ENHANCED INTERFACES AND TRAIN CATEGORIES FOR DYNAMIC COMPATIBILITY ASSESSMENT OF EUROPEAN RAILWAY BRIDGES

Deliverable 1.3 –
Dynamic Train Categories (DTCs)

DELIVERABLE INFORMATION	
Work package number:	WP1
Work package title:	Definition of Dynamic Train Categories (DTCs) for ensuring compatibility of the interface between trains and bridges
Deliverable number:	1.3
Deliverable title:	Dynamic Train Categories (DTCs)
Due date of deliverable:	28-02-2026
Actual submission date:	31-03-2026
Responsible partner	UPM
Revision:	V1
Dissemination level:	PU

This project has received funding from the Europe's Rail Joint Undertaking under Horizon Europe research and innovation programme under grant agreement No. 101121765 (HORIZON-ER-JU-2022-ExplR-02).

PUBLICATION HISTORY

Revision	Date	Description	Responsible
V1	13/04/2026	Initial submission	JM Goicolea

PROJECT CONSORTIUM

Coordinator

Universidade do Porto
UPORTO, Portugal

Beneficiaries

Kungliga Tekniska Hoegskolan
KTH, Sweden

Universidad Politecnica de Madrid
UPM, Spain

Bundesanstalt Fuer Materialforschung Und –Pruefung
BAM, Germany

Deutschen Bahn InfraGO AG
DB, Germany

Acoustique Et Vibrations Logiciels Scientifiques
AVLS, France

Affiliated Partners (to UPM)

Universitat Politecnica de Valencia
UPV, Spain

Universitat Jaume I de Castellon
UJI, Spain

Universidad de Sevilla
UdS, Spain

Administrador de Infraestructuras Ferroviarias
ADIF, Spain

Associated Partner

University Of Huddersfield
HUD, UK

Acknowledgments: This project has received funding from the Europe's Rail Joint Undertaking under Horizon Europe research and innovation programme under grant agreement No. 101121765 (HORIZON-ER-JU-2022-ExplR-02).

TABLE OF CONTENTS

EXECUTIVE SUMMARY

This study addresses the limitations of existing load models in representing the dynamic effects of modern passenger trains on railway bridges. A comprehensive database of 221 real passenger trains with maximum operating speeds of 200 km/h and above was analysed using three progressively refined methodologies: undamped train signatures, LIR-based calculations, and full time-stepping simulations. The dynamic response of 15 representative European bridges, covering a broad range of spans and fundamental frequencies, was evaluated across a wide spectrum of train speeds. Building upon the MU-class framework, three families of Dynamic Train Categories (DTCs) were developed. DTC0 and DTC1 extend the original reference trains to fill spectral gaps observed in train signatures. DTC2 introduces optimised resonant trains designed to capture dominant coach-length peaks, while DTC2e supplements these with real train configurations that exhibit richer axle patterns and transient effects not fully covered by idealised models. The combined DTC2 + DTC2e framework comprises 31 reference trains and successfully envelopes the dynamic response of all real trains across the entire bridge set, achieving more balanced safety margins than HSLM-A or DTC0+DTC1. For existing bridges, where the operating train subcategories are known, DTC2+DTC2e enables targeted and efficient dynamic compatibility checks without the need to consider non-relevant train configurations. For new bridge design, the framework provides a robust and validated load model that balances accuracy and conservatism. Therefore, this work proposes DTC2+DTC2e as the selected DTC, and it is organised in a practical workflow based on coach length and axle load categories, with full geometric details provided in the appendices.

1 Introduction

The dynamic interaction between railway traffic and bridges has become a governing aspect in both assessment of existing infrastructure and design of new structures. Modern passenger train fleets comprise a broad spectrum of vehicle configurations, axle loads and speed ranges, producing widely different dynamic effects on bridges depending on their vibration properties. To enable consistent and safe verification, this work aims at establishing Dynamic Train Categories (DTCs) which are representative of, and envelop, the dynamic actions induced by families of real passenger trains with similar configurations. For each DTC, a set of representative load models is defined such that the resulting bridge response bounds the effects of the corresponding train family under relevant conditions.

The proposed approach for DTCs builds upon the concept of Multiple Unit (MU) classes first introduced in EN 15528:2015, which provided a categorisation of train configurations for dynamic compatibility checks. This standard introduced as a novelty dynamic line categories in addition to the traditional static ones. However, in a subsequent edition (EN 15528:2021) it was decided to limit the scope to static line categories. Additionally, the original MU-class framework presented some limitations with respect to its applicability to real train fleets and their induced vibrations in bridges. This is one of the main reasons prompting this project, which aims at proposing categories and procedures for dynamic compatibility checks. The DTCs developed in the present work attempt to improve and generalise the initial concept of MU classes, from the extensive train database collected by University of Huddersfield (HUD) in Deliverable 1.1, complemented with additional trains added more recently, and proposing new DTCs that will cover the dynamic effects of modern trains on real bridges of the European railway network.

The structure of the DTC framework is presented in Figure 1. It is intended to be directly applicable in dynamic checks of bridges, both for verifying the compatibility of existing bridges with current and future traffic, and for the design of new bridges to ensure adequate dynamic performance.

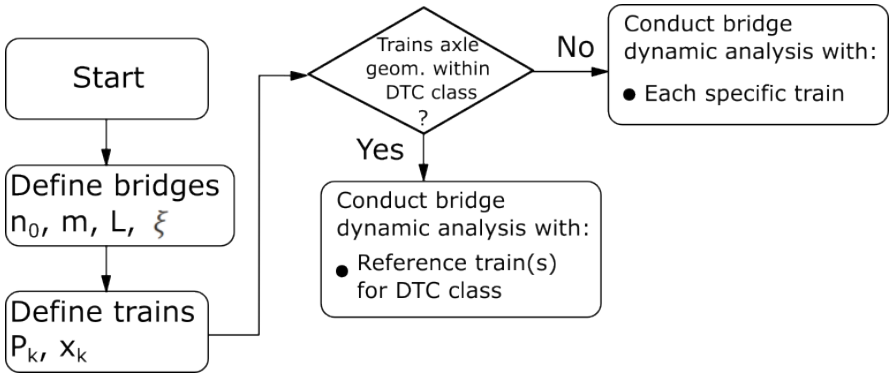

Figure 1: Workflow to use DTCs.

The work presents two complementary types of Dynamic Train Categories.

- **DTC1**: defined as an extension of the original MU-based reference trains from EN 15528:2015 (hereafter referred to as DTC0), with the objective of covering wavelength (λ) ranges in which modern passenger trains exceed the spectral limits of DTC0 and the HSLM load models. DTC1 categories are therefore conceived to fill the identified spectral gaps and are intended to be used in combination with DTC0 to ensure a consistent and conservative envelope of dynamic effects at category level.

- **DTC2**: derived through a systematic optimisation procedure, DTC2 categories are designed to represent refined sub-categories of passenger trains on a standalone basis. They are formulated to directly envelope the dynamic effects of specific train families without requiring combination with DTC0 and DTC1, providing a more targeted and scalable solution for dynamic compatibility verification.
- **DTC2e**: defined as a family of supplemental trains intended to be used in combination with the resonant trains obtained from the systematic optimisation process in DTC2. While the DTC2 reference trains capture the dominant resonant excitation associated with coach length and bogie spacing, certain real trains exhibit more complex configurations - featuring variations in unit couplings, transition cars, and axle arrangements - that produce a richer signature content with significant excitation at wavelengths beyond those captured by the idealised DTC2 formations. The DTC2e trains are therefore formulated to complement the DTC2 families, providing additional coverage of these secondary spectral features and ensuring a more comprehensive envelope of the dynamic effects induced by real trains.
-

2 Methodology

The methodology for development of DTCs follows a three-step process, from train signatures to full dynamic interaction with bridges.

1. Train signatures are first compared, neglecting bridge interaction and damping. This very fast screening allows capturing the dominant excitation wavelengths of real trains and defining initial Dynamic Train Categories (DTCs) that bound these signatures. The step is also used to explore the sensitivity of geometric parameters of the trains in their dynamic signatures. In addition to supporting the definition of DTC0 and DTC1 through direct envelope comparison of raw train signatures, this step provides the basis for the DTC2 methodology by introducing dimensionless train signatures normalised by maximum axle load. Smoothed envelope spectra are derived for refined train sub-categories, which serve as target functions in a subsequent optimisation process used to define idealised “resonant” reference trains representative of each sub-category.
2. The candidate DTCs are then checked against the response of a set of 15 representative European bridges, agreed with WP2 and documented in deliverable D1.1, covering a realistic range of spans and structural typologies known to be vibration-sensitive. Peak mid-span vertical accelerations are computed using the LIR method, which is sufficiently fast to permit systematic sensitivity studies while incorporating basic bridge dynamics. The adequacy of the DTC envelopes is verified against real trains and bridges in this step.
3. Finally, the selected configurations are analysed with accurate time-stepping simulations using the software CALDINTAV (Nguyen & Goicolea, 2024) to compute peak accelerations. This step is used to validate that the proposed DTCs provide a robust envelope. Additionally, for those real passenger trains whose dynamic effects are consistently not covered by the optimised DTC2 reference trains, a complementary family (designated DTC2e) is developed. These supplemental trains are obtained by identifying real trains that exhibit richer signature content beyond the dominant resonant peaks captured by DTC2, and which remain uncovered across multiple bridges. The axle spacing of these trains is then normalised by their maximum axle load, preserving their exact geometric configuration, to serve as supplementary reference trains within the DTC2 category

In the three analysis steps the comparison also includes the HSLM-A trains defined in EN 1991-2:2023 for dynamic design and assessment of passenger railway bridges. This is done in order to have a reference, but HSLM-A is not considered in the definition of the DTCs in this work.

3 Train database

The Dynamic Train Categories (DTCs) developed in this work are based on a refined subset of the rolling stock database compiled by the University of Huddersfield (UoH) in Deliverable D1.1 of the InBridge4EU project. The original passenger database comprised 3025 trains collected from previous EU projects (In2Track2, In2Track3, DLM (DZSF)), manufacturer spreadsheets, standards and reference documents, and was subsequently processed to remove duplicates and generate consistent single- and multi-unit configurations. After consolidation, the database included 806 unique train configurations and 2701 multiple-unit (MU) arrangements.

For the purposes of the present work, only passenger trains with maximum operating speeds greater than or equal to 200 km/h have been considered. Furthermore, in order to ensure consistency in load representation and compatibility with EN 15528 and EN 15663 definitions, only Normal Design Payload (MND) axle loads have been used. This filtering ensures that the database reflects realistic operational loading conditions while avoiding inconsistencies associated with mixed load definitions (e.g. MVD or MND160).

After applying these criteria, the initial dataset resulted in 200 passenger trains suitable for dynamic signature analysis and DTC development. Subsequently, additional data were incorporated from manufacturers of regular passenger rolling stock currently operating in Europe, in particular recent single-axle train configurations (e.g. TALGO-type trains). This update included 21 new passenger train configurations (including ICE-L, FLIX and S-units with different geometric arrangements and coupling configurations), ensuring that the database reflects the most recent developments in European passenger traffic.

The final database used for the DTC analyses therefore comprises 221 passenger trains, classified according to bogie configuration as follows:

- Trains with Conventional Bogies (CB): 140 trains.
- Trains with Articulated bogies (AB): 32 trains.
- Trains with Regular / Single Axle configurations (SA): 49 trains.

This categorisation separates the database into three basic Train Categories and it is consistent with the MU-based framework of EN 15528. It will also form the basis for the definition and refinement of the DTCs in this work. The database provides the axle spacing and axle load distributions required to compute train signatures, derive envelope spectra, perform sensitivity analyses, and conduct both simplified (LIR-based) and full time-stepping dynamic simulations.

By focusing exclusively on passenger trains with harmonised load definitions and incorporating the most recent rolling stock developments, the goal is that the resulting DTCs are representative of current and near-future European passenger train traffic, and are suitable for robust dynamic compatibility verification of bridges.

3.1 Signatures of passenger trains in the database

First, the dynamic signatures of all the trains in the database are computed. These are expressed in terms of the wavelength λ associated with the running speed v of the train, defined as $\lambda = v/n_0$, where n_0 is the fundamental vertical frequency of the bridge. For a given wavelength λ, the train spectrum is defined as:

$$G(\lambda,\xi) = \max_{k=1,\dots,N}\left\{\left[\sum_{i=1}^{k} P_i \cos\left(2\pi\frac{d_k-d_i}{\lambda}\right)e^{-2\pi\xi\frac{d_k-d_i}{\lambda}}\right]^{1/2} + \left[\sum_{i=1}^{k} P_i \sin\left(2\pi\frac{d_k-d_i}{\lambda}\right)e^{-2\pi\xi\frac{d_k-d_i}{\lambda}}\right]^{2}\right\}^{1/2} \quad (1)$$

where P_i and d_i are the vertical load and the cumulative longitudinal position of axle i (d_i measured from the front axle of the train), N is the total number of axles in the train, and ξ is the damping ratio of the bridge. Ignoring the effect of the bridge and considering $\xi = 0$ gives the dynamic signature of the train as:

$$S_0(\lambda) = \max_{k=1,\dots,N}\left\{\left[\sum_{i=1}^{k} P_i \cos\left(2\pi\frac{d_k-d_i}{\lambda}\right)\right]^{1/2} + \left[\sum_{i=1}^{k} P_i \sin\left(2\pi\frac{d_k-d_i}{\lambda}\right)\right]^{2}\right\}^{1/2} \quad (2)$$

The signature $S_0(\lambda)$ isolates the pure geometric excitation characteristics of the train and is used to define and compare train signatures independently of the bridge properties.

Figure 2 presents the undamped train signatures $S_0(\lambda)$ obtained for the 221 real passenger trains included in the database. A comparison with the HSLM-A envelope reveals several exceedances at specific wavelength ranges. In particular:

- Several CB trains exceed the HSLM-A envelope at long wavelengths, around $\lambda \approx 28$m. This is due to new passenger trains with longer coaches, such as ICE4.
- A limited number of AB trains exceed the envelope in the characteristic “valley” of the HSLM-A signature, at approximately $\lambda \approx 17$m.
- SA trains exceed the HSLM-A peak at shorter characteristic wavelengths, around $\lambda \approx 13$m, exceeding the HSLM-A limits in some cases.

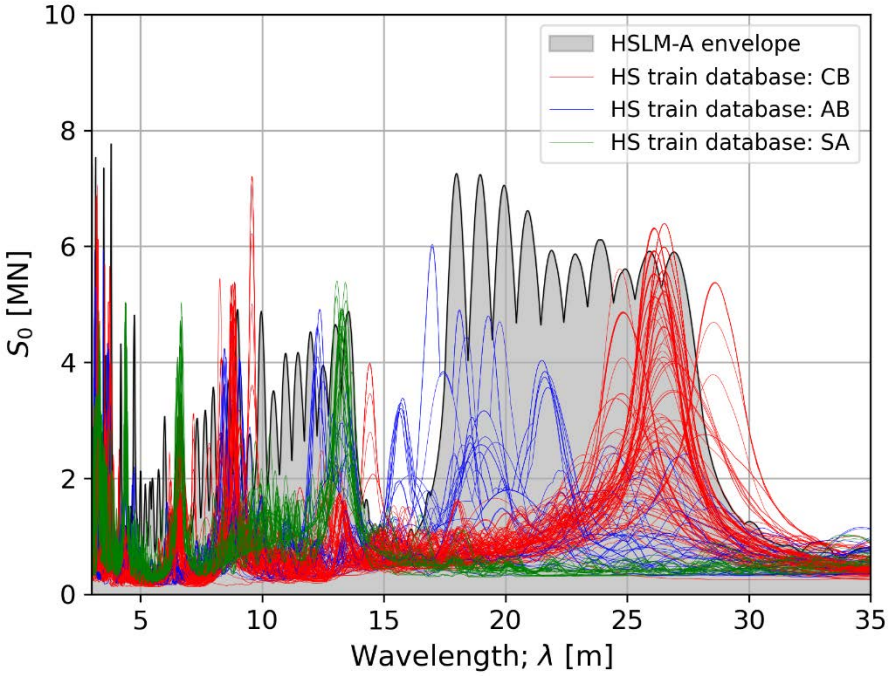

Figure 2. Signatures of the real passenger trains (with speeds above or equal to 200 km/h) in the database, compared with the HSLM-A envelope.

These observations indicate that modern passenger trains currently operating on European lines exhibit excitation characteristics that are not fully covered by the HSLM-A signature. While this comparison is based solely on undamped train signatures and therefore constitutes a preliminary indication, it provides an early warning regarding potential gaps in the representativeness of the HSLM-A load model. As demonstrated in the subsequent sections, these spectral exceedances translate into cases where real trains induce peak bridge accelerations that exceed those predicted by HSLM-A for several bridge types and operating speeds. However, train signatures have well known limitations: 1) they represent only resonant effects due to the first (fundamental) mode of simply-supported bridges; 2) some ranges of the wavelength may not be reached for realistic bridges / speeds. These limitations will be tackled in this report by using more advanced analysis methods.

4 Representative set of bridges

The same set of 15 bridges of the European passenger railway network employed in Deliverable D1.1 has been considered in this work. Most of these bridges were originally selected because they are located in the lower range of the fundamental frequency band typically encountered in passenger lines, and they are therefore potentially prone to train-induced vibration problems. At the same time, they are representative of different structural typologies and span lengths commonly found in European railway infrastructure. Table 1 (taken from D1.1) summarises the main characteristics of the structures analysed. All bridges are simply supported, torsional effects induced by the trains are neglected, and a single train crossing is considered in all simulations.

Bridge	Damping (%)	EN1991-2 damp (%)	Span (m)	Mass (kg/m)	EI (Nm²)	Frequency (Hz)	Max Speed (km/h)	Max Wavelength (m)	Max acceleration (m/s²)
1	2	1.5	27	28453	1.5E+11	4.96	400	22.40	4.391
2	2	1.5	20	47160	1.2E+11	6.24	400	17.81	3.97
3	2.4	1.78	16	28035	2.9E+10	6.29	250	11.04	2.127
4	-	2.5815	4.55	10060	4.8E+08	16.51	220	3.70	15.85
5	-	0.5	25.63	7650	2E+10	3.86	160	11.51	10.47
6	2	0.5875	19.3	7130	2E+10	4.45	220	13.73	10.53
7	1.4585	1.4585	13.45	14365.2	1.1E+10	7.53	200	7.38	5.704
8	0.5	0.5	20	8803.9	2.8E+10	6.95	210	8.39	7.767
9	1.65	1.65	10.8	973.39	4.2E+09	27.9	200	1.99	6.009
10	2.13	1.625	11	12250	3.4E+09	6.8	200	8.17	5.112
11	1.5	0.5	21.18	11220	2.4E+10	5.12	200	10.85	6.513
12	1.913	1.913	14.1	31531	2.4E+10	6.85	330	13.38	7.383
13	2.382	2.382	7.4	11750	1E+10	26.9	200	2.07	0.9193
14	1.5	1.5	30	21754	1.2E+11	4.12	300	20.23	3.051
15	0.5	0.5	36	17000	1.7E+11	3.86	160	11.51	2.591

Table 1. Bridge parameters. Taken from deliverable D1.1, prepared by University of Huddersfield (HUD).

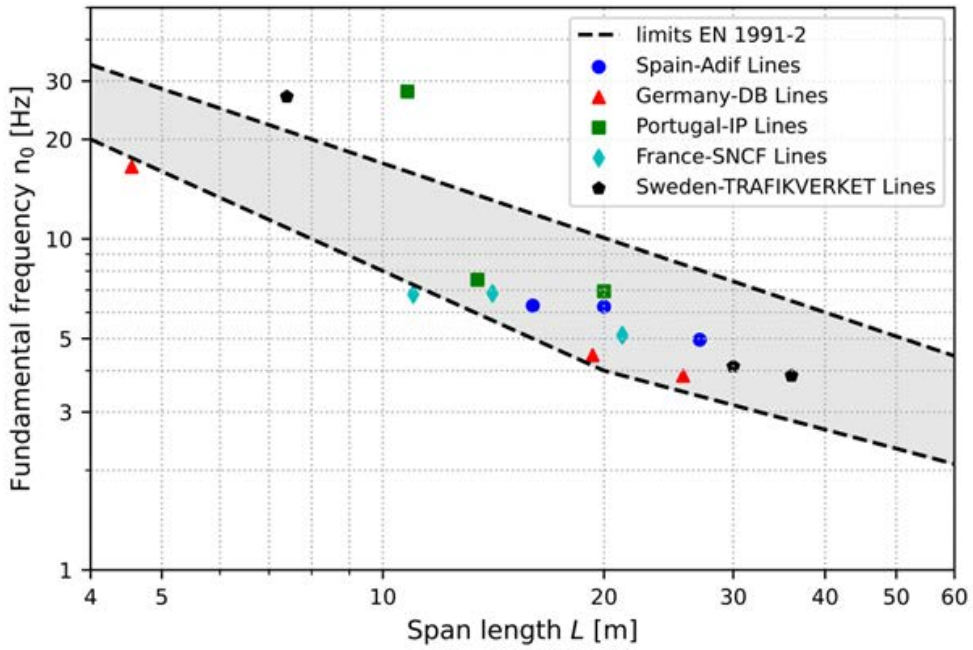

Figure 3. Signatures of the real passenger trains (with speeds above or equal to 200 km/h) in the database, compared with the HSLM-A envelope.

For clarity of interpretation, the bridges can be grouped according to their fundamental vertical frequency n_0, which is a governing parameter for resonance susceptibility:

- **Low-frequency bridges** (IDs 1, 5, 6, 14 and 15 in Table 1): Fundamental frequency n_0 between 3.8 and 5 Hz, with spans ranging from 19.3 m to 36 m. These bridges are more prone to resonance with longer excitation wavelengths typically associated with passenger trains.

- **Intermediate-frequency bridges** (IDs 2, 3, 8, 10, 11 and 12): n_0 between 5 and 7 Hz, with spans from 11 m to 21 m. These structures represent a transition range where both geometric and speed-related excitation mechanisms may govern the response.
- **High-frequency bridges** (IDs 4, 7, 9 and 13): $n_0$between 7 and 27 Hz, with spans from 4.5 m to 13.5 m. These shorter, stiffer bridges are mainly sensitive to shorter excitation wavelengths and higher-frequency axle-passing effects.

This classification allows systematic evaluation of the dynamic effects of real trains and proposed DTCs across bridges of different dynamic characteristics, trying to verify the proposed DTCs against a sufficiently broad range of structural behaviours representative of the European passenger infrastructure network.

5 Dynamic Train Categories 1: DTC1

The MU-classes defined in EN 15528:2015 are taken as the starting point for the definition of Dynamic Train Categories, referred to as DTC0 in the following. In that standard, multiple units are organised into three main MU-Groups according to their main configuration: conventional bogies (CB), articulated bogies (AB), and predominantly single-axle arrangements (SA). Within these groups, the following MU-Classes are defined:

- MU-Group CB (conventional bogies): CB1 and CB2.
- MU-Group AB (articulated bogies): AB1, AB2, AB3 and AB4.
- MU-Group SA (single-axle units): SA1 and SA2.

The geometric load patterns associated with these MU-Classes are specified in Annex E of EN 15528:2015. In addition to the axle spacing layout, the standard requires the definition of an axle load parameter P_{MUclass}, representing the maximum axle load under normal design payload conditions (MND), in accordance with Annex D. All axle loads within a given MU load model are taken as equal to P_{MUclass}.

Four recommended levels of P_{MUclass} are provided in the standard EN 15528:2015: 21.5 t, 19.0 t, 17.0 t and 15.0 t (Table E.9). These correspond to the line categories D2, C2, B1 and A, respectively. In particular, a value of 19.0 t corresponds to line category C2, associated with a maximum line category axle load of 20.0 t. In the present work, a uniform axle load of 19.0 t is adopted as a representative value for the general definition of DTC0. This is consistent with line category C2, which is widely representative of European passenger infrastructure.

In this work a new group of Dynamic Train Categories, referred to as DTC1, is introduced as an extension of DTC0. The geometric configurations of DTC1 are derived to cover wavelength ranges in which modern passenger trains exceed the spectral limits of the original MU-Classes and HSLM-A. As in DTC0, all axle loads within each DTC1 configuration are taken as equal, with a value of 19.0 t per axle.

It is noted that in Section 8, when all the DTCs are presented together (DTC0, 1, 2 and 2e) the load P_{MUclass} is the same in these reference trains to facilitate comparison, at it is set from the four different values defined in Table E.9 of EN 15528:2015.

5.1 Trains with Conventional Bogies: CB

The definition of DTC1 for the CB group begins with a comparative analysis between the envelope of the DTC0 conventional-bogie reference trains (CB1 and CB2) and the signatures of the real CB trains contained in the passenger train database. In order to maintain consistency with the Infrastructure TSI classification, the trains are first distinguished according to their maximum operating speed: those with maximum running speeds between 200 and 250 km/h (corresponding to Traffic Code P2, according to INF TSI) and those exceeding 250 km/h (Traffic Code P1).

At this stage of the analysis, no further subdivision based on geometric train parameters (e.g. coach length or bogie spacing) is introduced. All conventional-bogie (CB) trains are therefore considered together within each speed category, and the envelope of the two DTC0 CB reference configurations is directly compared against the signatures of all real CB trains. A more refined grouping is examined in subsequent sections.

Figures 4 and 5 show that the most significant exceedances occur at long wavelengths, around $\lambda \approx 28$ m, where several real CB trains clearly exceed both the HSLM-A envelope and the DTC0 reference envelope. These exceedances are predominantly associated with trains belonging to Traffic Code P1 (maximum speed above 250 km/h), typically characterised by longer coach lengths that generate dominant excitation components in this wavelength range.

Furthermore, the comparison indicates that the combined DTC0 and HSLM-A envelopes fall below that of real CB train signatures for certain wavelength ranges, in both P2 and P1 categories. This demonstrates that the existing reference models do not fully capture the excitation characteristics of modern passenger CB trains.

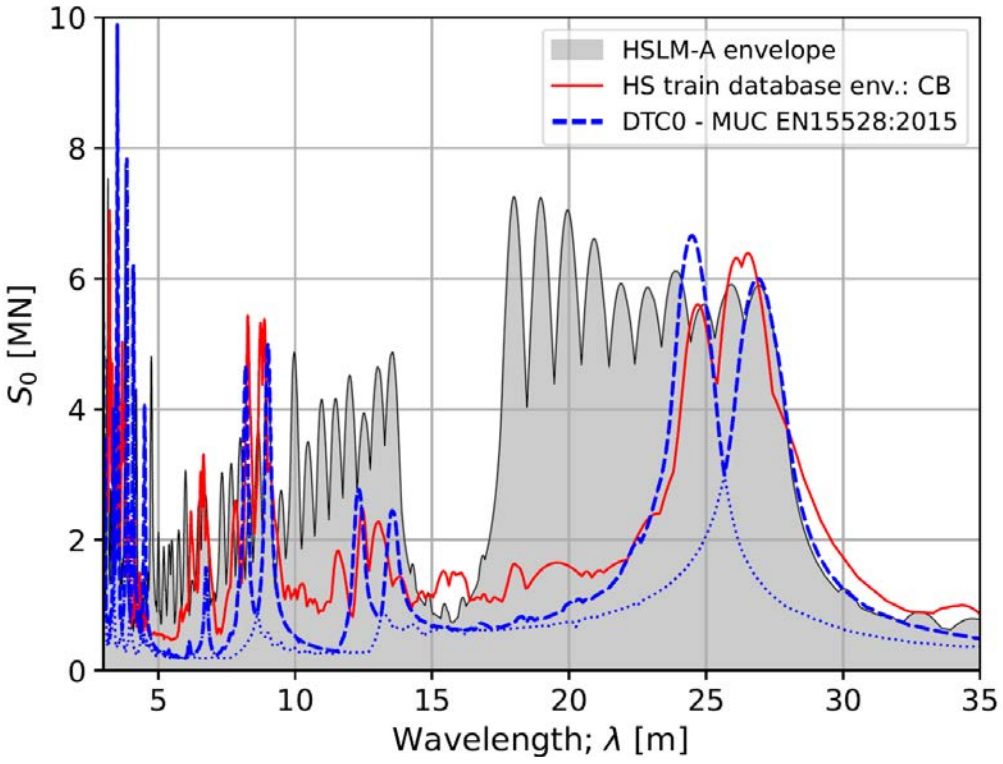

Figure 4. Envelope of the signatures of real CB trains with speeds from 200 to 250 km/h, compared with the reference CB trains in DTC0 - MUC EN 5528:2015, and with the HSLM-A envelope.

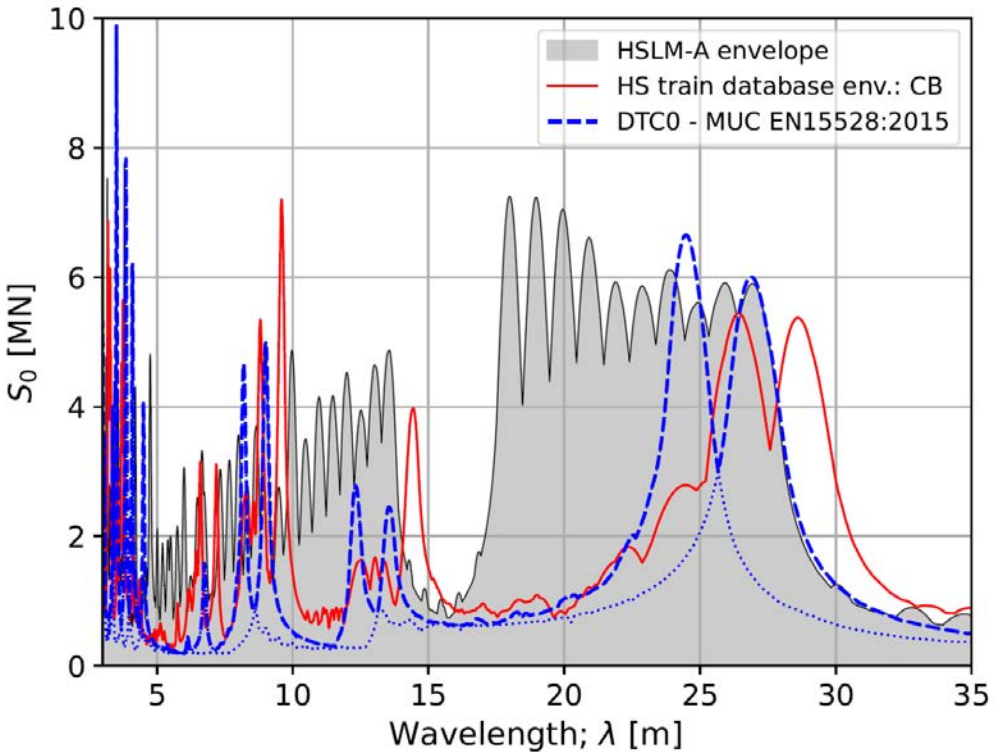

Figure 5. Envelope of the signatures of real CB trains with speeds above 250 km/h, compared with the reference CB trains in DTC0 - MUC EN 5528:2015, and with the HSLM-A envelope.

Based on the previous observations, the DTC1 configurations are proposed to cover the wavelength bands where DTC0 has a signature that falls clearly below that of the real train envelope. More specifically, a reference train named CB1_1, with coach length in the order of 28 m and axle distances similar to those in the new ICE4 train, is proposed in DTC1 to capture the envelope of the real CB train signatures around $\lambda \approx 28$ m, as well as the second order peak that occurs $\lambda \approx 28/2 = 14$ m. The axle distribution of this train is included in Figure 6, along with the other two CB trains that are already part of DTC0. The train CB1_1 has a length of approximately 400 m, which is the maximum size that can be considered due to limitations in the size of the train stations, and it features a very repetive load patter to maximise resonance. Appendix A of this report includes the axle spacing of the proposed train CB1_1, along with the DTC0 CB trains for reference.

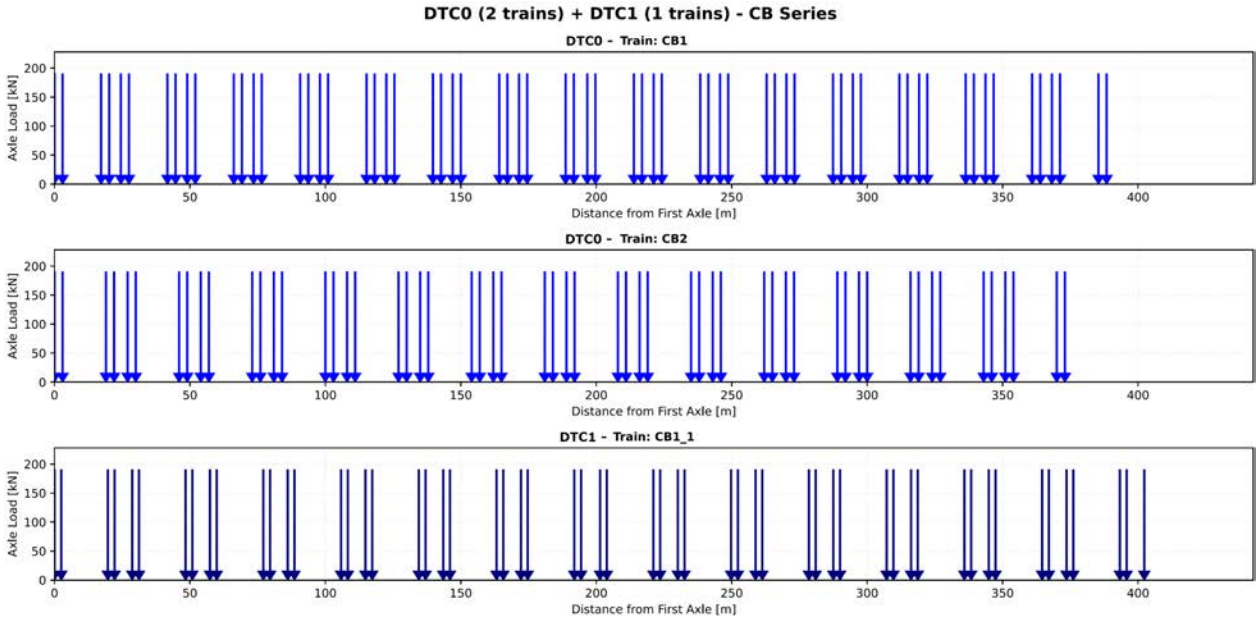

Figure 6. Axle spacing in the CB trains of DTC0 and DTC1.

The signature of the reference train DTC1 - CB1 presented in Figure 7 shows that it covers the envelope of the real CB trains in the region of very large wavelengths, as well as in the "valley" of λ between 12 and 15 m. In addition, the proposed CB1_1 train covers a narrow peak for $\lambda \approx 9$ m in which both the HSLM-A envelop and the CB trains of DTC0 are below the envelope of real trains. It can also be observed that the combination of DTC0, DTC1 and HSLM-A covers most of envelope of the real CB train signatures, with the exception of regions around $\lambda \approx 7$ m, $\lambda \approx 15 - 16$ m and $\lambda \approx 26 - 27$ m. How this translates into vertical accelerations in the proposed bridges will be discussed in the following

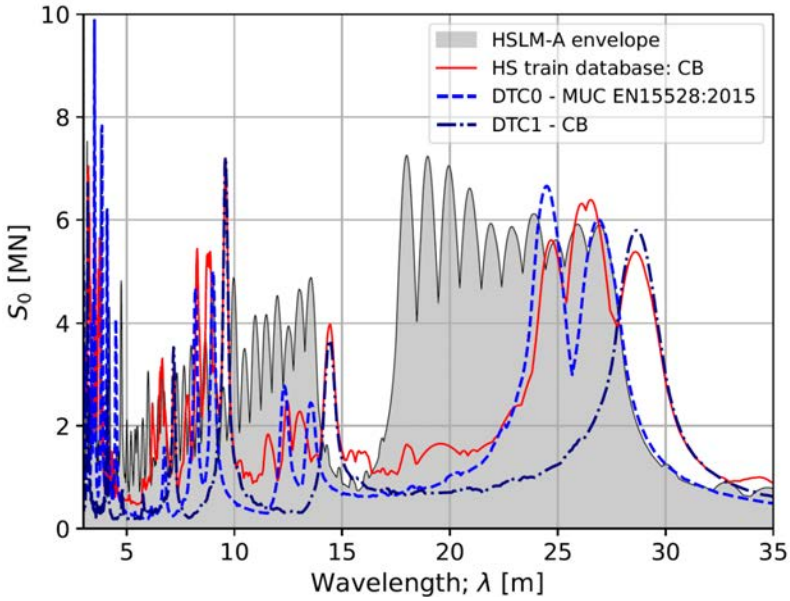

Figure 7. Signature of the proposed CB train in DTC1 (CB1_1) along with the envelope of the signatures of real CB trains (all trains, above 200 km/h). The reference CB trains in DTC0 - MUC EN 5528:2015 and the HSLM-A envelopes are also included for reference.

5.2 Trains with Articulated Bogies: AB

The definition of DTC1 for the AB group begins with a comparative analysis between the envelope of the DTC0 reference trains with articulated bogies (AB1 to AB4) and the signatures of the real AB trains contained in the passenger train database. Figures 8 and 9 shows this comparison distinguishing trains in the Traffic Codes P2 and P1, respectively. It is apparent that the envelope of the reference AB trains in DTC0 contributes to capturing the dynamic effects of real AB trains in the so-called "valley" of wavelengths in HSLM-A, from $\lambda \approx 14$ m to 17 m, that separates the main peaks related to coach wavelengths and the corresponding subharmonics. Indeed, this "valley" is narrower in the AB1-AB4 trains of DTC0, but there is still a region of wavelengths in which some real trains have signatures that exceed the original reference trains, with $\lambda \approx 16$ m in Traffic Code P2 (Figure 8), and $\lambda \approx 17$ m in Traffic Code P1 (Figure 9).

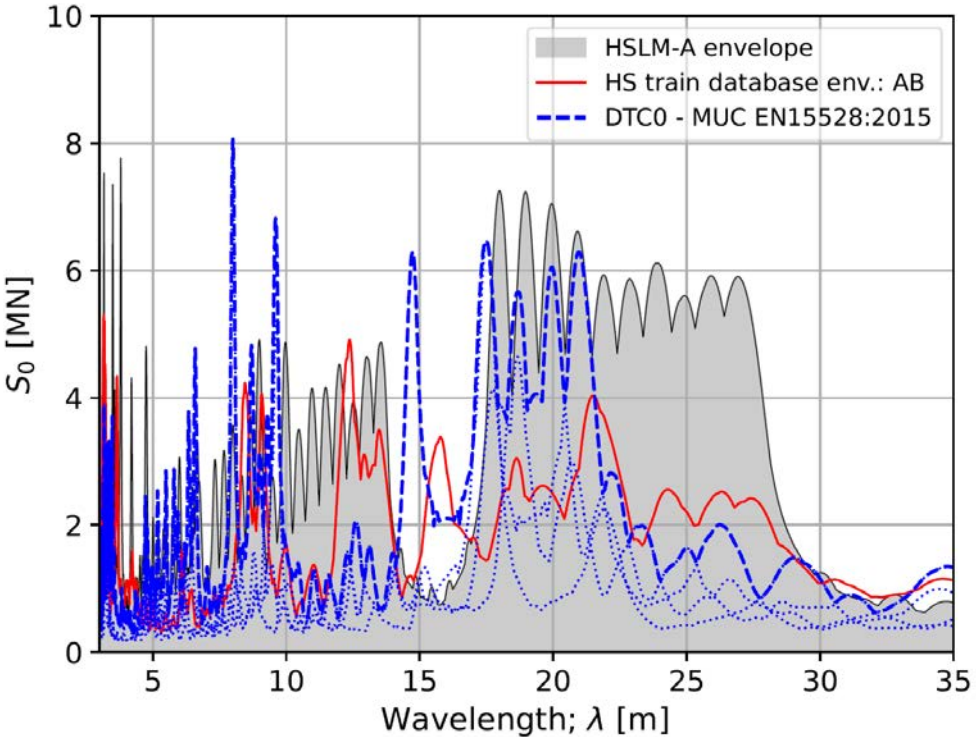

Figure 8. Envelope of the signatures of real AB trains with speeds from 200 to 250 km/h, compared with the reference AB trains in DTC0 - MUC EN 5528:2015, and with the HSLM-A envelope.

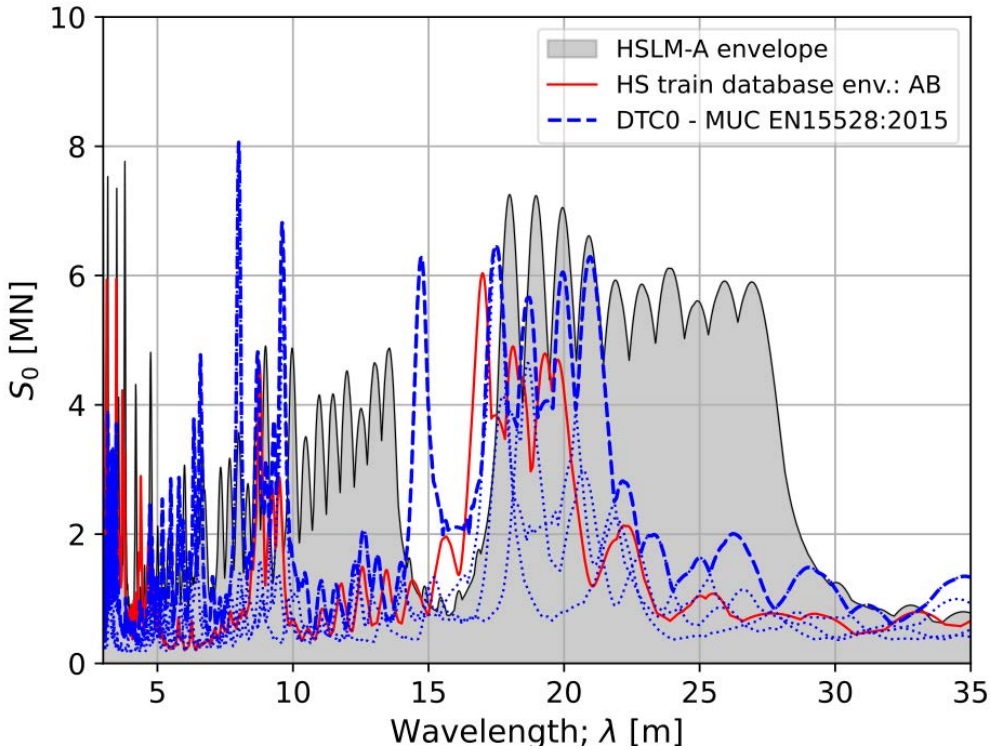

Figure 9. Envelope of the signatures of real AB trains with speeds above 250 km/h, compared with the reference AB trains in DTC0 - MUC EN 5528:2015, and with the HSLM-A envelope.

To address the identified spectral gaps, two new AB configurations, designated as AB1_1 and AB2_1, are proposed as part of DTC1. These are defined as modifications of existing DTC0 reference trains and critical real passenger trains for which significant signature exceedances are observed, with the objective of covering the wavelength regions where the original envelopes are not sufficient. The geometric layout of the proposed AB1_1 and AB2_1 configurations is illustrated in Figure 10, along with the other four reference AB trains in DTC0. The main characteristics of the DTC1 AB trains are as follows:

- AB1_1 is derived from a real articulated train consisting of two units. The configuration has a total length of approximately 400 m, with a coupling between units located at approximately 200 m from the front axle.
- AB2_1 is defined as a modification of the DTC0 reference train AB2. It is created by connecting four units to obtain a total length of approximately 400 m. This configuration has a coach length of 15 m to cover the spectral gap in that region.

Appendix A of this report includes the axle spacing of the proposed trains AB1_1 and AB2_1, as well as the DTC0 AB trains for reference.

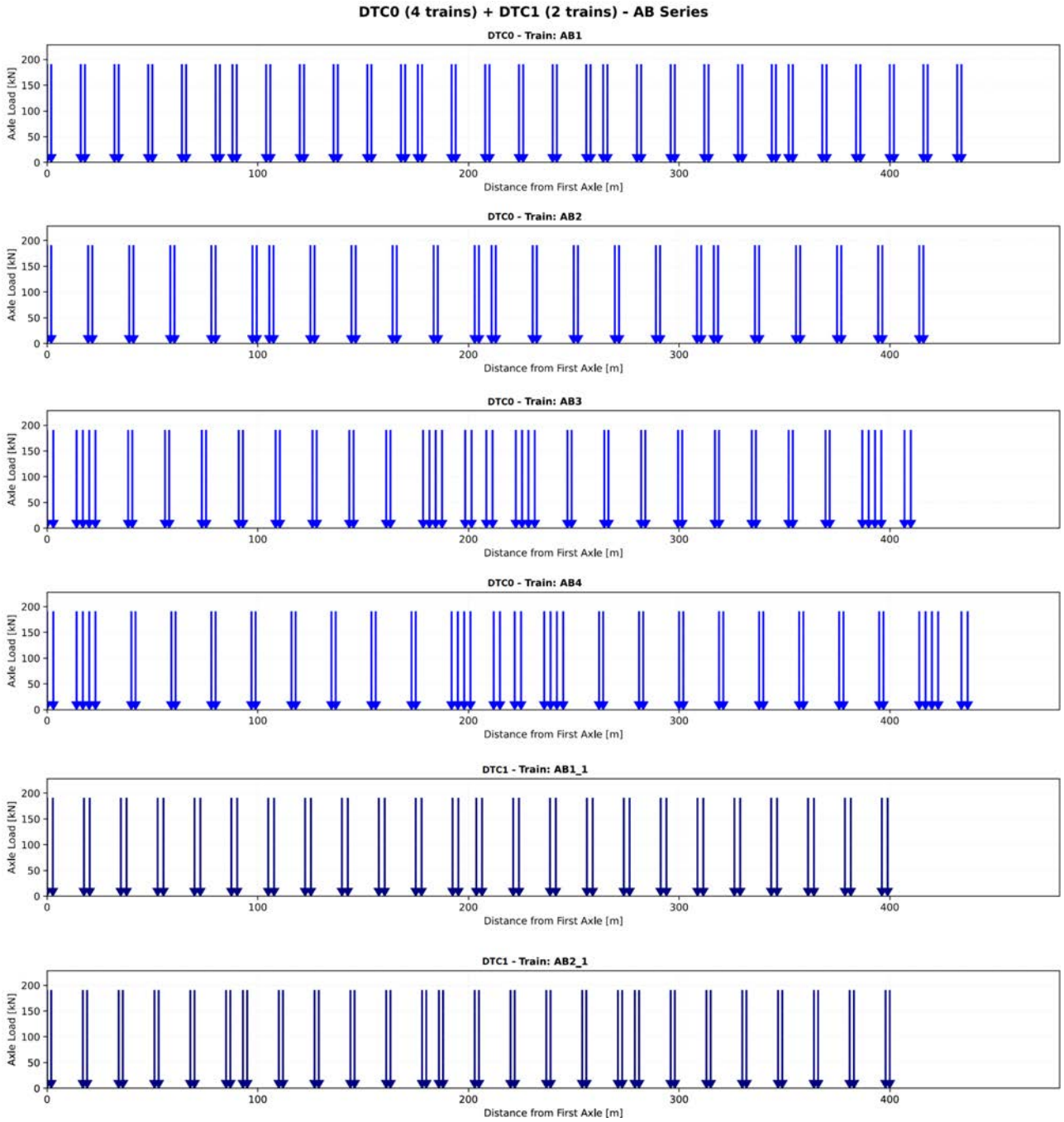

Figure 10. Axle spacing in the AB trains of DTC0 and DTC1.

Figure 11 shows the signature of the proposed DTC1 AB trains. When combined with the four reference trains of DTC0 (AB1–AB4), the resulting envelope clearly covers the spectral gap identified around λ ≈ 16–17 m. Including the contribution of HSLM-A for longer wavelengths, it is observed that most of the signature range is adequately covered, with real AB trains remaining below the combined DTC0 + DTC1 + HSLM-A envelope. The only exception is a small region around $\lambda \approx 12$ m, where some real AB trains marginally exceed the envelope. This residual exceedance will be examined in the subsequent dynamic analyses to assess its practical significance in terms of bridge acceleration response.

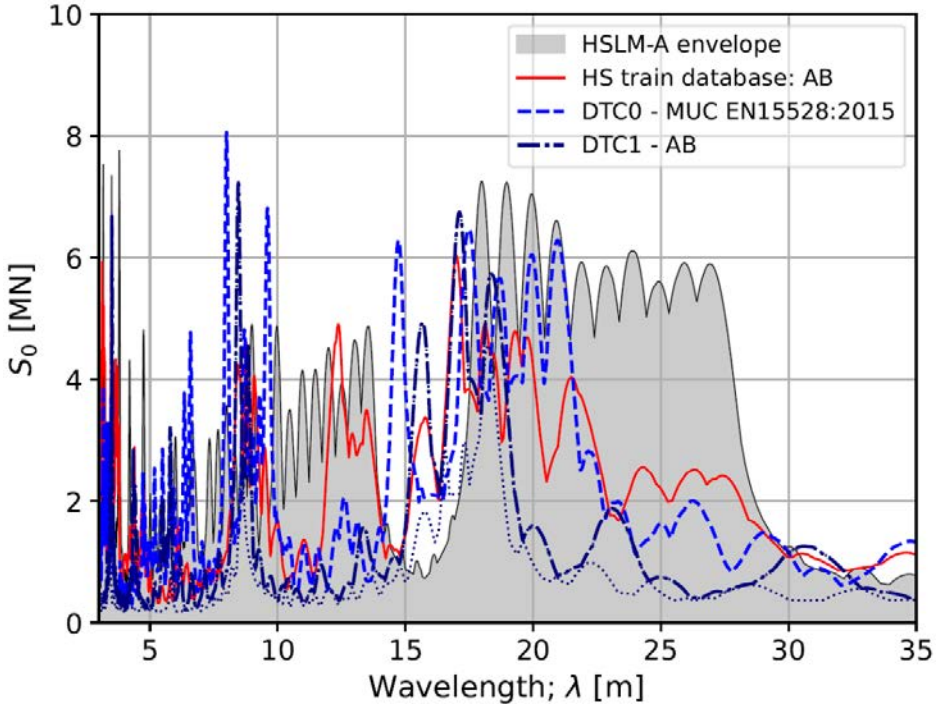

Figure 11. Signature of the proposed AB train in DTC1 (AB1_1 and AB1_2) along with the envelope of the signatures of real AB trains (all trains, above 200 km/h). The reference AB trains in DTC0 - MUC EN 5528:2015 and the HSLM-A envelopes are also included for reference.

5.3 Single Axle trains: SA

Figures 12 and 13 show the envelope of the signatures of real SA trains for Traffic Codes P2 and P1, respectively. SA trains are characterised by a coach length of approximately $\lambda \approx$ 13.1 m, which produces a marked peak in their signatures at that wavelength and the associated subharmonics, e.g. at $\lambda \approx$ 6.6 m. Both peaks lie above the HSLM-A envelope in the two Traffic Codes considered. DTC0 proposes two reference trains for the SA group, shown in Figure 14: SA1, with a total length of approximately 300 m, and SA2, composed of two units coupled at the centre and extending to nearly 400 m. The envelope of their signatures covers the main peak associated with the coach length for real trains, unlike HSLM-A. However, the subharmonic at $\lambda \approx$ 6.6 m exhibited by real SA trains lies above the DTC0 envelope, particularly for Traffic Code P2.

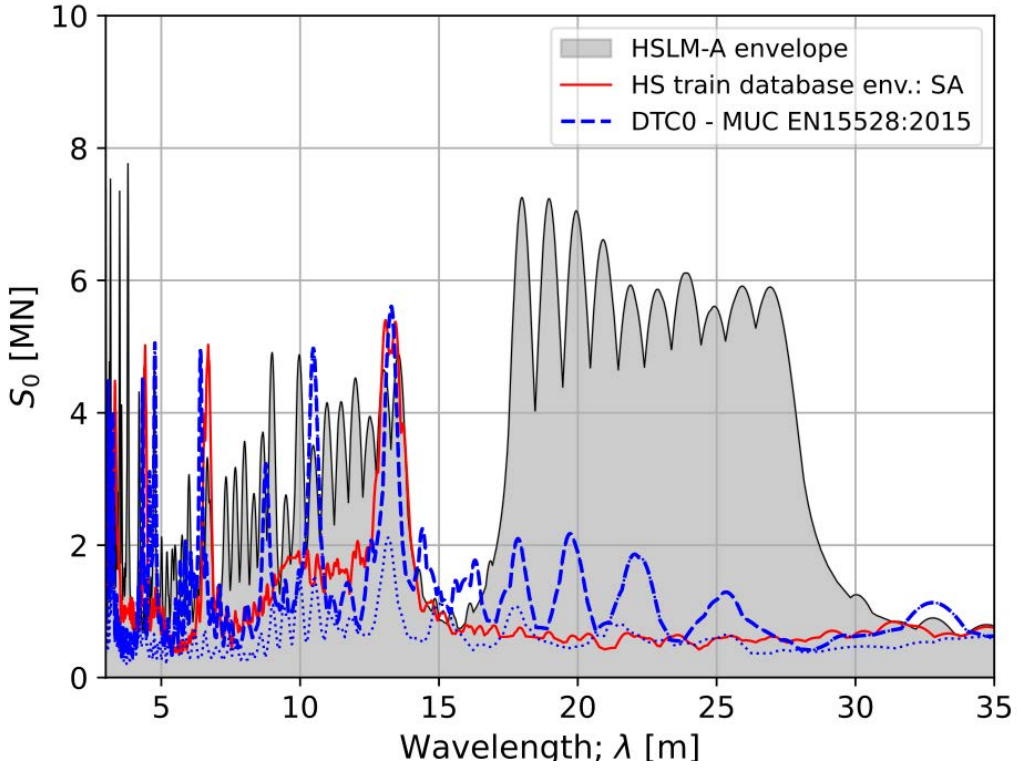

Figure 12. Envelope of the signatures of real SA trains with speeds from 200 to 250 km/h, compared with the reference SA trains in DTC0 - MUC EN 5528:2015, and with the HSLM-A envelope.

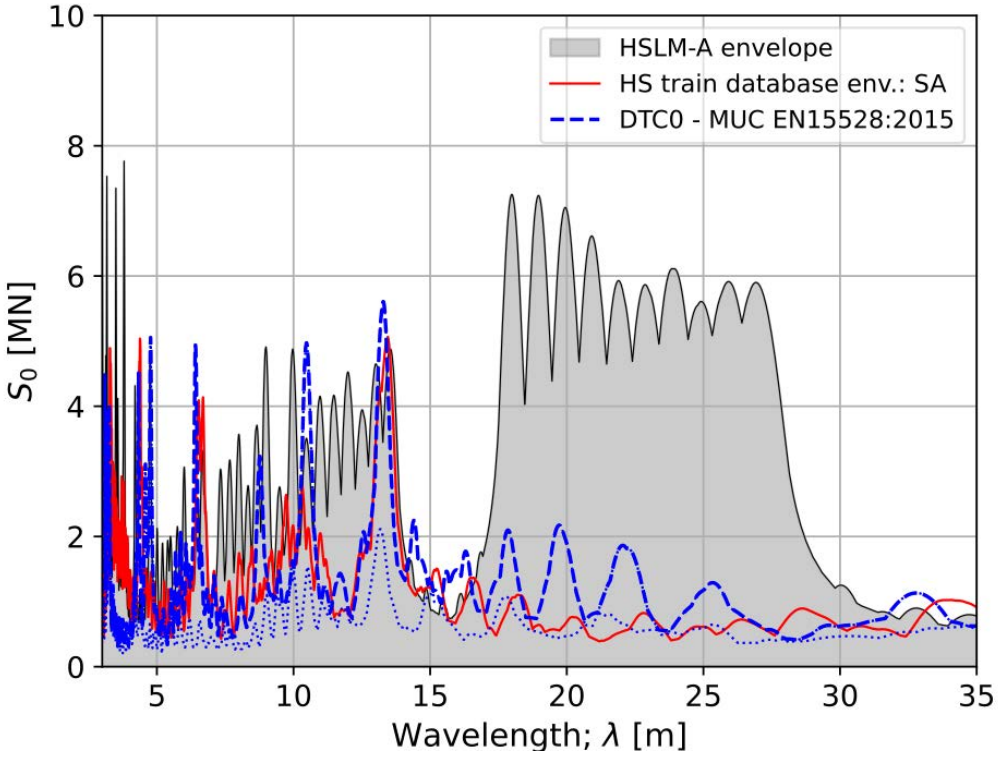

Figure 13. Envelope of the signatures of real SA trains with speeds above 250 km/h, compared with the reference SA trains in DTC0 - MUC EN 5528:2015, and with the HSLM-A envelope.

A modification of the SA2 train from DTC0 is proposed for DTC1, referred to as SA2_1, designed to cover precisely the subharmonic mentioned previously. As shown in Figure 14, SA2_1 adopts a slightly longer coach length of 13.4 m to shift the second peak to the right in the signature plot, at approximately $\lambda \approx 13.4/2 = 6.7$ m. The total train length is approximately 400 m to ensure sufficient buildup of resonant effects in longer bridges. The axle spacing of the proposed train SA2_1 is included in Appendix A, along with the DTC0 SA trains for reference.

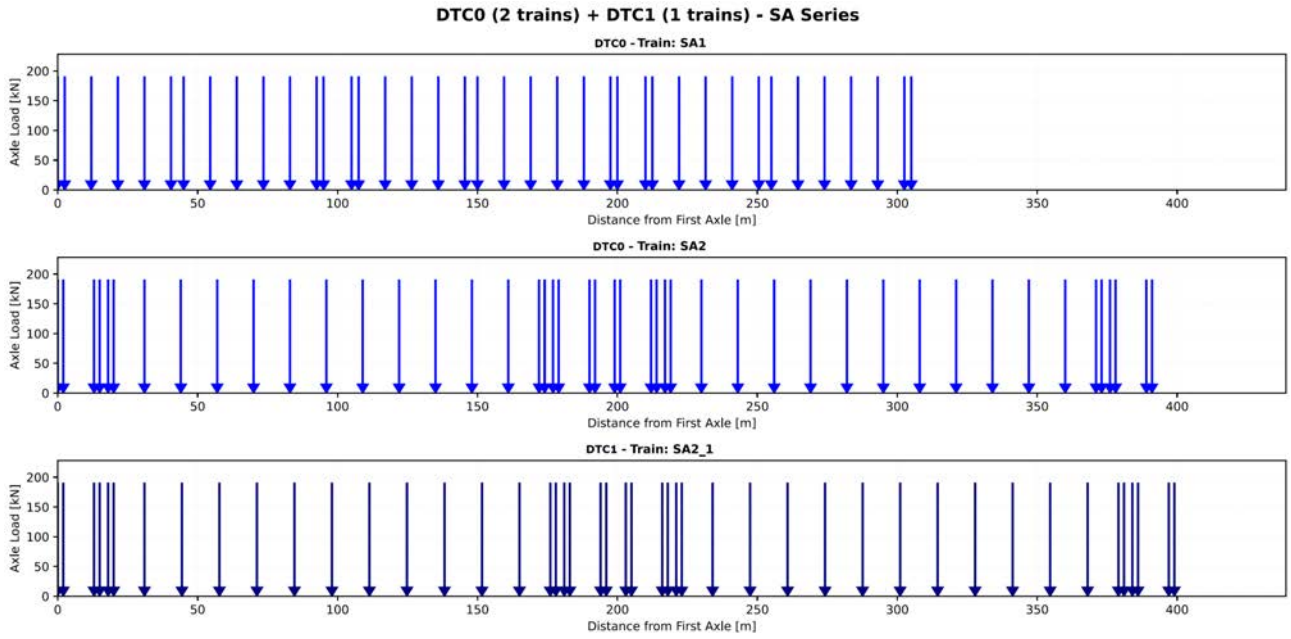

Figure 14. Axle spacing in the SA trains of DTC0 and DTC1.

Figure 15 presents the signature of the proposed SA2_1 train, along with the envelopes of the DTC0 SA trains, HSLM-A and the real SA trains, irrespective of line category. SA2_1 exhibits a signature larger than the existing reference trains at the subharmonic, and nearly covers the effects of real trains in terms of their signatures. It is noted that the resonant peak at $\lambda \approx 13$ m is relatively easy to reach, and indeed the combination of HSLM-A + DTC0 + DTC1 covers almost the entire envelope of the real SA train signatures. However, it is observed that the reference trains have smaller signatures over a wide range of wavelengths below the coach length. While this region is covered by HSLM-A, it reduces the ability of the DTCs to represent the characteristics of real train families on a standalone basis, as it will be discussed later.

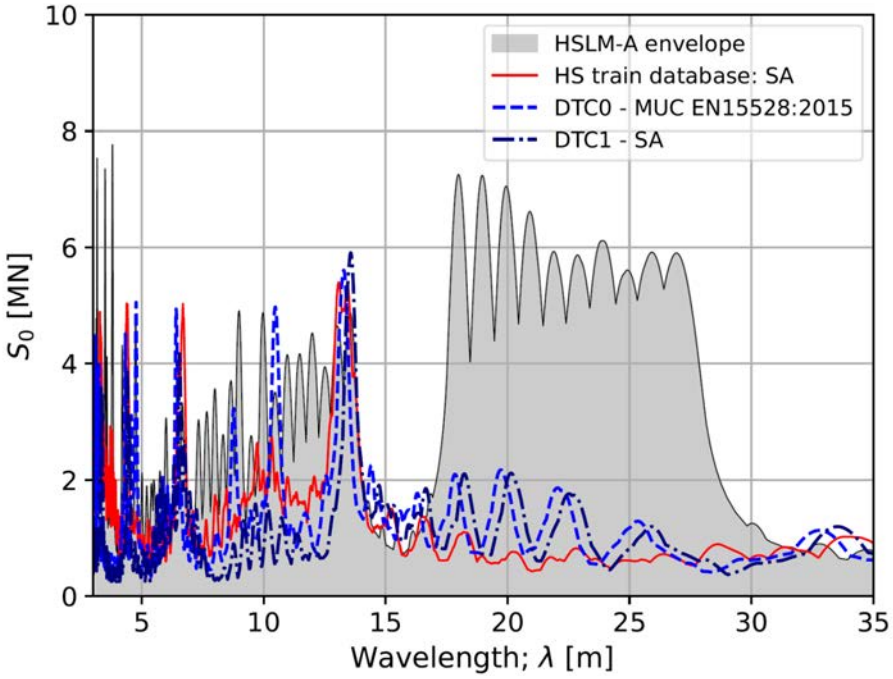

Figure 15. Signature of the proposed SA train in DTC1 (SA2_1) along with the envelope of the signatures of real SA trains (all trains, above 200 km/h). The reference SA trains in DTC0 - MUC EN 5528:2015 and the HSLM-A envelopes are also included for reference.

5.4 Peak accelerations obtained with LIR method

It is acknowledged that the undamped train signatures provide a useful screening tool to identify potential excitation wavelengths and spectral gaps, but they do not account for the dynamic filtering effect of the bridge structure nor the influence of the mass of the deck and its damping. To assess the practical significance of the observed signature exceedances, it is necessary to evaluate the actual acceleration response of representative bridges. For this purpose, the set of 15 real European passenger railway bridges introduced in Section 4 is employed.

The peak vertical acceleration at the center of the deck is computed first using the LIR method as:

$$a_{max} = \frac{2}{mL} \cdot A(K,\xi) \cdot G(\lambda,\xi) \tag{3}$$

where m and L are the distributed mass and the span of the bridge, respectively; $G(\lambda,\xi)$ is the train spectrum defined in Eq. (1) evaluated for the specific damping ratio (ξ) of the bridge under consideration; $A(K,\xi)$ is the influence line of the bridge that captures the resonant response of a simply supported beam subjected to a moving load, and it is given as:

$$A(K,\xi) = \frac{K}{1-K^2}\sqrt{1+\exp\left(-\frac{2\xi\pi}{K}\right)+2\cos\left(\frac{\pi}{K}\right)\exp\left(-\frac{\xi\pi}{K}\right)} \tag{4}$$

in which $K = \lambda/(2L)$ is the reduced speed.

5.4.1 Trains with Conventional Bogies: CB

Figure 16 presents the peak vertical acceleration at mid-span induced by all trains crossing the low-frequency bridges. The results are plotted against the wavelength λ associated with the running speed v of the train, defined as $\lambda = v/n_0$, where n_0 is the fundamental vertical frequency of the bridge. This representation facilitates direct comparison with the previous signature analyses and the geometric characteristics of the trains. A wide range of train speeds is considered, extending up to the maximum speed allowed on the bridge (indicated by a vertical black dashed line) and beyond into the next category of permissible line speeds (red vertical dashed line). The results show that HSLM-A does not envelope some of the vibrations induced by modern trains over a significant range of wavelengths, particularly at resonance in several bridges. Bridges ID 6 and 14 provide clear examples, with $\lambda \approx 9$ m and $\lambda \approx 14$ m, respectively, producing acceleration peaks well above those predicted by both HSLM-A and DTC0. However, the proposed DTC1 extension covers these cases in bridges with relatively low frequencies, primarily through the reference train with longer coaches CB1_1 (representative of trains such as ICE4). This effect is noticeable at $\lambda \approx 14$ m, corresponding to the subharmonic of the characteristic 28 m wavelength, since $\lambda \approx 28$ m would only be reached at very high train speeds beyond those considered. The combination of HSLM-A, DTC0 and DTC1 captures most of the effects of real conventional-bogie trains at operating speeds. Nevertheless, bridges ID 5 and ID 15 exhibit moderate exceedances in accelerations induced by real trains (with values above the vibration limit of 5 m/s² in bridge ID 5) at speeds slightly above the maximum speed allowed on the bridge.

Figure 17 presents the acceleration results for bridges with intermediate frequencies, which are in principle less dominated by long excitation wavelengths than the low-frequency bridges discussed previously. The results indicate that several real conventional-bogie trains, at or slightly above operating speeds, induce accelerations exceeding those predicted by HSLM-A. However, DTC0 and particularly the proposed DTC1 configuration CB1_1 help to cover these gaps, notably in bridge ID 11 at $\lambda \approx 9$ m. Although HSLM-A remains necessary to envelop some of the peak vibrations induced by real trains, the combination of HSLM-A, DTC0 and DTC1 falls slightly below the real train accelerations for very high speeds in certain cases, such as bridge ID 3.

Finally, Figure 18 shows the peak accelerations in the subset of bridges with relatively high frequencies, which are expected to be more sensitive to short wavelengths associated with axle spacing within bogies or higher-order subharmonics. The results exhibit clear resonant-antiresonant patterns for increasing values of λ. In bridge ID 4, HSLM-A falls below the vibrations induced by real trains in the range $\lambda \approx 2$–3 m, but DTC0 and DTC1 help to cover this exceedance almost completely. However, for bridges ID 9 and ID 13 at the resonant peak around $\lambda \approx 1.3$ m, the real trains induce accelerations that exceed both HSLM-A and the combined DTC0 and DTC1 envelope.

To provide a broader view of the results, Figures 19, 20 and 21 present the envelope of peak accelerations for all bridges with low, intermediate and high frequencies, respectively. In the low and intermediate frequency bridges (Figures 19 and 20), the combined effect of HSLM-A, DTC0 and DTC1 conventional-bogie trains covers most of the vibrations induced by real trains, with only marginal exceedances observed in the range $\lambda \approx 8$–9 m. For high-frequency bridges with short spans (Figure 21), the reference trains in HSLM-A, DTC0 and DTC1 also provide generally good coverage of the real train effects, although marginal exceedances persist at $\lambda \approx 1.3$ m and in the range $\lambda \approx 2$–3 m. Note that marked vertical drops in some of the large wavelengths occur due to the fact that only some bridges reach those regions, changing the number of structures included in the envelope at certain wavelengths.

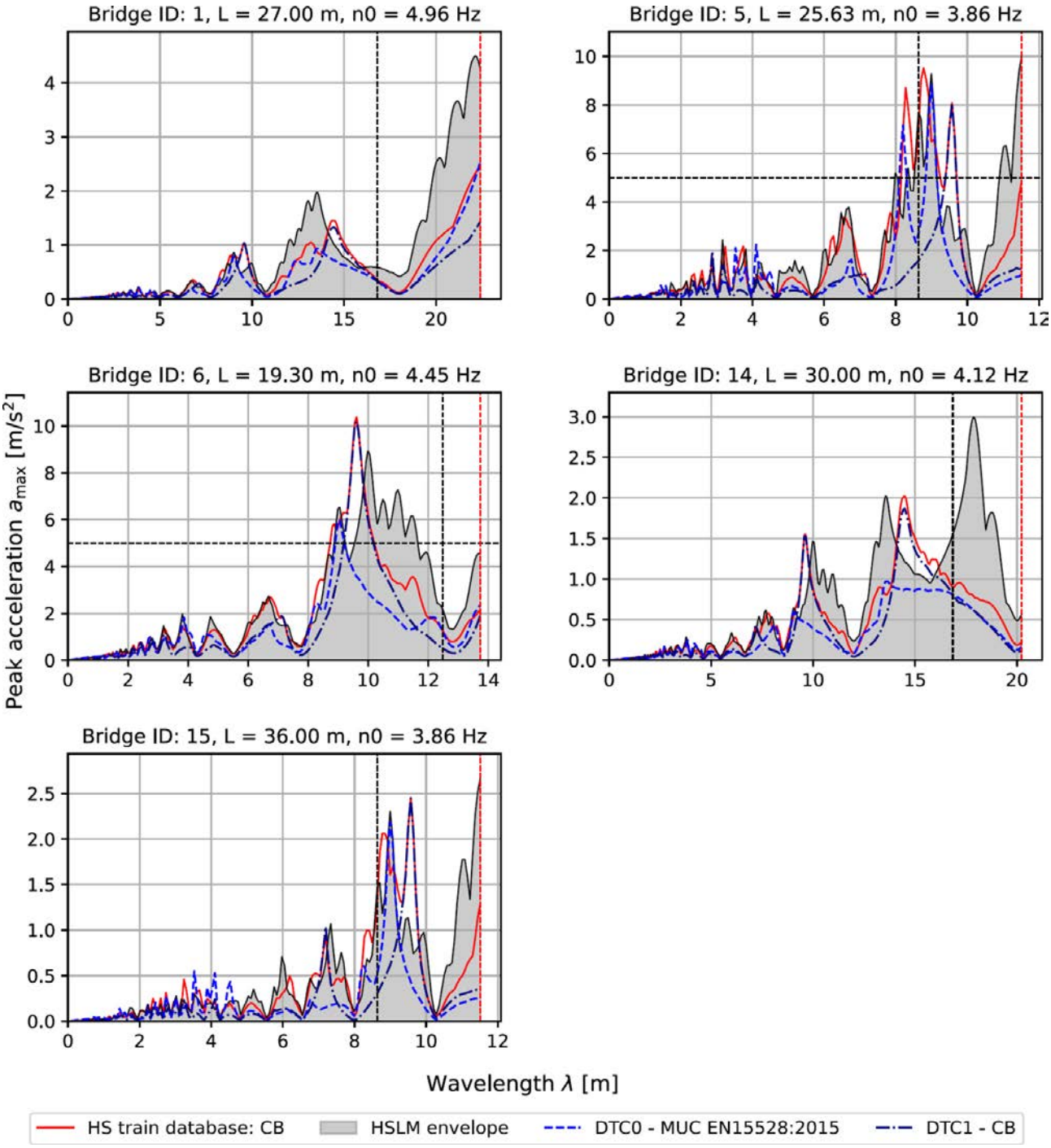

Figure 16. Envelope of the peak vertical acceleration in the bridges with 'low' frequency for different wavelengths. Comparison between real CB trains, reference CB trains in DTC0 and DTC1, and HSLM-A trains. LIR method.

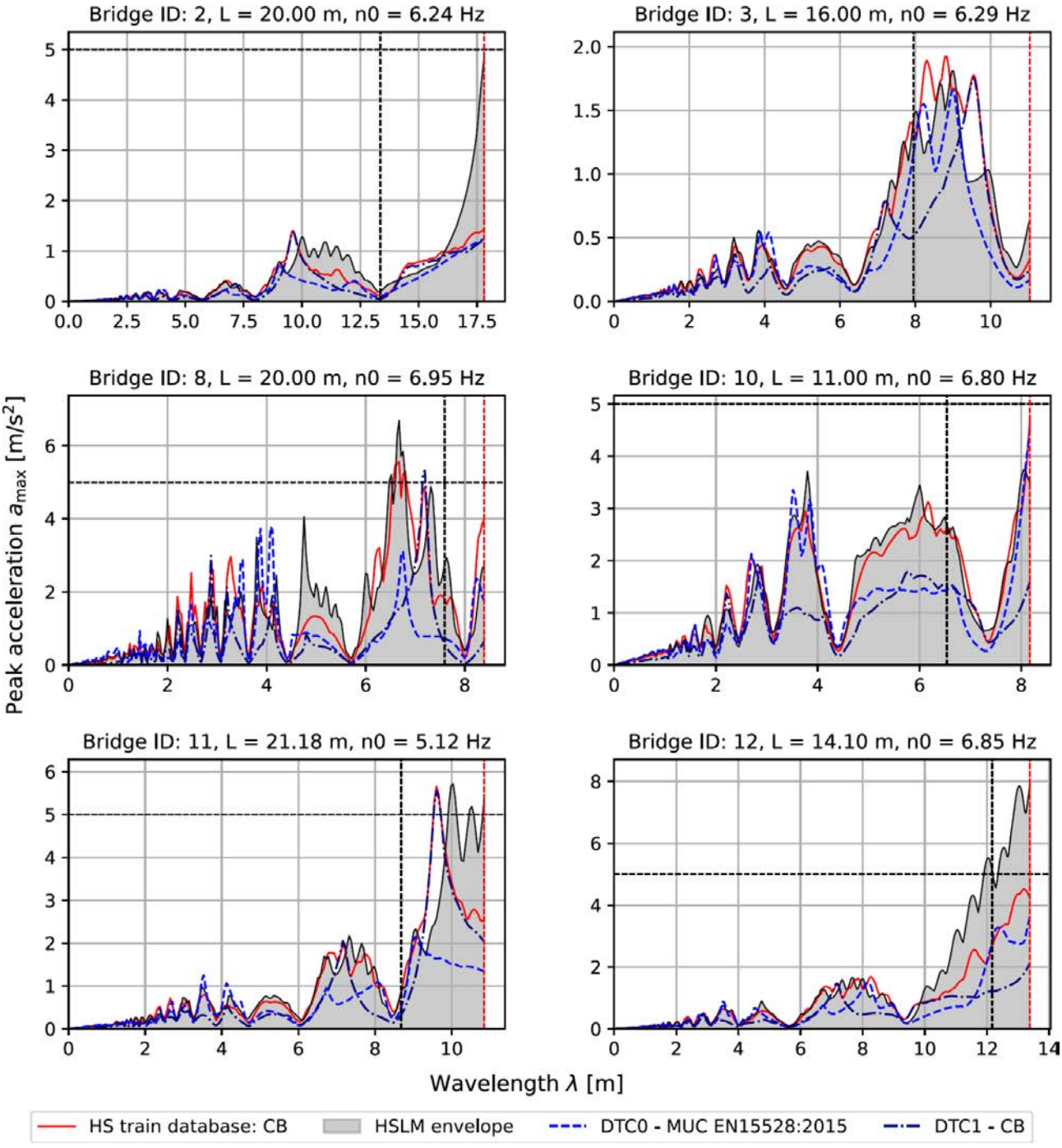

Figure 17. Envelope of the peak vertical acceleration in the bridges with 'intermediate' frequency for different wavelengths. Comparison between real CB trains, reference CB trains in DTC0 and DTC1, and HSLM-A trains. LIR method.

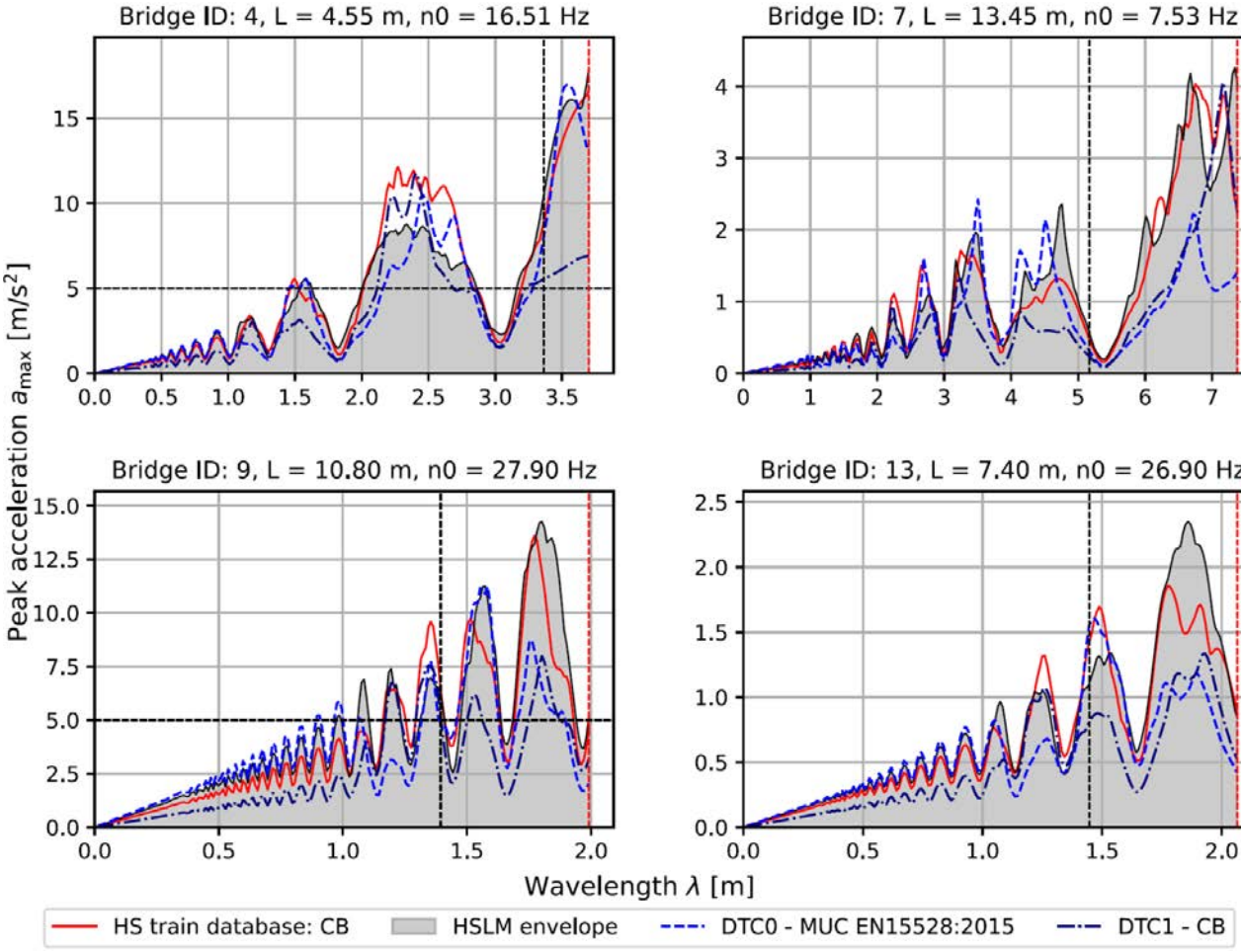

Figure 18. Envelope of the peak vertical acceleration in the bridges with 'high' frequency for different wavelengths. Comparison between real CB trains, reference CB trains in DTC0 and DTC1, and HSLM-A trains. LIR method.

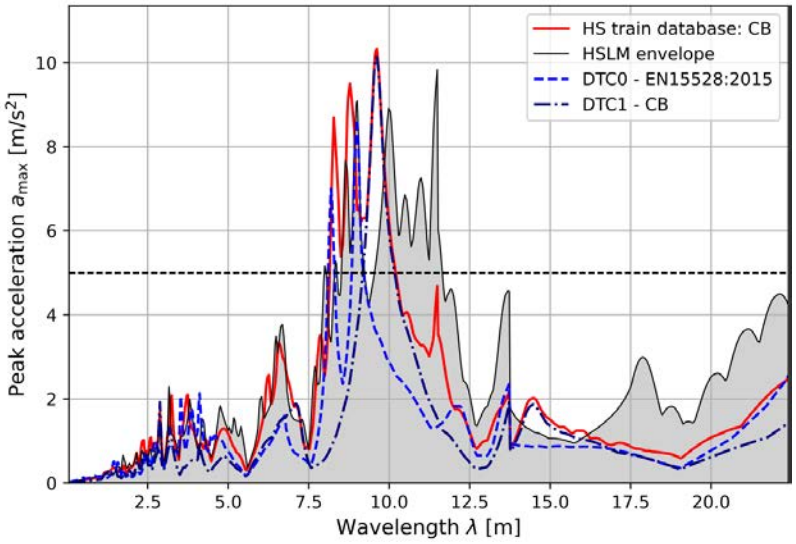

Figure 19. Envelope of the peak vertical acceleration in all the bridges with 'low' frequency for different wavelengths. Comparison between real CB trains, reference CB trains in DTC0 and DTC1, and HSLM-A trains. LIR method. Note that marked vertical drops in some of the large wavelengths occur due to the fact that only some bridges reach those regions, changing the number of structures included in the envelope at certain wavelengths.

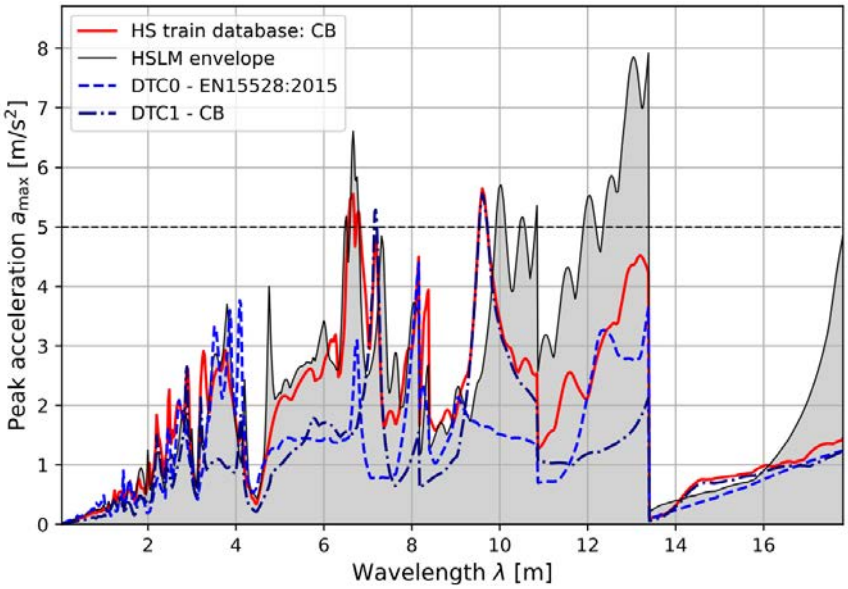

Figure 20. Envelope of the peak vertical acceleration in all the bridges with 'intermediate' frequency for different wavelengths. Comparison between real CB trains, reference CB trains in DTC0 and DTC1, and HSLM-A trains. LIR method. Note that marked vertical drops in some of the large wavelengths occur due to the fact that only some bridges reach those regions, changing the number of structures included in the envelope at certain wavelengths.

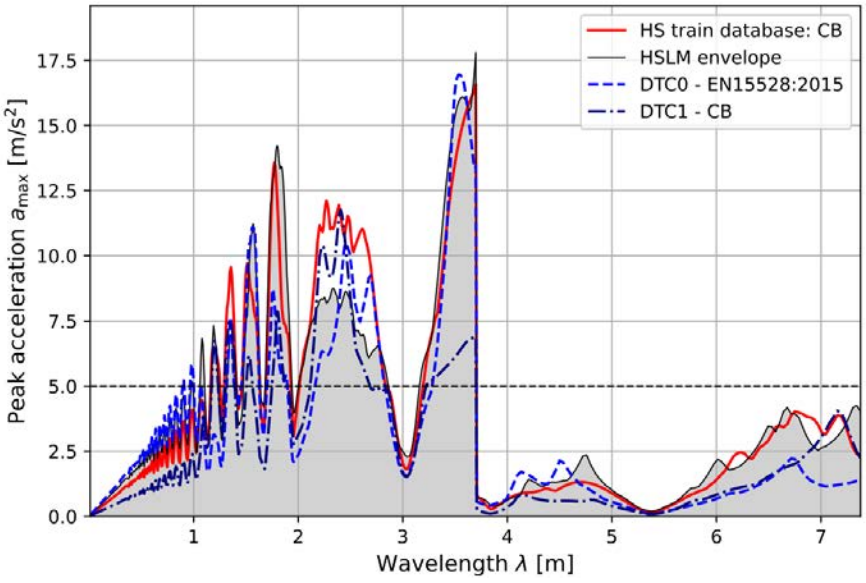

Figure 21. Envelope of the peak vertical acceleration in all the bridges with 'high' frequency for different wavelengths. Comparison between real CB trains, reference CB trains in DTC0 and DTC1, and HSLM-A trains. LIR method. Note that marked vertical drops in some of the large wavelengths occur due to the fact that only some bridges reach those regions, changing the number of structures included in the envelope at certain wavelengths.

5.4.2 Trains with Articulated Bogies: AB

Using the LIR method, the peak accelerations induced by real and reference trains in the bridge set are computed. Figure 22 shows the envelopes of peak accelerations for bridges with relatively low frequencies. It is noticeable that real articulated trains induce vibrations that significantly exceed the HSLM-A envelope for

wavelengths λ ≈ 15–16 m, which can be reached in the largest spans considered (L = 27 m and 30 m for bridge IDs 1 and 14, respectively), although the accelerations remain below the 5 m/s² limit. However, DTC0 and particularly DTC1 cover this spectral gap, which corresponds to the valley region in the HSLM-A signature.

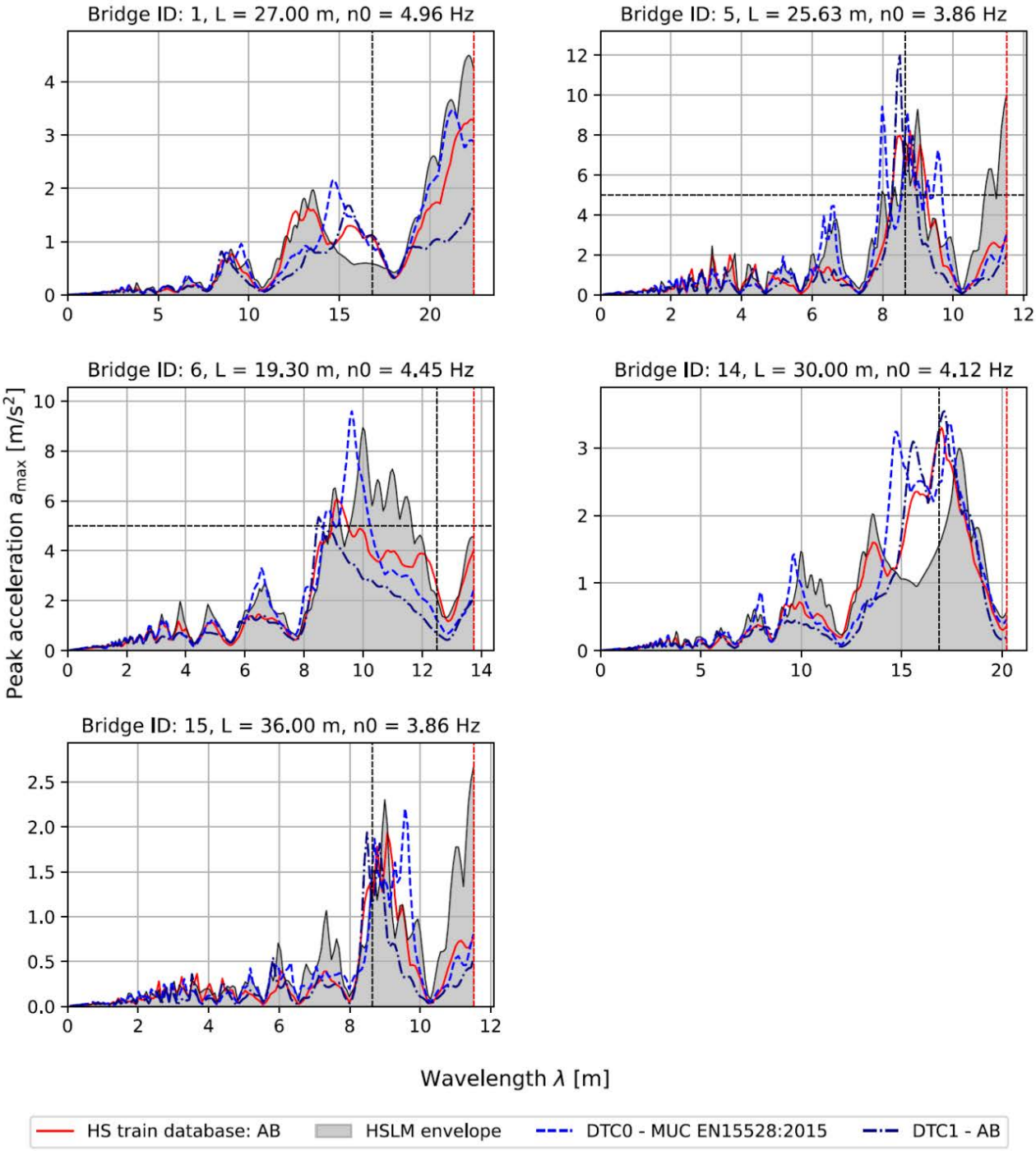

Figure 22. Envelope of the peak vertical acceleration in the bridges with 'low' frequency for different wavelengths. Comparison between real AB trains, reference AB trains in DTC0 and DTC1, and HSLM-A trains. LIR method.

The vibrations induced by articulated trains in bridges with intermediate frequencies are presented in Figure 23. At realistic operating speeds, these bridges cannot reach the wavelengths corresponding to the spectral valley where real AB trains are not covered by HSLM-A. Consequently, the HSLM-A load model generally provides adequate coverage of the effects of these trains, with the exception of some exceedance

around $\lambda \approx 12$ m in bridge ID 12, which is not captured by DTC0 and DTC1. It is also observed that the reference trains lie well above both other load models and the real train responses in certain wavelength ranges, leading to overconservative assessments around $\lambda \approx 8$–9 m, particularly in bridges ID 3 and ID 10.

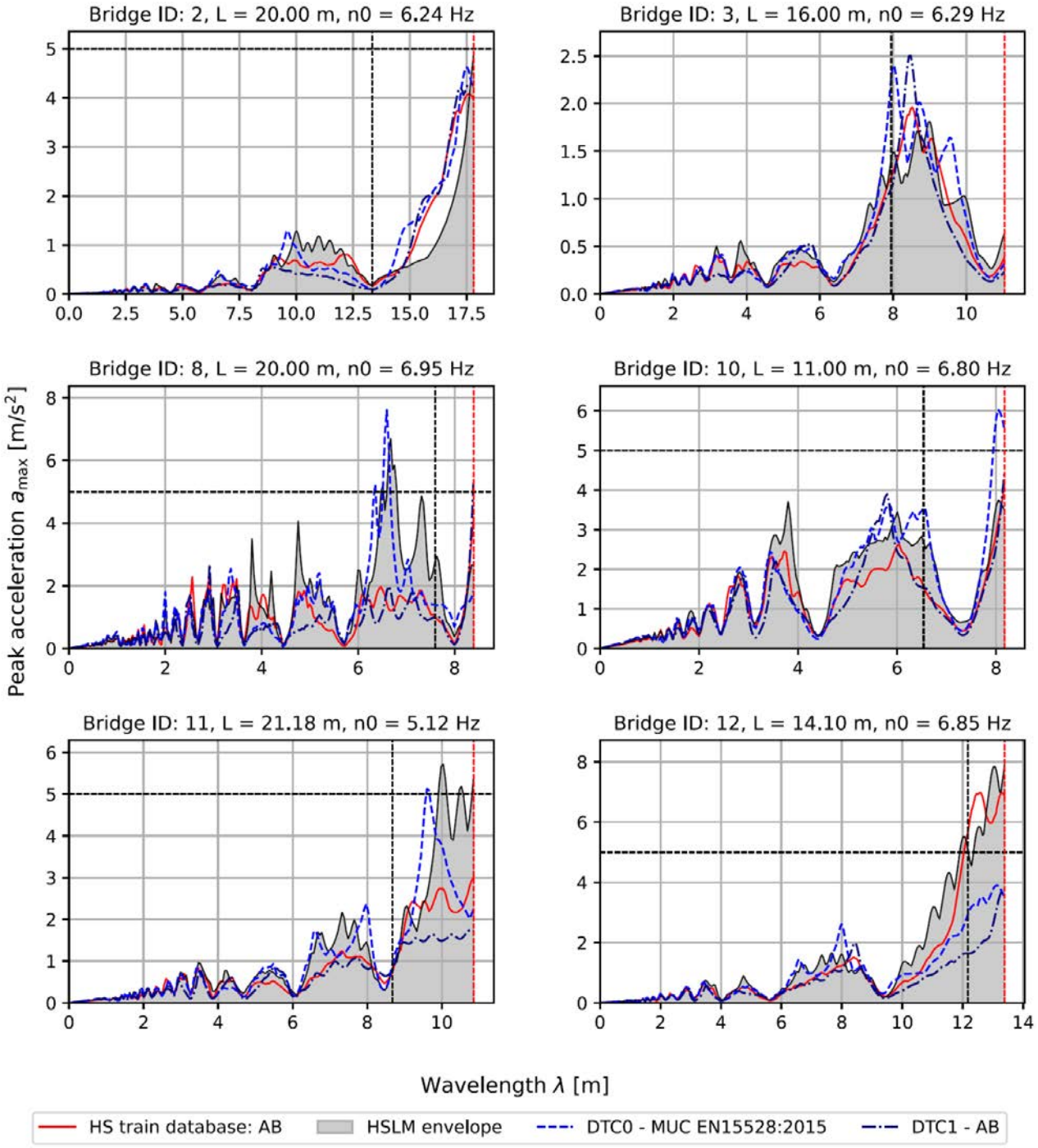

Figure 23. Envelope of the peak vertical acceleration in the bridges with 'intermediate' frequency for different wavelengths. Comparison between real AB trains, reference AB trains in DTC0 and DTC1, and HSLM-A trains. LIR method.

Figure 24 presents the vibrations induced by articulated trains in the high-frequency (short-span) bridges. In these structures, the range of wavelengths under operational speeds typically lies below 4 m, with excitation governed by bogie spacing and higher-order subharmonics. Some vibrations exceed the 5 m/s² limit and

marginally surpass the HSLM-A envelope in the range λ ≈ 2–3 m, an effect attributed to the wheel spacing within the bogies of AB trains. This behaviour is not fully enveloped by DTC0 and DTC1 alone. However, the combination of all reference trains collectively covers the effects of all real AB trains in these bridges.

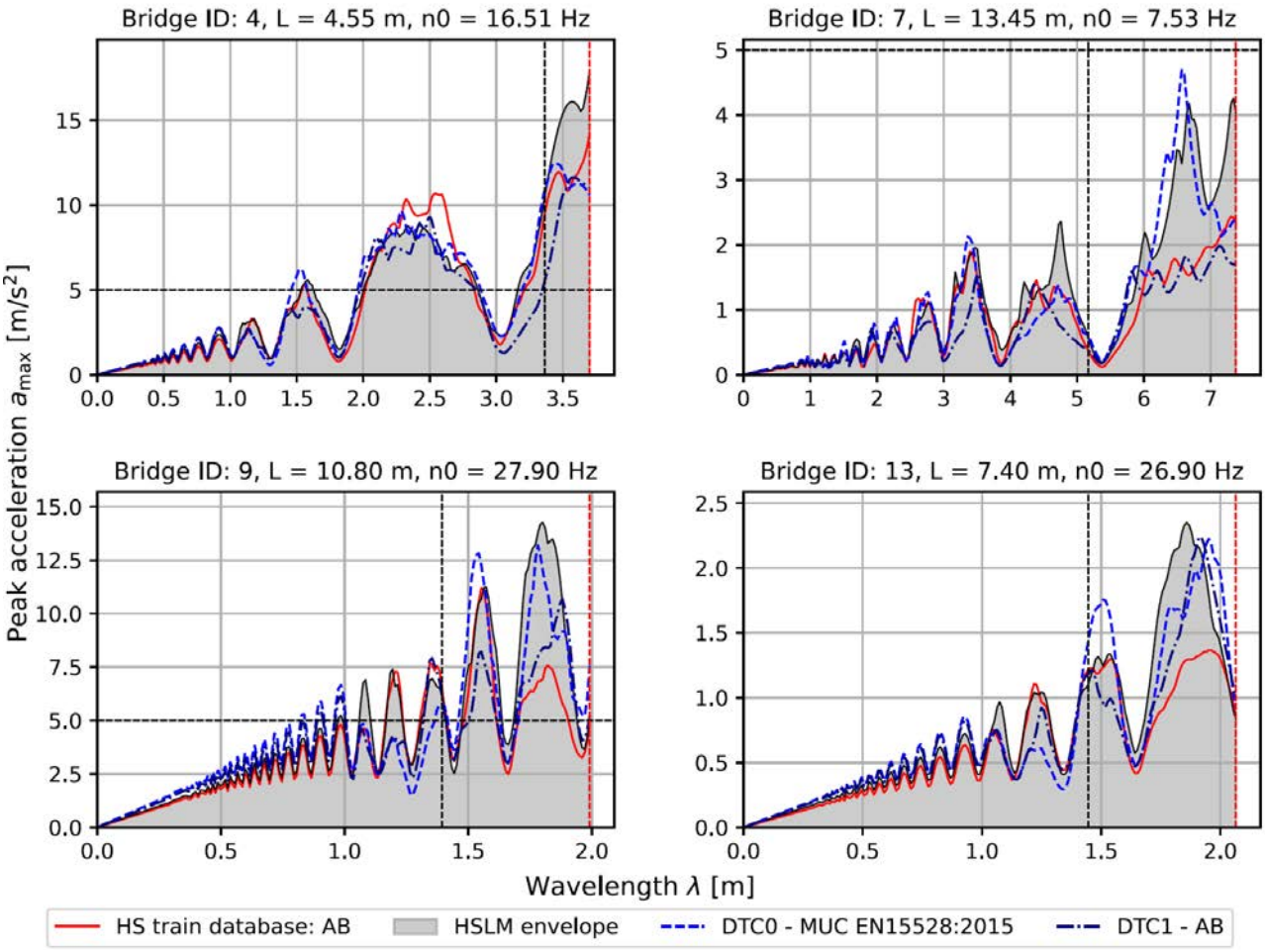

Figure 24. Envelope of the peak vertical acceleration in the bridges with 'high' frequency for different wavelengths. Comparison between real AB trains, reference AB trains in DTC0 and DTC1, and HSLM-A trains. LIR method.

Finally, Figures 25, 26 and 27 present the envelope of vibrations for the entire subset of low, intermediate and high-frequency bridges, respectively. It is clearly observed that the proposed DTC1 trains capture the peak vibrations induced by real articulated trains in the region around λ ≈ 8 m for low and intermediate frequency bridges, where both HSLM-A and DTC0 are exceeded, and the acceleration limit of 5 m/s² is also surpassed. Overall, the combination of DTC0, DTC1 and HSLM-A covers the envelope of accelerations induced by real AB trains across all bridges considered, with the exception of λ ≈ 12 m in relatively long spans and λ ≈ 2–3 m in shorter spans, although the discrepancies in these regions remain modest.

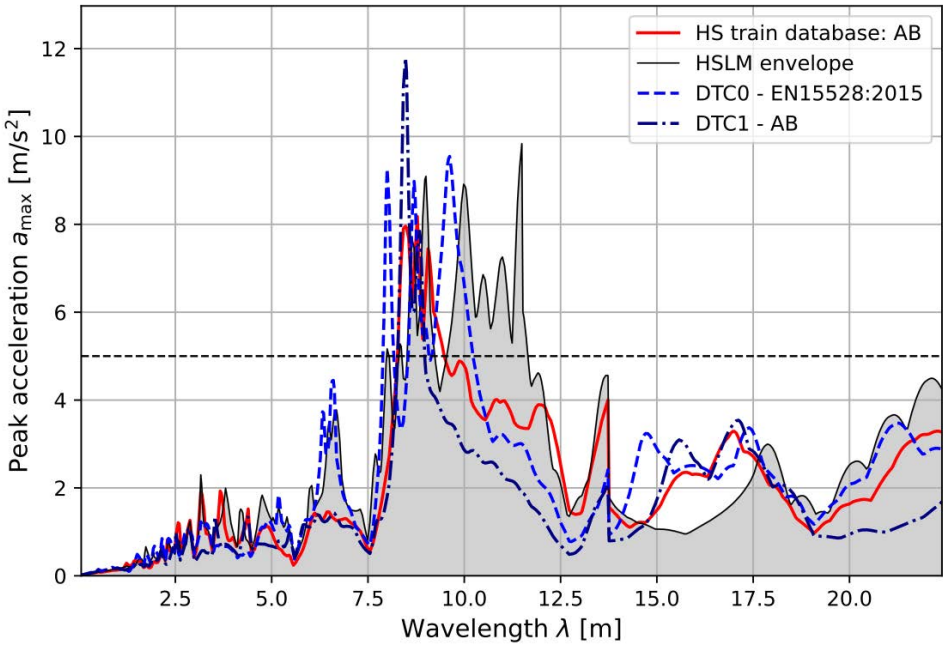

Figure 25. Envelope of the peak vertical acceleration in all the bridges with 'low' frequency for different wavelengths. Comparison between real AB trains, reference AB trains in DTC0 and DTC1, and HSLM-A trains. LIR method. Note that marked vertical drops in some of the large wavelengths occur due to the fact that only some bridges reach those regions, changing the number of structures included in the envelope at certain wavelengths.

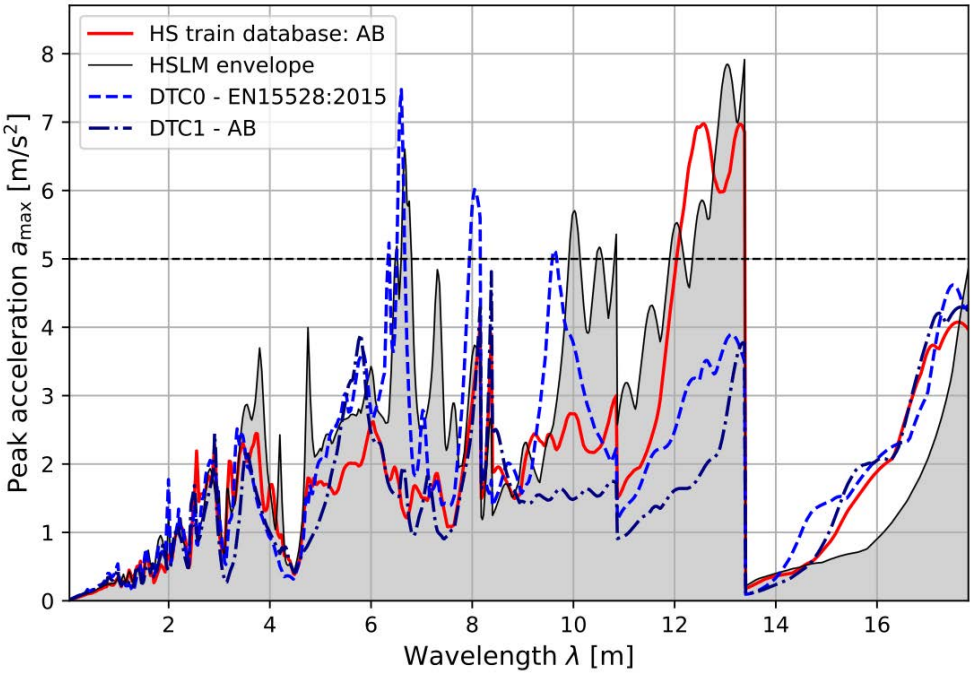

Figure 26. Envelope of the peak vertical acceleration in all the bridges with 'intermediate' frequency for different wavelengths. Comparison between real AB trains, reference AB trains in DTC0 and DTC1, and HSLM-A trains. LIR method. Note that marked vertical drops in some of the large wavelengths occur due to the fact that only some bridges reach those regions, changing the number of structures included in the envelope at certain wavelengths.

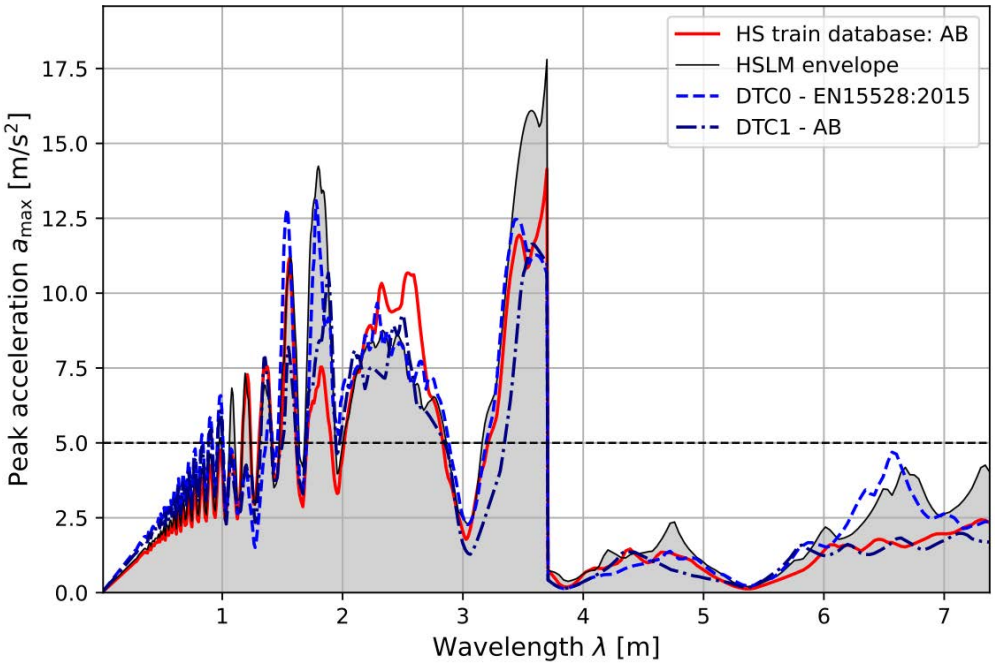

Figure 27. Envelope of the peak vertical acceleration in all the bridges with 'high' frequency for different wavelengths. Comparison between real AB trains, reference AB trains in DTC0 and DTC1, and HSLM-A trains. LIR method. Note that marked vertical drops in some of the large wavelengths occur due to the fact that only some bridges reach those regions, changing the number of structures included in the envelope at certain wavelengths.

5.4.3 Trains with Single Axles: SA

The vibrations induced by single-axle trains in low-frequency bridges are depicted in Figure 28, alongside those obtained from the reference trains and load models. In bridges where the excitation wavelengths approach the coach length, approximately 13 m, resonant vibration peaks are well covered by HSLM-A, DTC0 and DTC1 SA trains in that wavelength region. However, as noted earlier, DTC0 and DTC1 do not fully capture the frequency content of real train signatures between the coach length and the first subharmonic. Although this gap was covered by the HSLM-A envelope in the signature analysis, the filtering effect of the bridge influence line gives rise to notable vibrations in the region $\lambda \approx 9$ m for certain structures, particularly bridge ID 6. Exceedances are also observed, though of smaller magnitude, for the first subharmonic of real trains around $\lambda \approx 6.6$ m. In this region, the response is almost fully covered by the proposed SA2_1 configuration and the reference SA trains from DTC0.

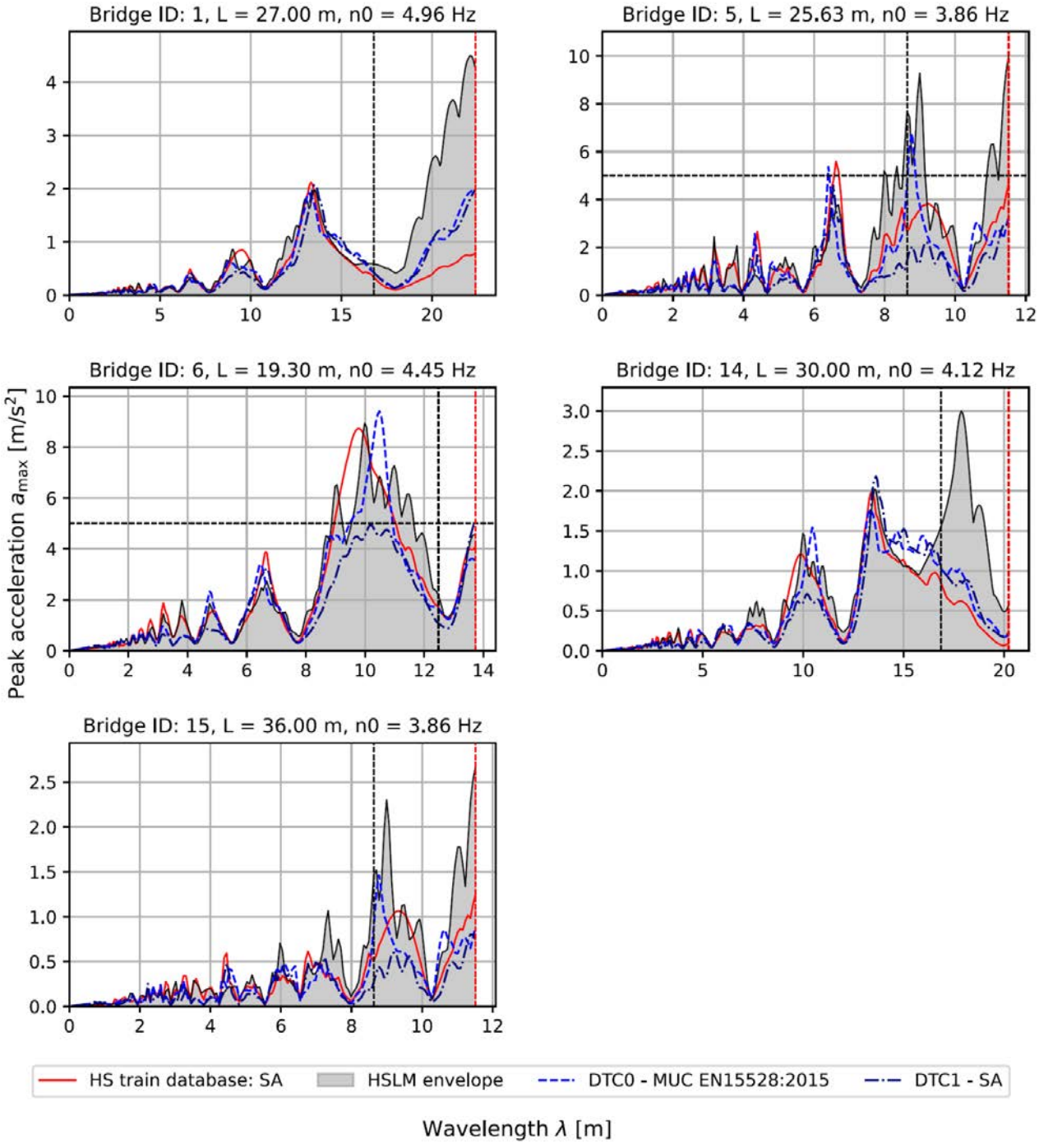

Figure 28. Envelope of the peak vertical acceleration in the bridges with 'low' frequency for different wavelengths. Comparison between real SA trains, reference SA trains in DTC0 and DTC1, and HSLM-A trains. LIR method.

The same trend is observed in the intermediate-frequency bridges shown in Figure 29, although the exceedances are locally more pronounced. In particular, bridge ID 3 exhibits larger vibrations in the region $\lambda \approx 10$ m, corresponding to the spectral valley of SA trains, while bridge ID 8 shows notable exceedances at the first subharmonic around $\lambda \approx 6.6$ m.

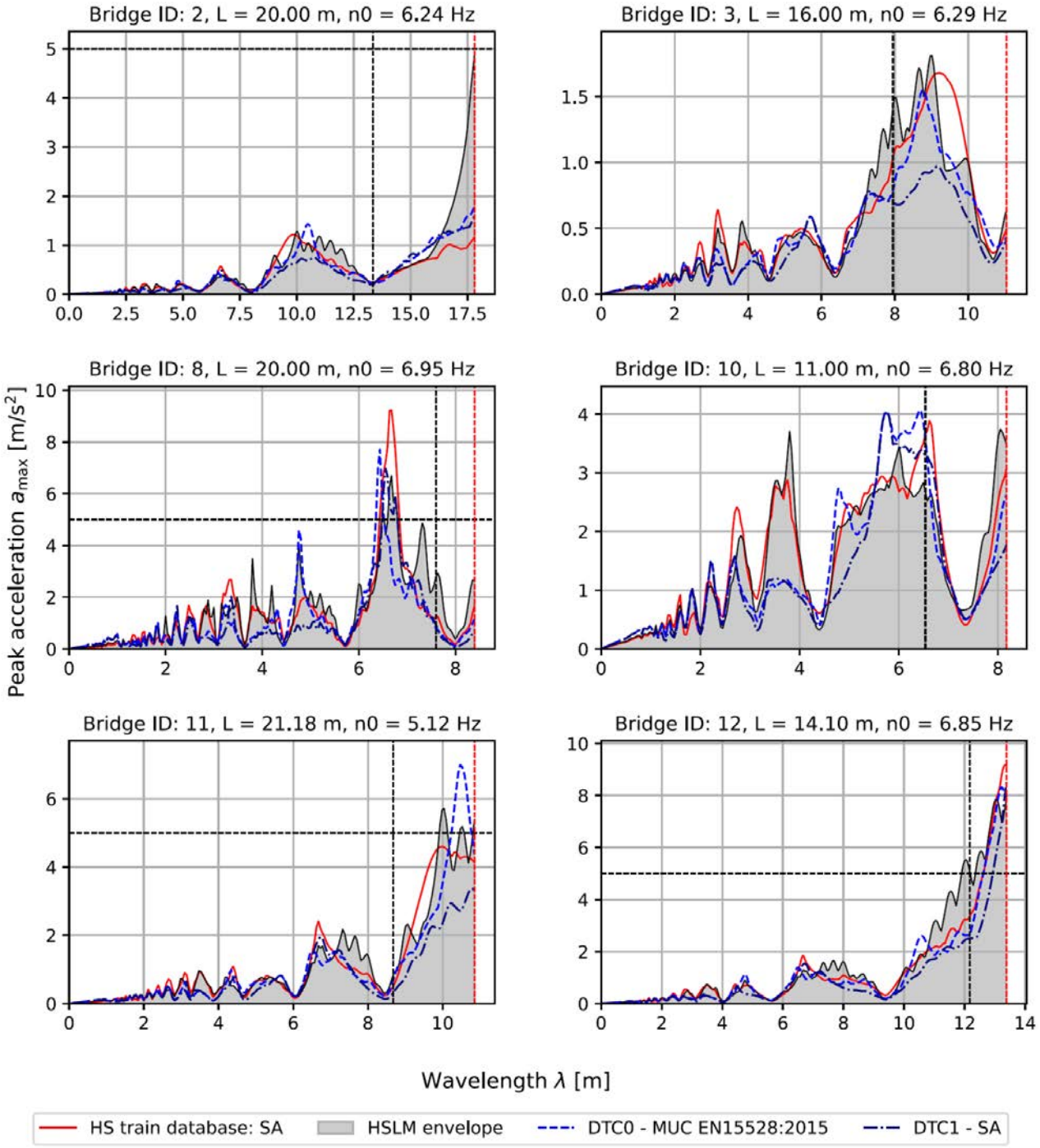

Figure 29. Envelope of the peak vertical acceleration in the bridges with 'intermediate' frequency for different wavelengths. Comparison between real SA trains, reference SA trains in DTC0 and DTC1, and HSLM-A trains. LIR method.

The largest discrepancies between real trains and the combination of DTC0, DTC1 and HSLM-A are observed in the vibrations of high-frequency bridges under single-axle trains, shown in Figure 30. These structures are significantly influenced by wavelengths in the range of 2 to 3 m, which may be attributed to the bogie axle spacing in locomotives or transition coaches. The reference trains are designed with highly repetitive patterns to capture the resonant peak associated with the coach length, which often results in fewer couplings and transition cars that could otherwise excite the short-wavelength content dominating high-frequency bridges. Although DTC0 and DTC1 nearly cover the effects in this spectral band for bridge ID 4,

even shorter wavelengths around 1–2 m in bridges ID 9 and ID 13 lead to exceedances of real SA train vibrations relative to the reference trains and HSLM-A.

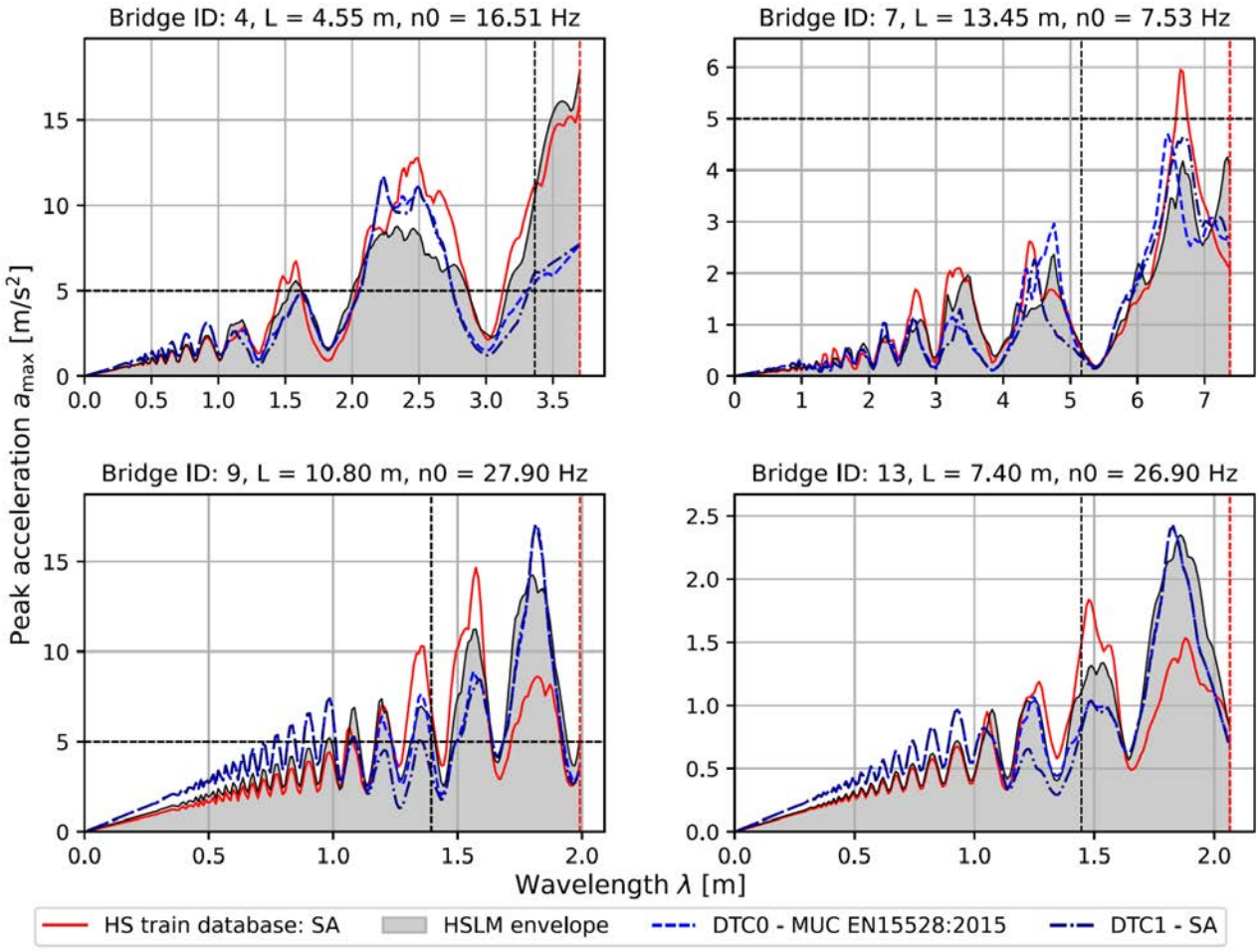

Figure 30. Envelope of the peak vertical acceleration in the bridges with 'high' frequency for different wavelengths. Comparison between real SA trains, reference SA trains in DTC0 and DTC1, and HSLM-A trains. LIR method.

Overall, Figures 31, 32 and 33 show that the envelope of vibrations induced by real single-axle trains across all low, intermediate and high-frequency bridges is generally covered by the combination of DTC0, DTC1 and HSLM-A. However, certain frequency bands exhibit noticeable exceedances, which are more pronounced than those observed for conventional and articulated trains. This behaviour is attributed to the inherent characteristics of SA trains: while their highly repetitive coach lengths are well captured in the region around $\lambda \approx 13$ m, the spectral valley between the coach length and its first subharmonic presents a richer content than that of the more idealised reference trains. This is due to the complex axle spacing configurations found in real SA formations, which give rise to significant dynamic effects around $\lambda \approx 8$–9 m in low and intermediate-frequency bridges that are not fully enveloped by the reference load models. In contrast, the response of high-frequency bridges under SA trains, shown in Figure 32, is better represented by the proposed reference trains.

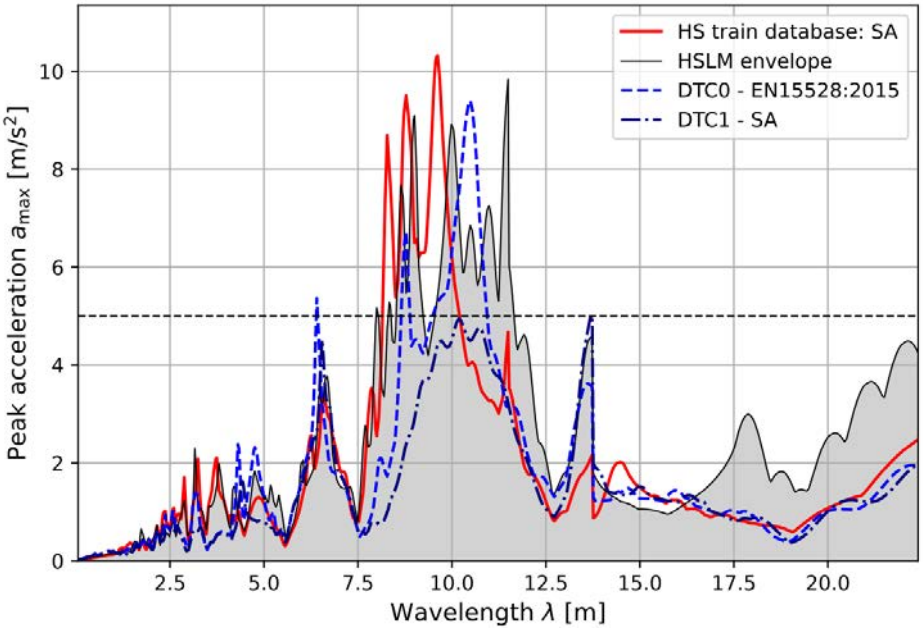

Figure 31. Envelope of the peak vertical acceleration in all the bridges with 'low' frequency for different wavelengths. Comparison between real SA trains, reference SA trains in DTC0 and DTC1, and HSLM-A trains. LIR method. Note that marked vertical drops in some of the large wavelengths occur due to the fact that only some bridges reach those regions, changing the number of structures included in the envelope at certain wavelengths.

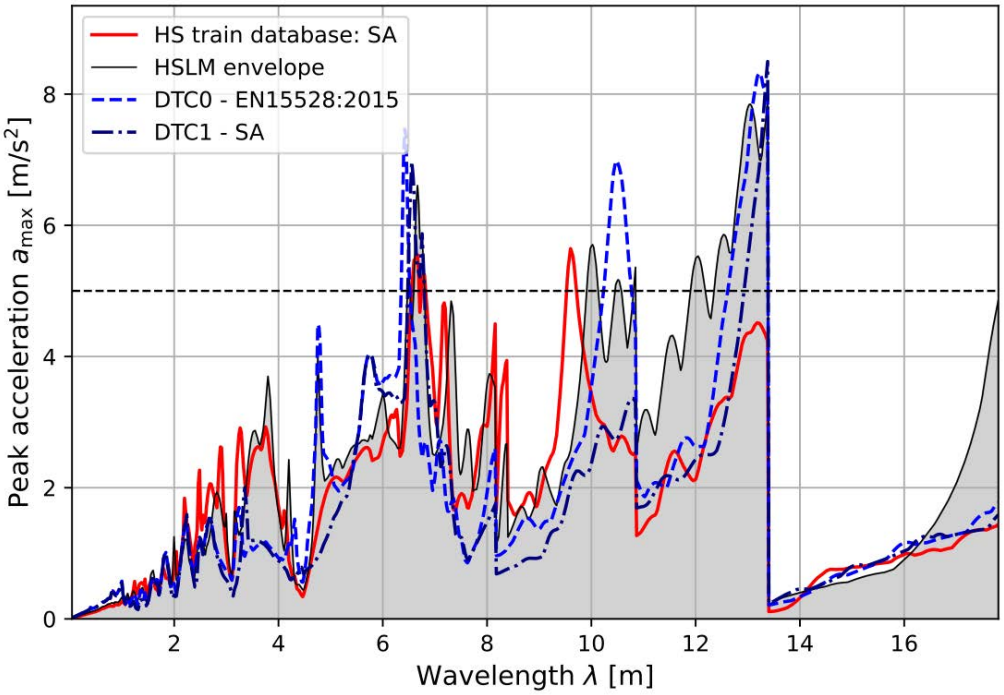

Figure 32. Envelope of the peak vertical acceleration in all the bridges with 'intermediate' frequency for different wavelengths. Comparison between real SA trains, reference SA trains in DTC0 and DTC1, and HSLM-A trains. LIR method. Note that marked vertical drops in some of the large wavelengths occur due to the fact that only some bridges reach those regions, changing the number of structures included in the envelope at certain wavelengths.

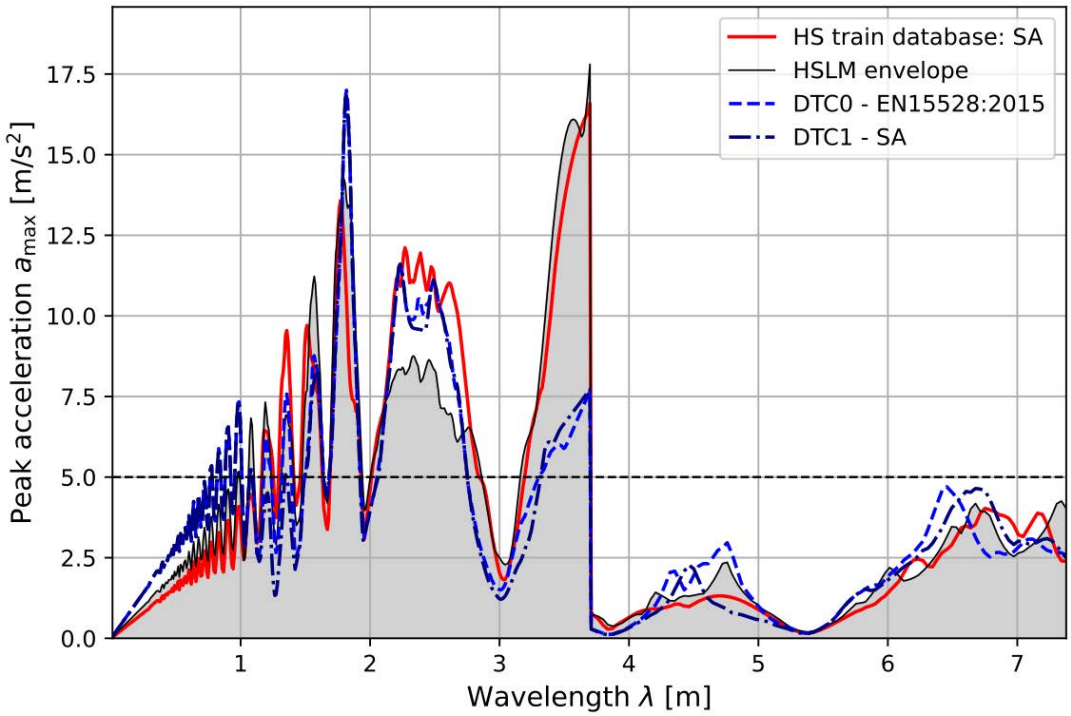

Figure 33. Envelope of the peak vertical acceleration in all the bridges with 'high' frequency for different wavelengths. Comparison between real SA trains, reference SA trains in DTC0 and DTC1, and HSLM-A trains. LIR method. Note that marked vertical drops in some of the large wavelengths occur due to the fact that only some bridges reach those regions, changing the number of structures included in the envelope at certain wavelengths.

5.5 Peak accelerations obtained with time-stepping analysis

The peak accelerations with DTC0 and DTC1, as well as HSLM-A and the real train database, were also calculated using a more accurate method, namely the time-stepping analysis in CALDINTAV (Nguyen & Goicolea, 2024). The results are included in Appendix D. Comparing them with those obtained with the LIR method included previously for the same bridges it is observed that the maximum accelerations in both methodologies are similar at resonance peaks. The improved coverage of the train-induced vibrations with the combination of DTC0 and DTC1, compared with HSLM-A, is generally observed. However, the results of the time-stepping analysis with DTC0 and DTC1 are not discussed in detail as they are similar to those with LIR, and because more attention will be given to DTC2.

6 Dynamic Train Categories 2: DTC2

The development of DTC2 arises from limitations identified in the DTC0+DTC1 framework when examined at the level of refined MU sub-categories. Although the combined DTC0+DTC1 sets generally provide a satisfactory envelope when all trains within a main group (CB, AB or SA) are considered together, as it was discussed previously, a more detailed assessment that will be presented in the following reveals that certain real trains classified within specific sub-categories have dynamic signatures above those from the reference trains DTC0+DTC1. More importantly, the peak bridge accelerations in these sub-groups can exceed for certain excitation wavelengths those predicted by the corresponding reference train(s) of that subgroup. This indicates that the geometric and excitation variability within some MU classes cannot be completely

represented by the corresponding reference configurations in DTC0 and DTC1. To address this shortcoming, DTC2 is introduced as a more systematic and optimisation-based formulation, aimed at defining reference trains that robustly envelope the dynamic effects of each refined sub-category while preserving simplicity and applicability for compatibility checks.

The general optimisation methodology for DTC2 is given composed of the following steps:

1. Normalisation of the real train signatures

In the present work, the optimisation of the DTC2 is based on the real train signatures. In order to obtain the optimum axle spacing of the reference trains without considering the axle weight (which is adjusted later depending on the line category and the corresponding value of P_{MUclass}), the signatures of the real trains are normalised with respect to the maximum axle load of each train (P), not with respect to the maximum value of the signature itself. The dimensionless normalised signature is therefore defined as:

$$S_0^*(\lambda) = \max_{k=1,\dots,N} \left\{ \left[\sum_{i=1}^{k} \cos\left(2\pi \frac{d_k - d_i}{\lambda}\right) \right]^2 + \left[\sum_{i=1}^{k} \sin\left(2\pi \frac{d_k - d_i}{\lambda}\right) \right]^2 \right\}^{1/2} \tag{5}$$

It is remarked that in the recent research project DLM (2023), in its work package 2, an optimisation of DTC is proposed from the signatures of real trains, but it explicitly included the axle load as an optimisation parameter. In contrast, the present approach explicitly separates:

- Geometric excitation effects (contained in the dimensionless signature),
- Load level effects (introduced later through a chosen reference axle load P_{MUclass}).

This distinction is physically meaningful because the signatures of the trains scale linearly with their loads: $S_0(\lambda) \propto P$. Therefore, normalising by P isolates the purely geometric–kinematic excitation characteristics of the train (axle spacing, coach length, bogie distances), independently of its axle weights. This is consistent with the philosophy of the DTC framework, where reference trains are later defined with uniform axle loads P_{MUclass} appropriate for the sub-group under consideration.

2. Envelope of the dimensionless signatures

For each wavelength value λ, the raw envelope is obtained by taking the maximum value among all normalised signature in the database of N trains:

$$S_{0,raw}^{*,\mathrm{env}}(\lambda) = \max_{j=1,\dots,N} \{S_{0,j}^*(\lambda)\} \tag{6}$$

where $S_{0,j}^*(\lambda)$ is the dimensionless signature of the j-th train.

This curve represents the worst-case dimensionless dynamic amplification within the group. However, since it is built from discrete train responses, it may contain narrow peaks or local irregularities caused by isolated configurations. For optimisation purposes, a smoother and more robust target curve is required.

3. Obtain a smooth envelope as the target signature

To eliminate short-wavelength irregularities while preserving dominant peaks, a window-based smoothing procedure is applied.

The wavelength axis is discretised with spacing $\Delta\lambda$. A smoothing window of length $\Delta\lambda_w = 0.5$ m is defined. Within each window:

a) The maximum value of the raw envelope is identified.

b) That maximum is retained as a representative point.

c) Consecutive retained maxima are connected by linear interpolation.

The smoothed envelope, referred to as $S^{*}_{0,target}$, is therefore constructed as a piecewise linear curve passing through the selected local maxima. The first and last wavelength points are always retained to ensure complete domain coverage.

The resulting curve preserves dominant dynamic amplification regions while removing artificial oscillations and providing a stable and conservative optimisation target. Therefore, this smoothed, dimensionless envelope is selected as the reference spectrum for the DTC2 optimisation.

4. Definition of the optimisation problem

The objective of DTC2 is to determine a parametric reference train whose dimensionless spectrum reproduces the smoothed envelope as closely as possible. The reference train is defined through a design vector **s** that contains the key geometric parameters of each train (e.g. coach length, bogie spacing, axle spacing) Figure 34 shows parameters included in the design vectors of the three train categories in this work. On the other hand, the number of coaches in the train is defined as a function of the coach length (D) so that the total length of the passenger cars (including transition cars if existing) do not exceed 400 m (excluding locomotives).

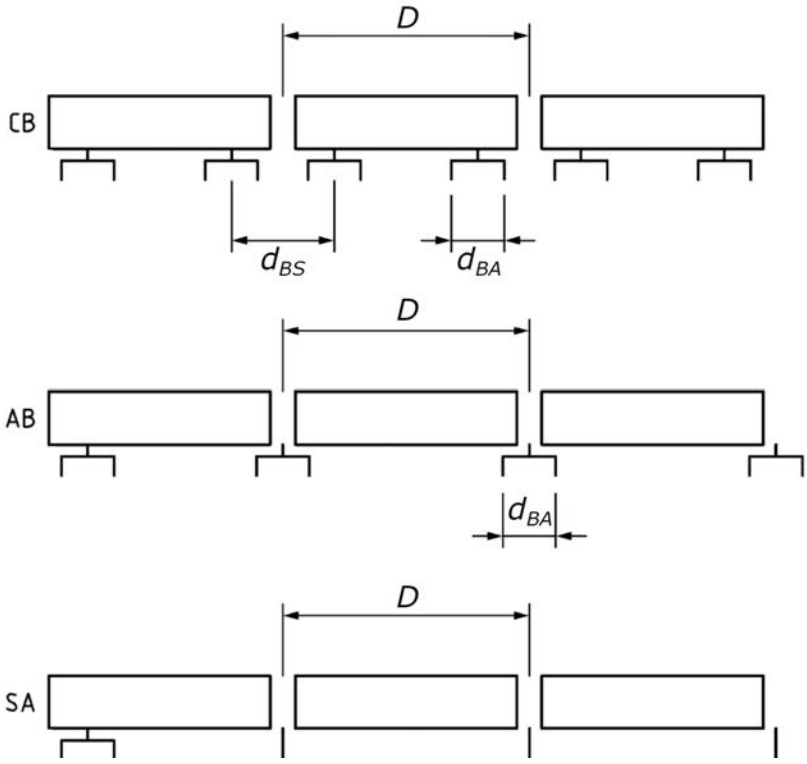

Figure 34. Train parameters defined in the design vector s *for the optimisation of CB, AB and SA trains in DTC2.*

From the design vector and the number of coaches, the axle positions are generated as it will be explained for each train category in the following sections, and its dimensionless signature $S_0^{*,model}$ (model signature) is obtained from Eq. (5).

The optimisation seeks to minimise the discrepancy between the model signature and the smoothed envelope. A discrete L^2 norm is adopted:

$$J(s) = \sqrt{\sum_{i=1}^{M} \left(S_0^{*,model}(\lambda_i; s) - S_{0,target}^{*}(\lambda_i) \right)^2} \tag{7}$$

Therefore, the optimisation is defined as a minimisation of the residual:

$$\min_{s \in \mathcal{D}} J(s), \tag{8}$$

where the domain $\mathcal{D}$ defines the physically admissible geometric properties that compose the optimisation vector **s**, which depend of each train sub-group as it will be described later.

The minimisation is performed using the L-BFGS-B algorithm (Zhu *et al*., 1997) implemented in PYTHON (Van Rossum, 2023), which is particularly suitable because the number of design variables is relatively small, and the objective is smooth (unless the number of coaches changes within the optimisation process) but computationally expensive.

6.1 Trains with Conventional Bogies: CB

Focusing first on the definition of optimised DTC2 for CB trains, Figure 34 shows the signatures of the real passenger trains that belong to the sub-groups CB1 and CB2 defined by EN 15528:2015 in DTC0, and it compares them with the corresponding reference trains in that normative. According to it, CB1 trains are CB trains with coach lengths (D in Figure 34) between 23.8 m and 25.3 m, as well as other geometric constraints that have been considered in the preparation of Figure 35. On the other hand, CB2 trains have coach lengths in the range between 25.3 m and 27.5 m. With this subgroups, it is clear that trains with longer coaches (e.g. ICE4) are not covered by the reference train models in DTC0 (and this was the reason why DTC1 proposed the train CB1_1, as explained previously), but now the attention is called on the trains that belong to one of the two existing groups of CB trains in DTC0; it is observed that there are two clear peaks in the signatures of CB1 and CB2, and these are related to their coach lengths. Therefore, within each CB sub-family there are distinct groups of trains, and for this reason the reference CB1 and CB2 trains, with specific coach lengths, cannot cover the effect of all the trains in the sub-groups that they represent.

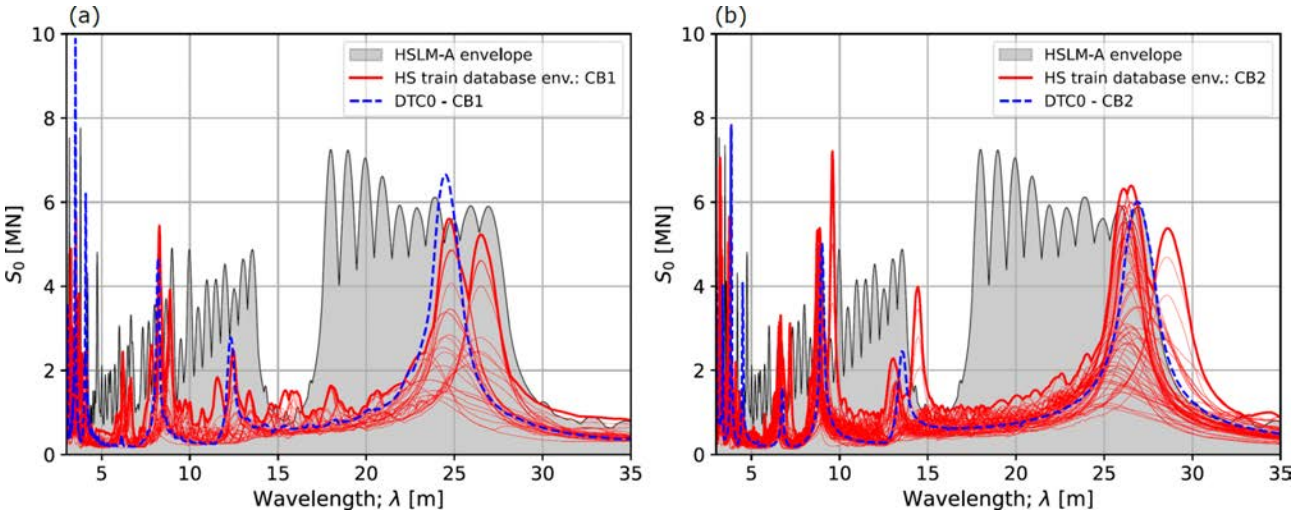

Figure 35. Envelope of the signatures of real CB trains grouped in the DTC0 sub-categories (all speeds above 200 km/h); (a) CB1 trains, (b) CB2 trains. The HSLM-A and DTC0 envelopes are also included for reference.

Acknowledging this issue, and based on the signatures of the real trains in Figure 34, a total of 3 new reference CB trains is proposed in DTC2 with the following categorisiation:

	Reference train CBa	**Reference train CBb**	**Reference train CBc**
Coach length *D* [m]	$23 \leq D < 25$	$25 \leq D < 27$	$27 \leq D < 29$

Table 2. Categorisation of CB trains in DTC2 in terms of their coach length.

It is noted that the rest of the geometric properties of CB trains included in the definition of the DTC0 sub-groups in EN 15528:2015 is intentionally ignored in the proposed DTC2. This is to facilitate the categorisation of real trains into relevant families with consistent induced vibrations in bridges, ignoring parameters with marginal effects that may not be available for all the trains.

The axle distribution of the reference CB trains is defined as a long and repetitive train given by the design vector $\mathbf{s} = (D, d_{BS}, d_{BA})$, with D, d_{BS} and d_{BA} being the coach length, bogie spacing in consecutive coaches, and axle spacing in a bogie, respectively. The graphical explanation of these geometric parameters of the train are included in Figure 34 (top). The reference CB trains in DTC2 are composed of a front and rear locomotives with two bogies in each of them and axle spacings at 0, 3, 14 and 17 m, followed by a gap of 3.525 m between the last axle of the locomotive and the first axle of the car attached to it (referred as L_{gap} in the following). Between locomotives, a total of N_{coach} passenger cars of identical axle arrangement given in Figure 34 (top) is included.

Consequently, the position of the first car is:

$$x_{1,0} = L_{\text{loco}} + L_{\text{gap}} \tag{9}$$

where x refers to the distance from the front axle of the train; L_{loco} is the length of the locomotive.

$$x_{k,0} = x_{1,0} + (k-1)D \quad \text{for } k = 1, \dots, N \tag{10}$$

The four axles of the k-th car are located at:

$$\text{Axle 1:} \quad x_{k,0} \tag{11}$$

$$\text{Axle 2:} \quad x_{k,0} + d_{\text{BA}} \tag{12}$$

$$\text{Axle 3:} \quad x_{k,0} + D - d_{\text{BS}} \tag{13}$$

$$\text{Axle 4:} \quad x_{k,0} + D - d_{\text{BS}} + d_{\text{BA}} \tag{14}$$

After the last car, the trailing locomotive is positioned with a coupling gap L_{gap} as:

$$x_{\text{last,loco}} = x_{N,0} + D + L_{\text{gap}} \tag{15}$$

6.1.1 CBa reference train

Figure 36(a) shows the dimensionless signatures of the real CBa trains in the database, and the corresponding smoothed signature ($S^*_{0,target}$) used in the optimisation process.

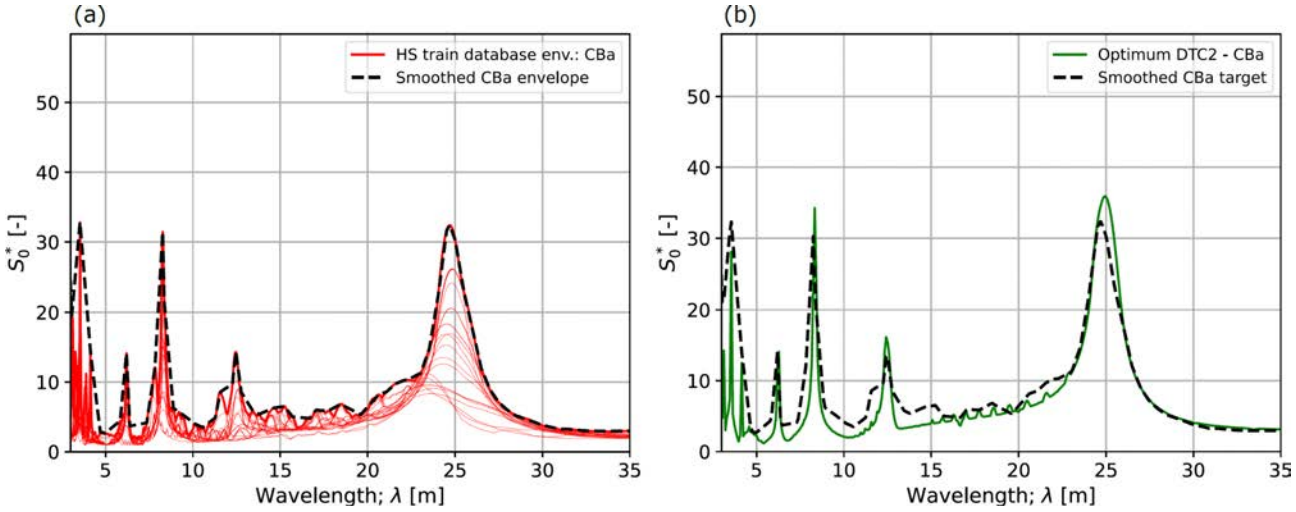

Figure 36. (a) Dimensionless signature of the real passenger trains in the CBa sub-group and smooth envelope $S^*_{0,target}$, (b) dimensionless signature of the optimised CBa train in DTC2 ($S_0^{*,model}$) compared with $S^*_{0,target}$.

The optimisation problem seeks to minimise the L^2-norm of the difference between the signature of the reference train and the target signature, as described in Eq. (7), using the reference CB axle distribution described en Eqs. (9)-(15). The optimisation problem in the CBa train starts with the initial guess vector as $\mathbf{s_{init}} = (24.0, 7.5, 2.5)$ m, and the search for the reference train is bounded within the coach lengths of CBa: $D \in (23, 25)$ m, in addition $d_{BS} \in (7, 8)$ m and $d_{BA} \in (2, 3)$ m. After several iterations in the optimisation process, the reference CBa train defined by the axle spacing included in Figure 37 (top) is obtained. It has 15 coaches and a total length of 411 m, with an optimised design vector of $\mathbf{s} = (D, d_{BS}, d_{BA}) = (25.0, 7.47, 2.43)$ m. Figure 36(b) compares the smooth target signature with that of the CBa train resulting from the optimisation process, and it can be seen that all the resonant peaks are well captured. Appendix B includes the axle spacing for this train, which is referred to as CBa_1 to distinguish it from the extended DTC2 trains (DTC2e) that will be introduced in Section 7.

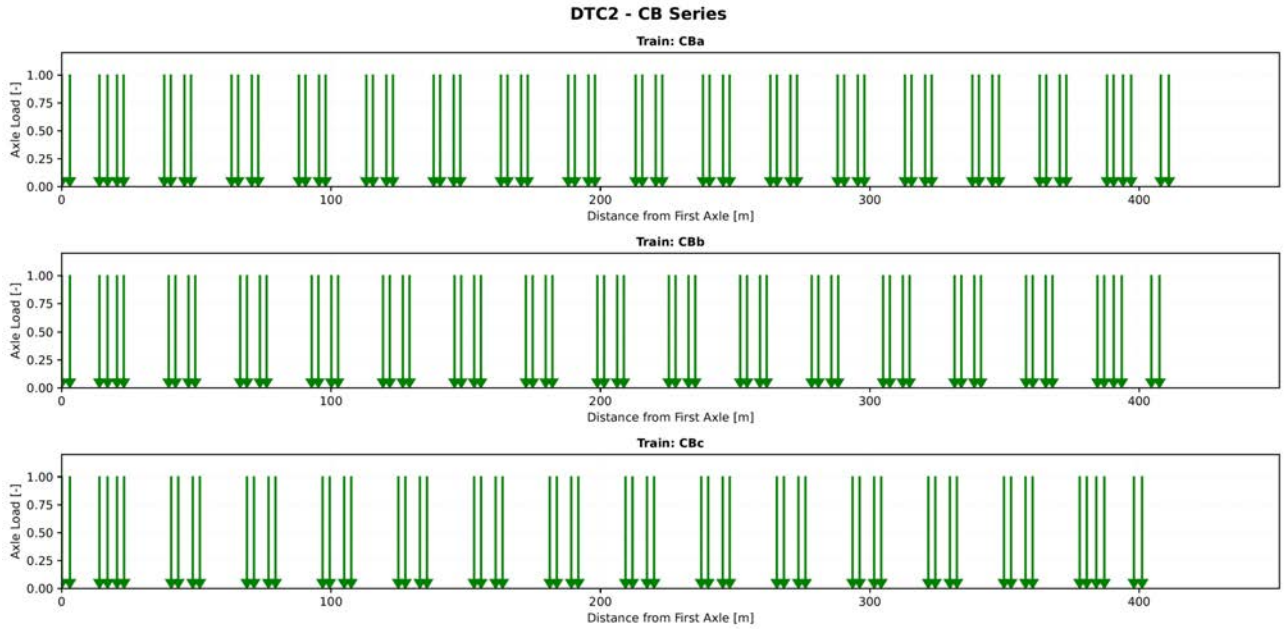

Figure 37. Axle spacing in the CB trains of DTC2.

Once the axle configuration of the CBa train is defined, the allocation of axle loads must be established. Following the same approach adopted for DTC0 and DTC1, the DTC2 reference trains feature uniform axle loads throughout their entire length, including locomotives. These loads are defined by the parameter P_{MUclass}, for which four recommended levels are provided in EN 15528:2015 (Table E.9): 21.5 t, 19.0 t, 17.0 t and 15.0 t. These values correspond to line categories D2, C2, B1 and A, respectively.

Consequently, four reference CBa trains are defined, each associated with one of these load levels. The comparison with real trains is performed according to their maximum axle load under MND (Normal Design Payload) conditions:

- If the maximum axle load of a real train is below 15 t, it is compared against the reference train with $P_{\mathrm{MUclass}} = 15$ t.
- If the maximum axle load lies between 15 t and 17 t, it is compared against the reference train with $P_{\mathrm{MUclass}} = 17$ t.
- If the maximum axle load lies between 17 t and 19 t, it is compared against the reference train with $P_{\mathrm{MUclass}} = 19$ t.
- If the maximum axle load lies between 19 t and 21.5 t, it is compared against the reference train with $P_{\mathrm{MUclass}} = 21.5$ t.

Figure 38 presents the signatures of the real trains grouped according to this classification, alongside the corresponding reference CBa trains. It can be observed that no real passenger CBa train falls into the $P_{\mathrm{MUclass}} = 15$ t category. Only three trains are found in the 17 t and 21.5 t categories, while the vast majority belong to the 19 t category, exhibiting a pronounced peak at approximately $\lambda \approx 25$ m corresponding to their coach length. In general, the reference CBa trains provide excellent coverage of the real train signatures across the entire wavelength range. Moreover, the differentiation by P_{MUclass} categories enables a more precise adjustment of the reference train weights, avoiding the overly conservative models that are significantly heavier than the real trains they are intended to represent, a limitation observed in the DTC0 and DTC1

frameworks. The vibrations induced by these trains in the set of selected bridges will be explored in the following sections.

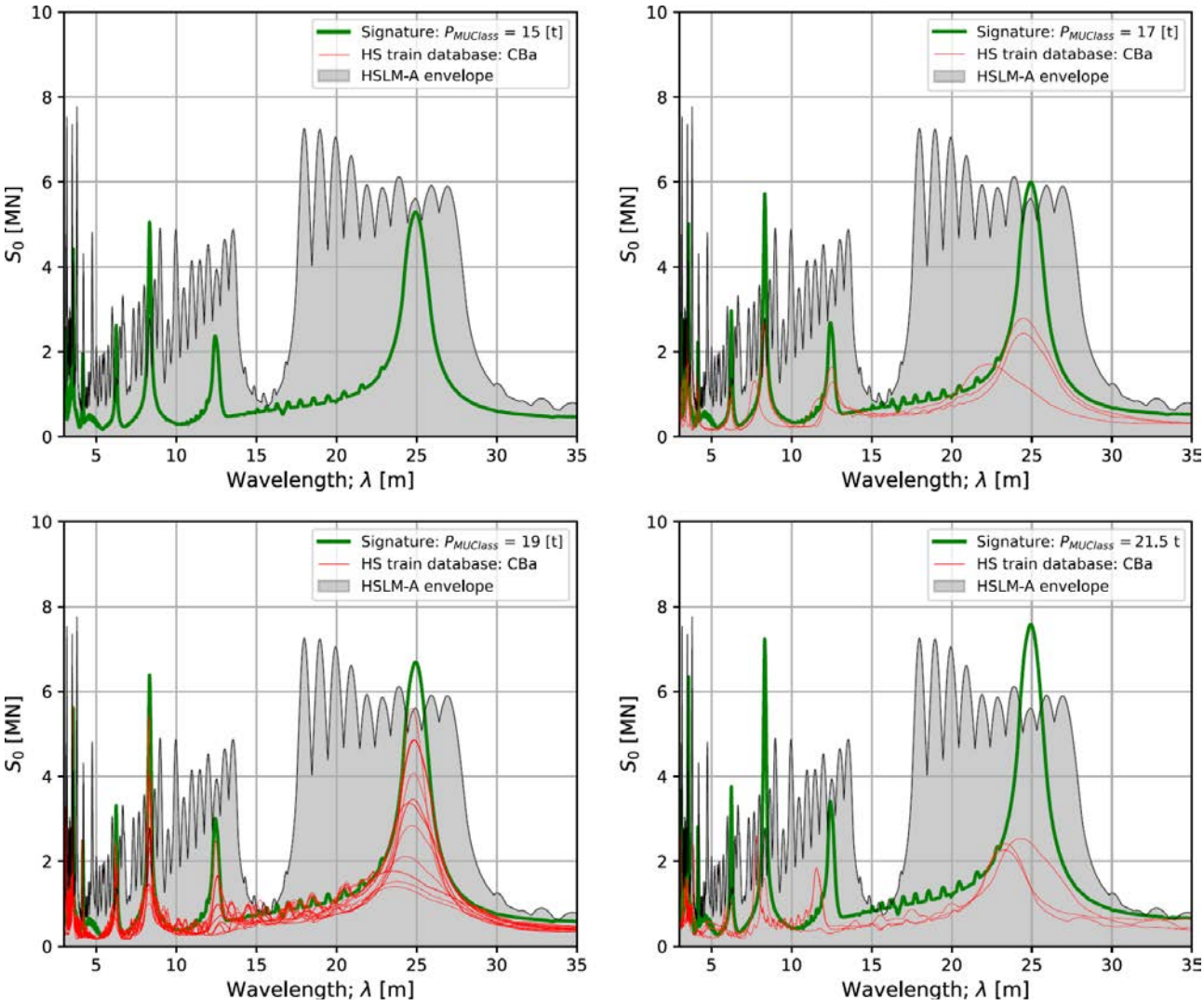

Figure 38. Comparison between the DTC2 CBa train signatures and the signatures of real CBa trains grouped in the DTC2 sub-categories (all speeds above 200 km/h); (top left) trains with $P_{max} \leq 15$ *t, (top right) trains with* $15 < P_{max} \leq 17$ *t, (bottom left) trains with* $17 < P_{max} \leq 19$ *t, and (bottom right) trains with* $19 < P_{max} \leq 21.5$ *t. The HSLM-A envelope is also included for reference.*

6.1.2 CBb reference train

Figure 39(a) presents the dimensionless signatures of the real CBb trains in the database, considering the coach length dimensions summarised in Table 2. The figure also includes the corresponding smoothed signature $S^*_{0,target}$, which serves as the target function in the subsequent optimisation process. It is clear from the signatures that real CBb trains have coach lengths in the order of 26 m, where there is a distinct peak in S^*_0 and consequently also in $S^*_{0,target}$, and this facilitates in principle finding a candidate reference train for this family.

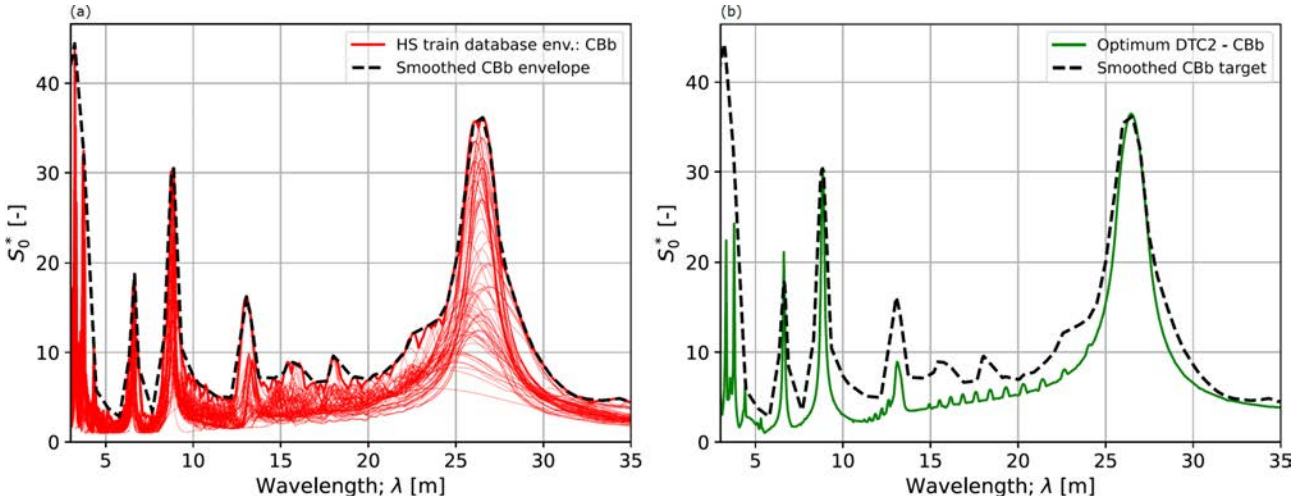

Figure 39. (a) Dimensionless signature of the real passenger trains in the CBb sub-group and smooth envelope $S^*_{0,target}$, (b) dimensionless signature of the optimised CBb train in DTC2 ($S_0^{*,model}$) compared with $S^*_{0,target}$.

The optimisation problem for the CBb train is formulated using the same reference axle distribution described in Eqs. (9)–(15). The initial guess is set to $\mathbf{s}_{\text{init}} = (26.0,7.5,2.5)$ m, and the search is constrained within the range of coach lengths observed for CBa trains: $D \in (25,27)$ m, with $d_{\text{BS}} \in (7,8)$ m and $d_{\text{BA}} \in (2,3)$ m. After several iterations, the optimised reference CBb train is obtained, with its axle configuration illustrated in Figure 37 (middle). The train comprises 14 coaches, has a total length of 407.5 m, and is defined by the optimised design vector $\mathbf{s} = (D, d_{\text{BS}}, d_{\text{BA}}) = (26.52,7.32,2.50)$ m. Figure 39(b) compares the smoothed target signature with that of the optimised CBb train. The results demonstrate that the largest resonant peaks are captured well by the reference train, although it is lower than the target in the first subharmonic around $\lambda \approx 12.5$ m. The axle spacing in this train is provided in Appendix B, where it is referred to as CBb_1 to distinguish it from the extended DTC2 trains (DTC2e) that will be introduced in Section 7.

Once the axle configuration of the CBb train is established, the axle loads are assigned according to the four P_{MUclass} category levels: 21.5 t, 19.0 t, 17.0 t and 15.0 t. Figure 40 presents the signatures of the real trains grouped according to this classification, alongside the corresponding reference CBb trains. It is first observed that the main resonant peak at $\lambda \approx 26$ m, associated with the coach length, is well captured by the reference CBb train across all four line categories. For the category that includes the majority of passenger trains, namely $P_{\text{MUclass}} = 19$ t, the signature of the CBb train closely follows the envelope of the real trains, thereby avoiding excessive conservatism. Other resonant peaks in the signatures are also adequately covered by the CBb train. However, some discrepancies are noted: the subharmonic at $\lambda \approx 13$ m (half the coach length) appears slightly underconservative for the lightest trains in the 17 t category. Additionally, a marginal exceedance of the reference signature is observed for the 17 t category in the spectral valley around $\lambda \approx$ 15–16 m.

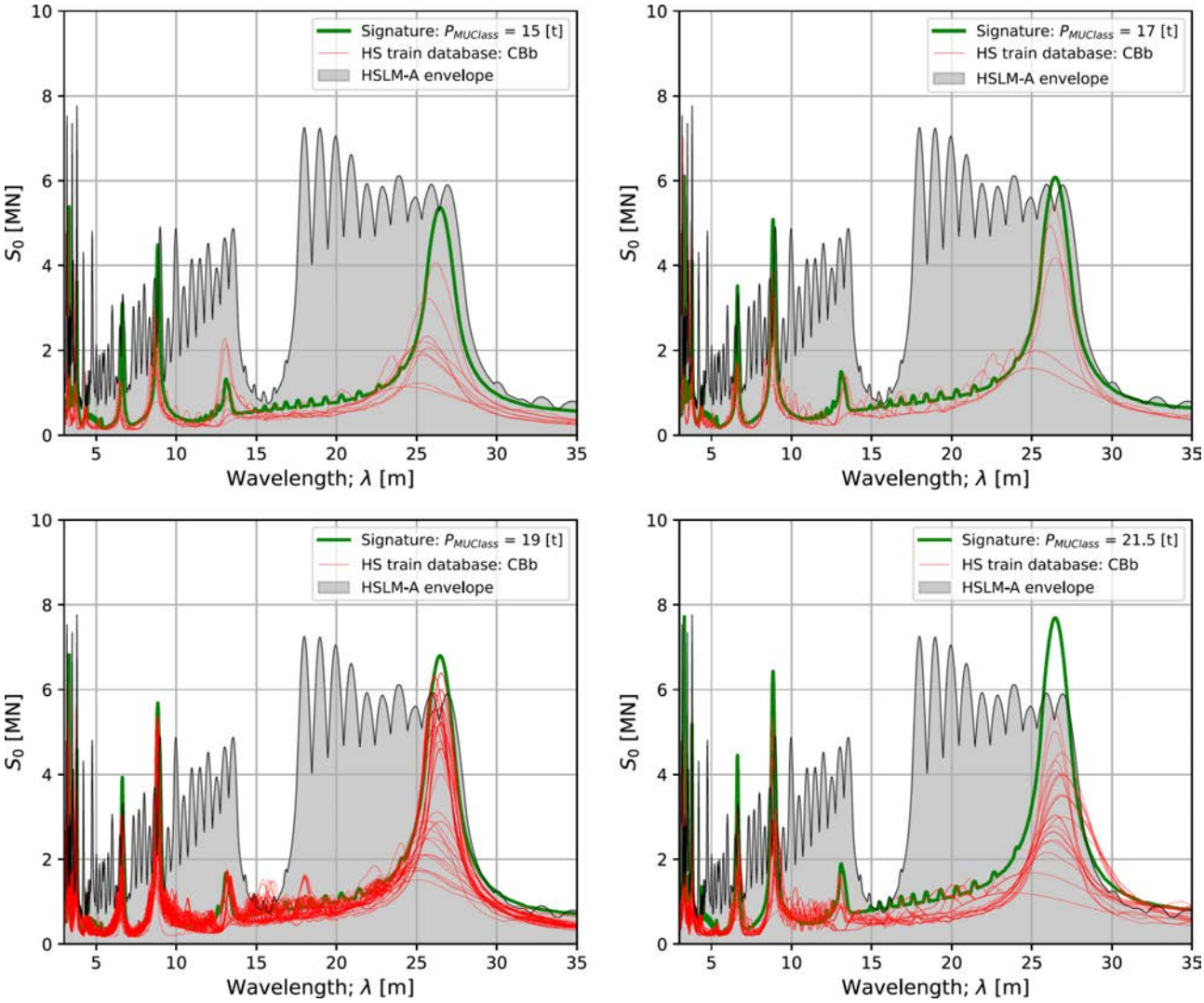

Figure 40. Comparison between the DTC2 CBb train signatures and the signatures of real CBb trains grouped in the DTC2 sub-categories (all speeds above 200 km/h); (top left) trains with $P_{max} \leq 15$ *t, (top right) trains with* $15 < P_{max} \leq 17$ *t, (bottom left) trains with* $17 < P_{max} \leq 19$ *t, and (bottom right) trains with* $19 < P_{max} \leq 21.5$ *t. The HSLM-A envelope is also included for reference.*

6.1.3 CBc reference train

Figure 41(a) presents the dimensionless signatures of the real CBc trains in the database, based on the coach length dimensions summarised in Table 2. The figure also includes the corresponding smoothed signature $S^*_{0,target}$, which serves as the target function in the subsequent optimisation process. Examination of the signatures reveals that the majority of real CBc trains exhibit coach lengths on the order of 28 m, characteristic of newer rolling stock such as the ICE4. However, a distinct secondary peak is also observed in some trains at approximately $\lambda \approx 27$ m. This variation contributes to a broader peak in the smoothed target signature $S^*_{0,target}$ within the long-wavelength region, and it poses a challenge for the definition of a single envelope CBc reference train in DTC2.

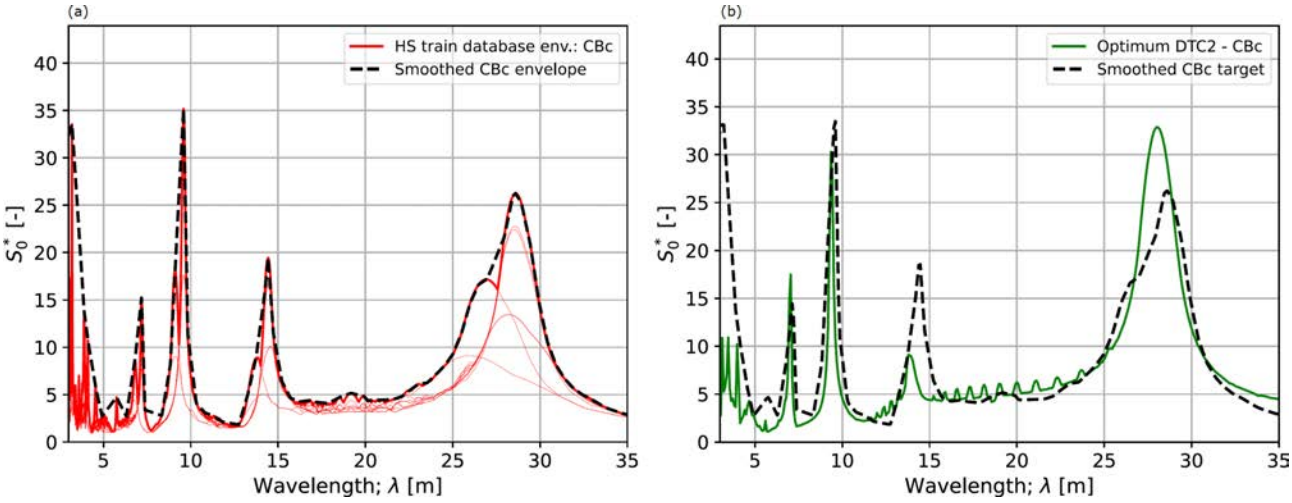

Figure 41. (a) Dimensionless signature of the real passenger trains in the CBc sub-group and smooth envelope $S^*_{0,target}$, (b) dimensionless signature of the optimised CBc train in DTC2 ($S_0^{*,model}$) compared with $S^*_{0,target}$.

The optimisation problem for the CBc train follows the same reference axle distribution described in Eqs. (9)–(15). An initial guess of $\mathbf{s}_{\text{init}} = (28.0,7.5,2.5)$ m is adopted, with the search constrained within the coach length range observed for CBc trains: $D \in (27,29)$ m, along with $d_{\text{BS}} \in (7,8)$ m and $d_{\text{BA}} \in (2,3)$ m. After several iterations, the optimised reference CBc train is obtained, with its axle configuration depicted in Figure 37 (bottom). The train consists of 13 coaches, has a total length of 401.1 m, and is defined by the optimised design vector $\mathbf{s} = (D, d_{\text{BS}}, d_{\text{BA}}) = (28.11,8.0,2.61)$ m. The axle spacing of this train is included in Appendix B, in which it is referred to as CBc_1 to distinguish it from the extended DTC2 trains (DTC2e) that will be presented in Section 7.

Figure 41(b) compares the smoothed target signature with that of the optimised CBc train. The results show that the dominant resonant peaks are well captured by the reference train. However, the reference signature falls noticeably below the target in the region of the first subharmonic, around $\lambda \approx 14$ m.

Once the axle configuration is established, axle loads are assigned according to the four P_{MUclass} category levels: 21.5 t, 19.0 t, 17.0 t and 15.0 t. Figure 42 presents the dimensional signatures of the real CBc trains, grouped by these load categories, alongside the corresponding reference CBc trains within the DTC2 framework. It is observed that the peak at approximately $\lambda \approx 27$ m is associated with relatively lightweight trains in the 17 t category, and this peak is adequately covered by HSLM-A. In contrast, heavier trains in the 19 t and particularly the 21.5 t categories exhibit a pronounced peak at $\lambda \approx 28$ m, corresponding to their longer coach lengths. The proposed CBc train effectively envelopes this behaviour. Nevertheless, for these heavier subcategories, the first subharmonic at $\lambda \approx 14$ m reveals signatures of real trains that lie well above those of the reference trains. This region coincides with a spectral valley in HSLM-A, raising potential concerns. The implications of this discrepancy in terms of peak accelerations in the selected bridges are examined in the following sections.

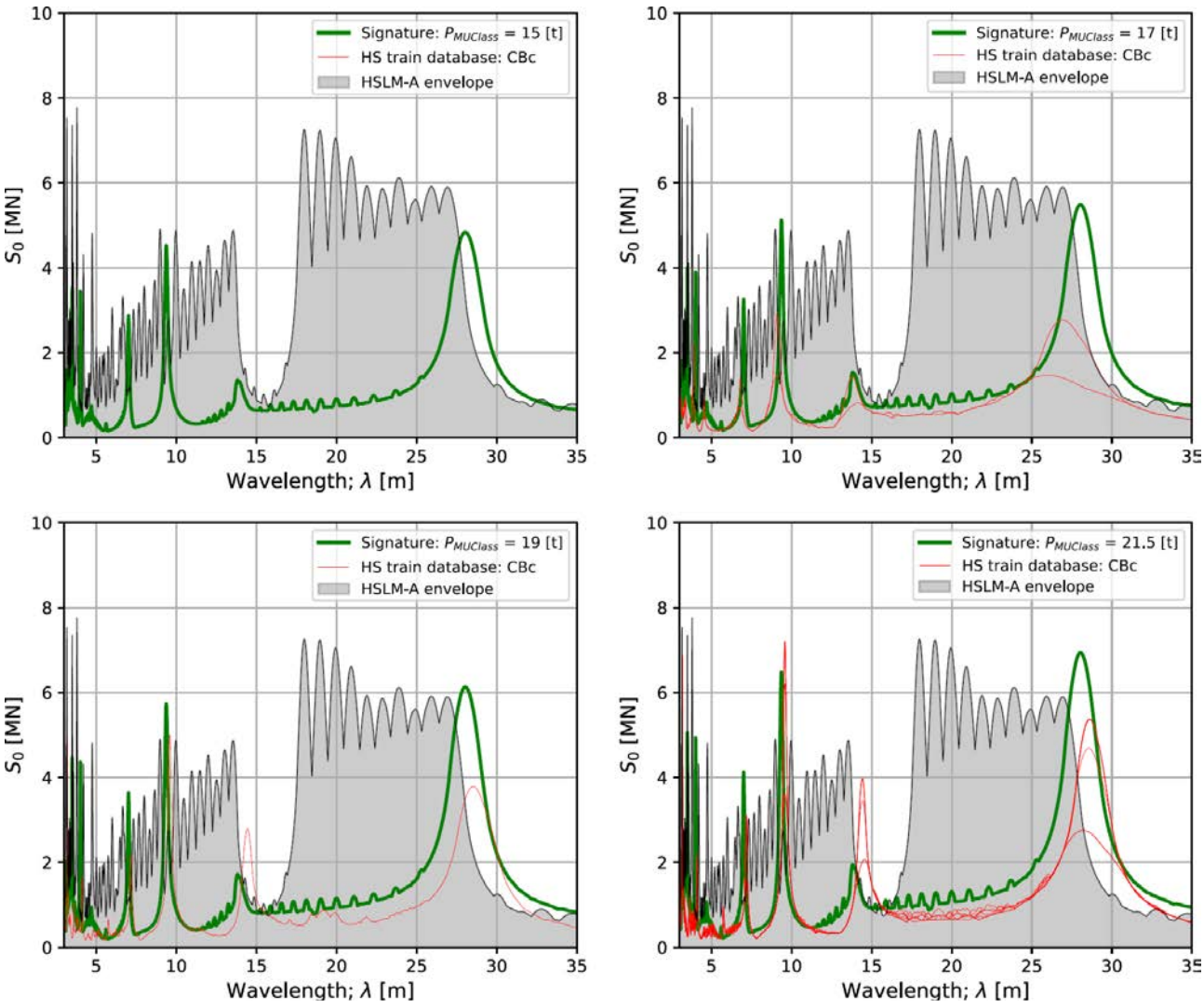

Figure 42. Comparison between the DTC2 CBc train signatures and the signatures of real CBc trains grouped in the DTC2 sub-categories (all speeds above 200 km/h); (top left) trains with $P_{max} \leq 15$ *t, (top right) trains with* $15 < P_{max} \leq 17$ *t, (bottom left) trains with* $17 < P_{max} \leq 19$ *t, and (bottom right) trains with* $19 < P_{max} \leq 21.5$ *t. The HSLM-A envelope is also included for reference.*

6.2 Trains with Articulated Bogies: AB

The starting point for the optimisation of AB trains within DTC2 is to identify the distinct subgroups present in this train type based on their signature characteristics. Figure 43 presents the signatures of real passenger trains belonging to the AB1, AB2, AB3 and AB4 subgroups defined in EN 15528:2015 (DTC0), alongside the corresponding reference trains from that standard. According to the classification, AB1 trains are characterised by coach lengths *D* (see Figure 34) between 14.9 m and 16 m, together with other geometric constraints considered in the preparation of Figure 43. AB2 trains have coach lengths in the range 18.8–19.5 m, AB3 trains between 17.0 m and 17.5 m, and AB4 trains between 18.7 m and 19.2 m.

From this subgrouping proposed in EN 15528:2015, it is evident that not all AB2 trains are adequately covered by the DTC0 reference train in the spectral valley region around 15–16 m, with additional exceedances observed elsewhere. The AB3 reference train provides better coverage for its corresponding subgroup, although the primary resonant peak occurs for mixed coach lengths in the 17–18 m range, appearing at slightly

shorter wavelengths than those of the AB3 reference train. These observations indicate that within each AB sub-family, there exist distinct groups of trains whose signature characteristics are not fully captured by the reference DTC0 trains.

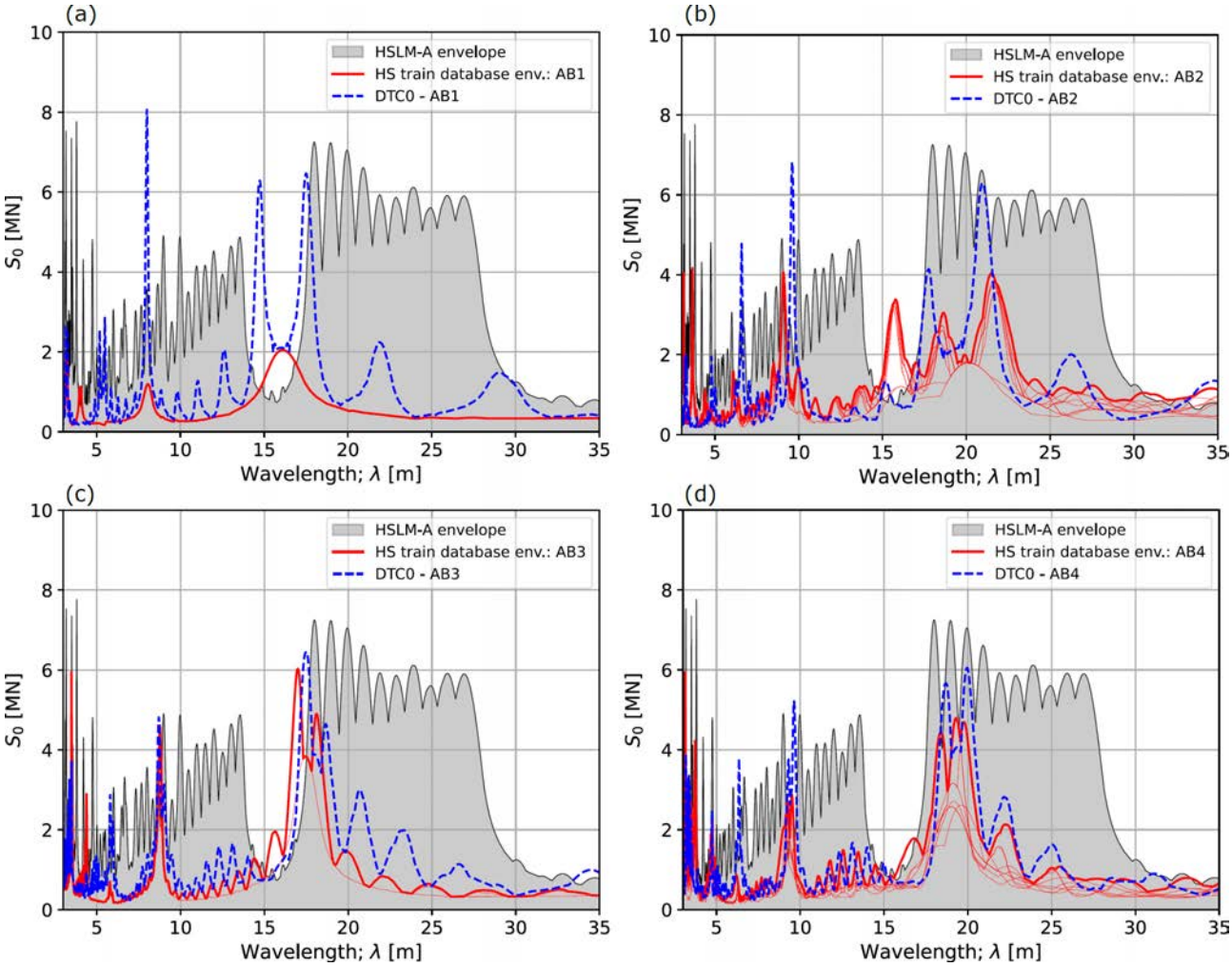

Figure 43. Envelope of the signatures of real AB trains grouped in the DTC0 sub-categories (all speeds above 200 km/h); (a) AB1 trains, (b) AB2 trains, (c) AB3 trains, (d) AB4 trains. The HSLM-A and DTC0 envelopes are also included for reference.

Based on this, 3 new reference AB trains are proposed in DTC2 with the following grouping:

	Reference train ABa	**Reference train ABb**	**Reference train ABc**
Coach length *D* [m]	$17 \leq D < 18$	$18 \leq D < 18.6$	$18.6 \leq D < 19.2$

Table 3. Categorisation of AB trains in DTC2 in terms of their coach length.

This classification yields three real passenger trains grouped into the ABa family, 11 into ABb, and 7 into ABc. A further 11 articulated trains with coach lengths below 11 m (approximately 10 m) are intentionally excluded from DTC2, as their geometry differs significantly from the rest and their maximum operating speed is limited to 200 km/h.

It is also remarked that other geometric parameters used in the DTC0 subgroup definitions from EN 15528:2015 are deliberately omitted in the proposed DTC2 framework. This simplification facilitates the

categorisation of real trains into families with consistent vibration signatures, disregarding parameters that have marginal influence on dynamic response or may not be readily available for all trains.

The axle configuration of the reference AB trains is defined as a long, repetitive formation characterised by the design vector $\mathbf{s} = (D, d_{\mathrm{BA}})$, where D is the coach length and d_{BA} is the axle spacing within each bogie. These geometric parameters are illustrated in Figure 34 (middle).

The reference AB trains in DTC2 are based on a simplified TGV-type pattern. Each train consists of front and rear locomotives, each equipped with two bogies and axle spacings at 0, 3, 14 and 17 m. A coupling gap of 3.15 m, denoted L_{gap}, separates the last axle of each locomotive from the first axle of the adjacent transition car. These transition cars feature a bogie with an axle spacing of 3 m located near the locomotive. The centre of this bogie is positioned at a distance D from the centre of the next bogie, which is shared between the transition car and the first normal passenger car. Between the two transition cars, a total of $N_{\mathrm{coach}} - 2$ identical passenger cars are inserted, each following the axle arrangement depicted in Figure 34 (middle). Note that N_{coach} refers to all the passenger coaches, including the two transition ones.

Consequently, the position of the first axle in the front bogie of the transition car is:

$$x_{1,0} = L_{\mathrm{loco}} + L_{\mathrm{gap}} \tag{16}$$

where x refers to the distance from the front axle of the train, L_{loco} is the length of the locomotive.

The centre of the subsequent i-th articulated bogie is located at:

$$x_{i,0} = x_{1,0} + i \cdot D \quad \text{for } i = 1, \ldots, N \tag{17}$$

in which N is the total number of articulated bogies (including those associated with transition cars and normal passenger cars), and D is the coach length (distance between successive bogie centres).

Each articulated bogie carries two axles. For the i-th bogie centre located at $x_{i,0}$, the two axles are positioned at:

$$\text{Axle 1:} \quad x_{i,0} - \frac{d_{\mathrm{BA}}}{2} \tag{18}$$

$$\text{Axle 2:} \quad x_{i,0} + \frac{d_{\mathrm{BA}}}{2} \tag{19}$$

6.2.1 ABa reference train

Figure 44(a) includes the dimensionless signatures of the real ABa trains in the database, and the corresponding smoothed signature ($S^*_{0,target}$) used in the optimisation process.

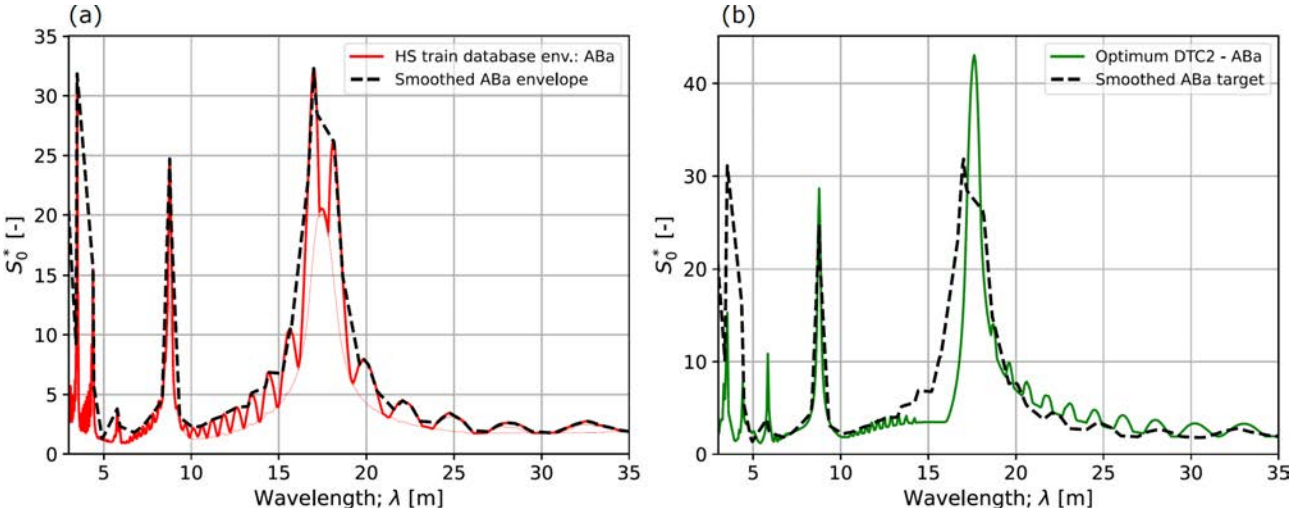

Figure 44. (a) Dimensionless signature of the real passenger trains in the ABa sub-group and smooth envelope $S^*_{0,target}$, (b) dimensionless signature of the optimised ABa train in DTC2 ($S_0^{*,model}$) compared with $S^*_{0,target}$.

The objective of the optimisation is to minimise the residual between the signature of the reference train and the target signature, as formulated in Eq. (7), using the reference AB axle distribution described in Eqs. (16)–(19). For the ABa train, the optimisation begins with an initial guess vector $\mathbf{s}_{\text{init}} = (17.5, 2.5)$ m, and the search is constrained within the coach length range observed for the ABa family: $D \in (17, 18)$ m, together with $d_{\text{BA}} \in (2, 3)$ m.

After several iterations, the optimised reference ABa train is obtained, with its axle configuration illustrated in Figure 45 (top). The train comprises 22 coaches, has a total length of 428.4 m, and is defined by the optimised design vector $\mathbf{s} = (D, d_{\text{BA}}) = (17.53, 2.49)$ m. The axle spacing in this train is given in Appendix B. In that appendix the train is referred to as ABa_1 to distinguish it from the extended DTC2 trains (DTC2e) that will be introduced in Section 7.

Figure 44(b) compares the smoothed target signature with that of the optimised ABa train. The results show that the main resonant peaks are adequately captured. However, the peak corresponding to the coach length at approximately $\lambda \approx 17.5$ m is narrower than the target, reflecting the variation in coach lengths among real AB trains. As a consequence, portions of the target signature lie above the reference model in this region.

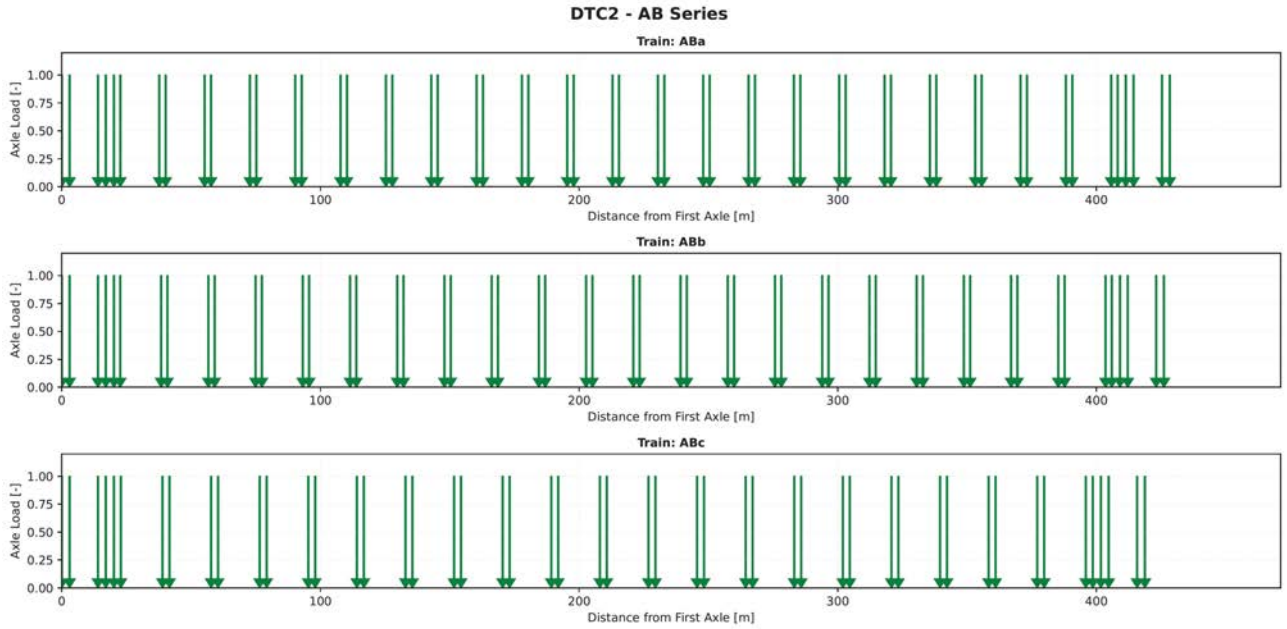

Figure 45. Axle spacing in the AB trains of DTC2.

Once the axle configuration of the ABa train is established, axle loads are assigned according to the four P_{MUclass} categories: 21.5 t, 19.0 t, 17.0 t and 15.0 t. Figure 46 presents the signatures of the real trains grouped by this classification, alongside the corresponding reference ABa trains. It is observed that real passenger ABa trains fall exclusively into the $P_{\mathrm{MUclass}} = 21.5$ t category. Overall, the reference ABa trains provide adequate coverage of the real train signatures across the entire wavelength range, with the exception of a marginal exceedance in the region between $\lambda \approx 16$ m and 17 m. The vibrations induced by these trains in the selected set of bridges will be examined in the following sections.

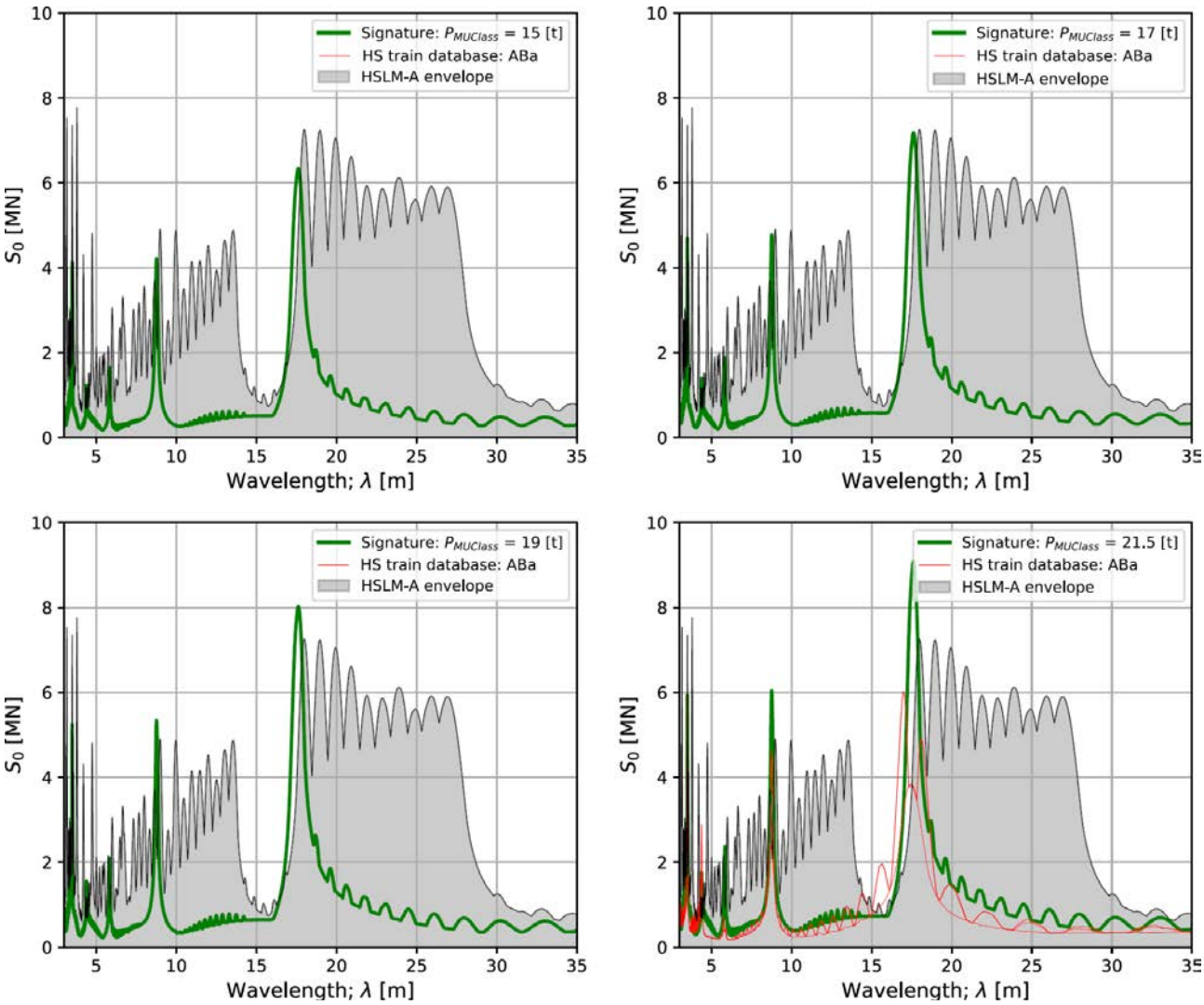

Figure 46. Comparison between the DTC2 ABa train signatures and the signatures of real ABa trains grouped in the DTC2 sub-categories (all speeds above 200 km/h); (top left) trains with $P_{max} \leq 15$ *t, (top right) trains with* $15 < P_{max} \leq 17$ *t, (bottom left) trains with* $17 < P_{max} \leq 19$ *t, and (bottom right) trains with* $19 < P_{max} \leq 21.5$ *t. The HSLM-A envelope is also included for reference.*

6.2.2 ABb reference train

Figure 47(a) includes the dimensionless signatures of the real ABb trains in the database, and the corresponding smoothed signature ($S^*_{0,target}$).

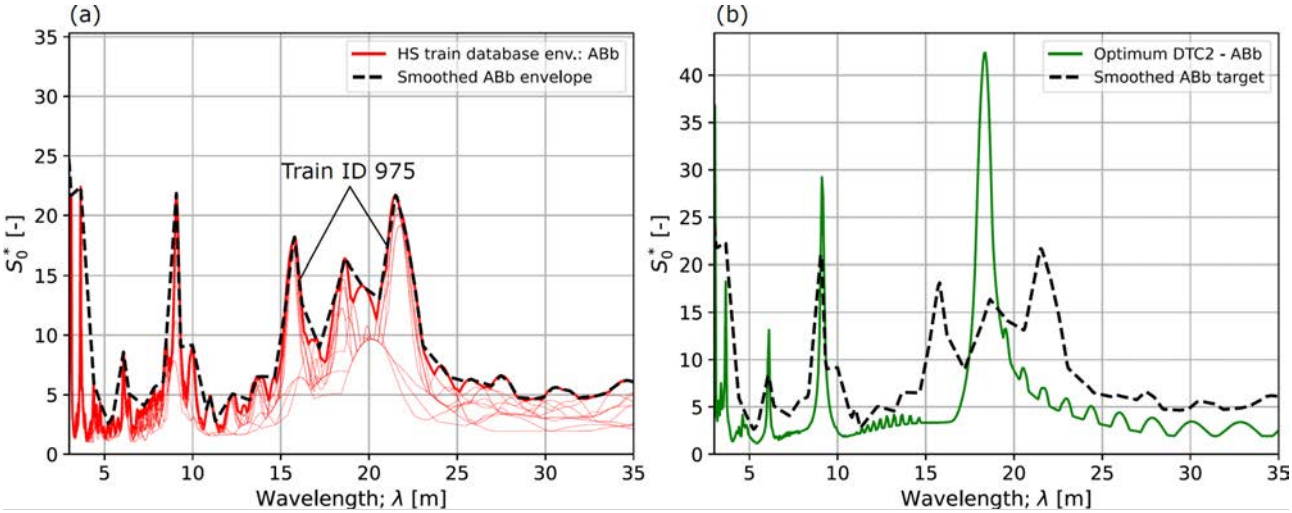

Figure 47. (a) Dimensionless signature of the real passenger trains in the ABb sub-group and smooth envelope $S^*_{0,target}$, (b) dimensionless signature of the optimised ABb train in DTC2 ($S_0^{*,model}$) compared with $S^*_{0,target}$.

The optimisation for the ABb train follows the reference axle distribution defined in Eqs. (16)–(19). An initial guess of $\mathbf{s}_{\text{init}} = (18.3, 2.5)$ m is adopted, with the search constrained within the coach length range characteristic of the ABb family: $D \in (18,18.6)$ m and $d_{\text{BA}} \in (2,3)$ m. After several iterations, the optimised reference ABb train is obtained, with its axle configuration shown in Figure 45 (middle). The train consists of 21 coaches, has a total length of 426.2 m, and is defined by the optimised design vector $\mathbf{s} = (D, d_{\text{BA}}) = (18.26,2.44)$ m. The detailed axle spacing is provided in Appendix B, which is referred to as ABb_1 to distinguish it from the extended DTC2 trains (DTC2e) that will be introduced in Section 7.

Figure 47(b) compares the smoothed target signature with that of the optimised ABb train. Although the optimised train significantly exceeds the target at the coach length peak near 18 m, it deviates notably from the target at wavelengths of approximately 16 m and 23 m. This discrepancy arises from a subset of real ABb trains for which the coach length is not the sole contributor to long-wavelength excitation. A representative example is train ID 975 in the database, which has a coach length of around 18 m but exhibits distinct signature peaks at 23 m and 16 m. These features are likely attributable to axle patterns associated with coupling between different units. Such effects cannot be captured by the simplified, highly idealised AB train formulation described in Eqs. (16)–(19), which lacks intermediate couplings or other complex features along the train length. Consequently, the proposed ABb train in DTC2 is designed as a resonant train that exaggerates the coach-length peak while underestimating other peaks present in more complex real trains. Despite these limitations, it was decided to retain the proposed ABb train to evaluate the impact of these discrepancies on bridge acceleration responses and to maintain consistency with the other reference trains developed in this work.

Following the definition of the axle configuration, the magnitude of the axle loads is assigned according to the four P_{MUclass} categories: 21.5 t, 19.0 t, 17.0 t and 15.0 t. Figure 48 presents the signatures of real trains grouped by this classification, alongside the corresponding reference ABb trains. It is observed that real passenger ABb trains fall exclusively into the $P_{\text{MUclass}} = 19$ t category. The substantial differences between the dimensionless spectrum of the reference ABb train and the target translate into significant exceedances in the dimensional

signature at wavelengths of 16 m and 23 m. While the latter is covered by HSLM-A, the former is not. This provides an early indication that the ABb reference train may not fully capture the dynamic effects induced by real ABb trains in bridges, a point that will be further explored in the following sections.

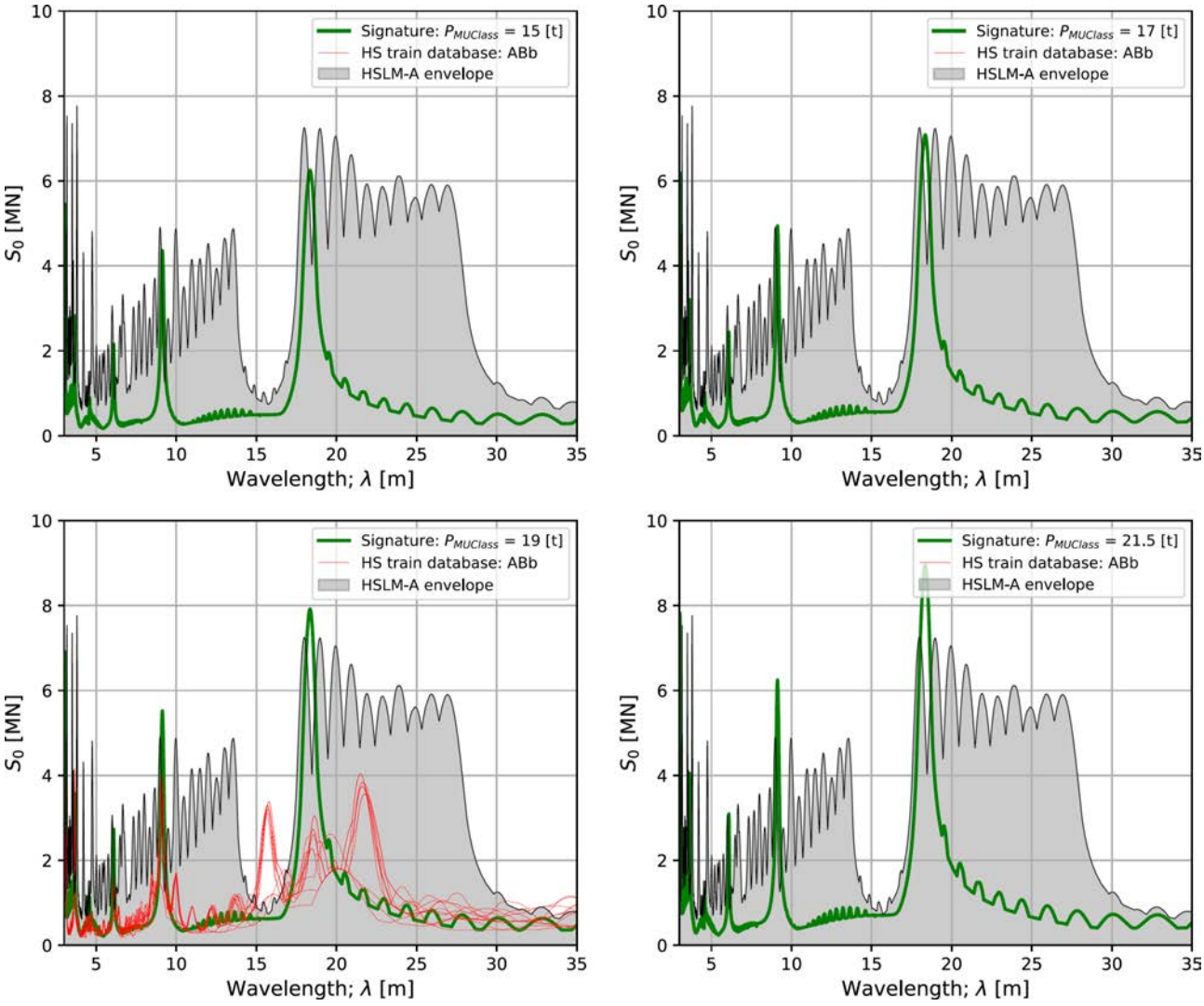

Figure 48. Comparison between the DTC2 ABb train signatures and the signatures of real ABb trains grouped in the DTC2 sub-categories (all speeds above 200 km/h); (top left) trains with $P_{max} \leq 15$ *t, (top right) trains with* $15 < P_{max} \leq 17$ *t, (bottom left) trains with* $17 < P_{max} \leq 19$ *t, and (bottom right) trains with* $19 < P_{max} \leq 21.5$ *t. The HSLM-A envelope is also included for reference.*

6.2.3 ABc reference train

Figure 49(a) presents the dimensionless signatures of the real ABc passenger trains in the database, and the associated smooth signature ($S^*_{0,target}$) taken as a target in the optimisation framework.

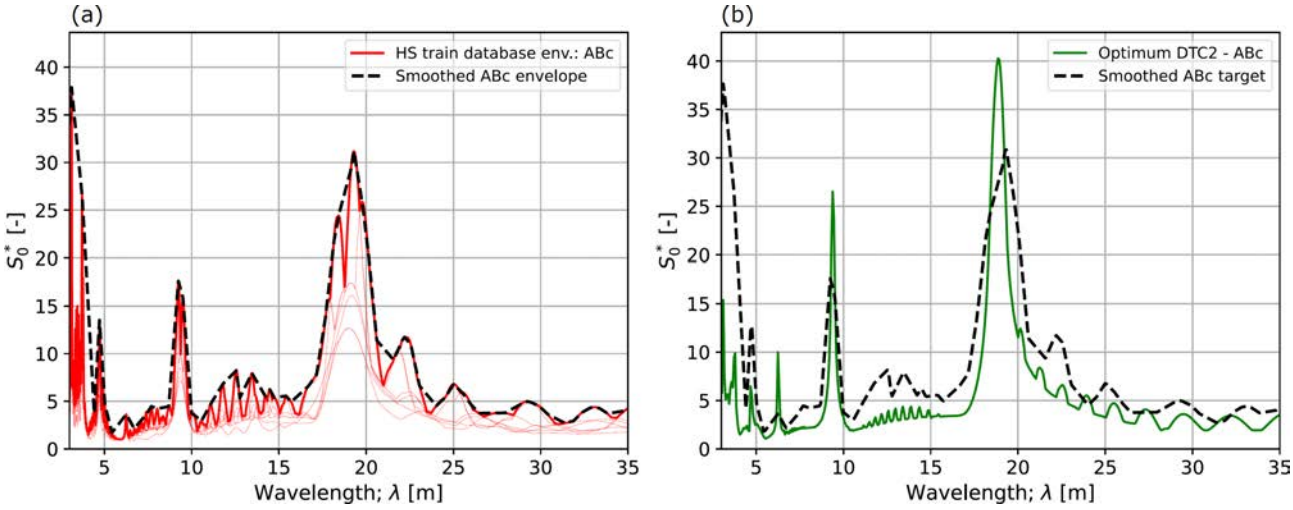

Figure 49. (a) Dimensionless signature of the real passenger trains in the ABc sub-group and smooth envelope $S^*_{0,target}$, (b) dimensionless signature of the optimised ABc train in DTC2 ($S_0^{*,model}$) compared with $S^*_{0,target}$.

The optimisation for the ABc train follows the reference axle distribution defined in Eqs. (16)–(19), with the objective of minimising the residual between the reference train signature and the target signature as formulated in Eq. (7). The optimisation begins with an initial guess vector $\mathbf{s}_{\text{init}} = (18.9, 2.5)$ m, and the search is constrained within the coach length range characteristic of the ABc family: $D \in (18.6, 19)$ m, together with $d_{\text{BA}} \in (2, 3)$ m. After several iterations, the optimised reference ABc train is obtained, with its axle configuration shown in Figure 45 (bottom). The train comprises 20 coaches, has a total length of 418.8 m, and is defined by the optimised design vector $\mathbf{s} = (D, d_{\text{BA}}) = (18.80, 2.68)$ m. The detailed axle spacing is provided in Appendix B, in which this train is referred to as ABc_1 to differentiate it from the extended DTC2 trains (DTC2e) that will be introduced in Section 7. Figure 49(b) compares the smoothed target signature with that of the optimised ABc train. The results indicate that the main resonant peaks are adequately captured.

Once the axle configuration is defined, axle loads are assigned according to the four P_{MUclass} categories: 21.5 t, 19.0 t, 17.0 t and 15.0 t. Figure 50 presents the signatures of real trains grouped by this classification, alongside the corresponding reference ABc trains. It is observed that the signatures of real passenger ABc trains are generally well covered by the reference ABc trains. However, for the $P_{\text{MUclass}} = 19$ t category, some exceedances are noted in the wavelength ranges of 12–15 m and 20–22 m.

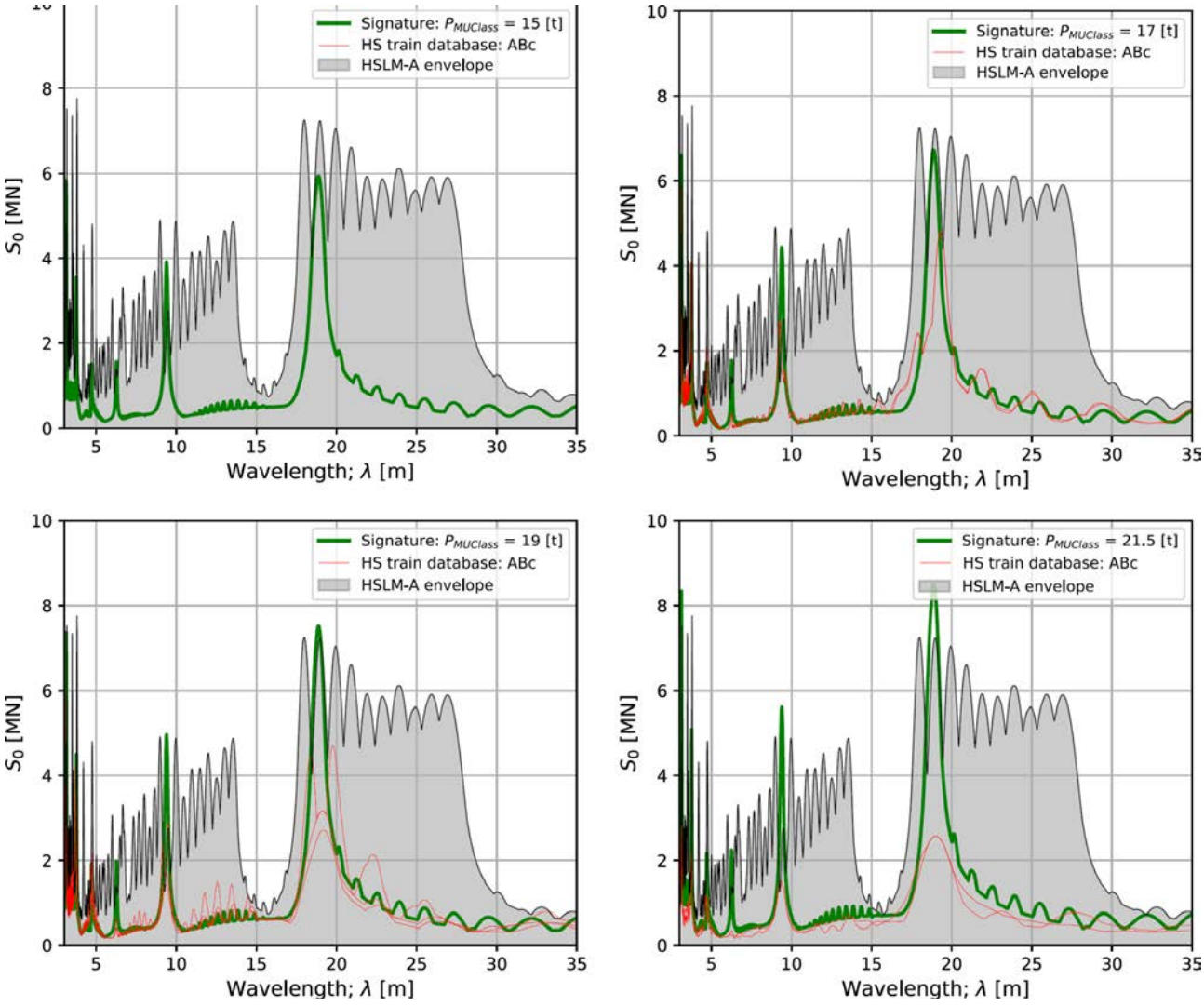

Figure 50. Comparison between the DTC2 ABc train signatures and the signatures of real ABc trains grouped in the DTC2 sub-categories (all speeds above 200 km/h); (top left) trains with $P_{max} \leq 15$ *t, (top right) trains with* $15 < P_{max} \leq 17$ *t, (bottom left) trains with* $17 < P_{max} \leq 19$ *t, and (bottom right) trains with* $19 < P_{max} \leq 21.5$ *t. The HSLM-A envelope is also included for reference.*

6.3 Trains with Single Axles: SA

As with the other train categories, the optimisation of SA trains within DTC2 begins by identifying distinct subgroups based on their signature characteristics. A classification of passenger SA trains according to the subgroups defined in EN 15528:2015 (DTC0) revealed that only those meeting all geometric conditions specified in the standard fall into the SA2 subgroup, while no trains in the database correspond to SA1.

Figure 51 presents the signatures of real trains in both subgroups (SA1 empty, SA2 populated), alongside the corresponding reference trains from DTC0. The SA2 trains exhibit a clear resonant peak at approximately $\lambda \approx 13.1$ m, corresponding to the characteristic coach length of single-axle formations. This peak is well represented by the reference SA2 train in DTC0. However, the first subharmonic of the reference train is slightly shifted, leaving the signatures of real trains uncovered around $\lambda \approx 6$ m. Furthermore, in the wavelength region between the resonant peak and its subharmonic, from approximately 7 m to 12 m, real trains exhibit higher signature amplitudes than the reference train, indicating a richer axle spacing configuration not

captured by the idealised DTC0 model. These observations highlight that, within the SA family, there exist trains whose signature characteristics are not fully enveloped by the reference DTC0 trains, motivating the refinement proposed in DTC2.

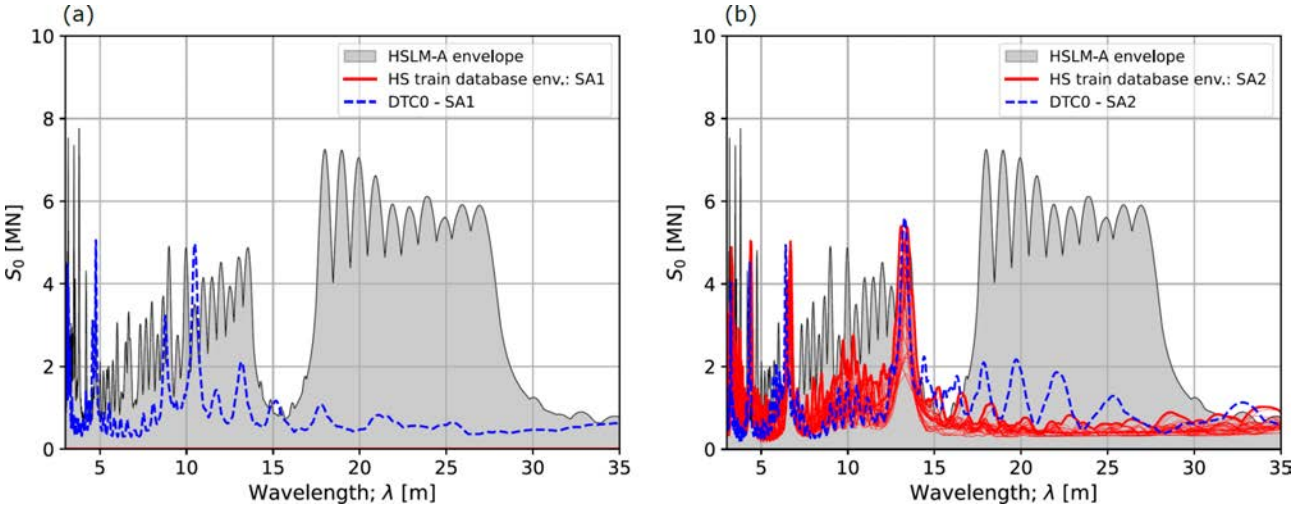

Figure 51. Envelope of the signatures of real SA trains grouped in the DTC0 sub-categories (all speeds above 200 km/h); (a) SA1 trains, (b) SA2 trains. The HSLM-A and DTC0 envelopes are also included for reference.

Based on the signature analysis, two new reference SA trains are proposed within DTC2, with the following grouping:

	Reference train SAa	**Reference train SAb**
Coach length *D* [m]	$13 \leq D < 13.2$	$13.2 \leq D < 13.4$

Table 4. Categorisation of SA trains in DTC2 in terms of their coach length.

In this categorisation the sub-group Saa has 7 real passenger trains, and SAb includes 43 trains.

As noted previously, other geometric parameters from the DTC0 subgroup definitions in EN 15528:2015 are deliberately omitted in the proposed DTC2 framework. This simplification enables a more practical categorisation of real trains into families with consistent vibration signatures, disregarding parameters that have marginal influence on dynamic response or may not be readily available for all trains.

The axle configuration of the reference SA trains is defined as a long, repetitive formation characterised by the design vector $\mathbf{s} = (D, d_{\mathrm{BA}})$, where D is the coach length. These geometric parameters are illustrated in Figure 34 (bottom). The reference SA trains in DTC2 are based on a simplified version of the S106 train configuration. Each train consists of front and rear locomotives, each equipped with two bogies and axle spacings at 0.0, 2.8, 10.8 and 13.6 m. A coupling gap of 4.4 m, denoted L_{gap}, separates the last axle of each locomotive from the first axle of the adjacent transition car. These transition cars feature a single axle at their connection point, located at a distance D from the interface between the transition car and the first conventional coach. Between the two transition cars, a total of $N_{\mathrm{coach}} - 2$ identical passenger cars are inserted, each following the axle arrangement shown in Figure 34 (bottom), with single axles located at the car connections. Note that N_{coach} refers to all passenger coaches, including the two transition cars.

The position of the first transition axle (located after the front locomotive) is:

$$x_{\mathrm{trans},1} = L_{\mathrm{loco}} + L_{\mathrm{gap}} \tag{20}$$

The position of the first rodal axle (at the connection between the transition car and the first normal car) is:

$$x_{\text{rodal},1} = x_{\text{trans},1} + D \tag{21}$$

For the subsequent k normal cars, where $k = 1, \ldots, N_{\text{coach}} - 1$ and N_{coach} is the total number of passenger coaches (including transition cars), the rodal axles are located at:

$$x_{\text{rodal},k+1} = x_{\text{rodal},1} + k \cdot D \tag{22}$$

The rear transition axle (after the last normal car) is positioned at:

$$x_{\text{trans},2} = x_{\text{rodal},1} + N_{\text{coach}} \cdot D \tag{23}$$

Finally, the rear locomotive starts at:

$$x_{\text{rear,loco}} = x_{\text{trans},2} + L_{\text{gap}} \tag{24}$$

6.3.1 SAa reference train

Figure 52(a) presents the dimensionless signatures of the real SAa trains in the database, and the corresponding smoothed signature ($S^*_{0,target}$) used in the optimisation process.

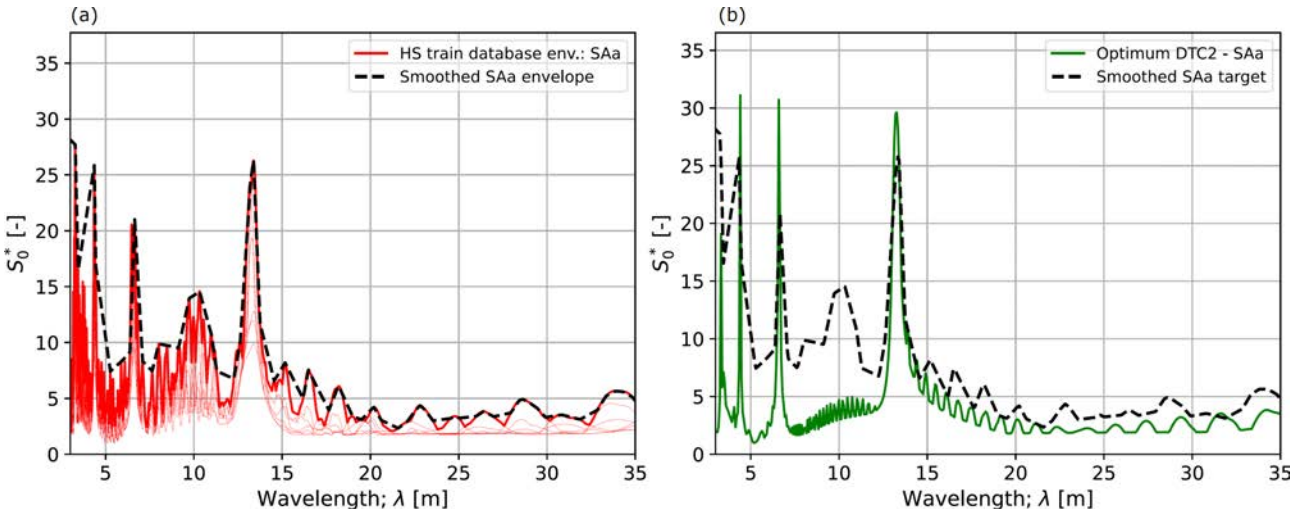

Figure 52. (a) Dimensionless signature of the real passenger trains in the SAa sub-group and smooth envelope $S^*_{0,target}$, (b) dimensionless signature of the optimised SAa train in DTC2 ($S_0^{*,model}$) compared with $S^*_{0,target}$.

The simplicity of the SA reference train formulation described in Eqs. (20)–(24) allows the optimised axle configuration to be obtained through a manual adjustment process. By varying the coach length D and the number of coaches until the maximum admissible train length is reached, the signature can be fitted to the target shown in Figure 52(a). Given that the design vector reduces to a single scalar $s = D$, a formal optimisation procedure is not required for the SA reference trains. The resulting reference SAa train is presented in Appendix B, with its axle configuration illustrated in Figure 53 (top). In Appendix B this train is referred to as SAa_1 to distinguish it from the extended DTC2 trains (DTC2e) that will be introduced in Section 7. The train comprises 29 coaches, has a total length of 432.0 m, and is defined by a coach length of $D =$ 13.2 m.

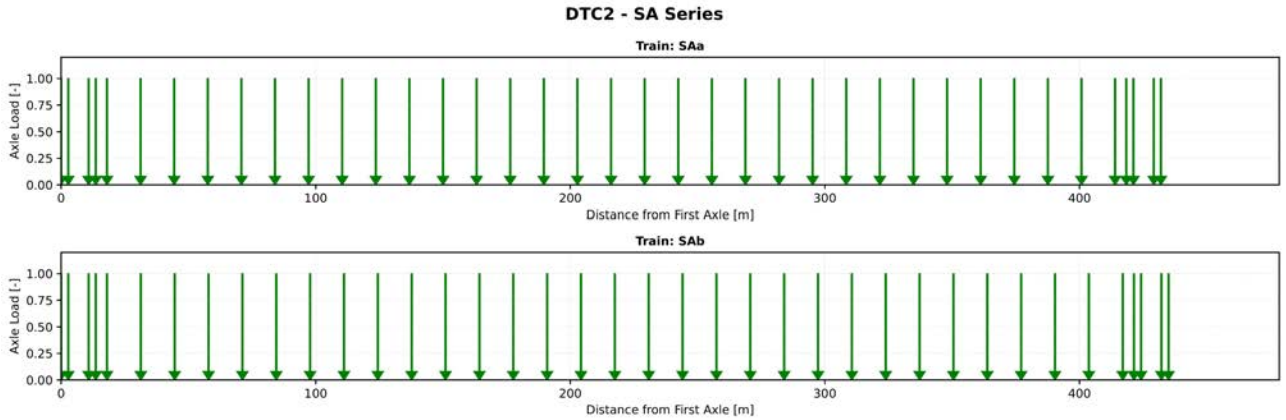

Figure 53. Axle spacing in the SA trains of DTC2.

Figure 52(b) compares the smoothed target signature with that of the optimised SAa train. The results indicate that while the main resonant peaks are adequately captured by the reference train, the signature in the intermediate regions between peaks falls below that of the real SAa trains. This discrepancy, which may be problematic for certain bridges, is attributed to the presence of patterns in real trains—such as couplers and unit arrangements—that are not represented in the idealised SA reference formulation.

Once the axle configuration of the SAa train is established, axle loads are assigned according to the four P_{MUclass} categories: 21.5 t, 19.0 t, 17.0 t and 15.0 t. Figure 54 presents the signatures of real trains grouped by this classification, alongside the corresponding reference SAa trains. It is observed that six of the real passenger SAa trains fall into the $P_{\mathrm{MUclass}} = 19$ t category, while only one belongs to the 21.5 t category. In both cases, the reference trains adequately cover the wavelength peak associated with the coach length and its first subharmonic. However, in the wavelength region between these two peaks, the real trains exhibit higher signature amplitudes than the reference train, although they generally remain below the HSLM-A envelope.

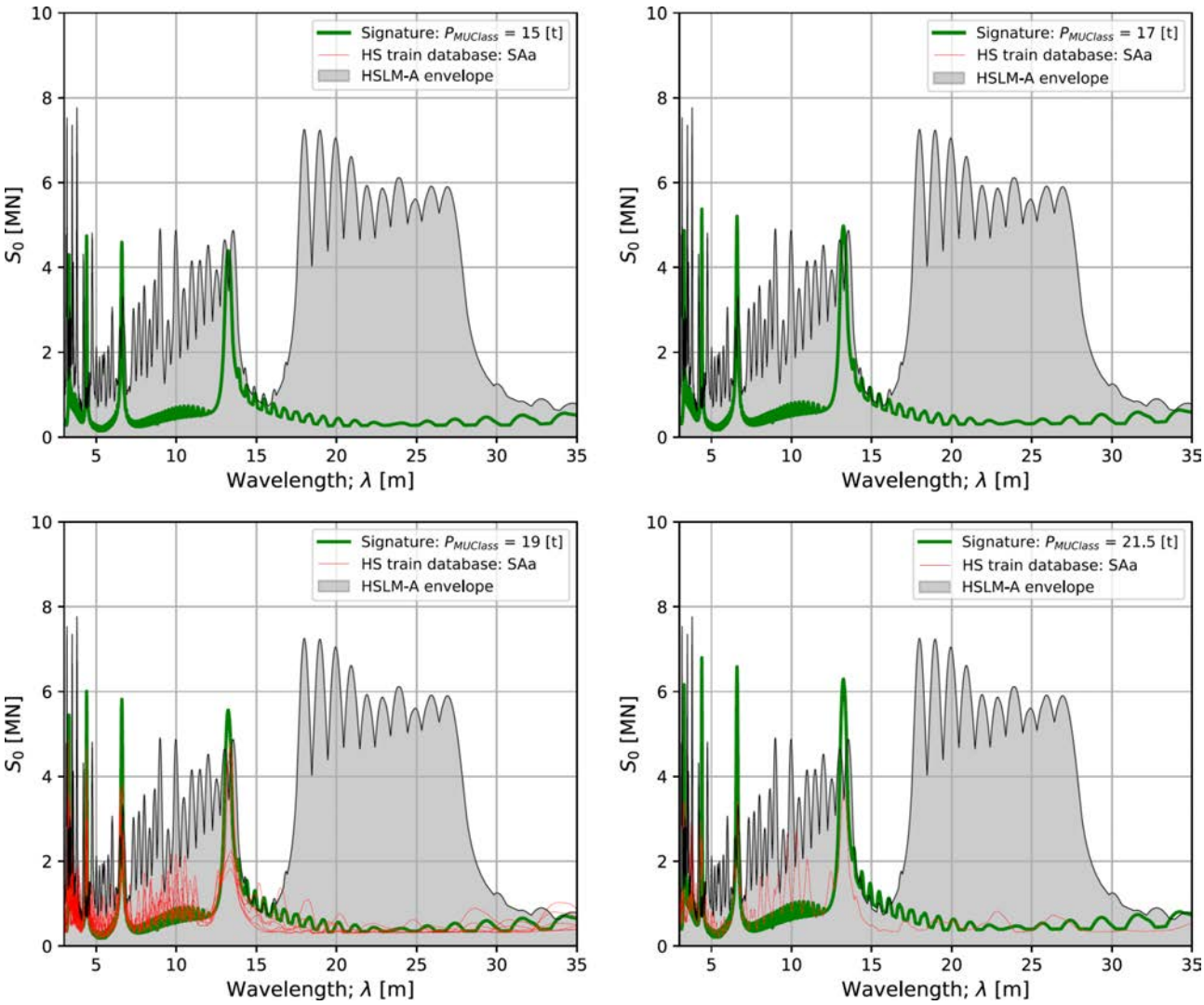

Figure 54. Comparison between the DTC2 SAa train signatures and the signatures of real SAa trains grouped in the DTC2 sub-categories (all speeds above 200 km/h); (top left) trains with $P_{max} \leq 15$ *t, (top right) trains with* $15 < P_{max} \leq 17$ *t, (bottom left) trains with* $17 < P_{max} \leq 19$ *t, and (bottom right) trains with* $19 < P_{max} \leq 21.5$ *t. The HSLM-A envelope is also included for reference.*

6.3.2 SAb reference train

The dimensionless signatures of the real SAb trains are shown in Figure 55(a), along with the corresponding smoothed signature ($S^*_{0,target}$).

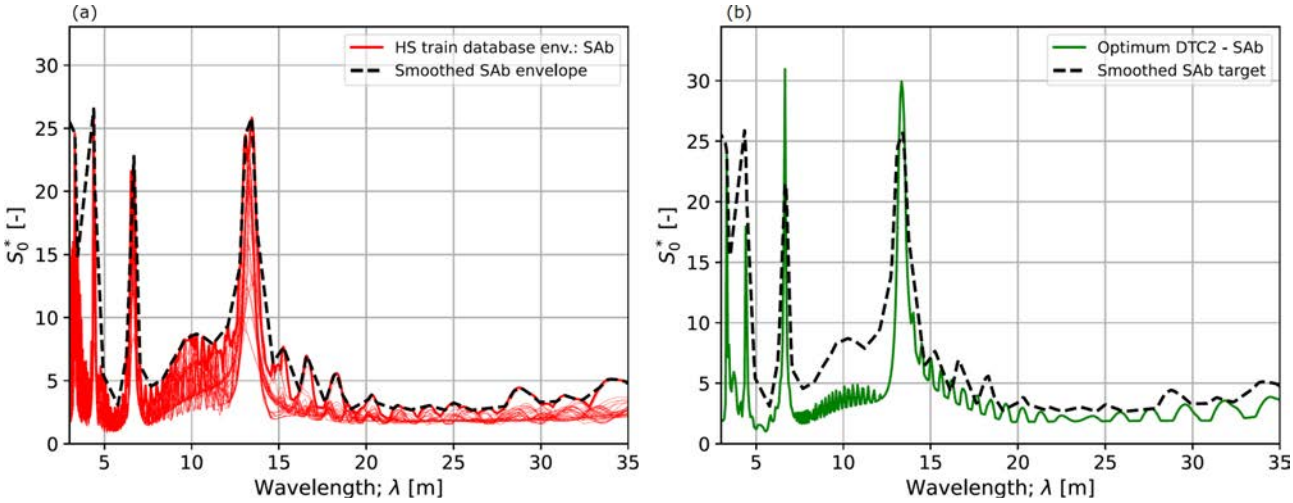

Figure 55. (a) Dimensionless signature of the real passenger trains in the SAa sub-group and smooth envelope $S^*_{0,target}$, (b) dimensionless signature of the optimised SAa train in DTC2 ($S_0^{*,model}$) compared with $S^*_{0,target}$.

The smoothed target signature shown in Figure 55(a) is used to adjust the coach length of the reference SAb train. The resulting configuration is presented in Appendix B, with its axle arrangement illustrated in Figure 53 (bottom). It is noted that in Appendix B the SAb train is referred to as SAb_1 to distinguish it from the extended DTC2 trains (DTC2e) that will be introduced in Section 7. The train comprises 29 coaches, has a total length of 435.0 m, and is defined by a coach length of $D = 13.3$ m.

Figure 55(b) compares the smoothed target signature with that of the optimised SAb train. As observed for the previous SA reference model, the main resonant peaks are adequately captured, but the signature in the intermediate regions between peaks falls below that of the real SAb trains.

Figure 56 presents the signatures of real trains meeting the SAb classification, alongside the corresponding reference SAb trains. Only one real passenger SAb train falls into the $P_{\mathrm{MUclass}} = 19$ t category, while the remaining 42 belong to the 21.5 t category. In the former case, the reference train provides adequate coverage of the real train signature. For the heavier trains in the 21.5 t category, the resonant peaks are well captured; however, in the wavelength region between these peaks, the real trains exhibit higher signature amplitudes than the reference train, although they generally remain below the HSLM-A envelope.

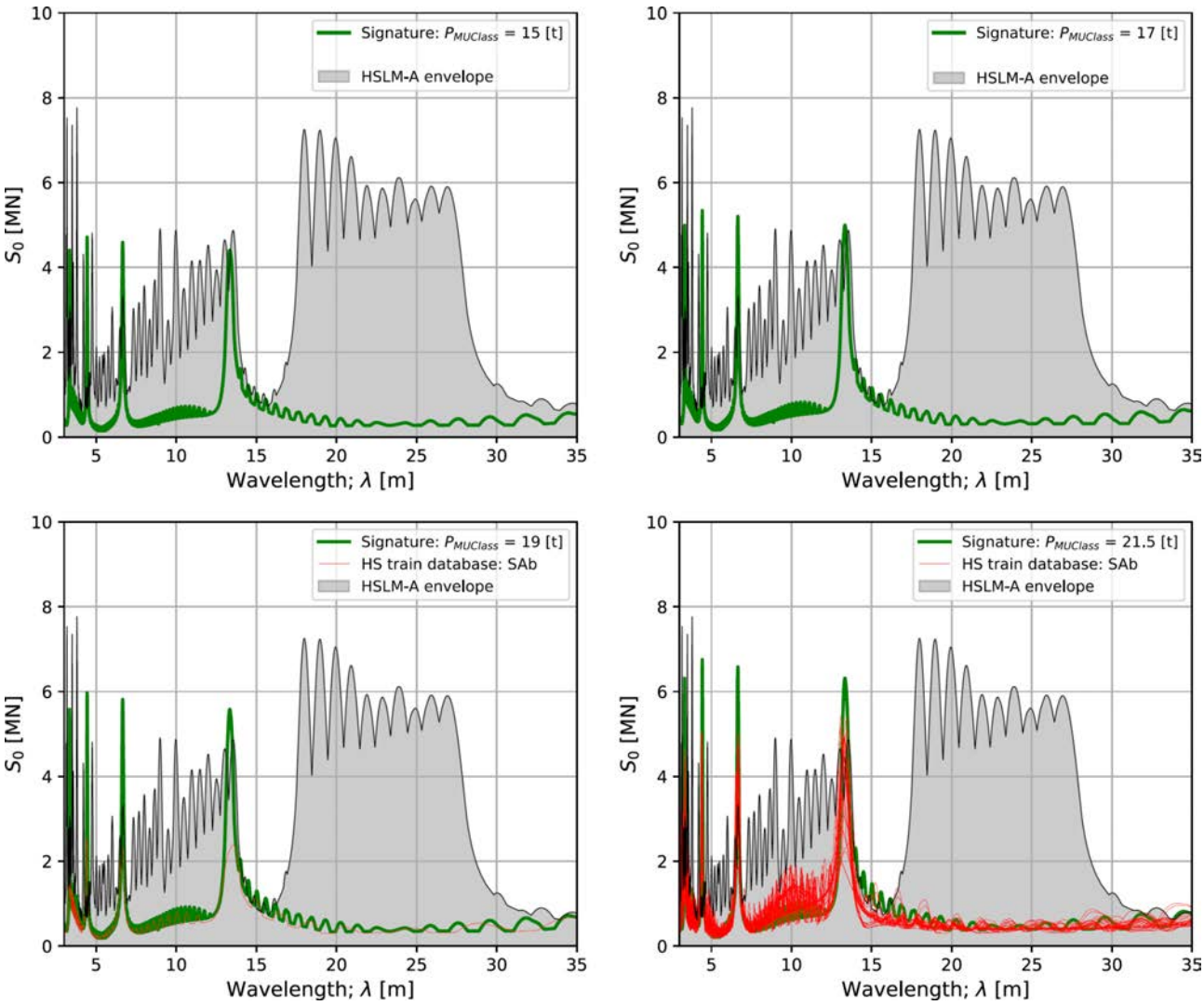

Figure 56. Comparison between the DTC2 SAb train signatures and the signatures of real SAb trains grouped in the DTC2 sub-categories (all speeds above 200 km/h); (top left) trains with $P_{max} \leq 15$ *t, (top right) trains with* $15 < P_{max} \leq 17$ *t, (bottom left) trains with* $17 < P_{max} \leq 19$ *t, and (bottom right) trains with* $19 < P_{max} \leq 21.5$ *t. The HSLM-A envelope is also included for reference.*

6.4 Peak accelerations obtained with LIR method

The dynamic response of the selected bridges under the proposed DTC2 trains was first evaluated using the LIR method. This section presents a selection of the resulting peak accelerations in a small subset of bridges and train typologies, comparing the effect of real trains and the existing reference load models (HSLM-A, DTC0 and DTC1). The results and detailed discussion on the accelerations obtained with LIR for all the trains crossing the whole set of bridges is not included for conciseness.

Figure 57 presents the peak vertical acceleration of bridge ID1 when subjected to real CBa trains across different weight categories, compared against the corresponding reference CBa train from DTC2 (formally denoted CBa_1 to differentiate it from the extended DTC2 trains presented in Section 7). The results show that the proposed CBa train closely matches the envelope of real train responses, demonstrating its representativeness of the dynamic effects induced by this subgroup in this specific bridge. This agreement holds across the various $P_{MUclass}$ categories, confirming that the weight-based differentiation in DTC2 enables

a more precise adjustment to the real trains of each line category. Similar results are obtained for other bridges subject to the action of the CBa resonant train.

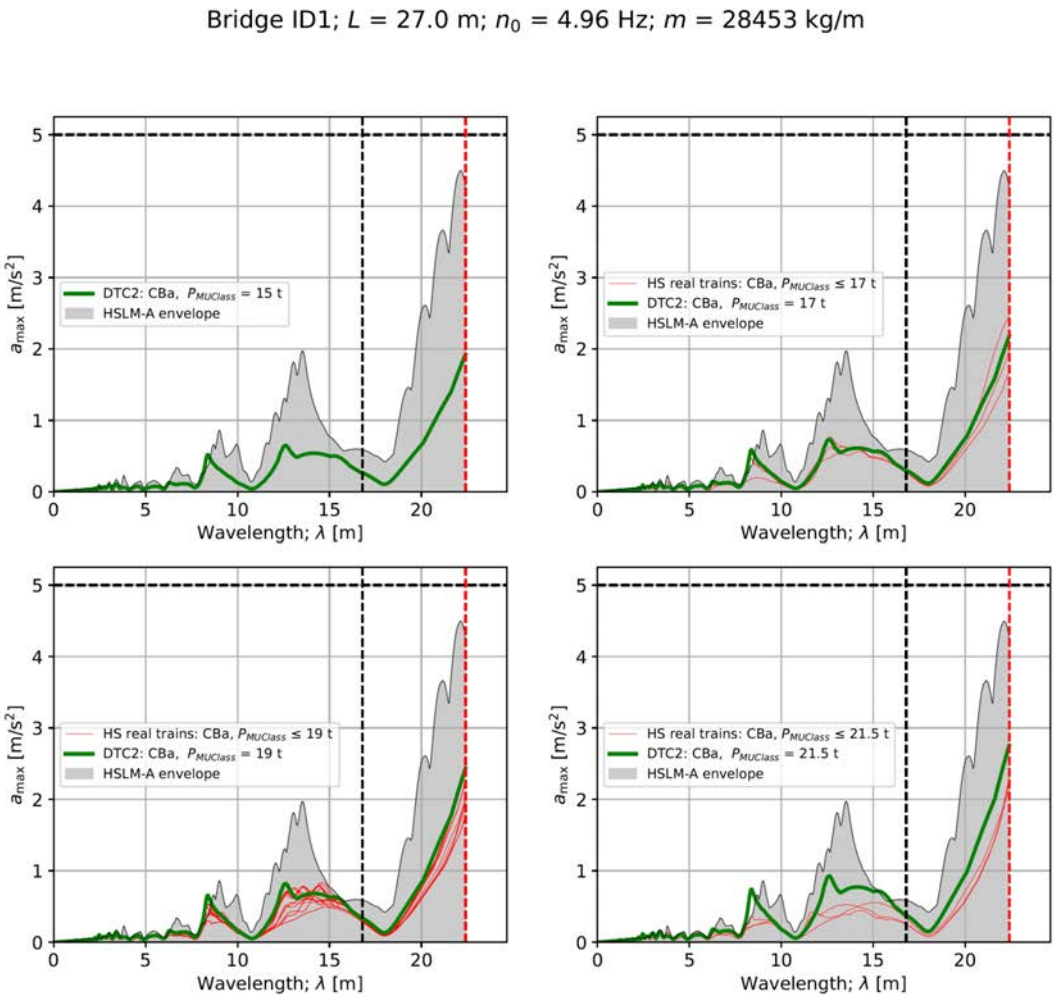

Figure 57. Peak vertical acceleration in the bridge ID1 when subject to real CBa trains of different weight categories, and comparison with the reference CBa train in DTC2. LIR method.

Focusing on the envelope of real train responses and on the aggregated behaviour of bridges grouped by their fundamental frequencies, Figure 58 presents the envelope of peak vertical accelerations for low-frequency bridges as a function of wavelength. This figure compares the response induced by real CBa trains with that of the reference CBa train from DTC2, the combined envelope of DTC0 and DTC1, and the HSLM-A trains. For consistency, the reference trains are shown with a uniform axle load of 19 t, corresponding to $P_{\mathrm{MUclass}} =$ 19 t in DTC2. It should be noted that while some real trains in the comparison may exceed this value (falling into higher weight categories), the envelope of peak accelerations is generally insensitive to the difference between 19 t and 21.5 t. This simplification is adopted for visual clarity, though weight category should be considered in detailed assessments, as it will be done later in Section 7. The results indicate that the CBa train in DTC2 generally captures the majority of peak accelerations induced by real CBa trains in low-frequency bridges. A notable exception occurs in the wavelength range $\lambda \approx$ 9–12 m for bridge ID 6, where real train responses exceed the DTC2 envelope, and this problem will be tackled later with the extension of the DTC2 in Section 7. However, it should be noted that the optimised DTC2 CBa train captures real train effects around $\lambda \approx$ 8.5 m that lie above the predictions of DTC0, DTC1 and HSLM-A. Overall, the combination of

the three DTCs provides a closer fit to the envelope of real train accelerations in low-frequency bridges under CBa traffic than HSLM-A alone, particularly considering DTC2.

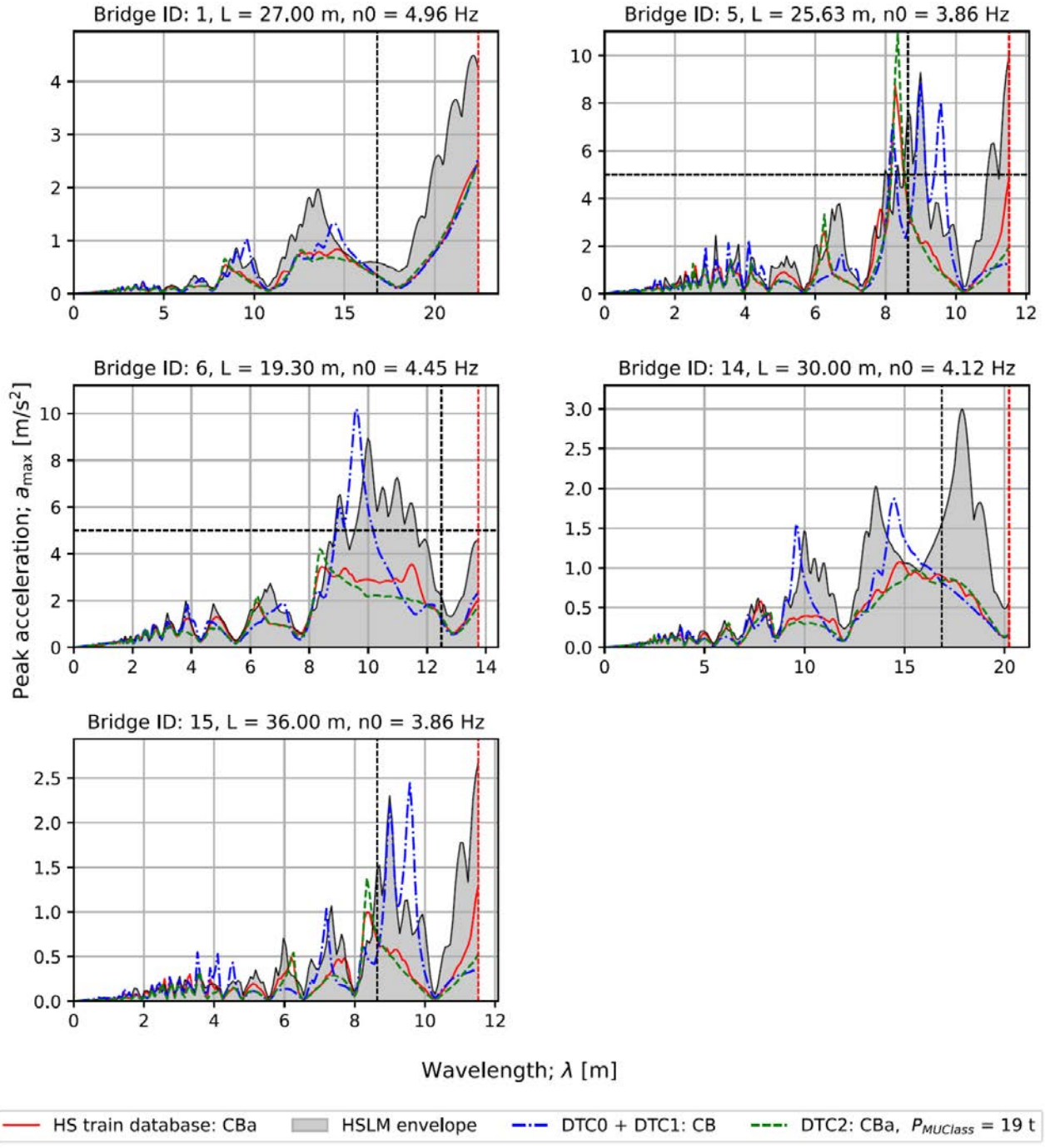

Figure 58. Envelope of the peak vertical acceleration in the bridges with 'low' frequency for different wavelengths. Comparison between real CBa trains, reference CBa train in DTC2, and reference trains in DTC0 and DTC1 (envelope of both), and HSLM-A trains. The reference trains have uniform axle weights of 19 t. LIR method.

The same observations can be drawn for different types of bridges and DTC2 trains. However, there are situations where real trains that can be categorised to specific DTC2 families exceed the accelerations induced in bridges, particularly in the cases in which the dimensionless signature of the optimised DTC2 train falls below the envelope of real trains in wavelengths regions that are usually between resonant peaks. As an example, Figure 59 shows the peak accelerations in the set of low-frequency bridges obtained with the SAa

reference train and with the real trains in the SAa family. It is clear that the reference DTC2 train is better adjusted to the envelope of the real trains than HSLM-A and DTC0+1 for most of the wavelengths, but there are localised regions in which real trains exceed the reference DTC2 vibrations. That is the case, for instance, of bridge ID14 for $12 < \lambda < 15$ m, and this is directly connected with the fact that the SAa reference train has a signature significantly below that of target obtained from real trains in this region of wavelengths, between the first and second subharmonics, as shown in Figure 52(b). Therefore, even though the SAa train produces vibrations that are generally enveloping those of the real trains in the corresponding family, it cannot be said that is completely representative of them for all the bridges.

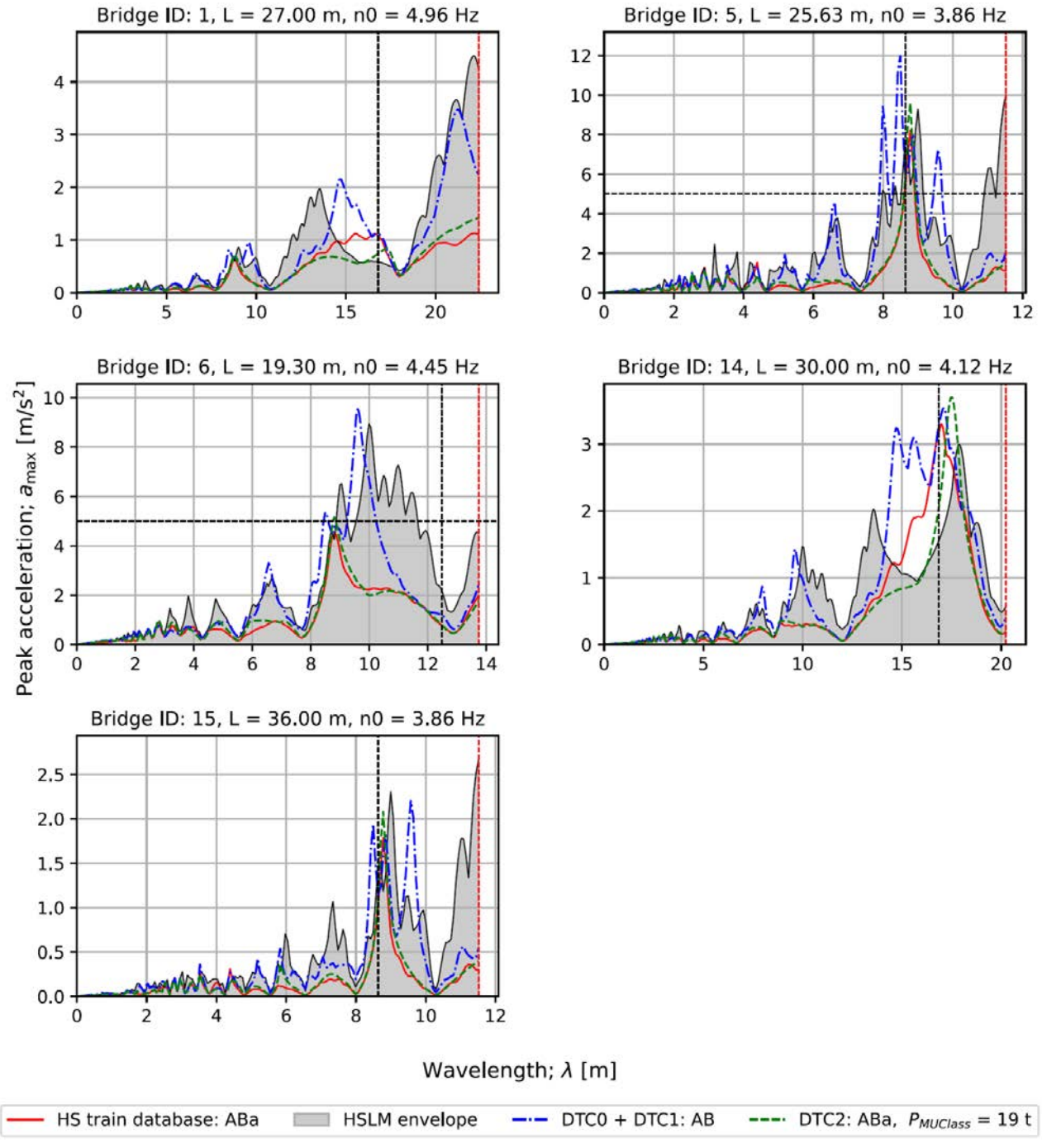

Figure 59. Envelope of the peak vertical acceleration in the bridges with 'low' frequency for different wavelengths. Comparison between real ABa trains, reference ABa train in DTC2, and reference trains in DTC0 and DTC1 (envelope of both), and HSLM-A trains. The reference trains have uniform axle weights of 19 t. LIR method.

The problem accentuates for the regular trains (SA) because the proposed optimised DTC2 trains are very specifically designed to target the resonant peaks by proposing a long and repetitive configuration, whilst real trains have a richer content of spatial frequencies given by details not included in the reference trains. The implications of this are observed, for example, in the SAa trains crossing the intermediate-frequency bridges, as shown in Figure 60. Clearly, the envelope of the bridge accelerations induced by real SAa trains is above that of the reference train SAa alone for wavelengths below 6 m (i.e. below the first subharmonic).

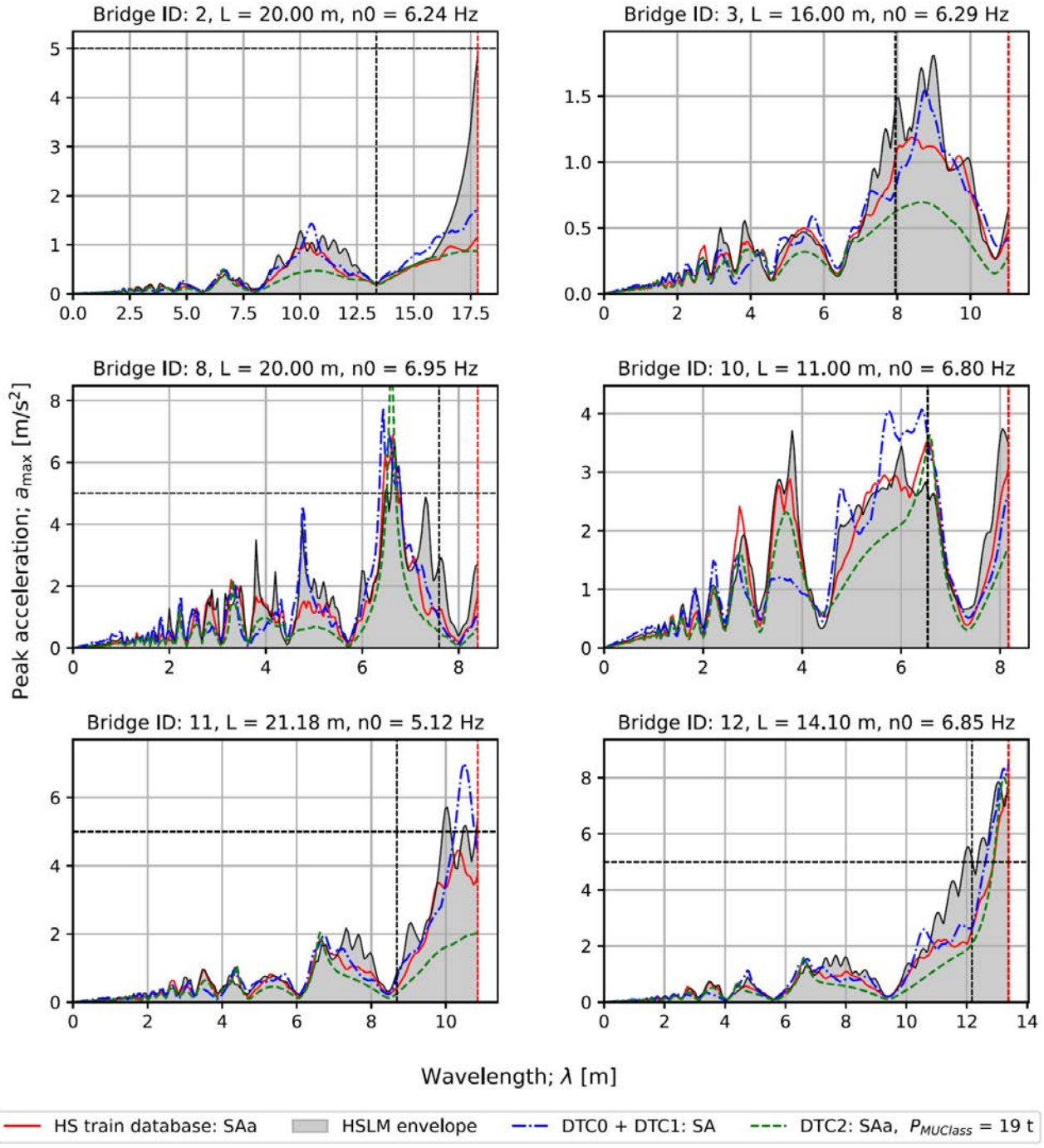

Figure 60. Envelope of the peak vertical acceleration in the bridges with 'intermediate' frequency for different wavelengths. Comparison between real SAa trains, reference SAa train in DTC2, and reference trains in DTC0 and DTC1 (envelope of both), and HSLM-A trains. The reference trains have uniform axle weights of 19 t. LIR method.

6.5 Peak accelerations obtained with time-stepping analysis

The accelerations introduced by the DTC2 reference trains in the proposed bridges were also calculated using Caldintav. These are consistent with those obtained with LIR and they will not be reported to avoid unnecessary details in the document.

7 DTC2e reference trains: an extension of DTC2

While the DTC2 resonant trains provide a robust envelope for the majority of real passenger trains within each sub-category, certain configurations exhibit dynamic effects that consistently exceed the DTC2 envelope across multiple bridges. These real trains are characterised by more complex axle arrangements that deviate from the idealised repetitive pattern of the DTC2 reference trains. Such complexities include distinct locomotive contributions at the train ends, couplings between different units that disrupt pure resonance while generating significant transient effects, and irregular axle spacing that produces excitation at wavelengths not captured by the dominant coach length.

To address these cases, a complementary family of reference trains, designated DTC2e, is introduced here. Unlike the DTC2 trains, which are derived through an optimisation procedure targeting the envelope of dimensionless smoothed signature envelope from real trains, the DTC2e trains are identified directly from time-stepping dynamic simulations (deemed as the most accurate analysis method in this context). For each bridge and load category, the peak accelerations induced by real trains are compared against the DTC2 envelope. Trains that consistently exceed this envelope across multiple bridges are flagged as candidates for inclusion in DTC2e. To this end, the following criteria are considered to select candidate trains for DTC2e in each sub-category of trains:

1. the exceedance of the acceleration in the original DTC2e is higher than 0.25 m/s²,
2. the total acceleration for the lambdas corresponding to these exceedance is higher than 2 m/s²,
3. the wavelength for which the exceedance is recorded is below that corresponding to the next category of permissible line speeds in the bridge.

The axle spacing of these candidate trains is then normalised by their maximum axle load, preserving their geometric configuration and allowing to scale the axle loads of the trains to the corresponding P_{MUclass}. These trains are incorporated as supplemental reference models within the DTC2 framework, intended to be used in combination with the resonant DTC2 trains.

7.1.1 Trains with Conventional Bogies: CB

7.1.1.1 CBa reference trains

Figure 61 presents the peak accelerations obtained from time-stepping analysis for bridge ID6, used to identify aggressive real CBa trains not covered by the corresponding DTC2 resonant train. It is observed that train ID 607 ($P_{\mathrm{MUclass}} = 17$ t) and train ID 948 ($P_{\mathrm{MUclass}} = 21.5$ t) clearly exceed the DTC2 reference envelope around $\lambda \approx 11$ m for this bridge. Examination of the remaining bridges confirms that these two trains, together with train ID 486, account for all exceedances relative to the original DTC2 envelope. The axle spacing and loading of these real trains are shown in Figure 62.

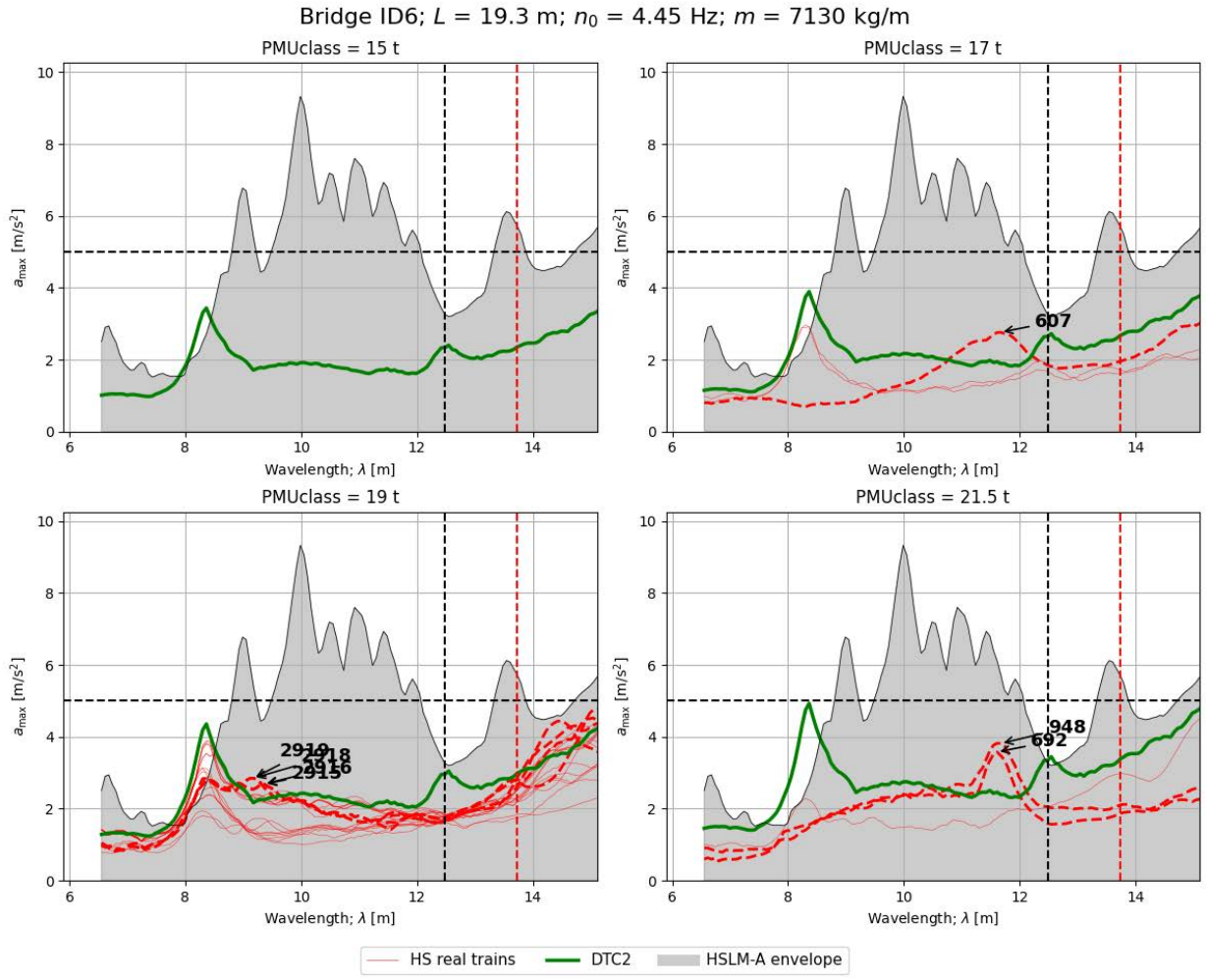

Figure 61. Identification of aggressive real CBa trains not covered by the CBa train in DTC2. Bridge ID 6. Time-stepping analysis.

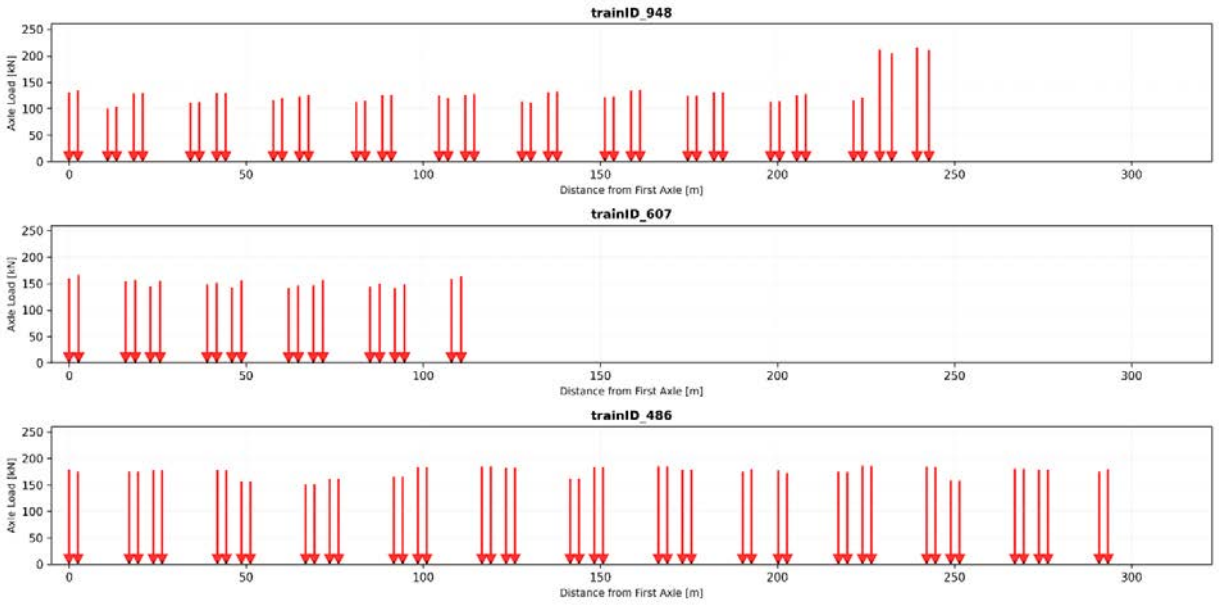

Figure 62. Axle spacing and load of real CBa trains that induce vibrations in bridges that are not covered by the reference DTC2 CBa train in some cases.

After identifying these three CBa trains, their axle loads are normalised with respect to the maximum load and they are renamed as CBa_2 to CBa_2 following Table 5. The axle spacing and normalised loads of these trains are included in Appendix C, which along with the train CBa_1 described previously (referred to simply as CBa) form the complete DTC (named DTC2 + DTC2e).

Real CBa train ID	DTC2e train
948	CBa_2
607	CBa_3
486	CBa_4

Table 5. Conversion of real CBa train to reference DTC2e trains after normalising their axle weight.

7.1.1.2 CBb reference trains

Figure 63 presents the peak accelerations obtained from time-stepping analysis for bridge ID4, used to identify aggressive real CBb trains not covered by the corresponding DTC2 resonant train (CBb_1). In this short-span bridge, a significant number of real trains across all P_{MUclass} categories induce accelerations that exceed the DTC2 reference envelope, particularly at short wavelengths below 4 m which dominate the dynamic response of this structure. Notably, train ID 3001 and train ID 2839 consistently produce the highest accelerations and effectively envelope the remaining real CBb trains. Across the remaining bridges, these two trains, together with train ID 1041 and 704, are found to account for all exceedances relative to the original DTC2 CBb envelope. The axle spacing and loading of these real trains are illustrated in Figure 64.

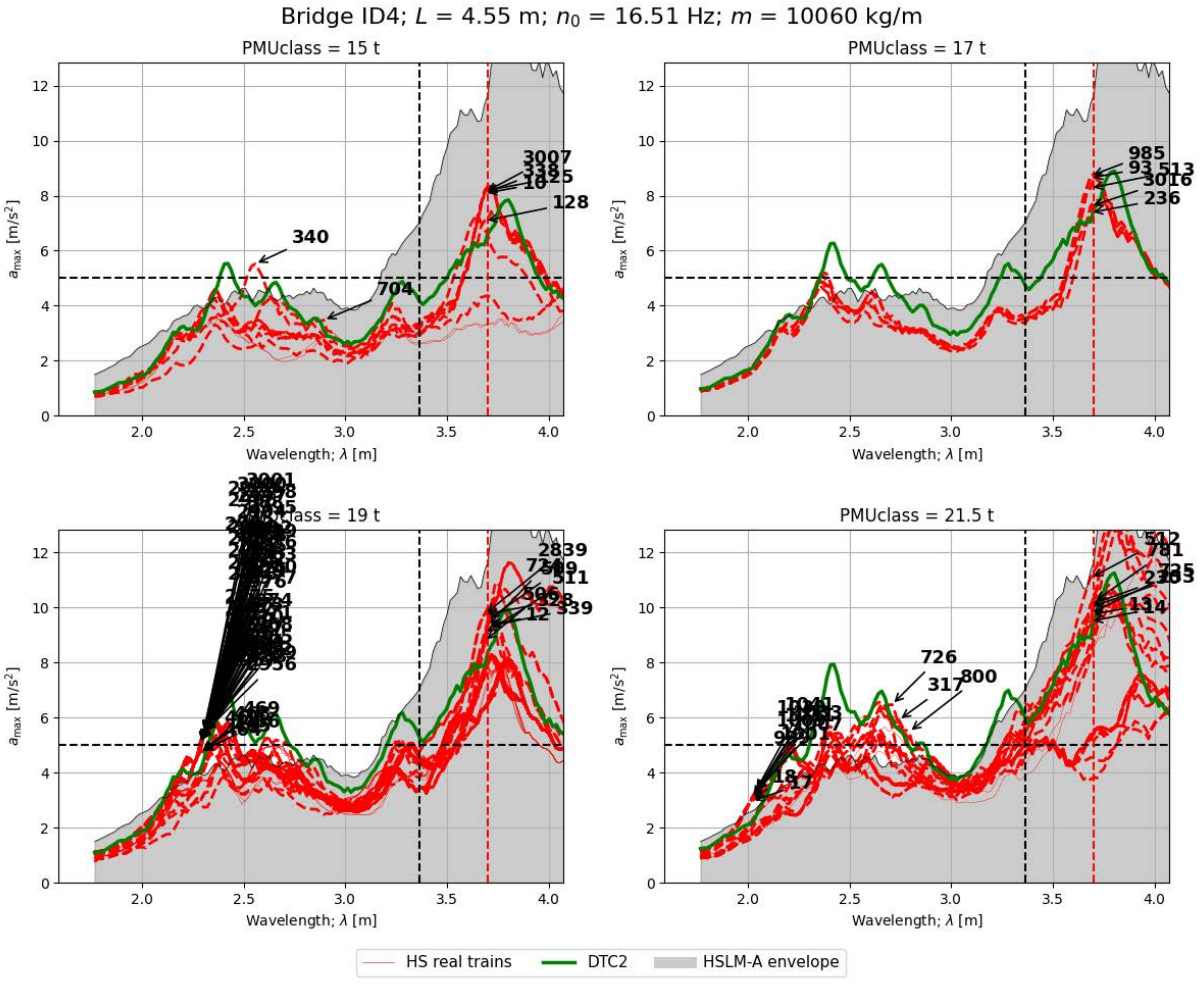

Figure 63. Identification of aggressive real CBb trains not covered by the CBb train in DTC2. Bridge ID 4. Time-stepping analysis.

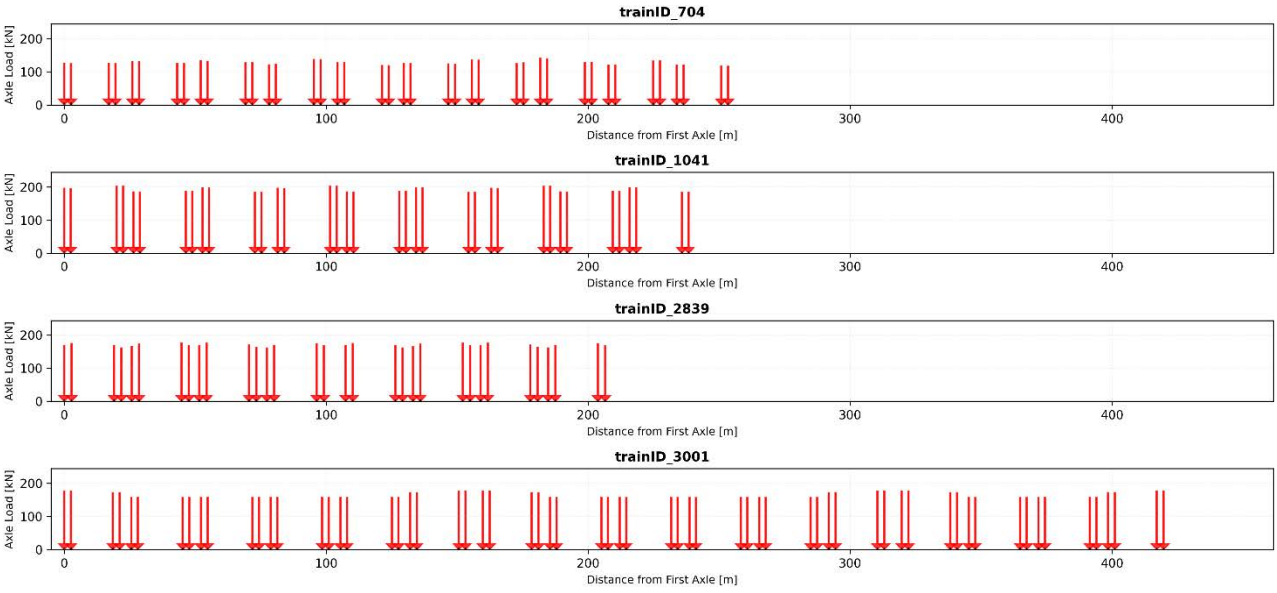

Figure 64. Axle spacing and load of real CBb trains that induce vibrations in bridges that are not covered by the reference DTC2 CBa train in some cases.

Following the identification of these four CBb trains, their axle loads are normalised by the maximum axle load, and they are renamed as CBb_2, CBb_3, CB_4 and CBa_5 according to Table 6. The axle spacing and normalised load distributions of these trains are provided in Appendix C. Together with the previously described CBb_1 train (referred to simply as CBb), these four configurations constitute the complete DTC set for the CBb family.

Real CBb train ID	DTC2e train
704	CBb_2
1041	CBb_3
2839	CBb_4
3001	CBb_5

Table 6. Conversion of real CBb train to reference DTC2e trains after normalising their axle weight.

7.1.1.3 CBc reference trains

Figure 65 presents the peak accelerations obtained from time-stepping analysis for bridge ID5, used to identify aggressive real CBc trains not covered by the corresponding DTC2 resonant train (CBc_1). In this bridge, the exceedances observed for real CBc trains ID 275 and 3012 are attributed to a shift in the resonant peak at approximately $\lambda \approx 9.4$ m, which is slightly offset from that of the reference CBc_1 train. Examination of the remaining bridges confirms that these two trains, together with train ID 521, are responsible for the exceedances relative to the DTC2 CBc envelope. The axle spacing and loading of these real trains are illustrated in Figure 66.

After the identification of these three CBc trains, their axle loads are normalised by the maximum axle load, and they are renamed CBc_2, CBc_3 and CBc_4 in accordance with Table 7. The axle spacing and normalised load distributions of these trains are provided in Appendix C. Together with the previously described CBc_1 train (referred to simply as CBc), these four configurations form the complete DTC set for the CBc family.

Real CBc train ID	DTC2e train
275	CBc_2
521	CBc_3
3012	CBc_4

Table 7. Conversion of real CBc trains to reference DTC2e trains after normalising their axle weight.

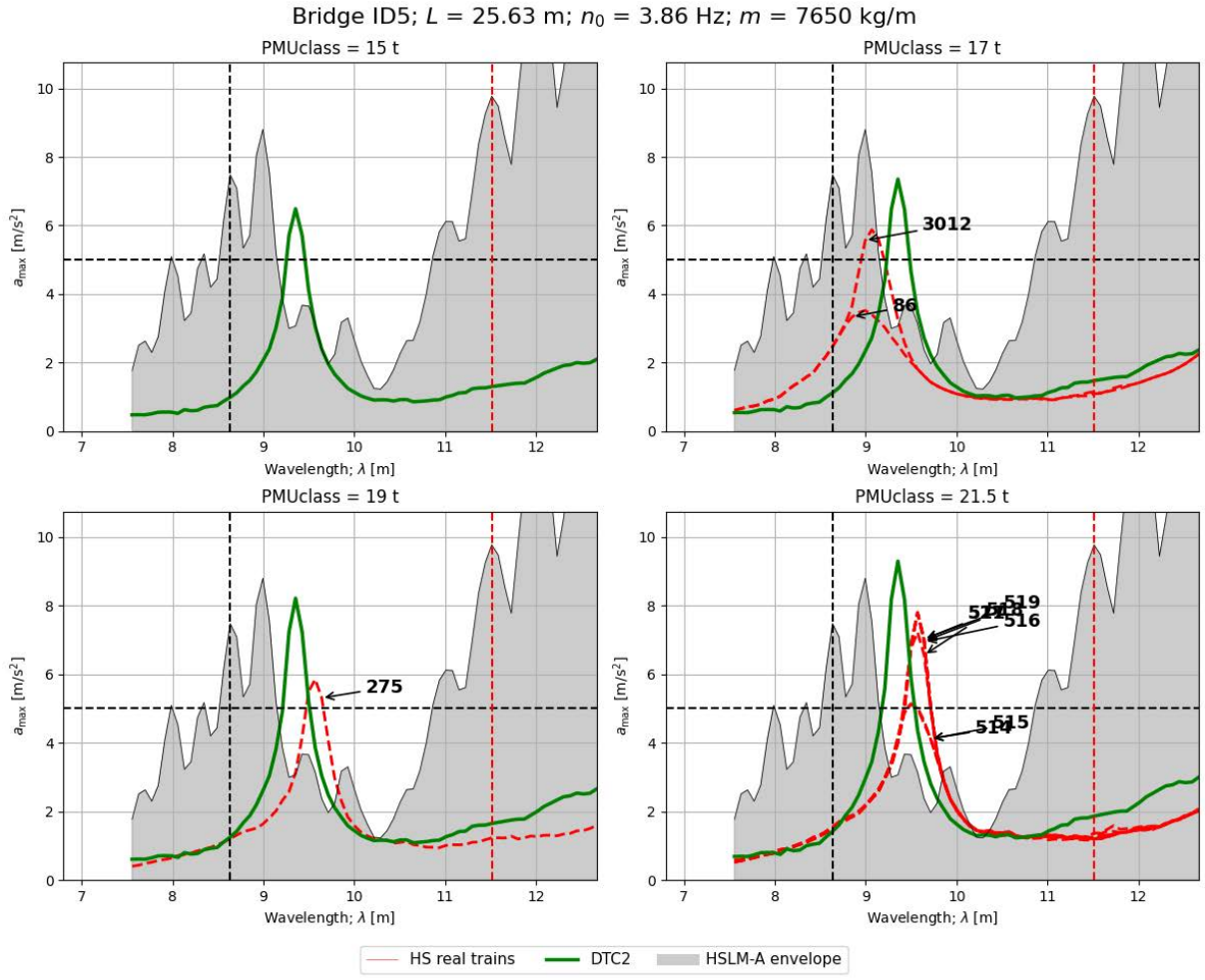

Figure 65. Identification of aggressive real CBc trains not covered by the CBc train in DTC2. Bridge ID 5. Time-stepping analysis.

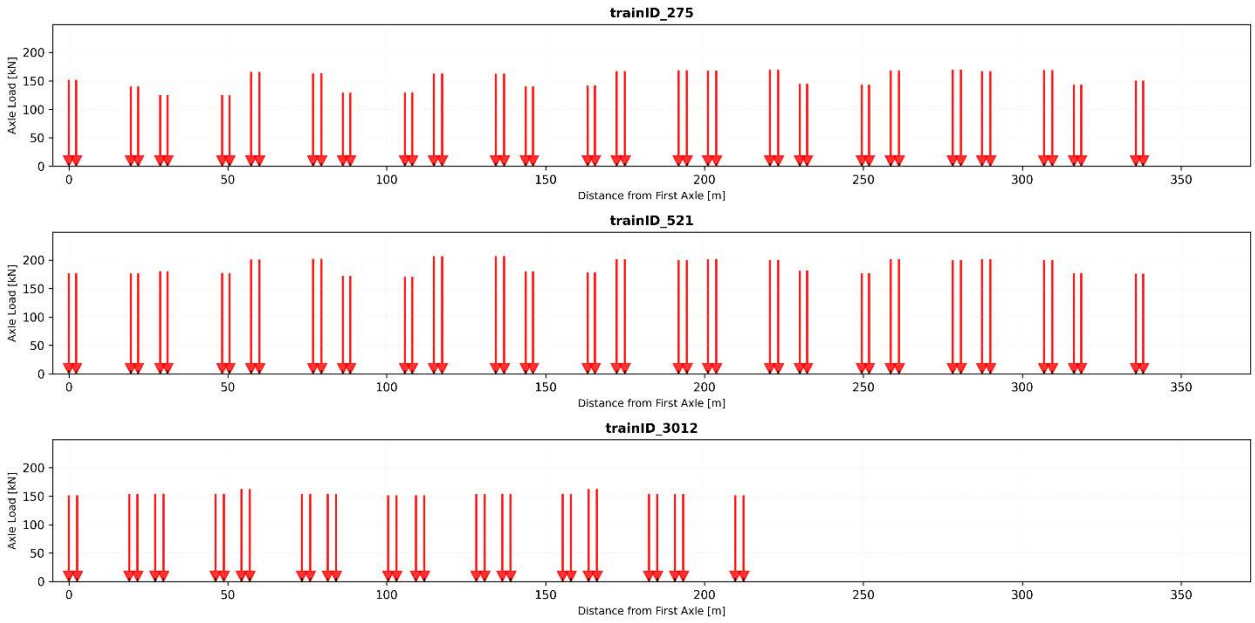

Figure 66. Axle spacing and load of real CBc trains that induce vibrations in bridges that are not covered by the reference DTC2 CBc train in some cases.

7.1.2 Trains with Articulated Bogies: AB

7.1.2.1 ABa reference trains

The DTC2 reference train for the ABa family provides adequate coverage of peak accelerations across almost all bridges, with a single exception. Figure 67 presents the peak accelerations obtained from time-stepping analysis for bridge ID12, where an aggressive real ABa train not covered by the DTC2 resonant train is identified. In this bridge, train ID 497 ($P_{\mathrm{MUclass}} = 21.5$ t) exceeds the DTC2 reference envelope in the wavelength range $\lambda = 12$ to 14 m. The axle spacing and loading of this train are illustrated in Figure 68.

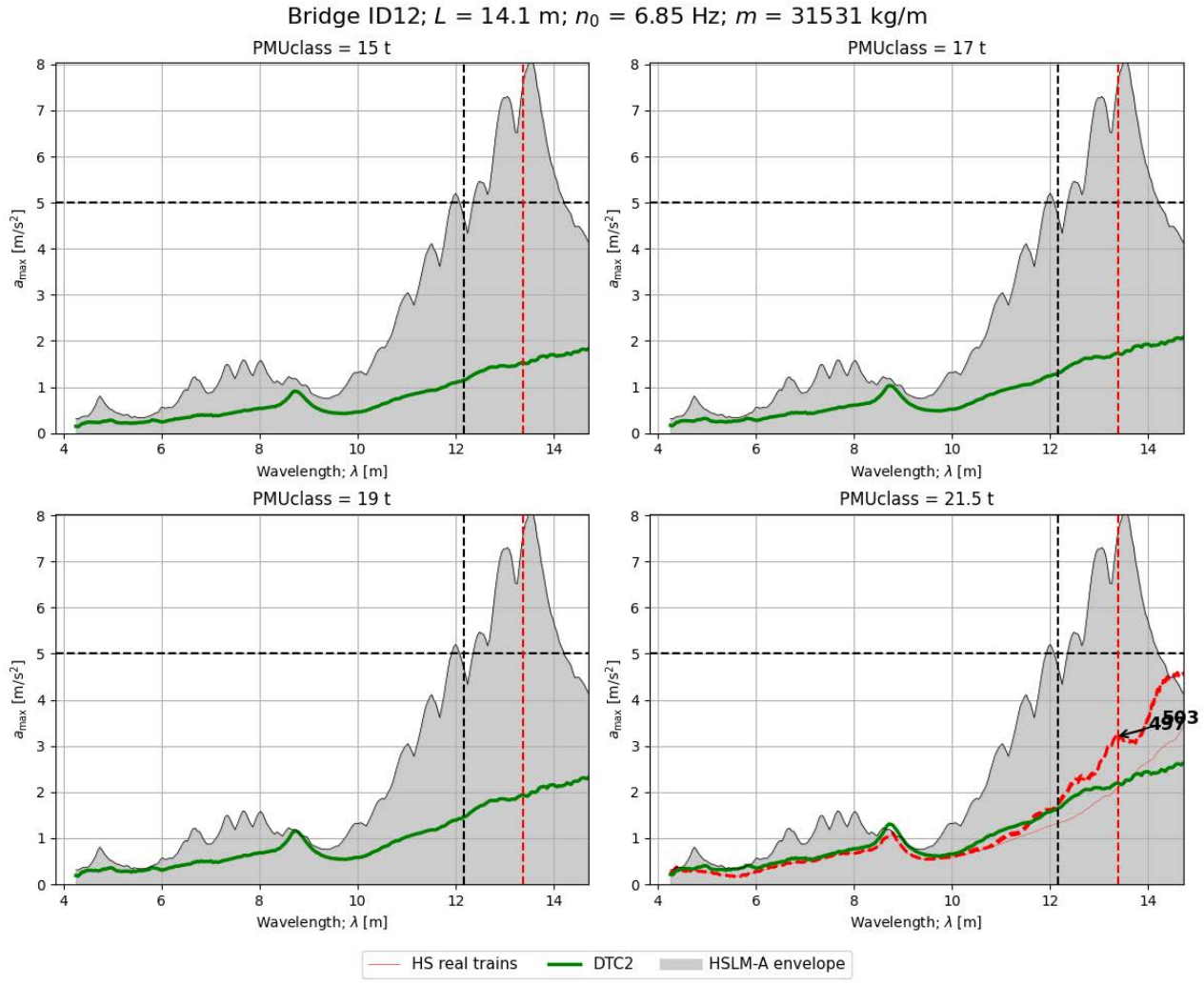

Figure 67. Identification of aggressive real ABa trains not covered by the ABa train in DTC2. Bridge ID 12. Time-stepping analysis.

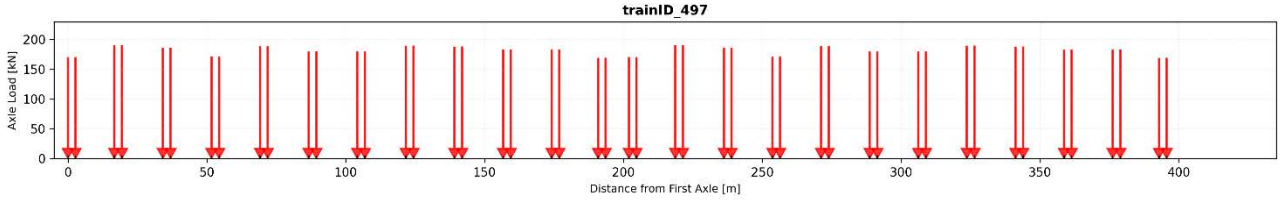

Figure 68. Axle spacing and load of a real ABa train that induce vibrations in bridges that are not covered by the reference DTC2 ABa train in some cases.

The axle loads of this real ABa train were normalised with respect to the maximum load and it was labelled as ABa_2 following Table 8. The axle spacing and normalised loads of this train is included in Appendix C, and it completes the DTC2 + DTC2e along with the reference train ABa_1 described previously.

Real ABa train ID	DTC2e train
497	ABa_2

Table 8. Conversion of real ABa train to a reference DTC2e train after normalising its axle weight.

7.1.2.2 ABb reference trains

The DTC2 reference train for the ABb family provides adequate coverage of resonant peak accelerations with $\lambda < 10$ m. However, there is a distinct group of trains with $P_{\mathrm{MUclass}} = 19$ t that consistently exceeds the reference accelerations for larger wavelengths, in most of the bridges. For example, Figure 69 shows the case of bridge ID1. This group of trains is represented and enveloped by train ID 976, and its axle distribution is illustrated in Figure 70.

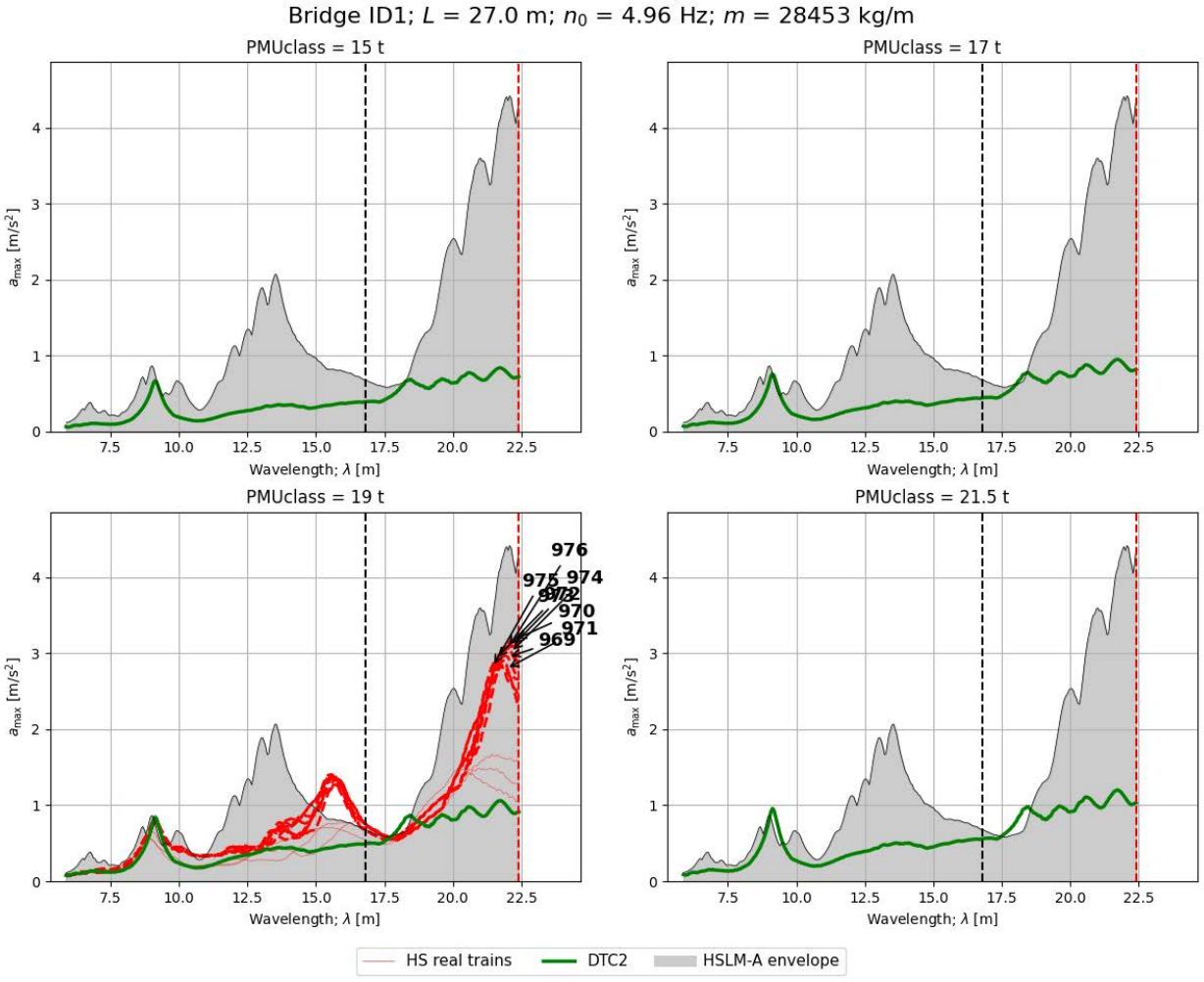

Figure 69. Identification of aggressive real ABb trains not covered by the ABb train in DTC2. Bridge ID 4. Time-stepping analysis.

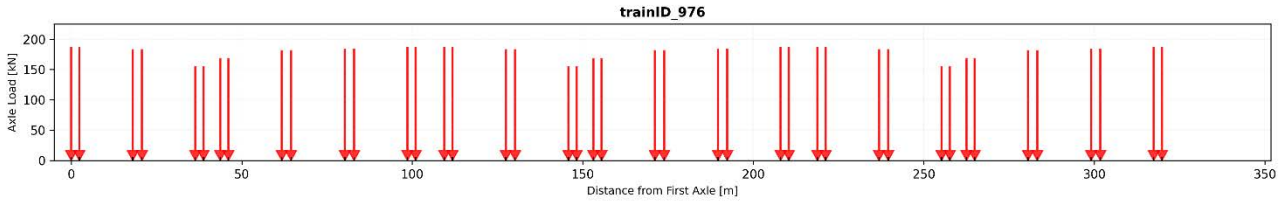

Figure 70. Axle spacing and load of a real ABb trains that induce vibrations in bridges that are not covered by the reference DTC2 ABb train in some cases.

The axle loads of train ID 976 were normalised and it was included in the DTC2+DTC2e as train ABb_2 (Table 9). Appendix C gathers the detailed axle spacing and loading in this train, which completes the DTC along with the resonant train ABa_1.

Real ABb train ID	DTC2e train
704	ABb_2

Table 9. Conversion of real ABb train to the reference DTC2e train after normalising its axle weight.

7.1.2.3 ABc reference trains

Figure 71 presents the peak accelerations obtained from time-stepping analysis for bridge ID5, used to identify aggressive real ABc trains not covered by the corresponding DTC2 resonant train (ABc_1). In this bridge, and also in other structures with intermediate and high frequencies, the exceedances correspond to train IDs 341 and 3014 due to a shift in a resonant peak at approximately $\lambda \approx 9.4$ m, which is slightly offset from that of the reference ABc_1 train, as well as certain exceedance for $\lambda > 10$ in the train ID 3014. The axle spacing and loading of these two real trains are described graphically in Figure 72. Then, their axle loads were normalised and labelled as ABc_2 and ABc_3 following Table 10 to complete along with the reference train ABc_1 the full ABc family in DTC2+DTC2e. Trains ABc_2 and ABc_3 are included in Appendix C.

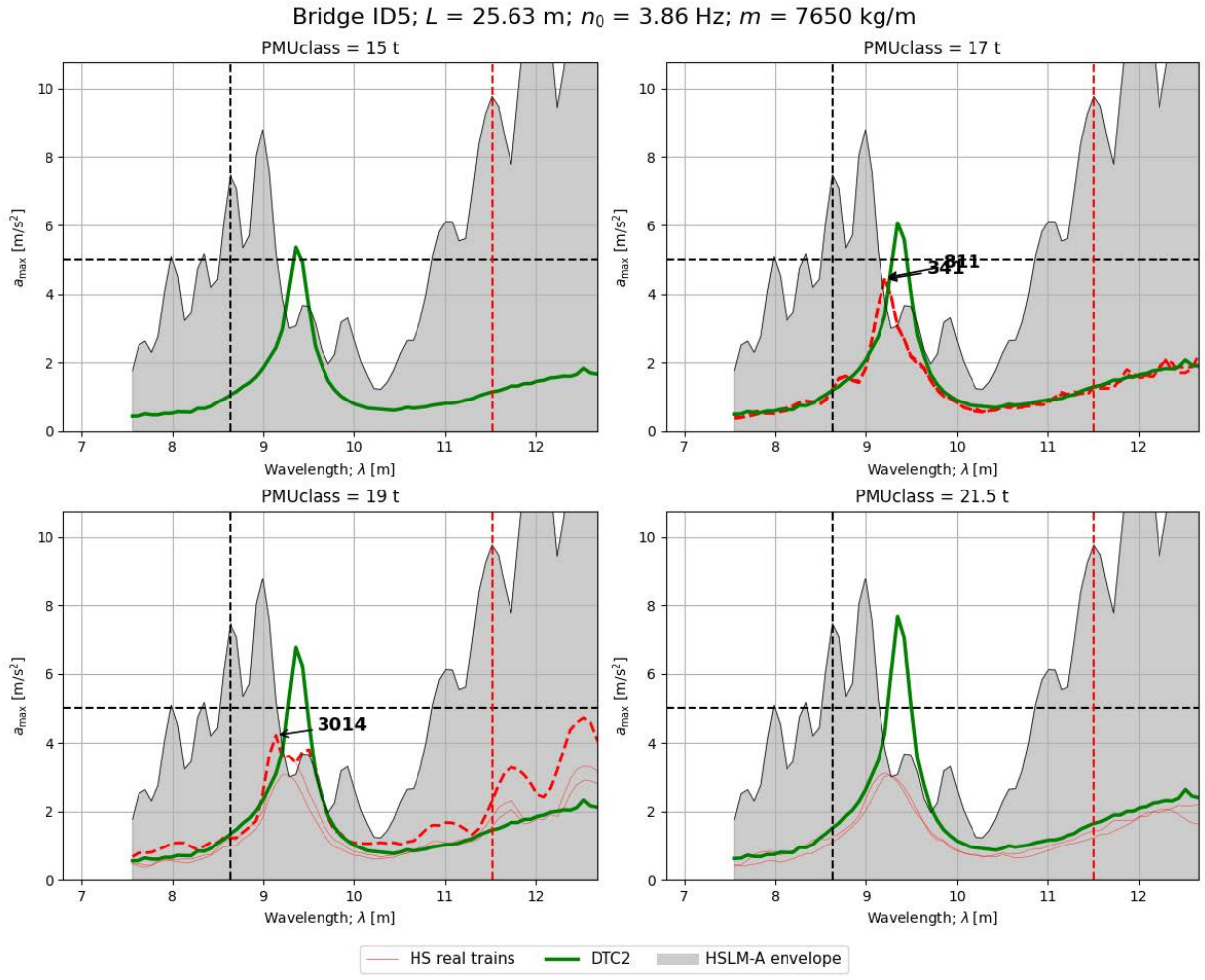

Figure 71. Identification of aggressive real ABc trains not covered by the ABc train in DTC2. Bridge ID 5. Time-stepping analysis.

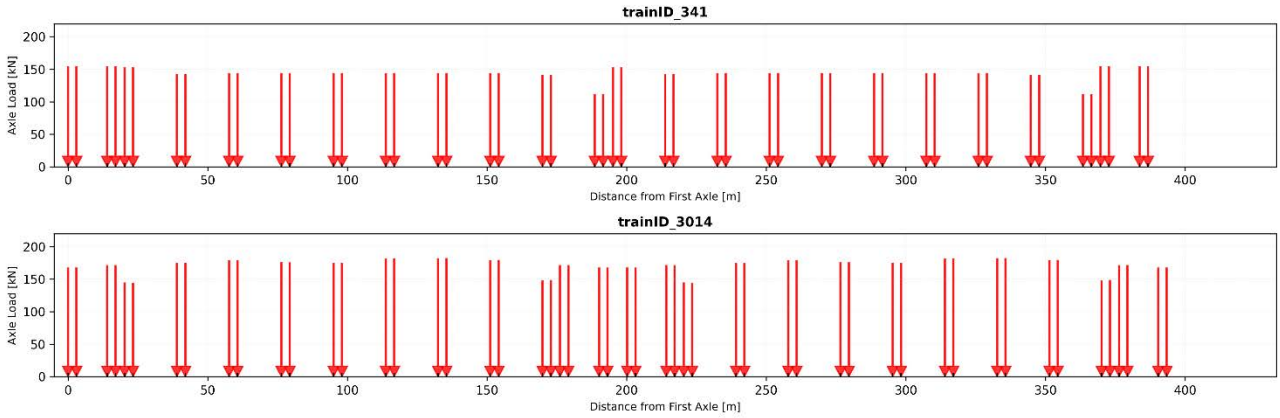

Figure 72. Axle spacing and load of real ABc trains that induce vibrations in bridges that are not covered by the reference DTC2 ABc train in some cases.

Real ABc train ID	DTC2e train
341	ABc_2
3014	ABc_3

Table 10. Conversion of real ABc trains to reference DTC2e trains after normalising their axle weight.

7.1.3 Regular Trains: SA

7.1.3.1 SAa reference trains

Figure 73 presents the peak accelerations obtained from time-stepping analysis for bridge ID5, used to identify aggressive real ABa trains not covered by the corresponding DTC2 resonant train (SAa_1). In this bridge, and across most of the other structures considered, the exceedances observed for real SAa trains are caused by trains ID 10002, 10003 and 10004. These correspond to modern SA trains recently provided by TALGO for this work. The exceedances occur at wavelengths between the resonant peak and the first subharmonic, which is a region not adequately covered by the resonant SAa_1 train, as noted previously. The axle spacing and loads of these three trains are shown in Figure 74. Following normalisation, they are labelled SAa_2, SAa_3 and SAa_4 as indicated in Table 11, with their detailed configurations provided in Appendix C. Together with the original reference SAa_1, these trains constitute the complete SAa family within the DTC2 + DTC2e framework.

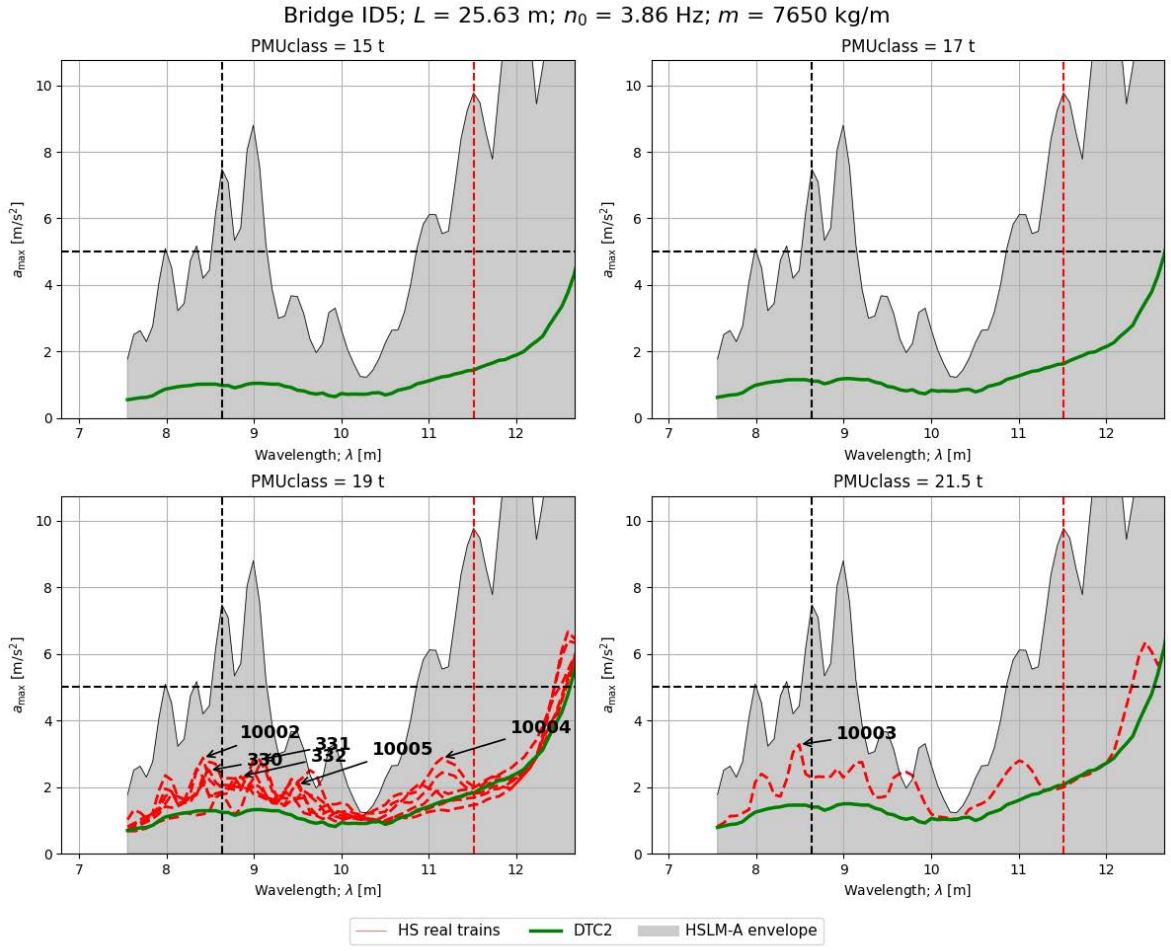

Figure 73. Identification of aggressive real SAa trains not covered by the SAa train in DTC2. Bridge ID 5. Time-stepping analysis.

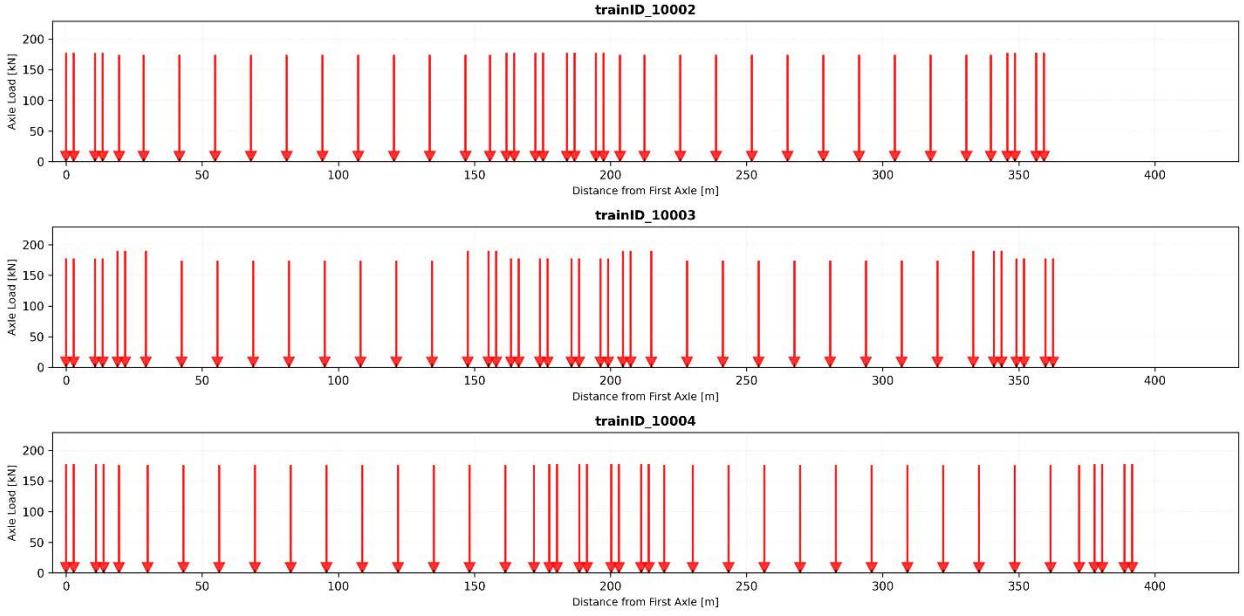

Figure 74. Axle spacing and load of real SAa trains that induce vibrations in bridges that are not covered by the reference DTC2 SAa train in some cases.

Real SAa train ID	DTC2e train
10002	SAa_2
10003	SAa_3
10004	SAa_4

Table 11. Conversion of real SAa trains to reference DTC2e trains after normalising their axle weight.

7.1.3.2 SAb reference trains

Unlike in the previous cases, a significant number of real SAb trains exceed the accelerations given by the corresponding DTC2 resonant train (SAb_1). Figure 75 presents the peak accelerations obtained from time-stepping analysis for bridge ID6, taken as an example to identify aggressive real ABa trains. In this, and other structures that reach operation wavelengths from 7 to 12 m, there are significant acceleration exceedance created by a large number of SAb trains. These occur because of the larger energy content of real SAb trains in this wavelgenth region between resonant peaks, particularly those with $P_{\mathrm{MUclass}} = 21.5$ t, due to the presence of heavier axle loads that break the resonance and introduce transient effects. A group of 6 real SAb trains were identified as representative of these effects in a wide range of wavelengths and bridges, and these are included in Figure 76. The axle loads of these trains was normalised and they are labelled as SAb_2 to SAb_7, following Table 12. Appendix C includes the details of these trains, which in addition to the reference SAb_1 train form the SAb DTC2 + DTC2e family.

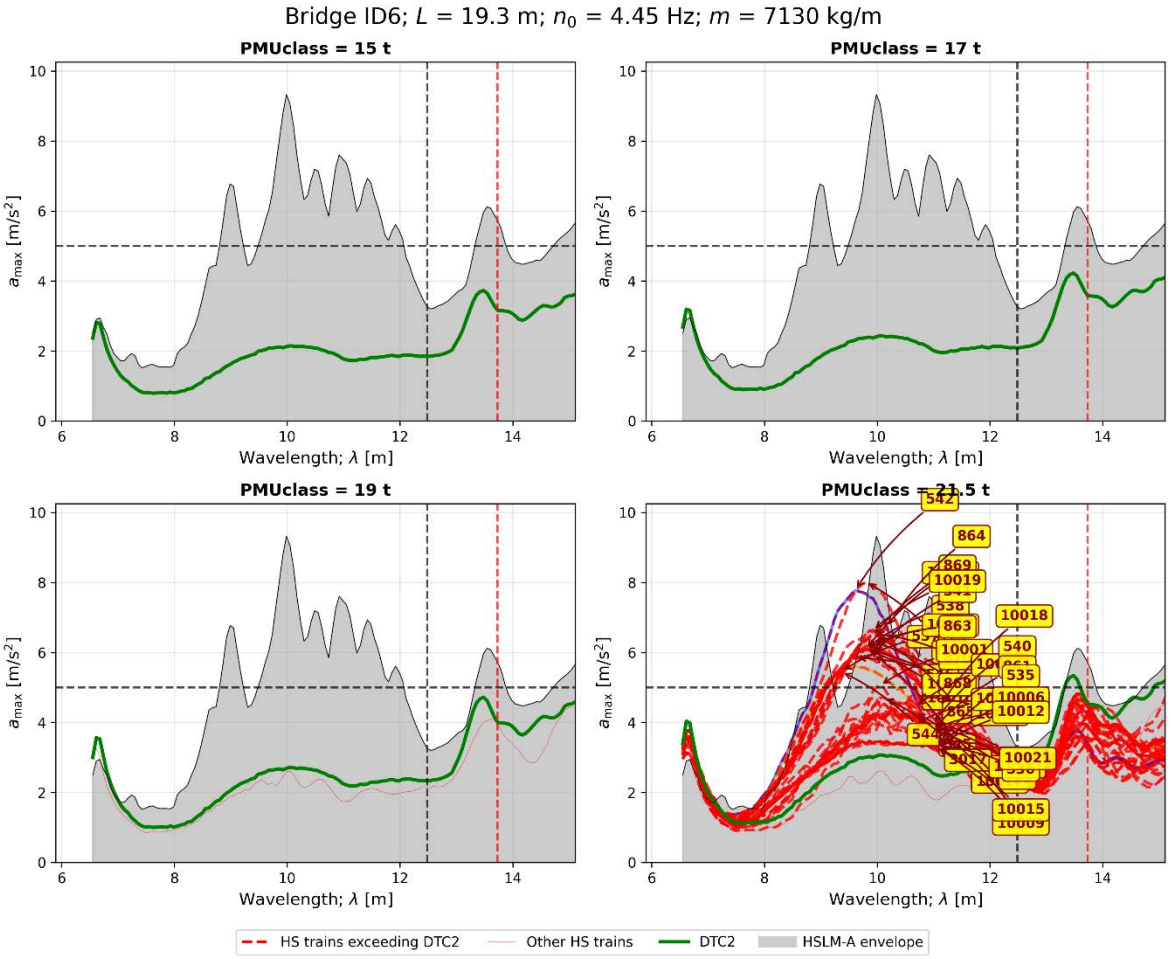

Figure 75. Identification of aggressive real SAb trains not covered by the SAb train in DTC2. Bridge ID 6. Time-stepping analysis.

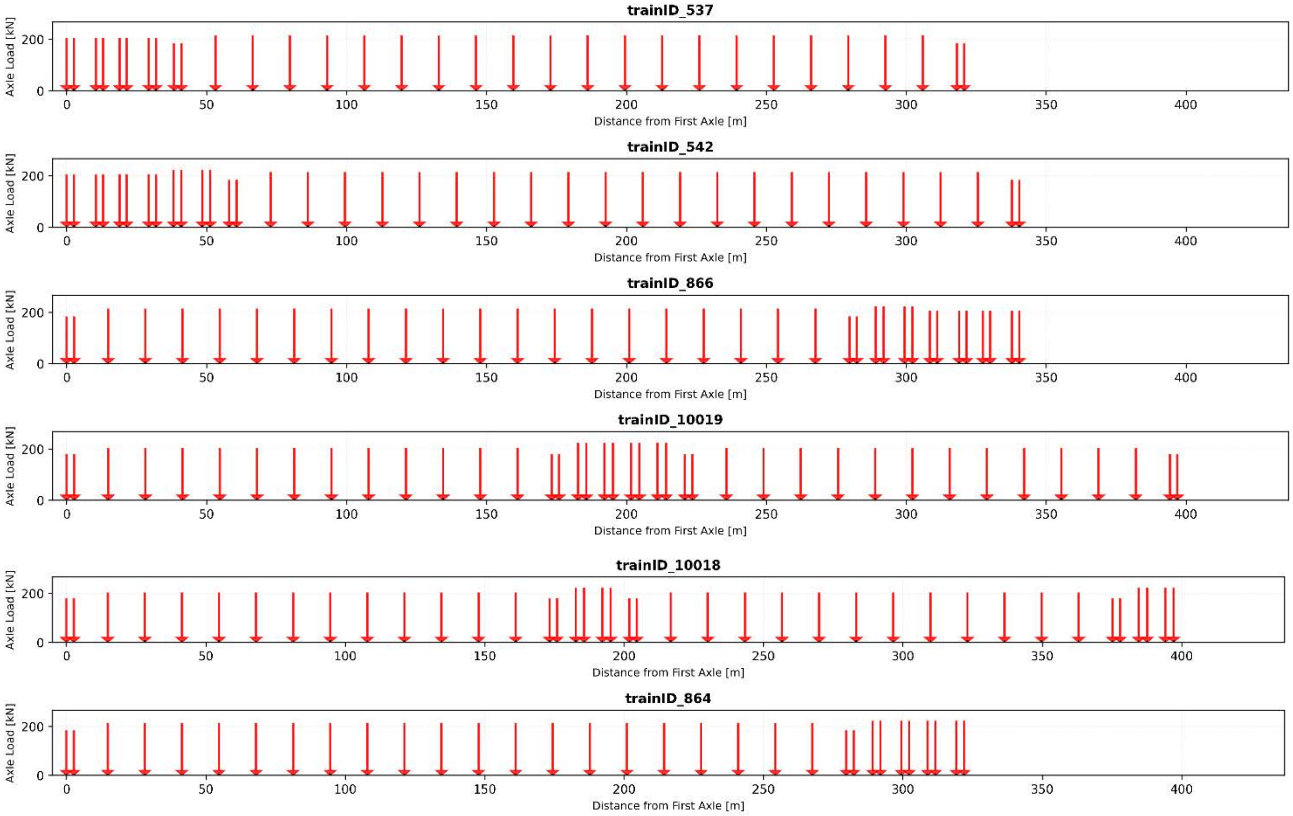

Figure 76. Axle spacing and load of real SAb trains that induce vibrations in bridges that are not covered by the reference DTC2 SAb train in some cases.

Real SAb train ID	DTC2e train
537	SAb_2
542	SAb_3
866	SAb_4
10019	SAb_5
10018	SAb_6
864	SAb_7

Table 12. Conversion of real SAb trains to reference DTC2e trains after normalising their axle weight.

8 Comparison of DTCs

This section presents a comparative assessment of vertical acceleration response envelopes for railway bridges, computed using the time-stepping method. The plots show the maximum peak acceleration as a function of the wavelength (λ) for a representative selection of bridges categorised by their natural frequency. The analysis includes four distinct train families: (i) the envelope of real passenger trains regardless of their P_{MUclass}; (ii) the combined envelope of DTC0 and DTC1 trains for a representative axle load of $P_{\mathrm{MUclass}} = 21.5$ t which corresponds to the heaviest MU Class category; (iii) the combined envelope of DTC2 and DTC2e trains also with $P_{\mathrm{MUclass}} = 21.5$ t; and (iv) the HSLM-A envelope that serves as a reference. For each bridge, the vertical lines indicate the maximum permissible wavelength corresponding to the operational speed limit (red dashed line) and the line speed limit (black dashed line), while the horizontal line at 5 m/s² indicates the acceleration limit threshold. The detailed accelerations obtained with time-stepping analysis for each bridge and P_{MUclass} are included in Appendix D.

8.1.1 Trains with Conventional Bogies: CB

8.1.1.1 CBa reference trains

The envelope of peak vertical accelerations across bridges and wavelengths is compared between real conventional passenger trains (CBa type) and the DTCs in Figures 77, 78 and 79 for low, intermediate and high-frequency bridges, respectively. The DTC2 + DTC2e combination exhibits excellent agreement with the envelope of real trains across all bridges and wavelengths. It remains slightly above the real train envelope, with only a few marginal cases where it falls slightly below. In these instances, the underprediction occurs either at very low acceleration levels where dynamic response is not critical. In contrast, the DTC0 + DTC1 combination shows significant deviations, either substantially overestimating or underestimating the real train envelope at certain wavelengths, while HSLM-A exhibits even larger mismatches.

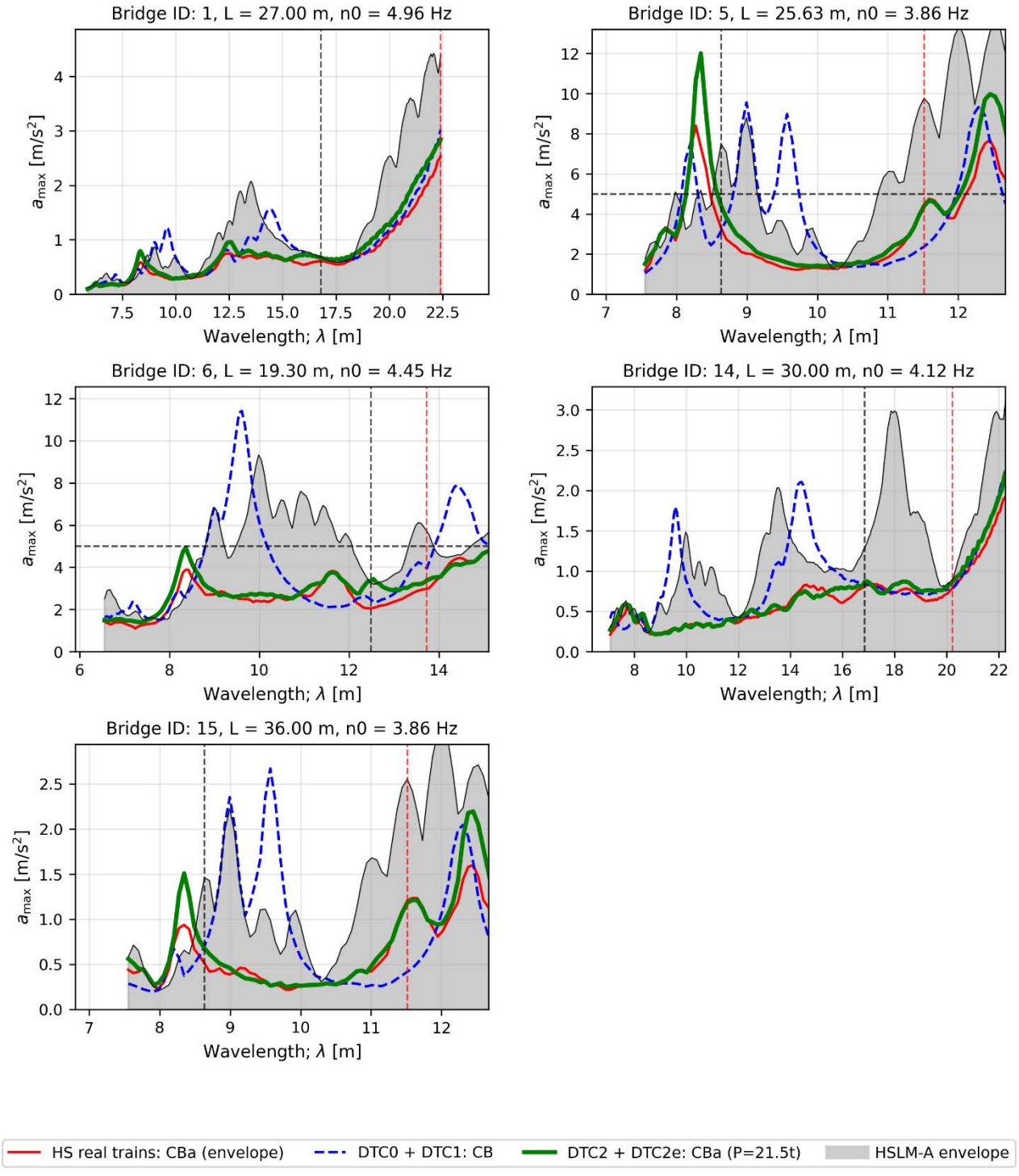

Figure 77. Envelope of the peak vertical acceleration in bridges with 'low' natural frequency for different wavelengths. Comparison between the envelope of real conventional passenger trains (CBa type), the combined envelope of DTC0 and DTC1 trains, the combined envelope of DTC2 and DTC2e trains, and the HSLM-A envelope. Results obtained with time-stepping analysis. All DTCs with $P_{MUclass} = 21.5\ t$.

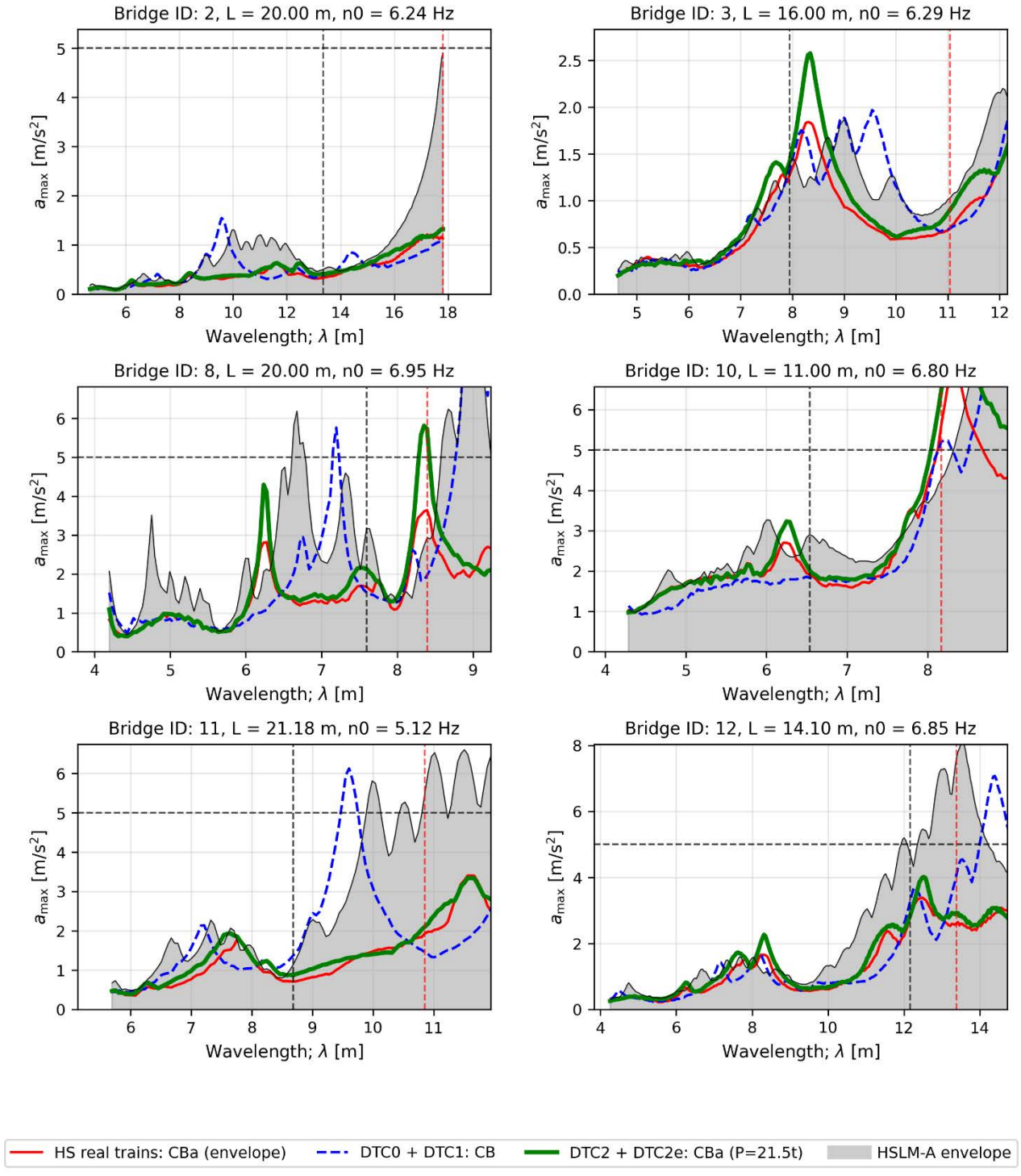

Figure 78. Envelope of the peak vertical acceleration in bridges with 'intermediate' natural frequency for different wavelengths. Comparison between the envelope of real conventional passenger trains (CBa type), the combined envelope of DTC0 and DTC1 trains, the combined envelope of DTC2 and DTC2e trains, and the HSLM-A envelope. Results obtained with time-stepping analysis. All DTCs with $P_{MUclass} = 21.5$ *t.*

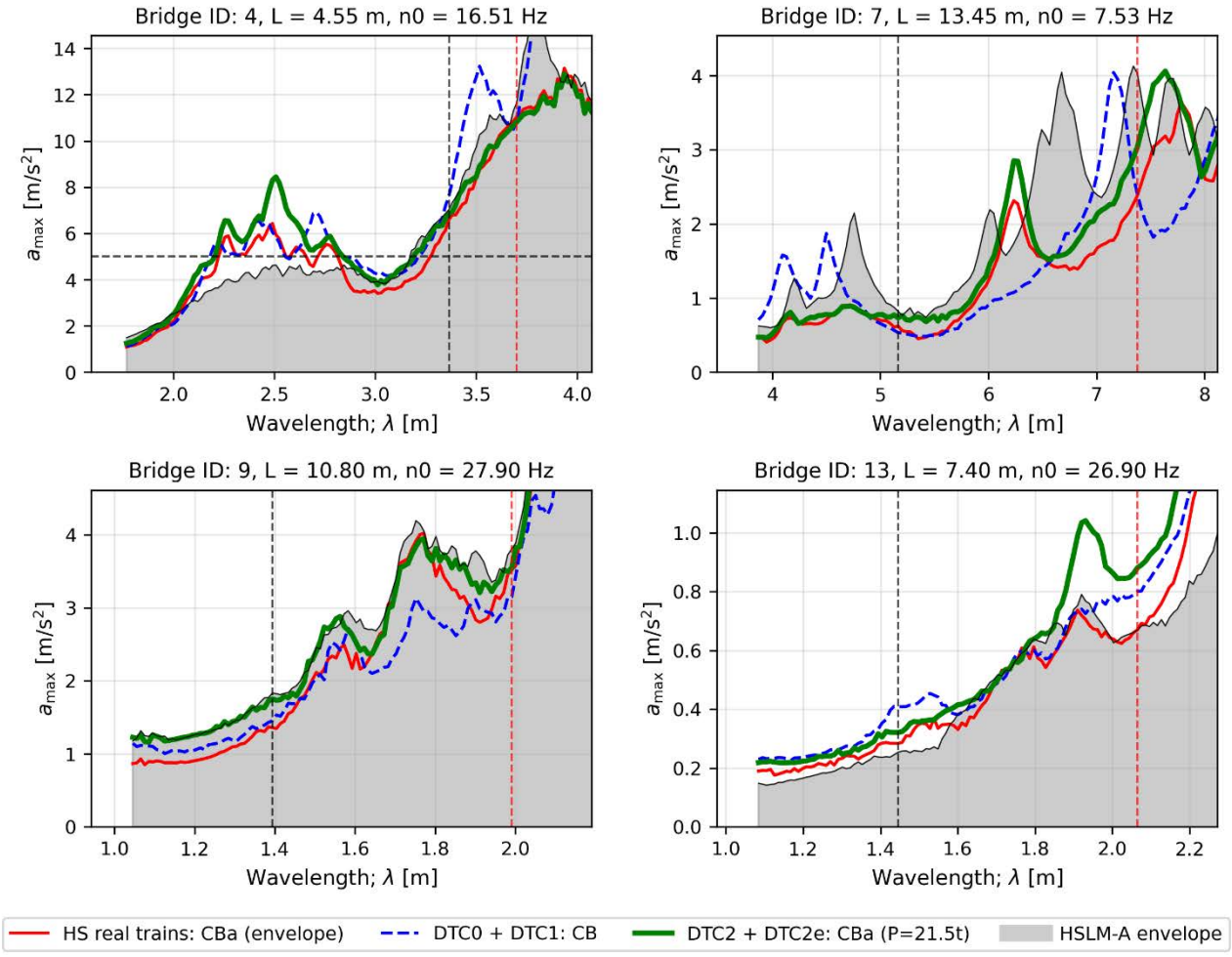

Figure 79. Envelope of the peak vertical acceleration in bridges with 'high' natural frequency for different wavelengths. Comparison between the envelope of real conventional passenger trains (CBa type), the combined envelope of DTC0 and DTC1 trains, the combined envelope of DTC2 and DTC2e trains, and the HSLM-A envelope. Results obtained with time-stepping analysis. All DTCs with $P_{MUclass} = 21.5$ *t.*

8.1.1.2 CBb reference trains

For the CBb family, Figures 80-82 shows that the combined DTC2 + DTC2e envelope provides adequate coverage of real train accelerations across all bridges, maintaining a consistent safety margin throughout the full range of operational wavelengths. Only marginal exceedances are observed, and these occur either at low acceleration levels that are not critical for bridge assessment, or at wavelengths corresponding to train speeds that cannot be attained in the shortest bridges, even when considering the next higher line category for which the trains were designed. In contrast, the DTC0 + DTC1 combination clearly overpredicts accelerations around $\lambda \approx 9.6$ m, while HSLM-A exhibits significant overpredictions at several wavelengths and, conversely, falls below the accelerations induced by real trains at certain resonant speeds.

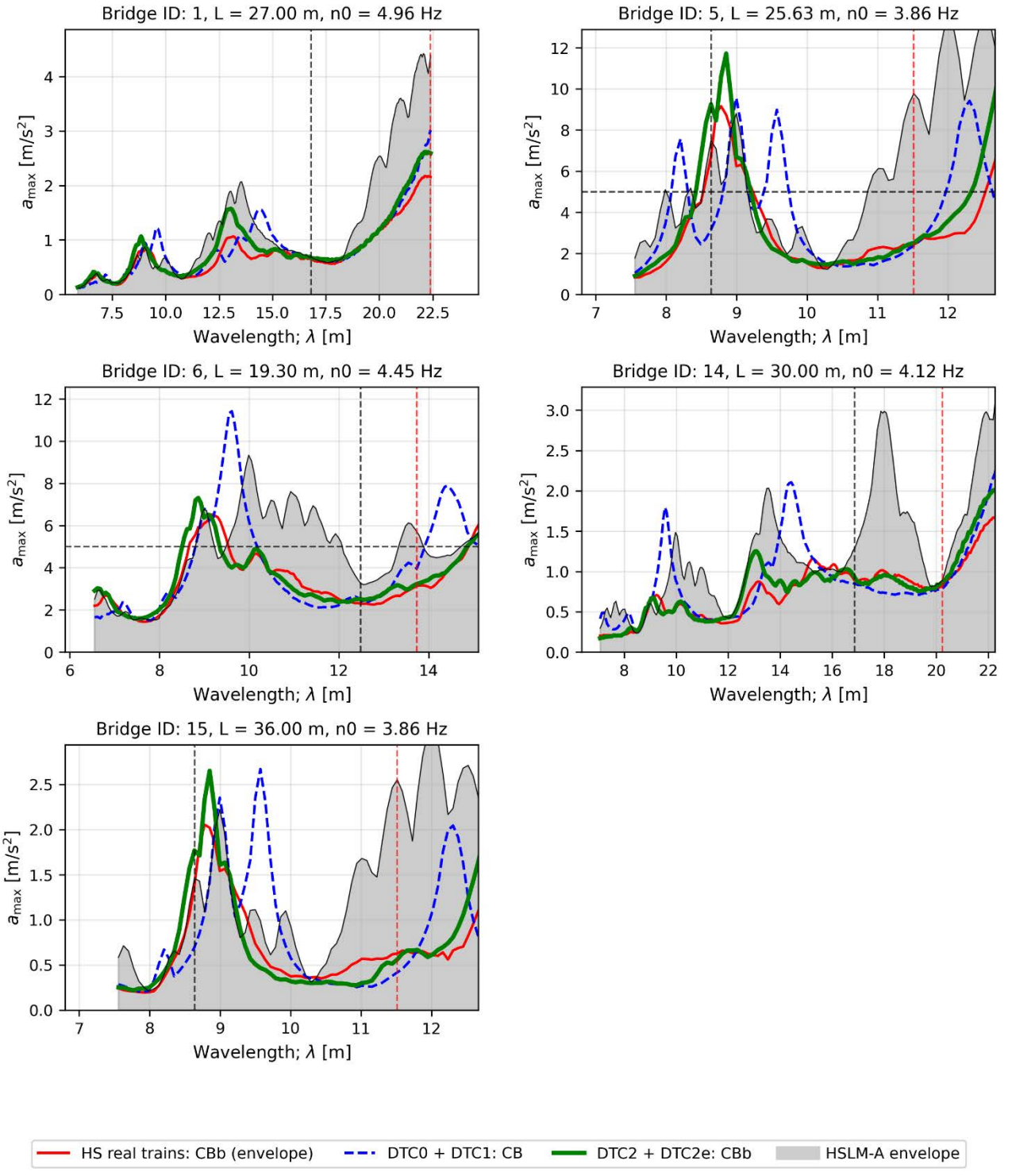

Figure 80. Envelope of the peak vertical acceleration in bridges with 'low' natural frequency for different wavelengths. Comparison between the envelope of real conventional passenger trains (CBb type), the combined envelope of DTC0 and DTC1 trains, the combined envelope of DTC2 and DTC2e trains, and the HSLM-A envelope. Results obtained with time-stepping analysis. All DTCs with $P_{MUclass} = 21.5$ *t.*

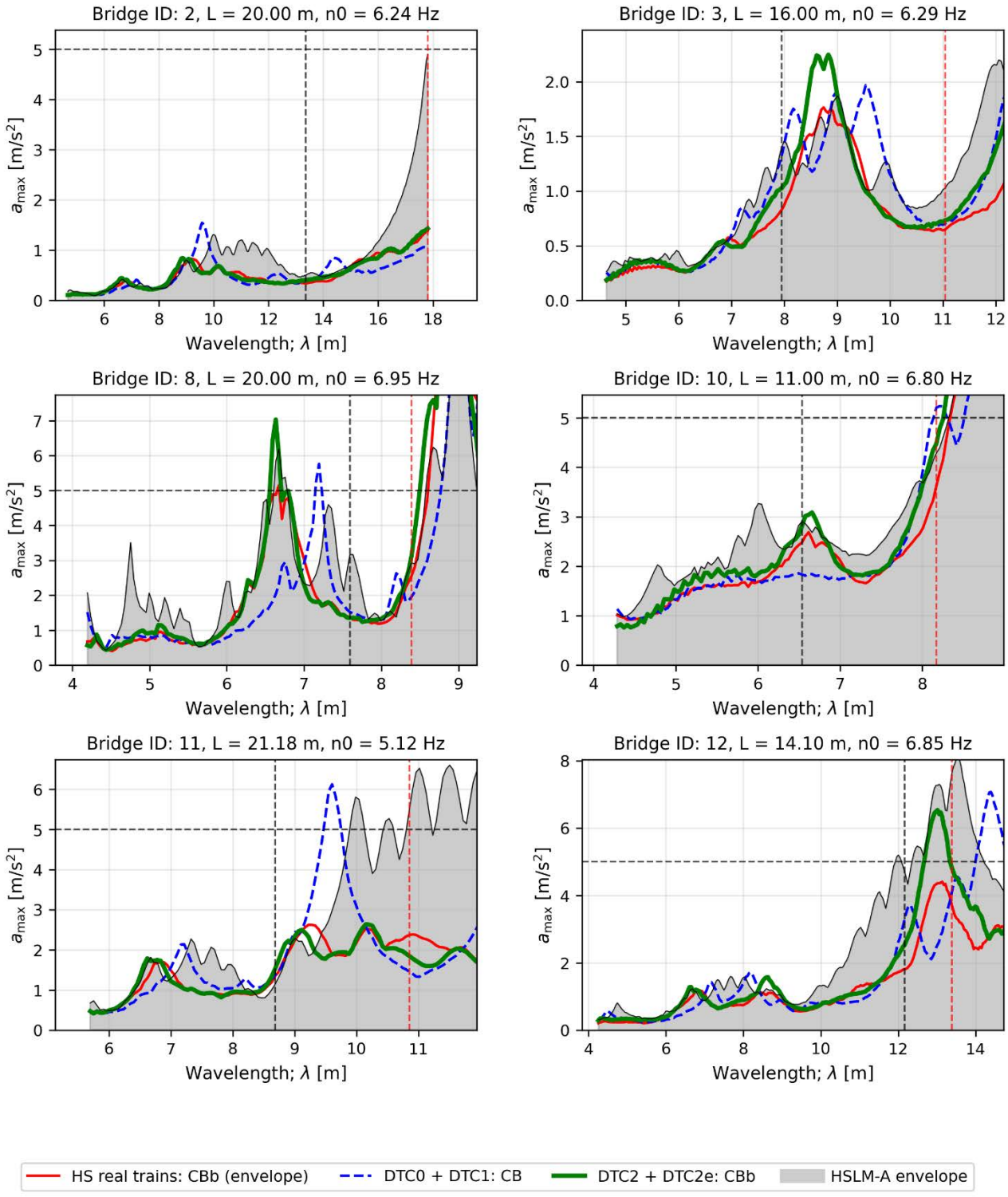

Figure 81. Envelope of the peak vertical acceleration in bridges with 'intermediate' natural frequency for different wavelengths. Comparison between the envelope of real conventional passenger trains (CBb type), the combined envelope of DTC0 and DTC1 trains, the combined envelope of DTC2 and DTC2e trains, and the HSLM-A envelope. Results obtained with time-stepping analysis. All DTCs with $P_{MUclass} = 21.5$ *t.*

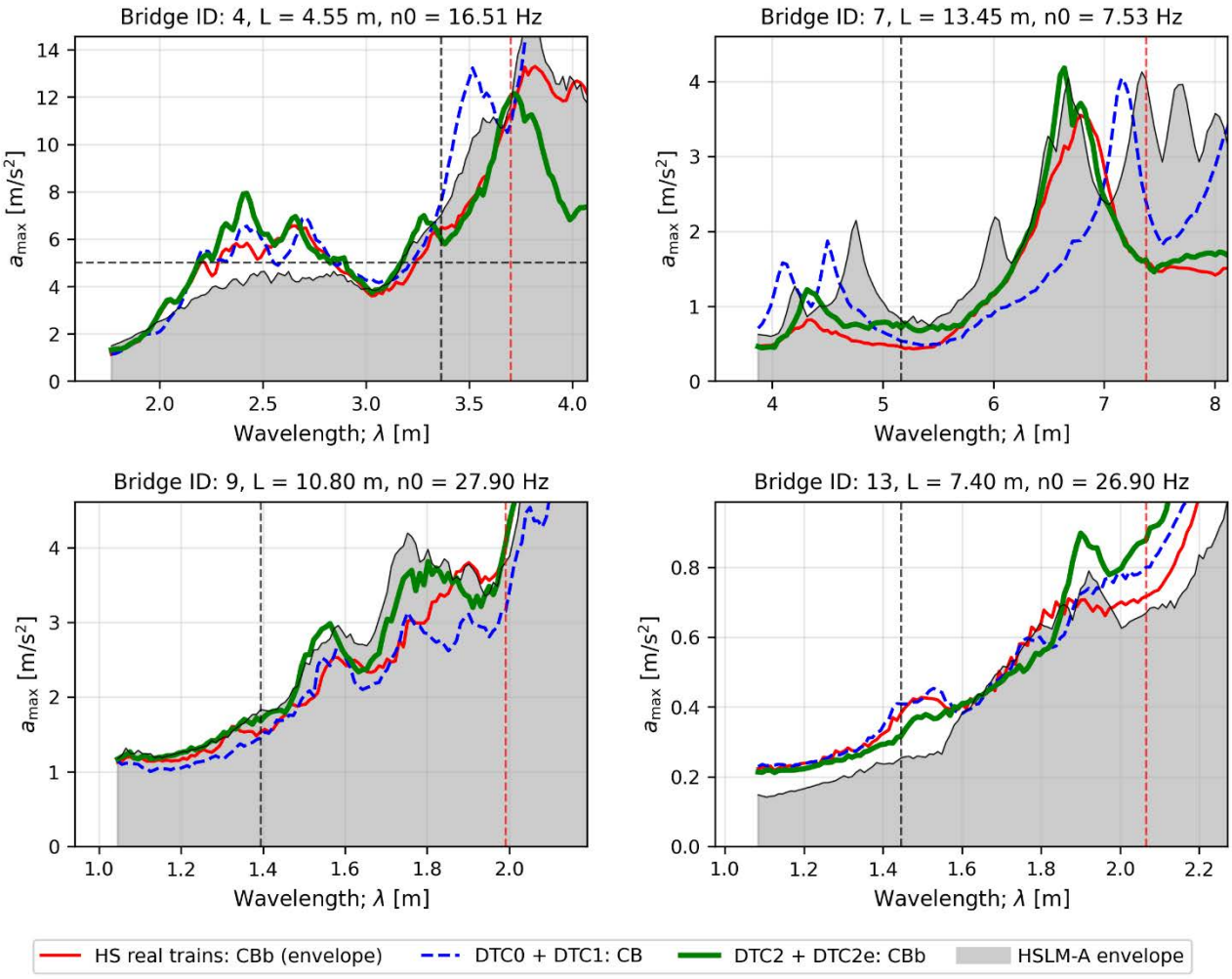

Figure 82. Envelope of the peak vertical acceleration in bridges with 'high' natural frequency for different wavelengths. Comparison between the envelope of real conventional passenger trains (CBb type), the combined envelope of DTC0 and DTC1 trains, the combined envelope of DTC2 and DTC2e trains, and the HSLM-A envelope. Results obtained with time-stepping analysis. All DTCs with $P_{MUclass} = 21.5$ *t.*

8.1.1.3 CBc reference trains

For the CBc family, the DTC2 + DTC2e and DTC0 + DTC1 combinations both cover the envelope of real trains in low-frequency bridges, as shown in Figure 83, although DTC2 + DTC2e provides a more refined fit to the actual demand. HSLM-A, in contrast, proves excessively conservative across a wide range of wavelengths. Similar trends are observed in intermediate-frequency bridges (Figure 84), where the proposed DTCs adapt well to the resonant peaks of real trains, while HSLM-A remains insensitive to these features—resulting in either significant overprediction or underprediction of the response. In the short wavelengths that govern the behaviour of high-frequency bridges (Figure 85), DTC2 + DTC2e achieves a closer match to real train accelerations compared to DTC0 + DTC1, and especially to HSLM-A.

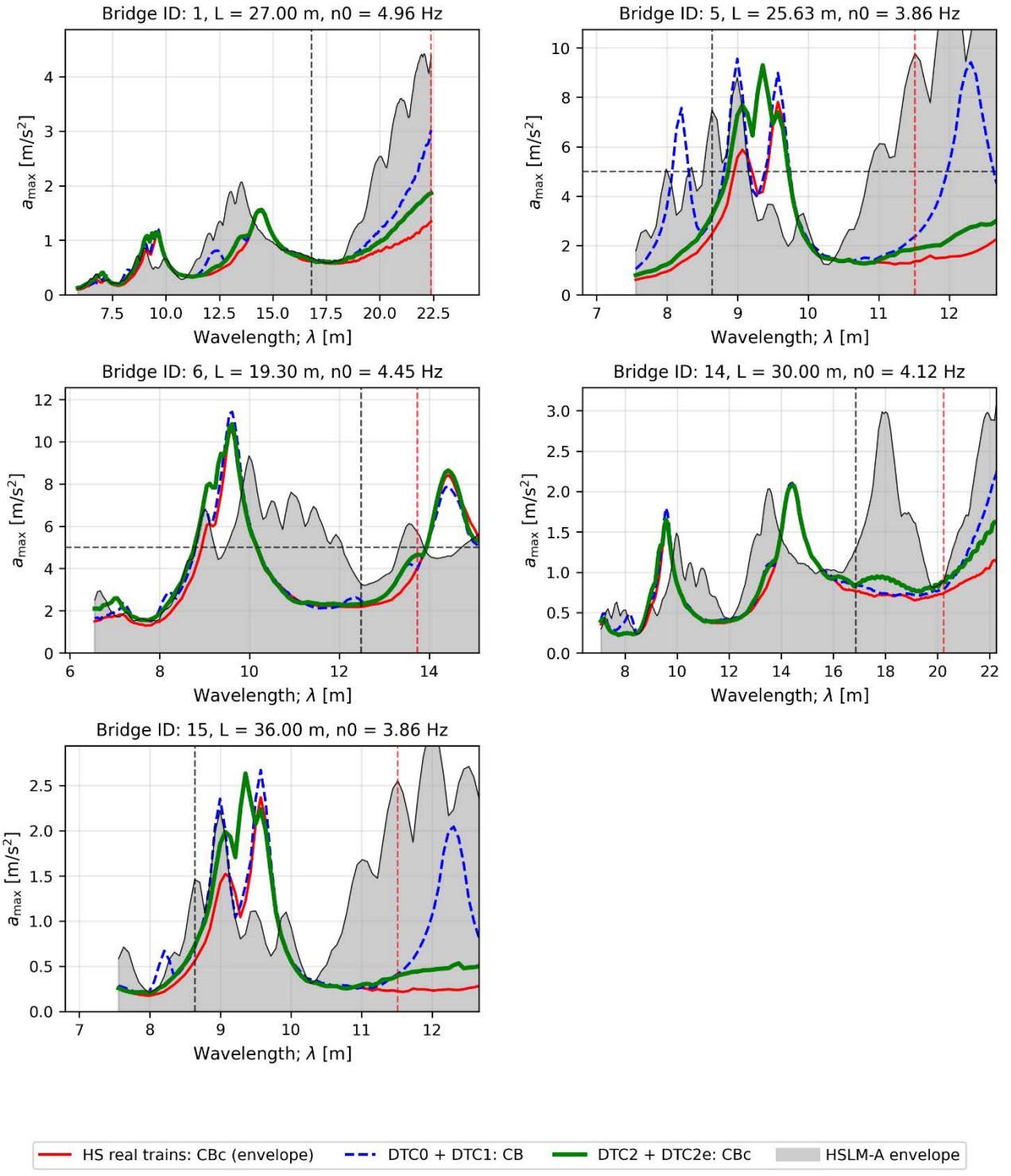

Figure 83. Envelope of the peak vertical acceleration in bridges with 'low' natural frequency for different wavelengths. Comparison between the envelope of real conventional passenger trains (CBc type), the combined envelope of DTC0 and DTC1 trains, the combined envelope of DTC2 and DTC2e trains, and the HSLM-A envelope. Results obtained with time-stepping analysis. All DTCs with $P_{MUclass} = 21.5$ *t.*

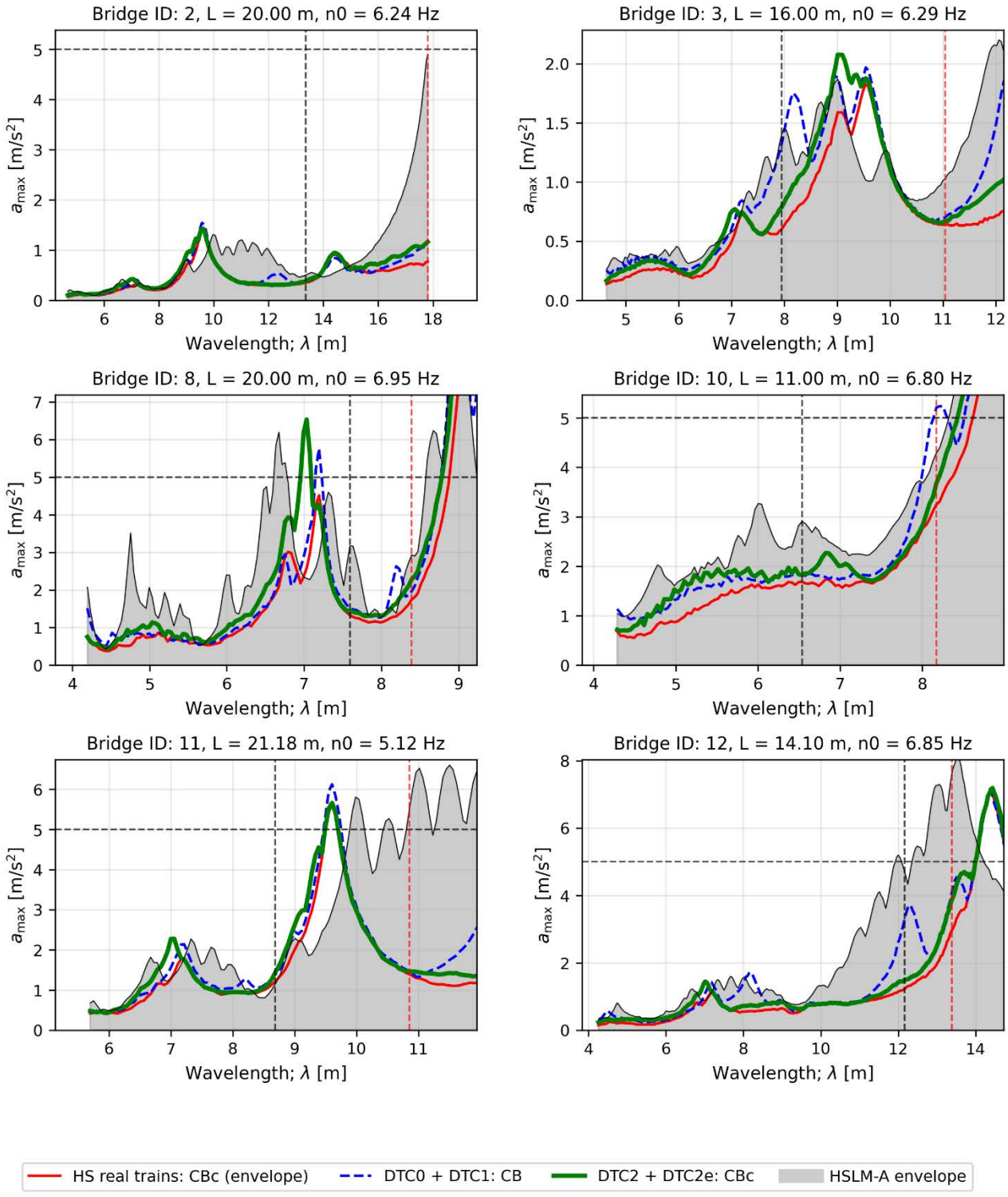

Figure 84. Envelope of the peak vertical acceleration in bridges with 'intermediate' natural frequency for different wavelengths. Comparison between the envelope of real conventional passenger trains (CBc type), the combined envelope of DTC0 and DTC1 trains, the combined envelope of DTC2 and DTC2e trains, and the HSLM-A envelope. Results obtained with time-stepping analysis. All DTCs with $P_{MUclass} = 21.5$ *t.*

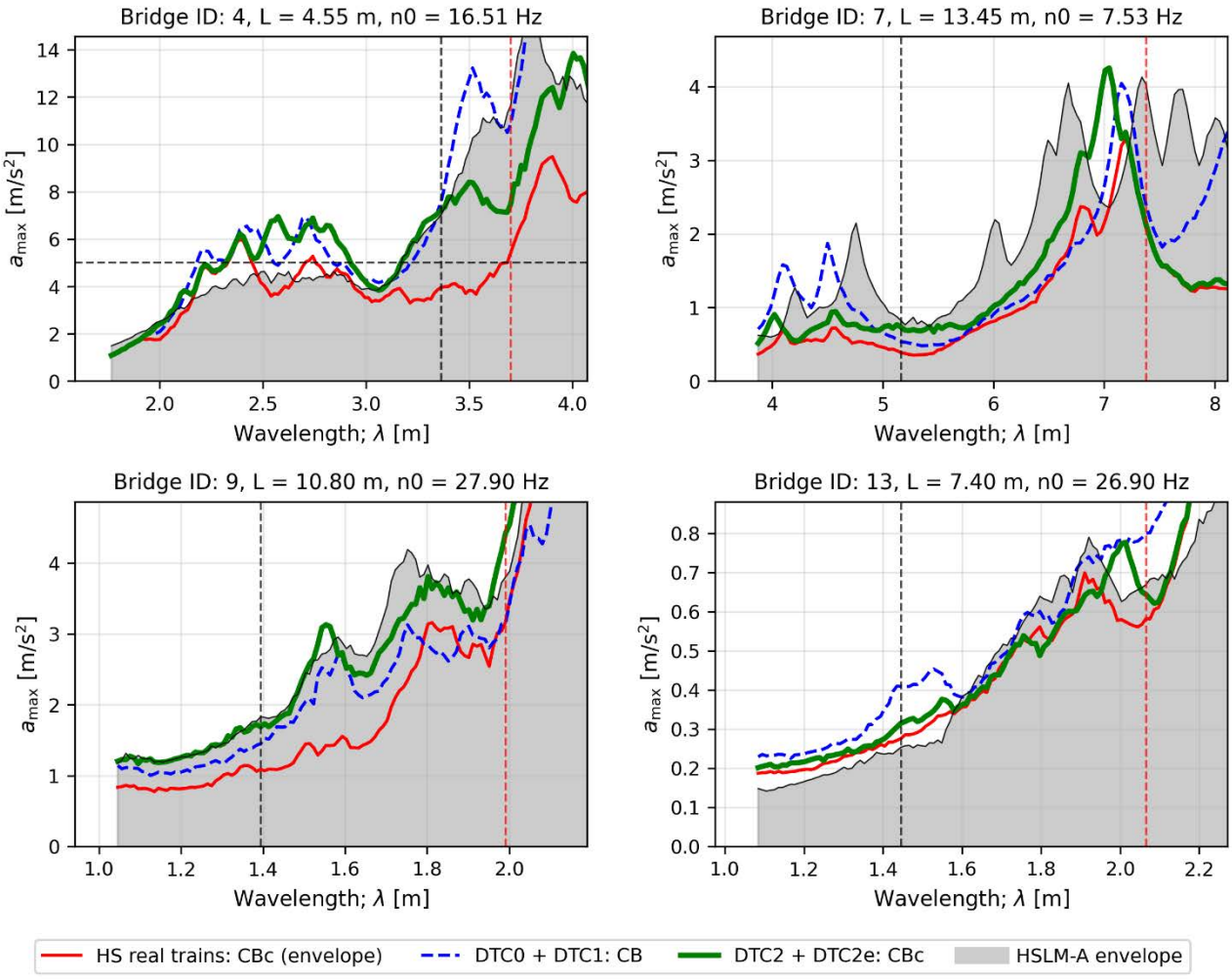

Figure 85. Envelope of the peak vertical acceleration in bridges with 'high' natural frequency for different wavelengths. Comparison between the envelope of real conventional passenger trains (CBc type), the combined envelope of DTC0 and DTC1 trains, the combined envelope of DTC2 and DTC2e trains, and the HSLM-A envelope. Results obtained with time-stepping analysis. All DTCs with $P_{MUclass} = 21.5$ *t.*

8.1.2 Trains with Articulated Bogies: AB

8.1.2.1 ABa reference trains

For the articulated ABa family, the DTC2 + DTC2e combination again exhibits excellent agreement with real trains, covering the envelope of real accelerations across all relevant wavelengths for low, intermediate and high-frequency bridges, as shown in Figures 86, 87 and 88, respectively. In contrast, DTC0 + DTC1 significantly overpredicts the accelerations—by factors of approximately 10, 8 and 5 in low, intermediate and high-frequency bridges, respectively, while HSLM-A is even more conservative at certain values of λ. Moreover, both DTC0 + DTC1 and HSLM-A also prove unsafe across a wide range of operating wavelengths, falling below the real train envelope in certain regions.

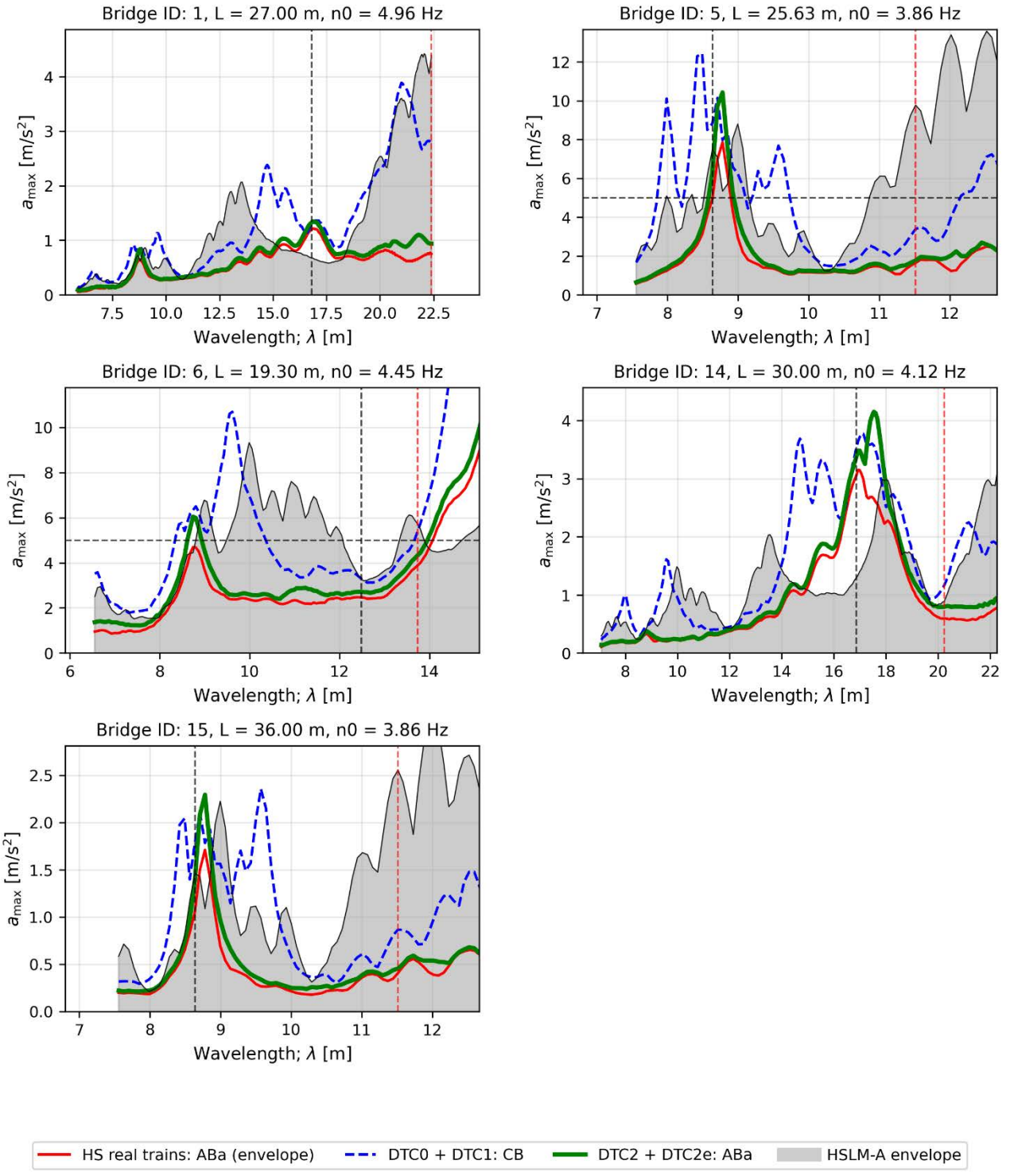

Figure 86. Envelope of the peak vertical acceleration in bridges with 'low' natural frequency for different wavelengths. Comparison between the envelope of real articulated passenger trains (ABa type), the combined envelope of DTC0 and DTC1 trains, the combined envelope of DTC2 and DTC2e trains, and the HSLM-A envelope. Results obtained with time-stepping analysis. All DTCs with $P_{MUclass} = 21.5$ *t.*

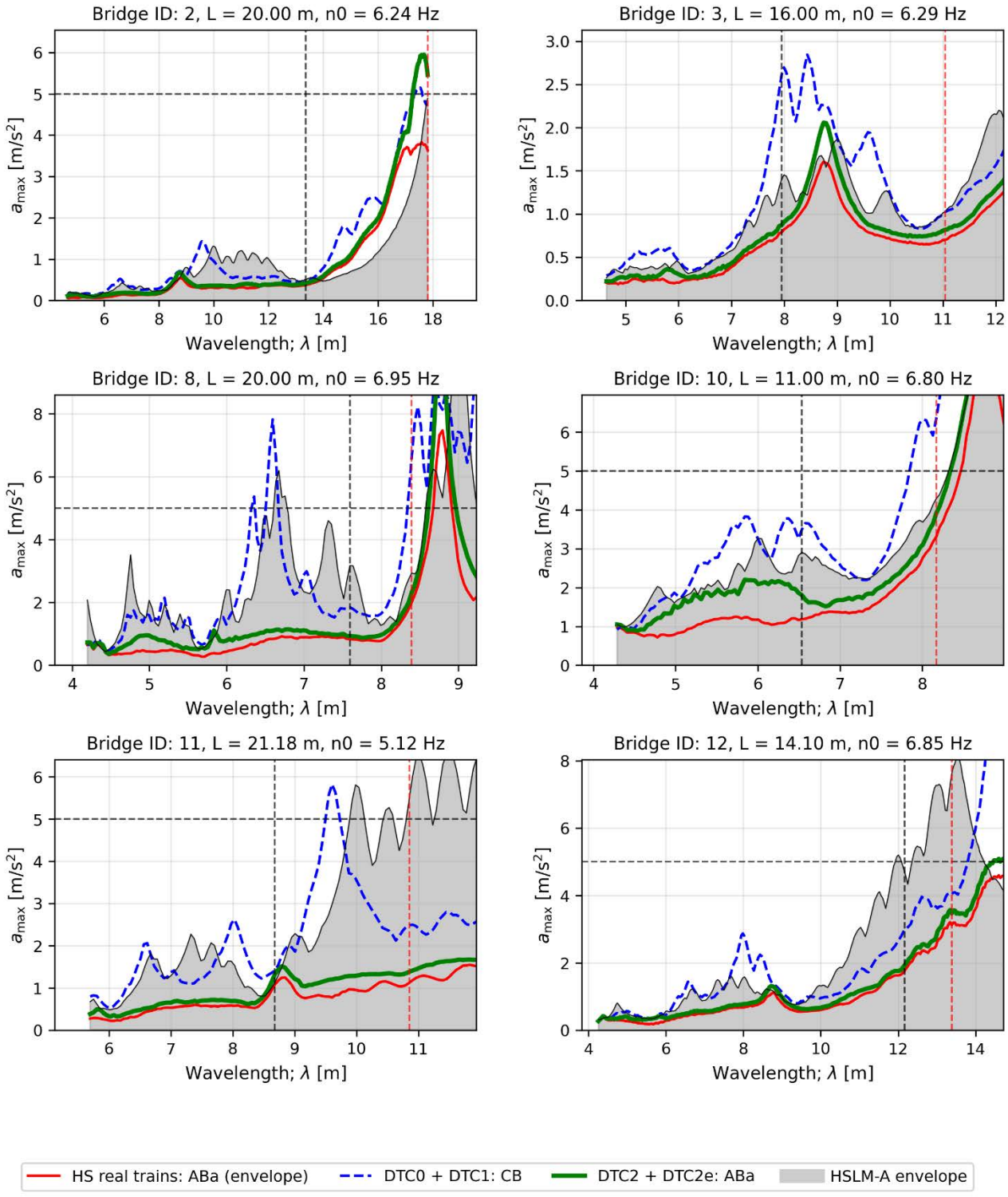

Figure 87. Envelope of the peak vertical acceleration in bridges with 'intermediate' natural frequency for different wavelengths. Comparison between the envelope of real articulated passenger trains (ABa type), the combined envelope of DTC0 and DTC1 trains, the combined envelope of DTC2 and DTC2e trains, and the HSLM-A envelope. Results obtained with time-stepping analysis. All DTCs with $P_{MUclass} = 21.5$ *t.*

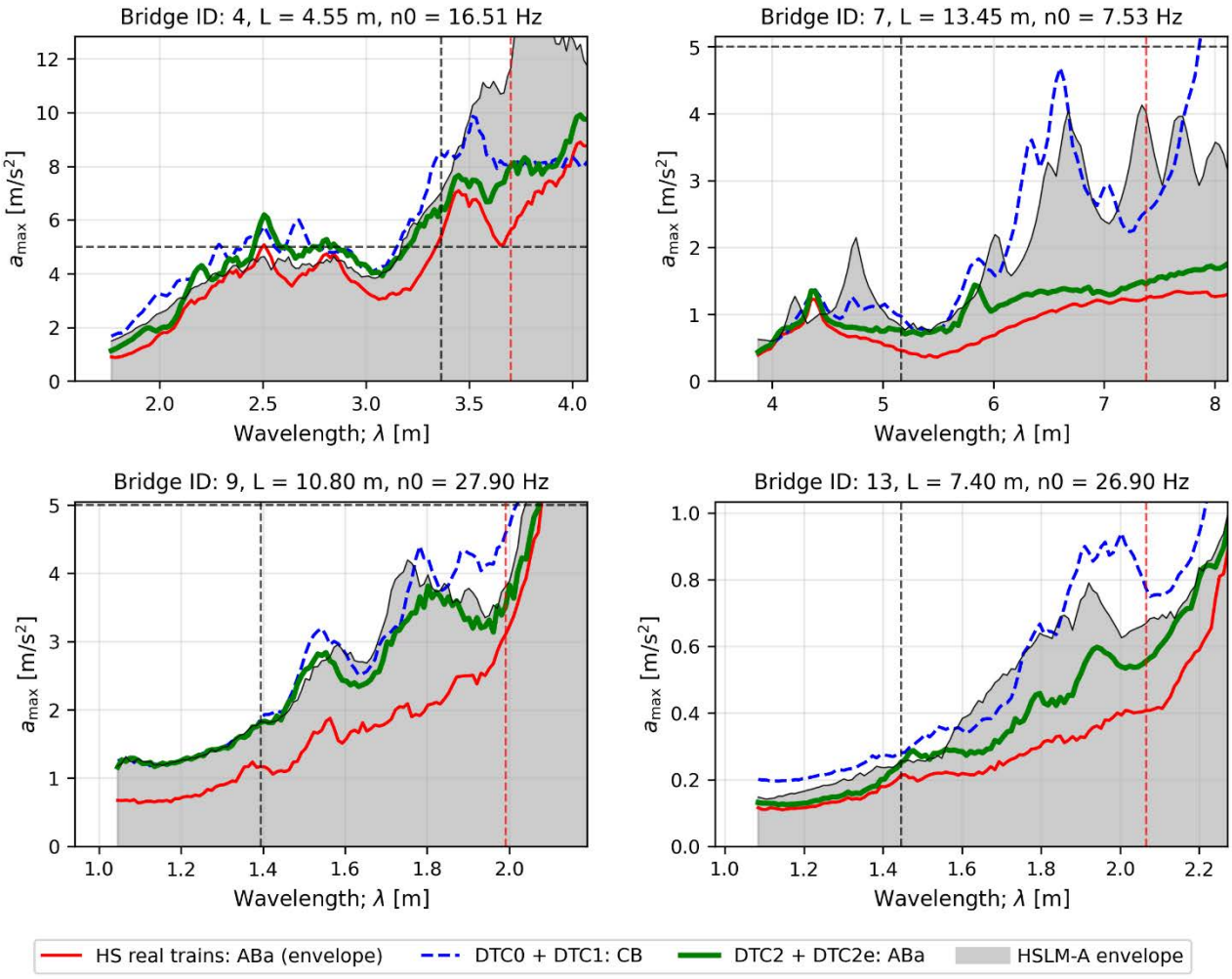

Figure 88. Envelope of the peak vertical acceleration in bridges with 'high' natural frequency for different wavelengths. Comparison between the envelope of real articulated passenger trains (ABa type), the combined envelope of DTC0 and DTC1 trains, the combined envelope of DTC2 and DTC2e trains, and the HSLM-A envelope. Results obtained with time-stepping analysis. All DTCs with $P_{MUclass} = 21.5$ *t.*

8.1.2.2 ABb reference trains

For the ABb family, the DTC2 + DTC2e combination again provides an excellent fit to the acceleration demand of real trains in low-frequency bridges, as shown in Figure 89. DTC0 + DTC1 offers reasonable alignment in the region of the resonant peak, but becomes excessively conservative at longer wavelengths. HSLM-A exhibits even greater variability, either severely overpredicting or significantly underpredicting the vibrations induced by real ABb trains in low-frequency bridges. Similar observations hold for intermediate and high-frequency bridges, as illustrated in Figures 90 and 91. In these cases, DTC2 + DTC2e consistently covers the full range of real train vibrations, while DTC0 + DTC1 substantially overpredicts the response at the relatively short wavelengths associated with operational train speeds.

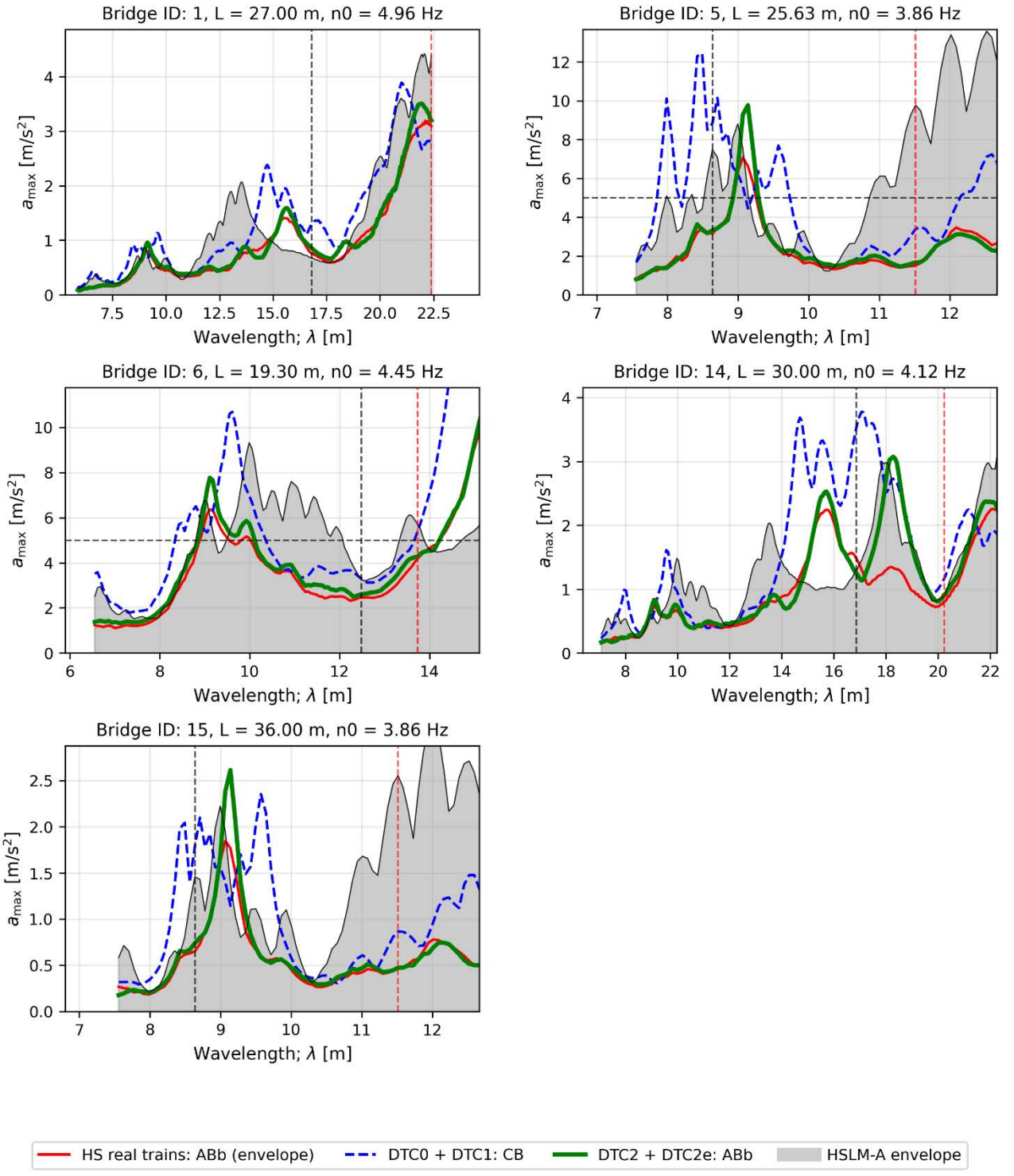

Figure 89. Envelope of the peak vertical acceleration in bridges with 'low' natural frequency for different wavelengths. Comparison between the envelope of real articulated passenger trains (ABb type), the combined envelope of DTC0 and DTC1 trains, the combined envelope of DTC2 and DTC2e trains, and the HSLM-A envelope. Results obtained with time-stepping analysis. All DTCs with $P_{MUclass} = 21.5$ *t.*

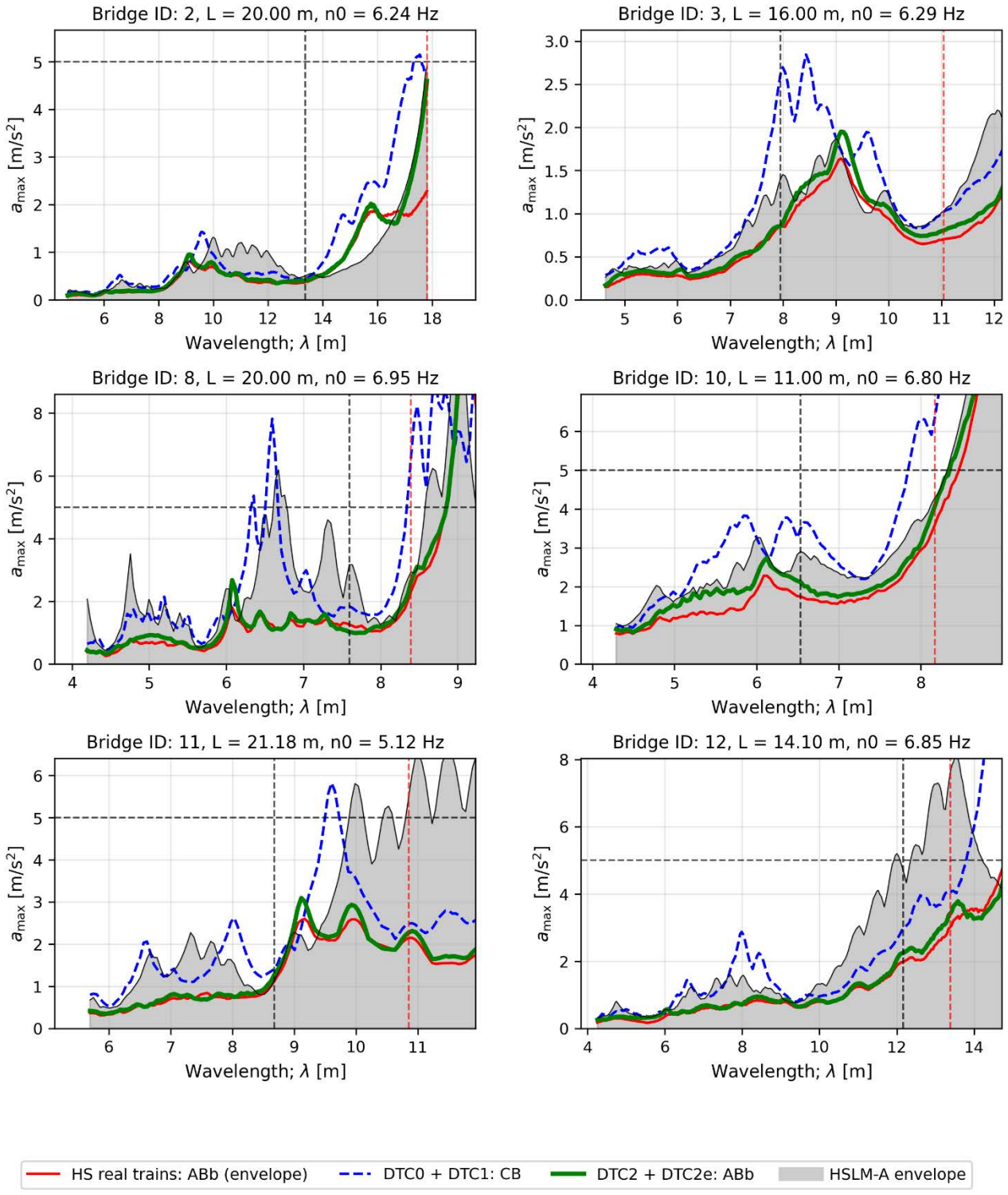

Figure 90. Envelope of the peak vertical acceleration in bridges with 'intermediate' natural frequency for different wavelengths. Comparison between the envelope of real articulated passenger trains (ABb type), the combined envelope of DTC0 and DTC1 trains, the combined envelope of DTC2 and DTC2e trains, and the HSLM-A envelope. Results obtained with time-stepping analysis. All DTCs with $P_{MUclass} = 21.5$ *t.*

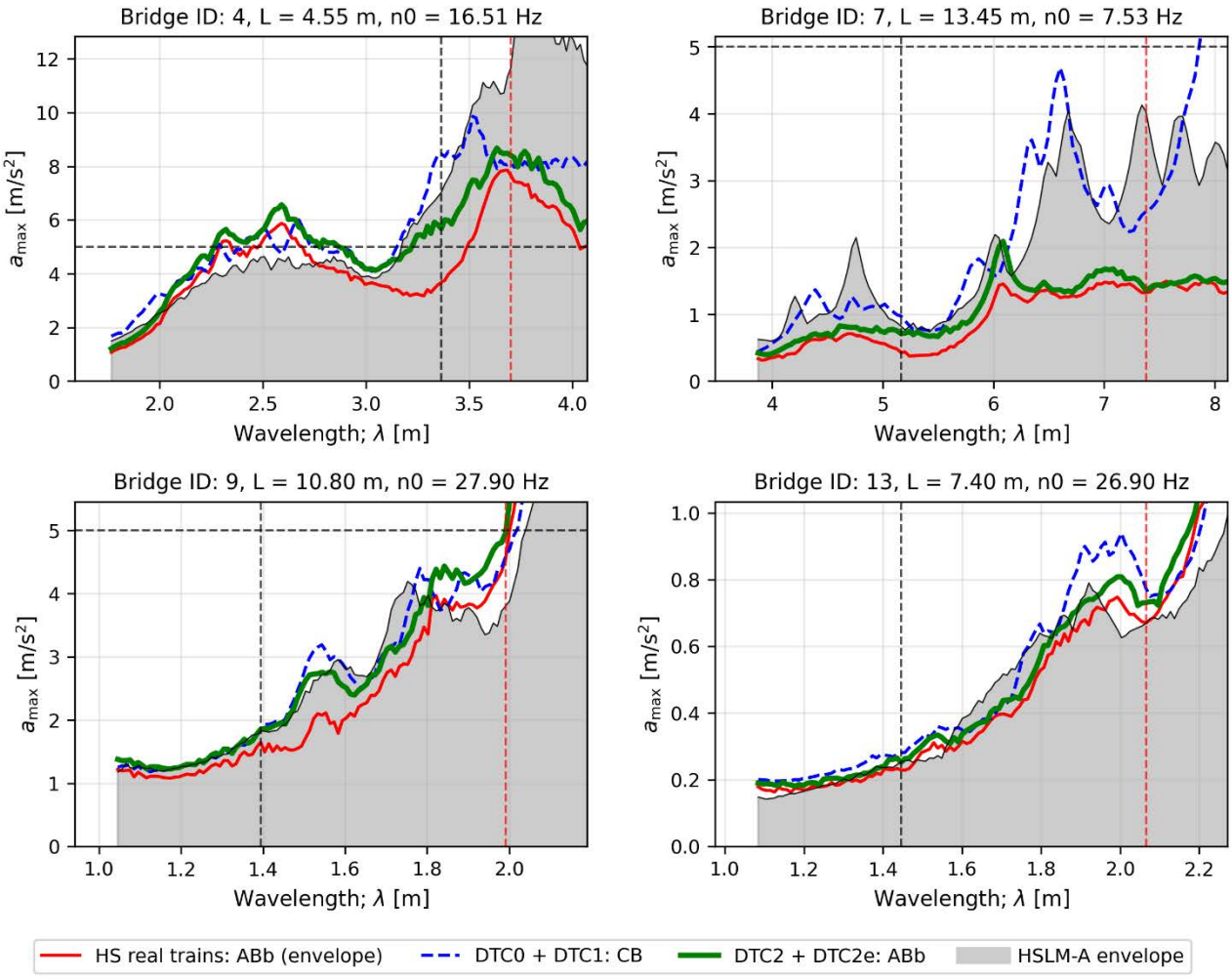

Figure 91. Envelope of the peak vertical acceleration in bridges with 'high' natural frequency for different wavelengths. Comparison between the envelope of real articulated passenger trains (ABb type), the combined envelope of DTC0 and DTC1 trains, the combined envelope of DTC2 and DTC2e trains, and the HSLM-A envelope. Results obtained with time-stepping analysis. All DTCs with $P_{MUclass} = 21.5$ *t.*

8.1.2.3 ABc reference trains

For the ABc family, Figure 92 shows that DTC2 + DTC2e achieves a good match to the dynamic response of real trains in relatively long-span bridges. In contrast, DTC0 + DTC1 significantly overpredicts the accelerations, particularly in the wavelength ranges $\lambda \approx 7$–10 m and above 14 m. HSLM-A also exhibits excessive conservatism in these wavelength regions, which dominate the response of low-frequency bridges. Similar observations are made in Figure 93 for intermediate-frequency bridges, where DTC0 + DTC1 proves overly conservative in the range $\lambda \approx 7$–10 m, while DTC2 + DTC2e remains well aligned with the real train demand. In high-frequency bridges, as shown in Figure 94, all DTCs and HSLM-A adequately cover the effects of ABc trains. However, DTC0 + DTC1 and HSLM-A are too conservative in the ranges $\lambda \approx 6$–8 m and $\lambda \approx$ 1.7–2 m.

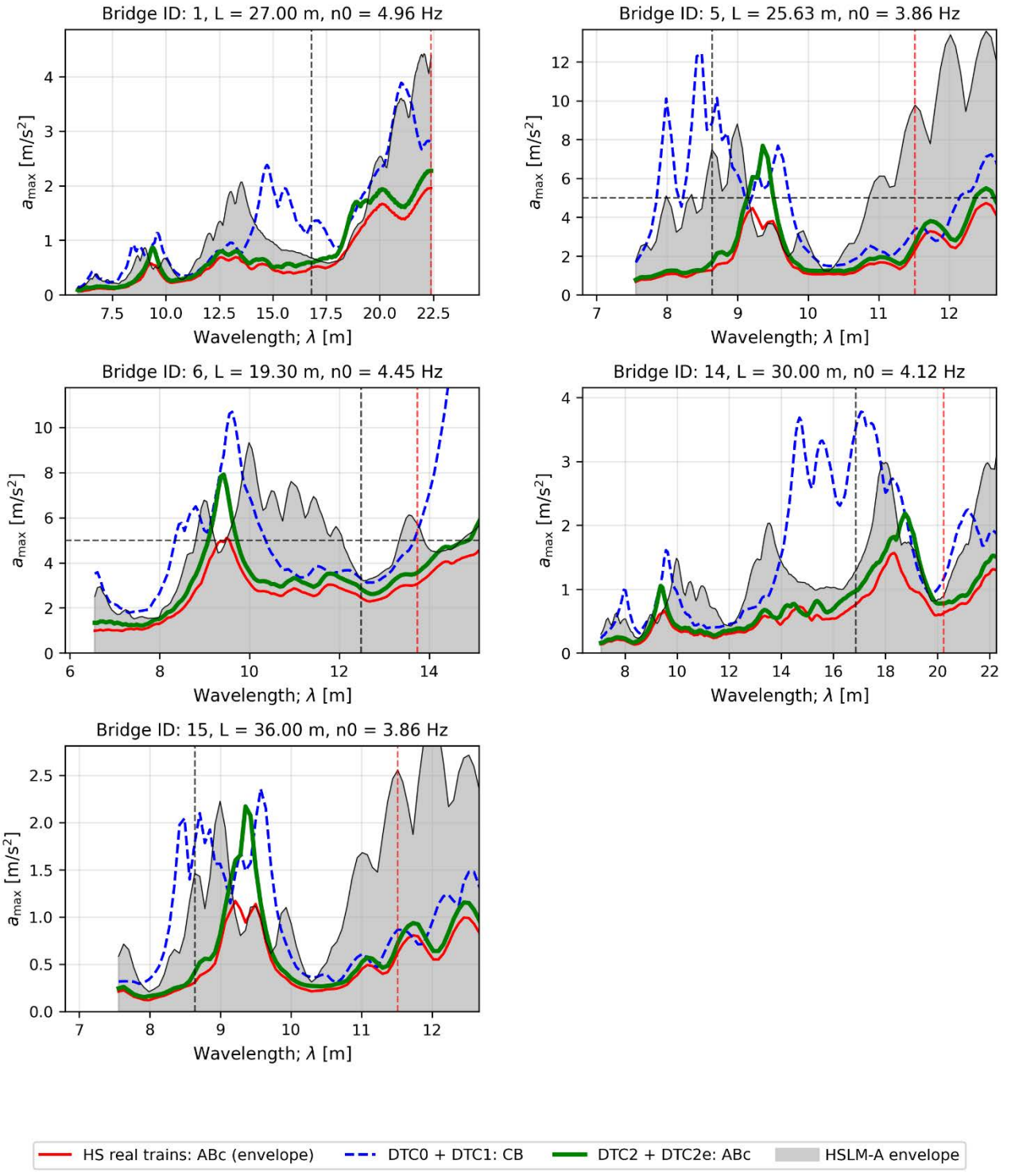

Figure 92. Envelope of the peak vertical acceleration in bridges with 'low' natural frequency for different wavelengths. Comparison between the envelope of real articulated passenger trains (ABc type), the combined envelope of DTC0 and DTC1 trains, the combined envelope of DTC2 and DTC2e trains, and the HSLM-A envelope. Results obtained with time-stepping analysis. All DTCs with $P_{MUclass} = 21.5$ *t.*

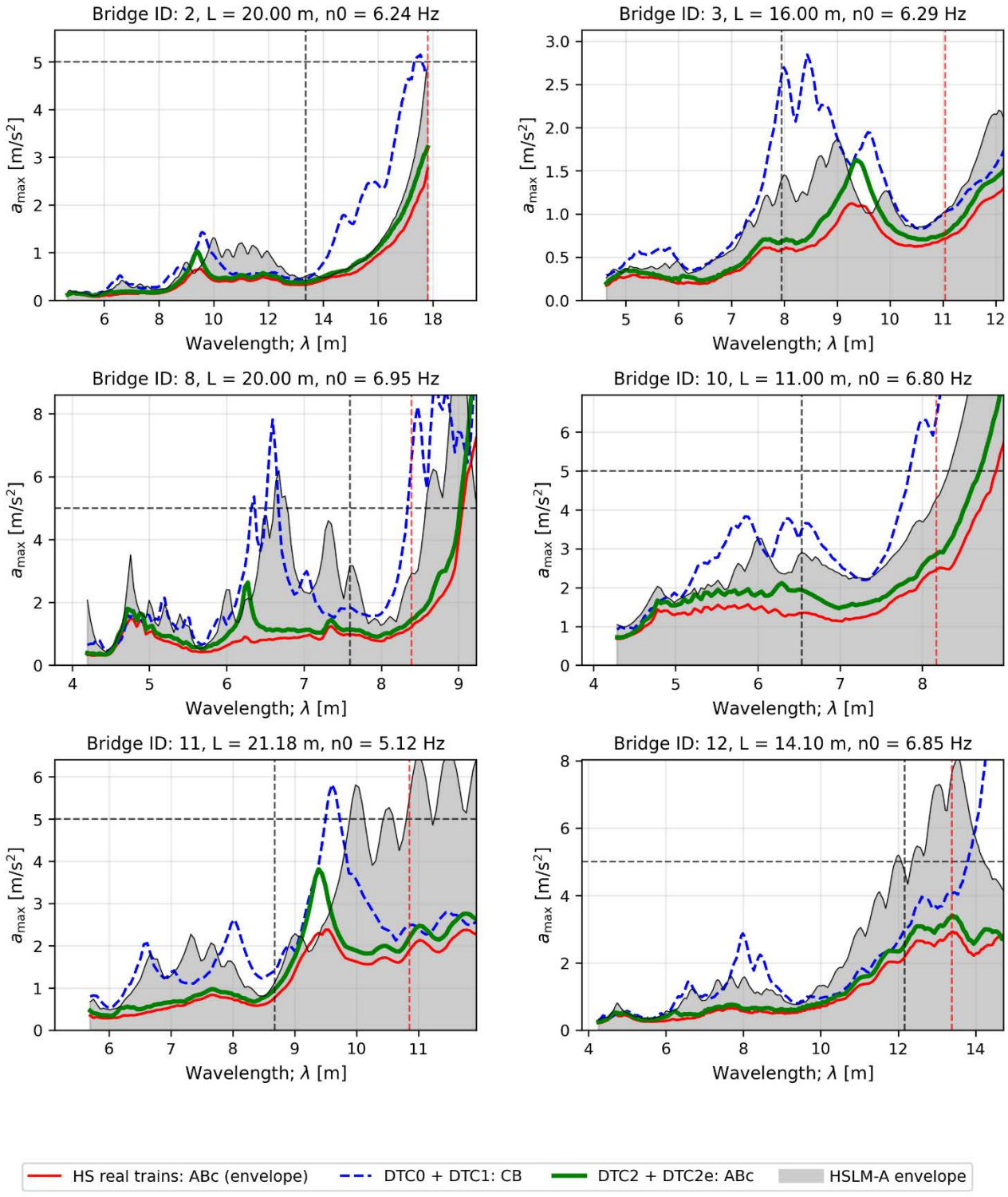

Figure 93. Envelope of the peak vertical acceleration in bridges with 'intermediate' natural frequency for different wavelengths. Comparison between the envelope of real articulated passenger trains (ABc type), the combined envelope of DTC0 and DTC1 trains, the combined envelope of DTC2 and DTC2e trains, and the HSLM-A envelope. Results obtained with time-stepping analysis. All DTCs with $P_{MUclass} = 21.5$ *t.*

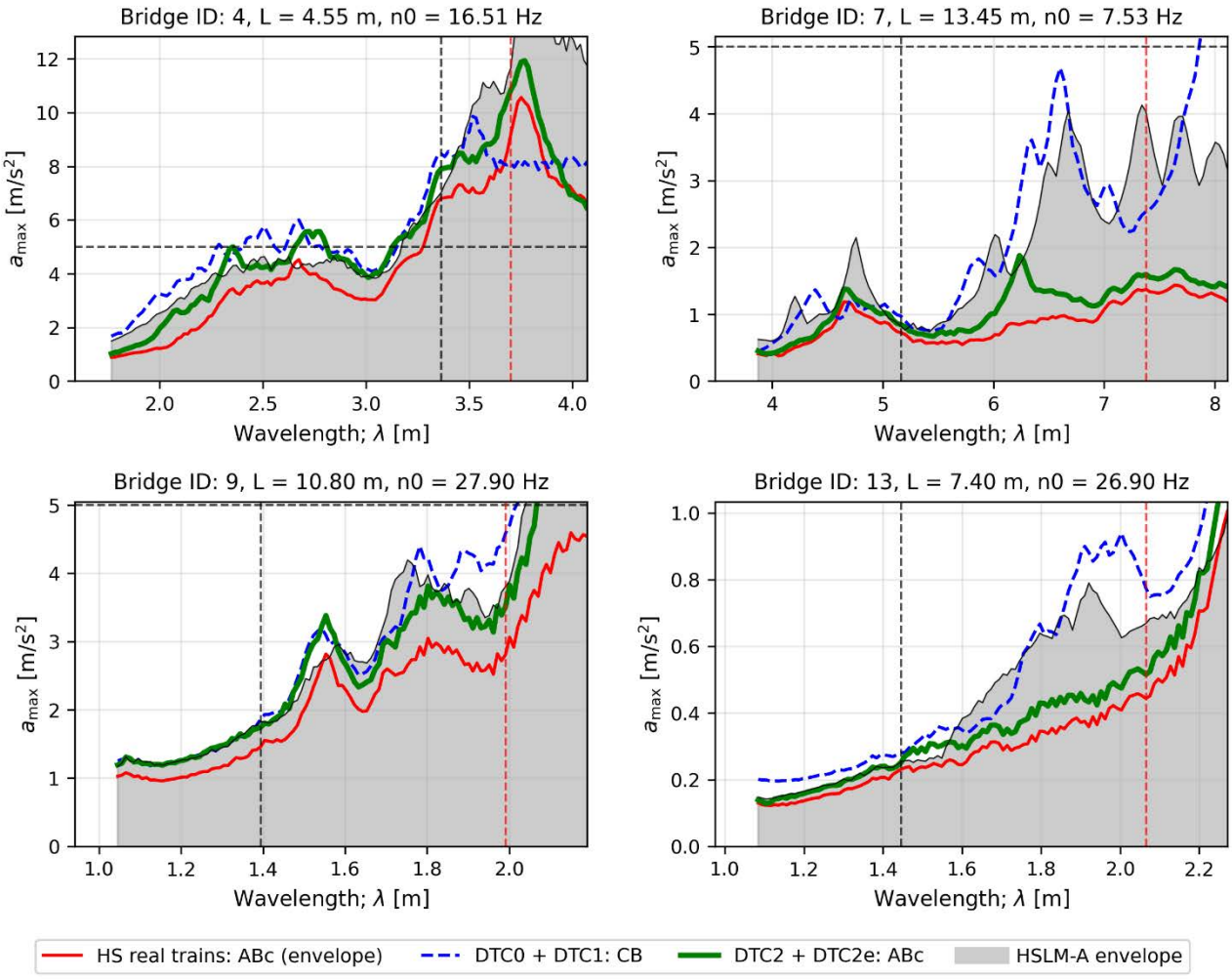

Figure 94. Envelope of the peak vertical acceleration in bridges with 'high' natural frequency for different wavelengths. Comparison between the envelope of real articulated passenger trains (ABc type), the combined envelope of DTC0 and DTC1 trains, the combined envelope of DTC2 and DTC2e trains, and the HSLM-A envelope. Results obtained with time-stepping analysis. All DTCs with $P_{MUclass} = 21.5$ *t.*

8.1.3 Regular trains: SA

8.1.3.1 SAa reference trains

For the SAa family, Figure 95 shows that all DTC envelopes and HSLM-A adequately cover the effects of real trains in low-frequency bridges. However, DTC2 + DTC2e provides a closer fit to the actual demand compared to the other models. The same trend is observed in Figure 96 for intermediate-frequency bridges, where it is notable that the resonant peak associated with the first subharmonic at $\lambda \approx 6.5$ m (half the coach length) is underestimated by both DTC0 + DTC1 and HSLM-A, but it is well captured by DTC2 + DTC2e. In high-frequency bridges (Figure 97), DTC2 + DTC2e again exhibits good alignment with the real train demand, whereas DTC0 + DTC1 overpredicts the response at very short wavelengths around $\lambda \approx 1.8$ m, which can have significant effects in the shortest structures.

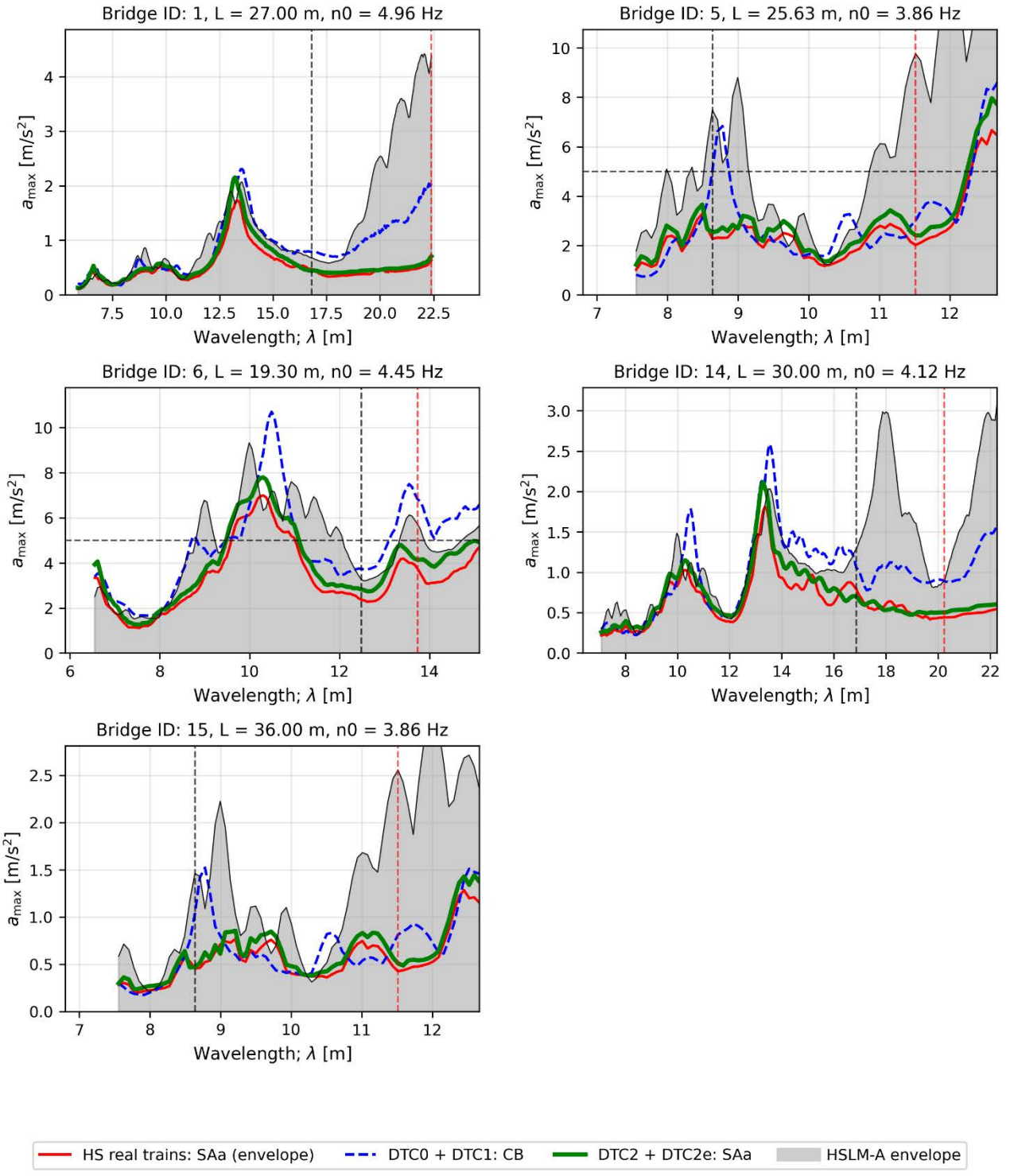

Figure 95. Envelope of the peak vertical acceleration in bridges with 'low' natural frequency for different wavelengths. Comparison between the envelope of real regular passenger trains (SAa type), the combined envelope of DTC0 and DTC1 trains, the combined envelope of DTC2 and DTC2e trains, and the HSLM-A envelope. Results obtained with time-stepping analysis. All DTCs with $P_{MUclass} = 21.5$ *t.*

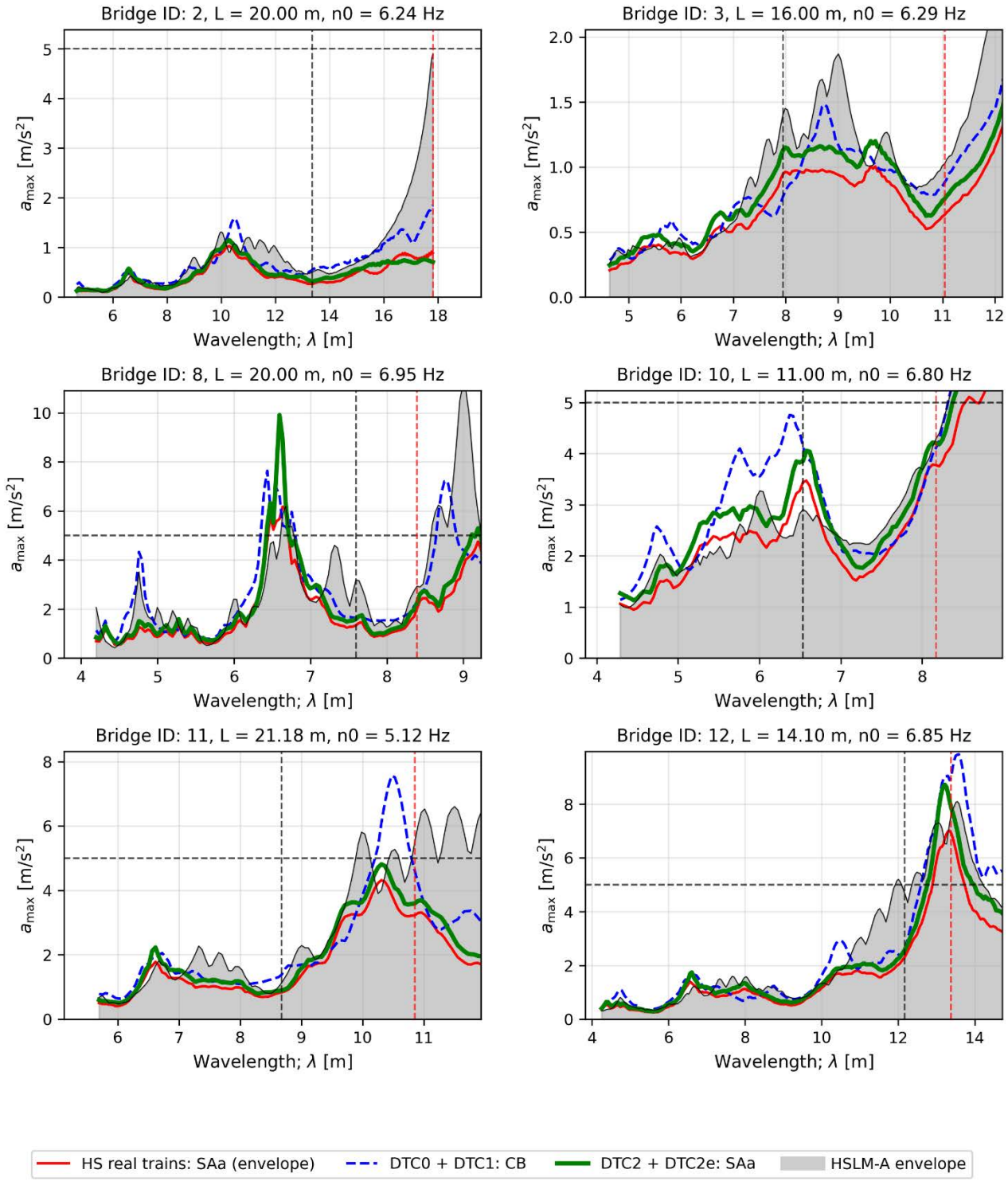

Figure 96. Envelope of the peak vertical acceleration in bridges with 'intermediate' natural frequency for different wavelengths. Comparison between the envelope of real regular passenger trains (SAa type), the combined envelope of DTC0 and DTC1 trains, the combined envelope of DTC2 and DTC2e trains, and the HSLM-A envelope. Results obtained with time-stepping analysis. All DTCs with $P_{MUclass} = 21.5$ *t.*

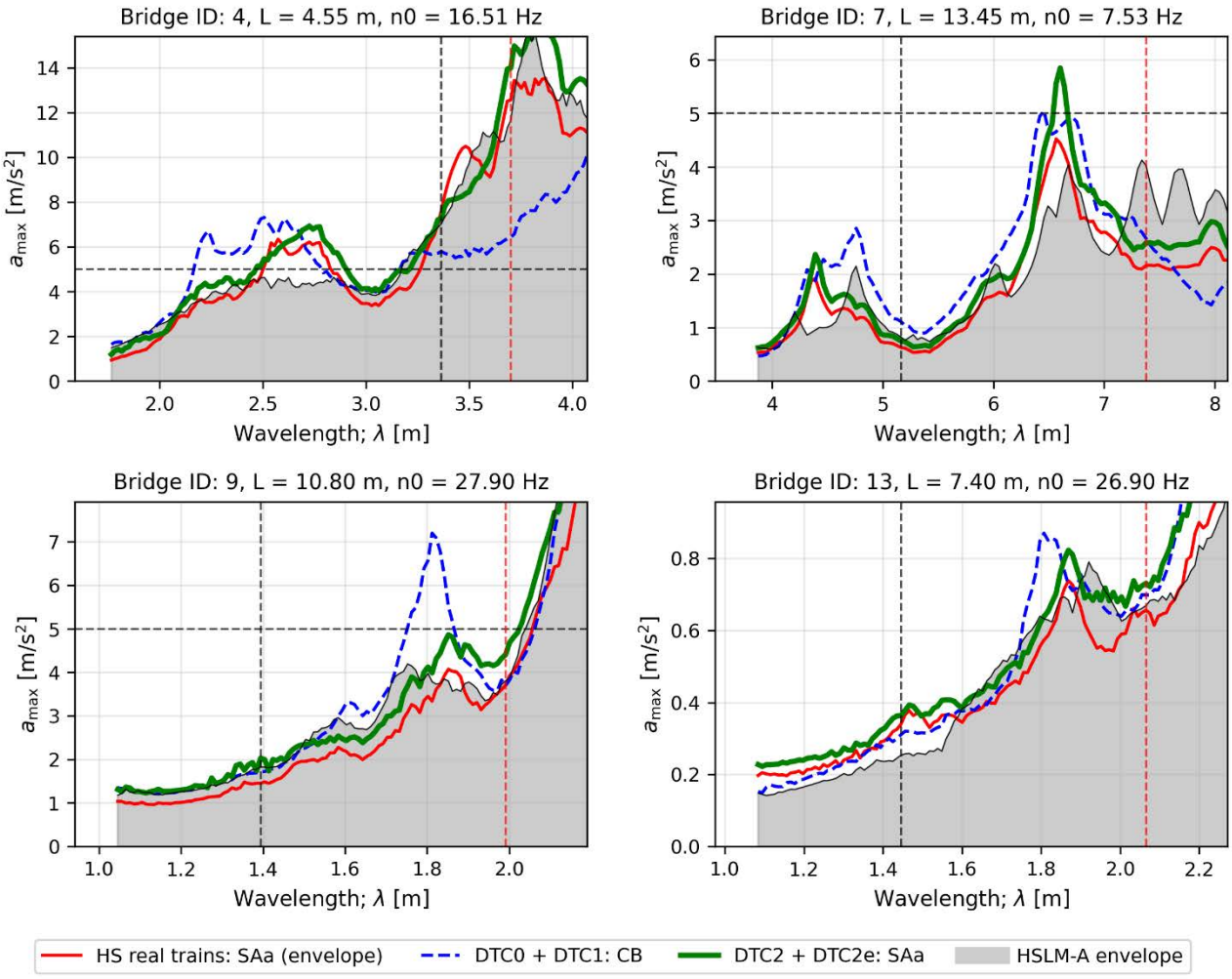

Figure 97. Envelope of the peak vertical acceleration in bridges with 'high' natural frequency for different wavelengths. Comparison between the envelope of real regular passenger trains (SAa type), the combined envelope of DTC0 and DTC1 trains, the combined envelope of DTC2 and DTC2e trains, and the HSLM-A envelope. Results obtained with time-stepping analysis. All DTCs with $P_{MUclass} = 21.5$ *t.*

8.1.3.2 SAb reference trains

The SAb family presents greater complexity due to the richer nature of the axle distributions in real trains. As shown in Figure 98, for the largest bridges the DTC2 + DTC2e model adequately covers the vibrations induced by real trains within this group. Although marginally below demand in a few cases (e.g., bridge ID6), this discrepancy is not deemed relevant, as the model remains capable of dynamically representing the action of real SAb trains. In contrast, DTC0 + DTC1 and HSLM-A are clearly overconservative across most wavelengths, while also strongly underpredicting the response near resonance in some instances. Similar observations are made for intermediate and high-frequency bridges, as illustrated in Figures 99 and 100.

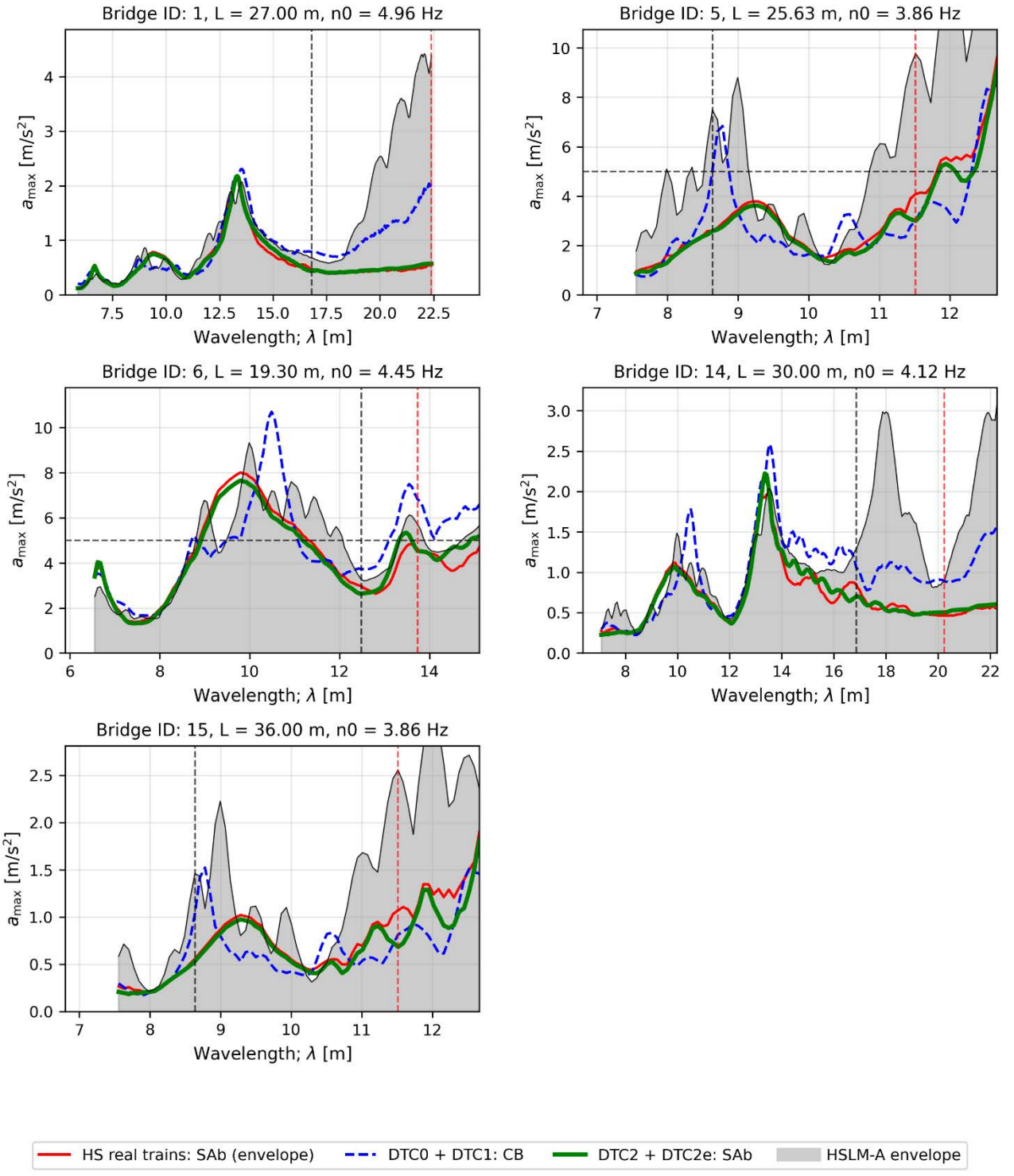

Figure 98. Envelope of the peak vertical acceleration in bridges with 'low' natural frequency for different wavelengths. Comparison between the envelope of real regular passenger trains (SAb type), the combined envelope of DTC0 and DTC1 trains, the combined envelope of DTC2 and DTC2e trains, and the HSLM-A envelope. Results obtained with time-stepping analysis. All DTCs with $P_{MUclass} = 21.5$ *t.*

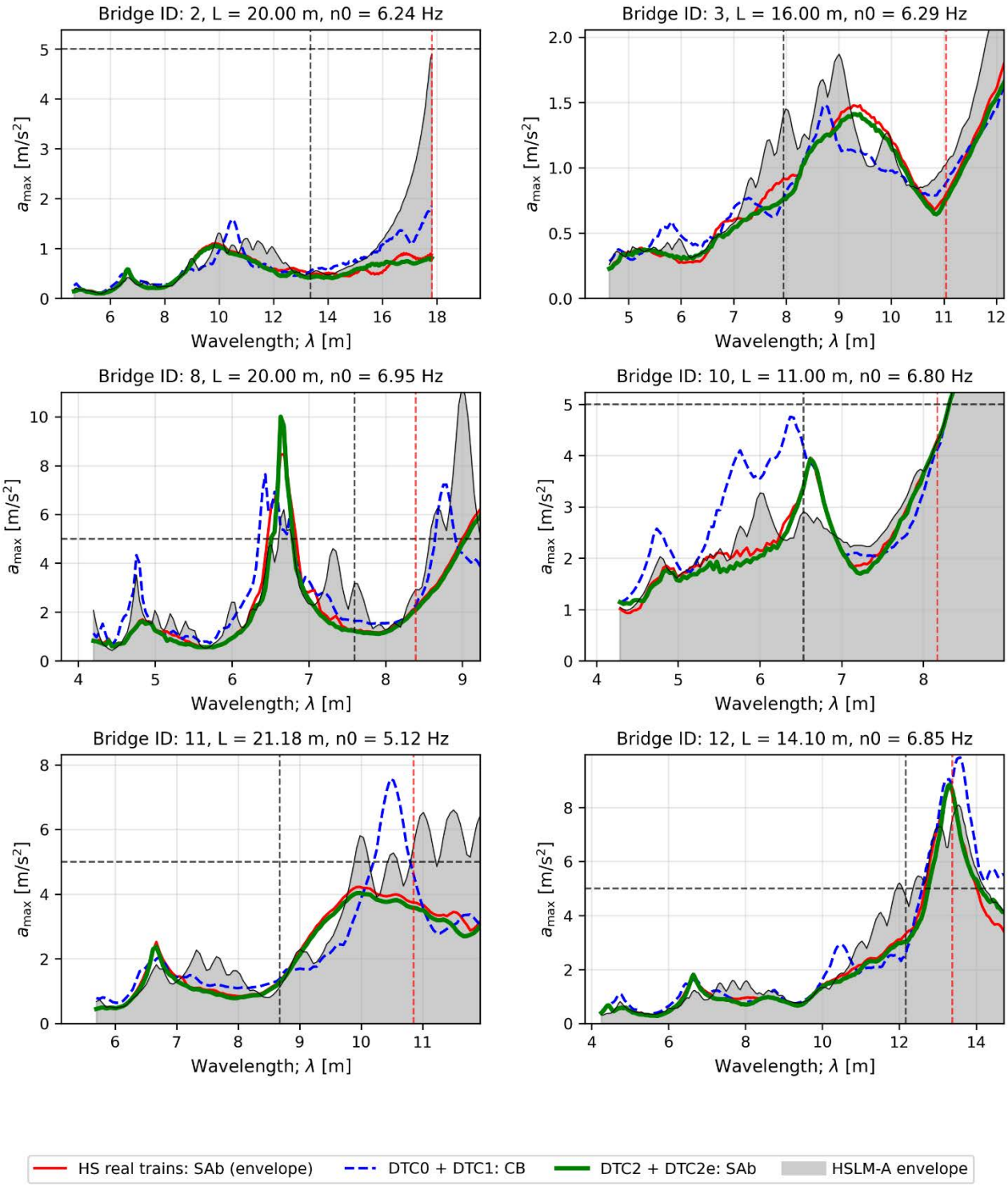

Figure 99. Envelope of the peak vertical acceleration in bridges with 'intermediate' natural frequency for different wavelengths. Comparison between the envelope of real regular passenger trains (SAb type), the combined envelope of DTC0 and DTC1 trains, the combined envelope of DTC2 and DTC2e trains, and the HSLM-A envelope. Results obtained with time-stepping analysis. All DTCs with $P_{MUclass} = 21.5$ *t.*

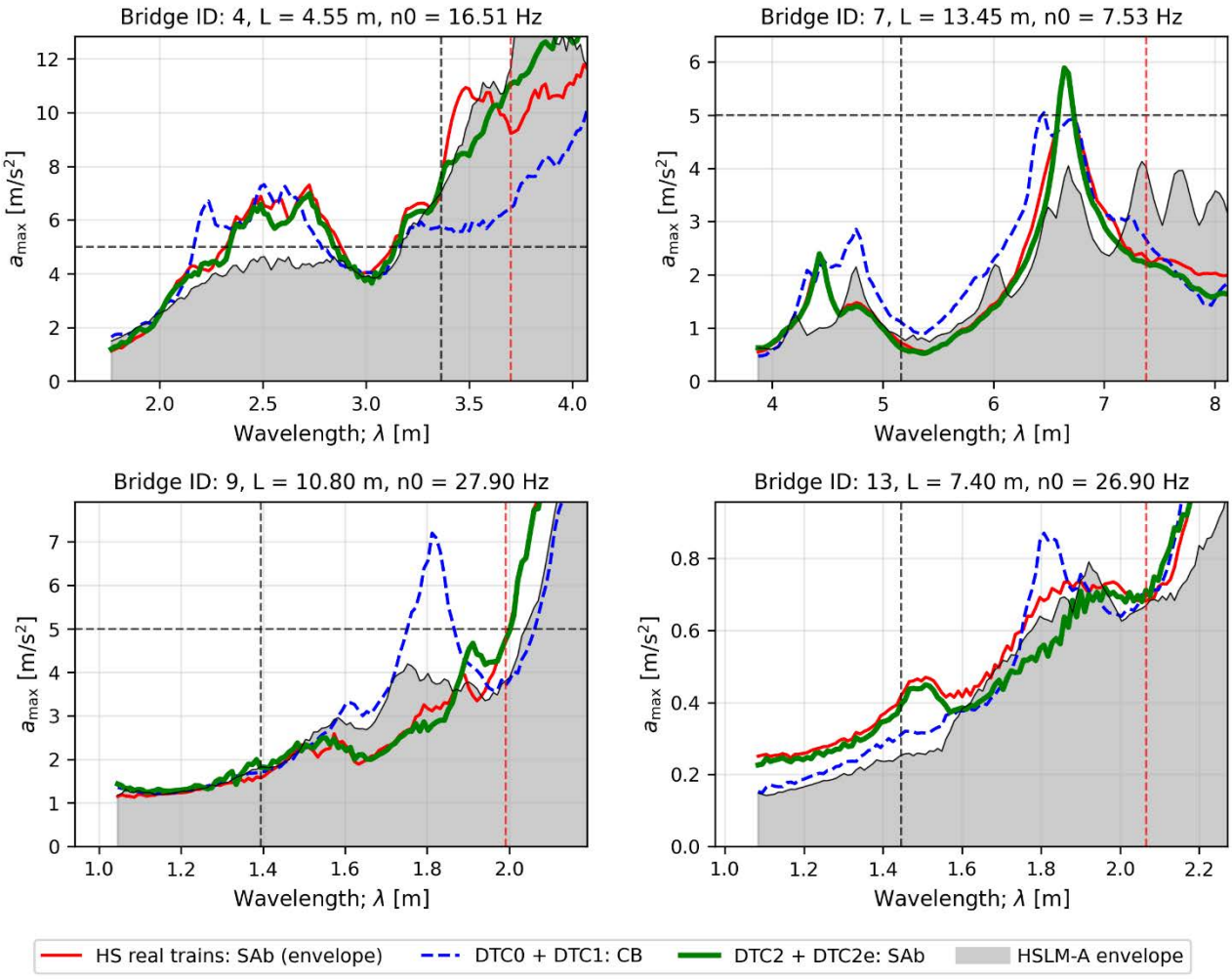

Figure 100. Envelope of the peak vertical acceleration in bridges with 'high' natural frequency for different wavelengths. Comparison between the envelope of real regular passenger trains (SAb type), the combined envelope of DTC0 and DTC1 trains, the combined envelope of DTC2 and DTC2e trains, and the HSLM-A envelope. Results obtained with time-stepping analysis. All DTCs with $P_{MUclass} = 21.5\ t$.

9 Conclusions and recommendations

This study has undertaken a comprehensive assessment of the dynamic behaviour of passenger railway bridges through an extensive analysis comprising three progressively refined methodologies: undamped train signatures, LIR-based calculations, and full time-stepping simulations. A total of 221 real passenger trains (with maximum speeds higher or equal 200 km/h) were analysed alongside 8 reference trains from DTC0, 4 from DTC1, 8 optimised resonant trains from DTC2, and an additional 23 supplemental trains in DTC2e, complemented by the 10 HSLM-A load models defined in EN 1991-2. This ensemble of 274 train configurations was systematically evaluated across 15 representative European bridges covering a broad range of spans, fundamental frequencies, and structural typologies, with each train considered over a wide range of operating speeds. The following conclusions are drawn:

- The results demonstrate that the HSLM-A load models, as defined in EN 1991-2, are unable to fully capture the dynamic effects induced by modern passenger trains on representative European

bridges. The combination of DTC0 and DTC1, based on EN 15528:2015 and extended in this work to address spectral gaps observed in train signatures, provides a closer overall alignment with the envelope of real train responses, but it exhibits notable limitations. Specifically, this combination tends to be overly conservative across a significant range of wavelengths, while also remaining under-conservative in certain regions. In addition, DTC0 reference trains do not always represent the real trains grouped in their corresponding subcategories.

- The proposed DTC2 framework, comprising idealised long trains optimised to capture the dominant resonant peaks of real train families, effectively envelopes these peaks across the selected bridges. However, certain train configurations (particularly those with richer axle spacing patterns, such as regular trains) exhibit significant dynamic effects at wavelengths lying between the main resonant peaks, which are not adequately captured by the optimised DTC2 models alone. To address this limitation, the DTC2e extension is introduced. DTC2e consists of supplemental trains derived directly from time-stepping analyses of real passenger trains that consistently exceed the DTC2 envelope across multiple bridges. These trains preserve the exact axle spacing and normalised load distribution of the original configurations, capturing the complex transient effects arising from features such as locomotive contributions, unit couplings, and irregular axle arrangements. When combined with the resonant DTC2 trains, the DTC2e models provide an envelope that accounts for both the dominant resonant response and the secondary spectral content characteristic of more complex train formations.
- The combined DTC2 + DTC2e framework, comprising a total of 31 model trains, demonstrates that the envelope of these reference trains successfully covers the dynamic effects of all real trains in the database across the full set of bridges considered. Importantly, this coverage is achieved with significantly more refined safety margins compared to HSLM-A and the other DTC combinations. These results suggest that the proposed **DTC2 + DTC2e load model is valid for the design of new bridges**.
- When considering specific train families and their subcategories, the DTC2 + DTC2e framework proves to be dynamically representative of real trains within each group. It also enables adjusting to the specific axle load levels and MU classes defined for each line category. Consequently, **DTC2 + DTC2e is suited for the assessment of existing bridges**, where the particular subgroups of trains operating on the line are known. This targeted approach eliminates the need to evaluate train configurations and axle loads that will not circulate on the bridge, thereby enabling more realistic and efficient dynamic compatibility checks.

The proposed DTCs in this work are the combination of DTC2 and DTC2e. For each sub-category, the corresponding DTC reference trains are listed. Trains marked with * cannot be assigned to any of the defined sub-categories and therefore require a specific dynamic analysis using their actual axle spacing and load distribution. All DTC reference trains are normalised with respect to the P_{MUclass} (axle load level) applicable to the line category under consideration. The detailed axle configurations of the DTC2 resonant trains and DTC2e supplemental trains are provided in Appendices B and C, respectively.

Train Category	Coach Length: D [m]	Sub-Category	DTC reference trains (DTC2+DTC2e)
Conventional Bogies (CB)	D < 23 m	x	Not covered*
	23 m <= D < 25 m	CBa	CBa_1; CBa_2; CBa_3; CBa_4
	25 m <= D < 27 m	CBb	CBb_1; CBb_2; CBb_3; CBb_4; CBb_5
	27 m <= D < 29 m	CBc	CBc_1; CBc_2; CBc_3; CBc_4
	D >= 29 m	x	Not covered*
Articulated Bogies (AB)	D < 17 m	x	Not covered*
	17 m <= D < 18 m	ABa	ABa_1; ABa_2
	18 m <= D < 18.6 m	ABb	ABb_1; ABb_2
	18.6 m <= D < 19.2 m	ABc	ABc_1; ABc_2; ABc_3
	D >= 19.2 m	x	Not covered*
Regular trains (SA)	D < 13 m	x	Not covered*
	13 m <= D < 13.2 m	SAa	SAa_1; SAa_2; SAa_3; SAa_4;
	13.2 m <= D < 13.4 m	SAb	SAb_1; SAb_2; SAb_3; SAb_4; SAb_5; SAb_6; SAb_7
	D >= 13.4 m	x	Not covered*

Table 13. Dynamic Train Categories (DTC2 + DTC2e) for passenger trains (with maximum running speeds above or equal 200 km/h), organised by train type and coach length range.

REFERENCES

DLM Project. (2023). *Bridge dynamics; dynamic load model*. Research project funded by Deutsches Zentrum für Schienenverkehrsforschung (DZSF) beim Eisenbahn-Bundesamt.

EN 15528:2015. (2015). Railway applications – Line categories for managing the interface between load limits of vehicles and infrastructure. European Committee for Standardization (CEN). Brussels: CEN.

EN 15528:2021. (2021). Railway applications – Line categories for managing the interface between load limits of vehicles and infrastructure. European Committee for Standardization (CEN). Brussels: CEN.

EN 15663:2017+A2:2024. (2024). Railway applications - Vehicle reference masses. European Committee for Standardization (CEN). Brussels: CEN.

EN 1991-2:2023. (2023). Eurocode 1. Actions on structures - Part 2: Traffic loads on bridges and other civil engineering works. European Committee for Standardization (CEN). Brussels: CEN.

Nguyen, K., & Goicolea, J. M. (2024). CALDINTAV: A simple software for dynamic analysis of passenger railway bridges using the semi-analytical modal method. *Software Impacts, 22*, 100700. doi:https://doi.org/10.1016/j.simpa.2024.100700.

Van Rossum, G., & Python Software Foundation. (2023). *Python* (Version 3.x) [Computer software]. Python.org. https://www.python.org/

Zhu, C., Byrd, R. H., Lu, P., & Nocedal, J. (1997). Algorithm 778: L-BFGS-B: Fortran subroutines for large-scale bound-constrained optimization. *ACM Transactions on Mathematical Software*, 23(4), 550-560.

APPENDIX A: REFERENCE DTC0 AND DTC1 TRAINS

All the trains in this appendix are defined from their cumulative axle spacing, in m. Their axle loads are defined dending on the corresponding line category, or $P_{MUclass}$, according to EN 15528:2015.

CB trains

CB1 (DTC0)

0	196.7
3	199.7
17.2	213.9
20.2	216.9
24.5	221.2
27.5	224.2
41.7	238.4
44.7	241.4
49	245.7
52	248.7
66.2	262.9
69.2	265.9
73.5	270.2
76.5	273.2
90.7	287.4
93.7	290.4
98	294.7
101	297.7
115.2	311.9
118.2	314.9
122.5	319.2
125.5	322.2
139.7	336.4
142.7	339.4
147	343.7
150	346.7
164.2	360.9
167.2	363.9
171.5	368.2
174.5	371.2
188.7	385.4
191.7	388.4

CB2 (DTC0)

0	189
3	192
19	208
22	211
27	216
30	219
46	235
49	238
54	243
57	246
73	262
76	265
81	270
84	273
100	289
103	292
108	297
111	300
127	316
130	319
135	324
138	327
154	343
157	346
162	351
165	354
181	370
184	373

CB1_1 (DTC1)

0	201.4
2.5	203.9
19.7	221.1
22.2	223.6
28.7	230.1
31.2	232.6
48.4	249.8
50.9	252.3
57.4	258.8
59.9	261.3
77.1	278.5
79.6	281
86.1	287.5
88.6	290
105.8	307.2
108.3	309.7
114.8	316.2
117.3	318.7
134.5	335.9
137	338.4
143.5	344.9
146	347.4
163.2	364.6
165.7	367.1
172.2	373.6
174.7	376.1
191.9	393.3
194.4	395.8
	402.3

AB trains

AB1 (DTC0)

0	224
2	226
16	240
18	242
32	256
34	258
48	264
50	266
64	280
66	282
80	296
82	298
88	312
90	314
104	328
106	330
120	344
122	346
136	352
138	354
152	368
154	370
168	384
170	386
176	400
178	402
192	416
194	418
208	432
210	434

AB2 (DTC0)

0	211
2	213
19.5	230.5
21.5	232.5
39	250
41	252
58.5	269.5
60.5	271.5
78	289
80	291
97.5	308.5
99.5	310.5
105.5	316.5
107.5	318.5
125	336
127	338
144.5	355.5
146.5	357.5
164	375
166	377
183.5	394.5
185.5	396.5
203	414
205	416

AB3 (DTC0)

0	208.5
3	211.5
14	222.5
17	225.5
20	228.5
23	231.5
38.5	247
40.5	249
56	264.5
58	266.5
73.5	282
75.5	284
91	299.5
93	301.5
108.5	317
110.5	319
126	334.5
128	336.5
143.5	352
145.5	354
161	369.5
163	371.5
178.5	387
181.5	390
184.5	393
187.5	396
198.5	407
201.5	410

AB4 (DTC0)

0	222
3	225
14	236
17	239
20	242
23	245
40	262
42	264
59	281
61	283
78	300
80	302
97	319
99	321
116	338
118	340
135	357
137	359
154	376
156	378
173	395
175	397
192	414
195	417
198	420
201	423
212	434
215	437

AB1_1 (DTC1)

0	203.75
2.75	206.5
17.5	221.25
20.25	224
35	238.75
37.75	241.5
52.5	256.25
55.25	259
70	273.75
72.75	276.5
87.5	291.25
90.25	294
105	308.75
107.75	311.5
122.5	326.25
125.25	329
140	343.75
142.75	346.5
157.5	361.25
160.25	364
175	378.75
177.75	381.5
192.5	396.25
195.25	399

AB2_1 (DTC1)

0	203
2	205
17	220
19	222
34	237
36	239
51	254
53	256
68	271
70	273
85	279
87	281
93	296
95	298
110	313
112	315
127	330
129	332
144	347
146	349
161	364
163	366
178	381
180	383
186	398
188	400

SA trains

SA1 (DTC0)

0	159.5
2.5	169
12	178.5
21.5	188
31	197.5
40.5	200
45	210
54.5	212.5
64	222
73.5	231.5
83	241
92.5	250.5
95	255
105	264.5
107.5	274
117	283.5
126.5	293
136	302.5
145.5	305
150	

SA2 (DTC0)

0	199
2	201
13	212
15	214
18	217
20	219
31	230
44	243
57	256
70	269
83	282
96	295
109	308
122	321
135	334
148	347
161	360
172	371
174	373
177	376
179	378
190	389
192	391

SA2_1 (DTC1)

0	203
2	205
13	216
15	218
18	221
20	223
31	234
44.4	247.4
57.8	260.8
71.2	274.2
84.6	287.6
98	301
111.4	314.4
124.8	327.8
138.2	341.2
151.6	354.6
165	368
176	379
178	381
181	384
183	386
194	397
196	399

APPENDIX B: REFERENCE DTC2 TRAINS

All the trains in this appendix are defined from their cumulative axle spacing, in m. Their axle loads are all equal and they are defined dending on the corresponding line category, or $P_{MUclass}$, as per EN 15528:2015.

CB trains

CBa_1 train

0	213.051
3	215.485
14	220.525
17	222.959
20.525	238.051
22.959	240.485
38.051	245.525
40.485	247.959
45.525	263.051
47.959	265.485
63.051	270.525
65.485	272.959
70.525	288.051
72.959	290.485
88.051	295.525
90.485	297.959
95.525	313.051
97.959	315.485
113.051	320.525
115.485	322.959
120.525	338.051
122.959	340.485
138.051	345.525
140.485	347.959
145.525	363.051
147.959	365.485
163.051	370.525
165.485	372.959
170.525	388.051
172.959	390.485
188.051	394.01
190.485	397.01
195.525	408.01
197.959	411.01

CBb_1 train

0	206.177
3	208.674
14	225.374
17	227.872
20.525	232.698
23.023	235.196
39.723	251.896
42.22	254.393
47.047	259.22
49.544	261.717
66.244	278.417
68.742	280.915
73.568	285.741
76.066	288.239
92.766	304.939
95.263	307.437
100.09	312.263
102.587	314.761
119.288	331.461
121.785	333.958
126.612	338.785
129.109	341.282
145.809	357.982
148.307	360.48
153.133	365.306
155.631	367.804
172.331	384.504
174.828	387.002
179.655	390.527
182.152	393.527
198.852	404.527
201.35	407.527

CBc_1 train

0	209.28
3	211.892
14	217.28
17	219.892
20.525	237.388
23.137	240
40.633	245.388
43.245	248
48.633	265.495
51.245	268.107
68.741	273.495
71.353	276.107
76.741	293.603
79.353	296.215
96.848	301.603
99.461	304.215
104.848	321.711
107.461	324.323
124.956	329.711
127.568	332.323
132.956	349.819
135.568	352.431
153.064	357.819
155.676	360.431
161.064	377.927
163.676	380.539
181.172	384.064
183.784	387.064
189.172	398.064
191.784	401.064

AB trains

ABa_1 train

0	215.45
3	230.488
14	232.978
17	248.017
20.15	250.506
22.64	265.545
37.678	268.034
40.168	283.073
55.206	285.563
57.696	300.601
72.735	303.091
75.224	318.129
90.263	320.619
92.752	335.658
107.791	338.147
110.281	353.186
125.319	355.675
127.809	370.714
142.847	373.204
145.337	388.242
160.376	390.732
162.865	405.77
177.904	408.26
180.393	411.41
195.432	414.41
197.922	425.41
212.96	428.41

ABb_1 train

0	220.99
3	223.425
14	239.248
17	241.684
20.15	257.506
22.585	259.942
38.408	275.765
40.844	278.2
56.666	294.023
59.102	296.458
74.925	312.281
77.36	314.716
93.183	330.539
95.618	332.975
111.441	348.797
113.876	351.233
129.699	367.055
132.135	369.491
147.957	385.314
150.393	387.749
166.215	403.572
168.651	406.007
184.474	409.157
186.909	412.157
202.732	423.157
205.167	426.157

ABc_1 train

0	210.736
3	226.844
14	229.526
17	245.634
20.15	248.316
22.832	264.424
38.94	267.107
41.623	283.215
57.731	285.897
60.413	302.005
76.521	304.687
79.203	320.795
95.311	323.478
97.994	339.586
114.102	342.268
116.784	358.376
132.892	361.058
135.574	377.166
151.682	379.849
154.365	395.957
170.473	398.639
173.155	401.789
189.263	404.789
191.945	415.789
208.053	418.789

SA trains

SAa_1 train

0	229.2
2.8	242.4
10.8	255.6
13.6	268.8
18	282
31.2	295.2
44.4	308.4
57.6	321.6
70.8	334.8
84	348
97.2	361.2
110.4	374.4
123.6	387.6
136.8	400.8
150	414
163.2	418.4
176.4	421.2
189.6	429.2
202.8	432
216	

SAb_1 train

0	230.8
2.8	244.1
10.8	257.4
13.6	270.7
18	284
31.3	297.3
44.6	310.6
57.9	323.9
71.2	337.2
84.5	350.5
97.8	363.8
111.1	377.1
124.4	390.4
137.7	403.7
151	417
164.3	421.4
177.6	424.2
190.9	432.2
204.2	435
217.5	

APPENDIX C: REFERENCE DTC2e TRAINS

All the trains in this appendix are defined from their cumulative axle spacing x, in m, and the dimensionless i-th axle weight, with $P_i^* = P_i/P_{MUclass}$.

CB trains

CBa trains

CBa_2 train

x	P_i^*	x	P_i^*
0	0.602447	127.9	0.52624
2.5	0.621615	130.4	0.517586
10.9	0.46278	135.3	0.605657
13.4	0.477389	137.8	0.611566
18.3	0.593328	151.3	0.562762
20.8	0.596073	153.8	0.566391
34.3	0.516191	158.7	0.616172
36.8	0.520285	161.2	0.623895
41.7	0.595608	174.7	0.57323
44.2	0.596073	177.2	0.572811
57.7	0.539453	182.1	0.606541
60.2	0.554527	184.6	0.603378
65.1	0.568205	198.1	0.52396
67.6	0.582395	200.6	0.526705
81.1	0.522564	205.5	0.577789
83.6	0.532149	208	0.588304
88.5	0.57965	221.5	0.535359
91	0.58193	224	0.558202
104.5	0.57644	228.9	0.980367
107	0.552712	232.3	0.945659
111.9	0.580534	239.4	1
114.4	0.589699	242.8	0.979436

CBa_3 train

x	P_i^*
0	0.962031
2.7	1
16	0.931197
18.7	0.943047
23	0.873035
25.7	0.934764
39	0.889661
41.7	0.910399
46	0.852902
48.7	0.938271
62	0.845163
64.7	0.881378
69	0.883736
71.7	0.943652
85	0.862999
87.7	0.902116
92	0.842201
94.7	0.892624
108	0.953688
110.7	0.982164

CBa_4 train

x	P_i^*	x	P_i^*
0	0.964708	148.3	0.988668
2.5	0.934272	150.8	0.990071
17	0.93805	166.4	0.993362
19.5	0.936593	168.9	0.994064
23.8	0.95807	173.2	0.961632
26.3	0.957369	175.7	0.963089
41.9	0.95807	190.2	0.936107
44.4	0.956667	192.7	0.966489
48.7	0.84329	200.24	0.954671
51.2	0.844045	202.74	0.924235
66.8	0.812692	217.24	0.934218
69.3	0.813448	219.74	0.932761
73.6	0.865307	224.04	1
76.1	0.866062	226.54	0.999298
91.7	0.883331	242.14	0.992175
94.2	0.884032	244.64	0.990772
98.5	0.987426	248.94	0.849657
101	0.98883	251.44	0.848956
116.6	0.992715	267.04	0.97032
119.1	0.993416	269.54	0.971022
123.4	0.981221	273.84	0.961632
125.9	0.982624	276.34	0.963089
141.5	0.870271	290.84	0.936107
144	0.870919	293.34	0.966489

CBb trains

CBb_2 train

x	P_i^*	x	P_i^*
0	0.894655	129.6	0.890461
2.6	0.886978	132.2	0.885627
17	0.893304	146.6	0.879301
19.6	0.88911	149.2	0.876528
26	0.93304	155.6	0.963676
28.6	0.931618	158.2	0.959554
43.1	0.891171	172.7	0.886338
45.7	0.891171	175.3	0.901621
52.1	0.94555	181.7	1
54.7	0.93375	184.3	0.98884
69.2	0.906525	198.7	0.905104
71.8	0.907947	201.3	0.914202
78.2	0.859824	207.7	0.854919
80.8	0.875178	210.3	0.858402
95.3	0.973486	224.8	0.943489
97.9	0.972775	227.4	0.94555
104.3	0.907947	233.8	0.858402
106.9	0.910719	236.4	0.851436
121.3	0.843759	250.8	0.827694
123.9	0.842337	253.4	0.826343

CBb_3 train

x	P_i^*
0	0.968786
2.5	0.963781
20	0.997919
22.5	1
26.4	0.914433
28.9	0.912005
46.4	0.924095
48.9	0.92568
52.8	0.976564
55.3	0.972056
72.8	0.907893
75.3	0.909528
81.5	0.968786
84	0.963781
101.5	0.997919
104	1
107.9	0.914433
110.4	0.912005
127.9	0.924095
130.4	0.92568
134.3	0.976564
136.8	0.972056
154.3	0.907893
156.8	0.909528
163	0.968786
165.5	0.963781
183	0.997919
185.5	1
189.4	0.914433
191.9	0.912005
209.4	0.924095
211.9	0.92568
215.8	0.976564
218.3	0.972056
235.8	0.907893
238.3	0.909528

CBb_4 train

x	P_i^*
0	0.961161
2.8	0.994696
19	0.962986
21.8	0.918558
25.78	0.942169
28.58	0.98654
44.78	1
47.58	0.955629
51.56	0.954374
54.36	0.998802
70.56	0.968062
73.36	0.923691
77.34	0.919072
80.14	0.963442
96.34	0.99213
99.14	0.958538
107.36	0.961161
110.16	0.994696
126.36	0.962986
129.16	0.918558
133.14	0.942169
135.94	0.98654
152.14	1
154.94	0.955629
158.92	0.954374
161.72	0.998802
177.92	0.968062
180.72	0.923691
184.7	0.919072
187.5	0.963442
203.7	0.99213
206.5	0.958538

CBb_5 train

x	P_i^*
0	0.999887
2.6	0.999887
18.576	0.97214
21.176	0.97214
25.626	0.888788
28.126	0.888788
45.236	0.888788
47.736	0.888788
52.236	0.888788
54.736	0.888788
71.846	0.888788
74.346	0.888788
78.846	0.888788
81.346	0.888788
98.456	0.888788
100.96	0.888788
105.46	0.888788
107.96	0.888788
125.07	0.888788
127.57	0.888788
132.02	0.97214
134.62	0.97214
150.59	0.999887
153.19	0.999887
159.81	0.999887
162.41	0.999887
178.386	0.97214
180.986	0.97214
185.436	0.888788
187.936	0.888788
205.046	0.888788
207.546	0.888788
212.046	0.888788

AB trains

ABa train

ABa_2 train

x	P_i^*	x	P_i^*
0	0.894562	202	0.894562
2.7	0.893875	204.7	0.893875
16.675	0.999208	218.68	0.999208
19.425	1	221.43	1
34.175	0.97735	236.18	0.97735
36.925	0.978089	238.93	0.978089
51.675	0.899472	253.68	0.899472
54.425	0.900053	256.43	0.900053
69.175	0.989757	271.18	0.989757
71.925	0.990338	273.93	0.990338
86.675	0.944615	288.68	0.944615
89.425	0.945195	291.43	0.945195
104.17	0.943664	306.18	0.943664
106.92	0.944245	308.93	0.944245
121.67	0.995143	323.68	0.995143
124.42	0.995882	326.43	0.995882
139.18	0.987276	341.18	0.987276
141.93	0.988015	343.93	0.988015
156.68	0.962724	358.68	0.962724
159.43	0.963358	361.43	0.963358
174.18	0.96188	376.18	0.96188
176.93	0.96246	378.93	0.96246
190.9	0.88717	392.9	0.88717
193.6	0.887856	395.6	0.887856

ABb train

ABb_2 train

x	P_i^*	x	P_i^*
0	1	155.5	0.903049
2.4	1	171.15	0.97349
18.05	0.98204	173.85	0.97349
20.75	0.98204	189.65	0.98688
36.4	0.830833	192.35	0.98688
38.8	0.830833	208	0.999946
43.7	0.903049	210.4	0.999946
46.1	0.903049	218.8	1
61.75	0.97349	221.2	1
64.45	0.97349	236.85	0.98204
80.25	0.98688	239.55	0.98204
82.95	0.98688	255.2	0.830833
98.6	0.999946	257.6	0.830833
101	0.999946	262.5	0.903049
109.4	1	264.9	0.903049
111.8	1	280.55	0.97349
127.45	0.98204	283.25	0.97349
130.15	0.98204	299.05	0.98688
145.8	0.830833	301.75	0.98688
148.2	0.830833	317.4	0.999946
153.1	0.903049	319.8	0.999946

ABc trains

ABc_2 train

x	P_i^*	x	P_i^*
0	1	195.1	0.98927
3	1	198.1	0.98927
14	1	213.8	0.922547
17	1	216.8	0.922547
20.28	0.98927	232.5	0.932236
23.28	0.98927	235.5	0.932236
38.98	0.922547	251.2	0.932236
41.98	0.922547	254.2	0.932236
57.68	0.932236	269.9	0.932236
60.68	0.932236	272.9	0.932236
76.38	0.932236	288.6	0.932236
79.38	0.932236	291.6	0.932236
95.08	0.932236	307.3	0.932236
98.08	0.932236	310.3	0.932236
113.78	0.932236	326	0.932236
116.78	0.932236	329	0.932236
132.48	0.932236	344.7	0.913377
135.48	0.932236	347.7	0.913377
151.18	0.932236	363.4	0.722182
154.18	0.932236	366.4	0.722182
169.88	0.913377	369.68	1
172.88	0.913377	372.68	1
188.58	0.722182	383.68	1
191.58	0.722182	386.68	1

ABc_3 train

x	P_i^*	x	P_i^*
0	0.91959	200.19	0.91959
3	0.91959	203.19	0.91959
14	0.940574	214.19	0.940574
17	0.940574	217.19	0.940574
20.275	0.793799	220.465	0.793799
23.275	0.790824	223.465	0.790824
38.975	0.960676	239.165	0.960676
41.975	0.959685	242.165	0.959685
57.675	0.982211	257.865	0.982211
60.675	0.981274	260.865	0.981274
76.375	0.965688	276.565	0.965688
79.375	0.964697	279.565	0.964697
95.075	0.960621	295.265	0.960621
98.075	0.961558	298.265	0.961558
113.775	0.997356	313.965	0.997356
116.775	0.998348	316.965	0.998348
132.475	0.999064	332.665	0.999064
135.475	1	335.665	1
151.175	0.983698	351.365	0.983698
154.175	0.984634	354.365	0.984634
169.875	0.811423	370.065	0.811423
172.875	0.814397	373.065	0.814397
176.15	0.940574	376.34	0.940574
179.15	0.940574	379.34	0.940574
190.15	0.91959	390.34	0.91959
193.15	0.91959	393.34	0.91959

SA trains

SAa trains

SAa_2 train

x	P_i^*	x	P_i^*
0	1	183.98	1
2.8	1	186.78	1
10.65	1	194.63	1
13.45	1	197.43	1
19.51	0.980722	203.49	0.980722
28.48	0.980722	212.46	0.980722
41.62	0.980722	225.6	0.980722
54.76	0.980722	238.74	0.980722
67.9	0.980722	251.88	0.980722
81.04	0.980722	265.02	0.980722
94.18	0.980722	278.16	0.980722
107.32	0.980722	291.3	0.980722
120.46	0.980722	304.44	0.980722
133.6	0.980722	317.58	0.980722
146.74	0.980722	330.72	0.980722
155.71	0.980722	339.69	0.980722
161.77	1	345.75	1
164.57	1	348.55	1
172.42	1	356.4	1
175.22	1	359.2	1

SAa_3 train

x	P_i^*	x	P_i^*
0	0.93314	185.65	0.93314
2.8	0.93314	188.45	0.93314
10.65	0.93314	196.3	0.93314
13.45	0.93314	199.1	0.93314
18.915	1	204.565	1
21.715	1	207.365	1
29.315	1	214.965	1
42.455	0.915152	228.105	0.915152
55.595	0.915152	241.245	0.915152
68.735	0.915152	254.385	0.915152
81.875	0.915152	267.525	0.915152
95.015	0.915152	280.665	0.915152
108.155	0.915152	293.805	0.915152
121.295	0.915152	306.945	0.915152
134.435	0.915152	320.085	0.915152
147.575	1	333.225	1
155.175	1	340.825	1
157.975	1	343.625	1
163.44	0.93314	349.09	0.93314
166.24	0.93314	351.89	0.93314
174.09	0.93314	359.74	0.93314
176.89	0.93314	362.54	0.93314

SAa_4 train

x	P_i^*	x	P_i^*
0	1	200.25	1
2.8	1	203.05	1
11	1	211.25	1
13.8	1	214.05	1
19.445	0.991889	219.695	0.991889
29.965	0.991889	230.215	0.991889
43.105	0.991889	243.355	0.991889
56.245	0.991889	256.495	0.991889
69.385	0.991889	269.635	0.991889
82.525	0.991889	282.775	0.991889
95.665	0.991889	295.915	0.991889
108.805	0.991889	309.055	0.991889
121.945	0.991889	322.195	0.991889
135.085	0.991889	335.335	0.991889
148.225	0.991889	348.475	0.991889
161.365	0.991889	361.615	0.991889
171.885	0.991889	372.135	0.991889
177.53	1	377.78	1
180.33	1	380.58	1
188.53	1	388.78	1
191.33	1	391.58	1

SAb trains

SAb_2 train

x	P_i^*
0	0.960642
2.6	0.960642
10.44	0.960642
13.04	0.960642
18.9	0.960642
21.5	0.960642
29.34	0.960642
31.94	0.960642
38.362	0.856489
41.012	0.856489
53.187	1
66.487	1
79.787	1
93.087	1
106.39	1
119.69	1
132.99	1
146.29	1
159.59	1
172.89	1
186.19	1
199.49	1
212.79	1
226.09	1
239.39	1
252.69	1
265.99	1
279.29	1
292.59	1
305.89	1
318.06	0.856489
320.71	0.856489

SAb_3 train

x	P_i^*
0	0.922213
2.6	0.922213
10.44	0.922213
13.04	0.922213
18.9	0.922213
21.5	0.922213
29.34	0.922213
31.94	0.922213
38.17	1
40.97	1
48.47	1
51.27	1
58.062	0.822226
60.712	0.822226
72.887	0.959996
86.187	0.959996
99.487	0.959996
112.79	0.959996
126.09	0.959996
139.39	0.959996
152.69	0.959996
165.99	0.959996
179.29	0.959996
192.59	0.959996
205.89	0.959996
219.19	0.959996
232.49	0.959996
245.79	0.959996
259.09	0.959996
272.39	0.959996
285.69	0.959996
298.99	0.959996
312.29	0.959996
325.59	0.959996
337.76	0.822226
340.41	0.822226

SAb_4 train

x	P_i^*
0	0.822226
2.65	0.822226
14.82	0.959996
28.12	0.959996
41.42	0.959996
54.72	0.959996
68.02	0.959996
81.32	0.959996
94.62	0.959996
107.92	0.959996
121.22	0.959996
134.52	0.959996
147.82	0.959996
161.12	0.959996
174.42	0.959996
187.72	0.959996
201.02	0.959996
214.32	0.959996
227.62	0.959996
240.923	0.959996
254.223	0.959996
267.523	0.959996
279.698	0.822226
282.348	0.822226
289.14	1
291.94	1
299.44	1
302.24	1
308.47	0.922213
311.07	0.922213
318.91	0.922213
321.51	0.922213
327.37	0.922213
329.97	0.922213
337.81	0.922213
340.41	0.922213

SAb_5 train

x	P_i^*
0	0.8
2.65	0.8
14.825	0.911111
28.125	0.911111
41.425	0.911111
54.725	0.911111
68.025	0.911111
81.325	0.911111
94.625	0.911111
107.925	0.911111
121.225	0.911111
134.525	0.911111
147.825	0.911111
161.125	0.911111
173.3	0.8
175.95	0.8
182.682	1
185.682	1
192.182	1
195.182	1
201.662	1
204.662	1
211.162	1
214.162	1
220.894	0.8
223.544	0.8
235.719	0.911111
249.019	0.911111
262.319	0.911111
275.619	0.911111
288.919	0.911111
302.219	0.911111
315.519	0.911111
328.819	0.911111
342.119	0.911111
355.419	0.911111
368.719	0.911111
382.019	0.911111
394.194	0.8
396.844	0.8

SAb_6 train

x	P_i^*
0	0.8
2.65	0.8
14.825	0.911111
28.125	0.911111
41.425	0.911111
54.725	0.911111
68.025	0.911111
81.325	0.911111
94.625	0.911111
107.925	0.911111
121.225	0.911111
134.525	0.911111
147.825	0.911111
161.125	0.911111
173.3	0.8
175.95	0.8
182.682	1
185.682	1
192.182	1
195.182	1
201.914	0.8
204.564	0.8
216.739	0.911111
230.039	0.911111
243.339	0.911111
256.639	0.911111
269.939	0.911111
283.239	0.911111
296.539	0.911111
309.839	0.911111
323.139	0.911111
336.439	0.911111
349.739	0.911111
363.039	0.911111
375.214	0.8
377.864	0.8
384.596	1
387.596	1
394.096	1
397.096	1

SAb_7 train

x	P_i^*
0	0.822226
2.65	0.822226
14.82	0.959996
28.12	0.959996
41.42	0.959996
54.72	0.959996
68.02	0.959996
81.32	0.959996
94.62	0.959996
107.92	0.959996
121.22	0.959996
134.52	0.959996
147.82	0.959996
161.12	0.959996
174.42	0.959996
187.72	0.959996
201.02	0.959996
214.32	0.959996
227.623	0.959996
240.923	0.959996
254.223	0.959996
267.523	0.959996
279.698	0.822226
282.348	0.822226
289.14	1
291.94	1
299.44	1
302.24	1
308.84	1
311.64	1
319.14	1
321.94	1

APPENDIX D: DETAILED VIBRATIONS INDUCED BY REAL AND REFERENCE DTC TRAINS – TIME-STEPPING ANALYSIS

Trains with Conventional Bogies: CB

CBa trains

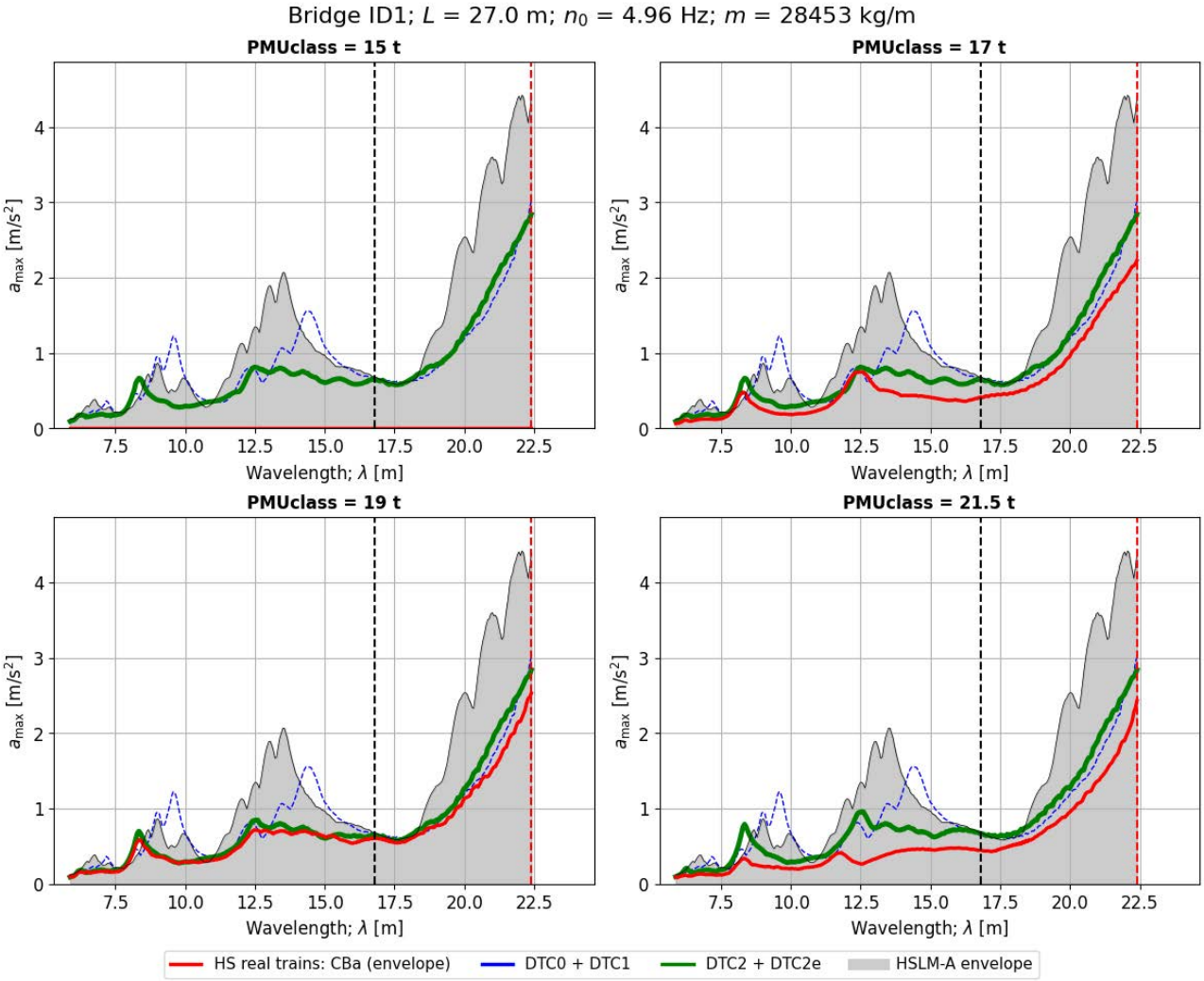

Figure 101. Peak vertical acceleration in the bridge ID1 when subject to real CBa trains of different weight categories, and comparison with the reference CBa train in DTCs. Time-stepping analysis.

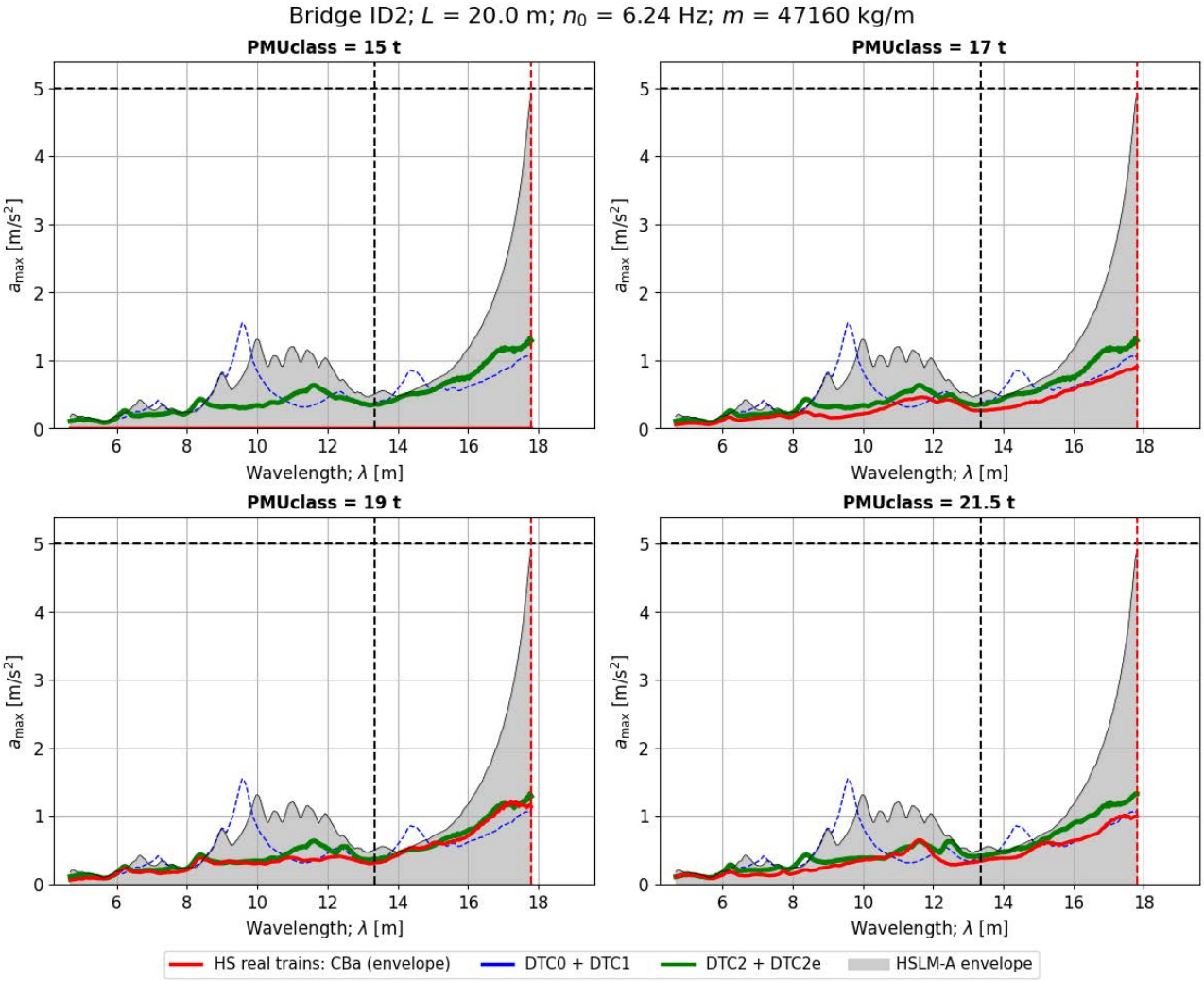

Figure 102. Peak vertical acceleration in the bridge ID2 when subject to real CBa trains of different weight categories, and comparison with the reference CBa train in DTCs. Time-stepping analysis.

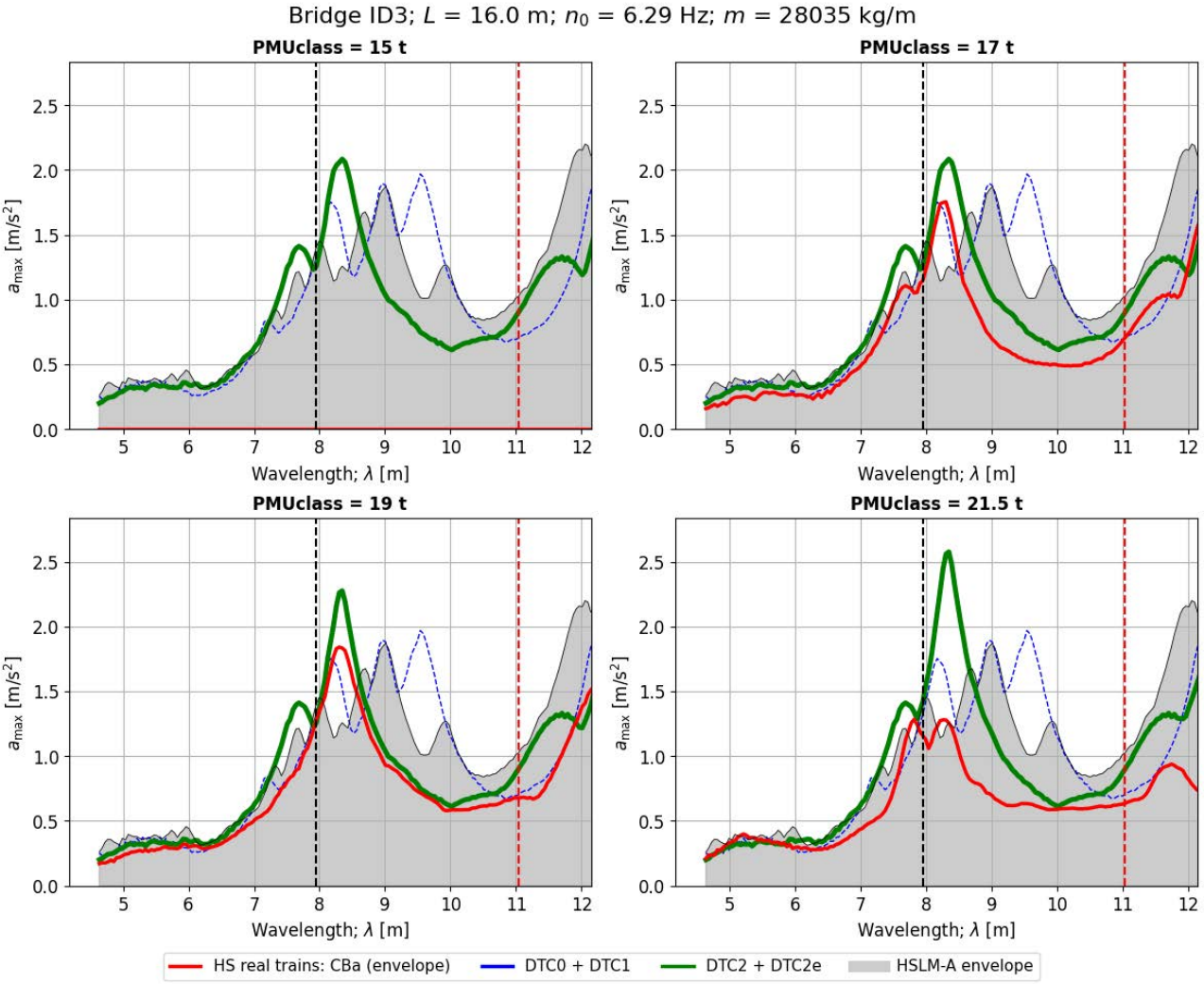

Figure 103. Peak vertical acceleration in the bridge ID3 when subject to real CBa trains of different weight categories, and comparison with the reference CBa train in DTCs. Time-stepping analysis.

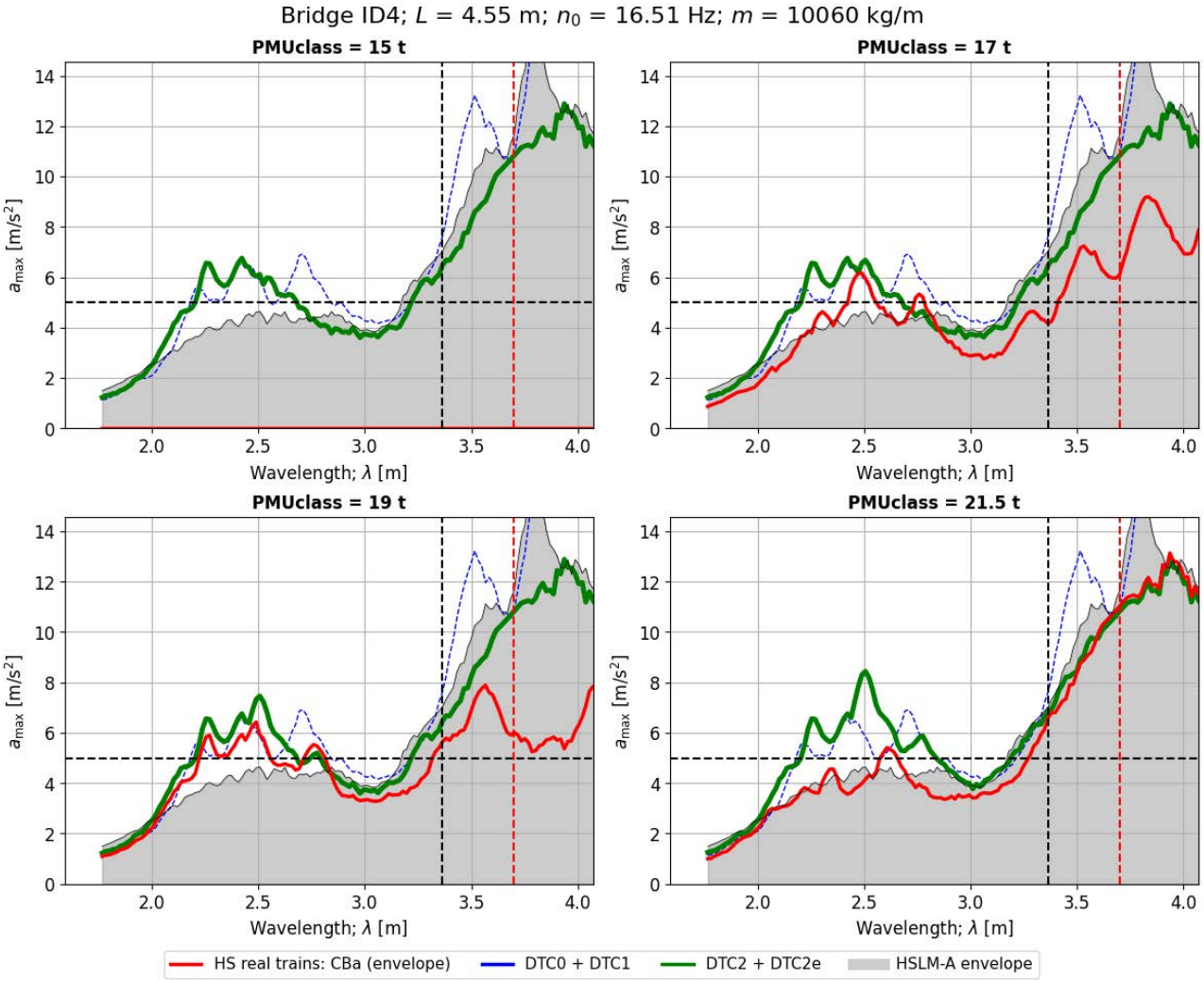

Figure 104. Peak vertical acceleration in the bridge ID4 when subject to real CBa trains of different weight categories, and comparison with the reference CBa train in DTCs. Time-stepping analysis.

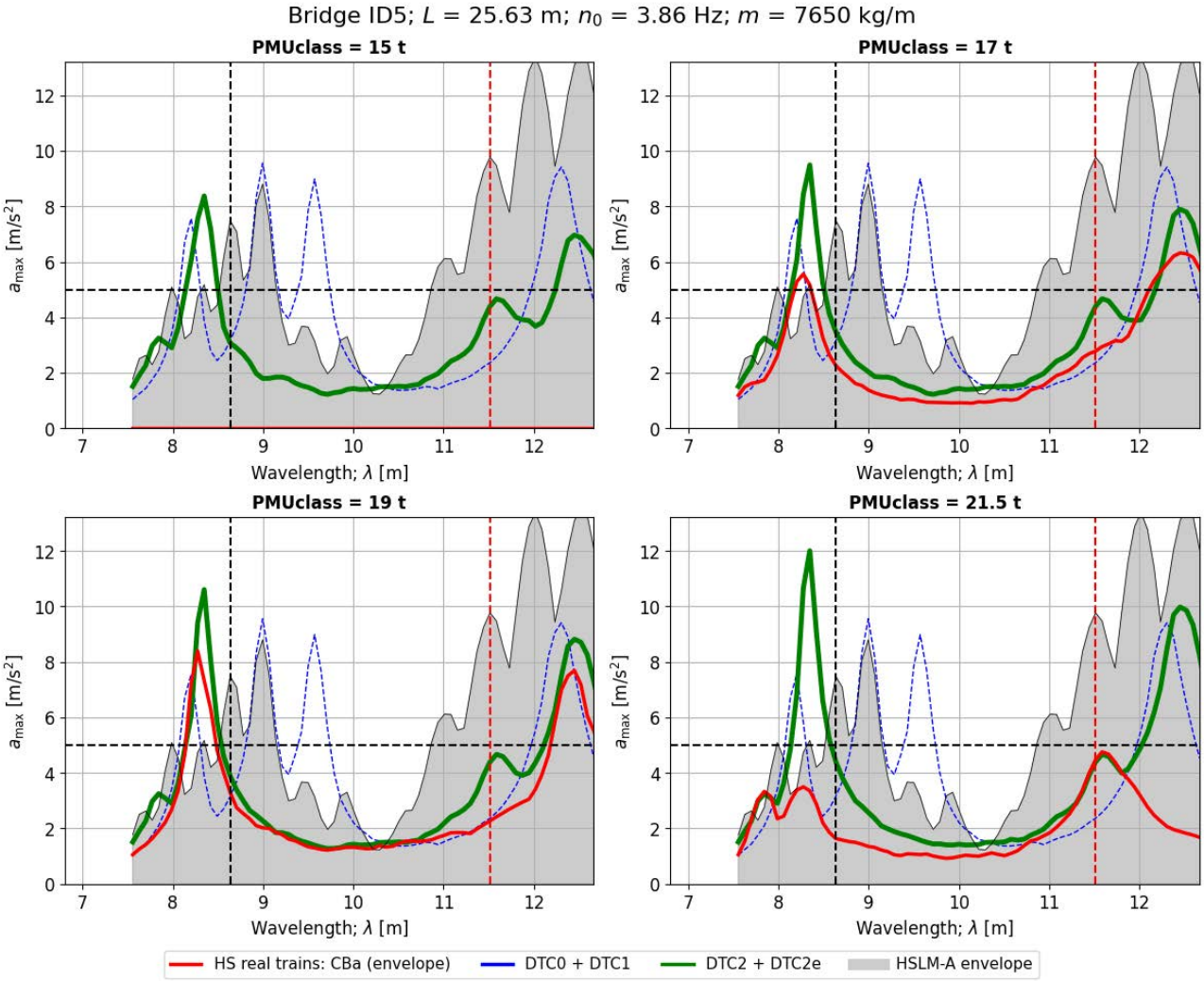

Figure 105. Peak vertical acceleration in the bridge ID5 when subject to real CBa trains of different weight categories, and comparison with the reference CBa train in DTCs. Time-stepping analysis.

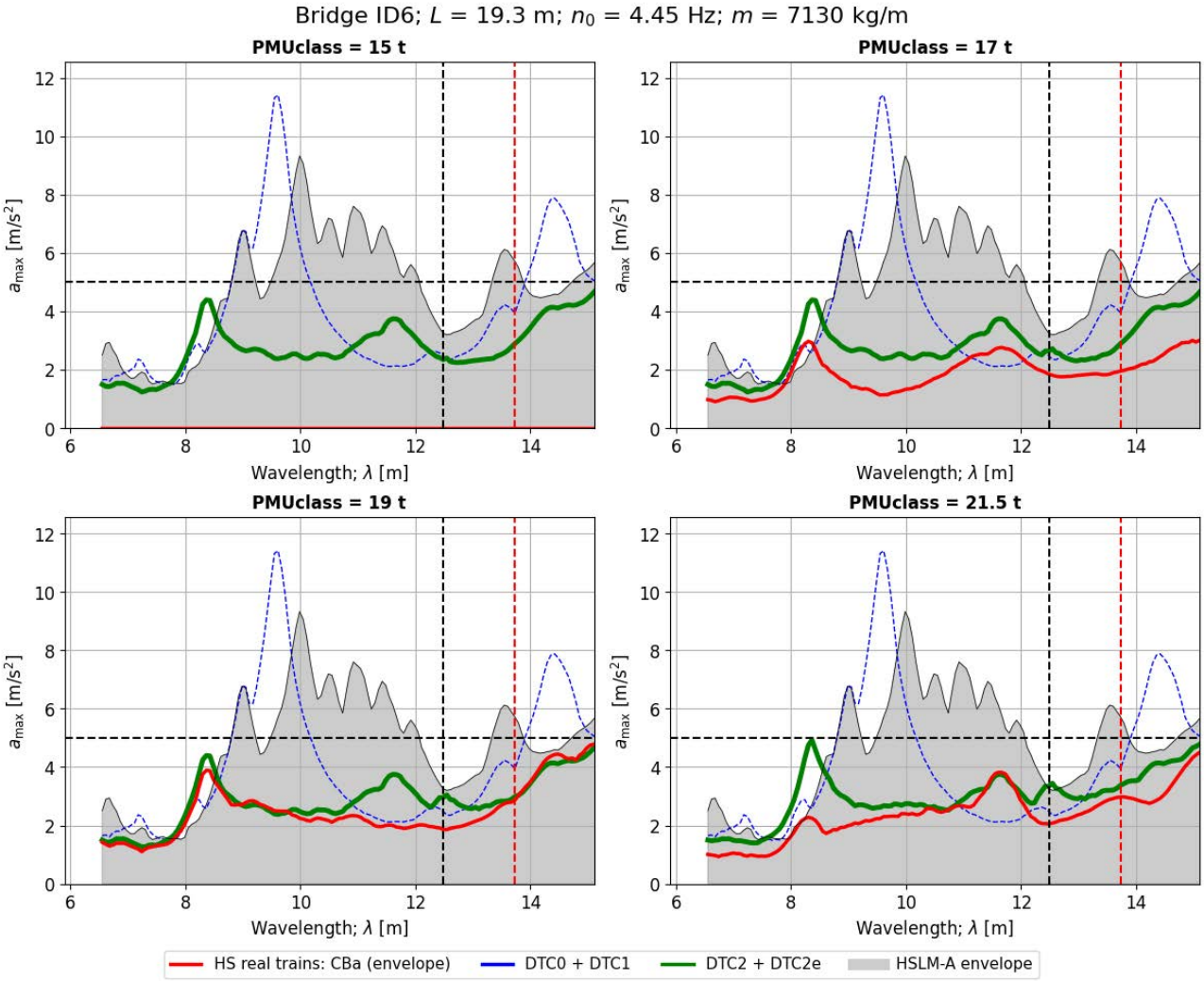

Figure 106. Peak vertical acceleration in the bridge ID6 when subject to real CBa trains of different weight categories, and comparison with the reference CBa train in DTCs. Time-stepping analysis.

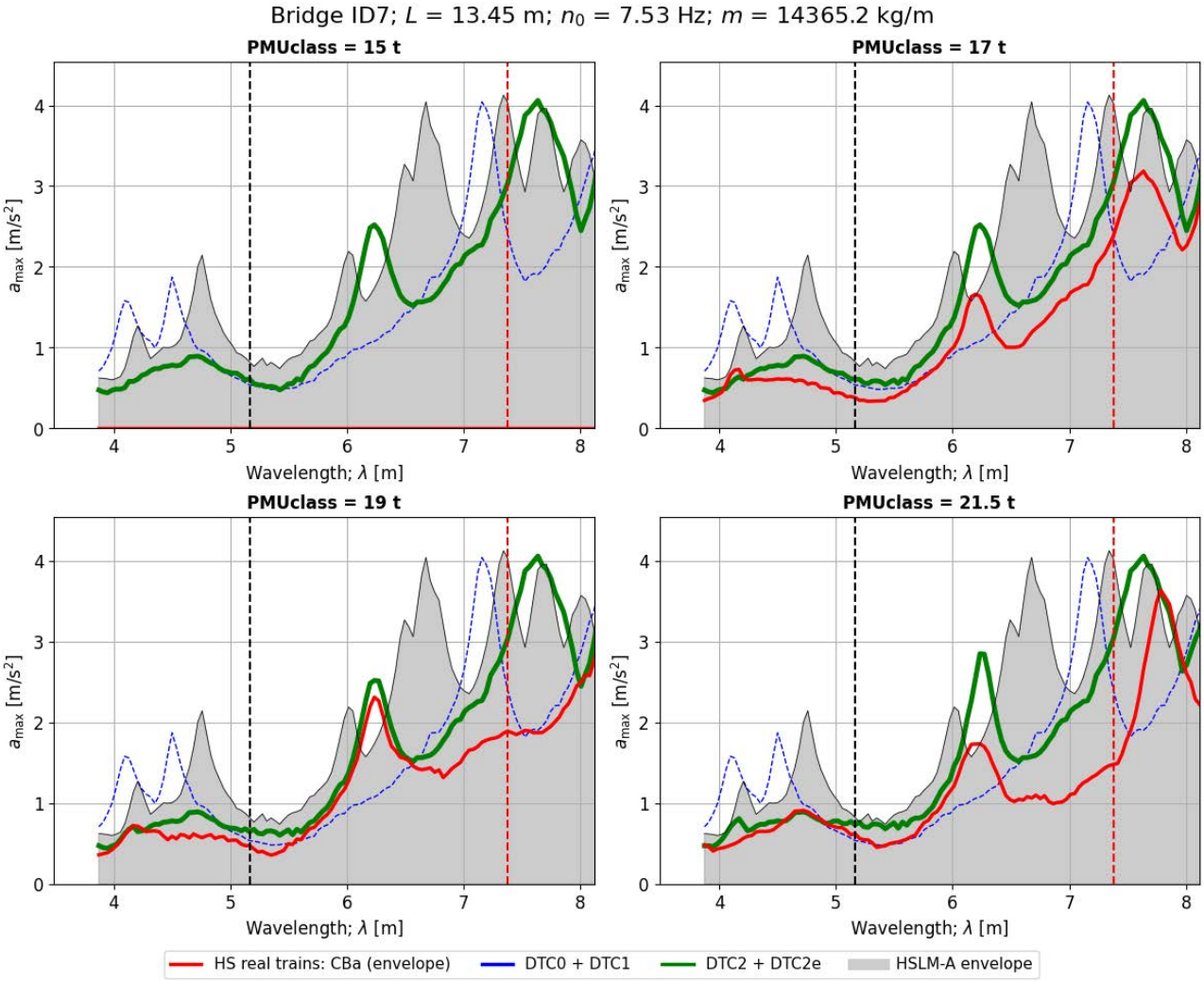

Figure 107. Peak vertical acceleration in the bridge ID7 when subject to real CBa trains of different weight categories, and comparison with the reference CBa train in DTCs. Time-stepping analysis.

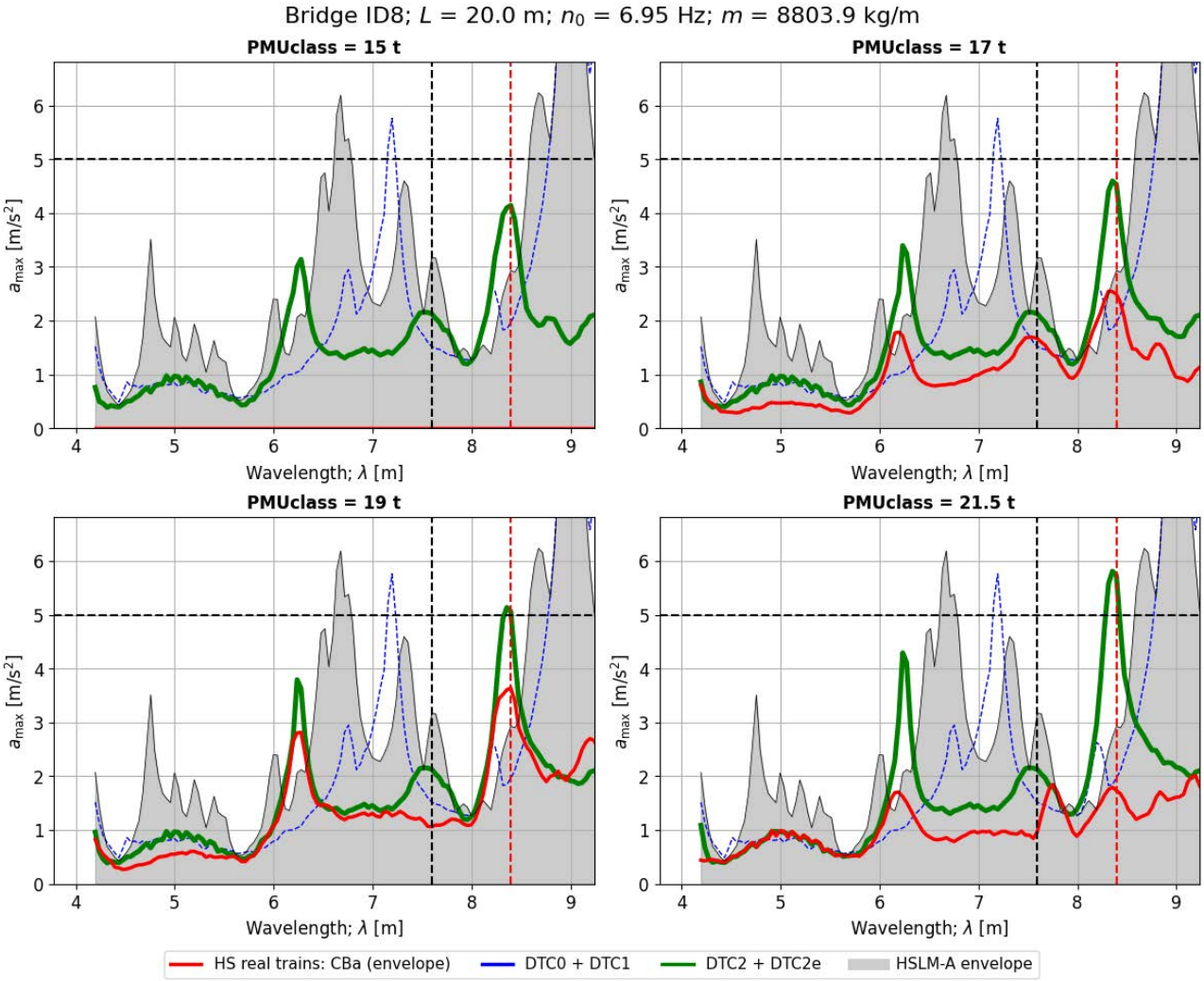

Figure 108. Peak vertical acceleration in the bridge ID8 when subject to real CBa trains of different weight categories, and comparison with the reference CBa train in DTCs. Time-stepping analysis.

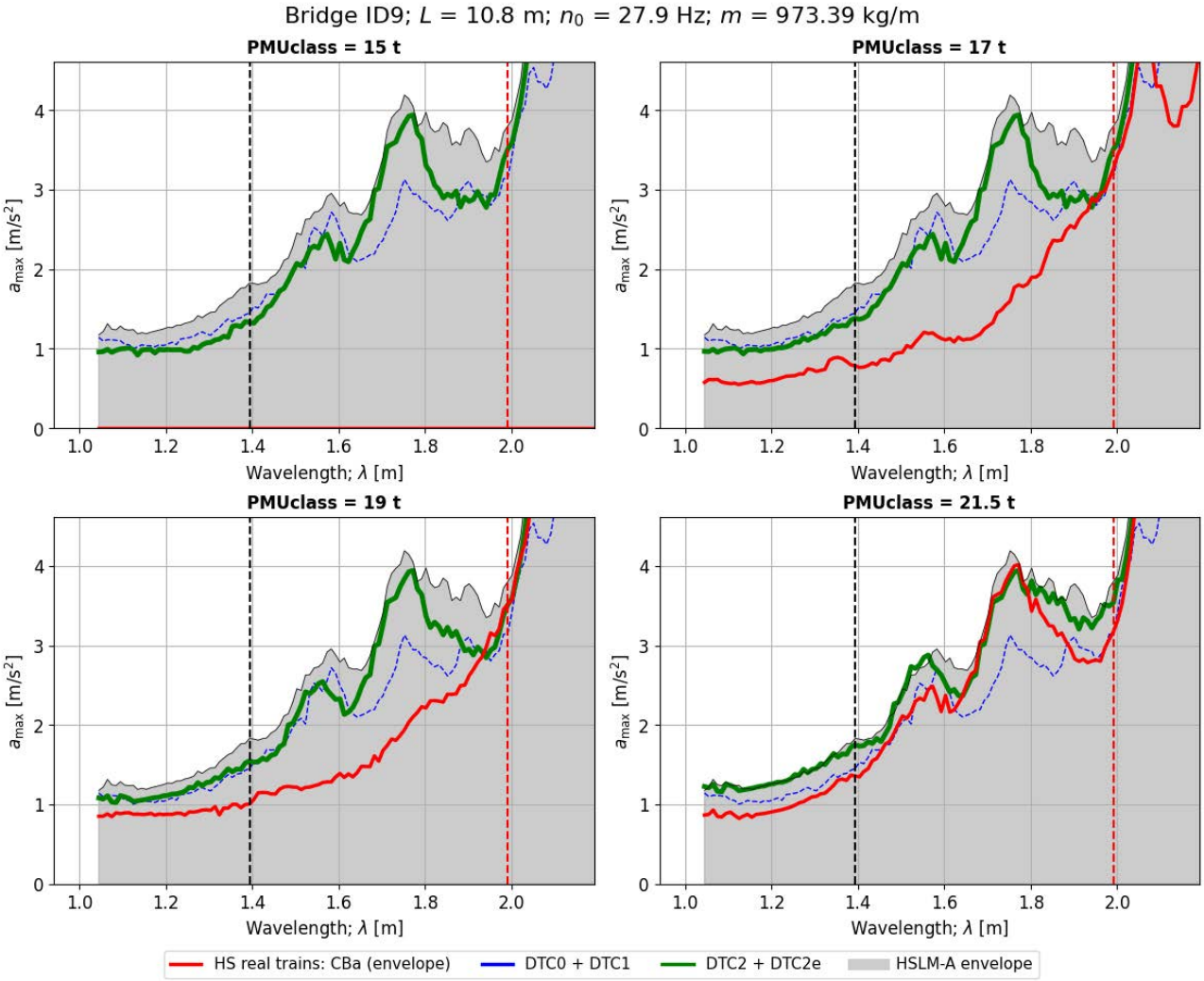

Figure 109. Peak vertical acceleration in the bridge ID9 when subject to real CBa trains of different weight categories, and comparison with the reference CBa train in DTCs. Time-stepping analysis.

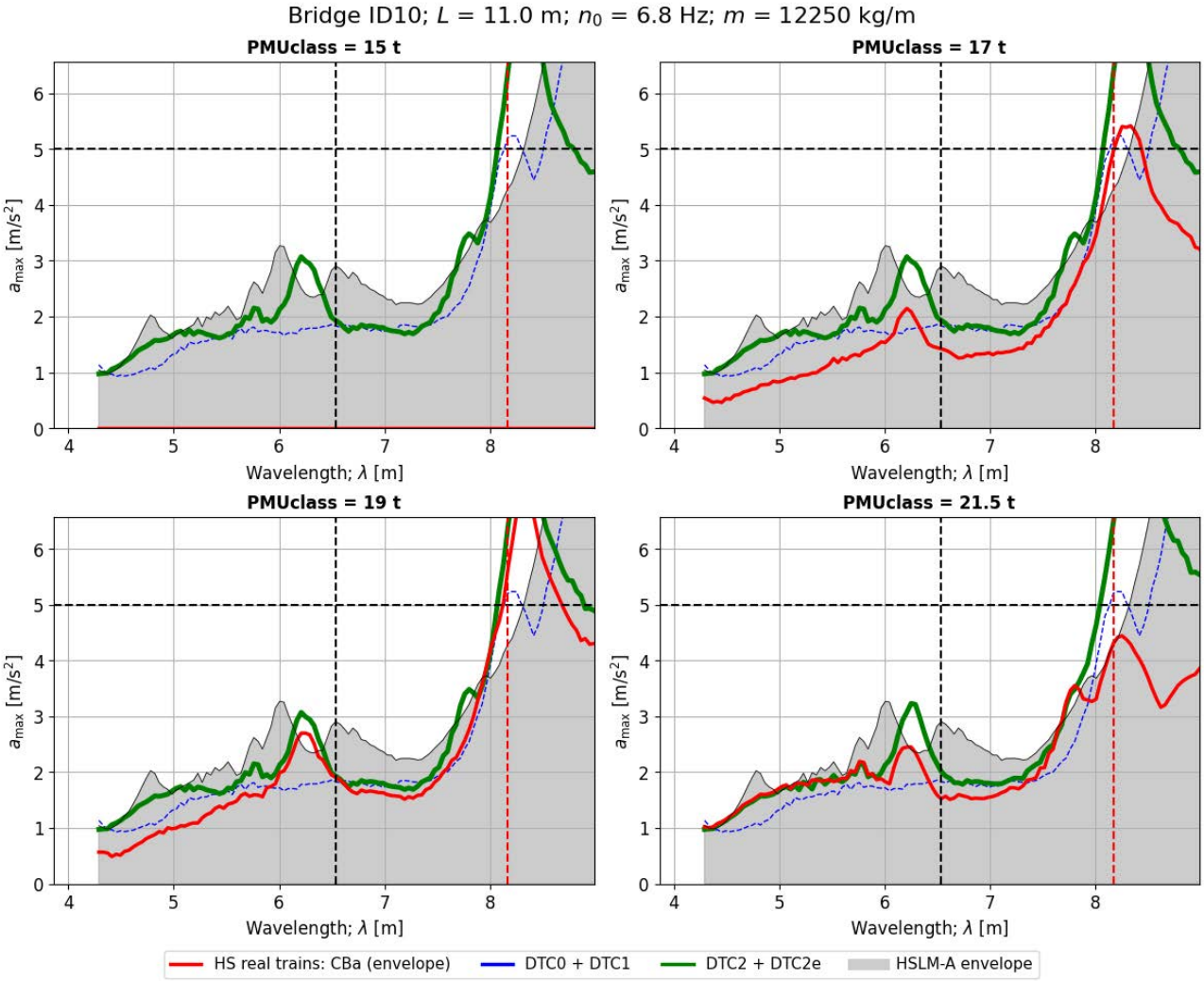

Figure 110. Peak vertical acceleration in the bridge ID10 when subject to real CBa trains of different weight categories, and comparison with the reference CBa train in DTCs. Time-stepping analysis.

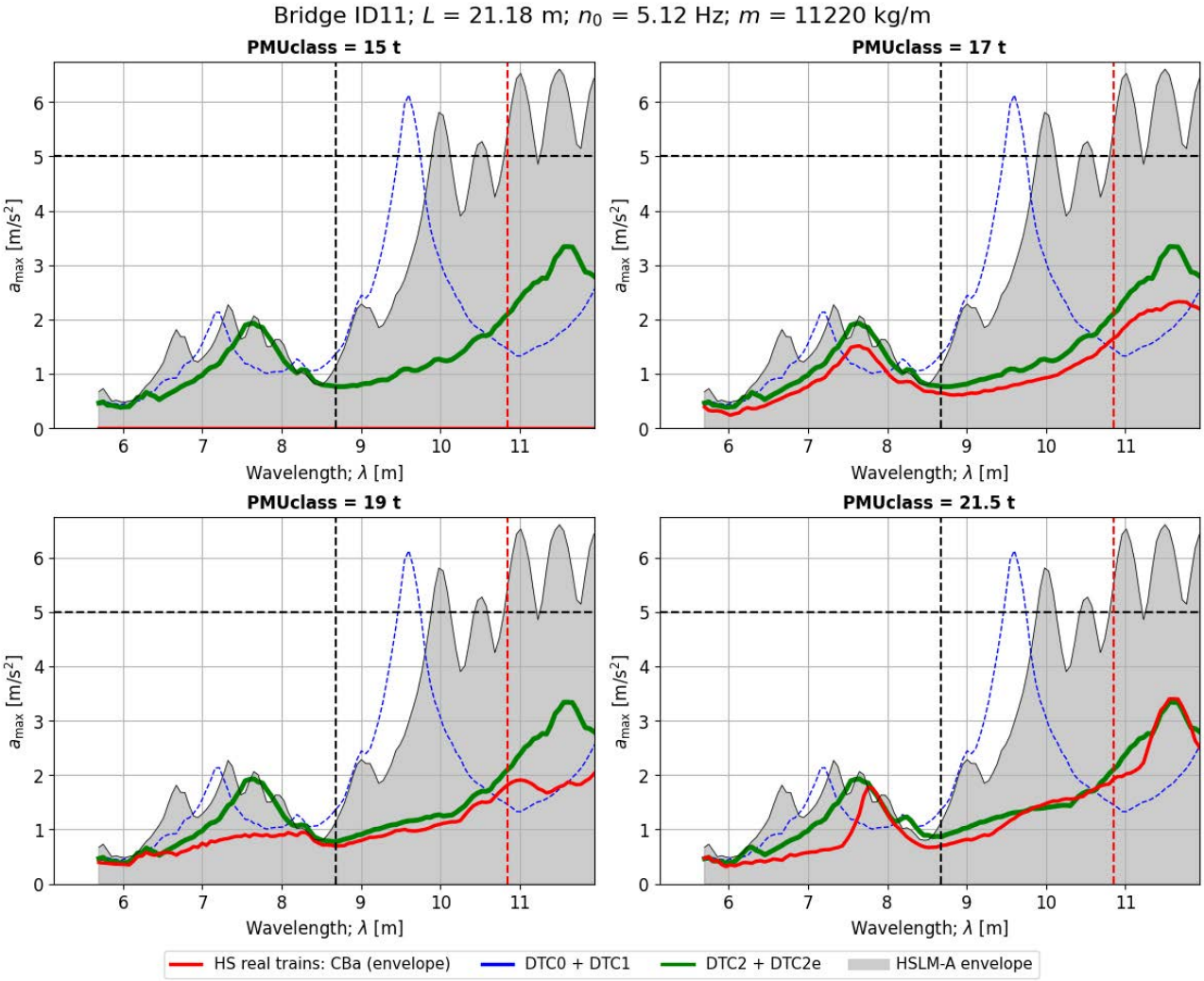

Figure 111. Peak vertical acceleration in the bridge ID11 when subject to real CBa trains of different weight categories, and comparison with the reference CBa train in DTCs. Time-stepping analysis.

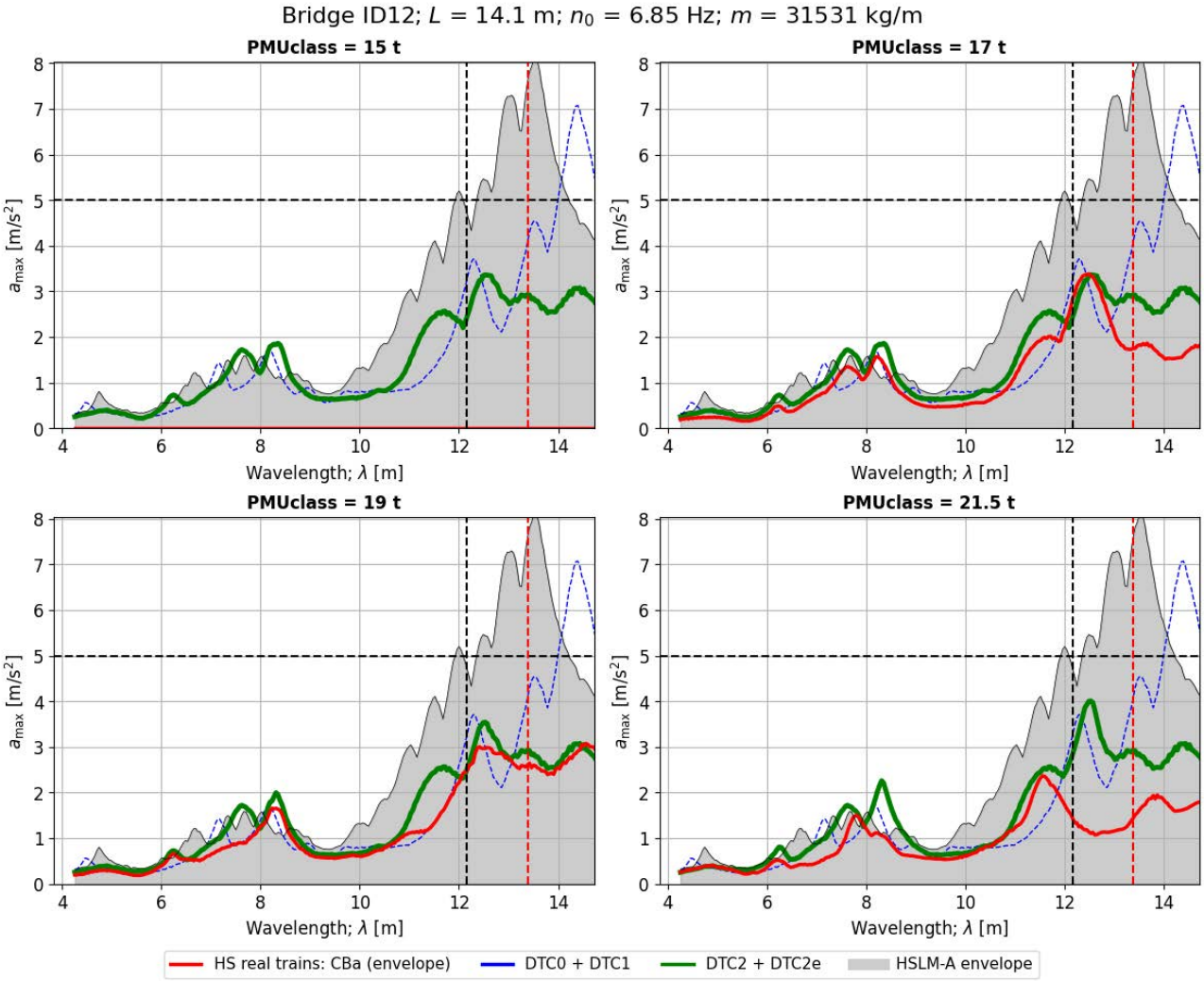

Figure 112. Peak vertical acceleration in the bridge ID12 when subject to real CBa trains of different weight categories, and comparison with the reference CBa train in DTCs. Time-stepping analysis.

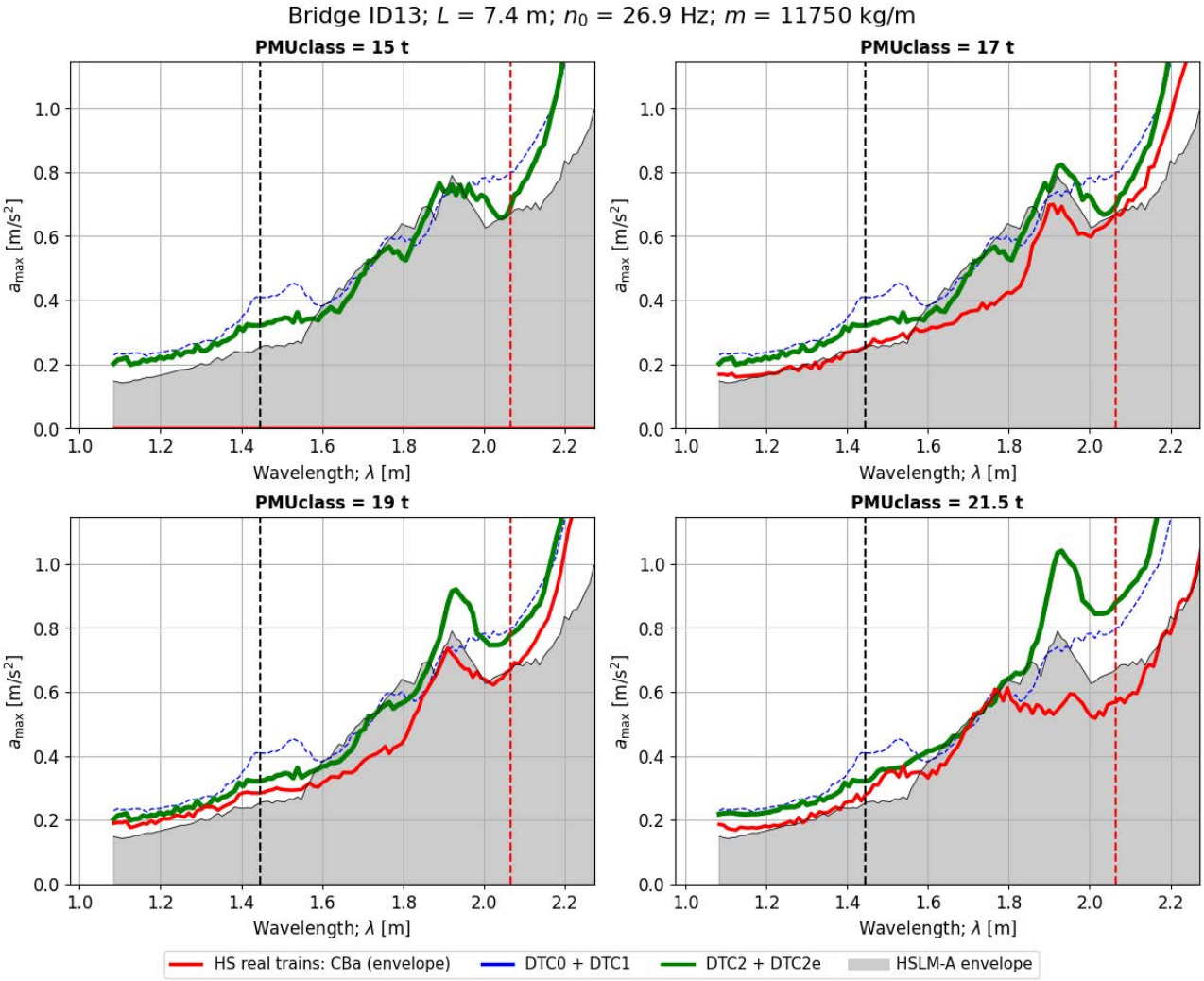

Figure 113. Peak vertical acceleration in the bridge ID13 when subject to real CBa trains of different weight categories, and comparison with the reference CBa train in DTCs. Time-stepping analysis.

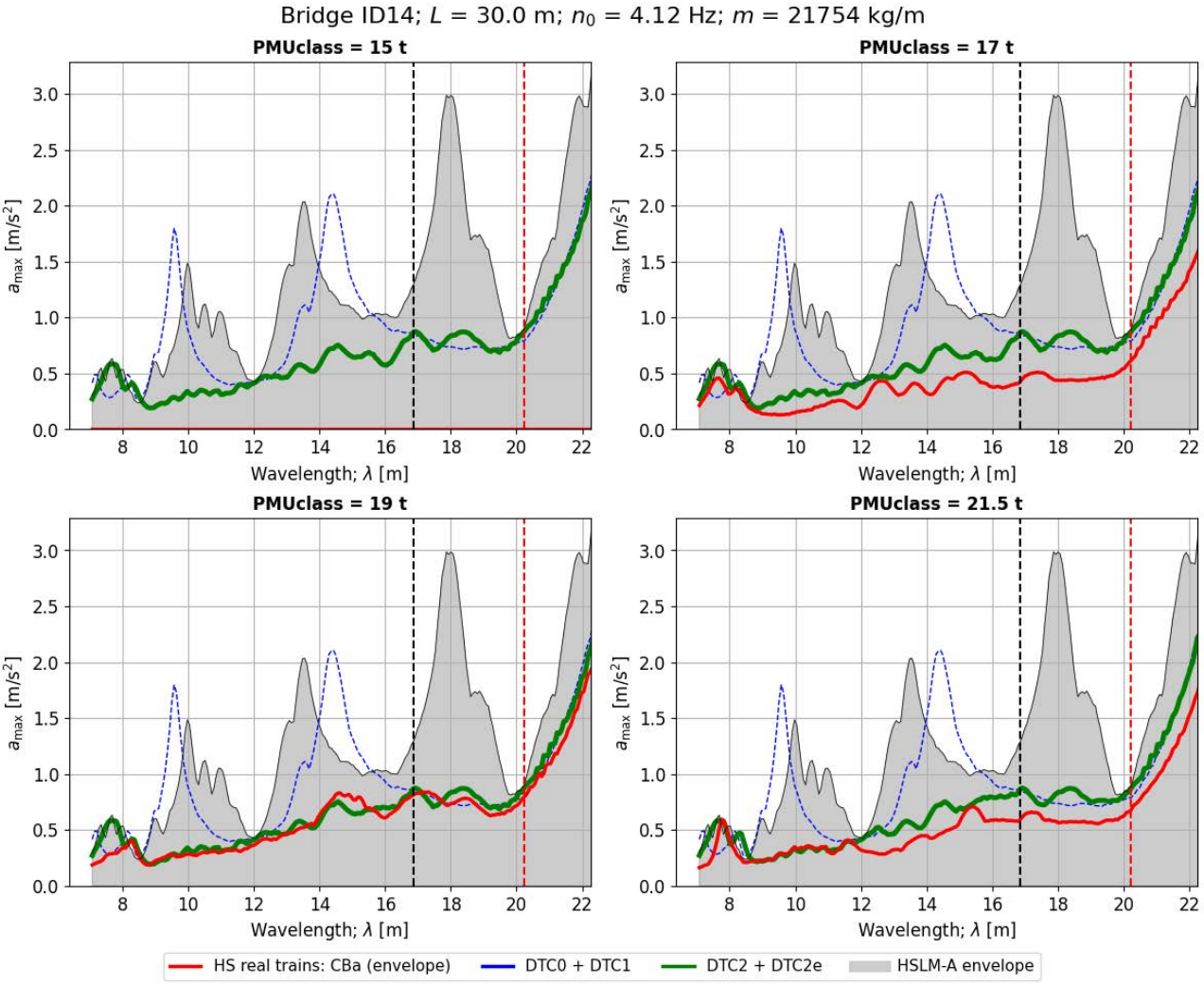

Figure 114. Peak vertical acceleration in the bridge ID14 when subject to real CBa trains of different weight categories, and comparison with the reference CBa train in DTCs. Time-stepping analysis.

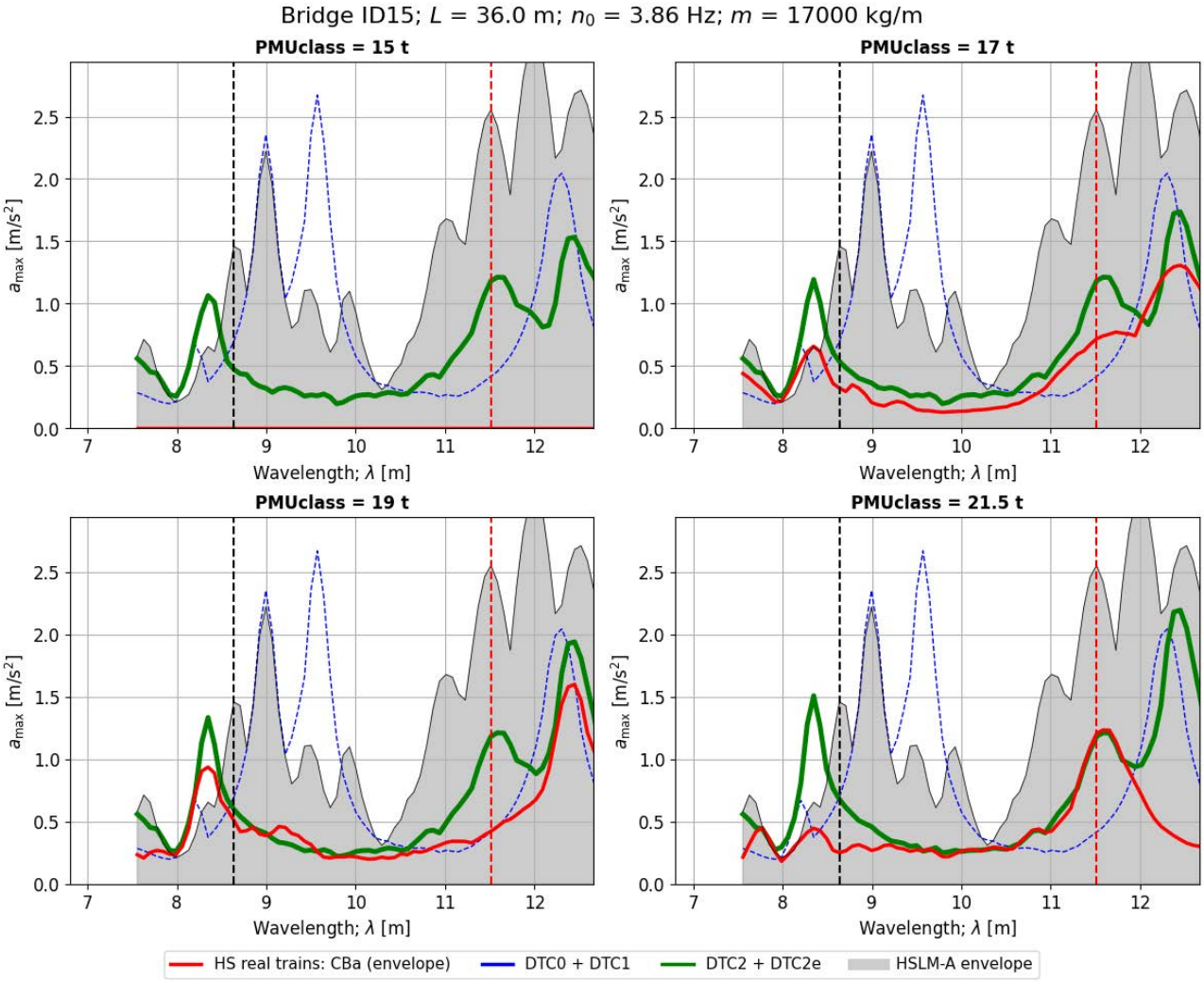

Figure 115. Peak vertical acceleration in the bridge ID15 when subject to real CBa trains of different weight categories, and comparison with the reference CBa train in DTCs. Time-stepping analysis.

CBb trains

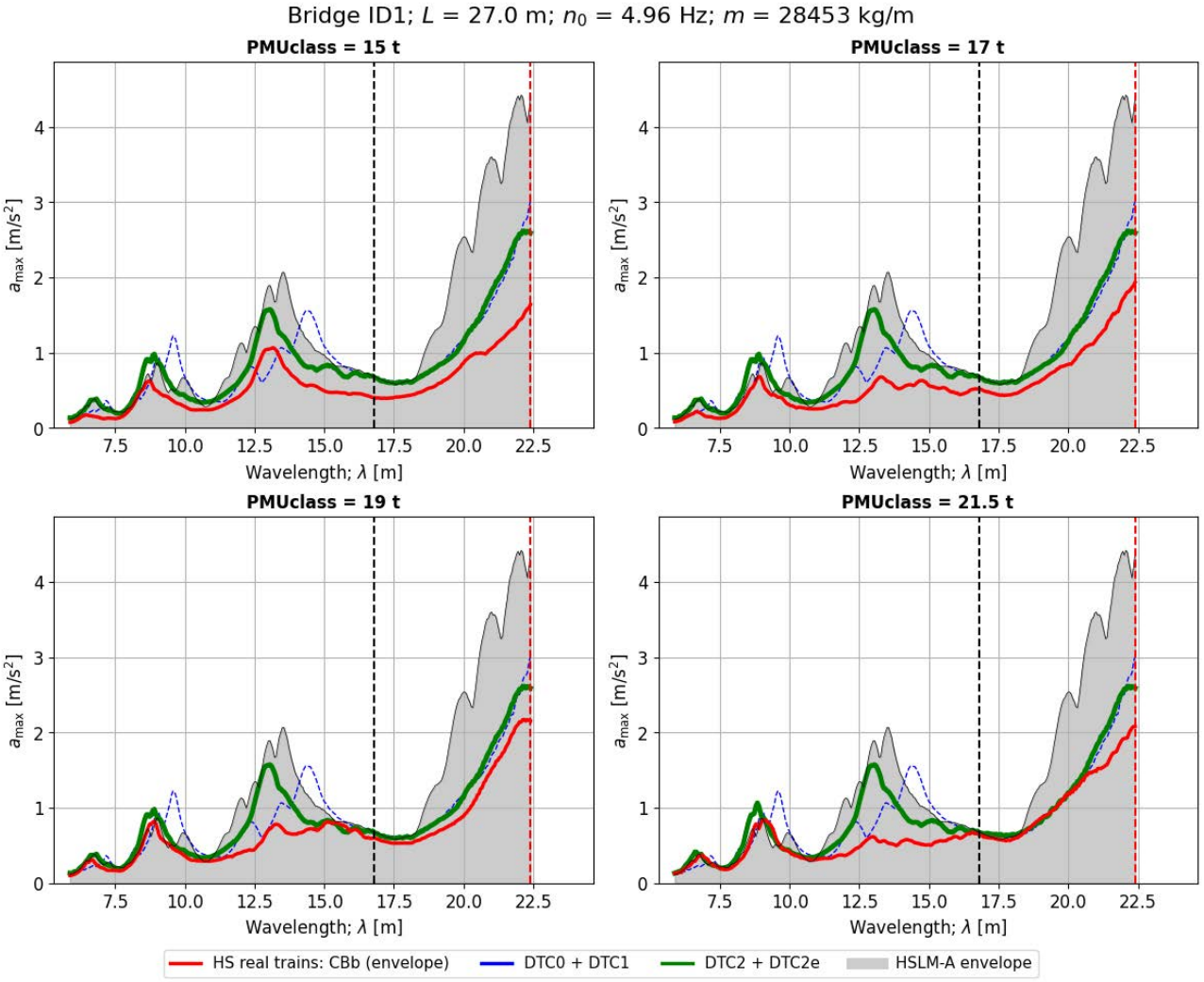

Figure 116. Peak vertical acceleration in the bridge ID1 when subject to real CBb trains of different weight categories, and comparison with the reference CBb train in DTCs. Time-stepping analysis.

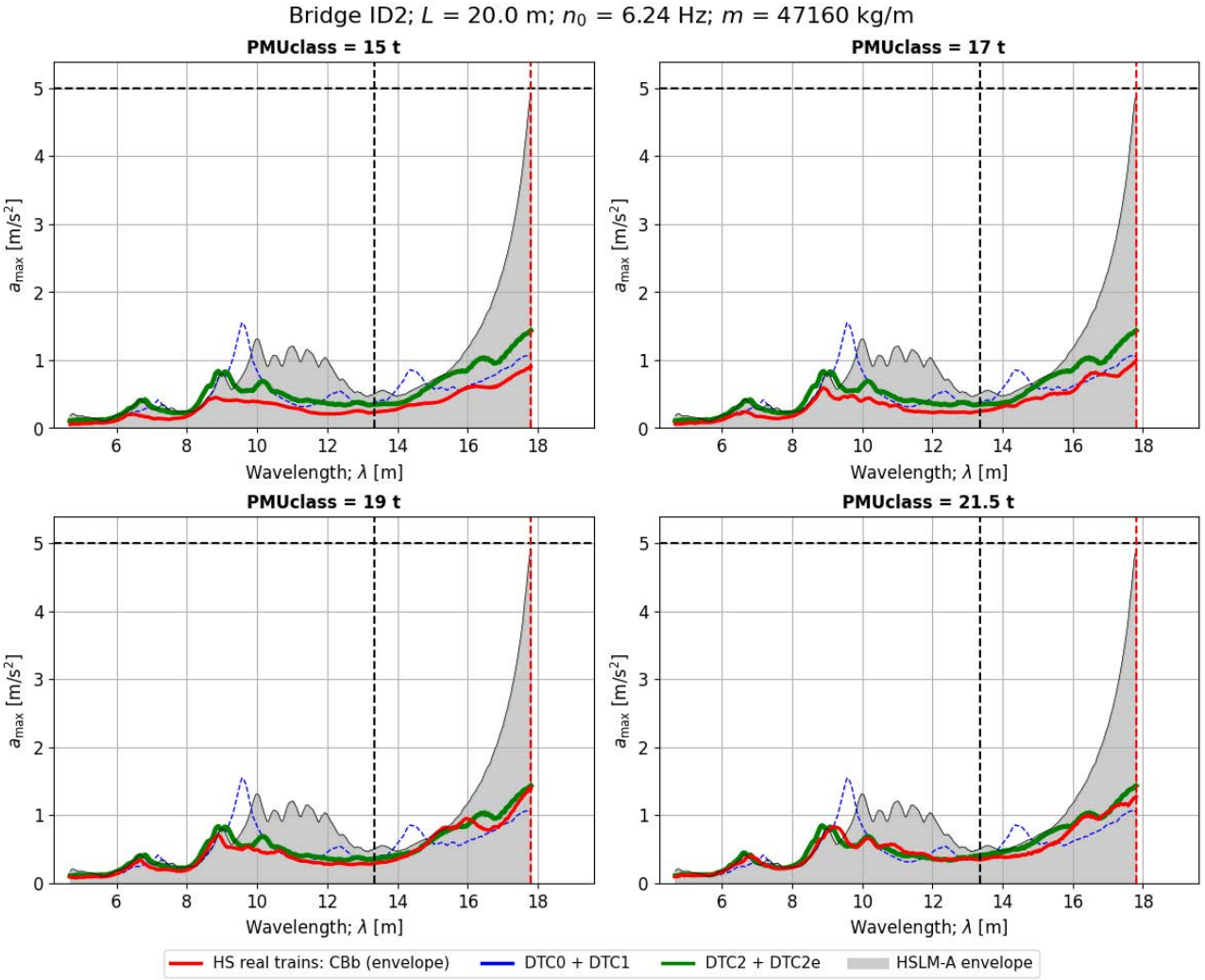

Figure 117. Peak vertical acceleration in the bridge ID2 when subject to real CBb trains of different weight categories, and comparison with the reference CBb train in DTCs. Time-stepping analysis.

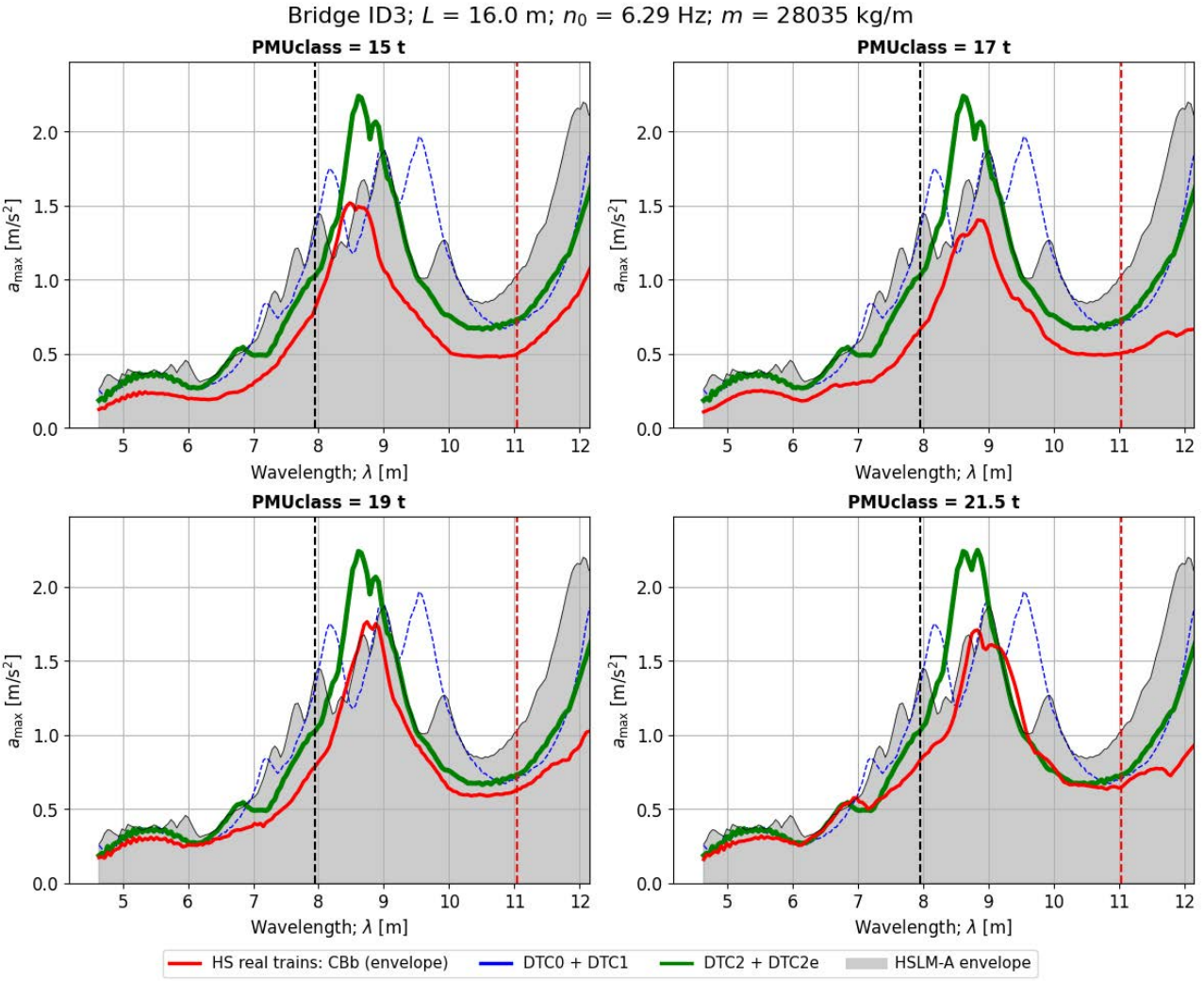

Figure 118. Peak vertical acceleration in the bridge ID3 when subject to real CBb trains of different weight categories, and comparison with the reference CBb train in DTCs. Time-stepping analysis.

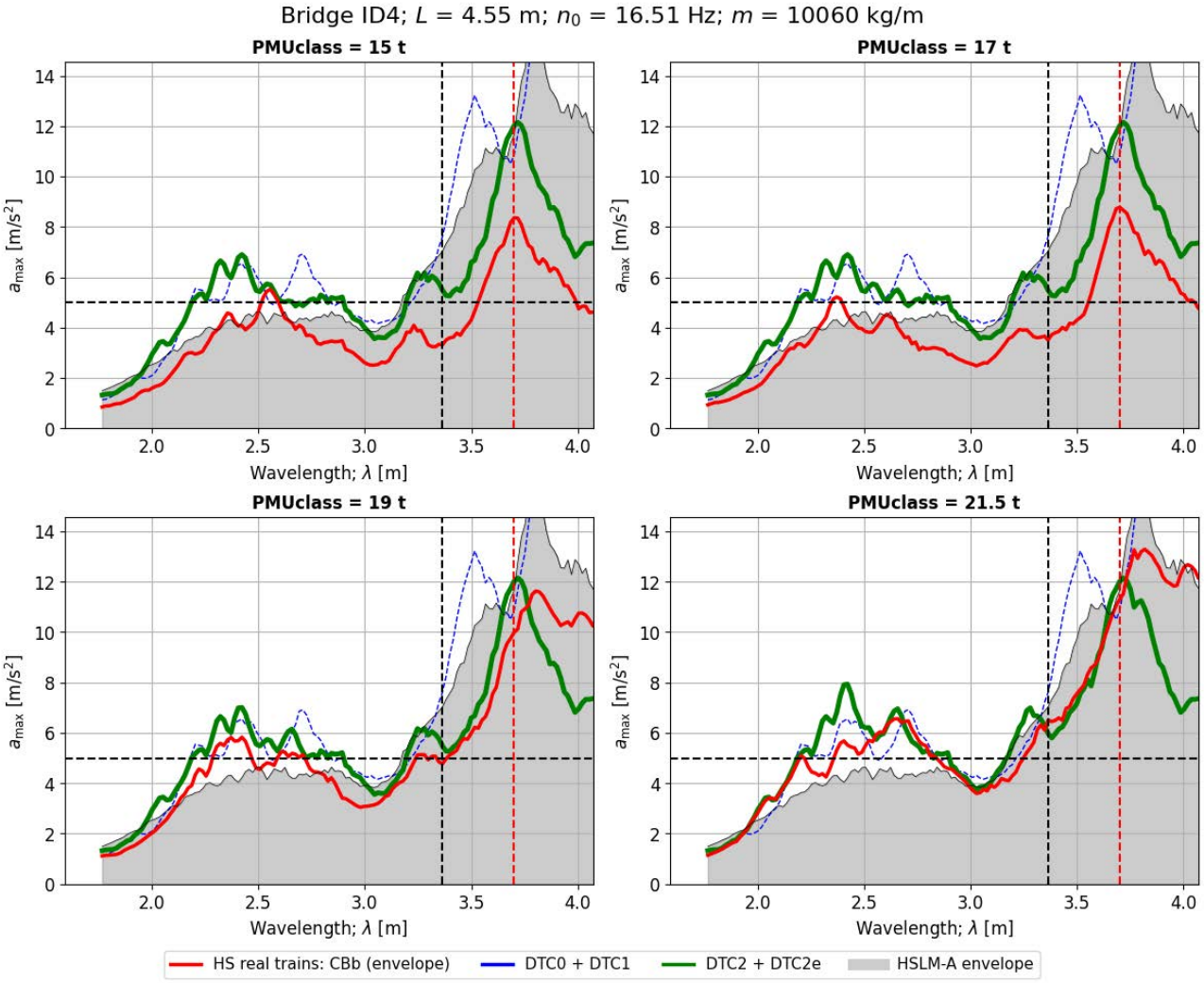

Figure 119. Peak vertical acceleration in the bridge ID4 when subject to real CBb trains of different weight categories, and comparison with the reference CBb train in DTCs. Time-stepping analysis.

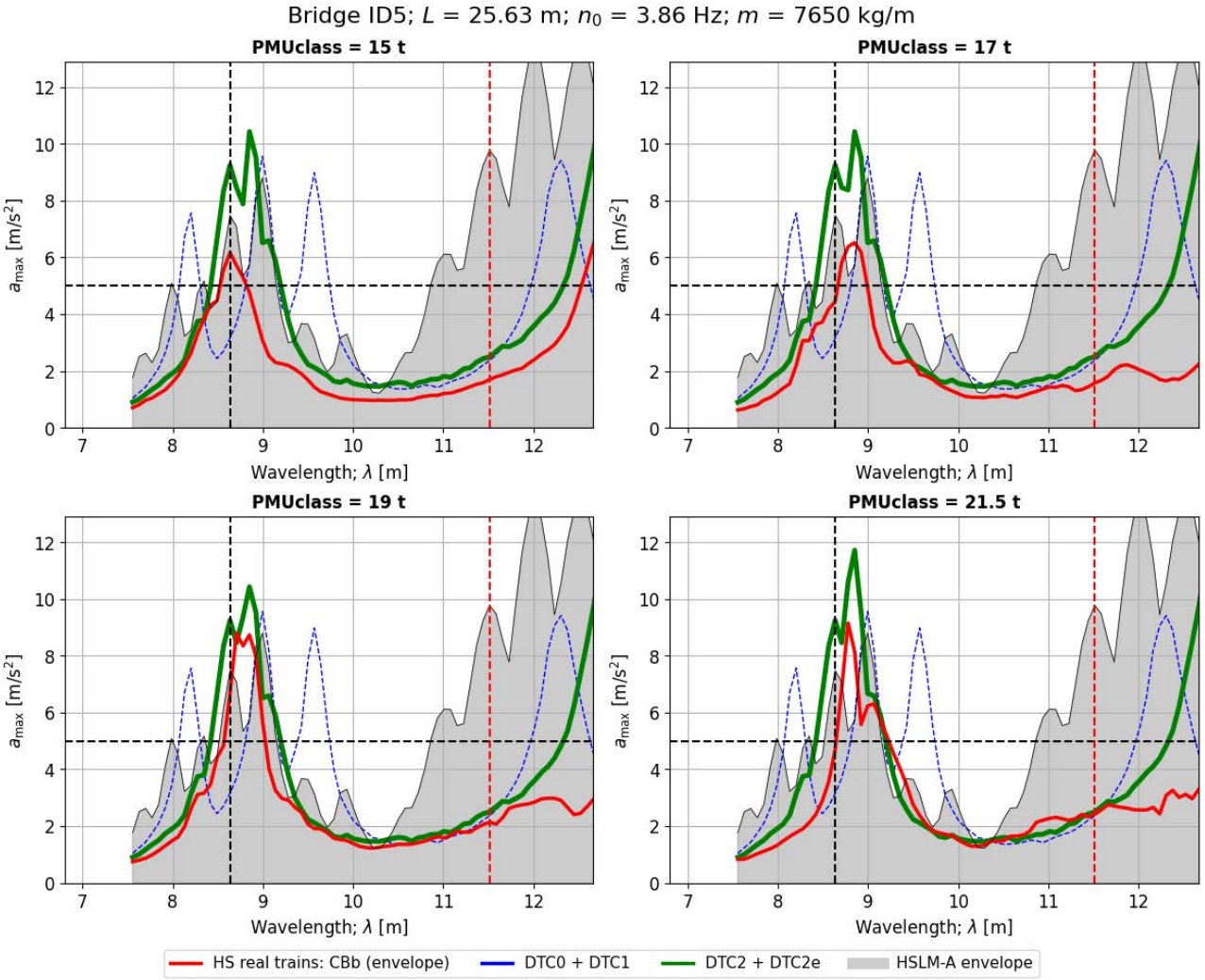

Figure 120. Peak vertical acceleration in the bridge ID5 when subject to real CBb trains of different weight categories, and comparison with the reference CBb train in DTCs. Time-stepping analysis.

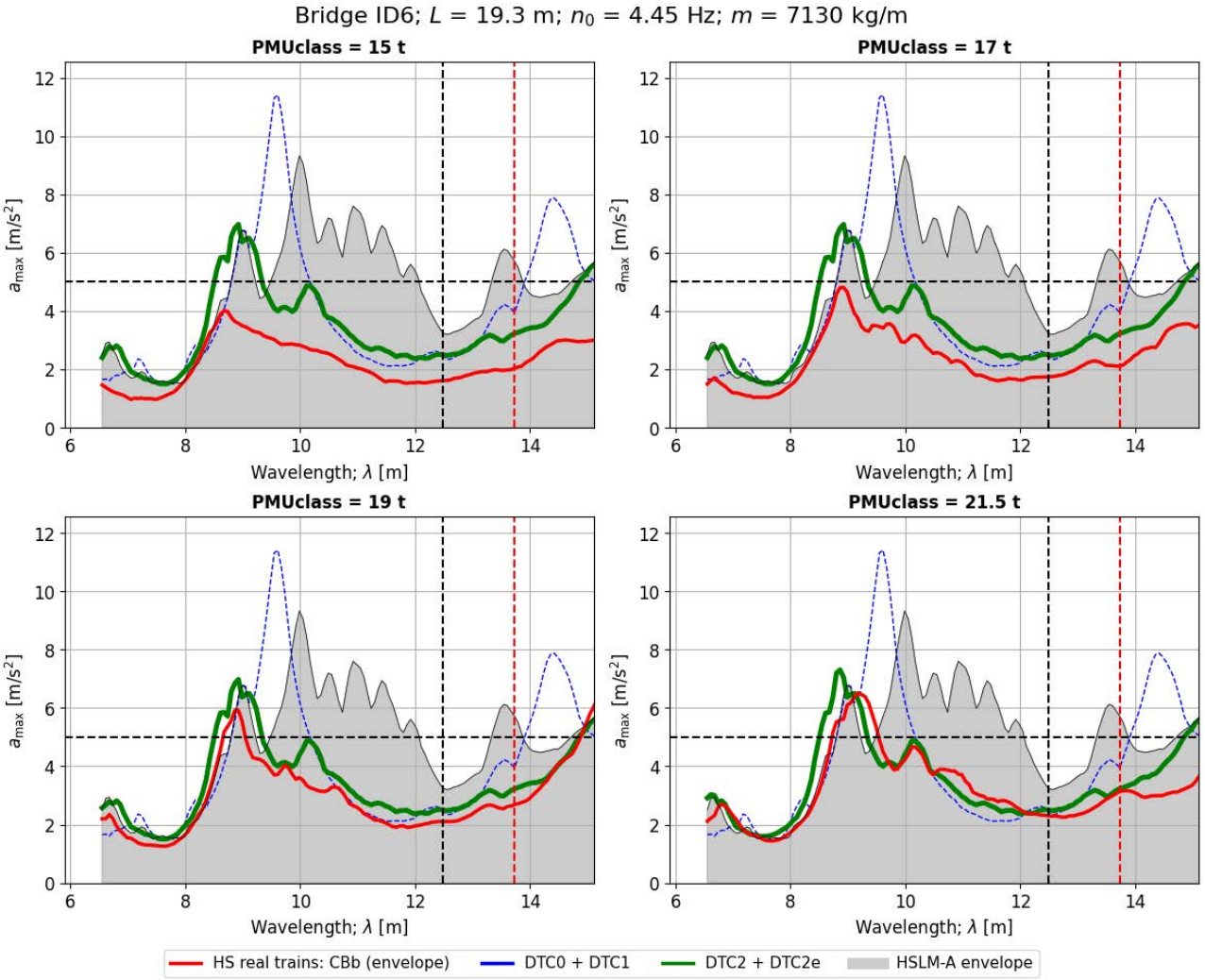

Figure 121. Peak vertical acceleration in the bridge ID6 when subject to real CBb trains of different weight categories, and comparison with the reference CBb train in DTCs. Time-stepping analysis.

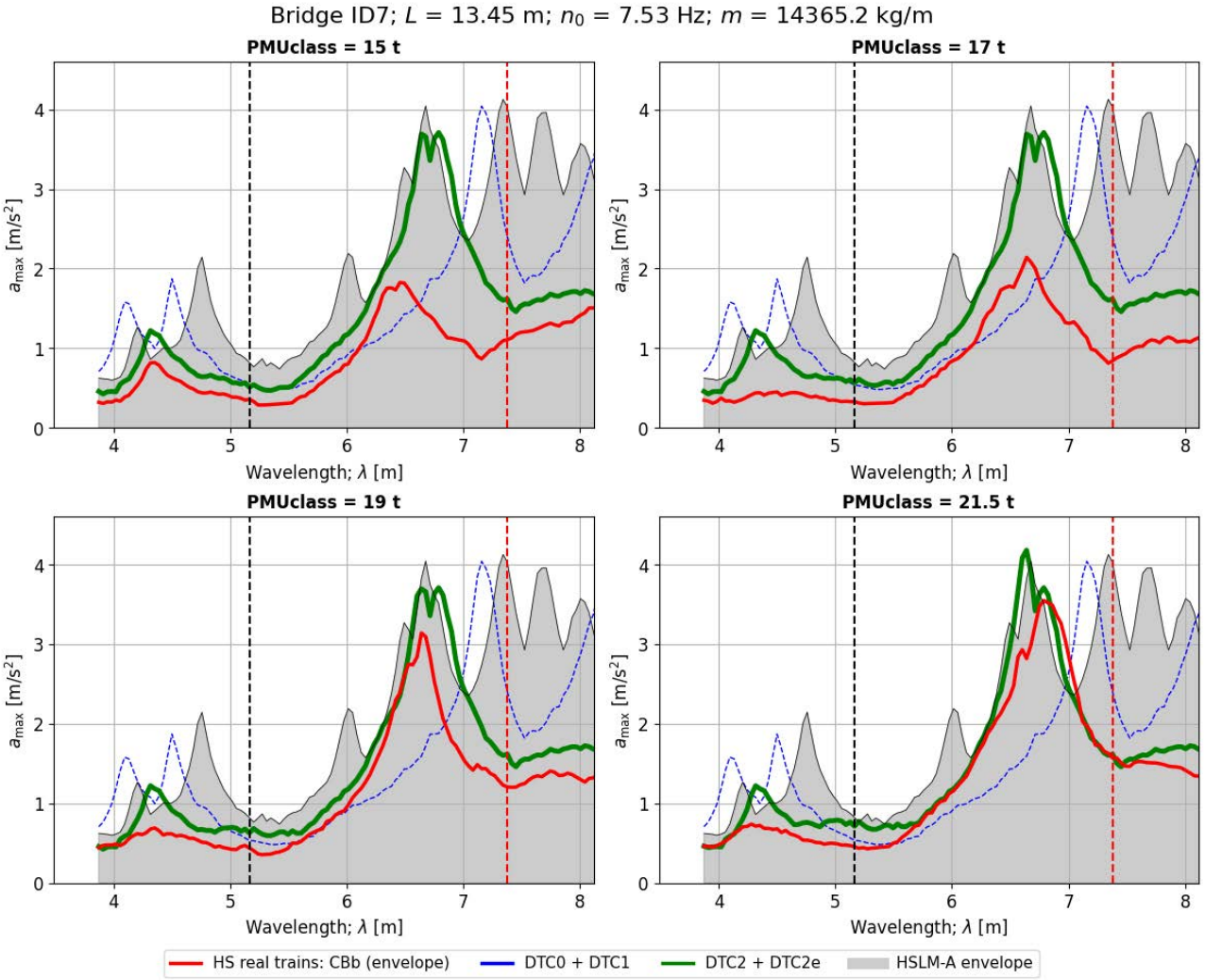

Figure 122. Peak vertical acceleration in the bridge ID7 when subject to real CBb trains of different weight categories, and comparison with the reference CBb train in DTCs. Time-stepping analysis.

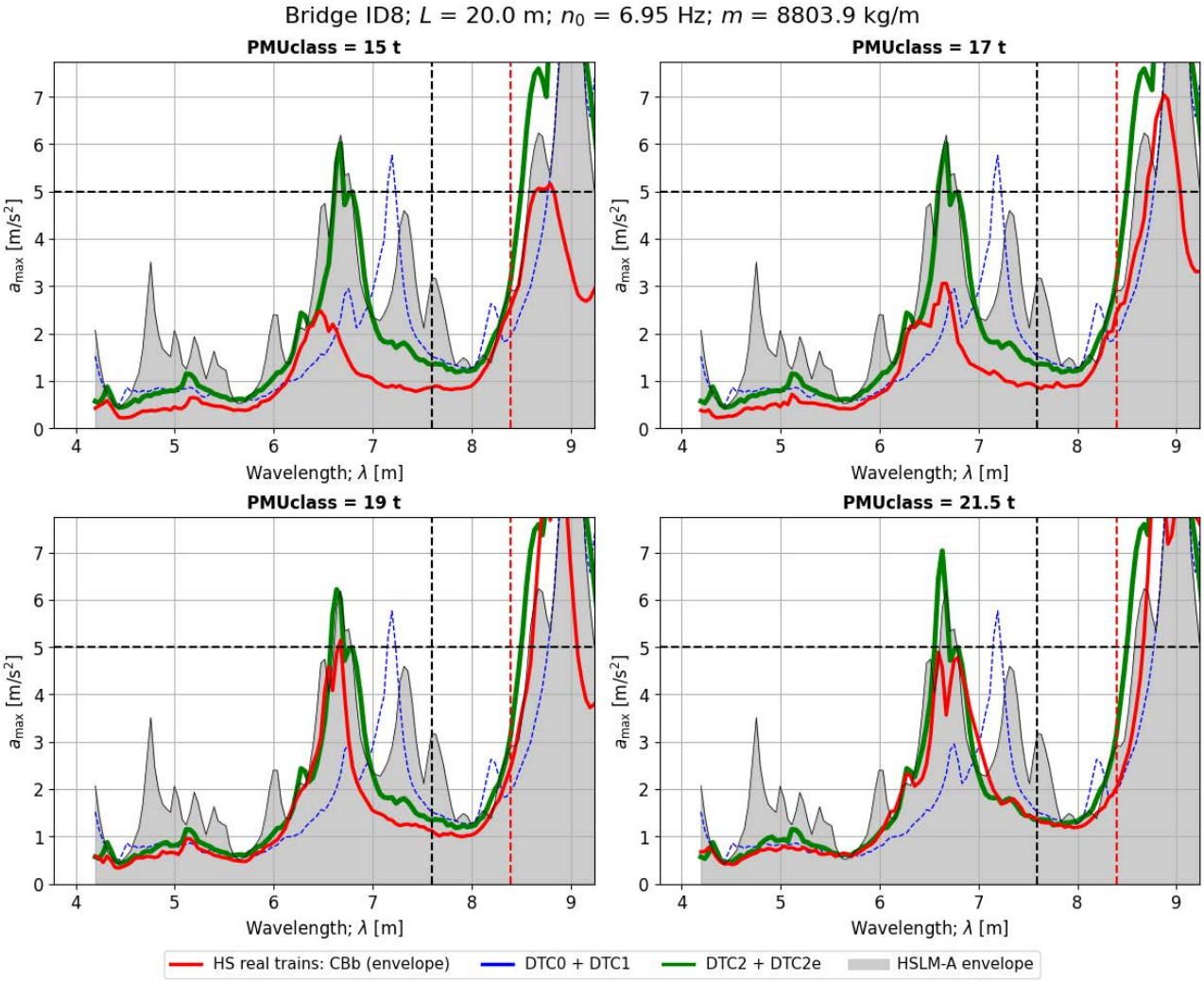

Figure 123. Peak vertical acceleration in the bridge ID8 when subject to real CBb trains of different weight categories, and comparison with the reference CBb train in DTCs. Time-stepping analysis.

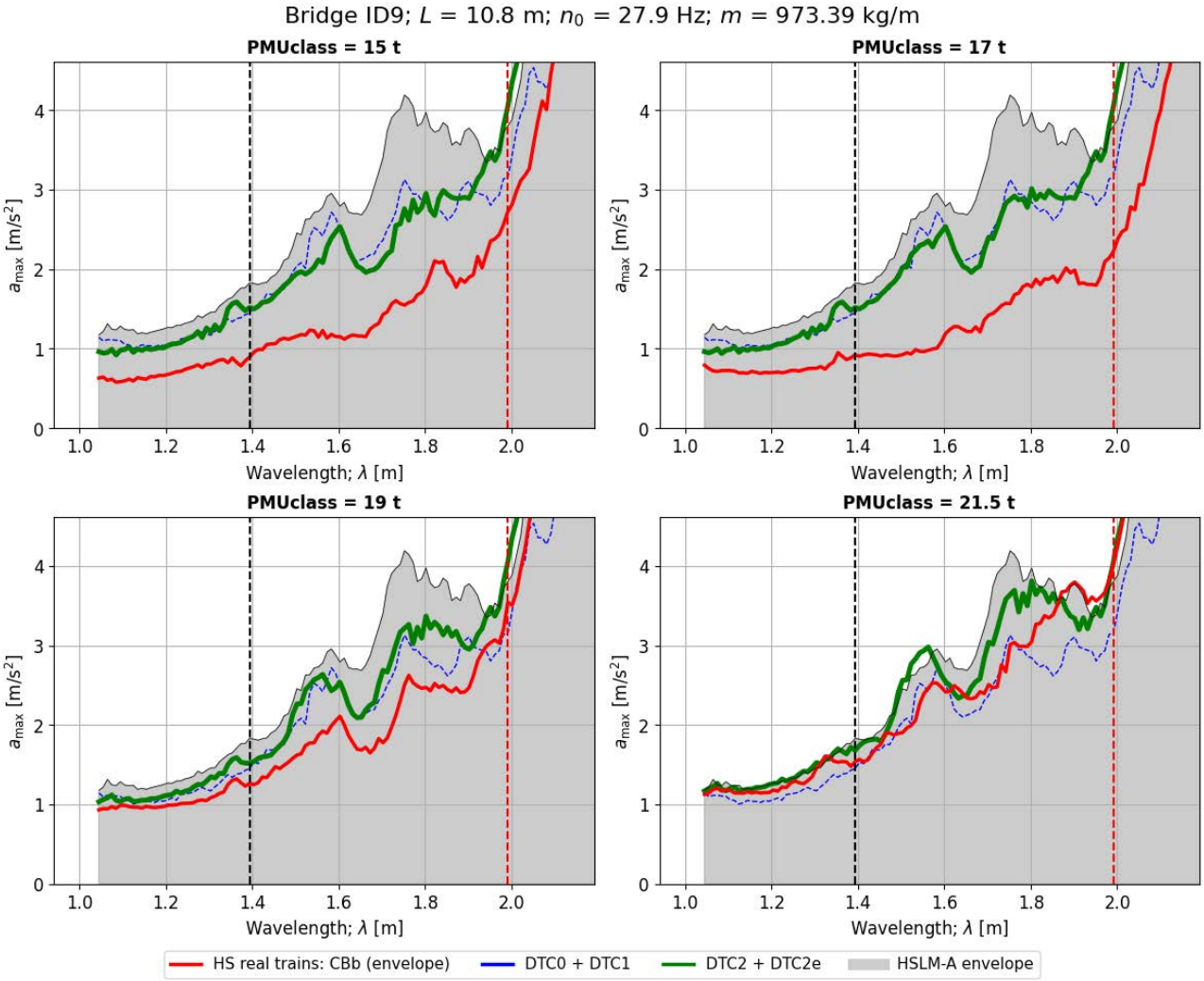

Figure 124. Peak vertical acceleration in the bridge ID9 when subject to real CBb trains of different weight categories, and comparison with the reference CBb train in DTCs. Time-stepping analysis.

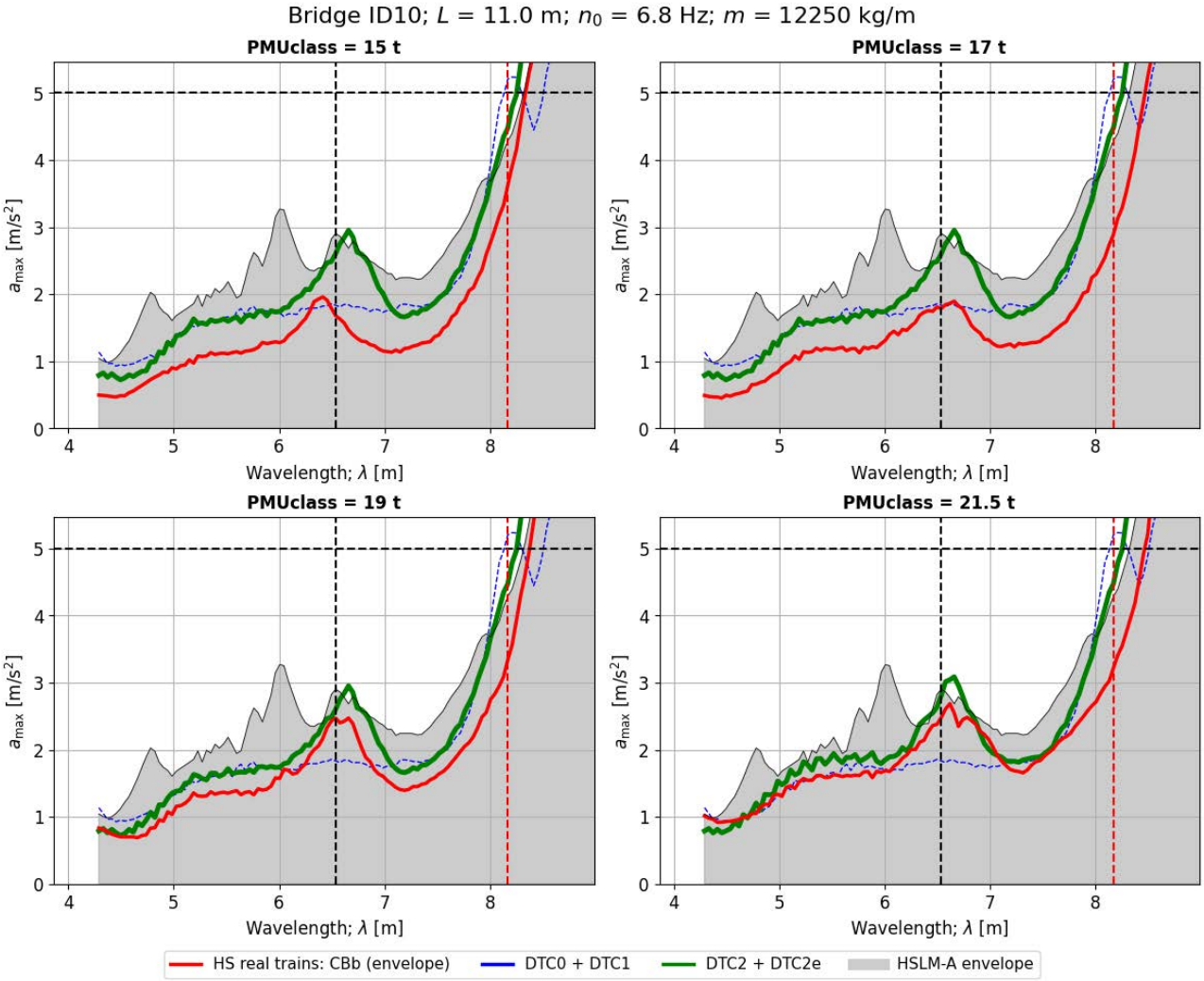

Figure 125. Peak vertical acceleration in the bridge ID10 when subject to real CBb trains of different weight categories, and comparison with the reference CBb train in DTCs. Time-stepping analysis.

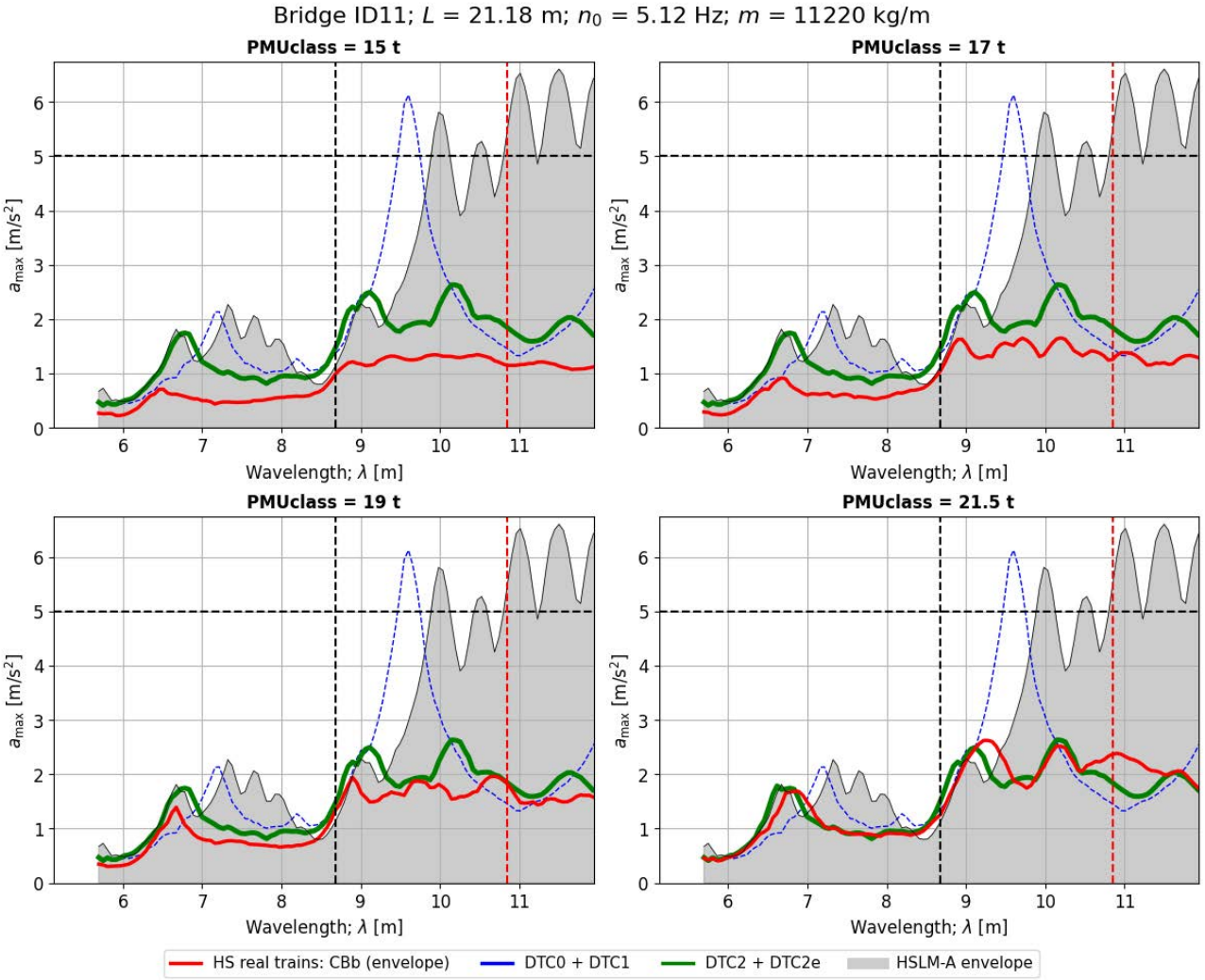

Figure 126. Peak vertical acceleration in the bridge ID11 when subject to real CBb trains of different weight categories, and comparison with the reference CBb train in DTCs. Time-stepping analysis.

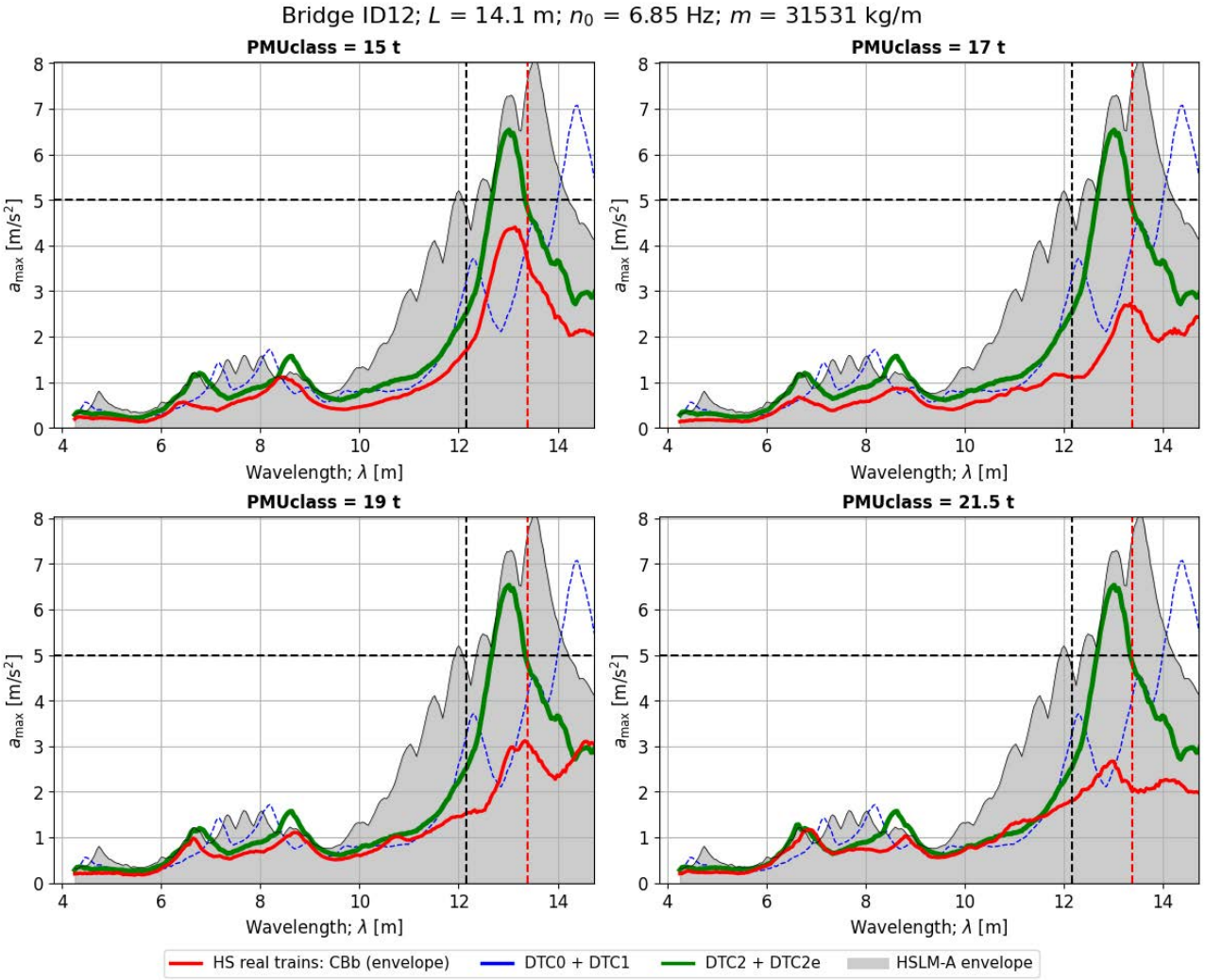

Figure 127. Peak vertical acceleration in the bridge ID12 when subject to real CBb trains of different weight categories, and comparison with the reference CBb train in DTCs. Time-stepping analysis.

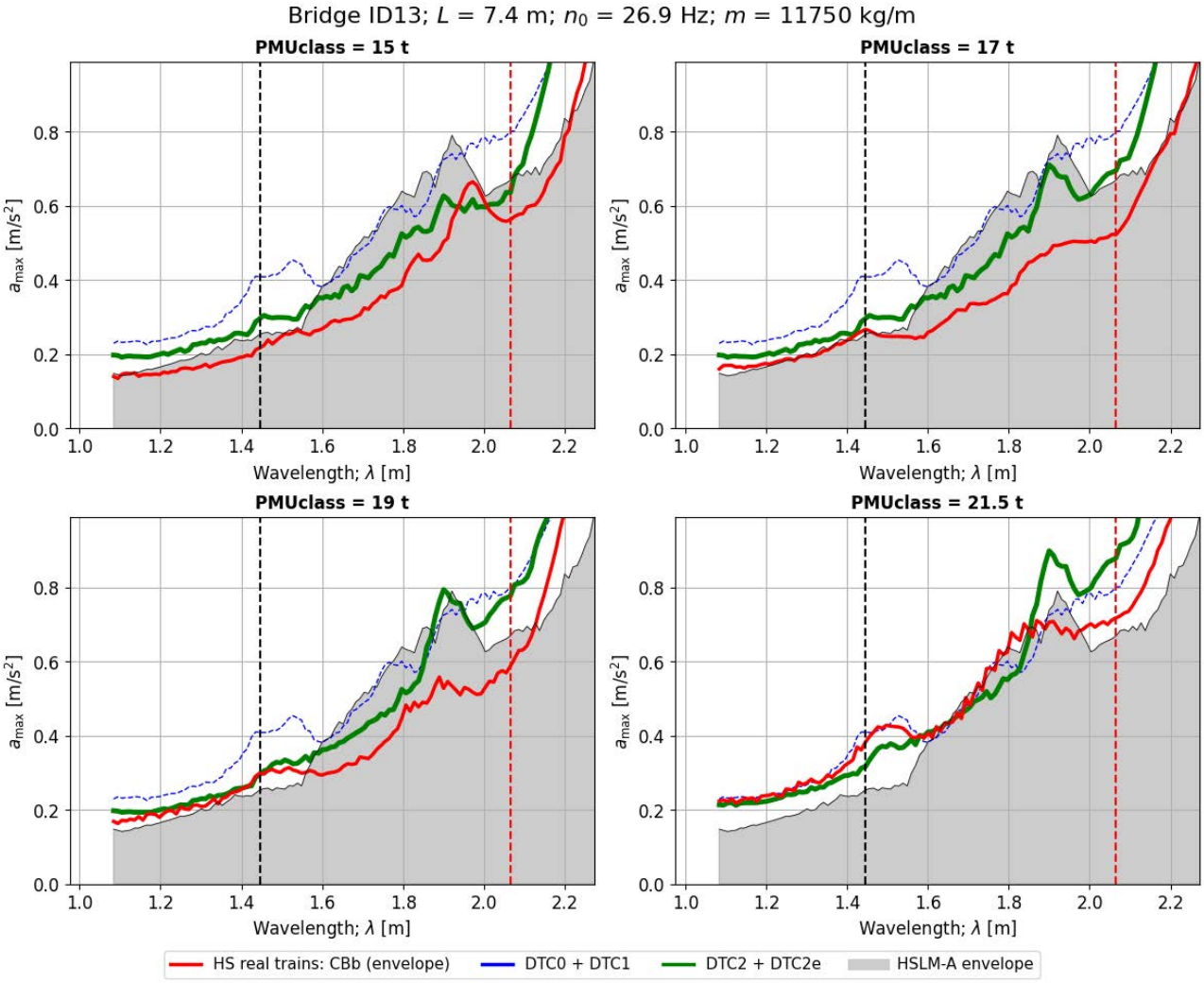

Figure 128. Peak vertical acceleration in the bridge ID13 when subject to real CBb trains of different weight categories, and comparison with the reference CBb train in DTCs. Time-stepping analysis.

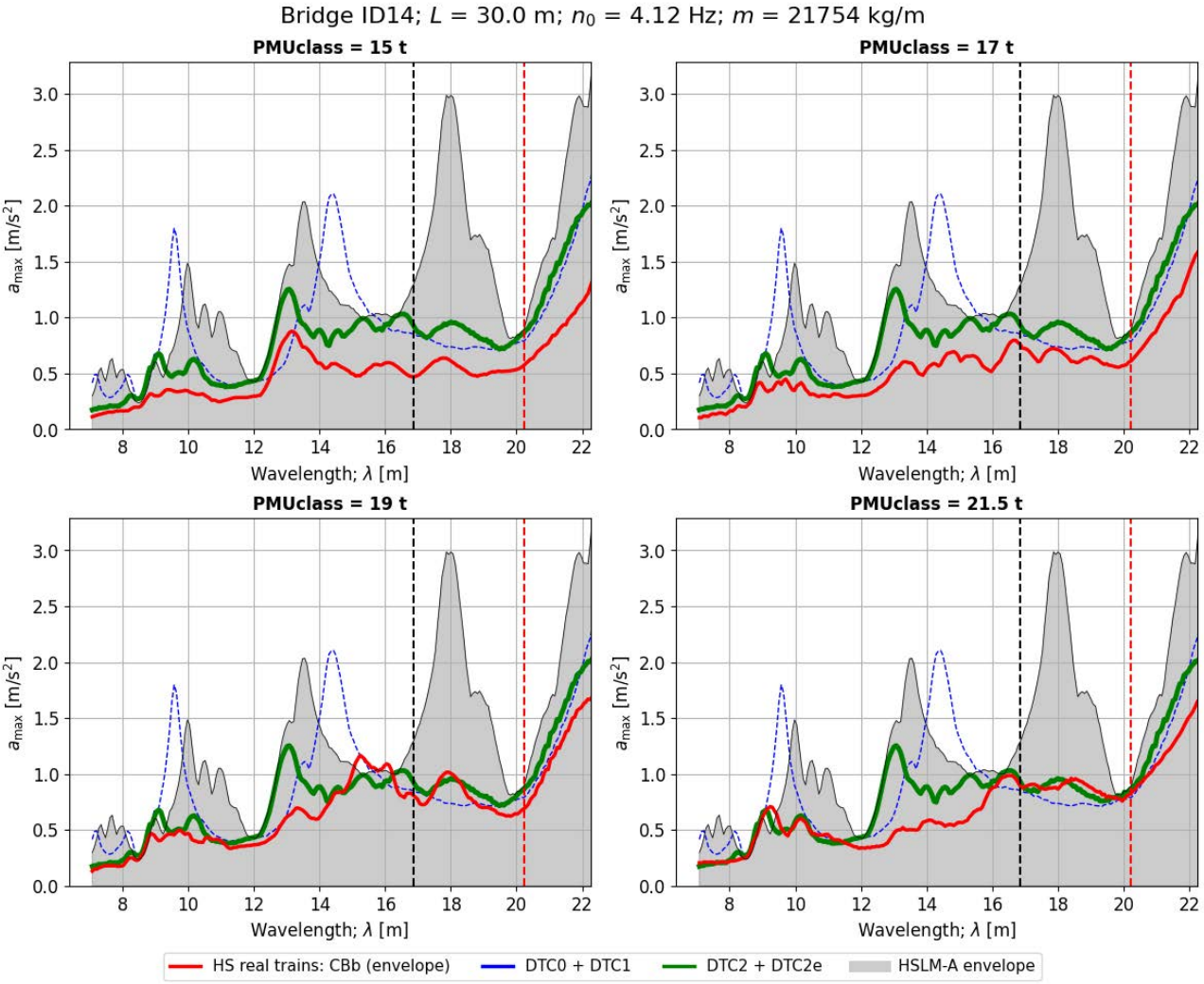

Figure 129. Peak vertical acceleration in the bridge ID14 when subject to real CBb trains of different weight categories, and comparison with the reference CBb train in DTCs. Time-stepping analysis.

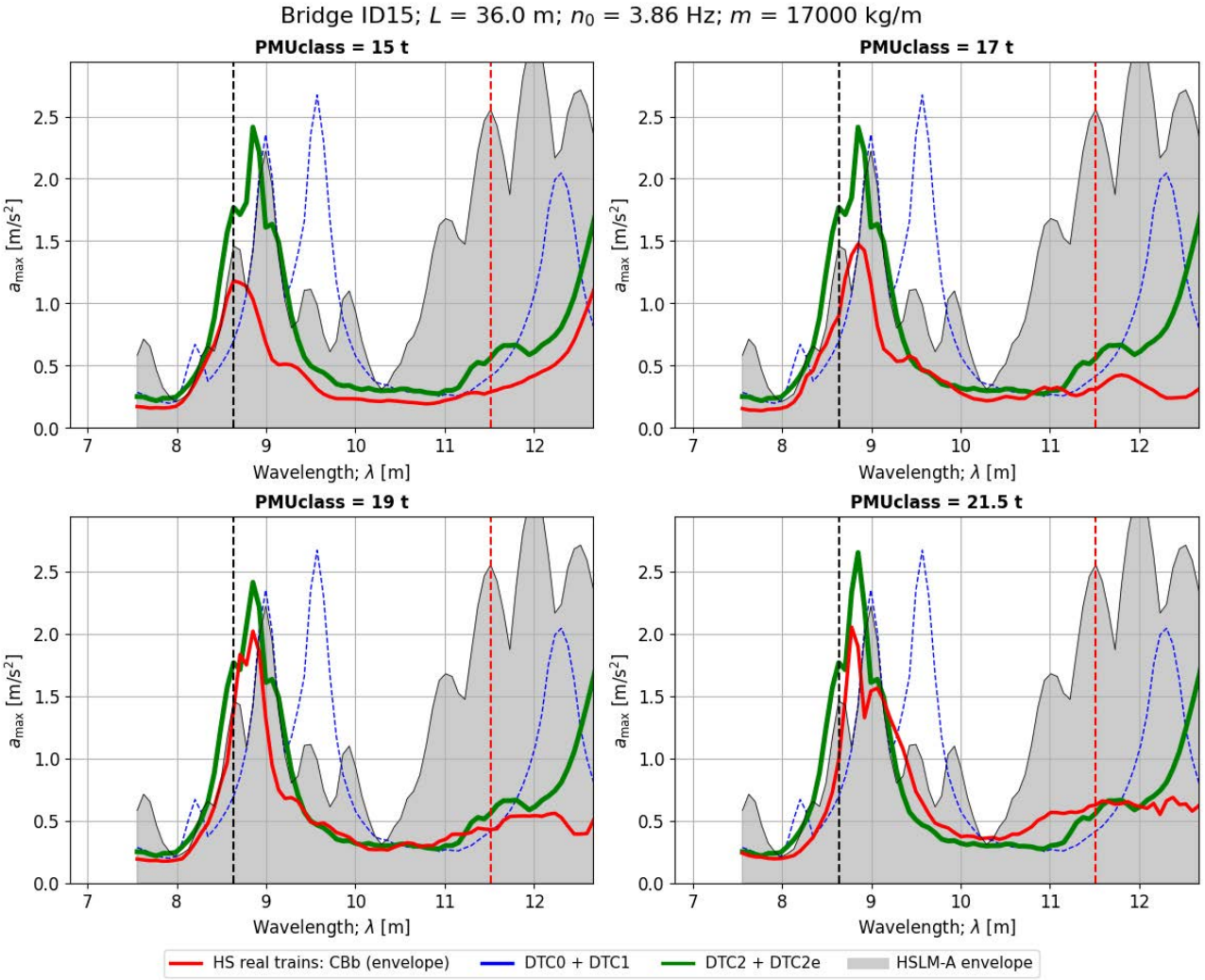

Figure 130. Peak vertical acceleration in the bridge ID15 when subject to real CBb trains of different weight categories, and comparison with the reference CBb train in DTCs. Time-stepping analysis.

CBc trains

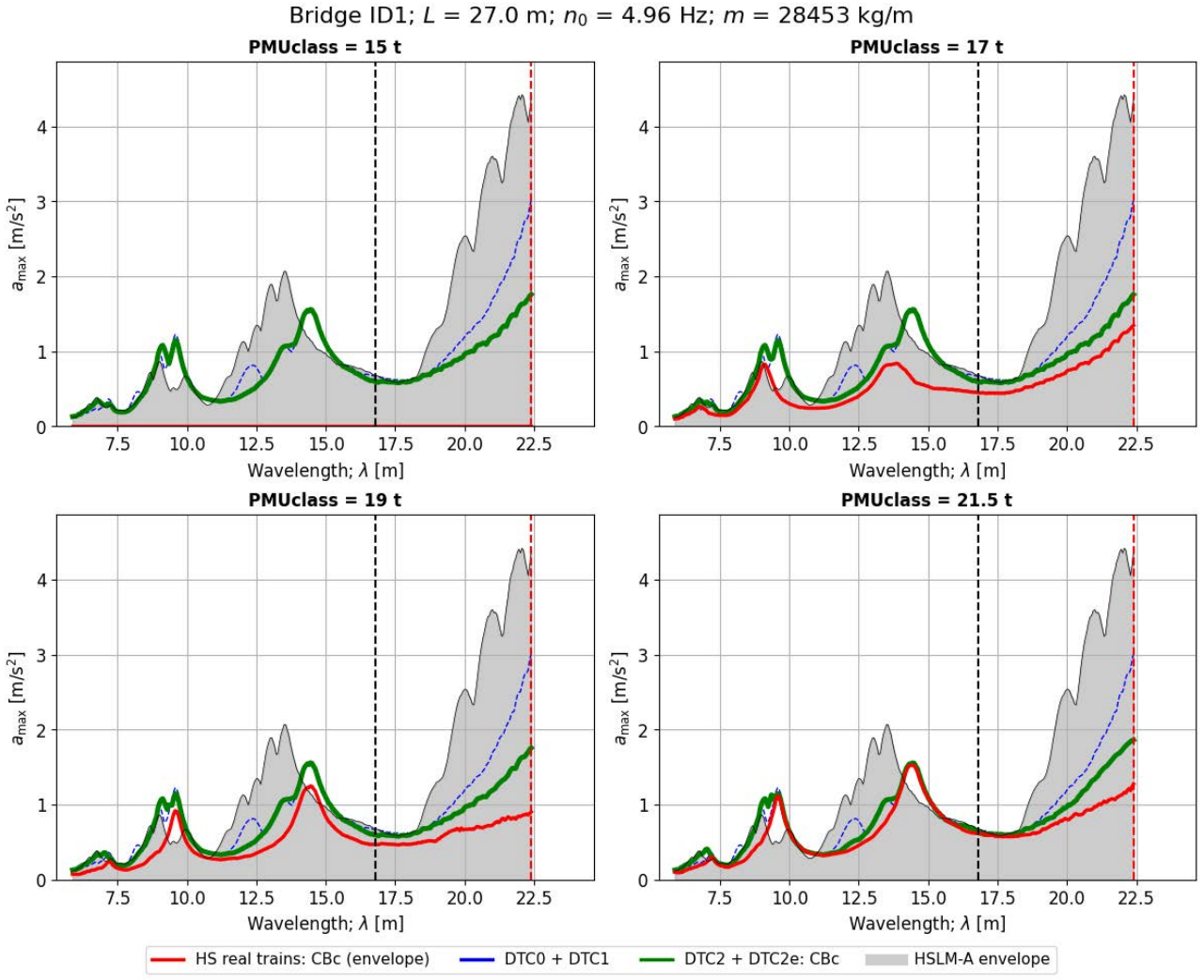

Figure 131. Peak vertical acceleration in the bridge ID1 when subject to real CBc trains of different weight categories, and comparison with the reference CBc train in DTCs. Time-stepping analysis.

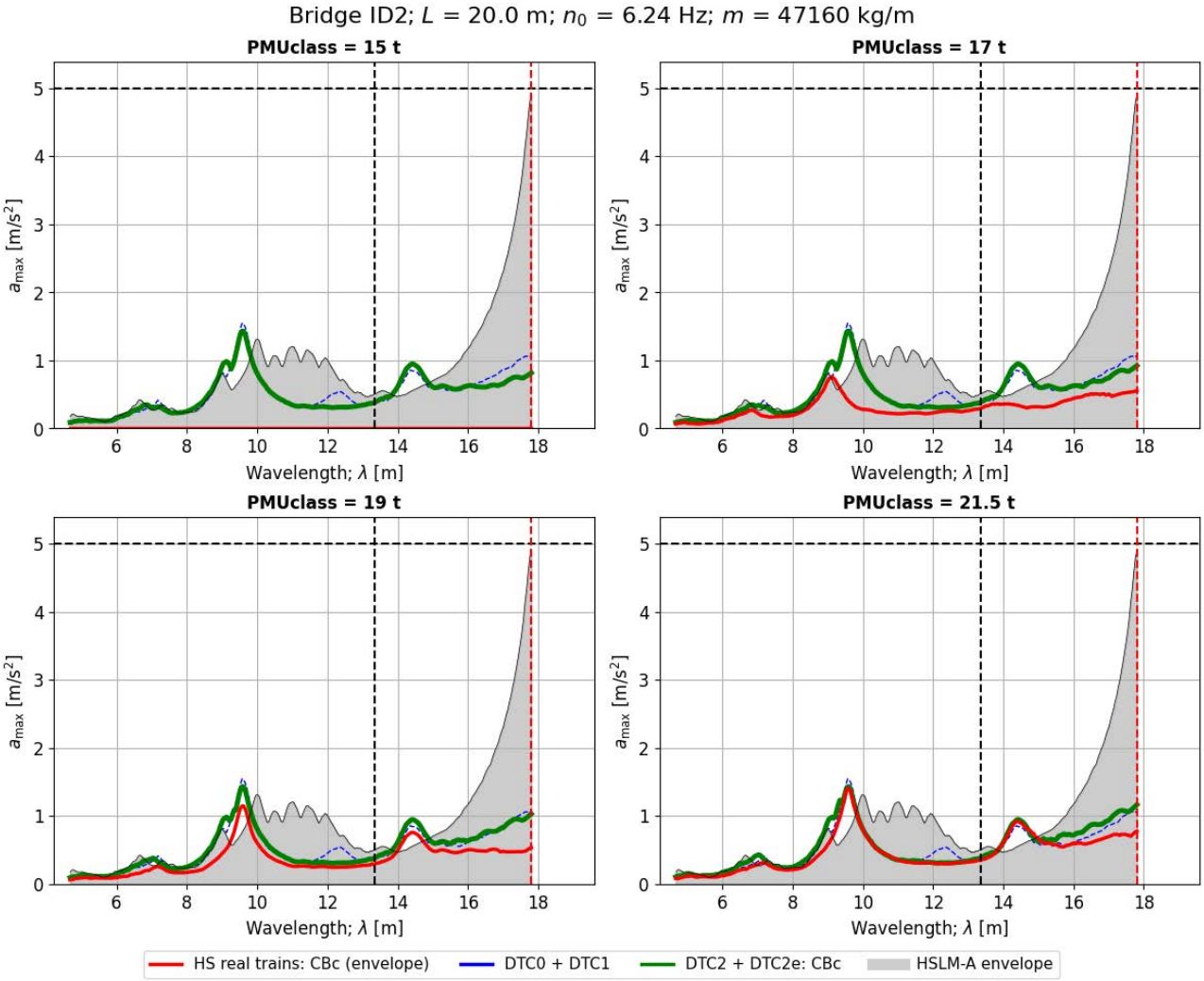

Figure 132. Peak vertical acceleration in the bridge ID2 when subject to real CBc trains of different weight categories, and comparison with the reference CBc train in DTCs. Time-stepping analysis.

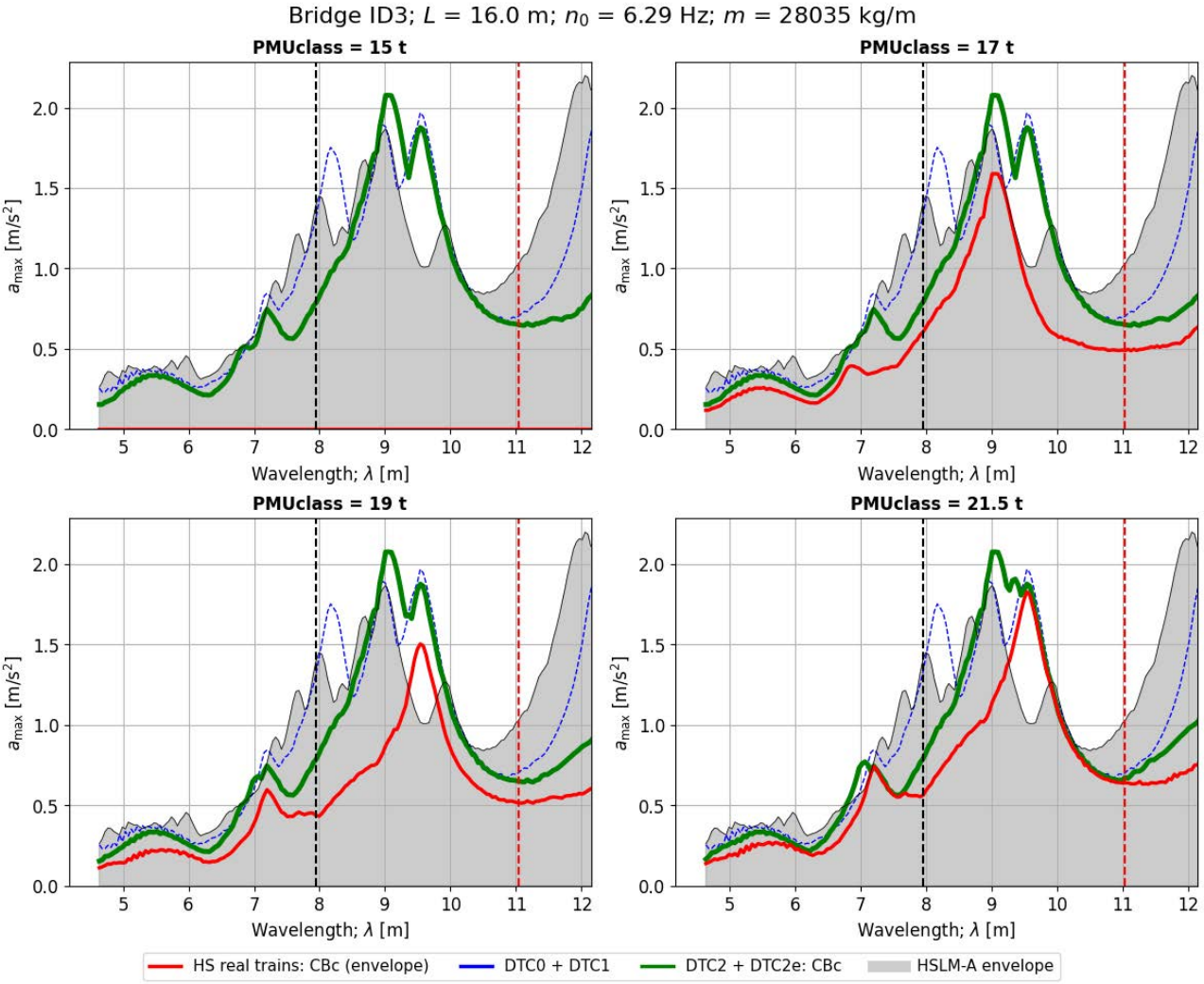

Figure 133. Peak vertical acceleration in the bridge ID3 when subject to real CBc trains of different weight categories, and comparison with the reference CBc train in DTCs. Time-stepping analysis.

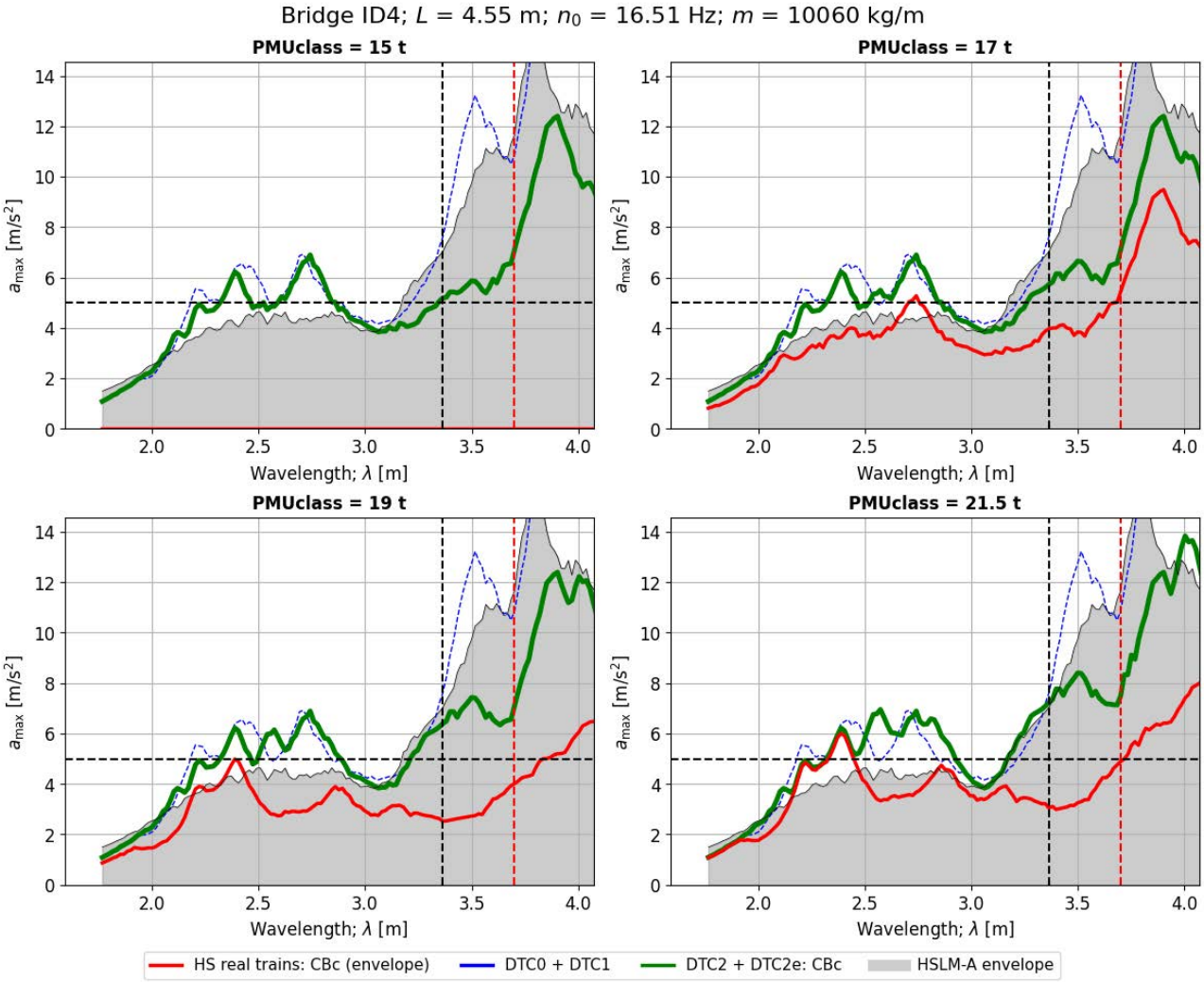

Figure 134. Peak vertical acceleration in the bridge ID4 when subject to real CBc trains of different weight categories, and comparison with the reference CBc train in DTCs. Time-stepping analysis.

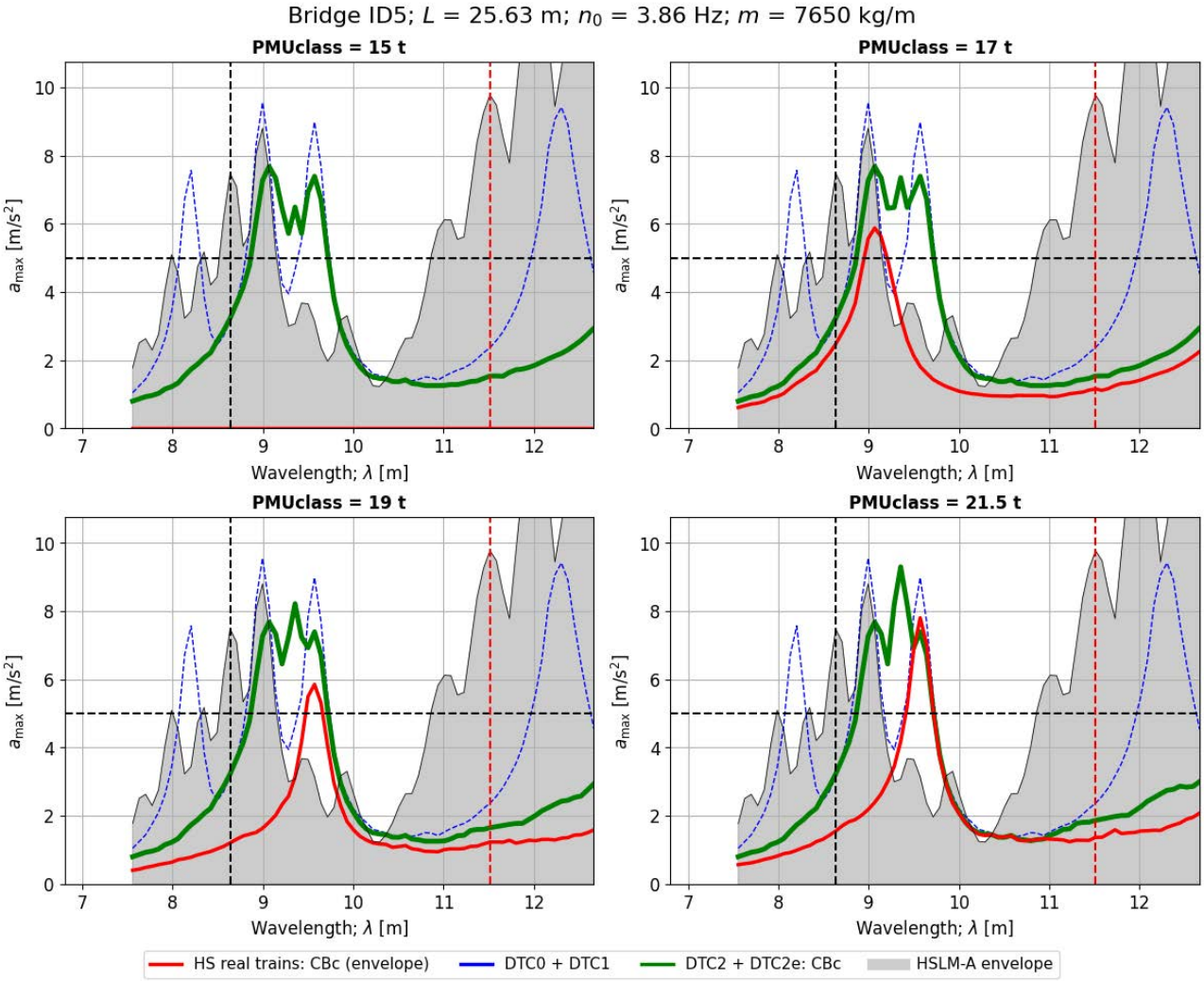

Figure 135. Peak vertical acceleration in the bridge ID5 when subject to real CBc trains of different weight categories, and comparison with the reference CBc train in DTCs. Time-stepping analysis.

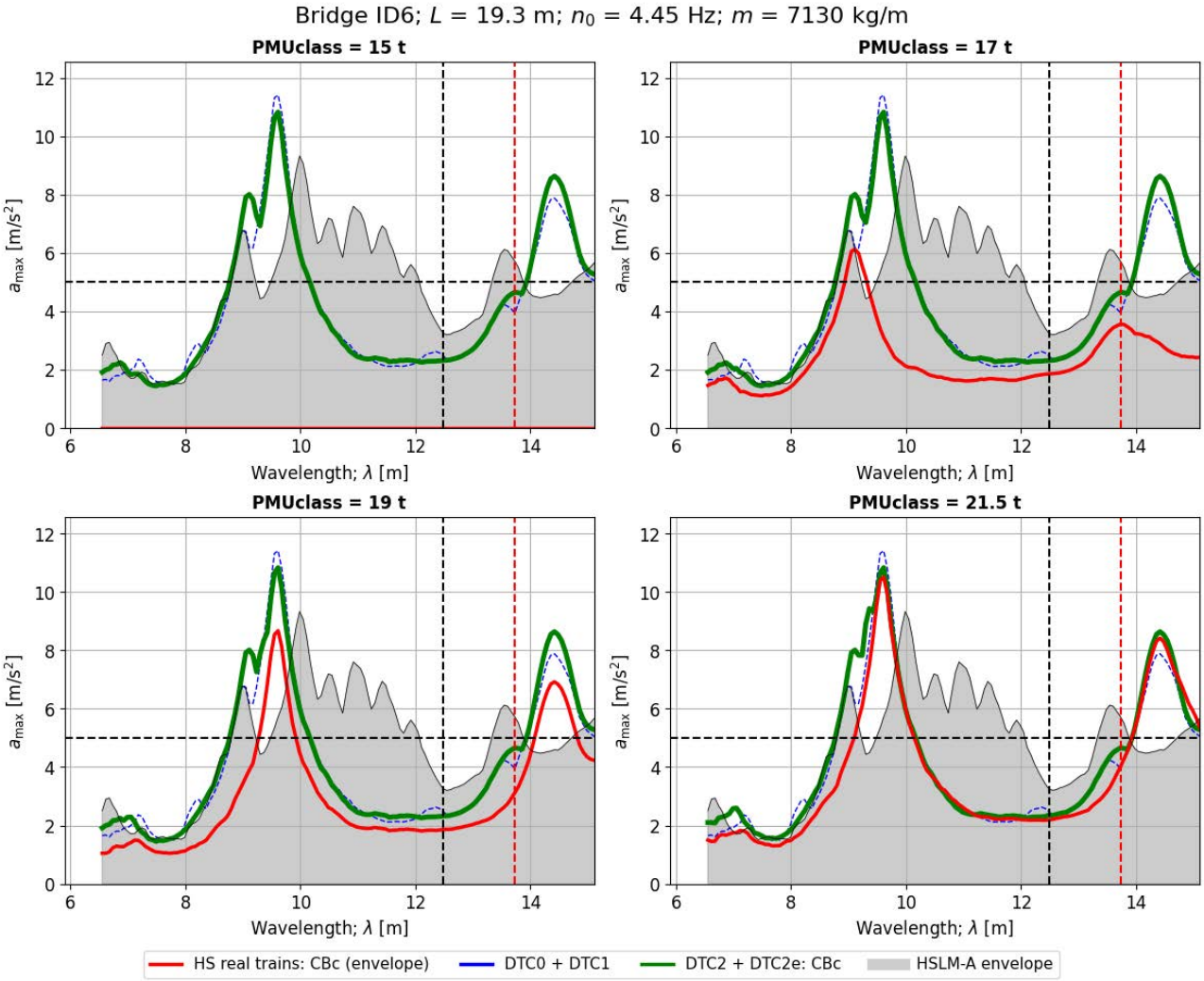

Figure 136. Peak vertical acceleration in the bridge ID6 when subject to real CBc trains of different weight categories, and comparison with the reference CBc train in DTCs. Time-stepping analysis.

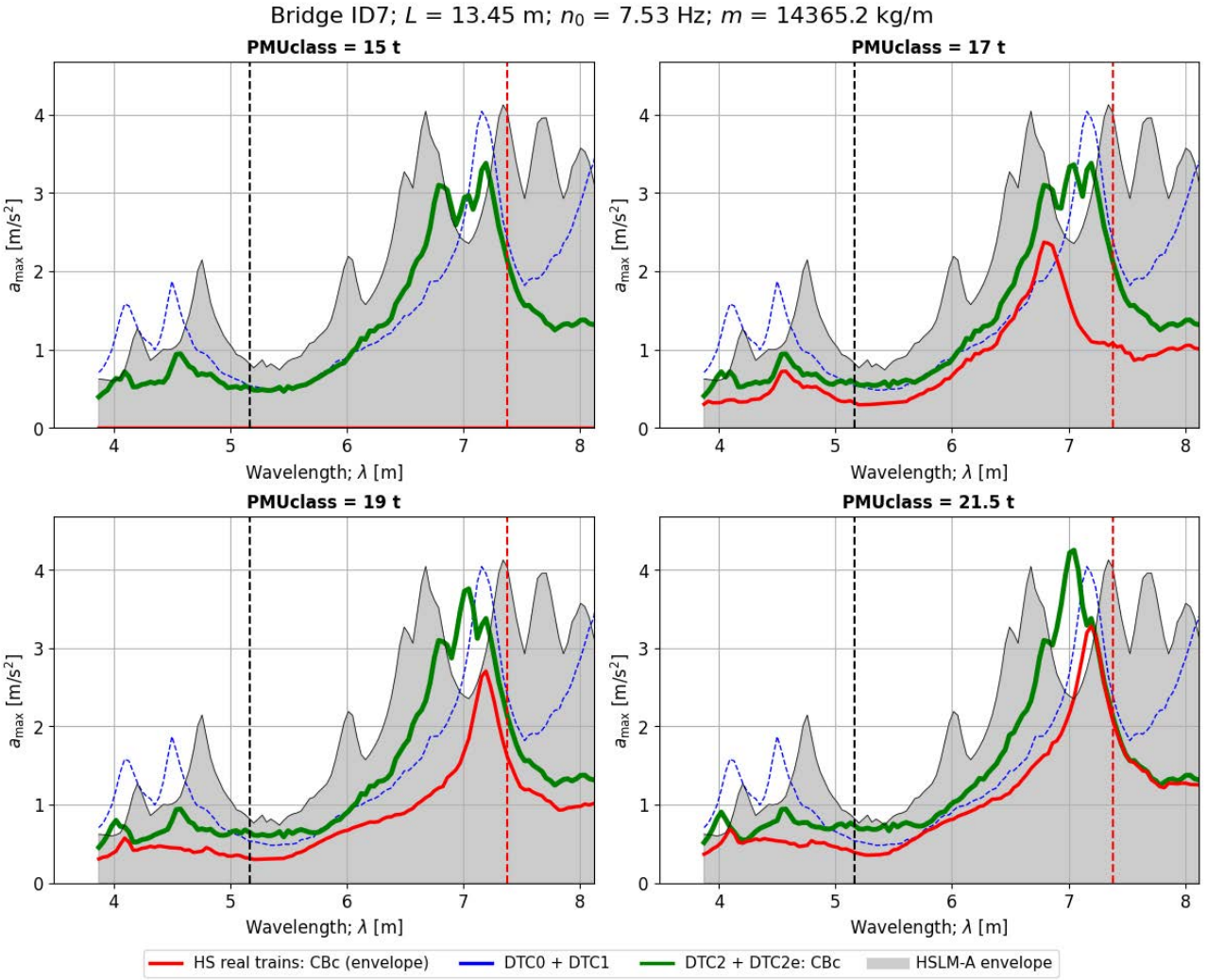

Figure 137. Peak vertical acceleration in the bridge ID7 when subject to real CBc trains of different weight categories, and comparison with the reference CBc train in DTCs. Time-stepping analysis.

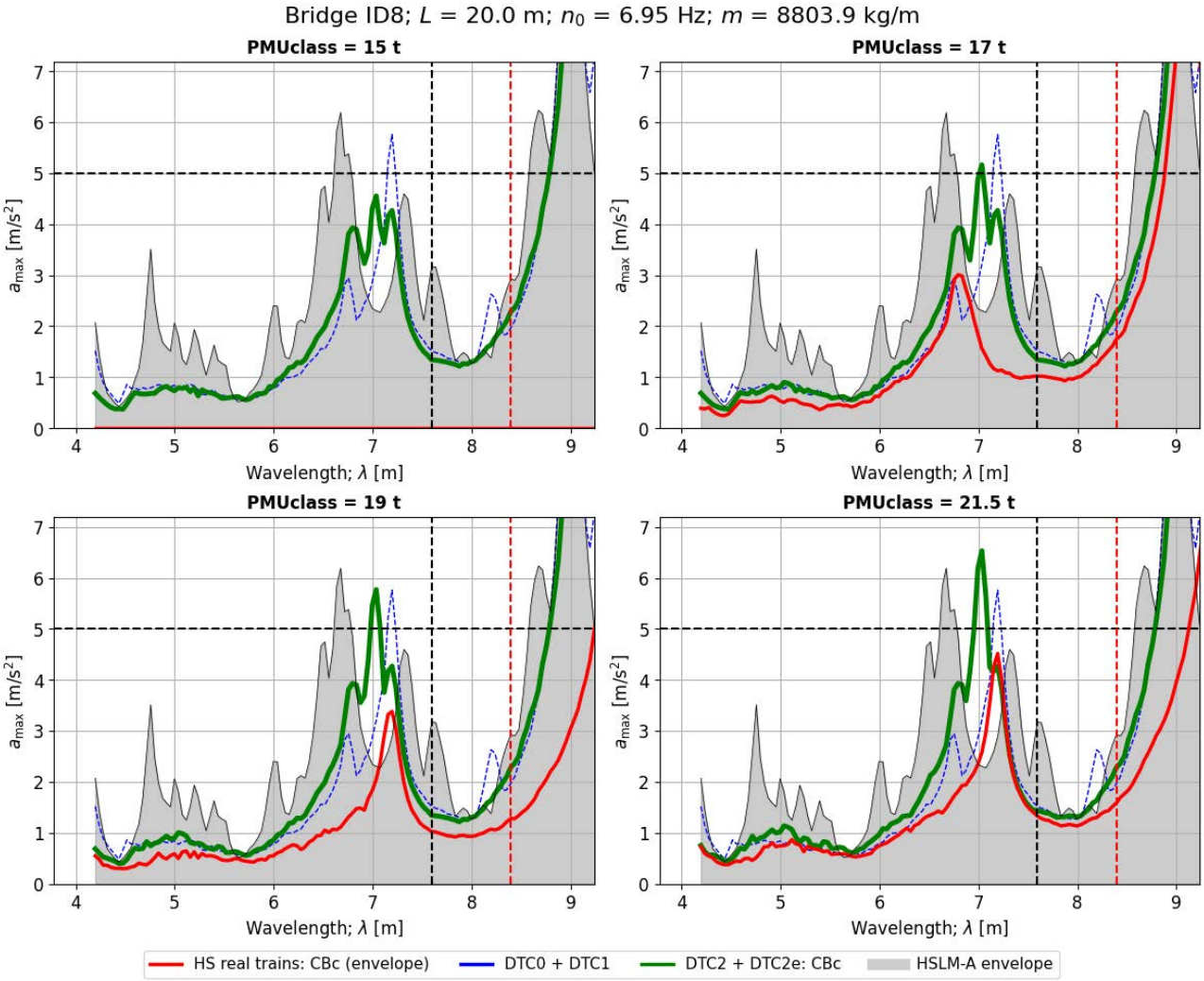

Figure 138. Peak vertical acceleration in the bridge ID8 when subject to real CBc trains of different weight categories, and comparison with the reference CBc train in DTCs. Time-stepping analysis.

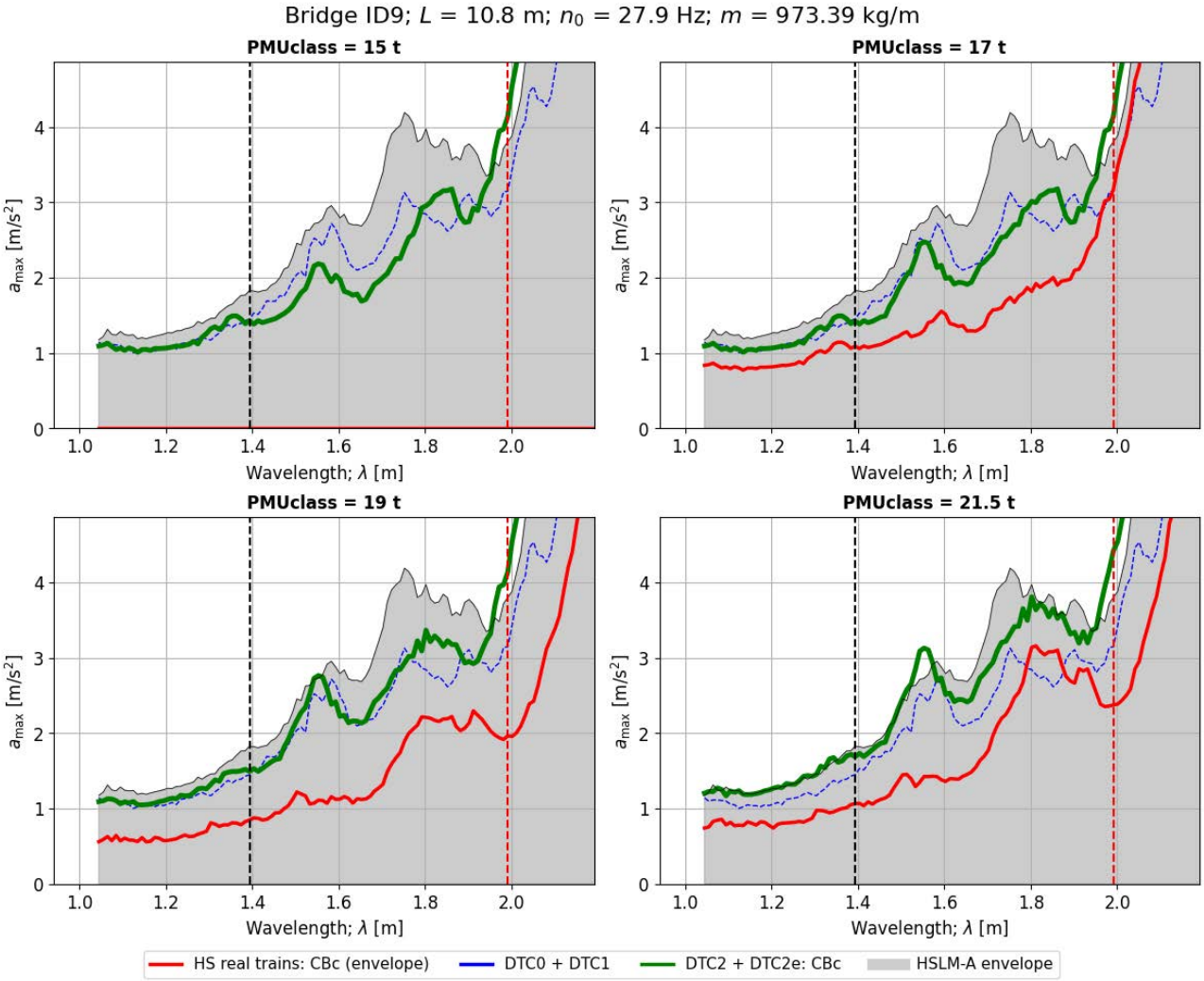

Figure 139. Peak vertical acceleration in the bridge ID9 when subject to real CBc trains of different weight categories, and comparison with the reference CBc train in DTCs. Time-stepping analysis.

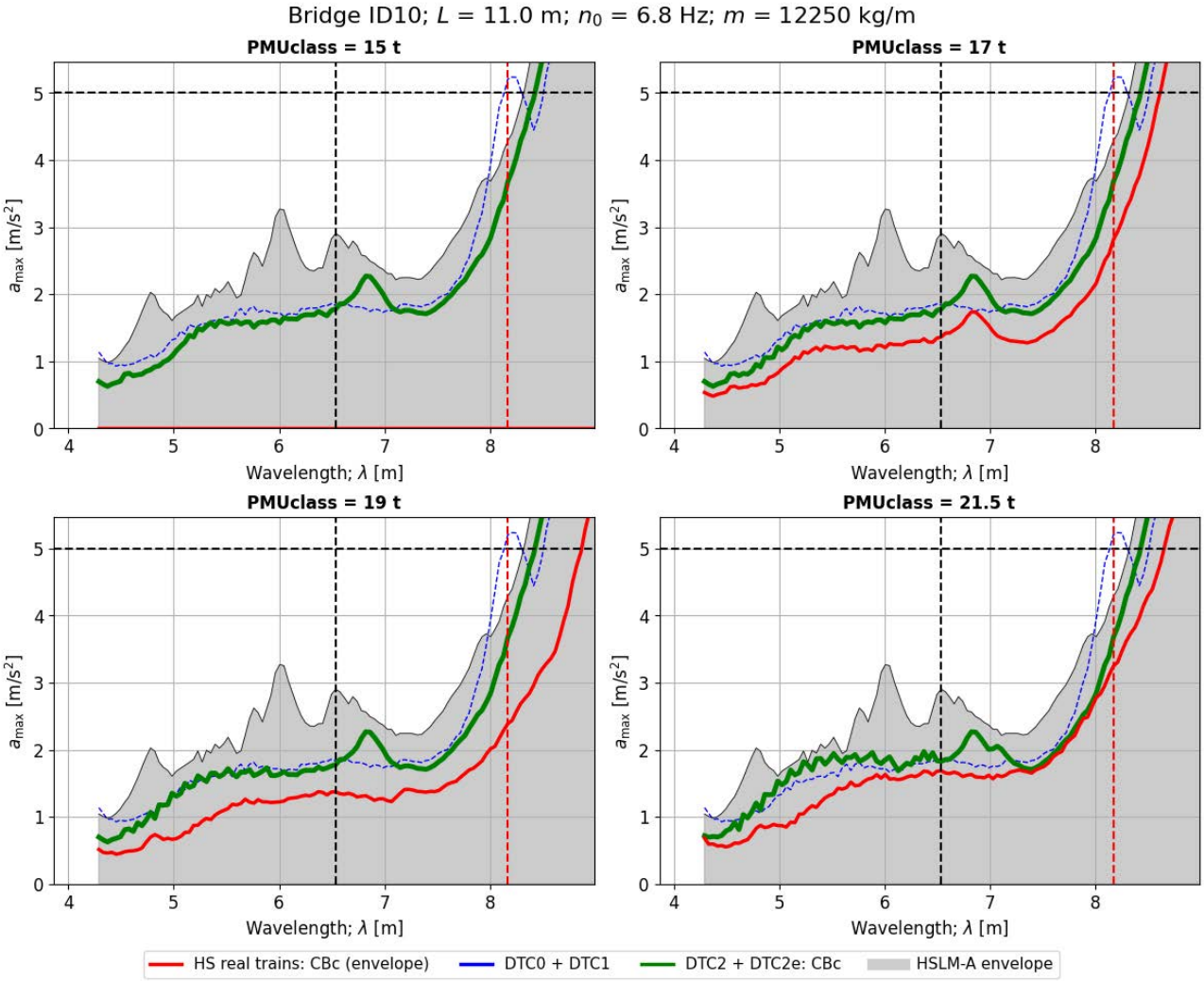

Figure 140. Peak vertical acceleration in the bridge ID10 when subject to real CBc trains of different weight categories, and comparison with the reference CBc train in DTCs. Time-stepping analysis.

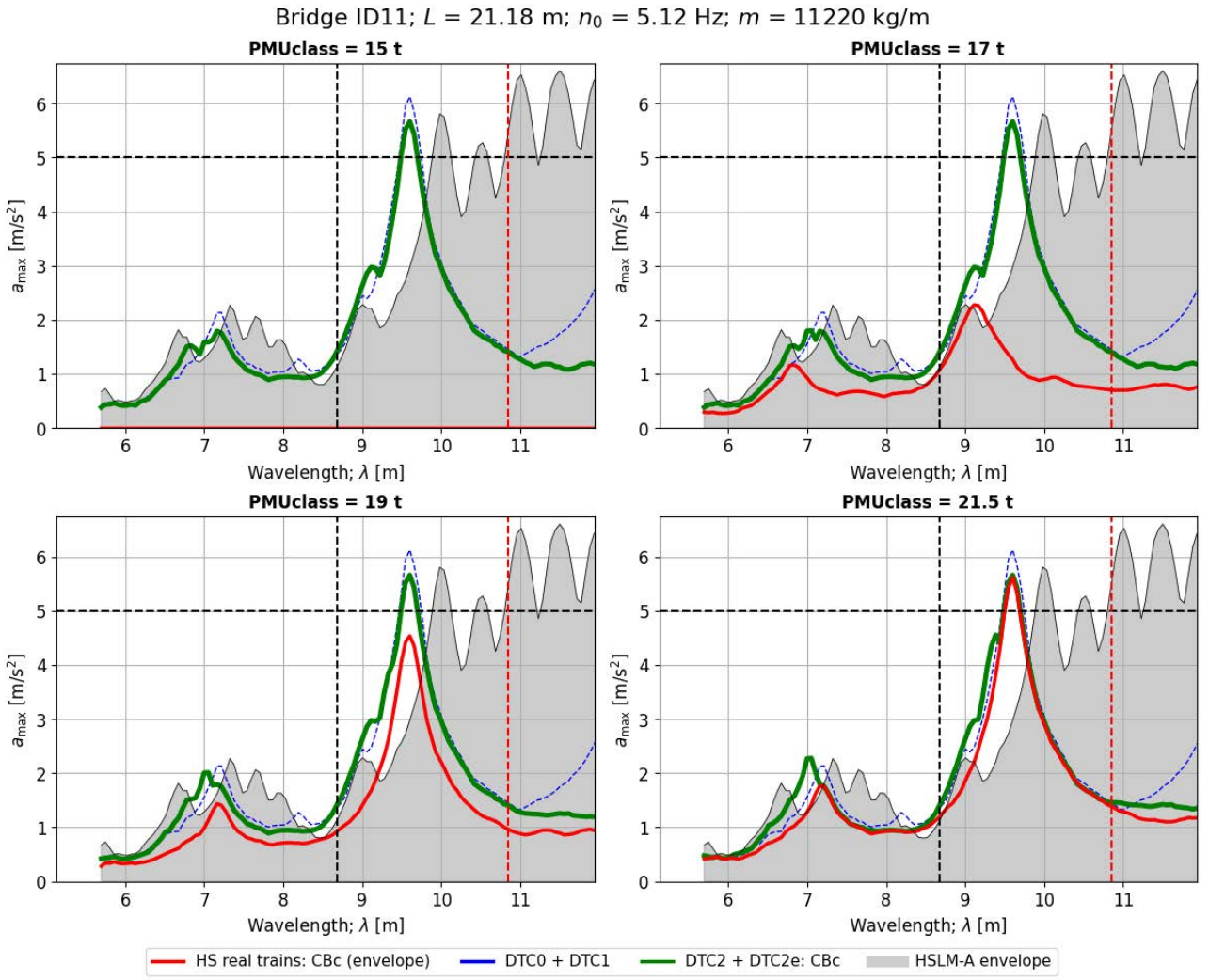

Figure 141. Peak vertical acceleration in the bridge ID11 when subject to real CBc trains of different weight categories, and comparison with the reference CBc train in DTCs. Time-stepping analysis.

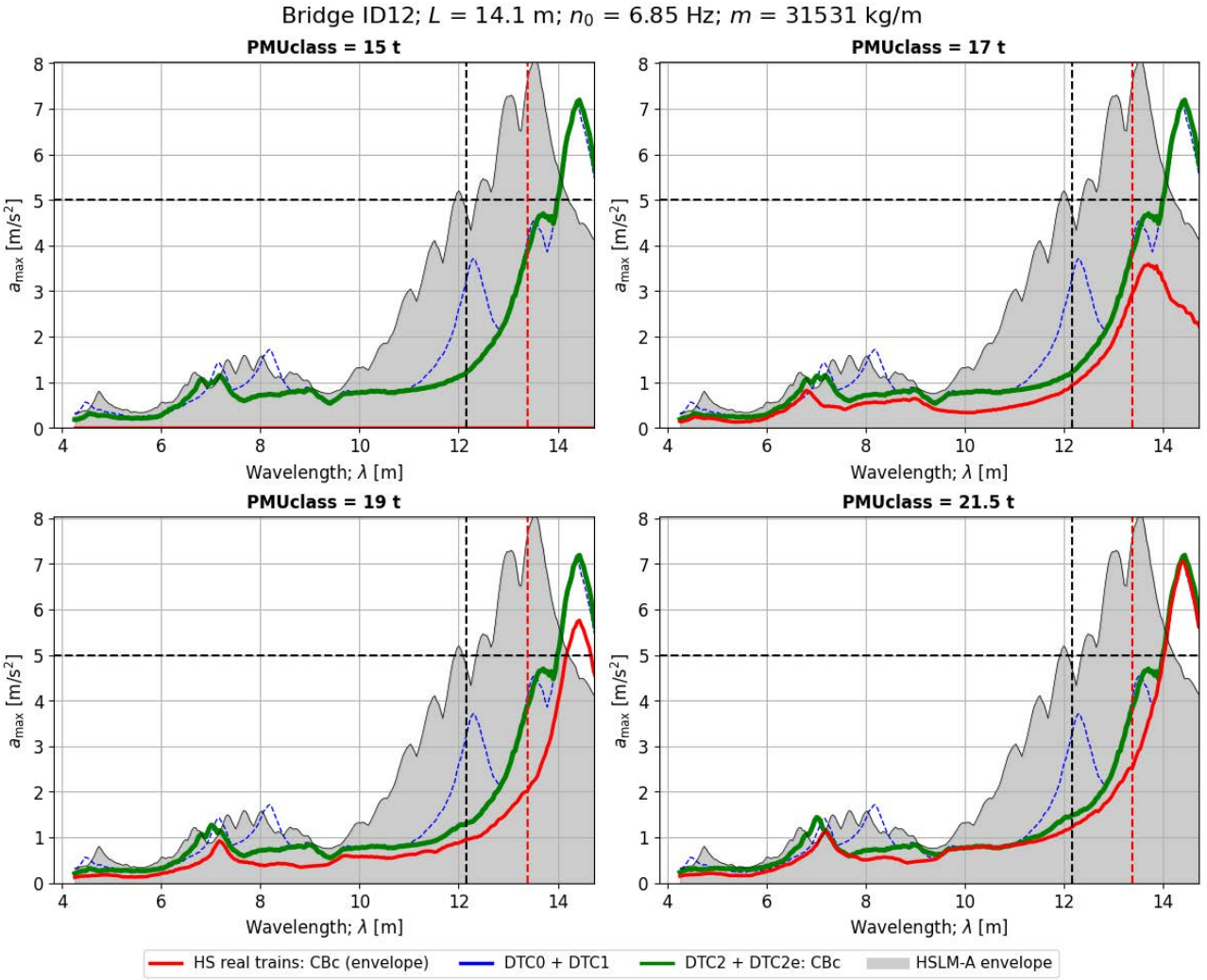

Figure 142. Peak vertical acceleration in the bridge ID12 when subject to real CBc trains of different weight categories, and comparison with the reference CBc train in DTCs. Time-stepping analysis.

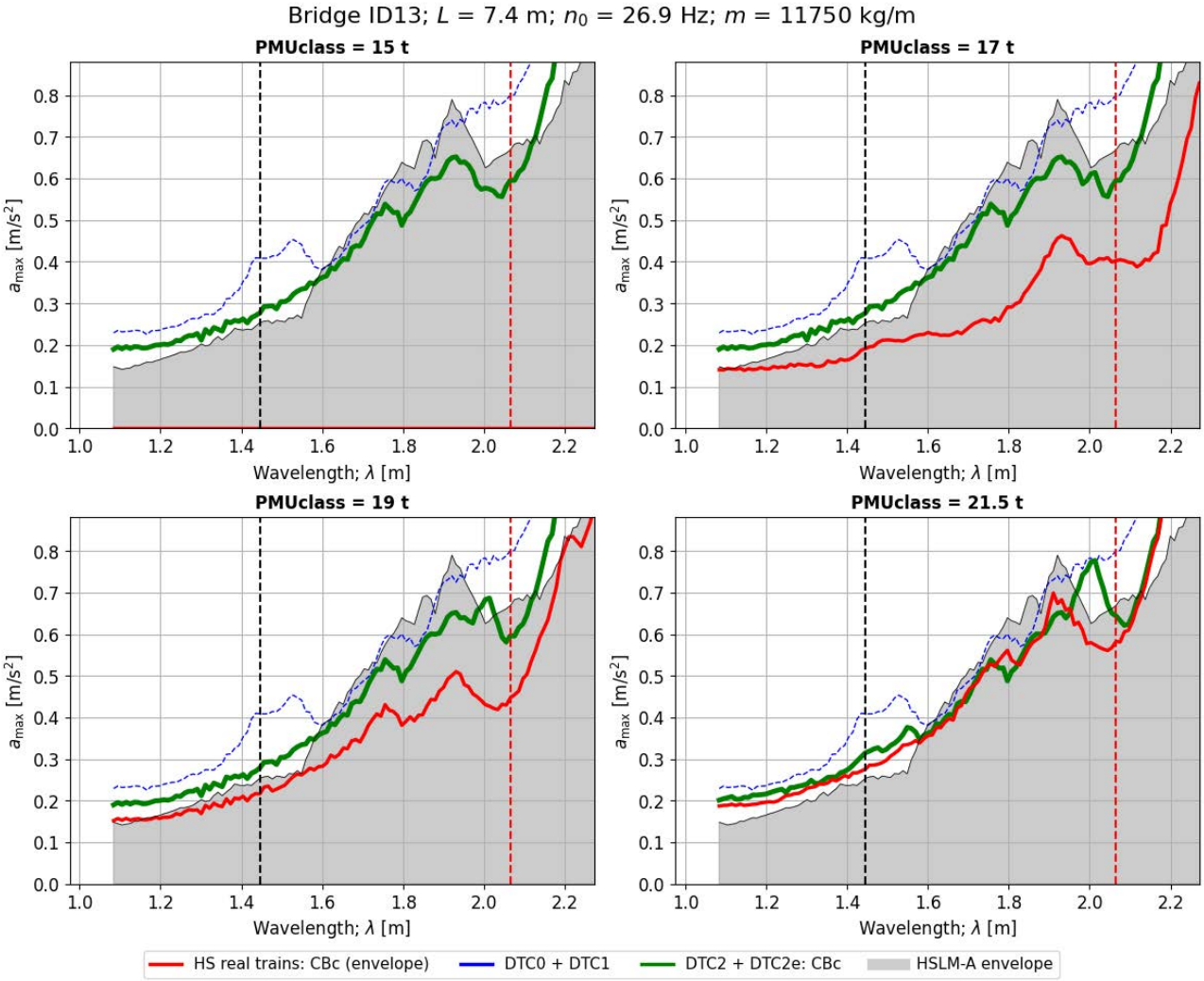

Figure 143. Peak vertical acceleration in the bridge ID13 when subject to real CBc trains of different weight categories, and comparison with the reference CBc train in DTCs. Time-stepping analysis.

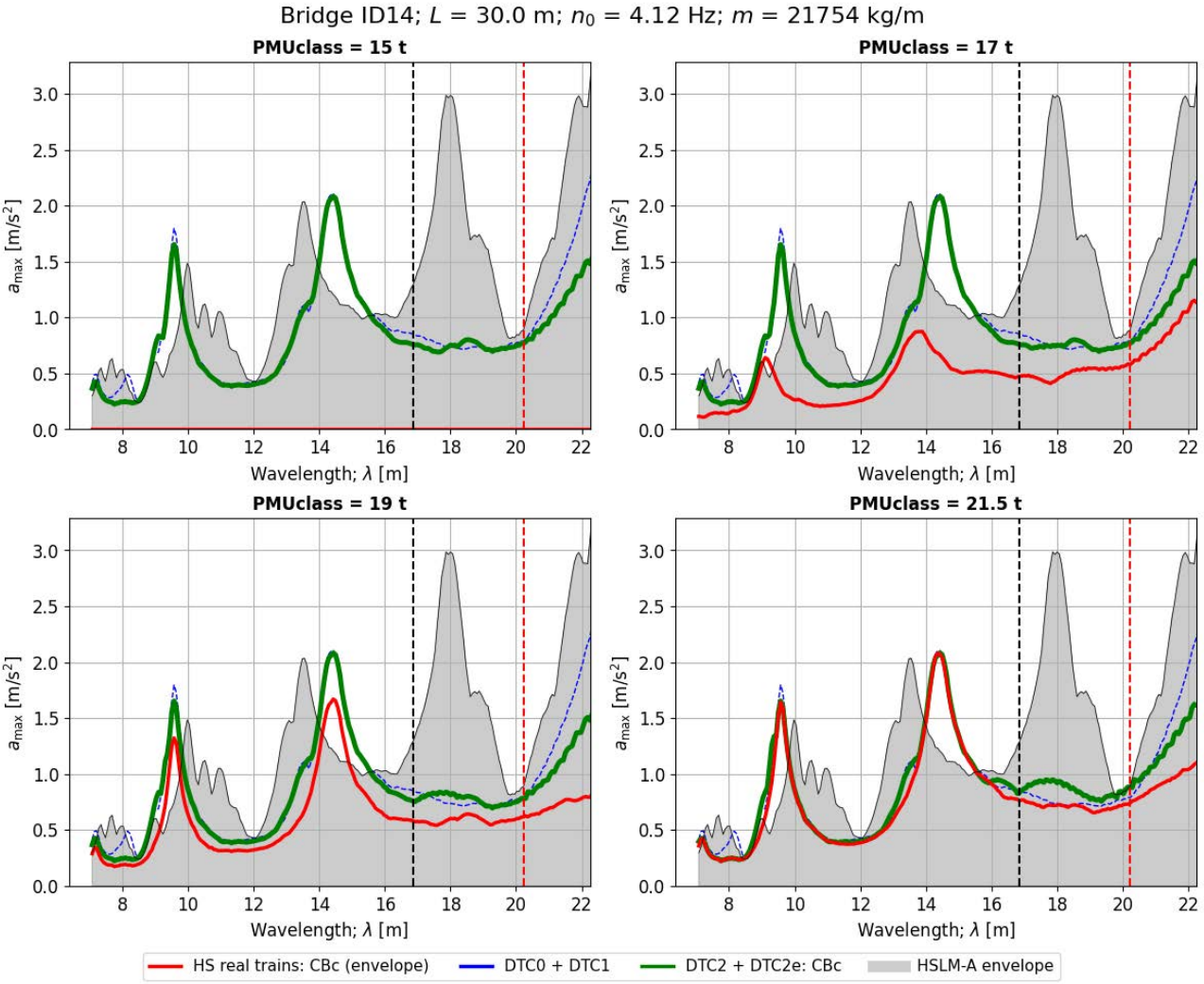

Figure 144. Peak vertical acceleration in the bridge ID14 when subject to real CBc trains of different weight categories, and comparison with the reference CBc train in DTCs. Time-stepping analysis.

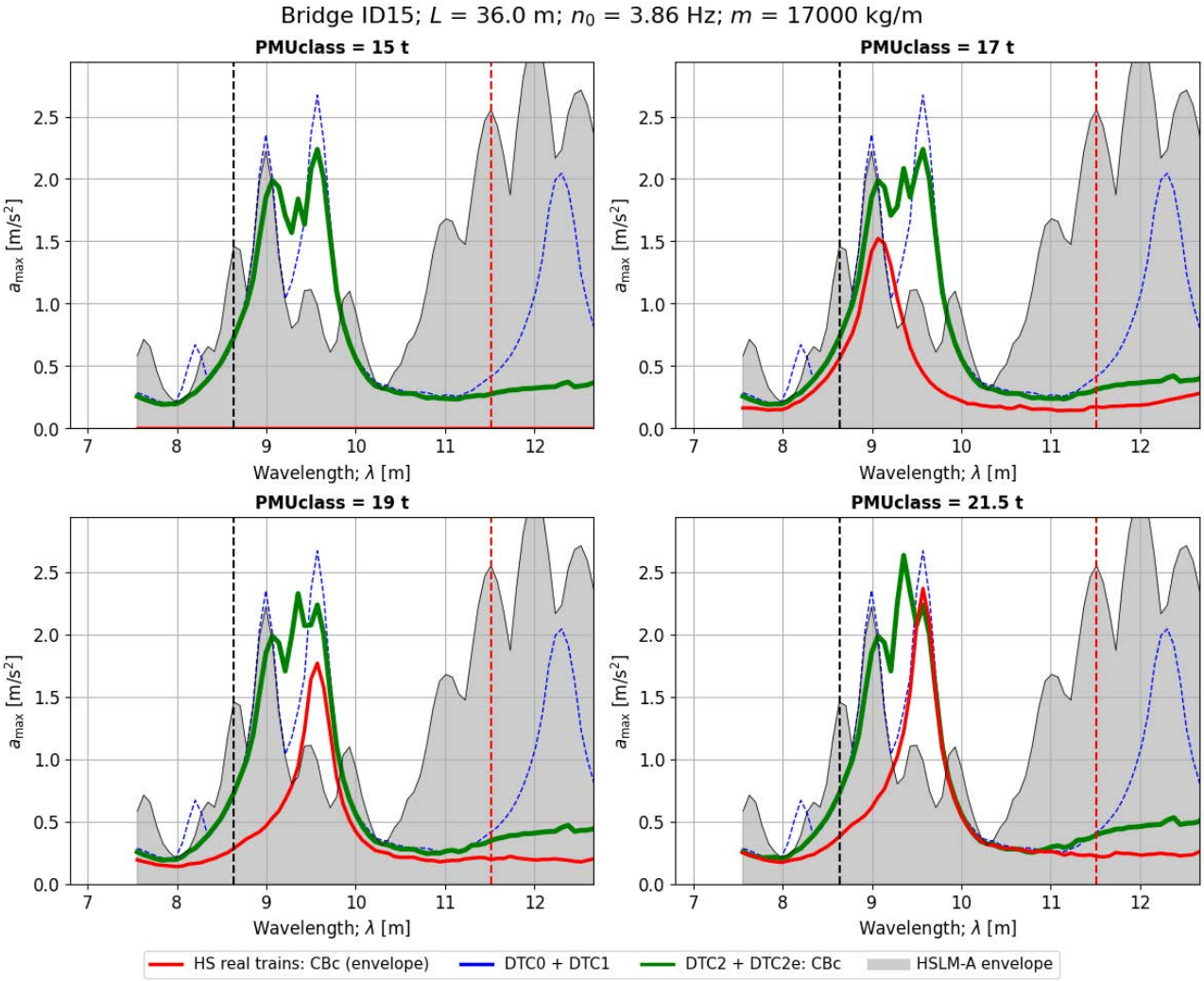

Figure 145. Peak vertical acceleration in the bridge ID15 when subject to real CBc trains of different weight categories, and comparison with the reference CBc train in DTCs. Time-stepping analysis.

Trains with Articulated Bogies: AB

ABa trains

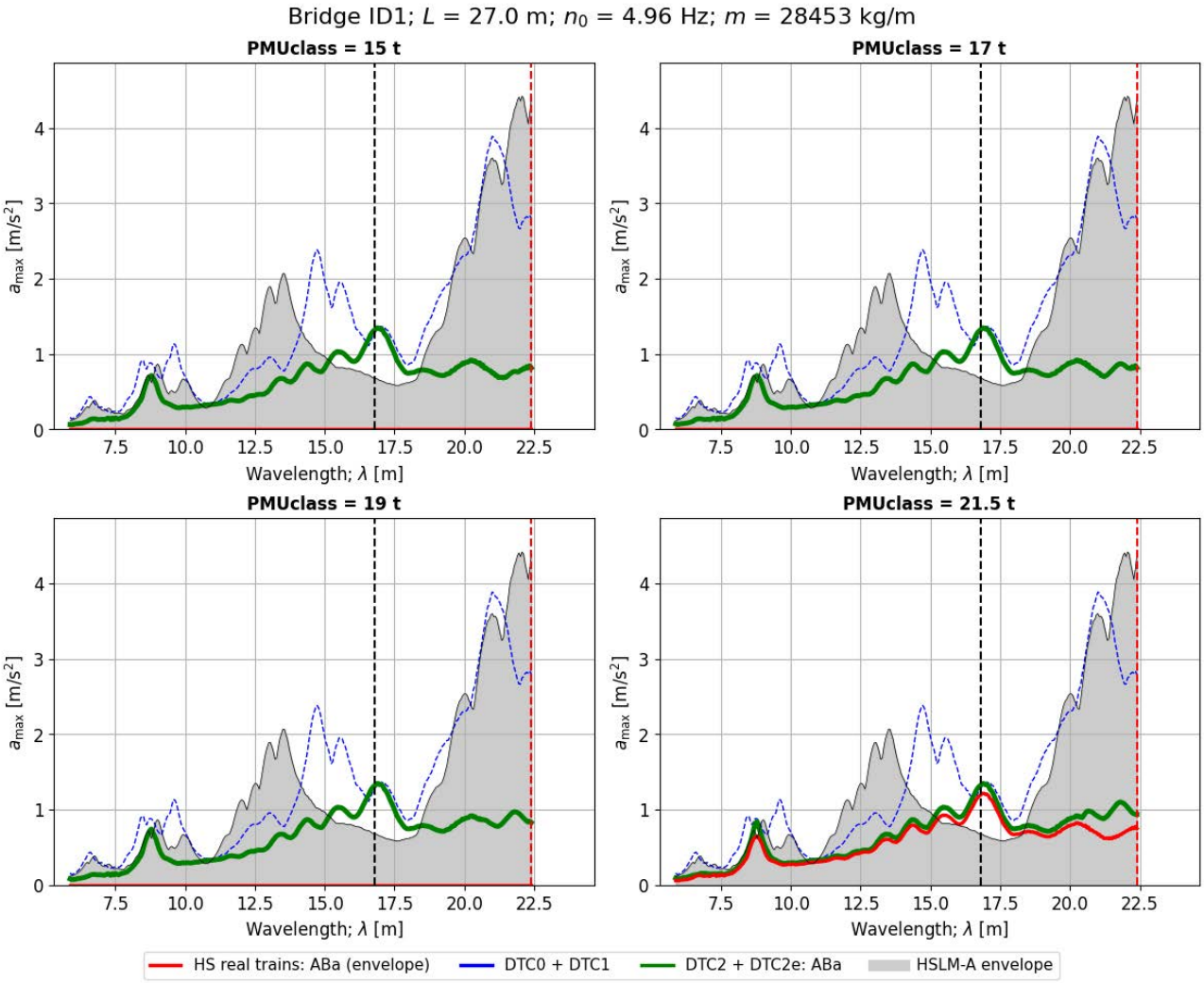

Figure 146. Peak vertical acceleration in the bridge ID1 when subject to real ABa trains of different weight categories, and comparison with the reference ABa train in DTCs. Time-stepping analysis.

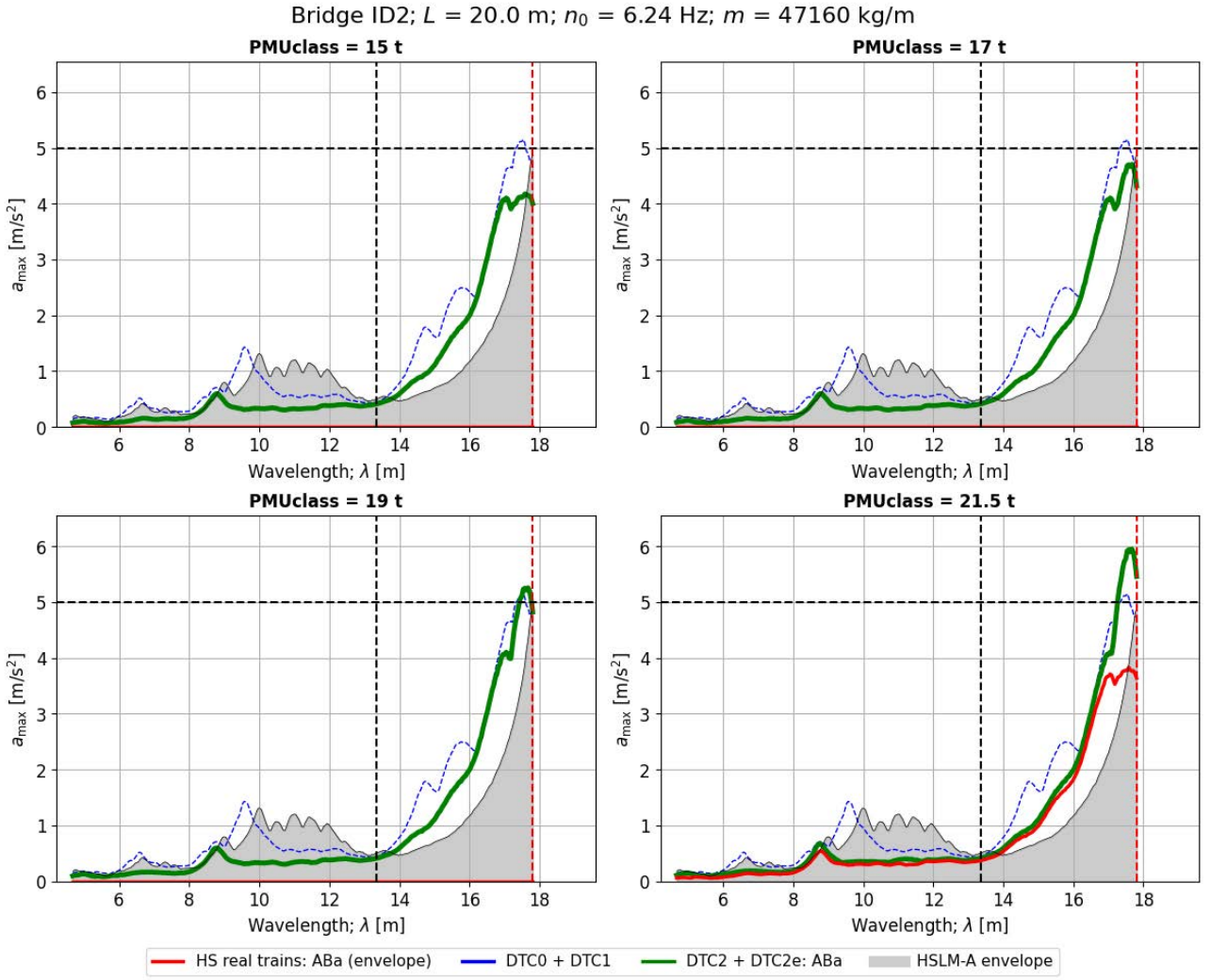

Figure 147. Peak vertical acceleration in the bridge ID2 when subject to real ABa trains of different weight categories, and comparison with the reference ABa train in DTCs. Time-stepping analysis.

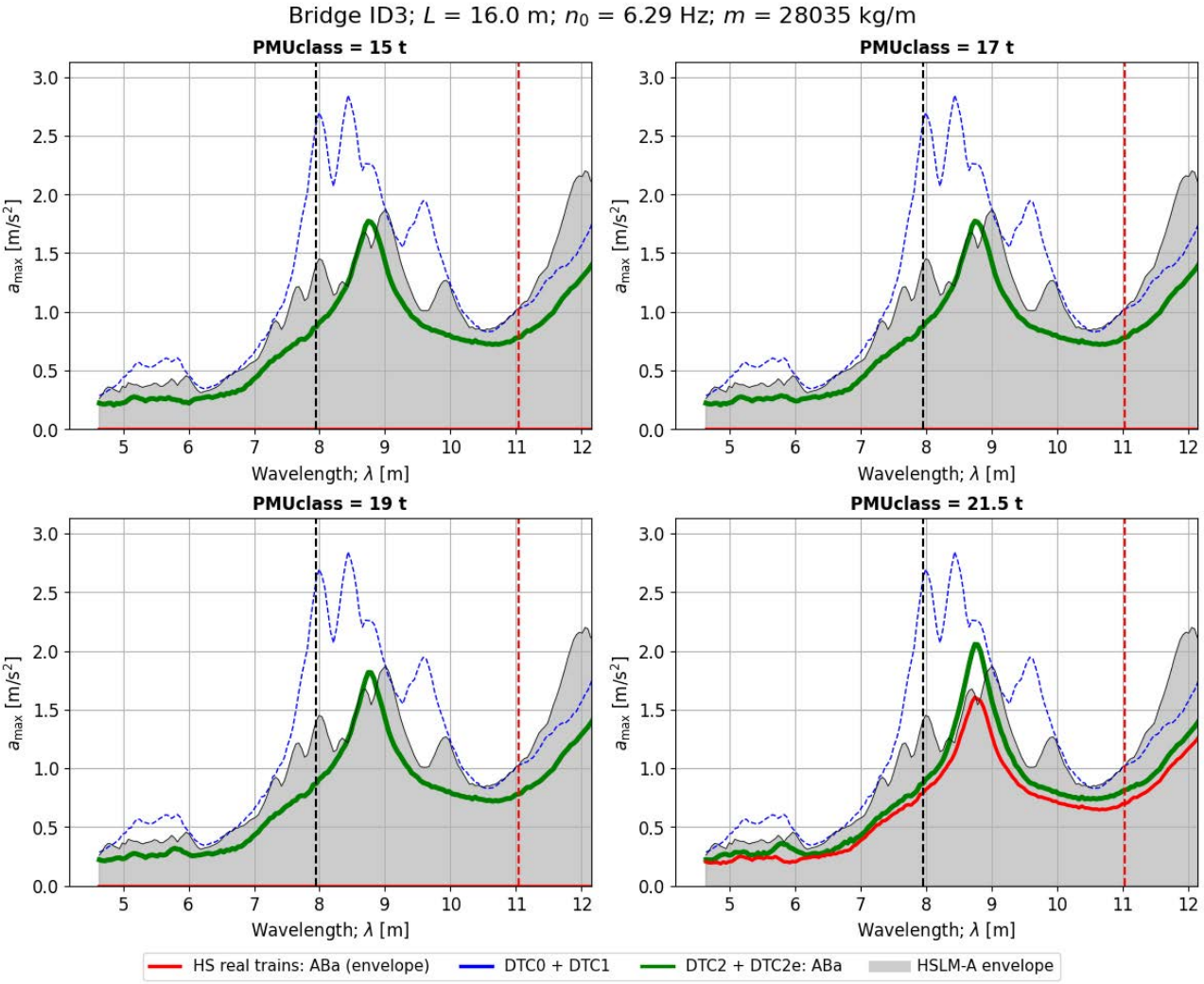

Figure 148. Peak vertical acceleration in the bridge ID3 when subject to real ABa trains of different weight categories, and comparison with the reference ABa train in DTCs. Time-stepping analysis.

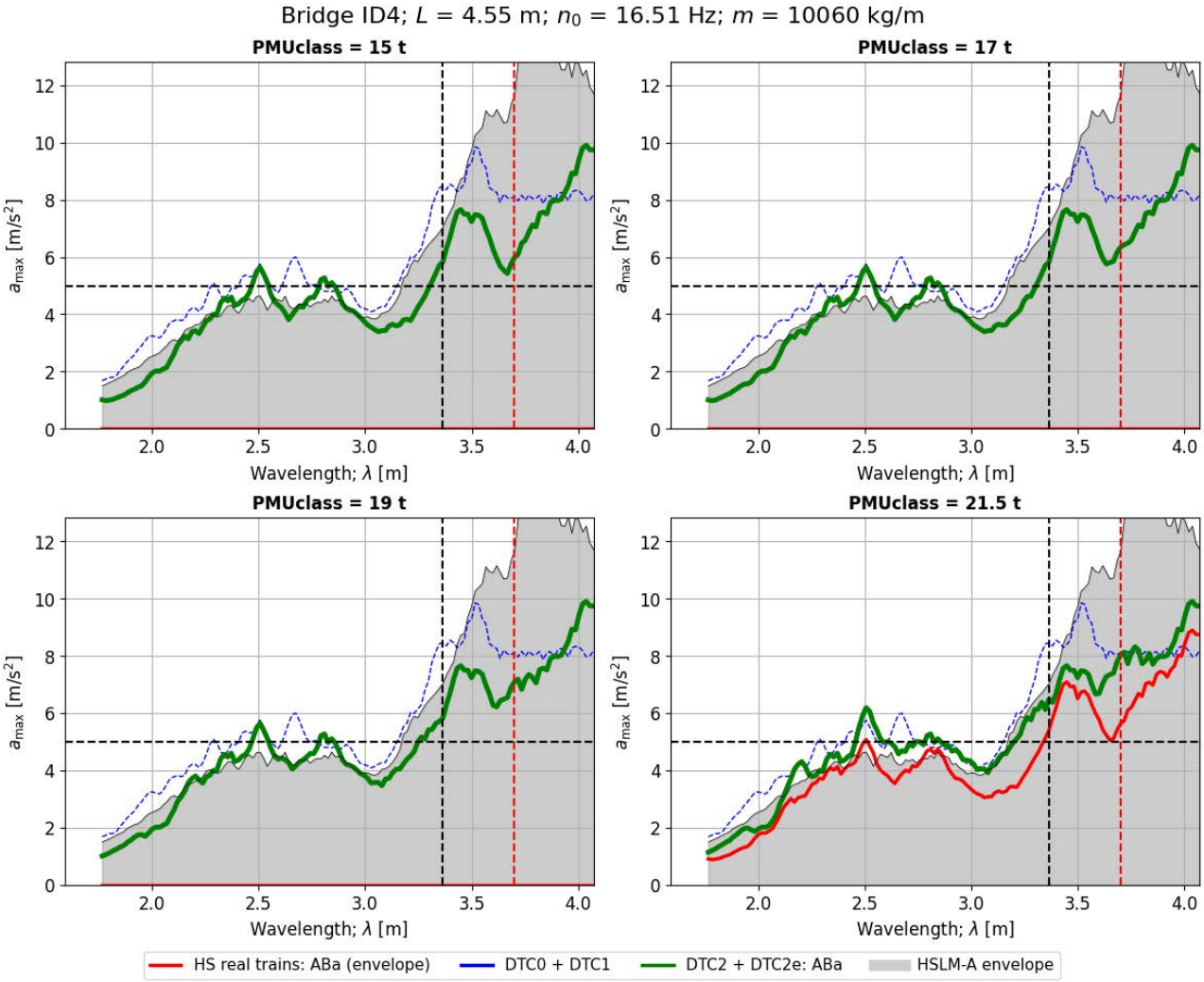

Figure 149. Peak vertical acceleration in the bridge ID4 when subject to real ABa trains of different weight categories, and comparison with the reference ABa train in DTCs. Time-stepping analysis.

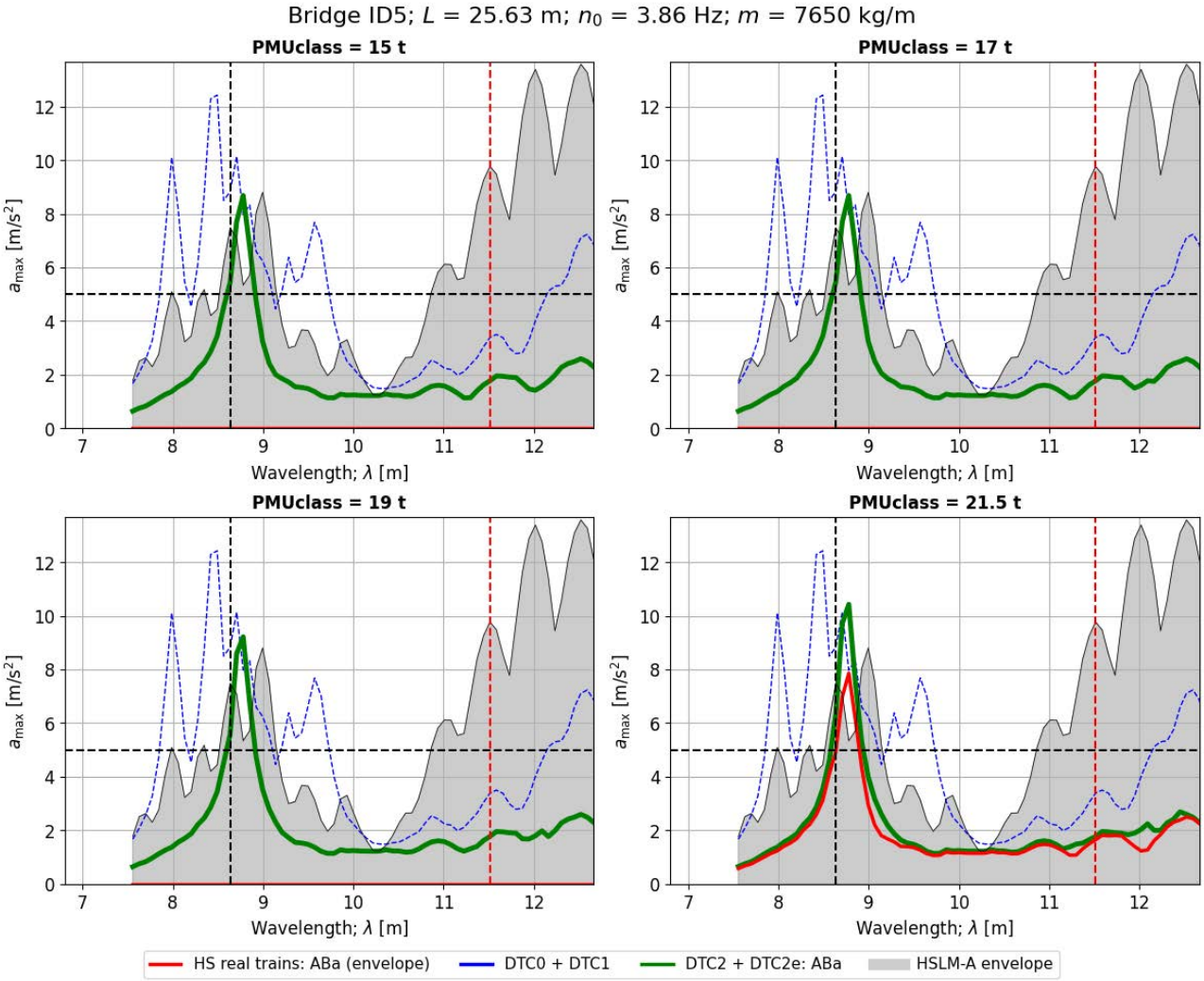

Figure 150. Peak vertical acceleration in the bridge ID5 when subject to real ABa trains of different weight categories, and comparison with the reference ABa train in DTCs. Time-stepping analysis.

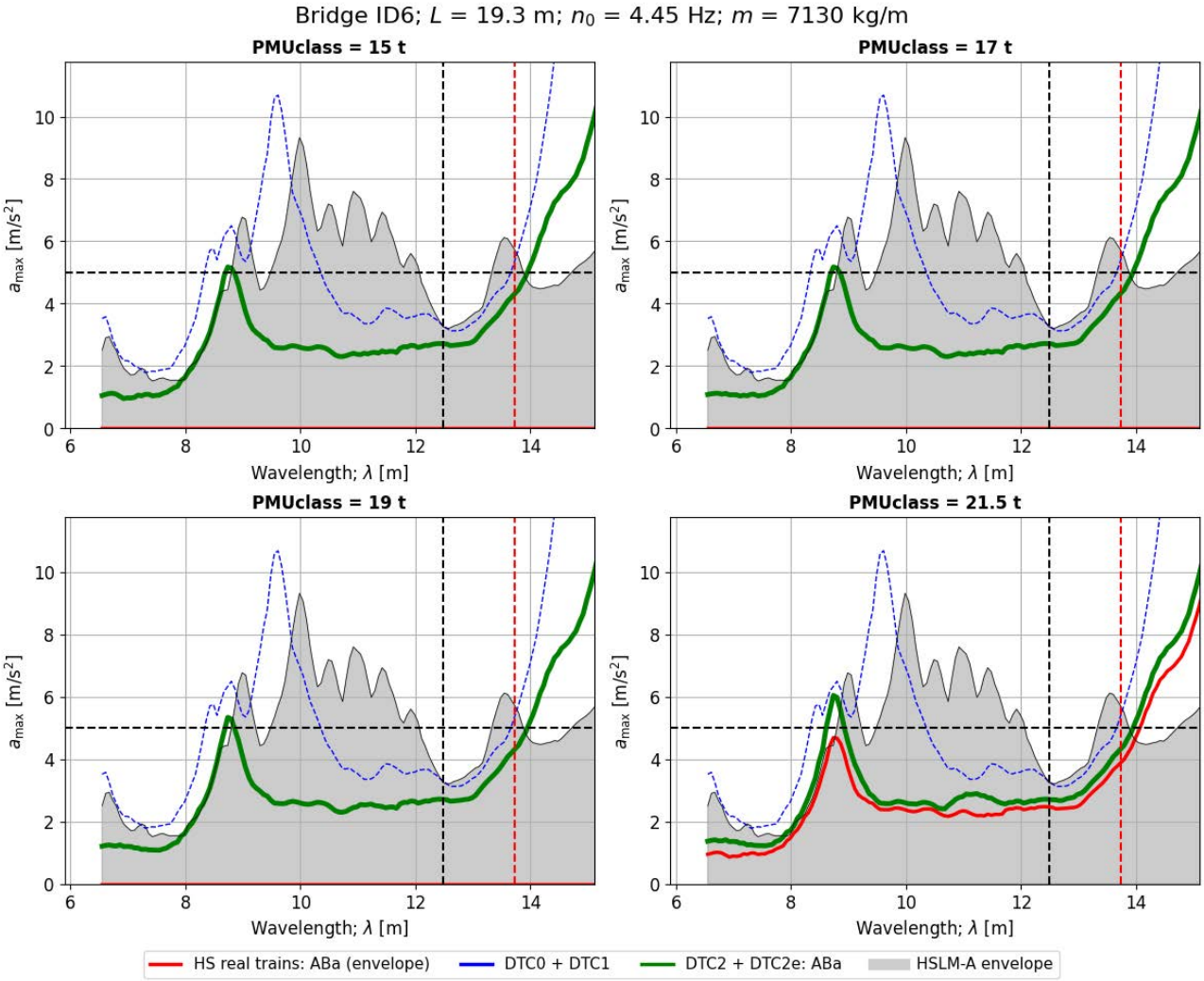

Figure 151. Peak vertical acceleration in the bridge ID6 when subject to real ABa trains of different weight categories, and comparison with the reference ABa train in DTCs. Time-stepping analysis.

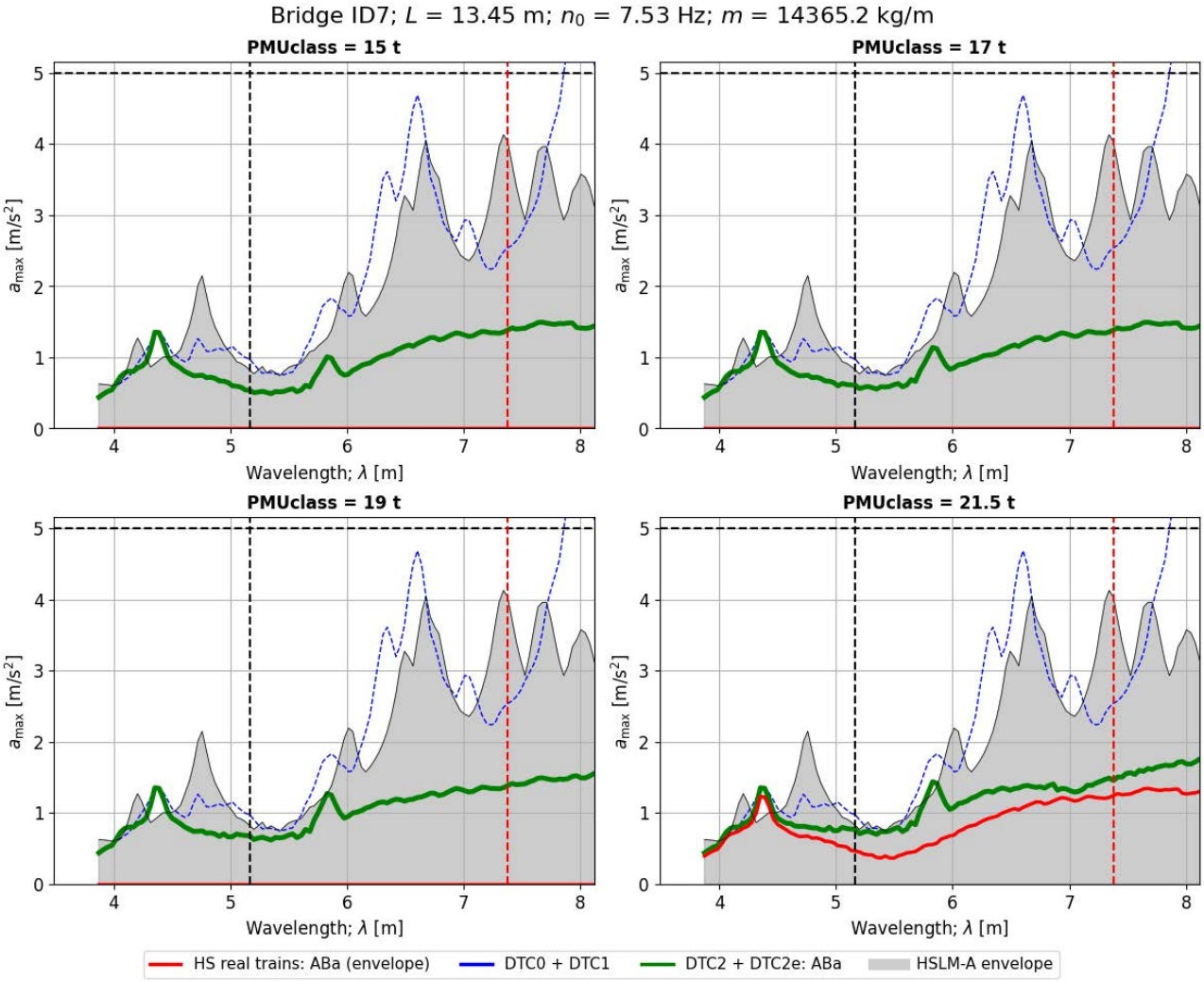

Figure 152. Peak vertical acceleration in the bridge ID7 when subject to real ABa trains of different weight categories, and comparison with the reference ABa train in DTCs. Time-stepping analysis.

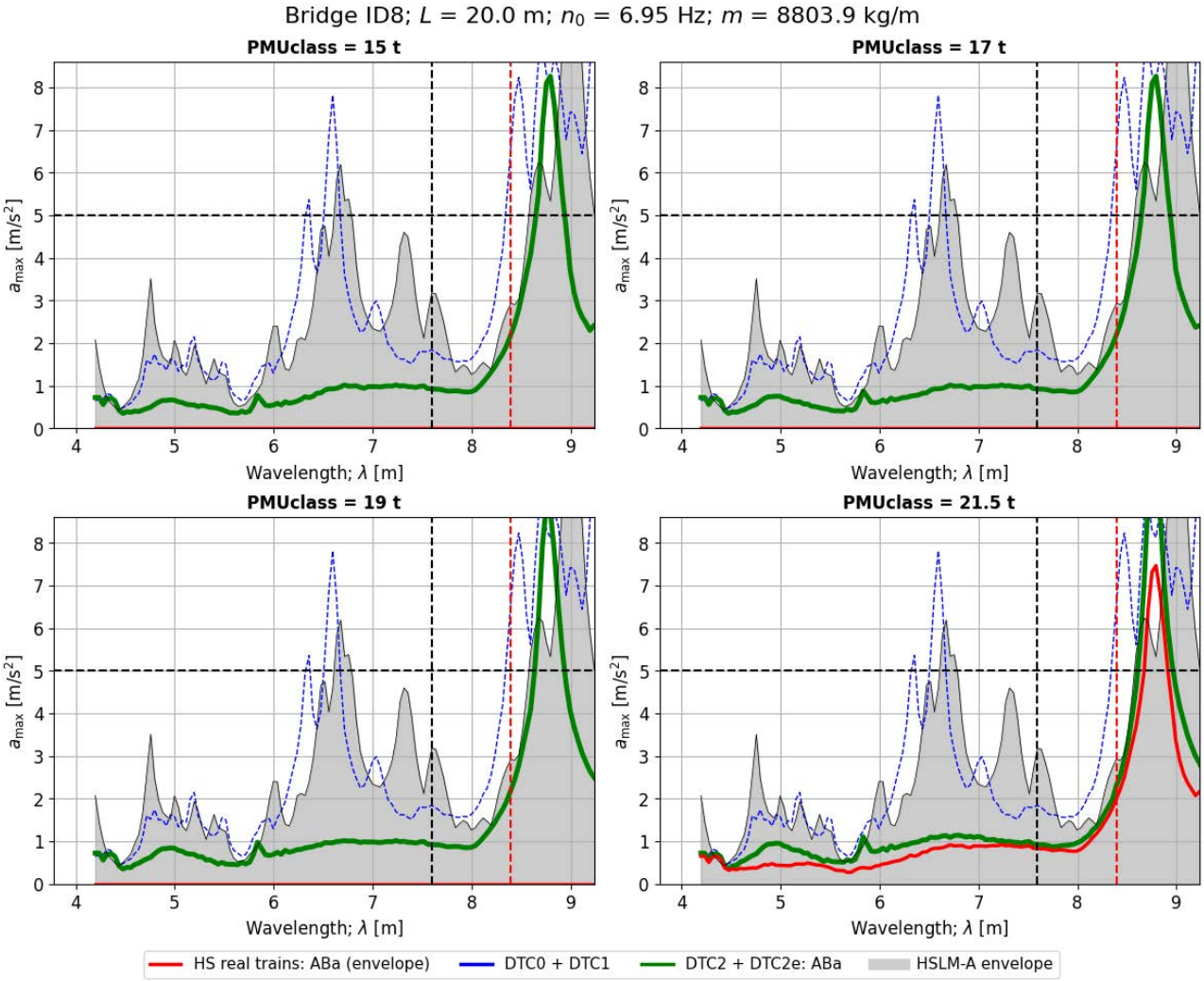

Figure 153. Peak vertical acceleration in the bridge ID8 when subject to real ABa trains of different weight categories, and comparison with the reference ABa train in DTCs. Time-stepping analysis.

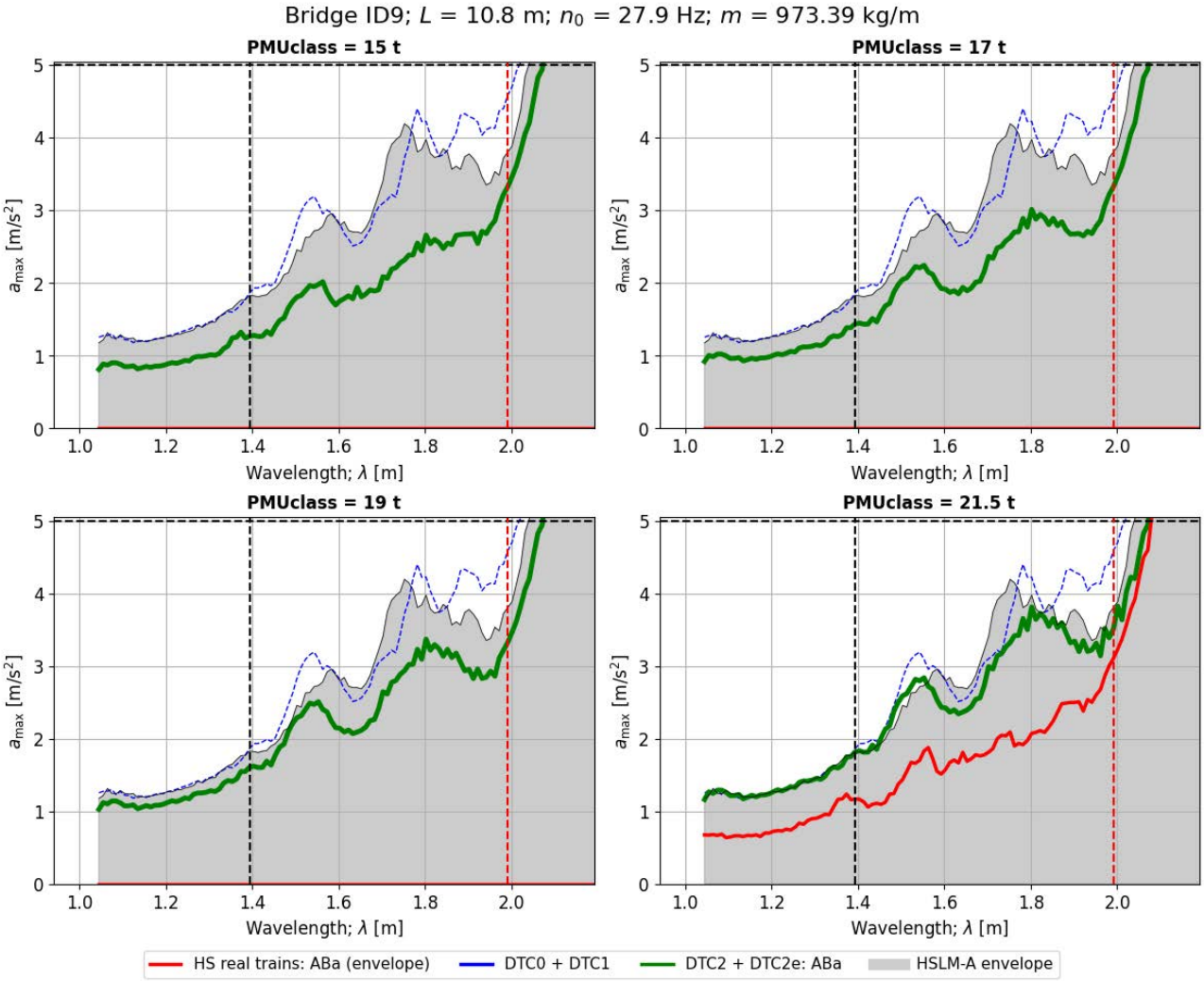

Figure 154. Peak vertical acceleration in the bridge ID9 when subject to real ABa trains of different weight categories, and comparison with the reference ABa train in DTCs. Time-stepping analysis.

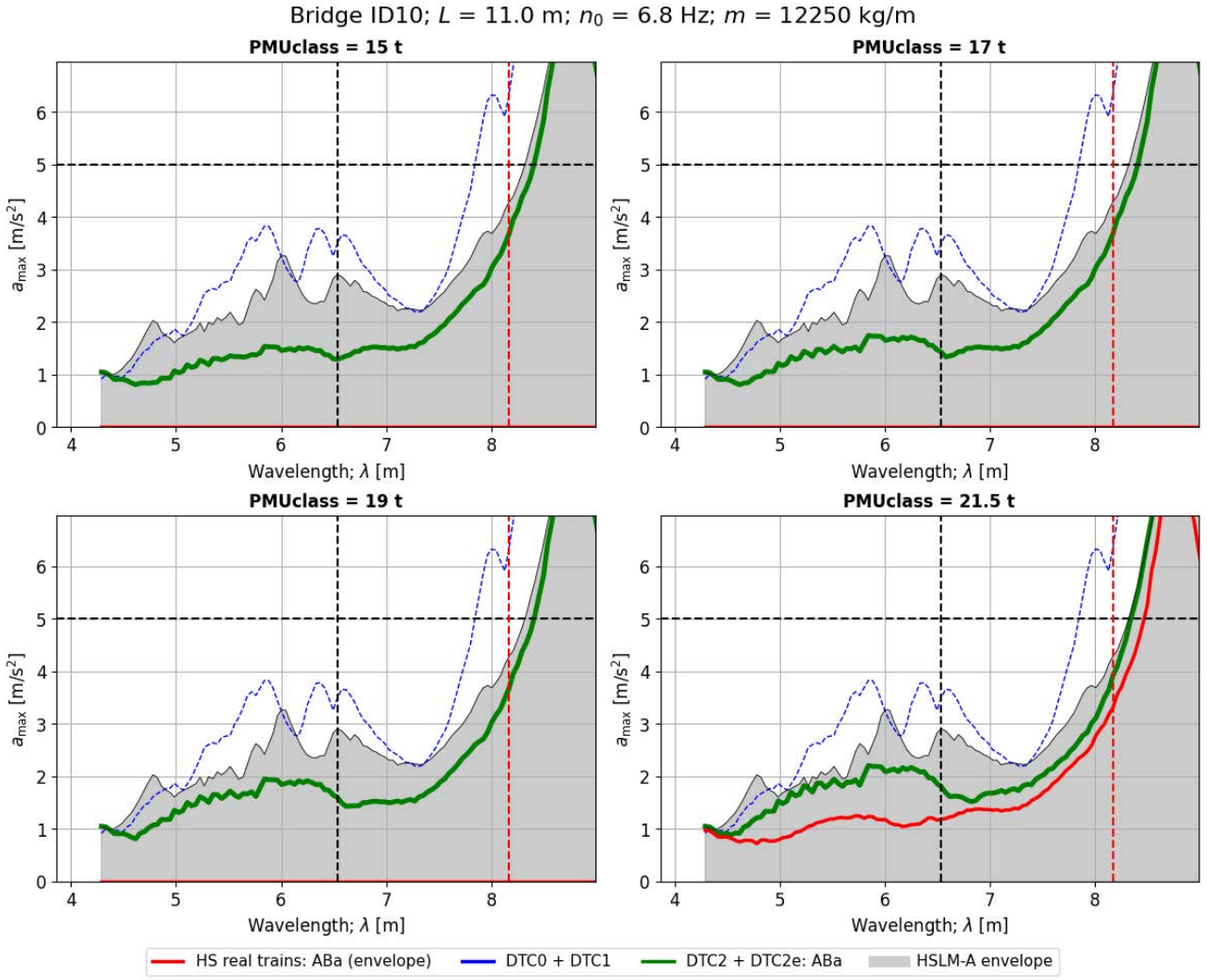

Figure 155. Peak vertical acceleration in the bridge ID10 when subject to real ABa trains of different weight categories, and comparison with the reference ABa train in DTCs. Time-stepping analysis.

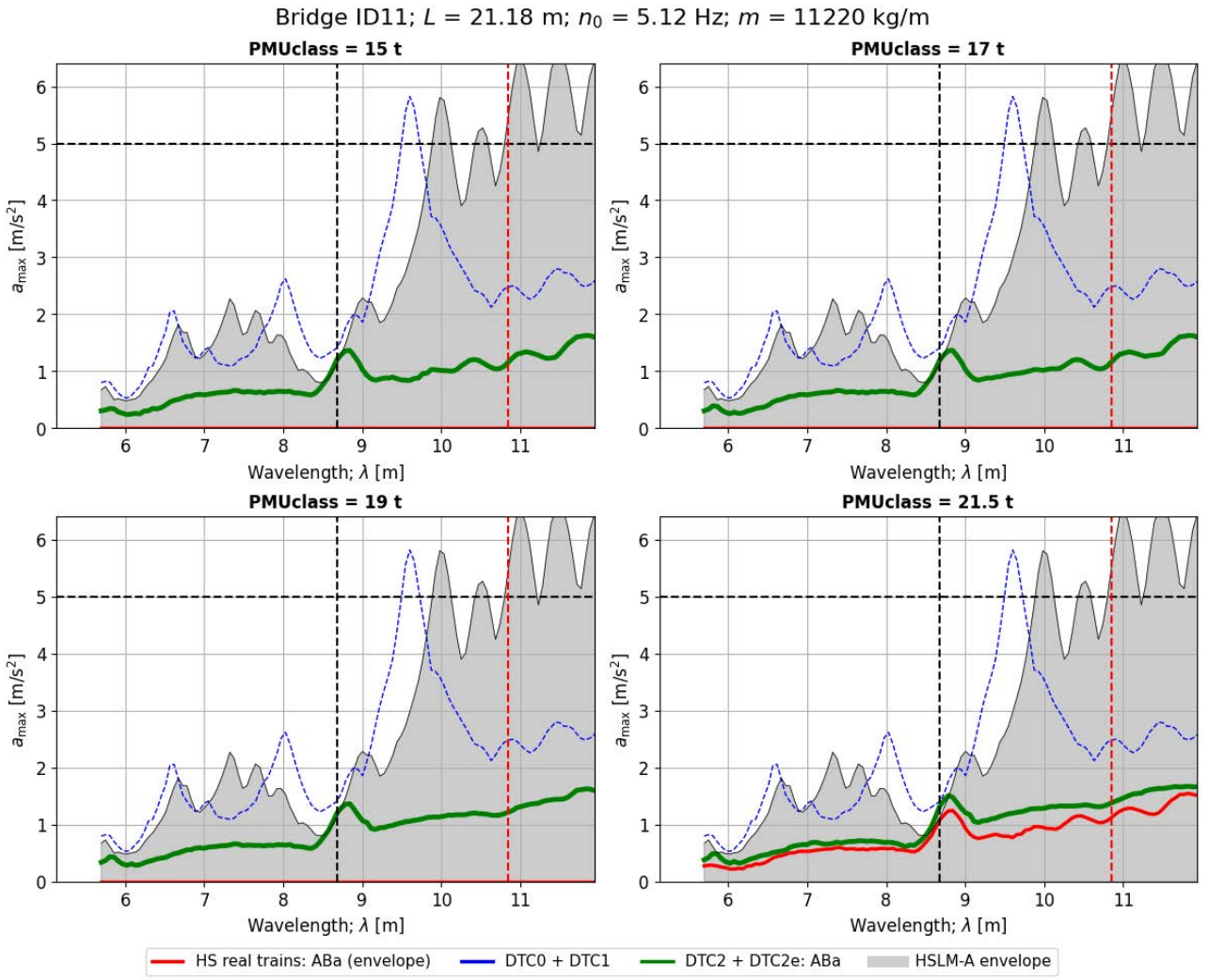

Figure 156. Peak vertical acceleration in the bridge ID11 when subject to real ABa trains of different weight categories, and comparison with the reference ABa train in DTCs. Time-stepping analysis.

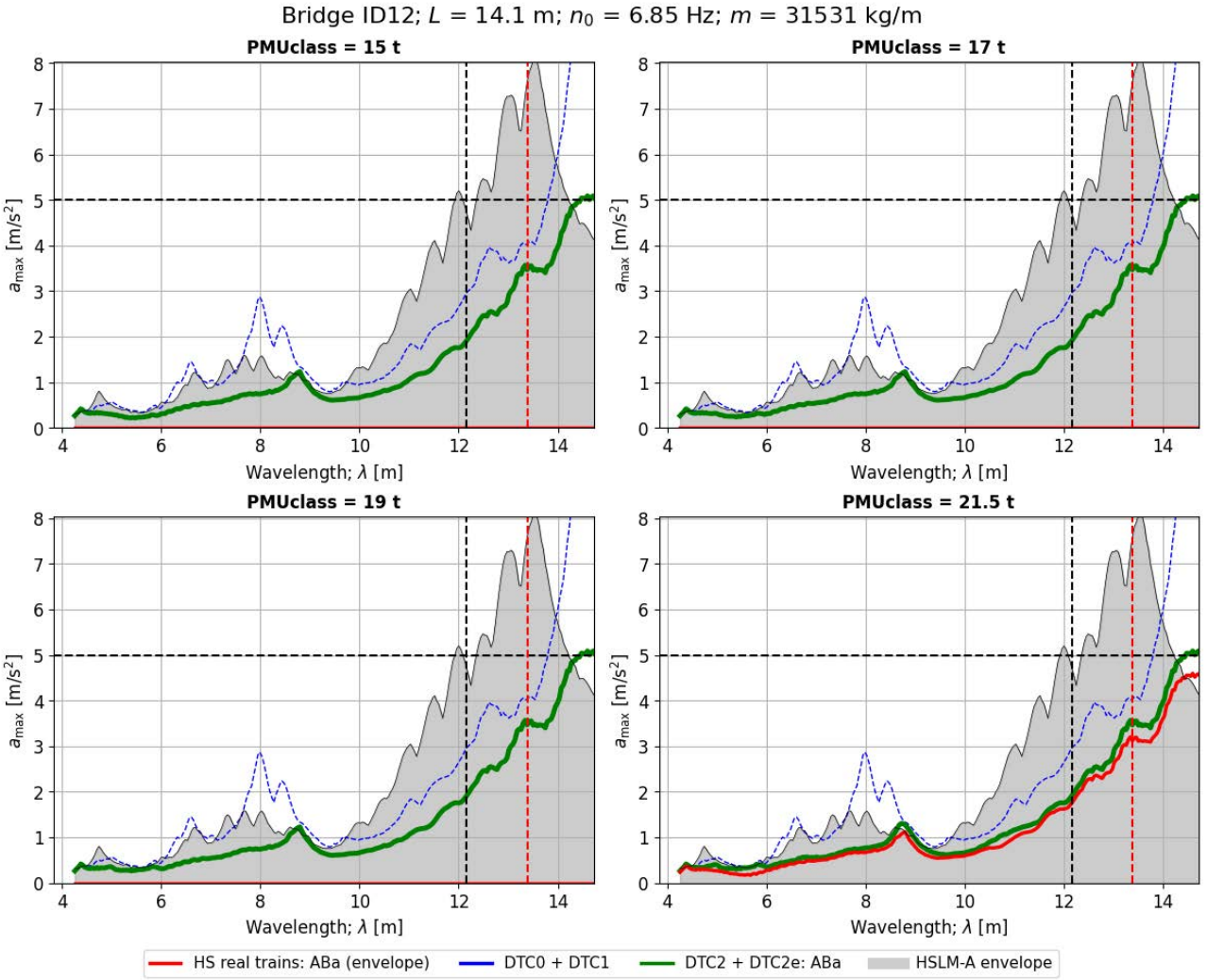

Figure 157. Peak vertical acceleration in the bridge ID12 when subject to real ABa trains of different weight categories, and comparison with the reference ABa train in DTCs. Time-stepping analysis.

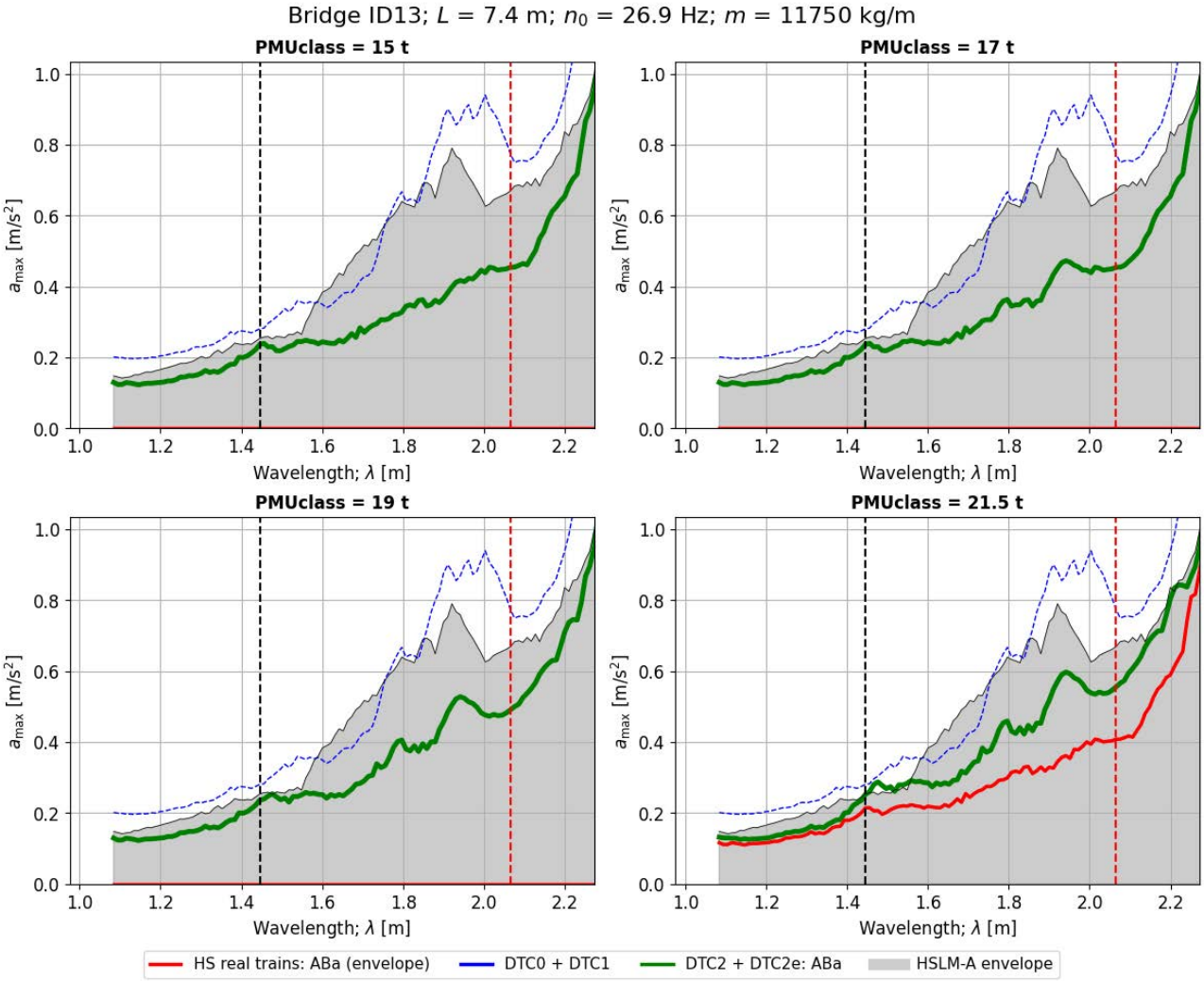

Figure 158. Peak vertical acceleration in the bridge ID13 when subject to real ABa trains of different weight categories, and comparison with the reference ABa train in DTCs. Time-stepping analysis.

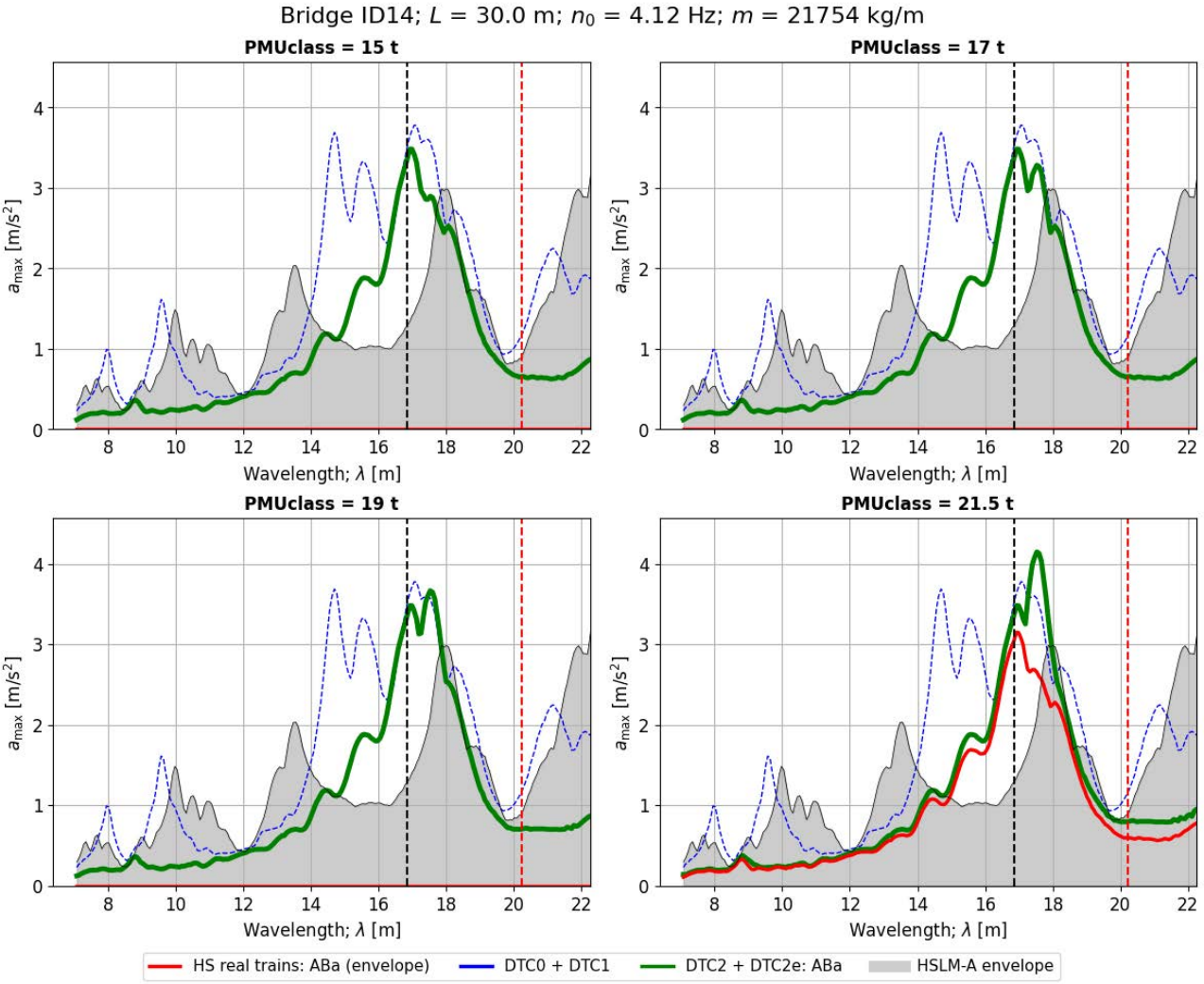

Figure 159. Peak vertical acceleration in the bridge ID14 when subject to real ABa trains of different weight categories, and comparison with the reference ABa train in DTCs. Time-stepping analysis.

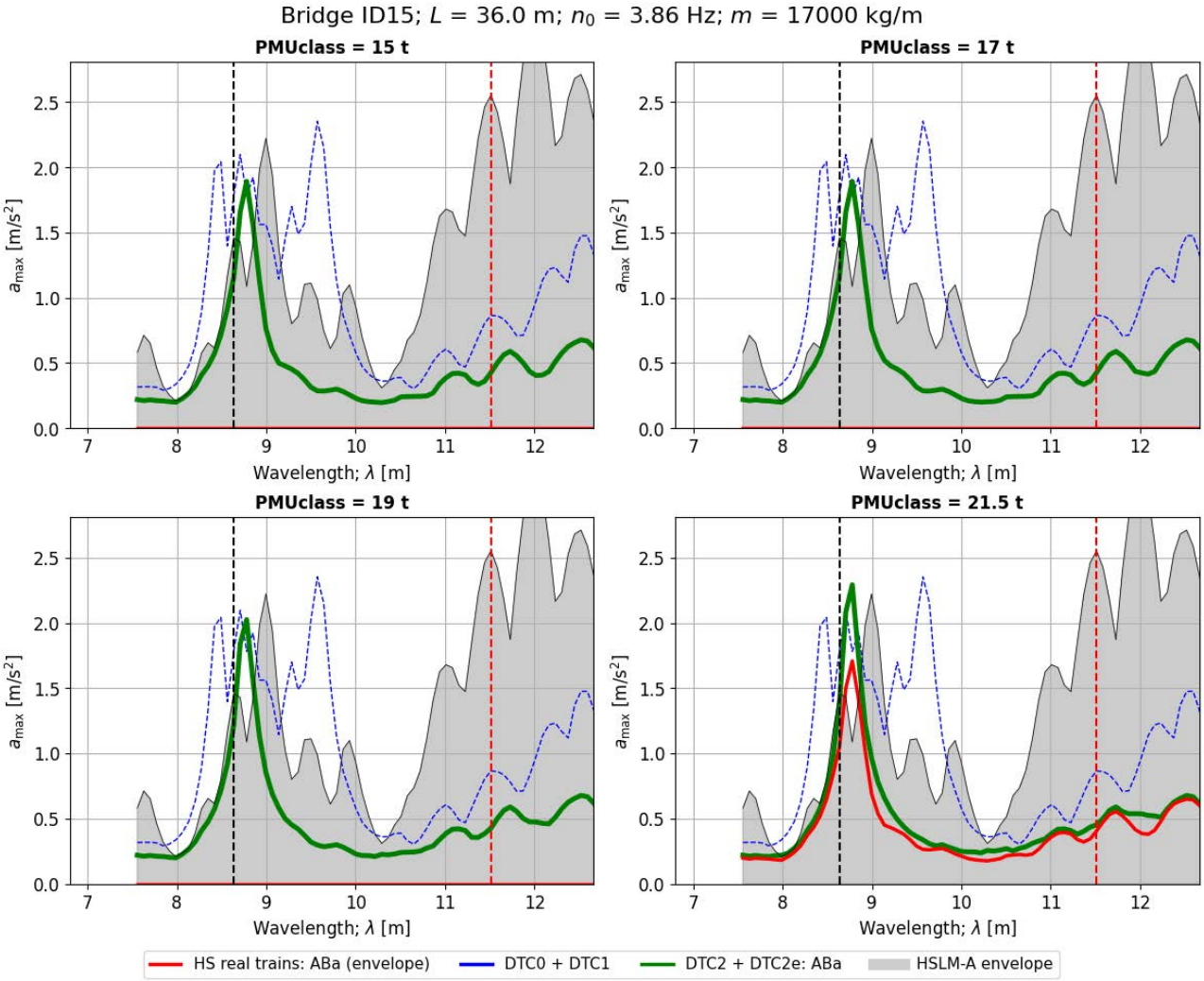

Figure 160. Peak vertical acceleration in the bridge ID15 when subject to real ABa trains of different weight categories, and comparison with the reference ABa train in DTCs. Time-stepping analysis.

ABb trains

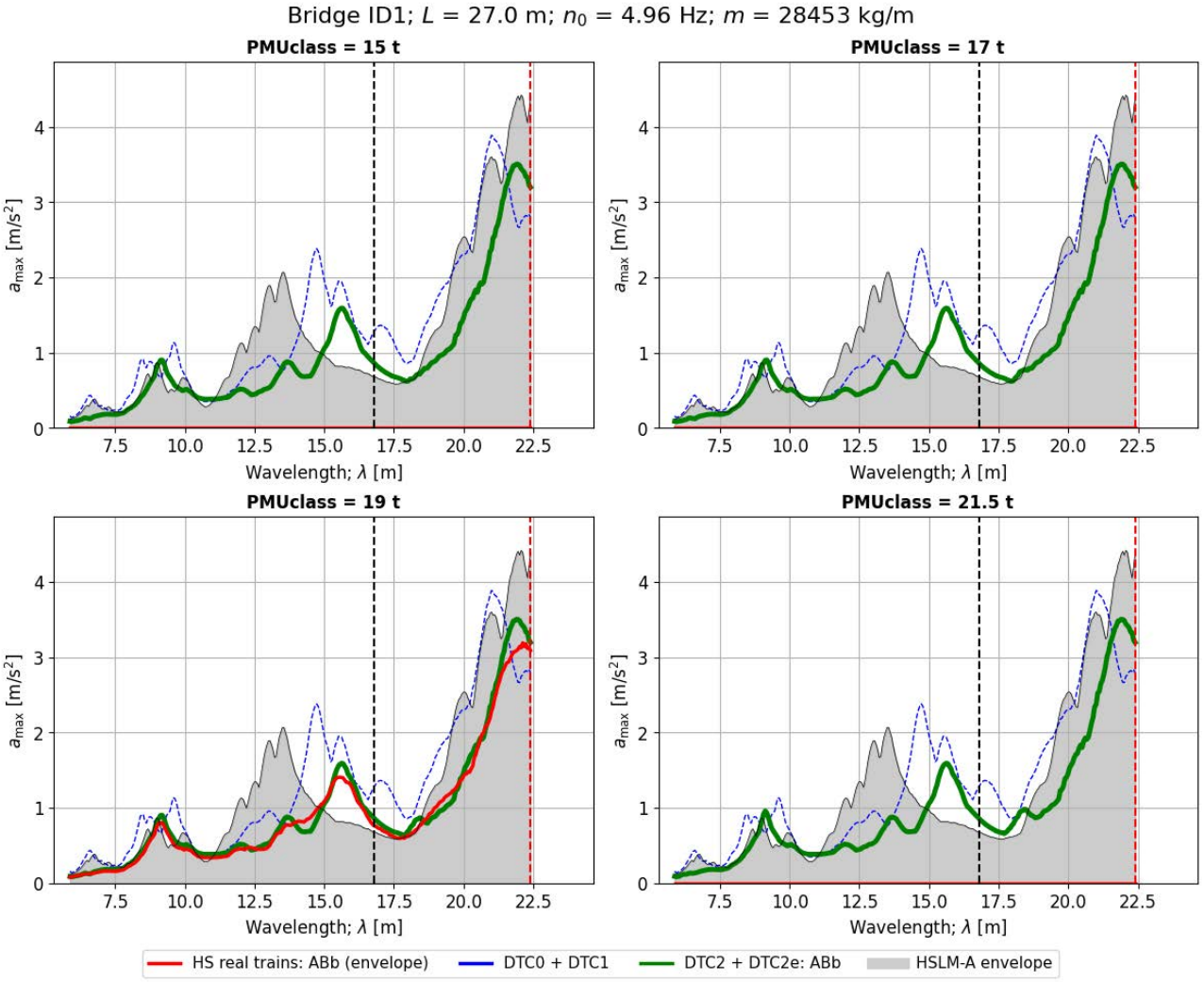

Figure 161. Peak vertical acceleration in the bridge ID1 when subject to real ABb trains of different weight categories, and comparison with the reference ABb train in DTCs. Time-stepping analysis.

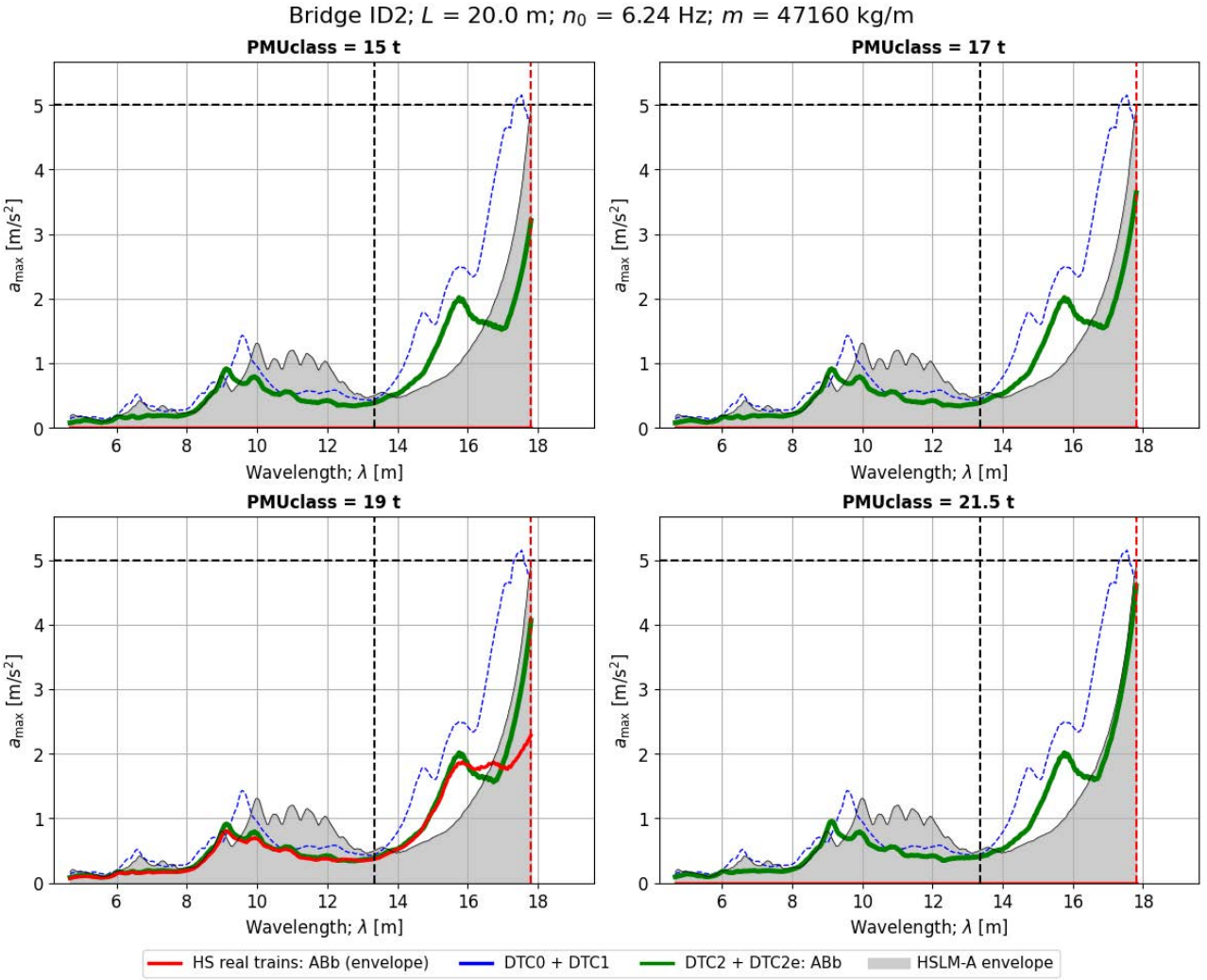

Figure 162. Peak vertical acceleration in the bridge ID2 when subject to real ABb trains of different weight categories, and comparison with the reference ABb train in DTCs. Time-stepping analysis.

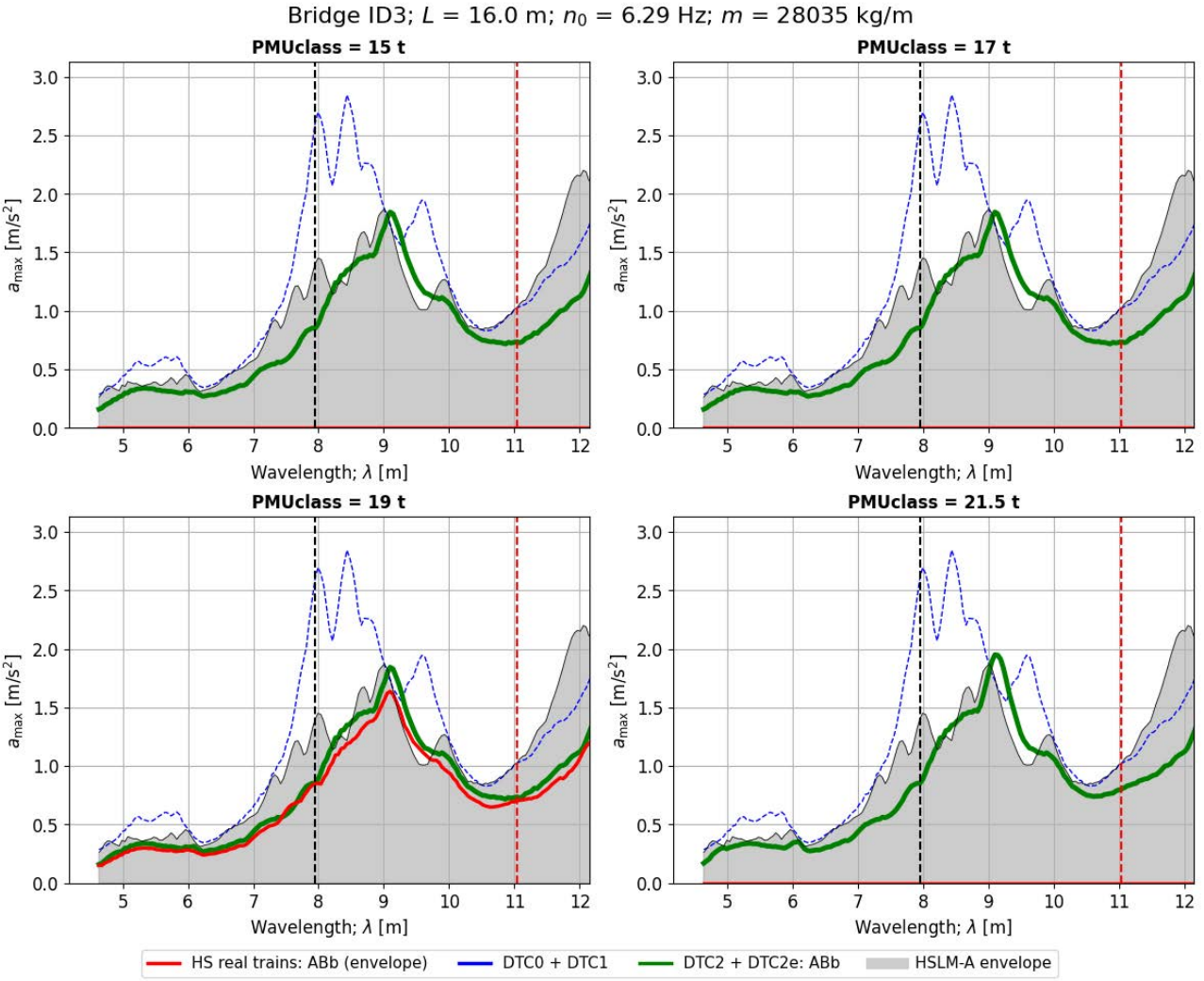

Figure 163. Peak vertical acceleration in the bridge ID3 when subject to real ABb trains of different weight categories, and comparison with the reference ABb train in DTCs. Time-stepping analysis.

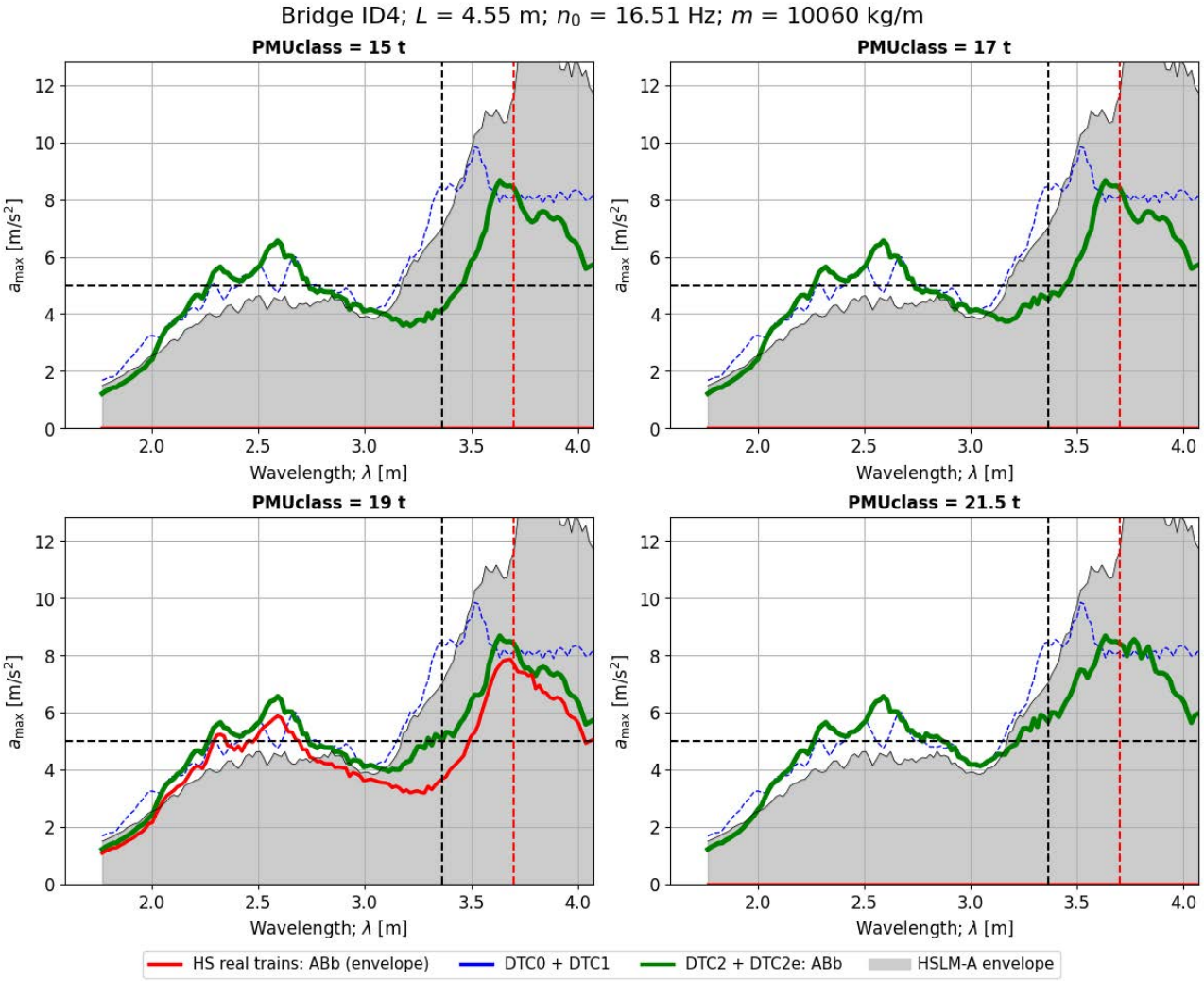

Figure 164. Peak vertical acceleration in the bridge ID4 when subject to real ABb trains of different weight categories, and comparison with the reference ABb train in DTCs. Time-stepping analysis.

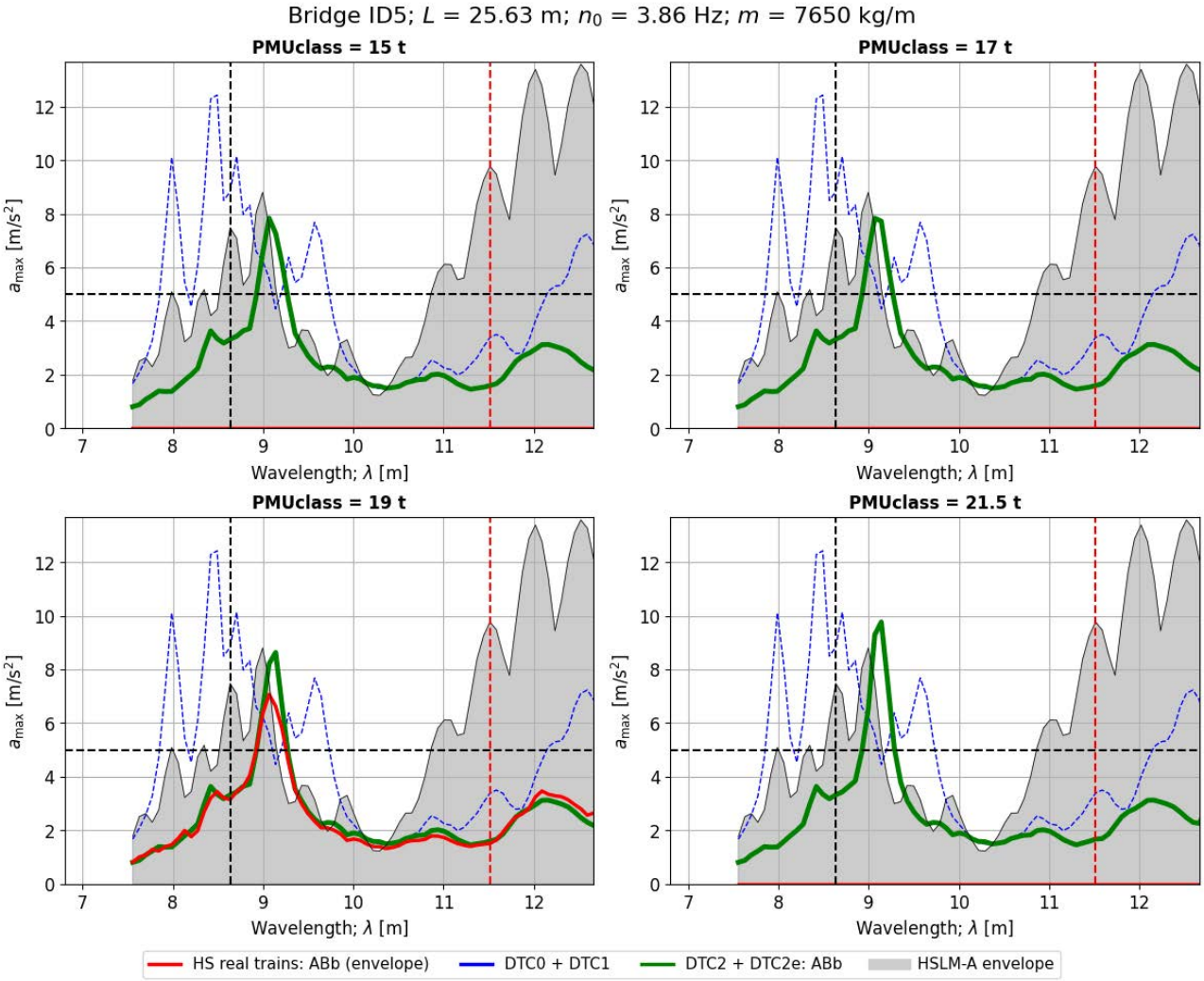

Figure 165. Peak vertical acceleration in the bridge ID5 when subject to real ABb trains of different weight categories, and comparison with the reference ABb train in DTCs. Time-stepping analysis.

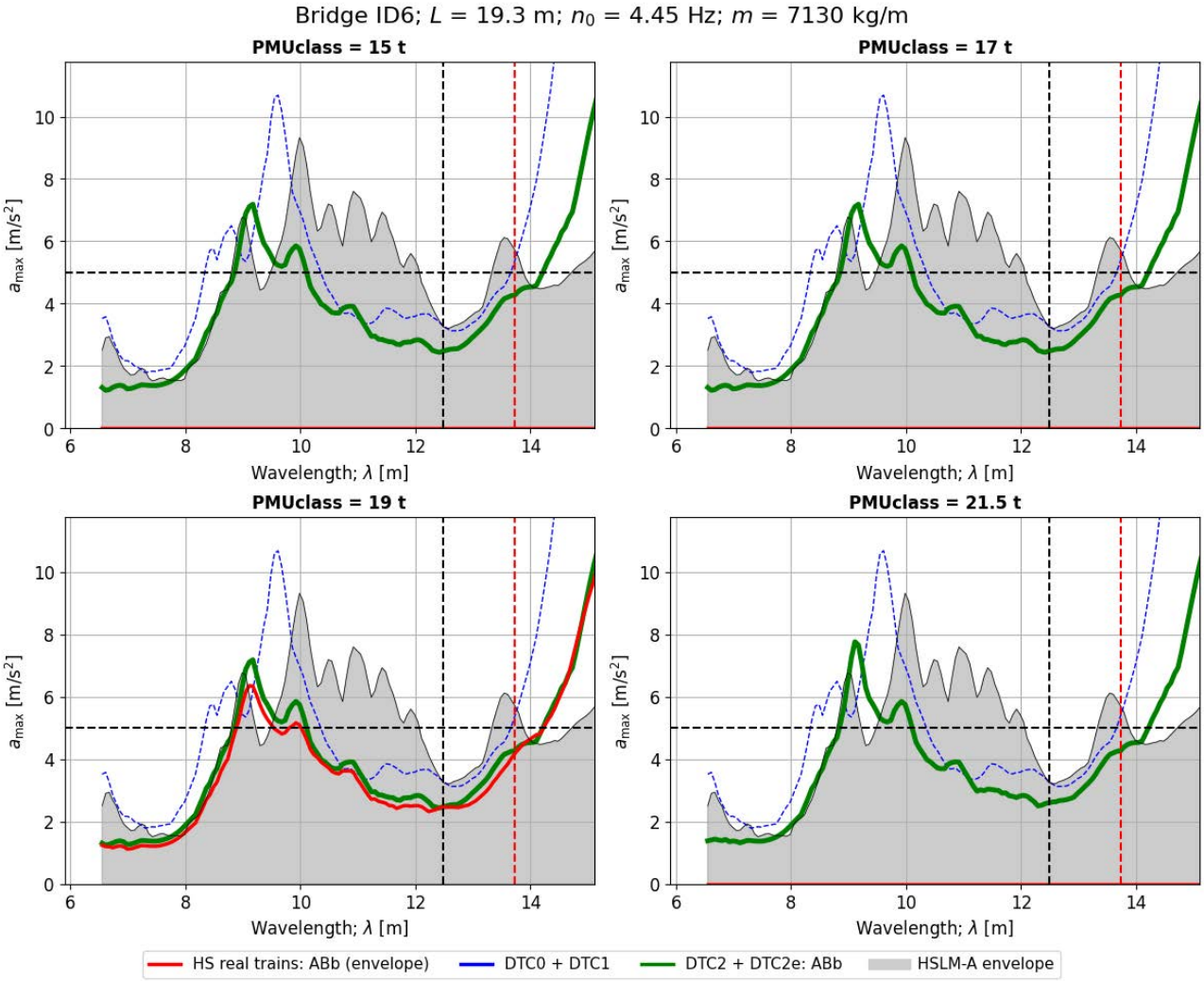

Figure 166. Peak vertical acceleration in the bridge ID6 when subject to real ABb trains of different weight categories, and comparison with the reference ABb train in DTCs. Time-stepping analysis.

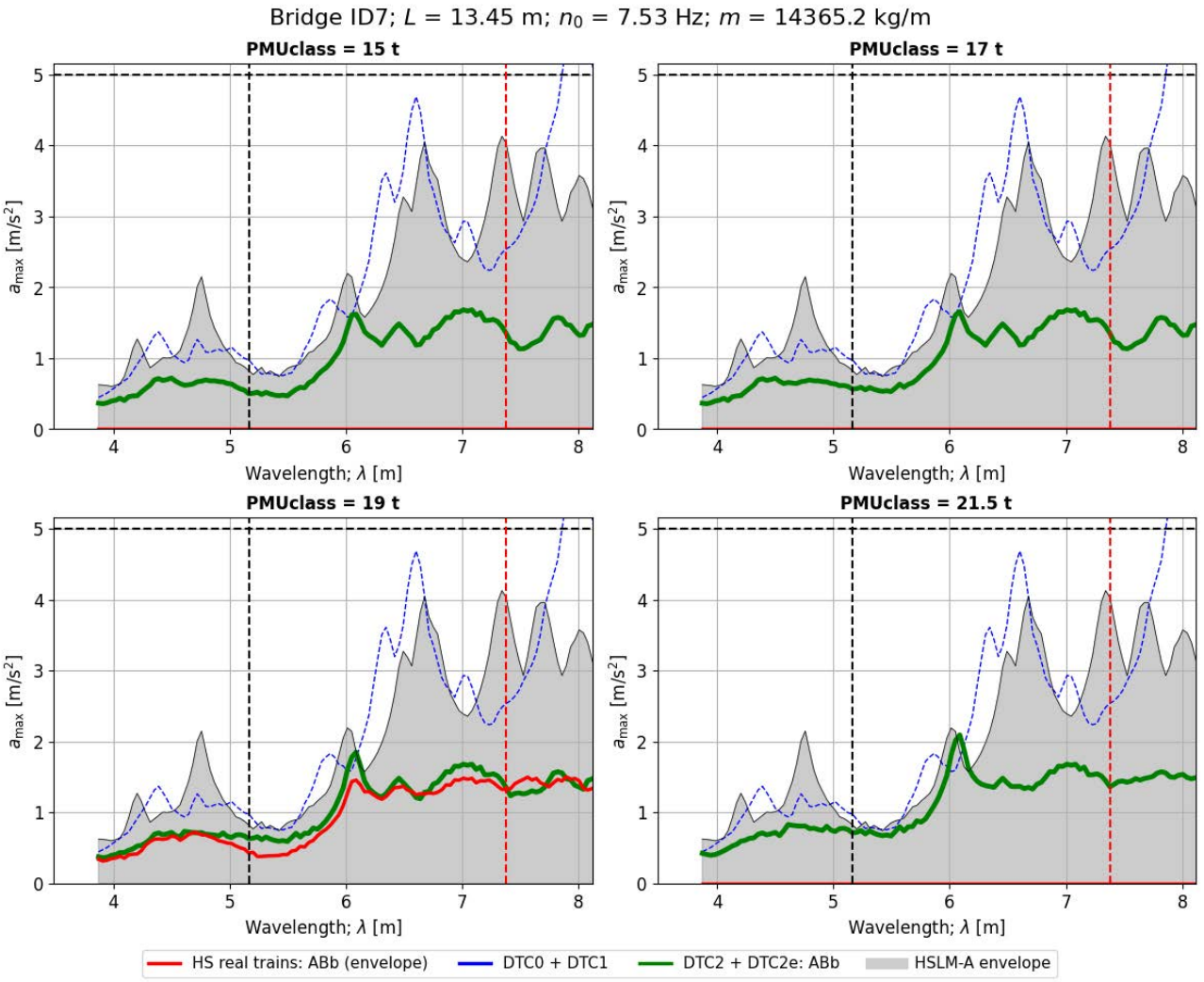

Figure 167. Peak vertical acceleration in the bridge ID7 when subject to real ABb trains of different weight categories, and comparison with the reference ABb train in DTCs. Time-stepping analysis.

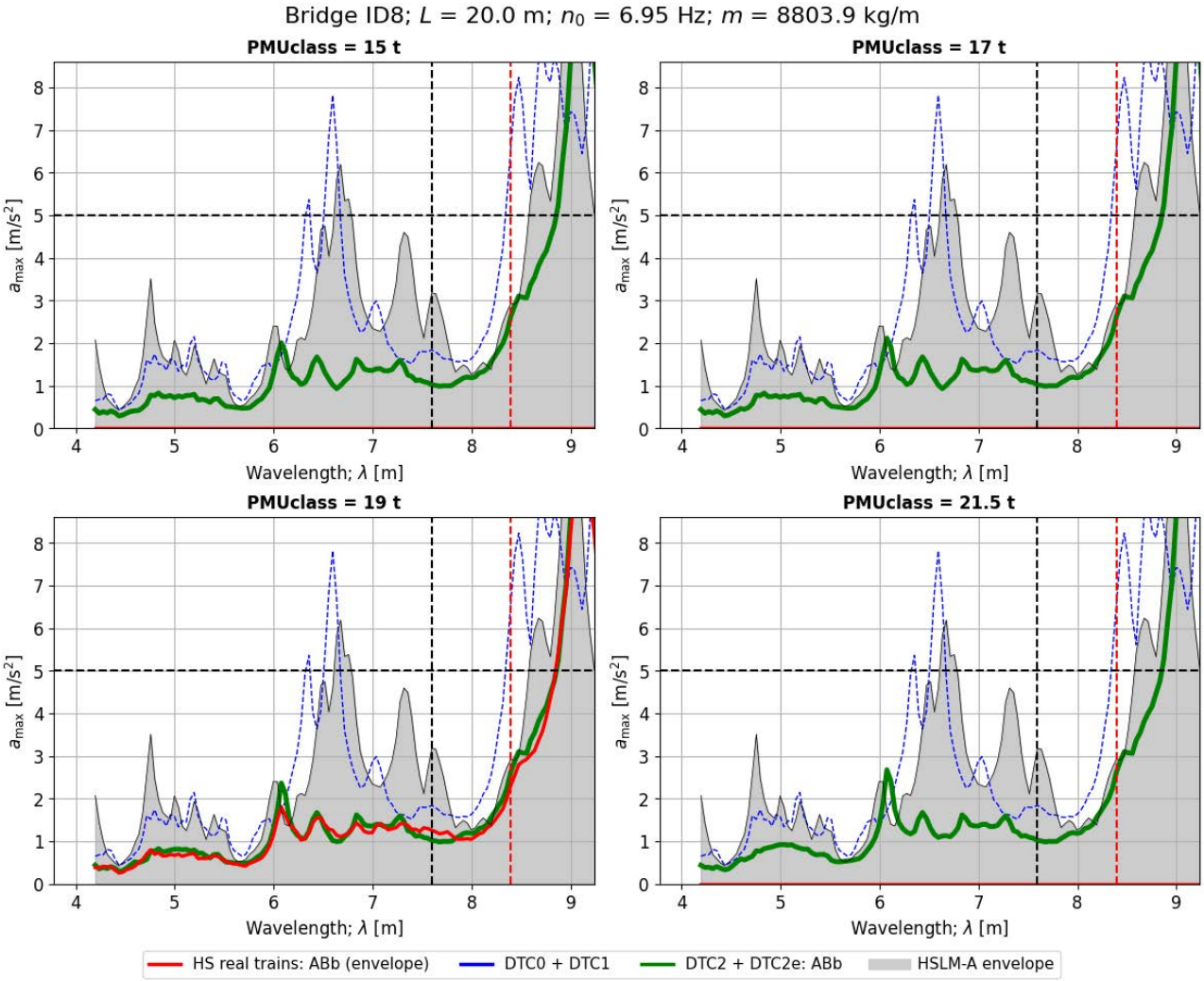

Figure 168. Peak vertical acceleration in the bridge ID8 when subject to real ABb trains of different weight categories, and comparison with the reference ABb train in DTCs. Time-stepping analysis.

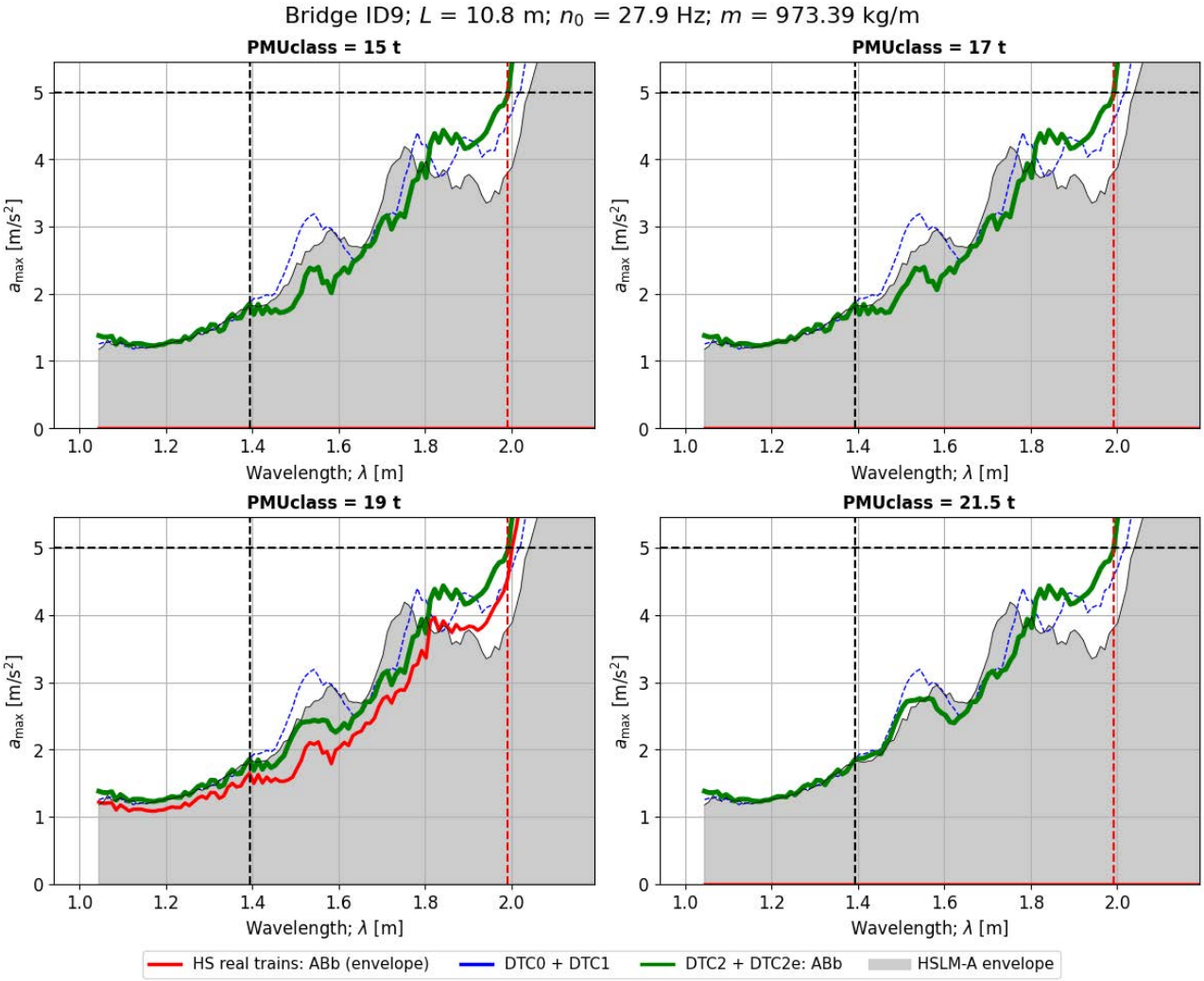

Figure 169. Peak vertical acceleration in the bridge ID9 when subject to real ABb trains of different weight categories, and comparison with the reference ABb train in DTCs. Time-stepping analysis.

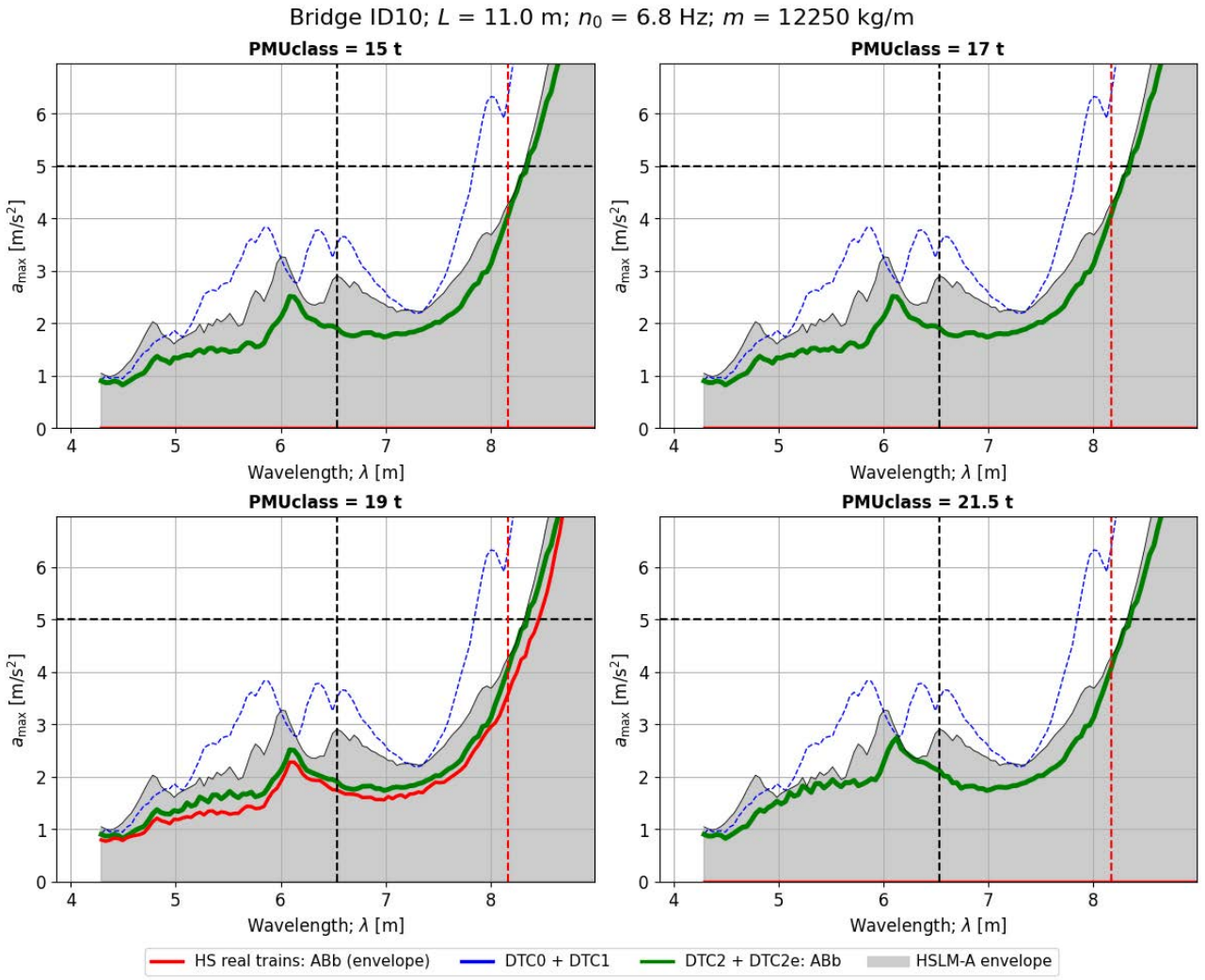

Figure 170. Peak vertical acceleration in the bridge ID10 when subject to real ABb trains of different weight categories, and comparison with the reference ABb train in DTCs. Time-stepping analysis.

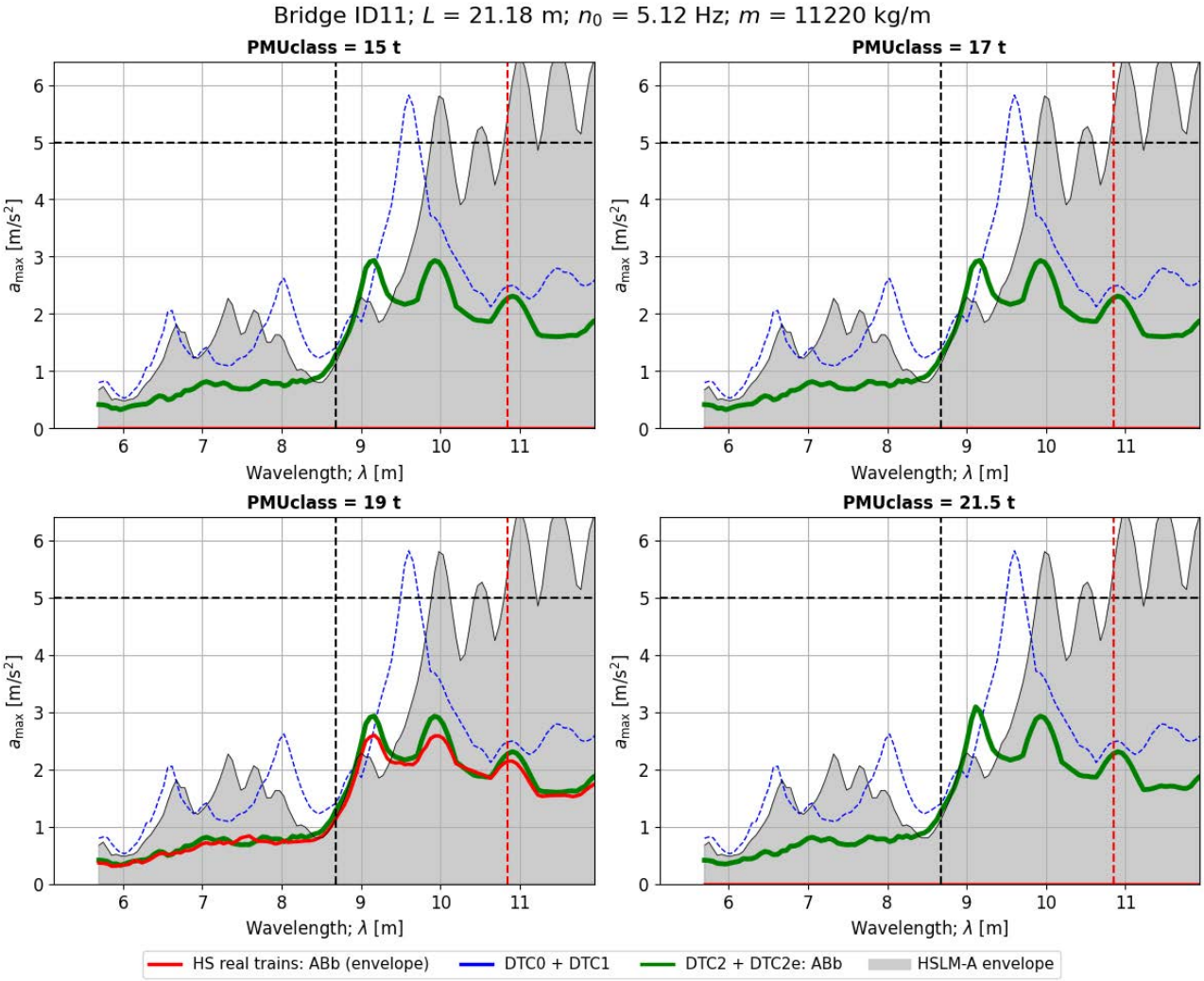

Figure 171. Peak vertical acceleration in the bridge ID11 when subject to real ABb trains of different weight categories, and comparison with the reference ABb train in DTCs. Time-stepping analysis.

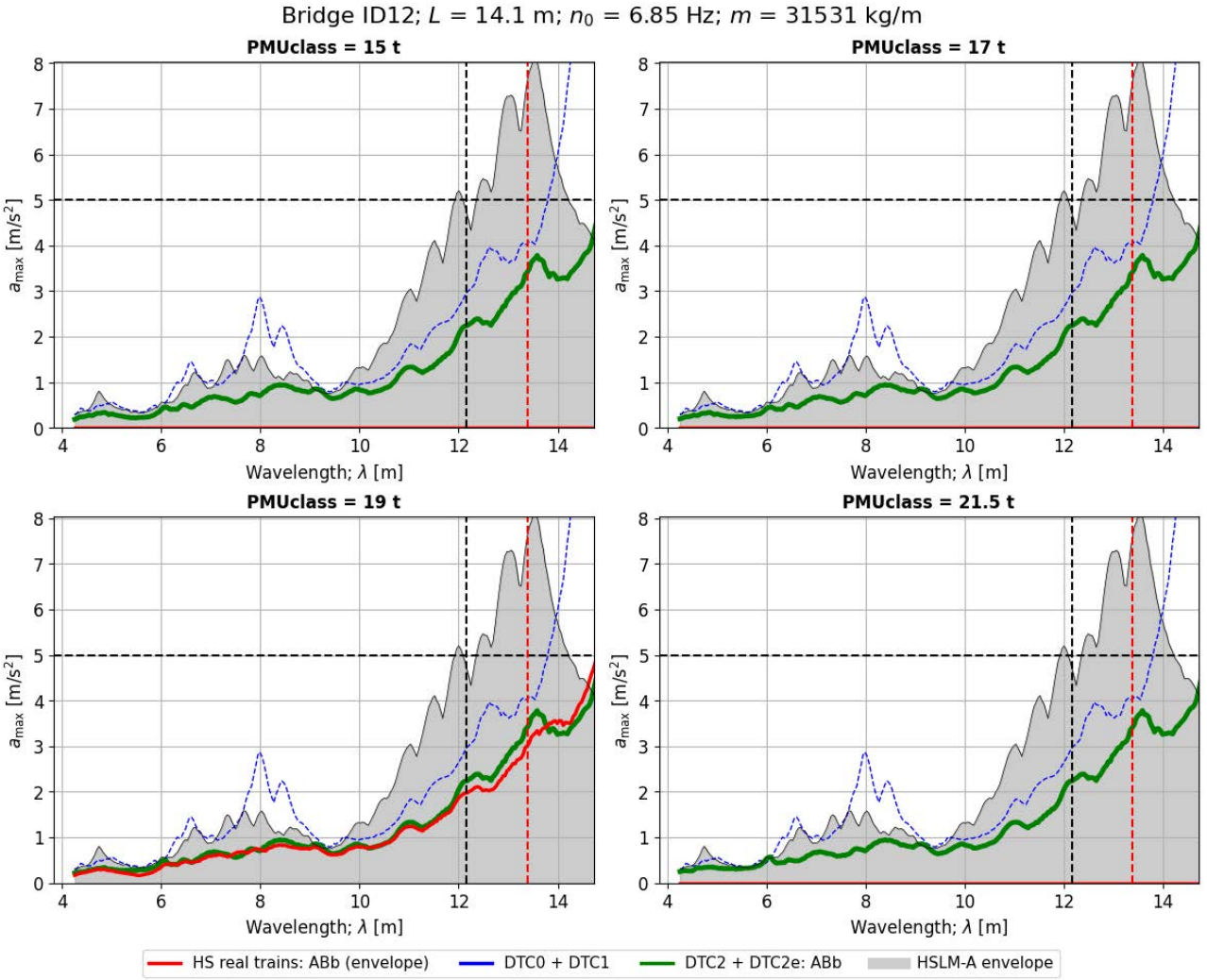

Figure 172. Peak vertical acceleration in the bridge ID12 when subject to real ABb trains of different weight categories, and comparison with the reference ABb train in DTCs. Time-stepping analysis.

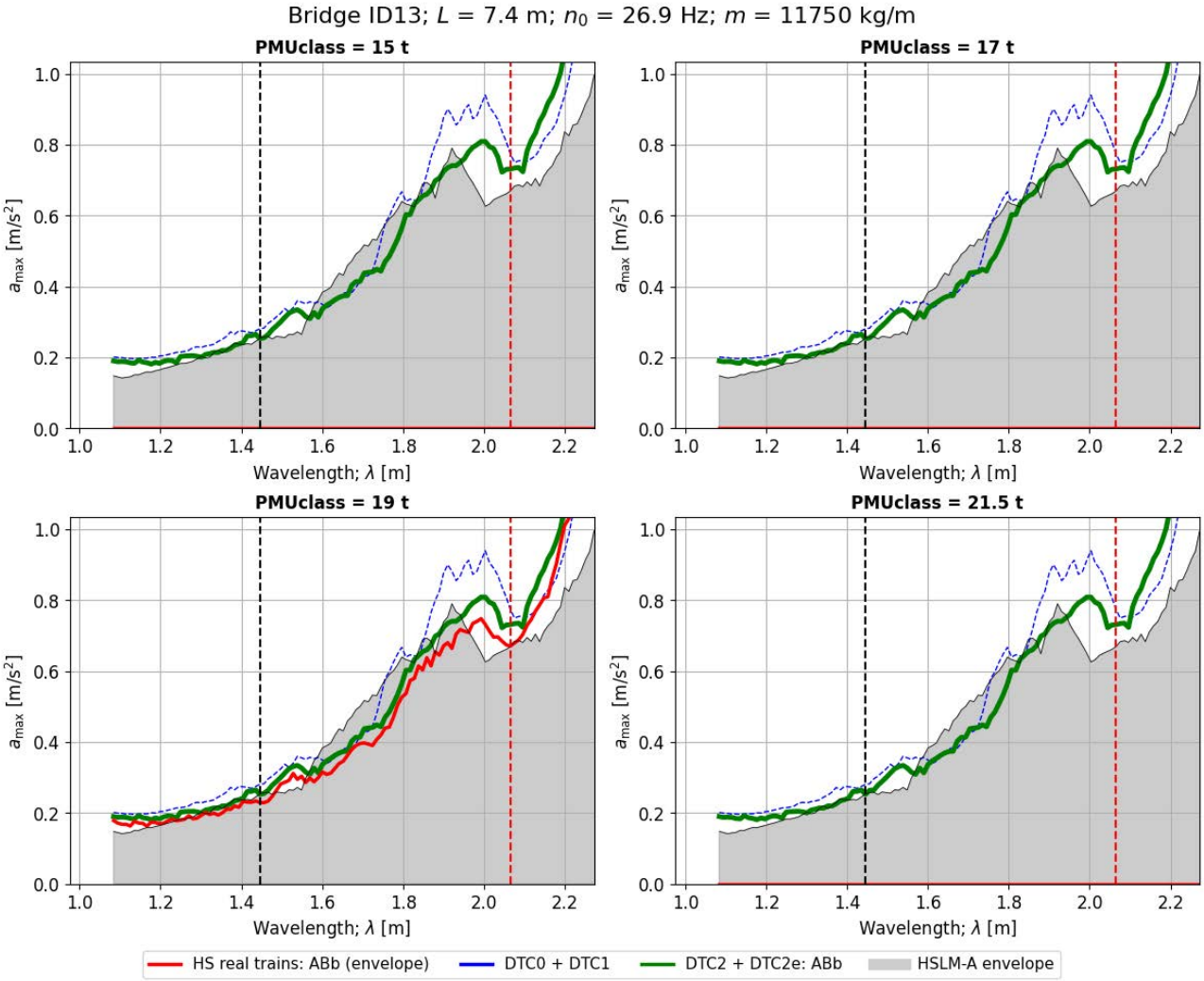

Figure 173. Peak vertical acceleration in the bridge ID13 when subject to real ABb trains of different weight categories, and comparison with the reference ABb train in DTCs. Time-stepping analysis.

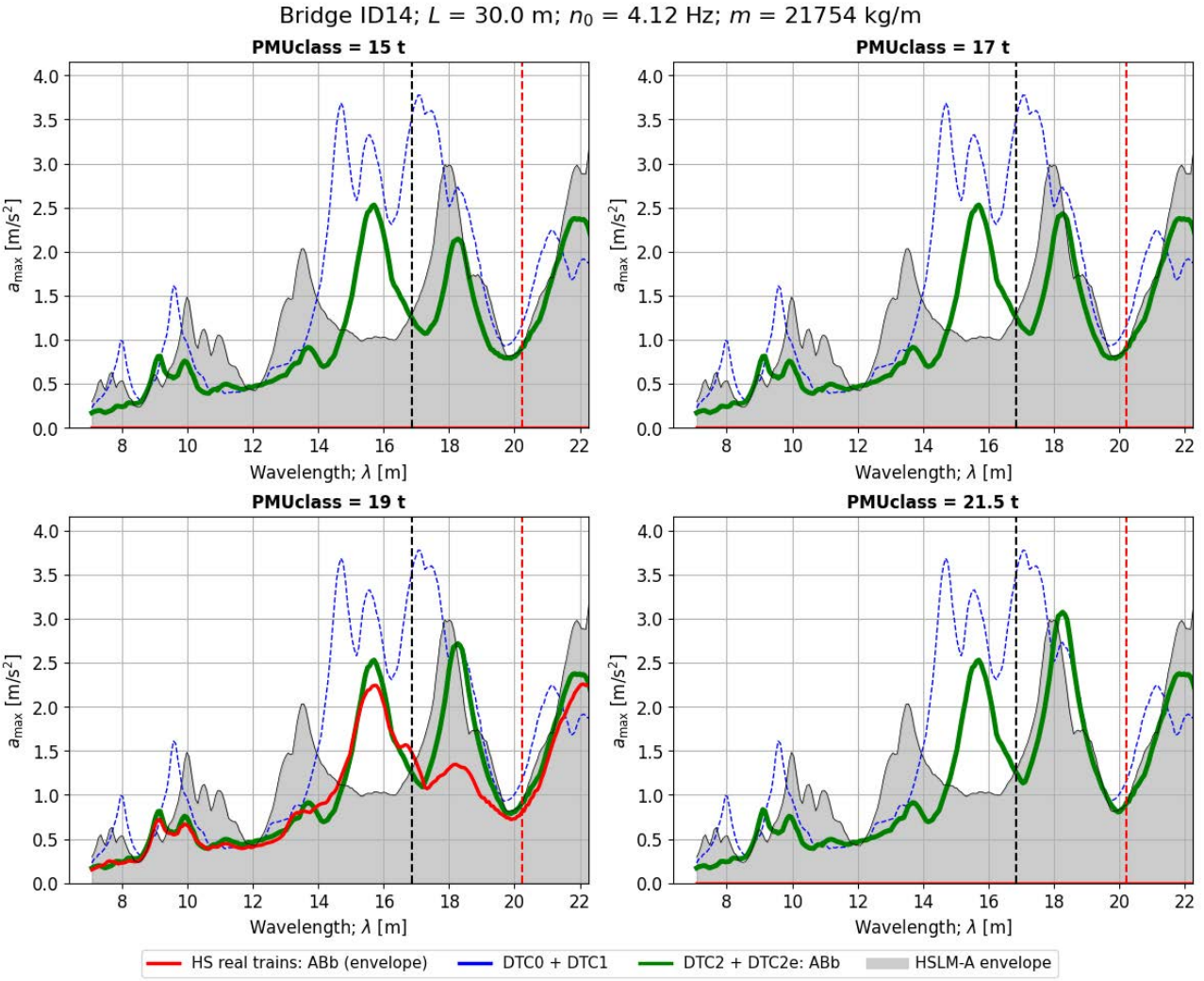

Figure 174. Peak vertical acceleration in the bridge ID14 when subject to real ABb trains of different weight categories, and comparison with the reference ABb train in DTCs. Time-stepping analysis.

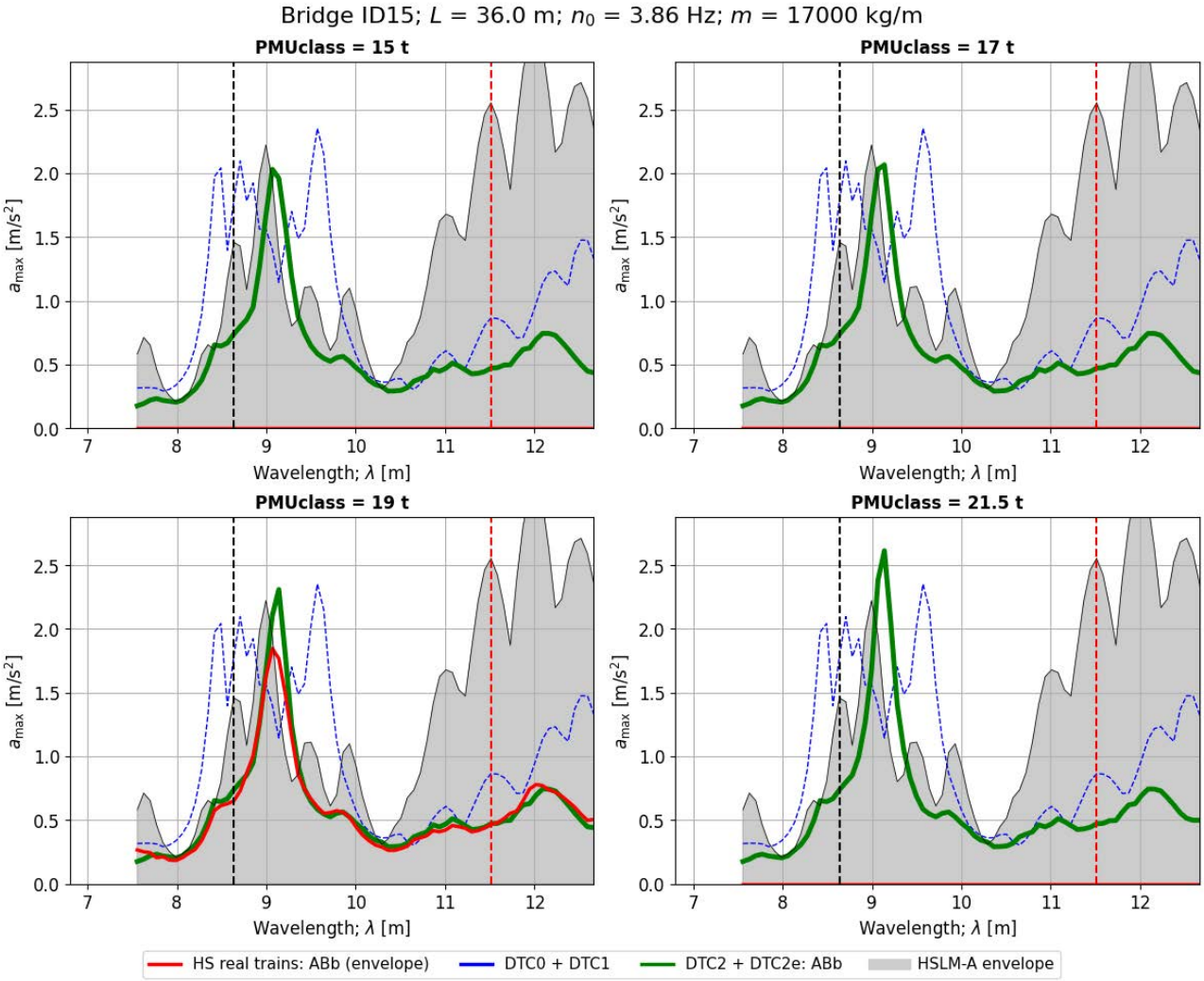

Figure 175. Peak vertical acceleration in the bridge ID15 when subject to real ABb trains of different weight categories, and comparison with the reference ABb train in DTCs. Time-stepping analysis.

ABc trains

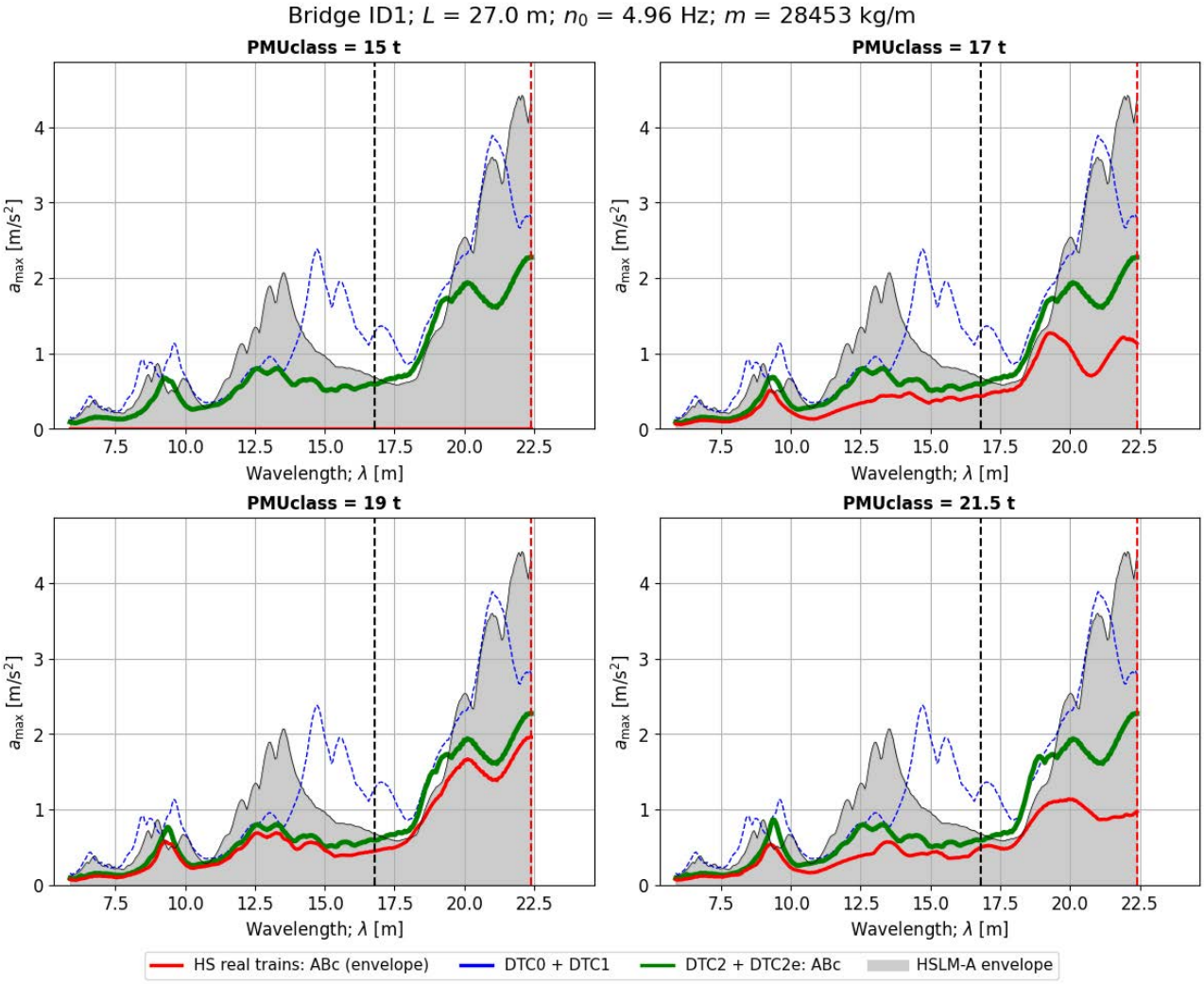

Figure 176. Peak vertical acceleration in the bridge ID1 when subject to real ABc trains of different weight categories, and comparison with the reference ABc train in DTCs. Time-stepping analysis.

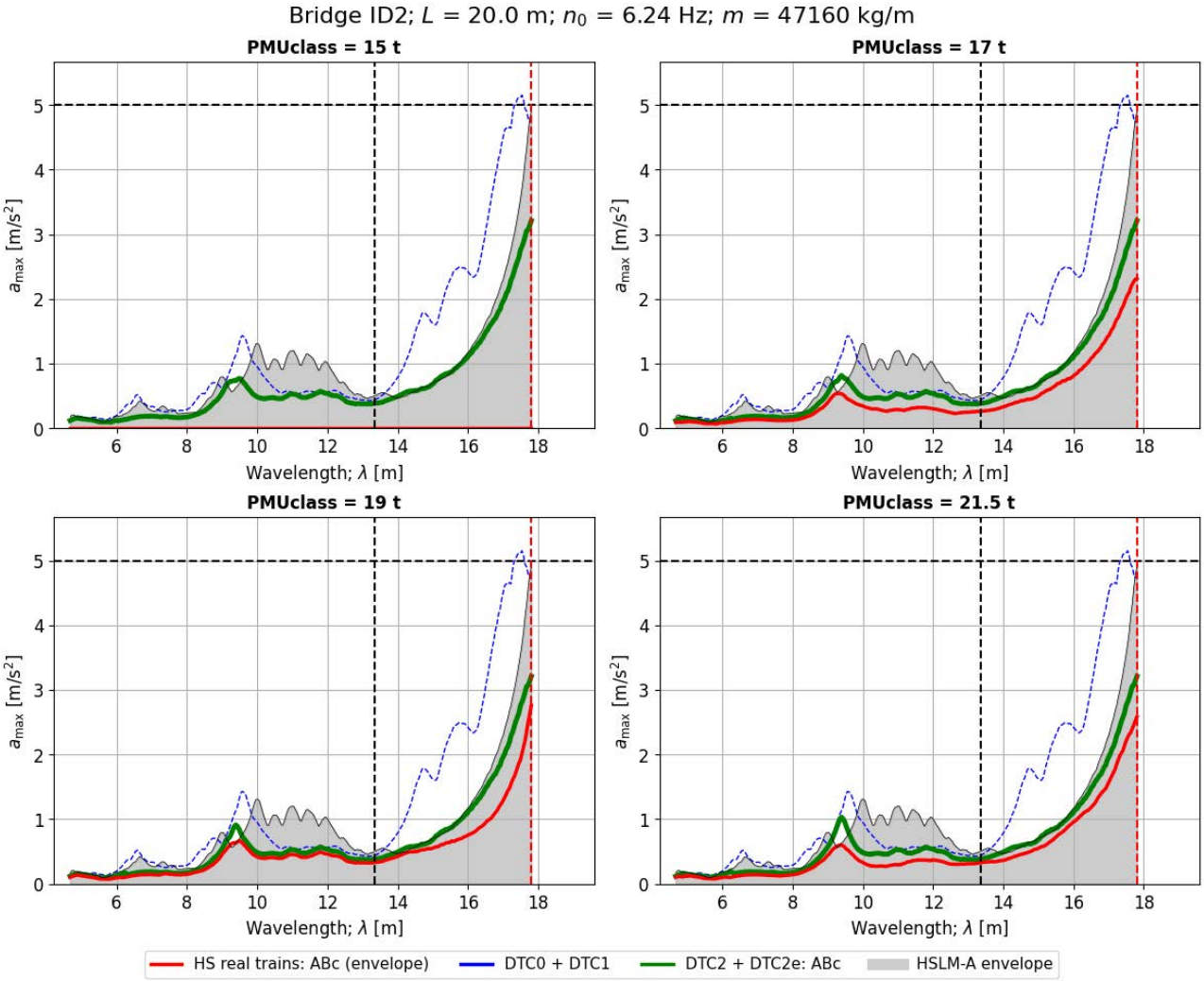

Figure 177. Peak vertical acceleration in the bridge ID2 when subject to real ABc trains of different weight categories, and comparison with the reference ABc train in DTCs. Time-stepping analysis.

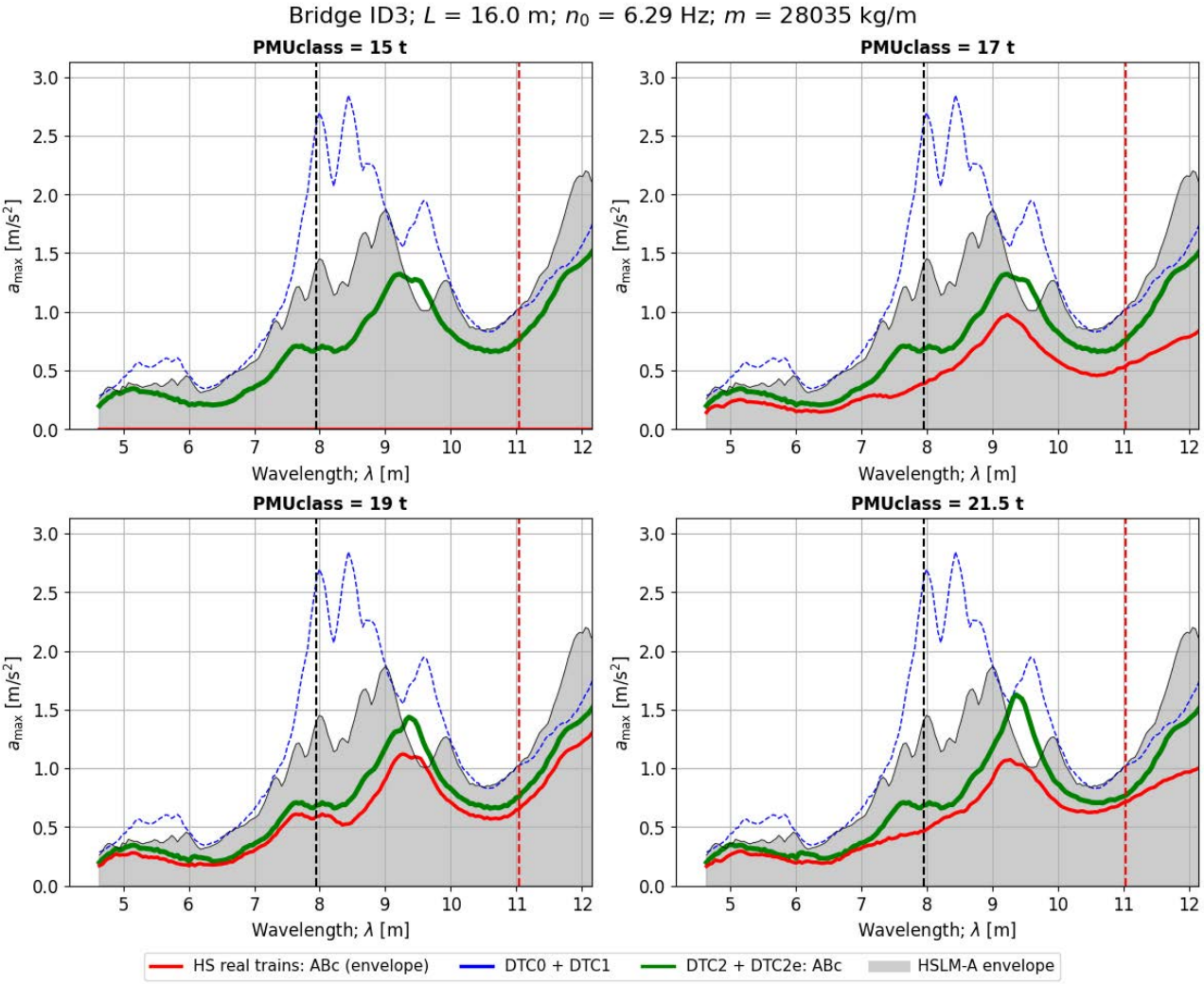

Figure 178. Peak vertical acceleration in the bridge ID3 when subject to real ABc trains of different weight categories, and comparison with the reference ABc train in DTCs. Time-stepping analysis.

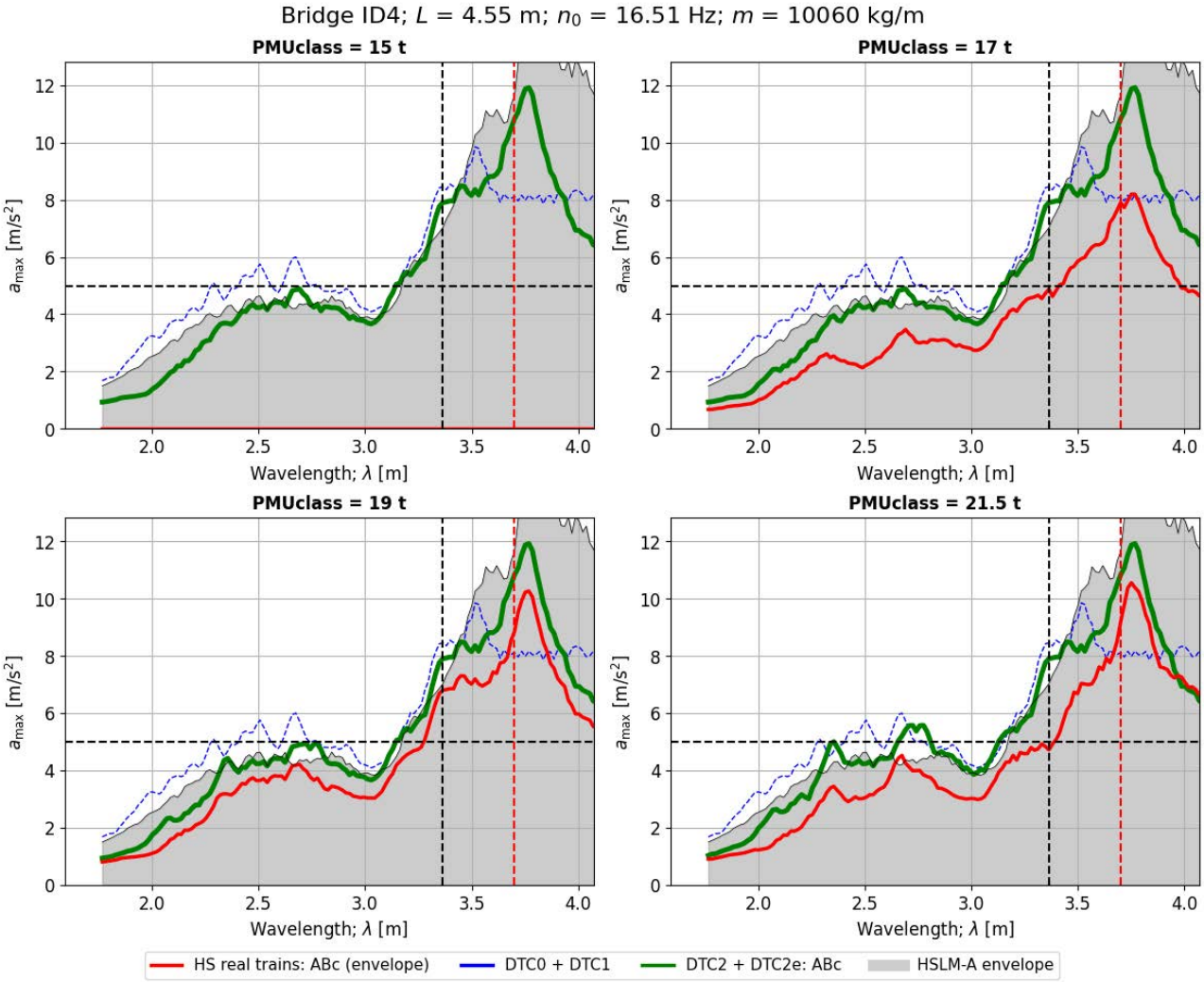

Figure 179. Peak vertical acceleration in the bridge ID4 when subject to real ABc trains of different weight categories, and comparison with the reference ABc train in DTCs. Time-stepping analysis.

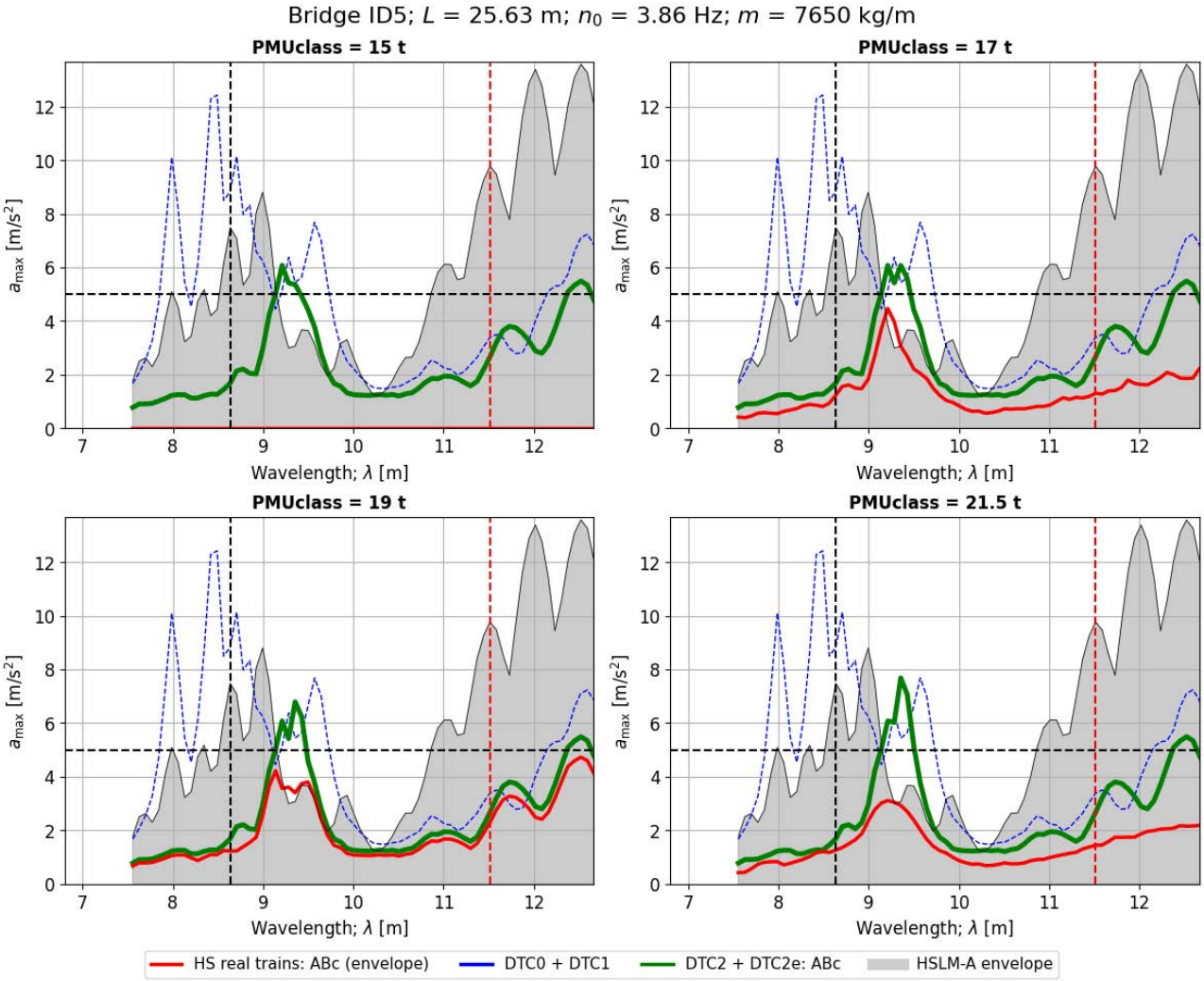

Figure 180. Peak vertical acceleration in the bridge ID5 when subject to real ABc trains of different weight categories, and comparison with the reference ABc train in DTCs. Time-stepping analysis.

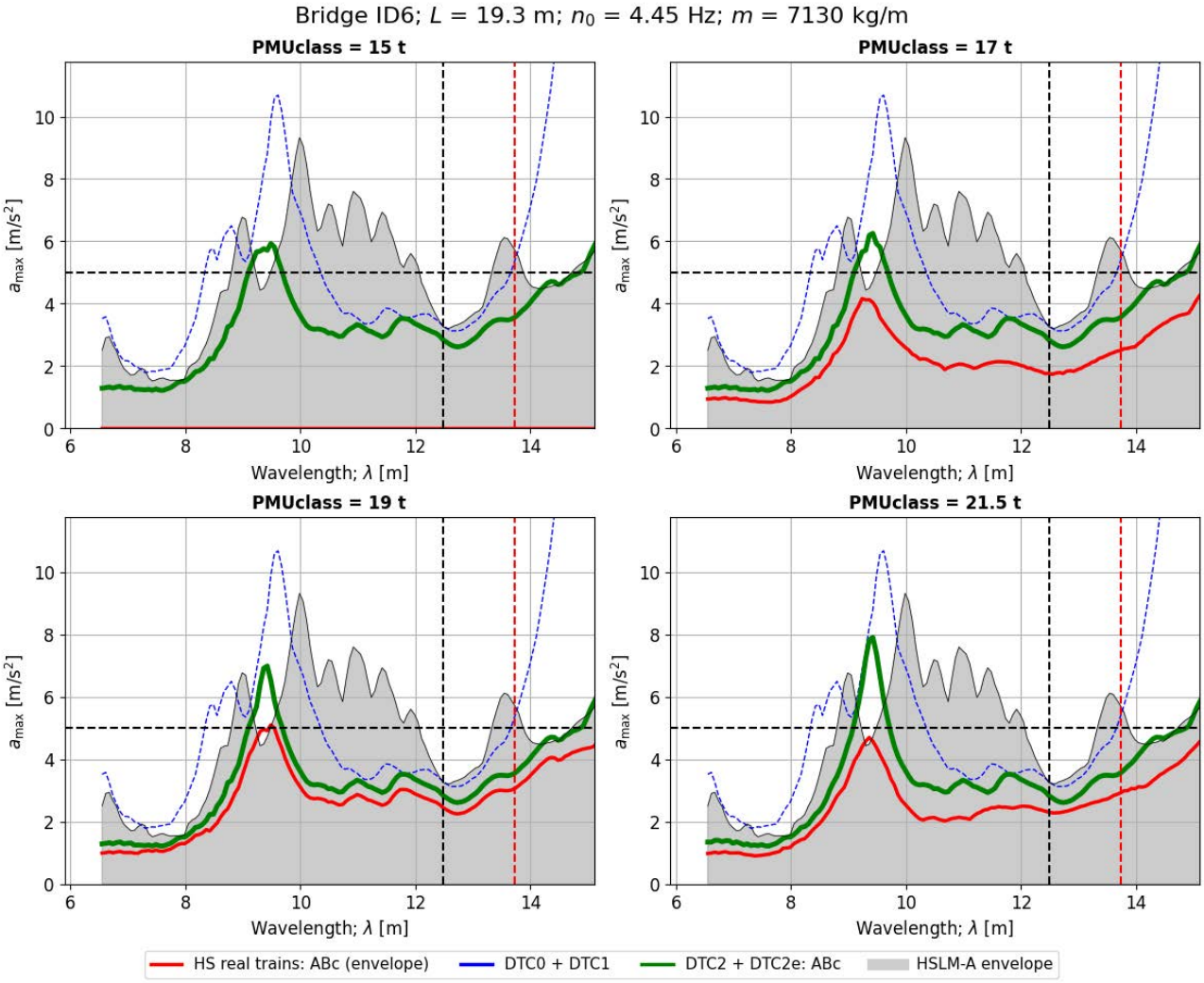

Figure 181. Peak vertical acceleration in the bridge ID6 when subject to real ABc trains of different weight categories, and comparison with the reference ABc train in DTCs. Time-stepping analysis.

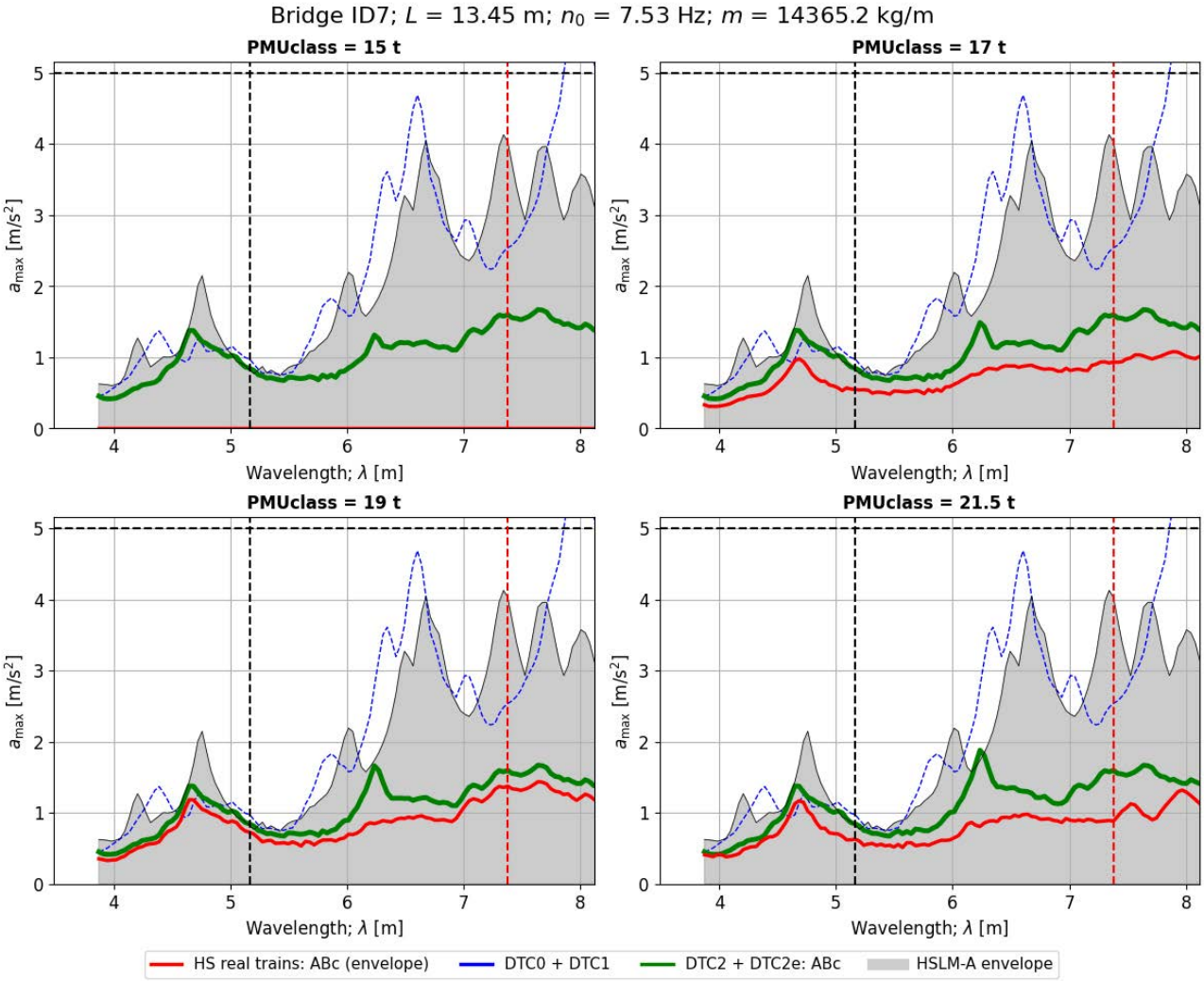

Figure 182. Peak vertical acceleration in the bridge ID7 when subject to real ABc trains of different weight categories, and comparison with the reference ABc train in DTCs. Time-stepping analysis.

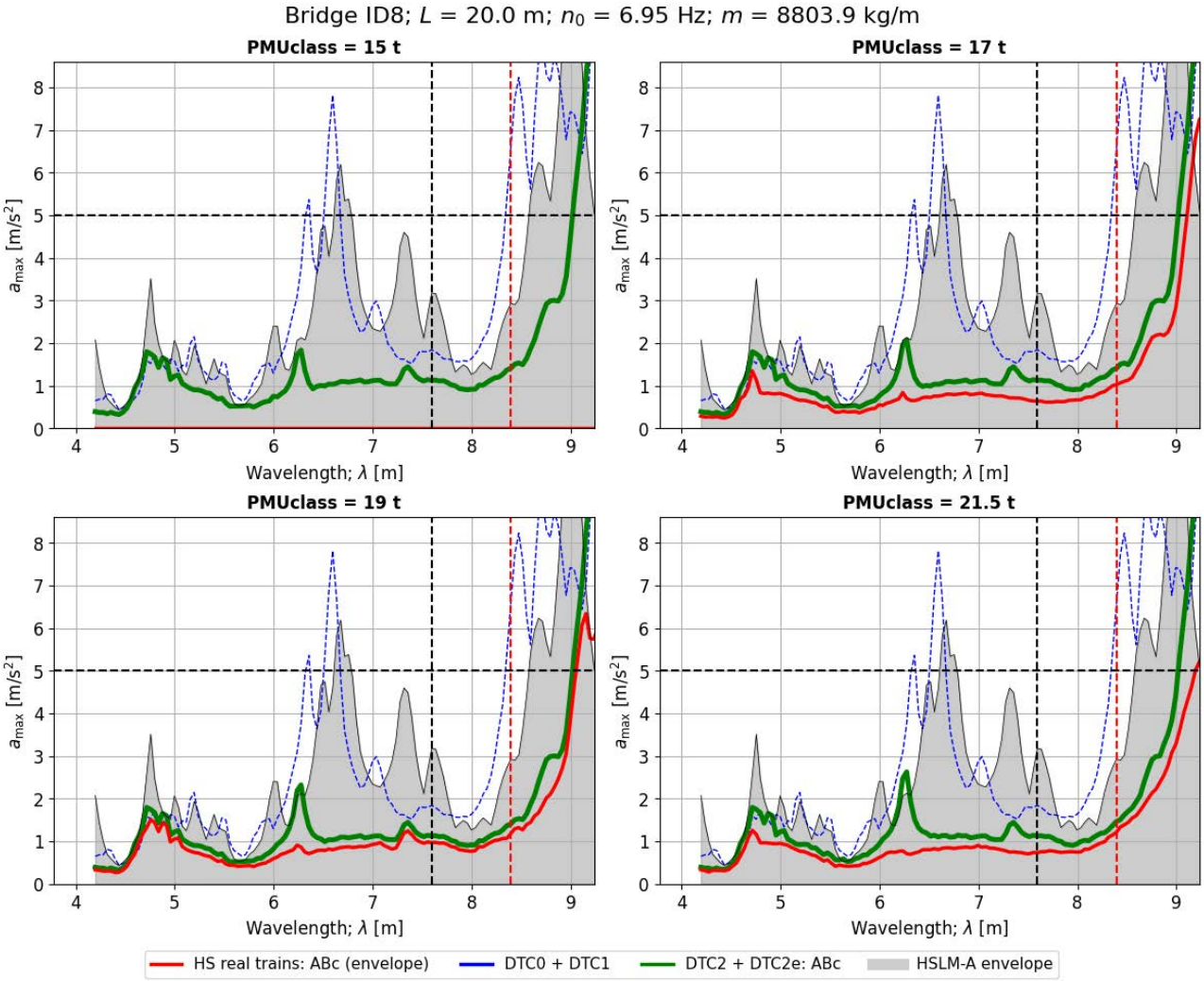

Figure 183. Peak vertical acceleration in the bridge ID8 when subject to real ABc trains of different weight categories, and comparison with the reference ABc train in DTCs. Time-stepping analysis.

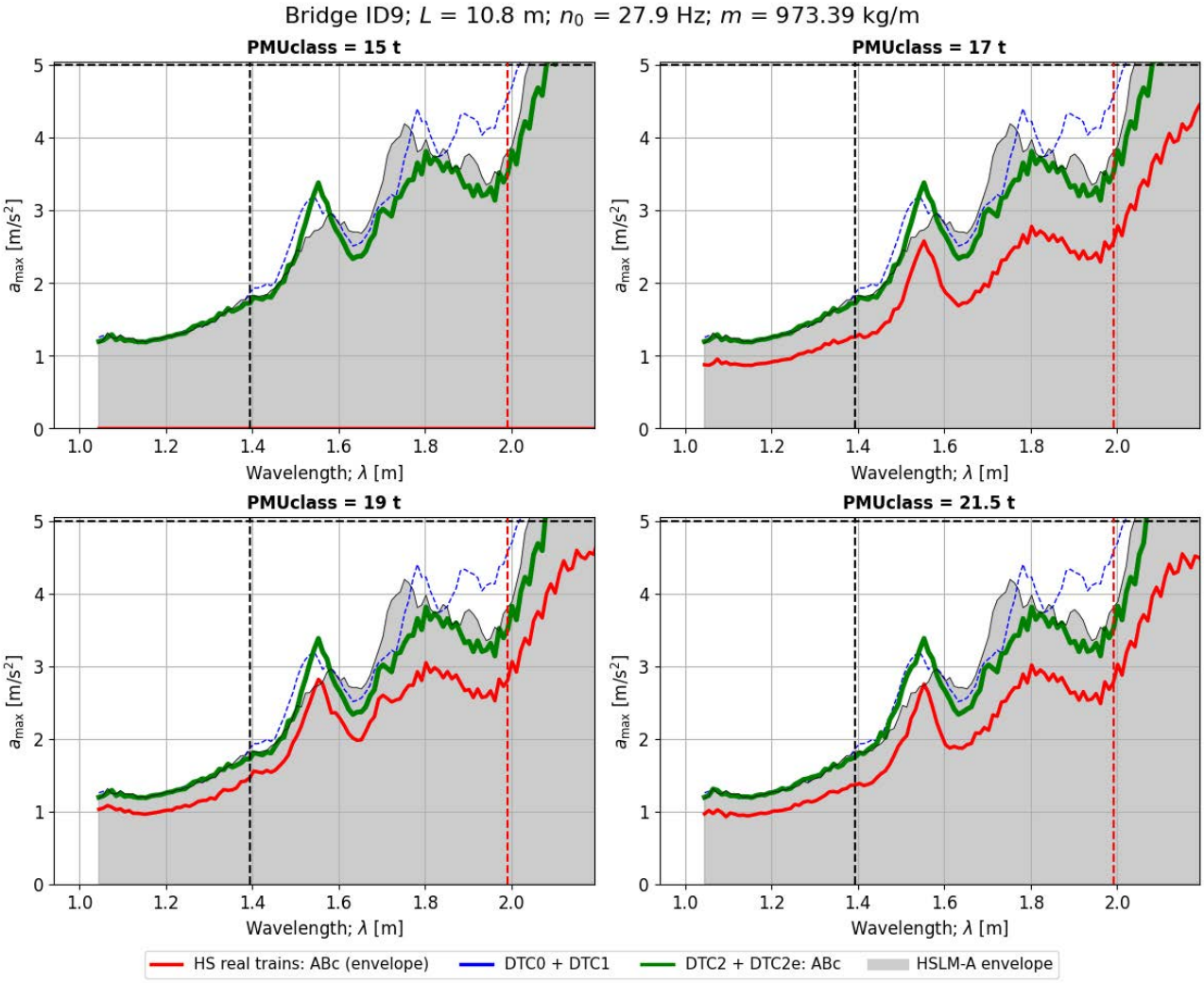

Figure 184. Peak vertical acceleration in the bridge ID9 when subject to real CBb trains of different weight categories, and comparison with the reference ABc train in DTCs. Time-stepping analysis.

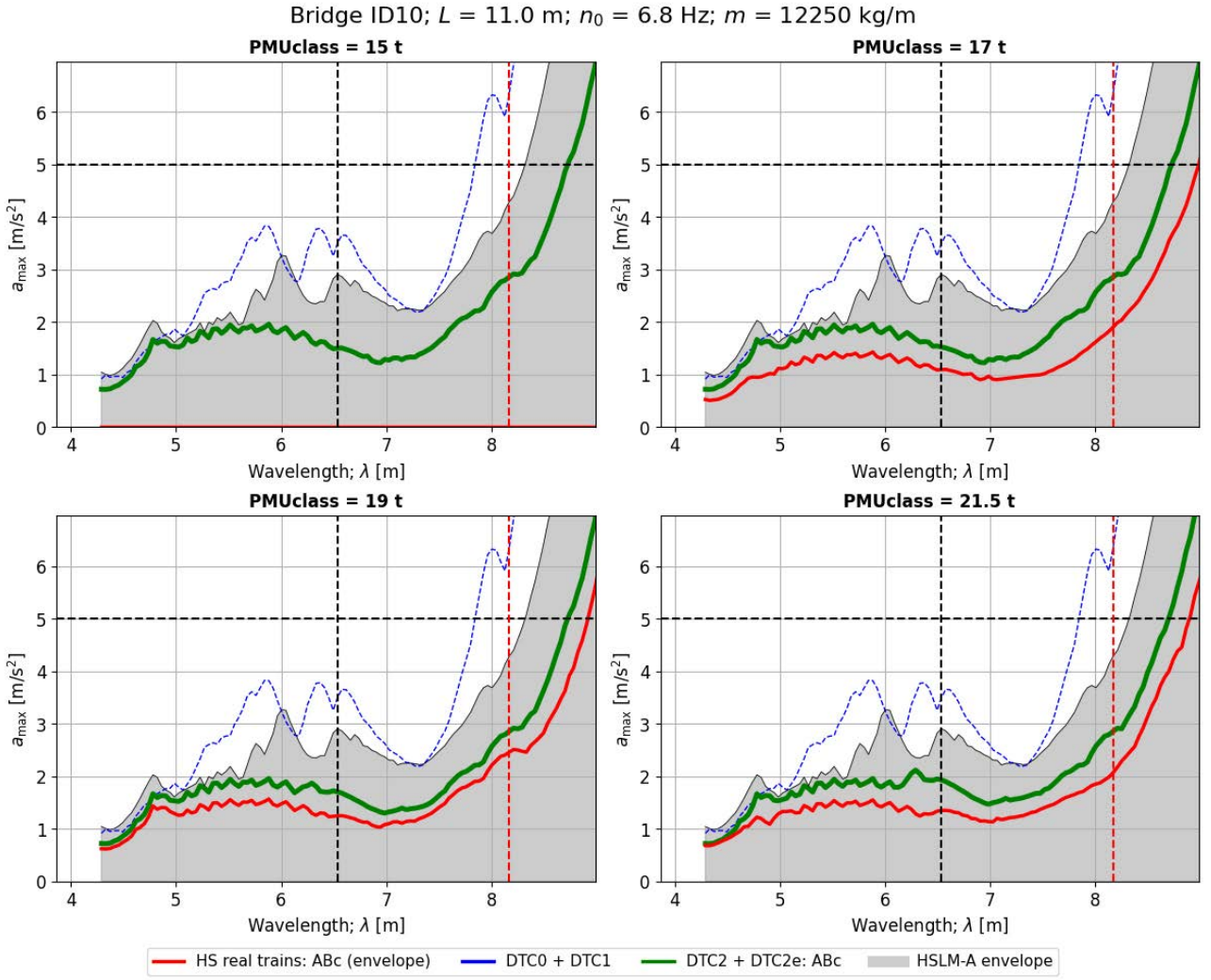

Figure 185. Peak vertical acceleration in the bridge ID10 when subject to real ABc trains of different weight categories, and comparison with the reference ABc train in DTCs. Time-stepping analysis.

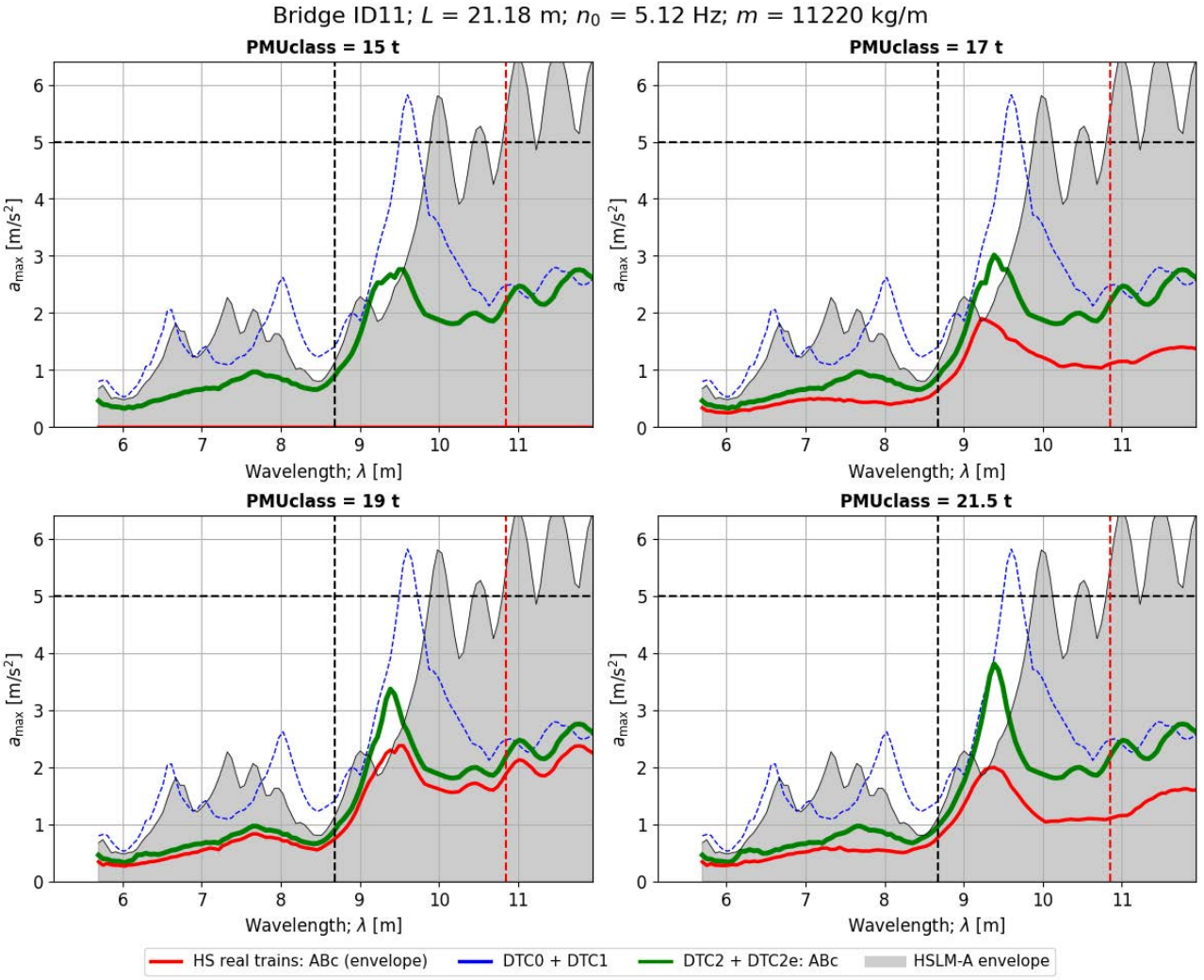

Figure 186. Peak vertical acceleration in the bridge ID11 when subject to real ABc trains of different weight categories, and comparison with the reference ABc train in DTCs. Time-stepping analysis.

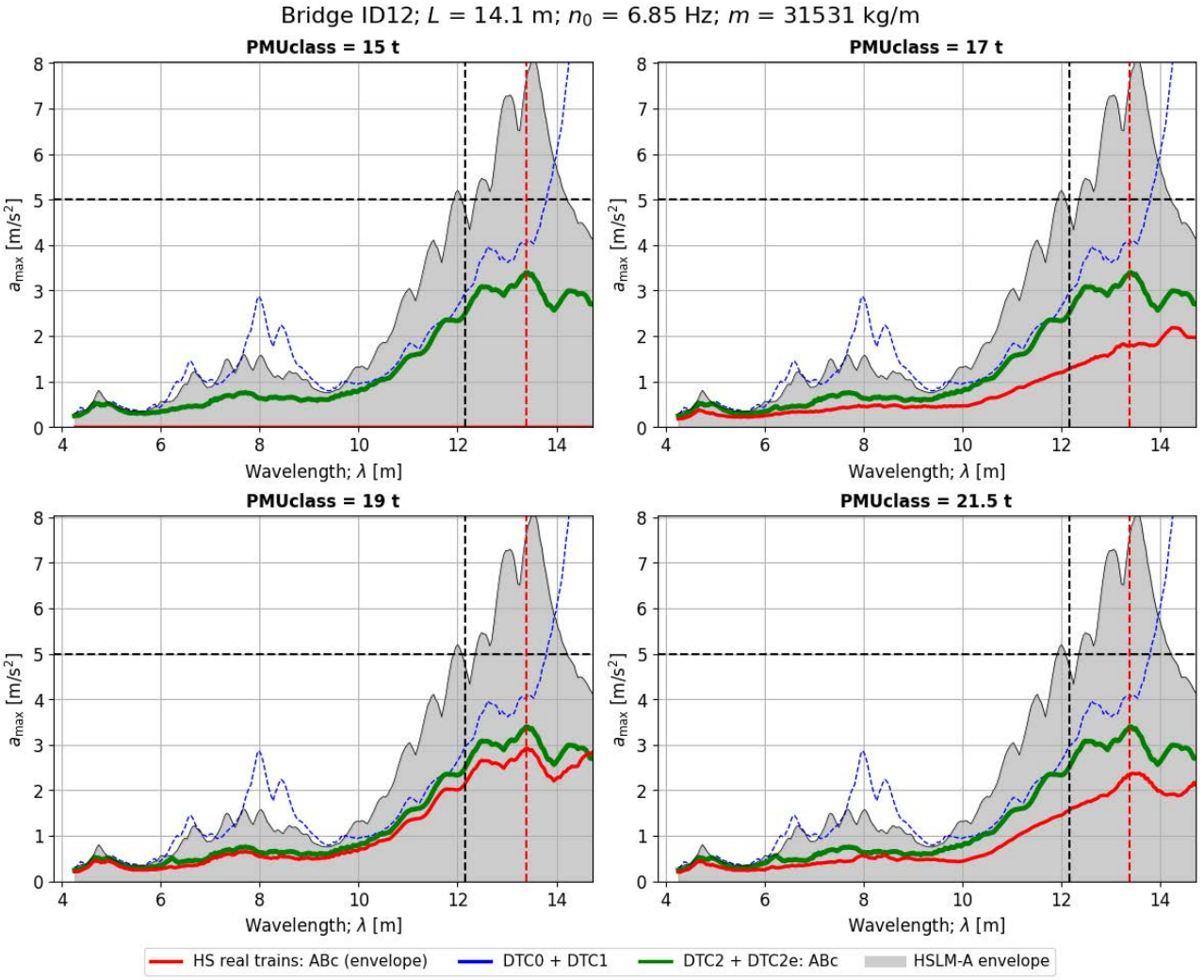

Figure 187. Peak vertical acceleration in the bridge ID12 when subject to real ABc trains of different weight categories, and comparison with the reference ABc train in DTCs. Time-stepping analysis.

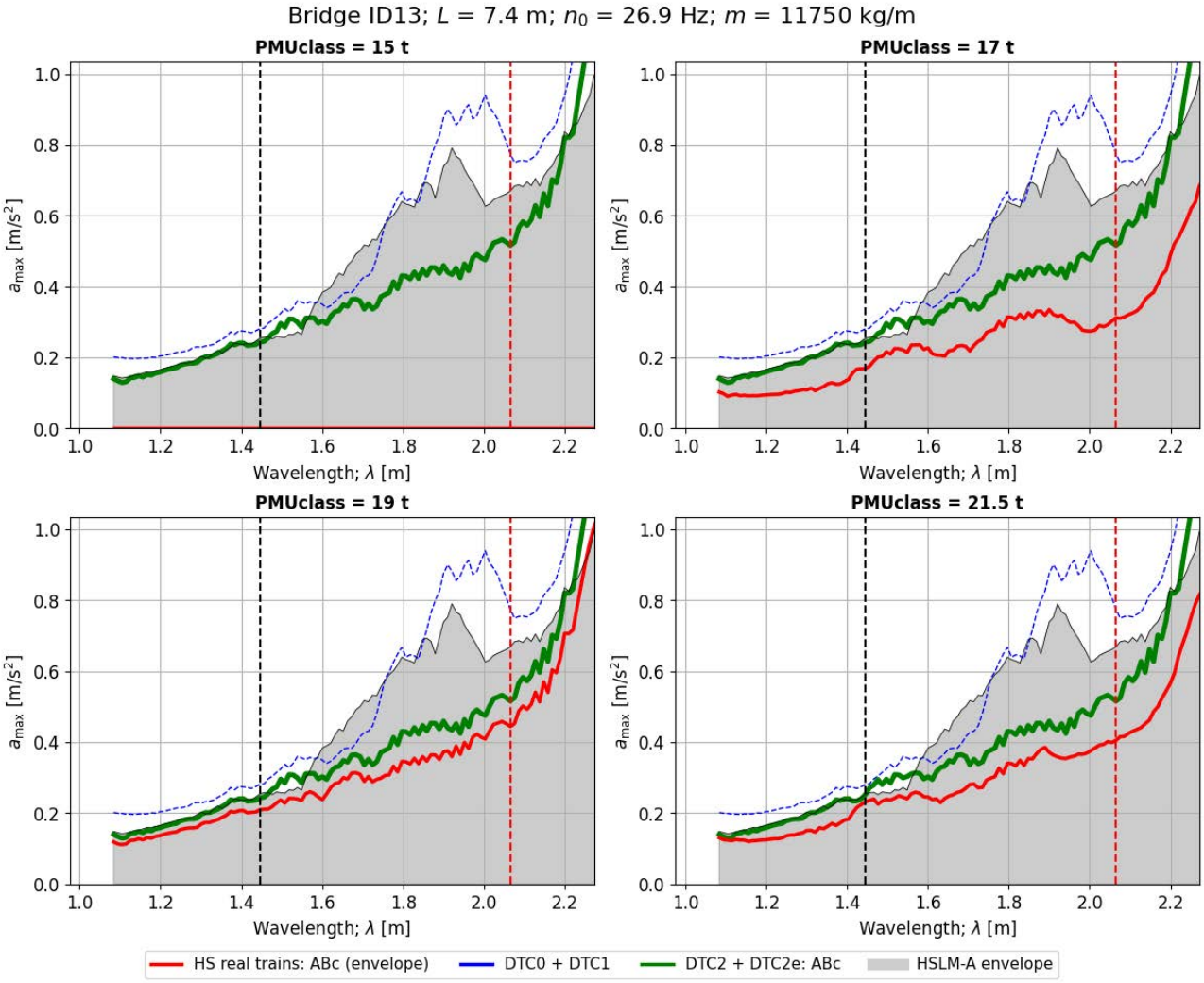

Figure 188. Peak vertical acceleration in the bridge ID13 when subject to real ABc trains of different weight categories, and comparison with the reference ABc train in DTCs. Time-stepping analysis.

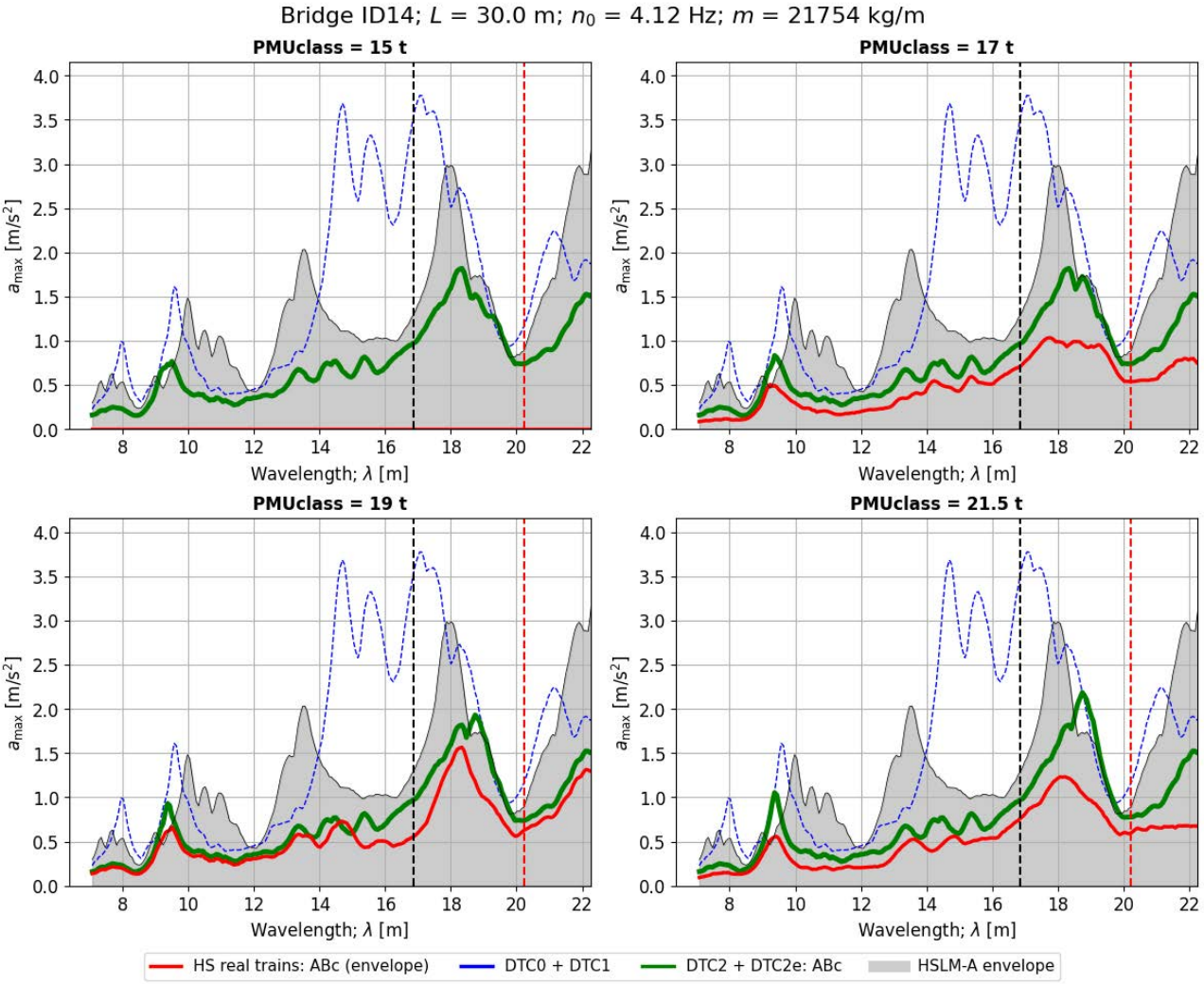

Figure 189. Peak vertical acceleration in the bridge ID14 when subject to real ABc trains of different weight categories, and comparison with the reference ABc train in DTCs. Time-stepping analysis.

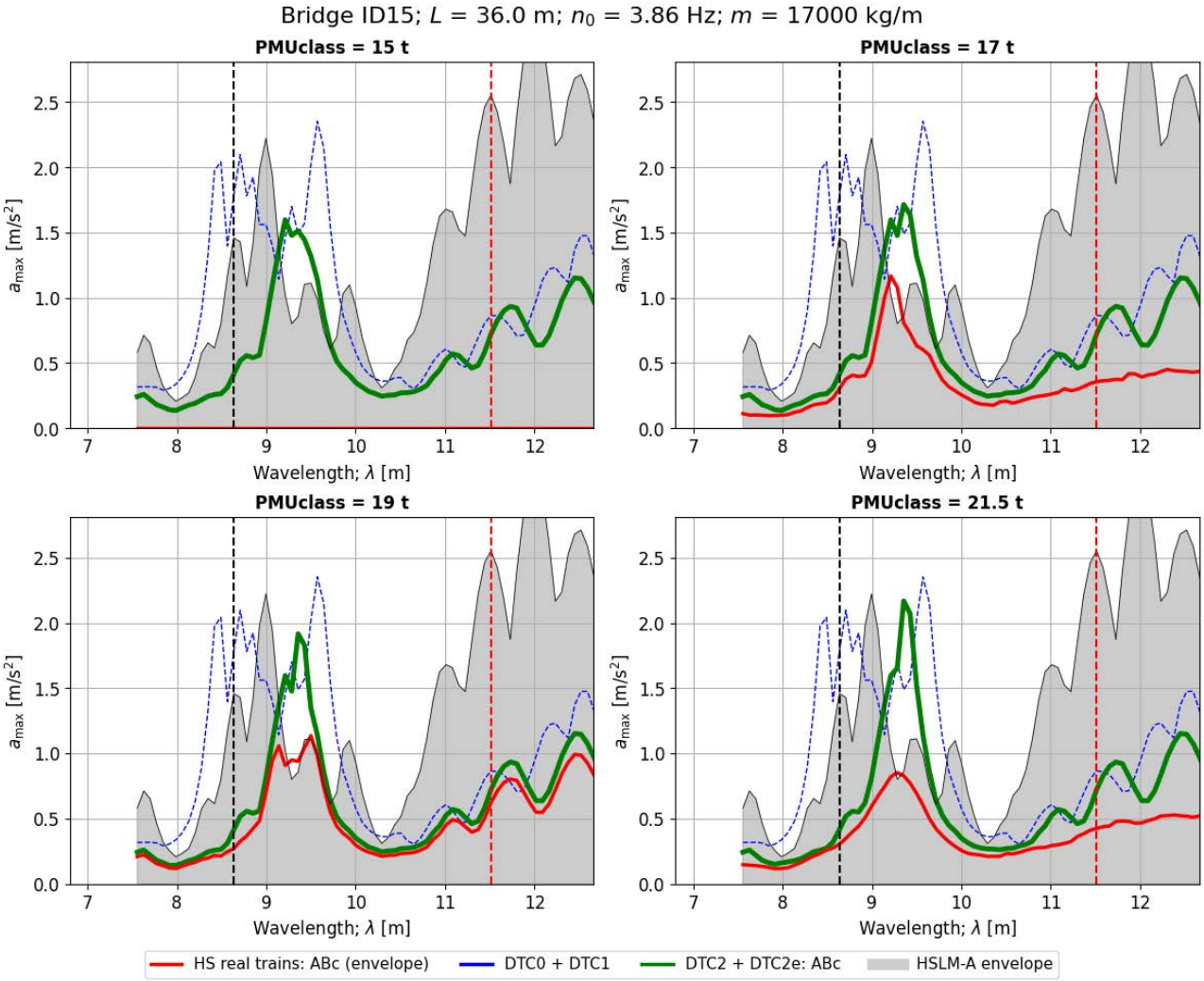

Figure 190. Peak vertical acceleration in the bridge ID15 when subject to real ABc trains of different weight categories, and comparison with the reference ABc train in DTCs. Time-stepping analysis.

Trains with Conventional Bogies: SA

SAa trains

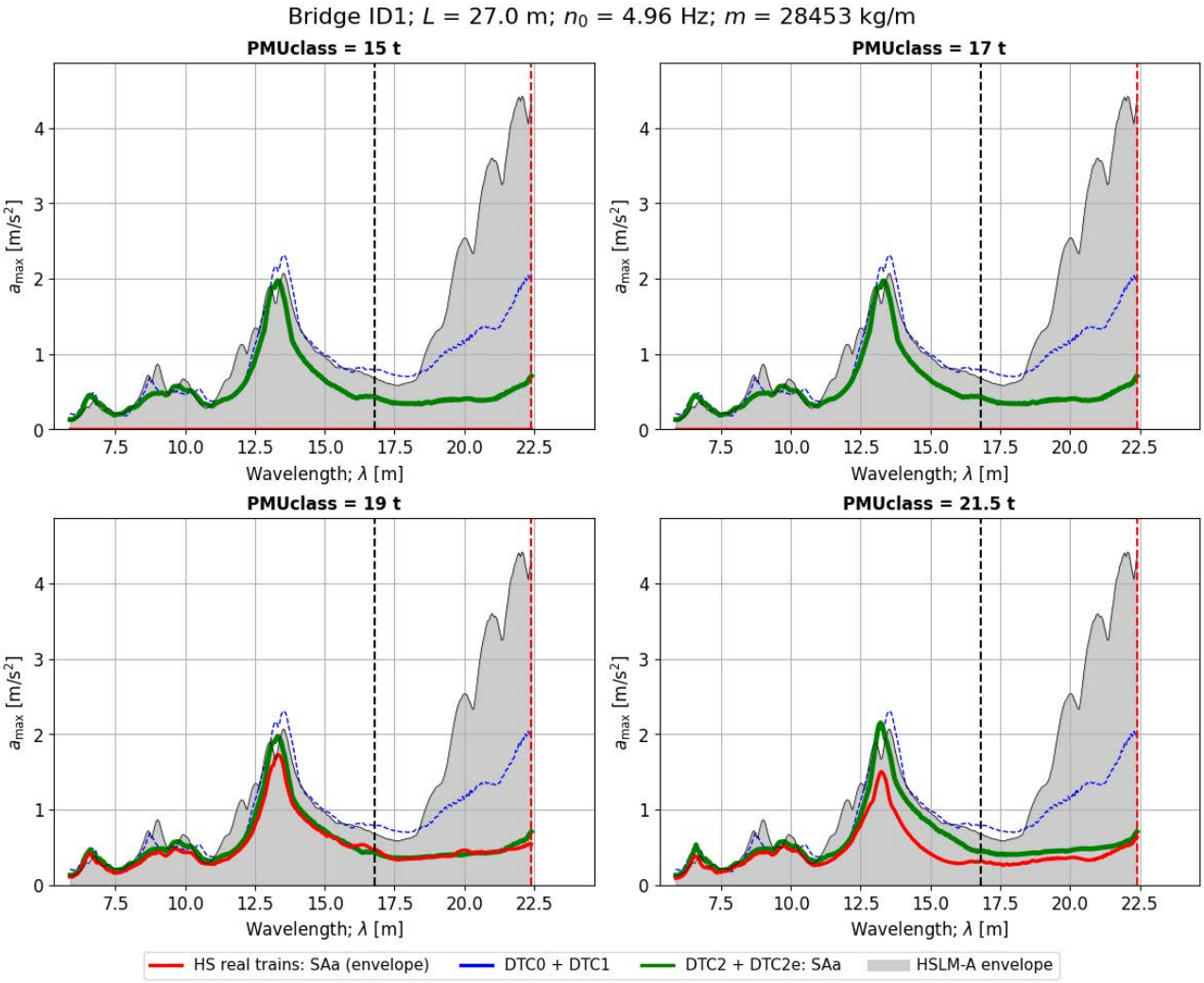

Figure 191. Peak vertical acceleration in the bridge ID1 when subject to real SAa trains of different weight categories, and comparison with the reference SAa train in DTCs. Time-stepping analysis.

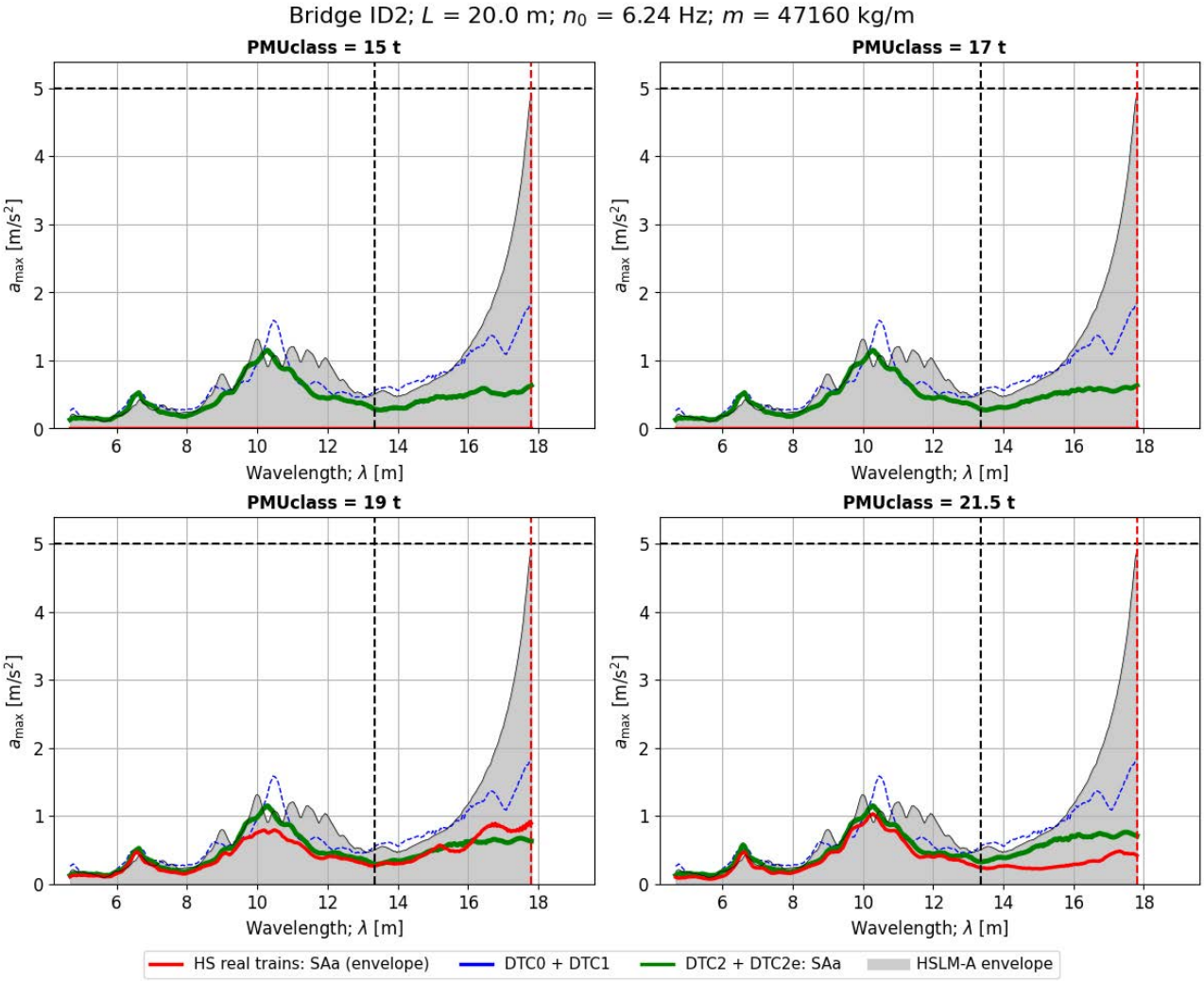

Figure 192. Peak vertical acceleration in the bridge ID2 when subject to real SAa trains of different weight categories, and comparison with the reference SAa train in DTCs. Time-stepping analysis.

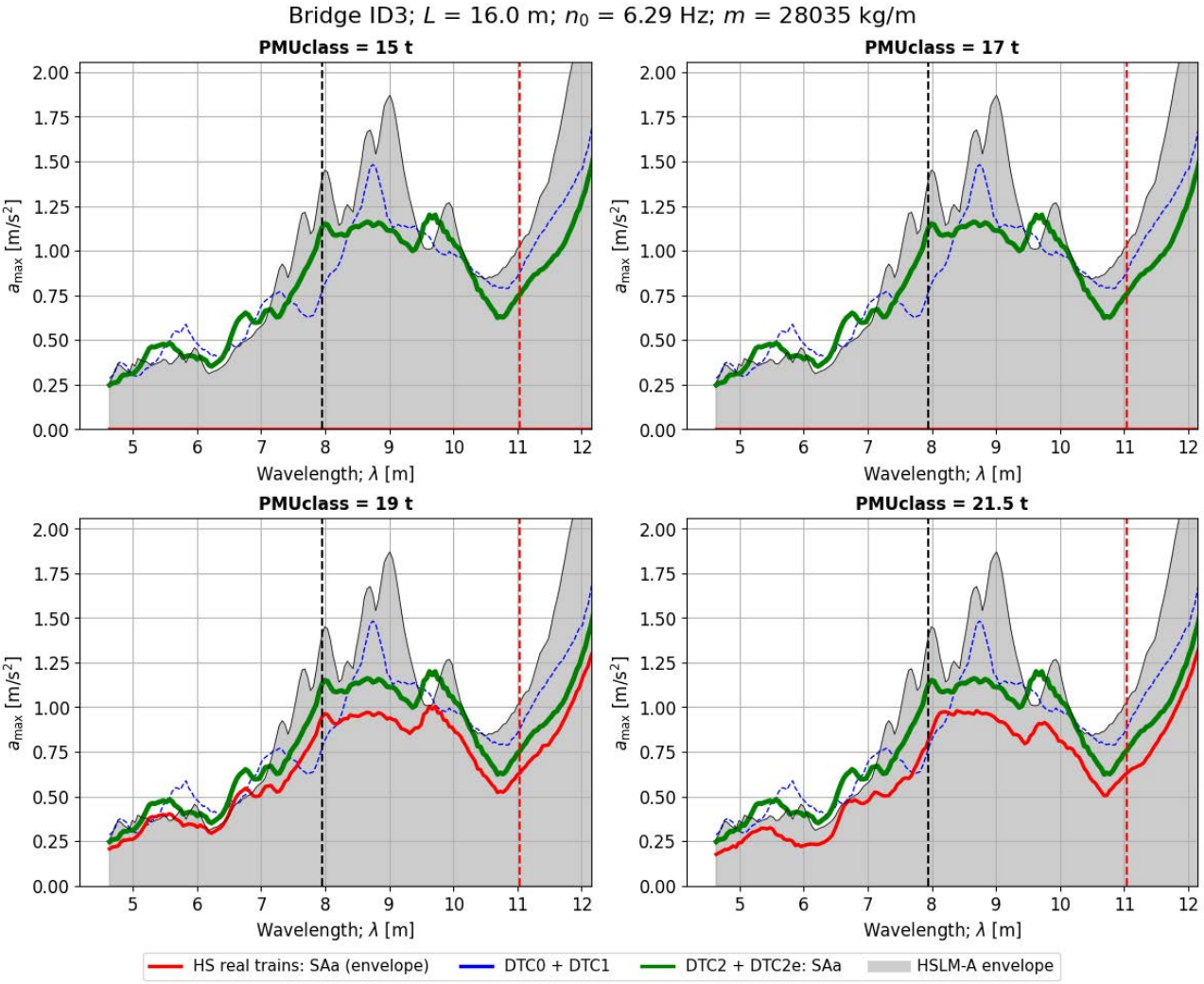

Figure 193. Peak vertical acceleration in the bridge ID3 when subject to real SAa trains of different weight categories, and comparison with the reference SAa train in DTCs. Time-stepping analysis.

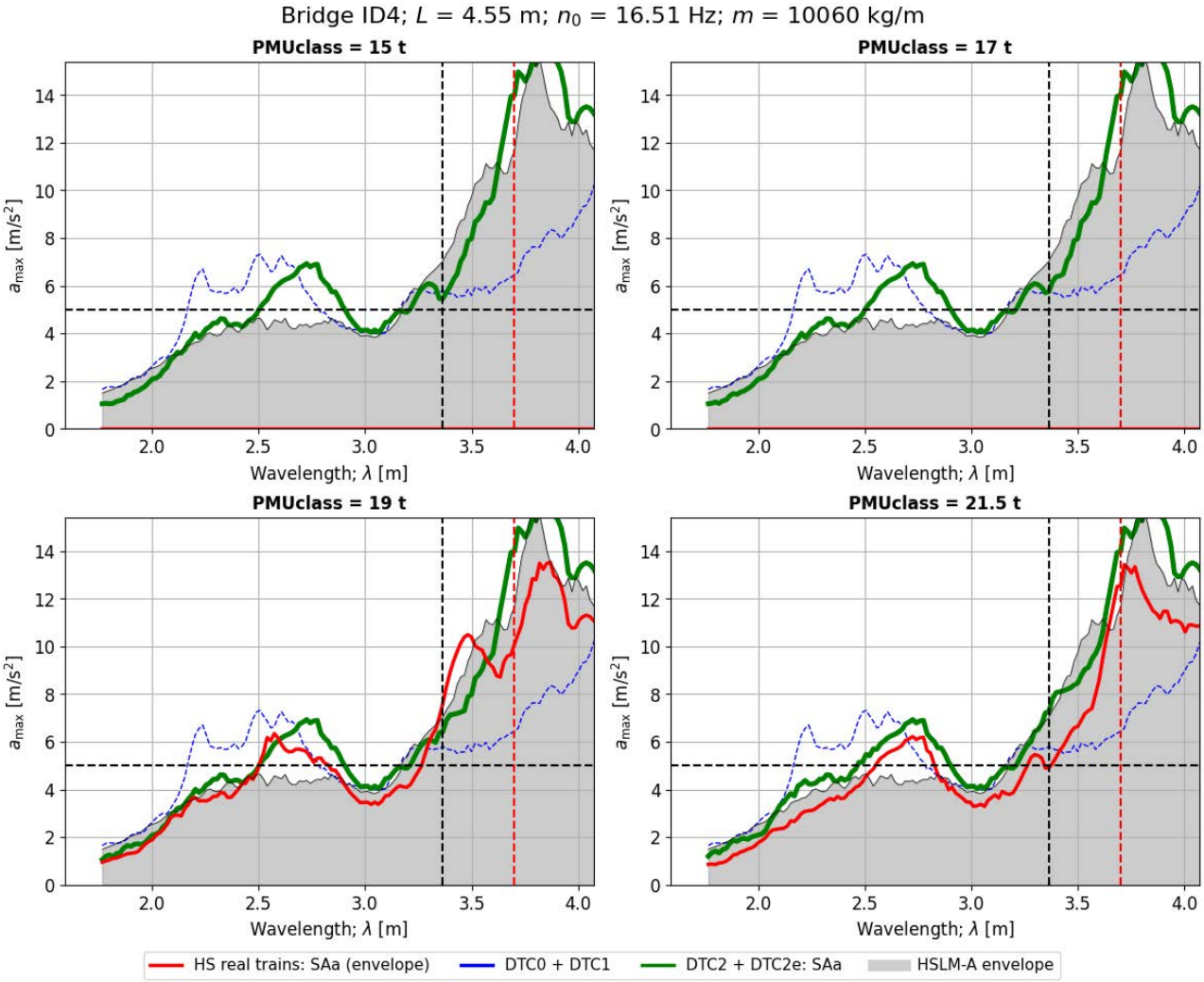

Figure 194. Peak vertical acceleration in the bridge ID4 when subject to real SAa trains of different weight categories, and comparison with the reference SAa train in DTCs. Time-stepping analysis.

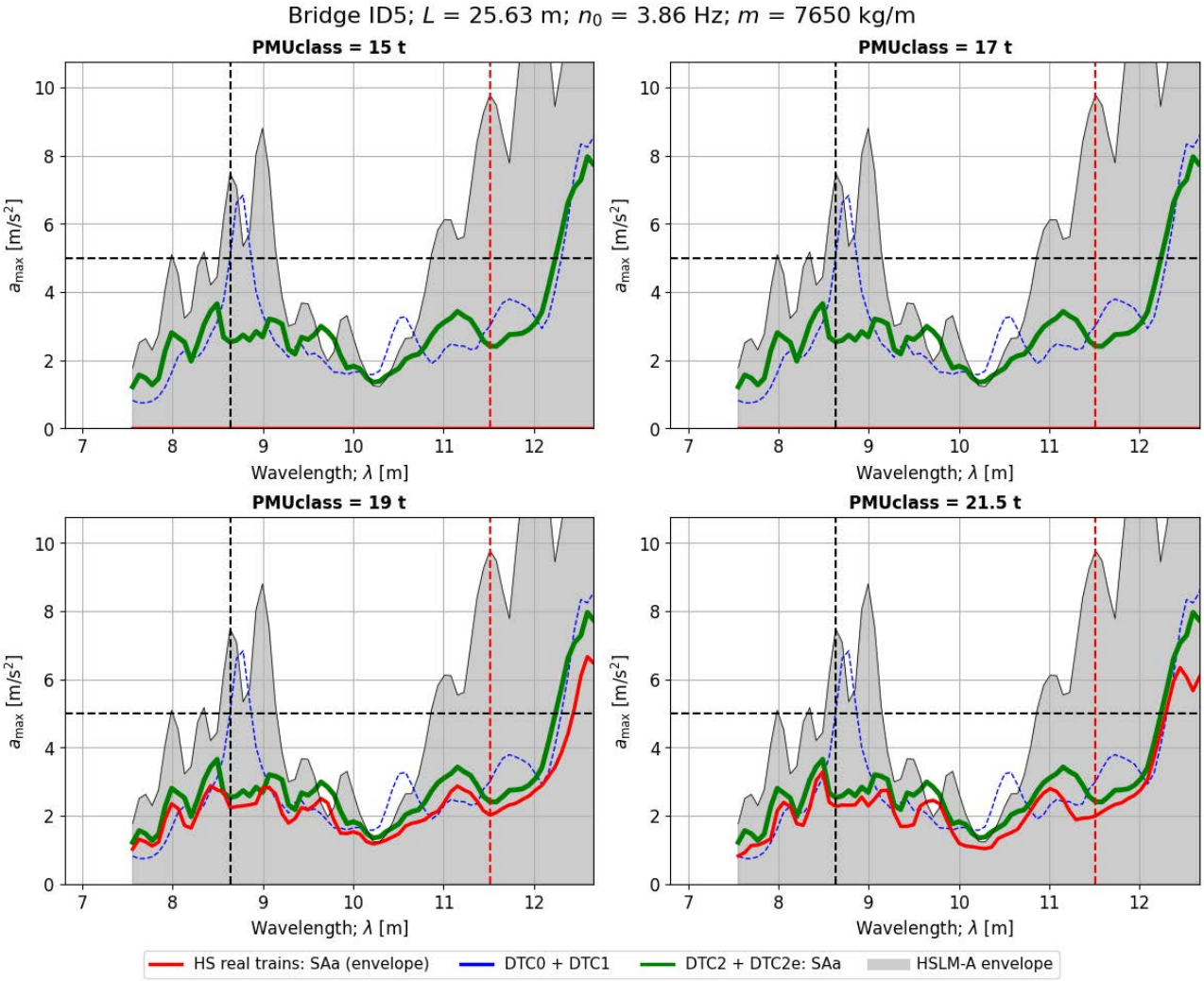

Figure 195. Peak vertical acceleration in the bridge ID5 when subject to real SAa trains of different weight categories, and comparison with the reference SAa train in DTCs. Time-stepping analysis.

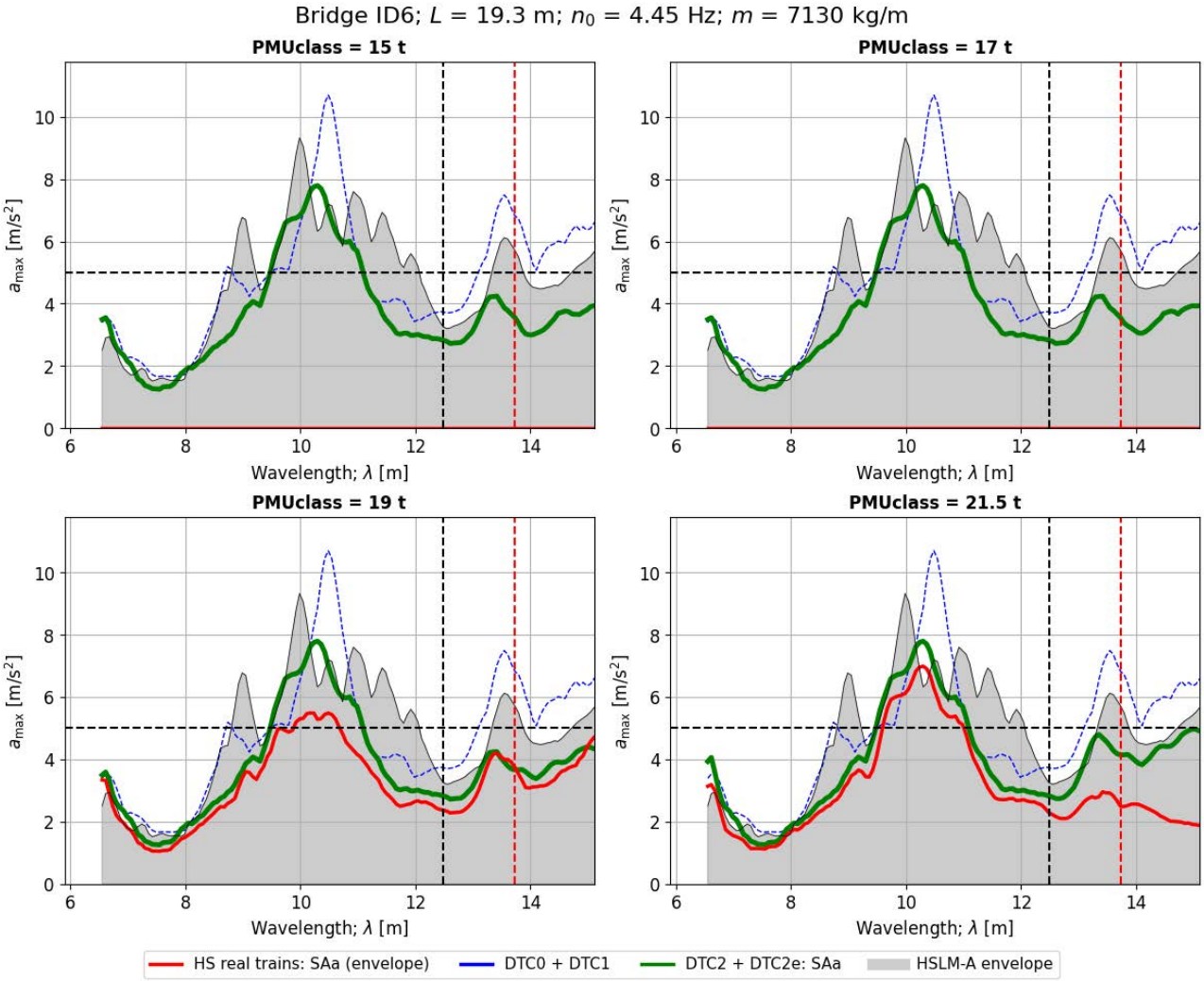

Figure 196. Peak vertical acceleration in the bridge ID6 when subject to real SAa trains of different weight categories, and comparison with the reference SAa train in DTCs. Time-stepping analysis.

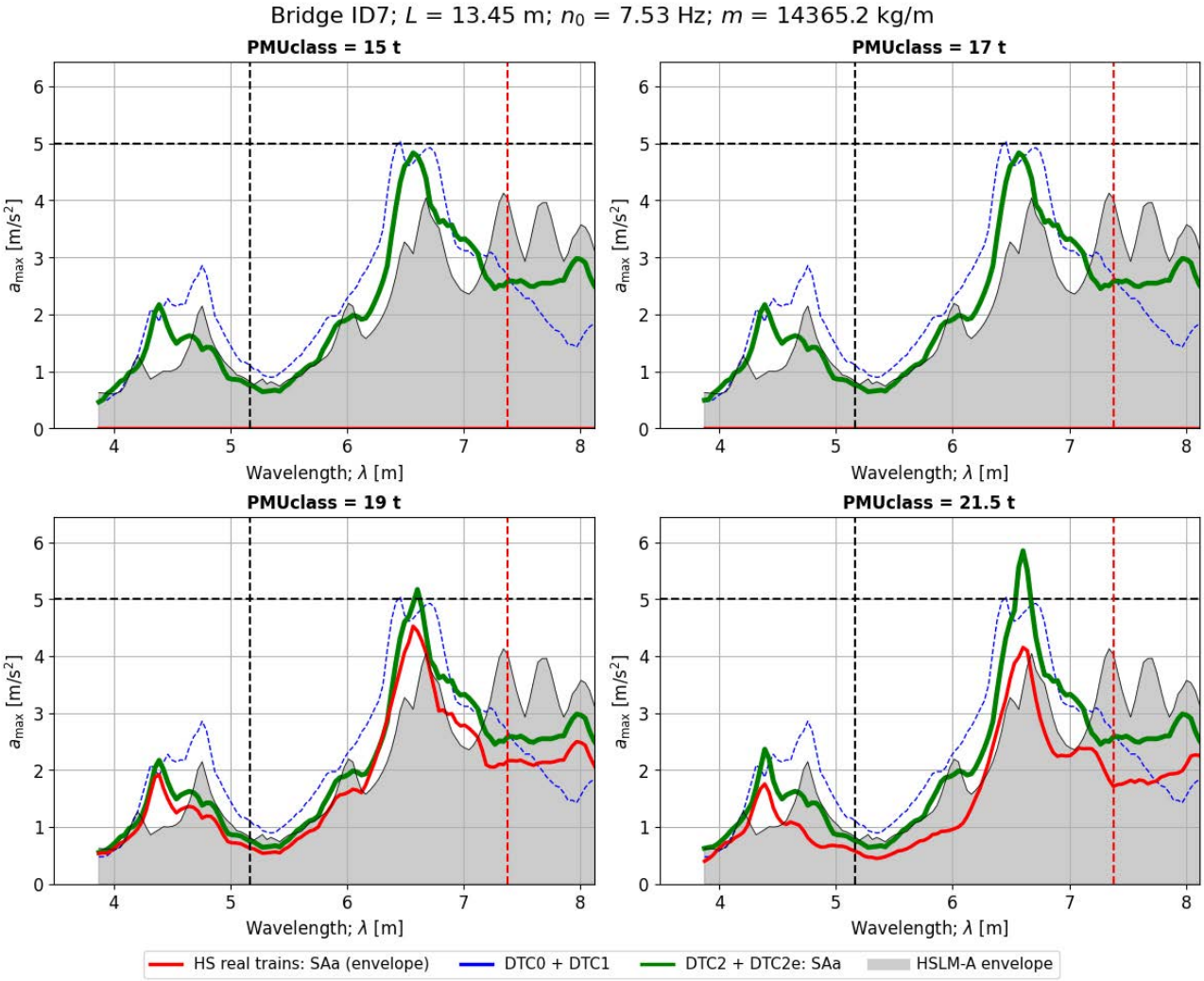

Figure 197. Peak vertical acceleration in the bridge ID7 when subject to real SAa trains of different weight categories, and comparison with the reference SAa train in DTCs. Time-stepping analysis.

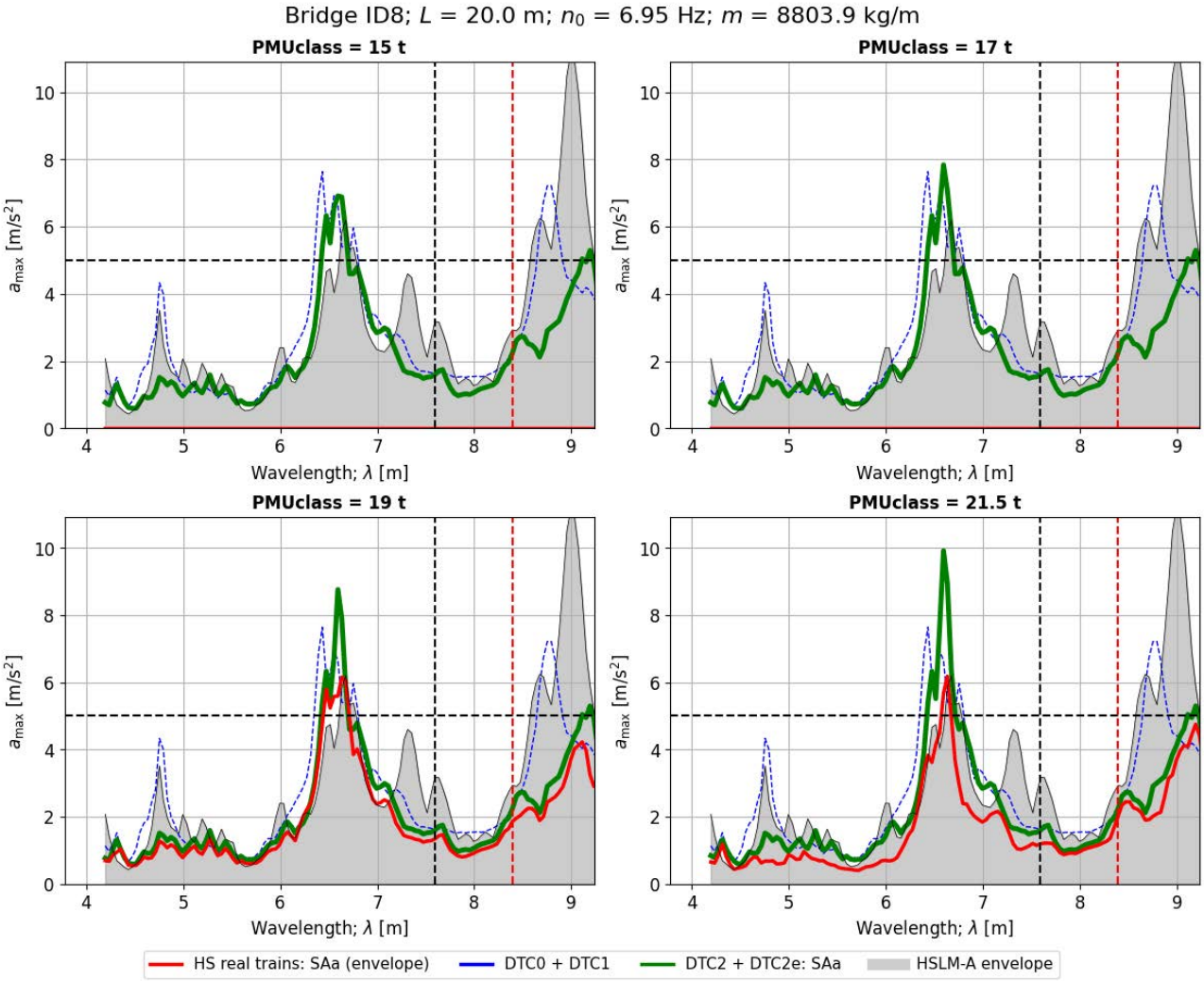

Figure 198. Peak vertical acceleration in the bridge ID8 when subject to real SAa trains of different weight categories, and comparison with the reference SAa train in DTCs. Time-stepping analysis.

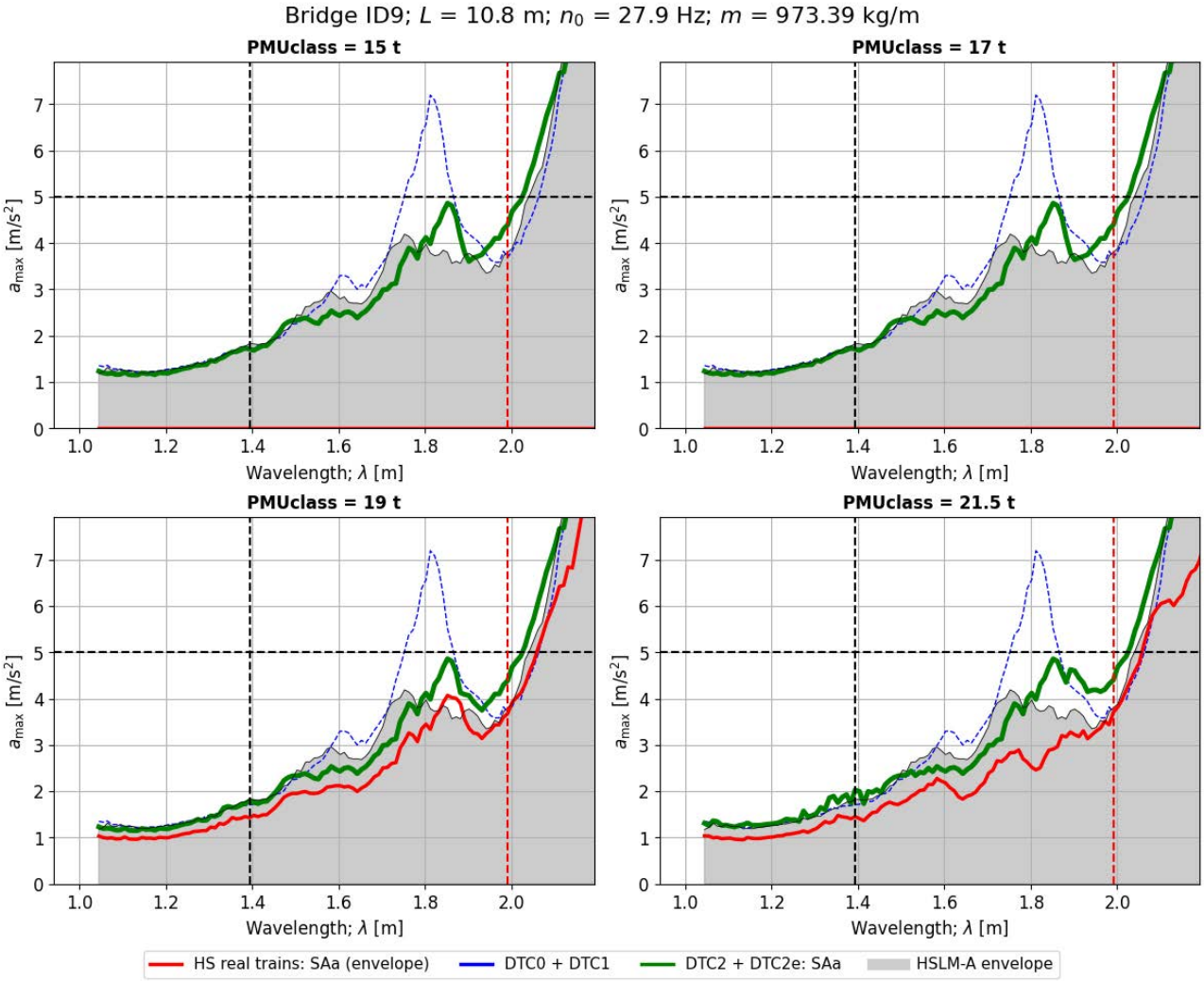

Figure 199. Peak vertical acceleration in the bridge ID9 when subject to real SAa trains of different weight categories, and comparison with the reference SAa train in DTCs. Time-stepping analysis.

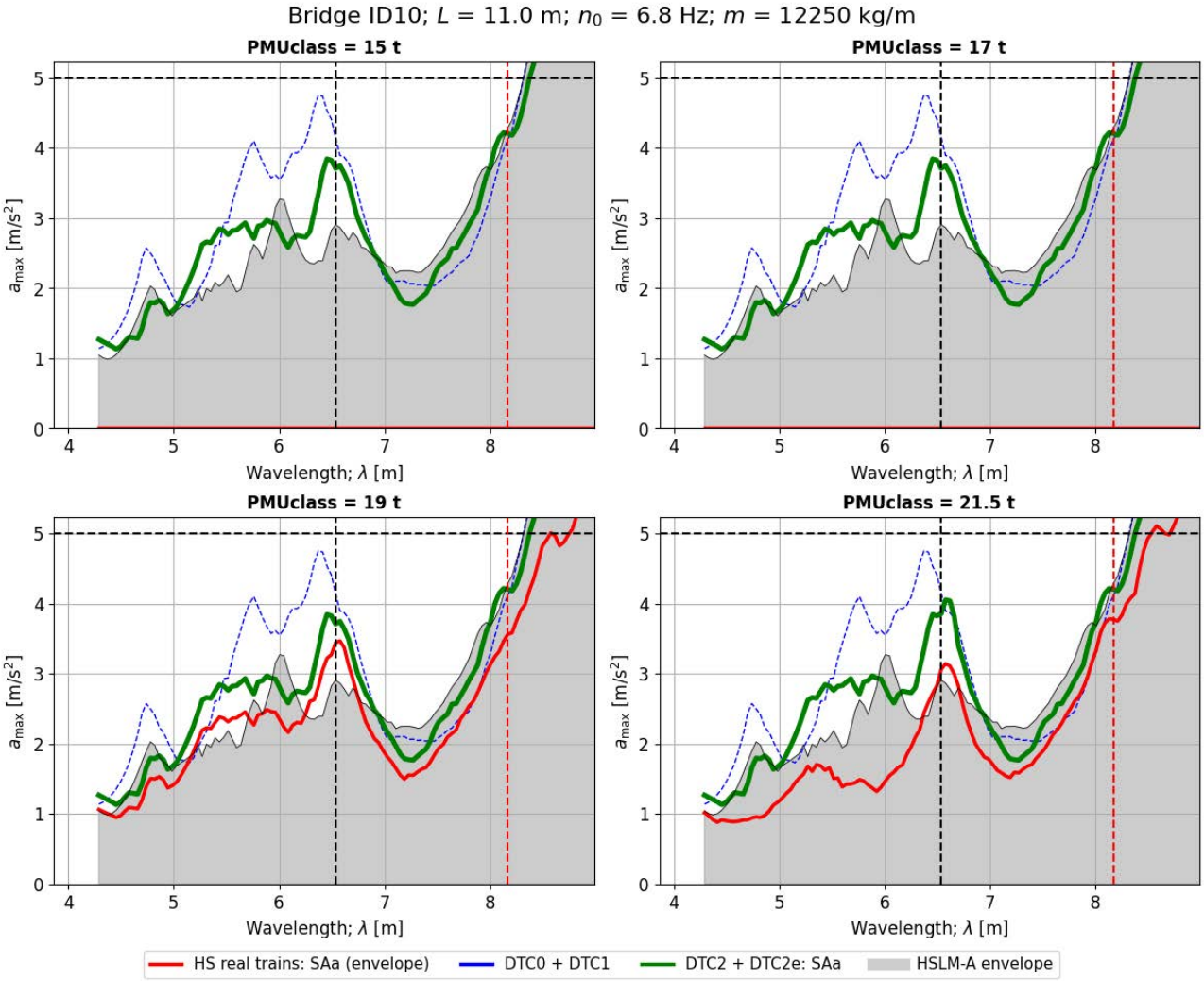

Figure 200. Peak vertical acceleration in the bridge ID10 when subject to real SAa trains of different weight categories, and comparison with the reference SAa train in DTCs. Time-stepping analysis.

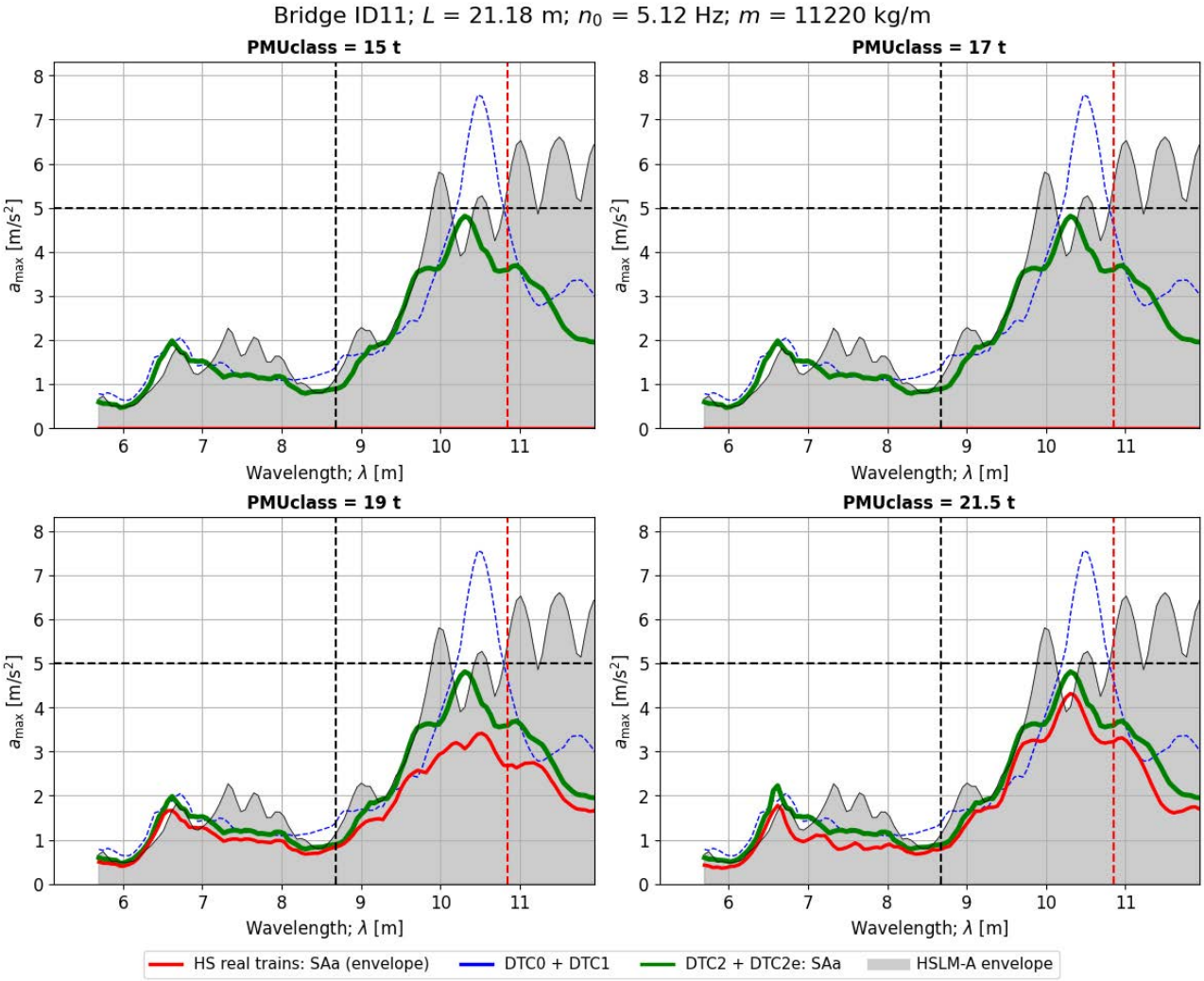

Figure 201. Peak vertical acceleration in the bridge ID11 when subject to real SAa trains of different weight categories, and comparison with the reference SAa train in DTCs. Time-stepping analysis.

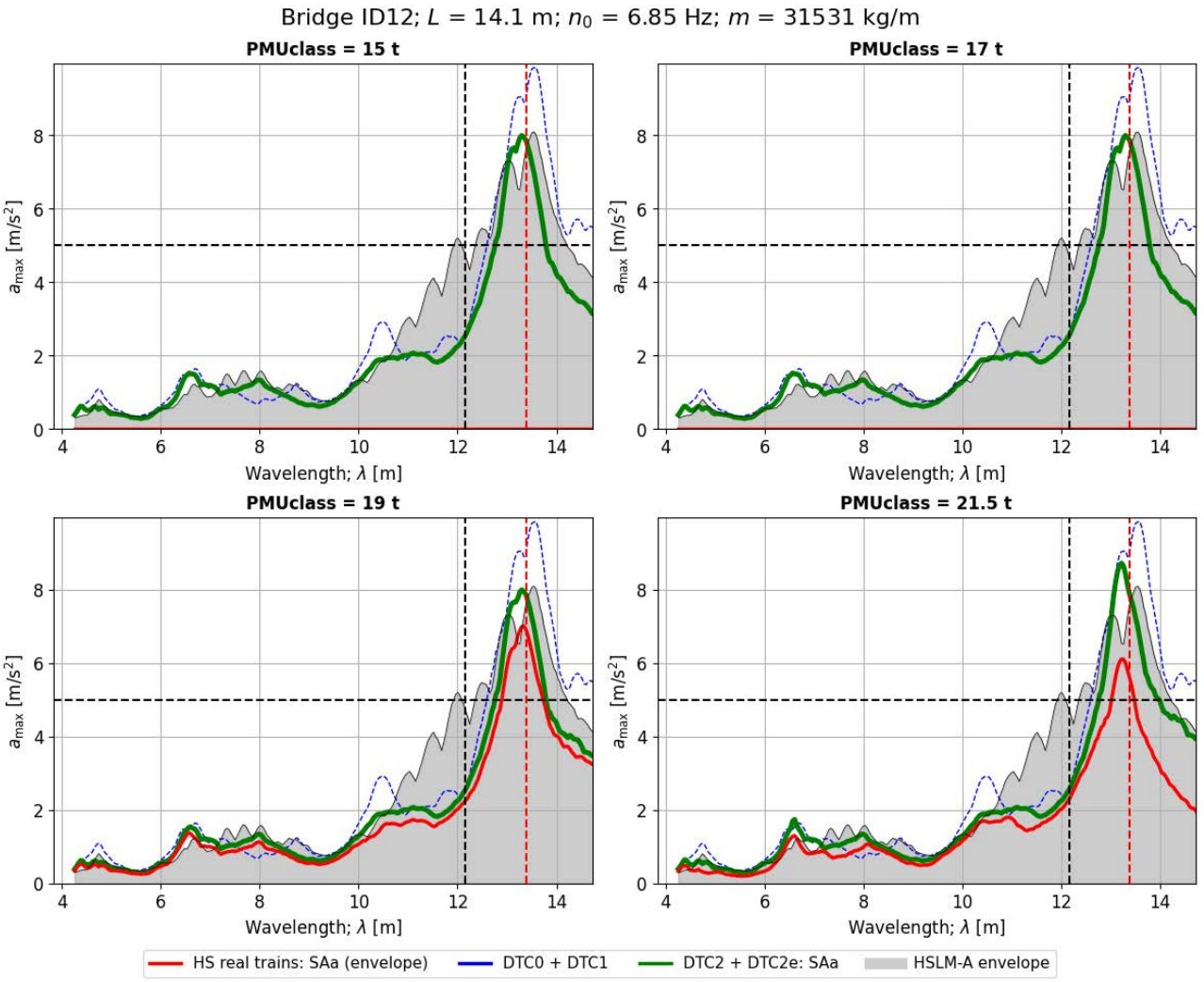

Figure 202. Peak vertical acceleration in the bridge ID12 when subject to real SAa trains of different weight categories, and comparison with the reference SAa train in DTCs. Time-stepping analysis.

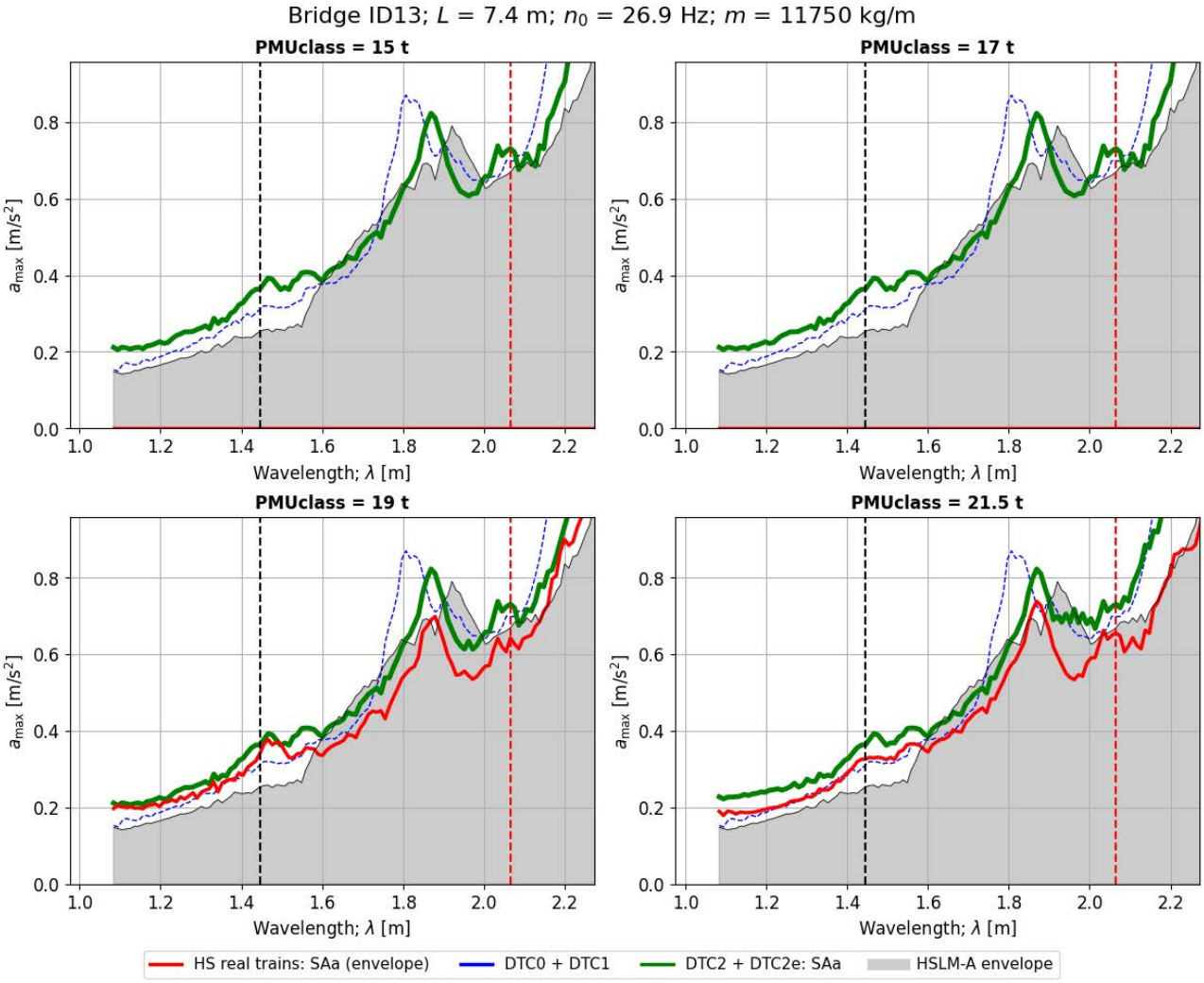

Figure 203. Peak vertical acceleration in the bridge ID13 when subject to real SAa trains of different weight categories, and comparison with the reference SAa train in DTCs. Time-stepping analysis.

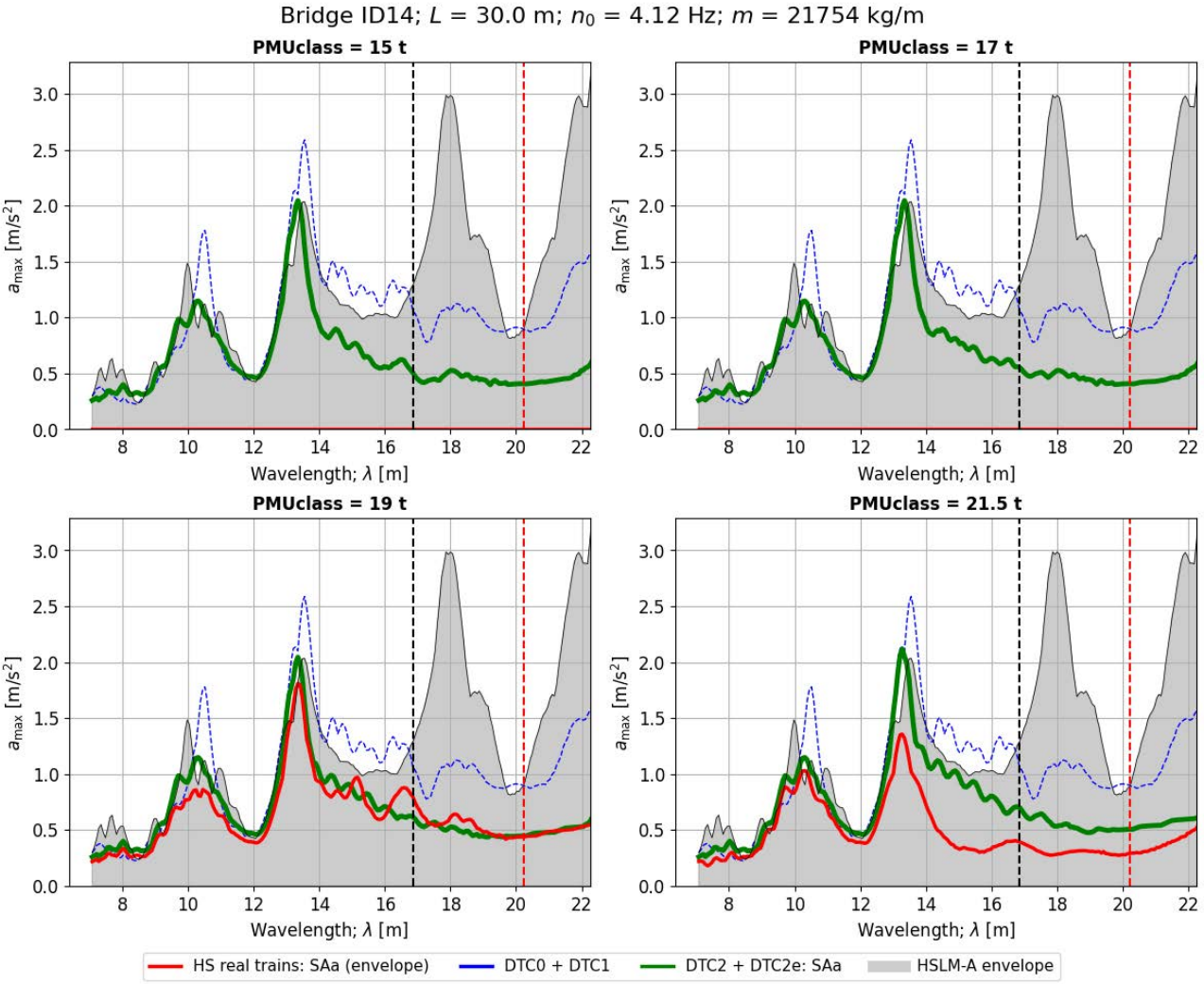

Figure 204. Peak vertical acceleration in the bridge ID14 when subject to real SAa trains of different weight categories, and comparison with the reference SAa train in DTCs. Time-stepping analysis.

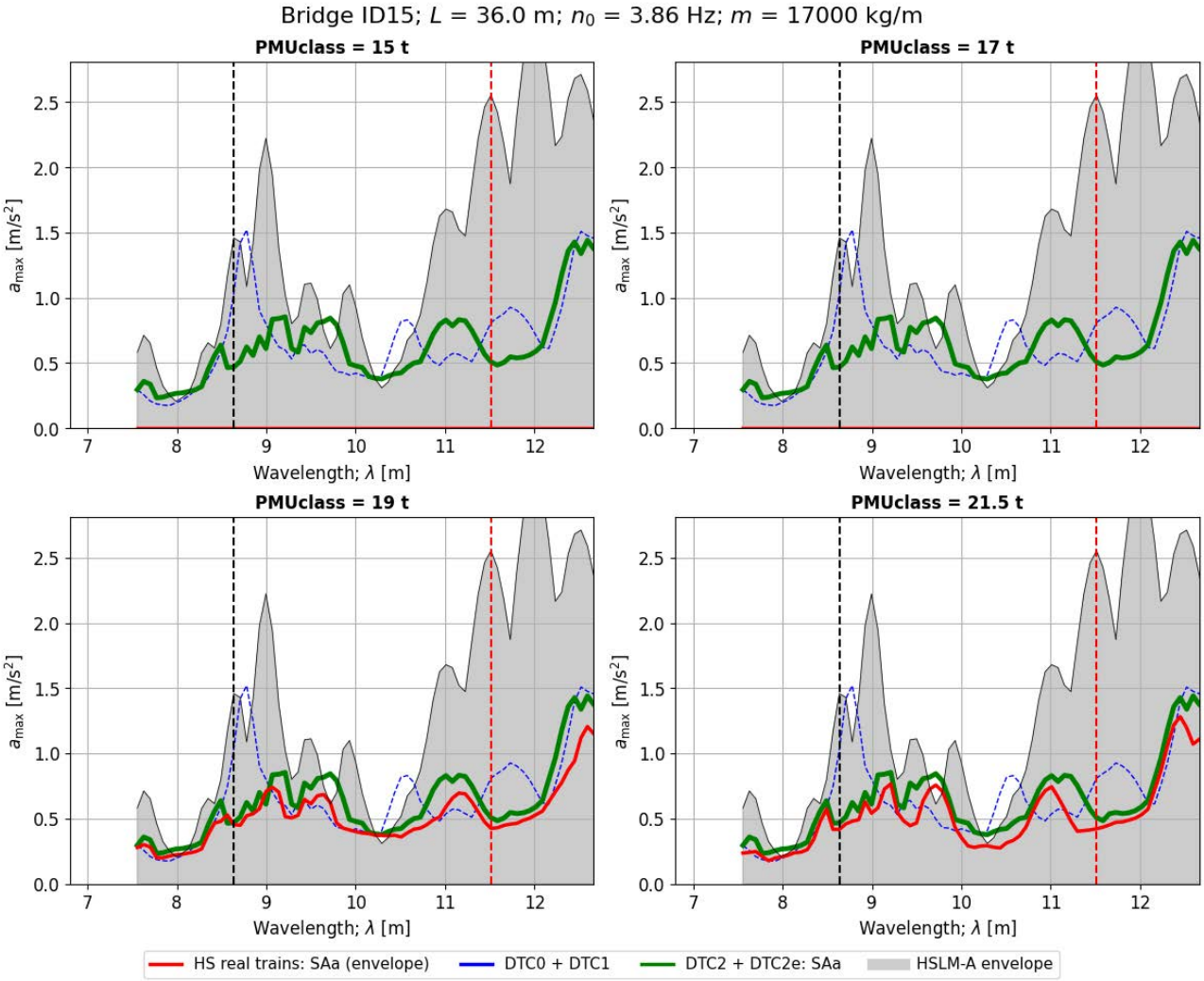

Figure 205. Peak vertical acceleration in the bridge ID15 when subject to real SAa trains of different weight categories, and comparison with the reference SAa train in DTCs. Time-stepping analysis.

SAb trains

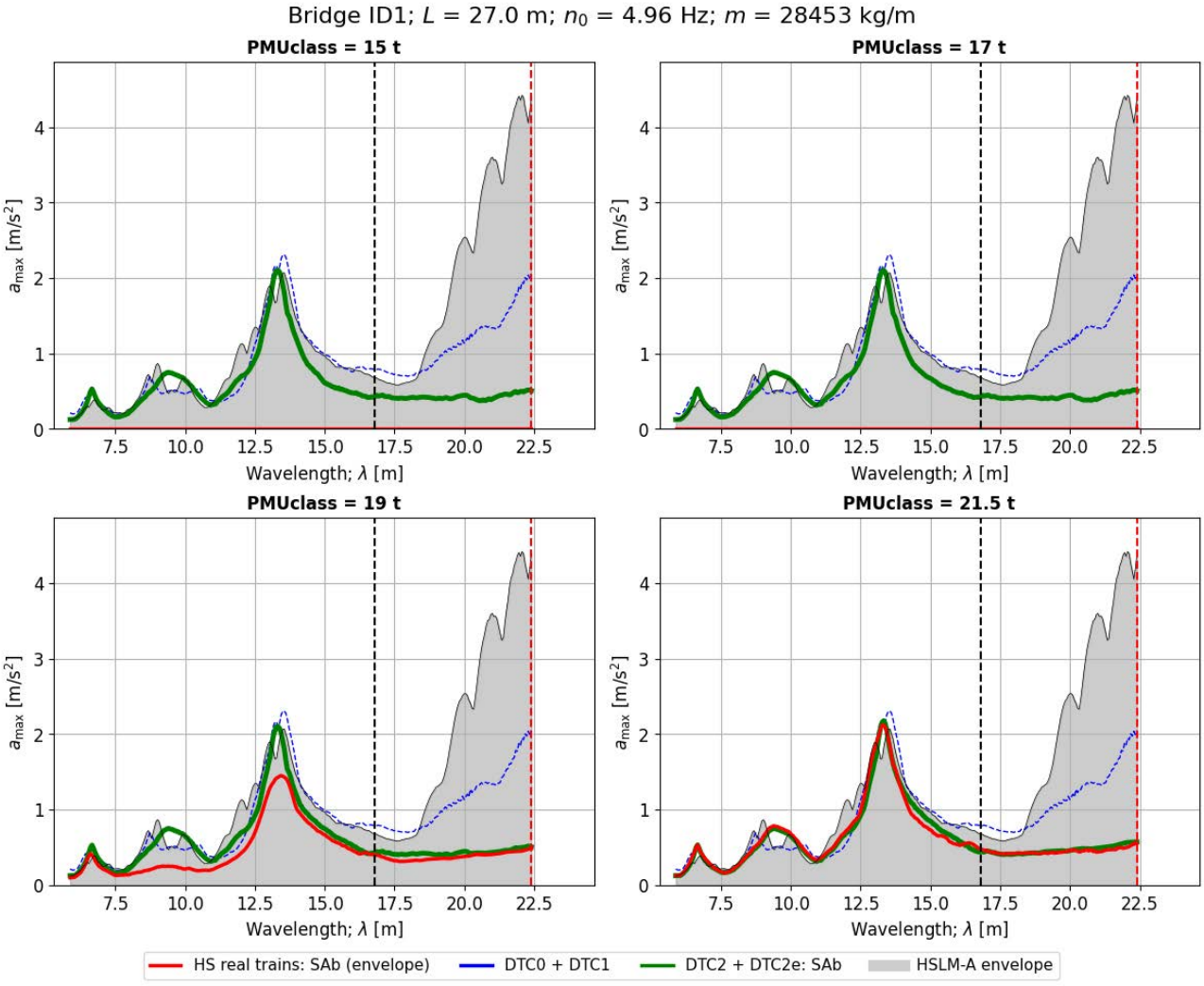

Figure 206. Peak vertical acceleration in the bridge ID1 when subject to real SAb trains of different weight categories, and comparison with the reference SAb train in DTCs. Time-stepping analysis.

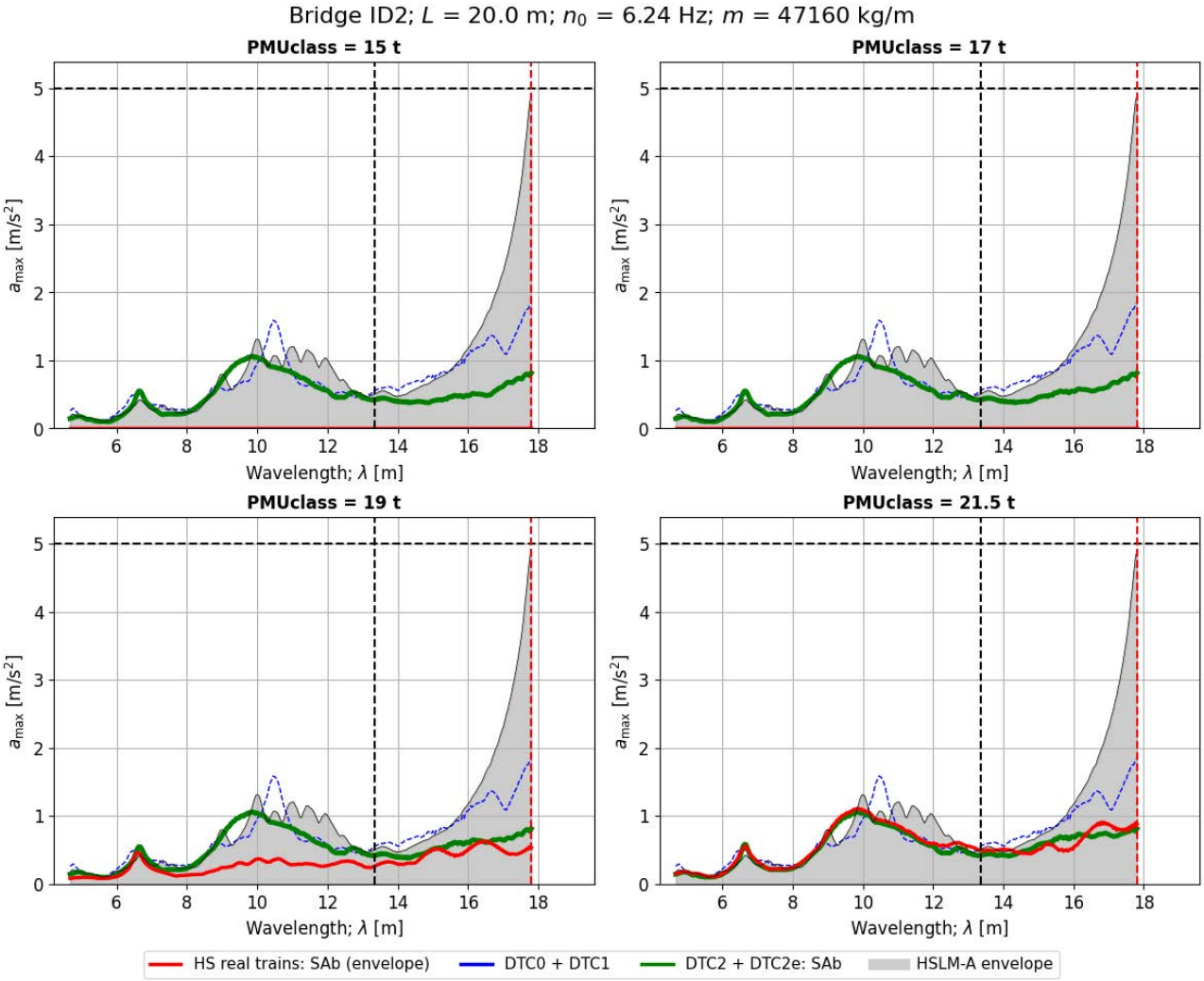

Figure 207. Peak vertical acceleration in the bridge ID2 when subject to real SAb trains of different weight categories, and comparison with the reference SAb train in DTCs. Time-stepping analysis.

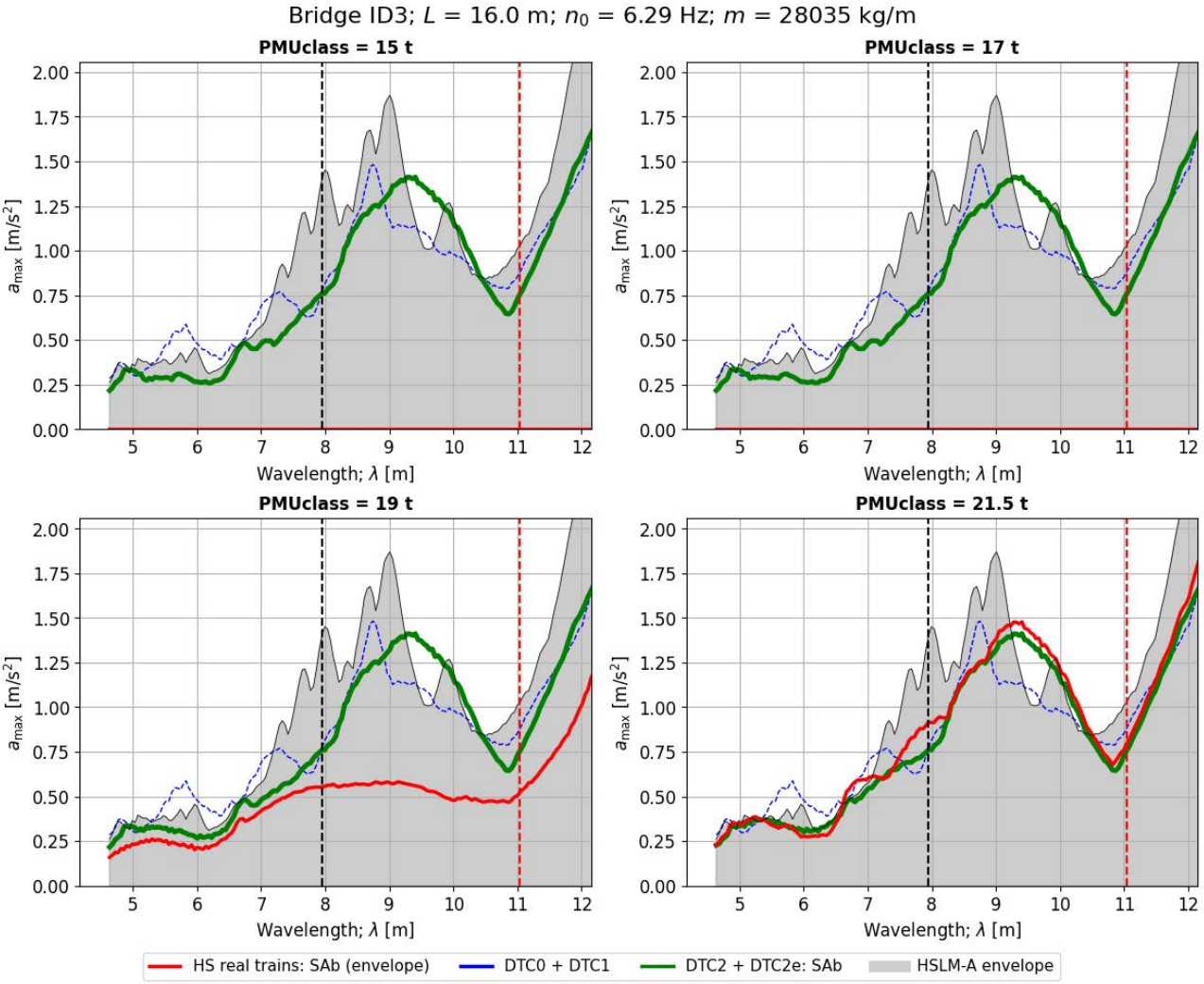

Figure 208. Peak vertical acceleration in the bridge ID3 when subject to real SAb trains of different weight categories, and comparison with the reference SAb train in DTCs. Time-stepping analysis.

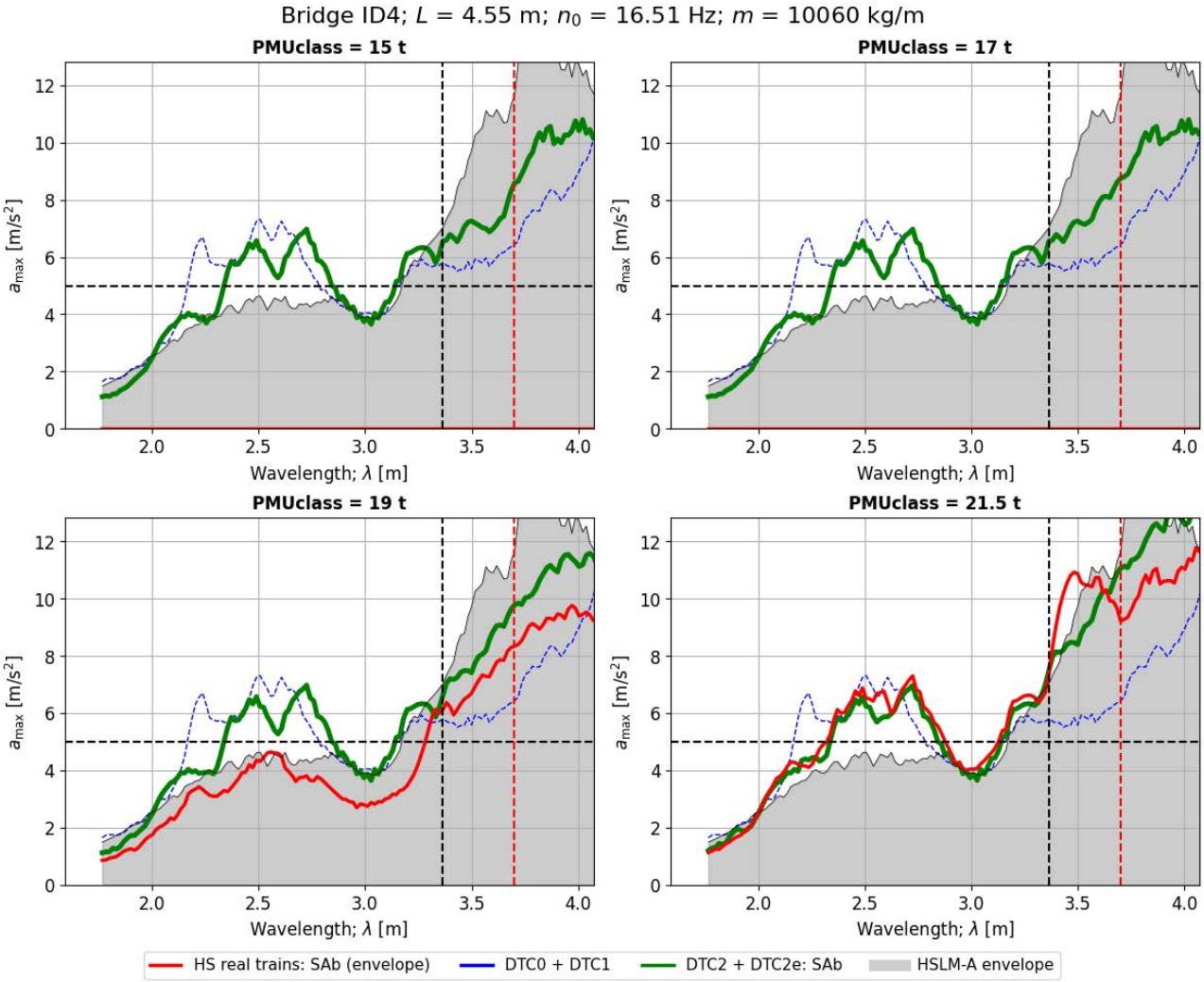

Figure 209. Peak vertical acceleration in the bridge ID4 when subject to real SAb trains of different weight categories, and comparison with the reference SAb train in DTCs. Time-stepping analysis.

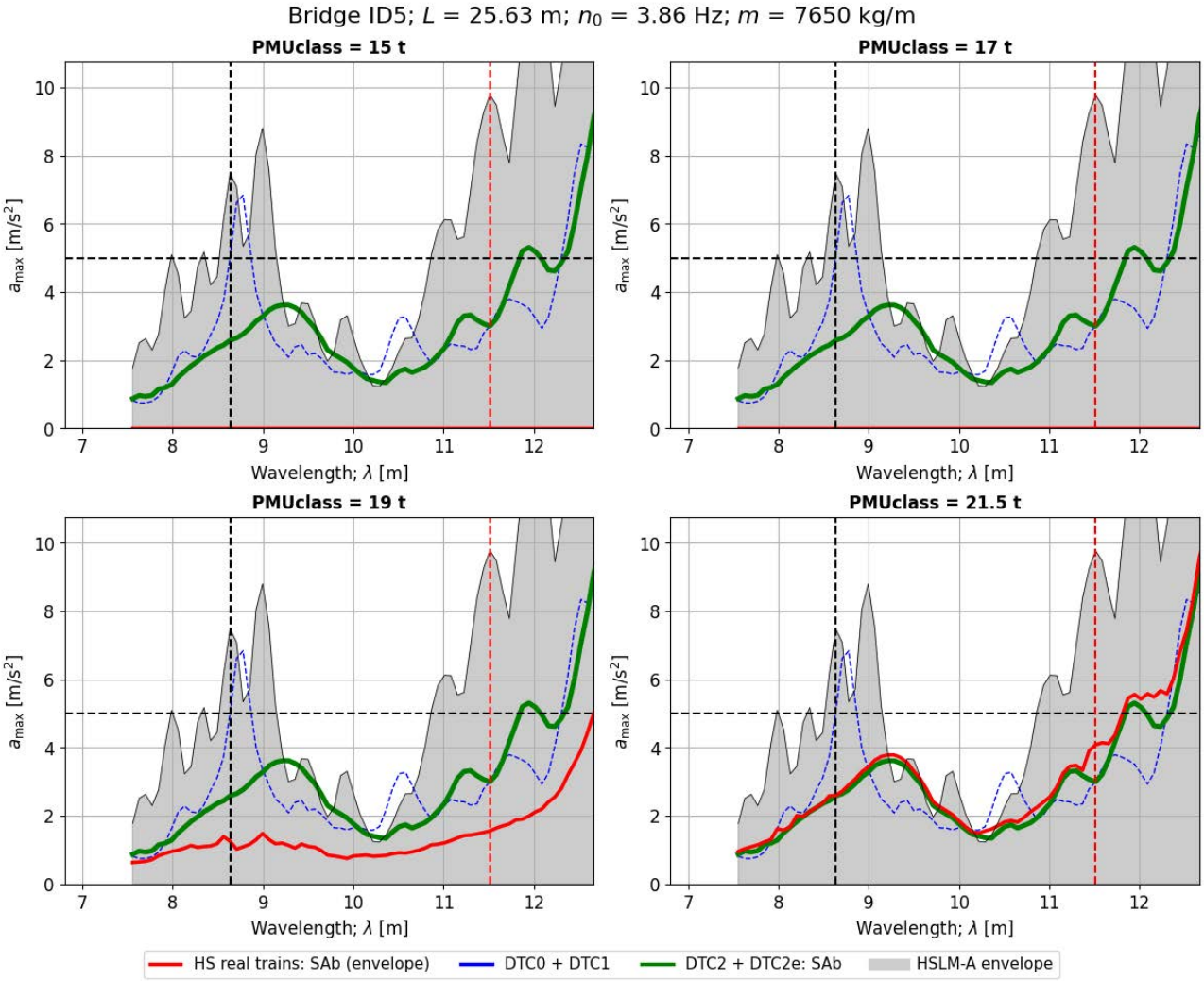

Figure 210. Peak vertical acceleration in the bridge ID5 when subject to real SAb trains of different weight categories, and comparison with the reference SAb train in DTCs. Time-stepping analysis.

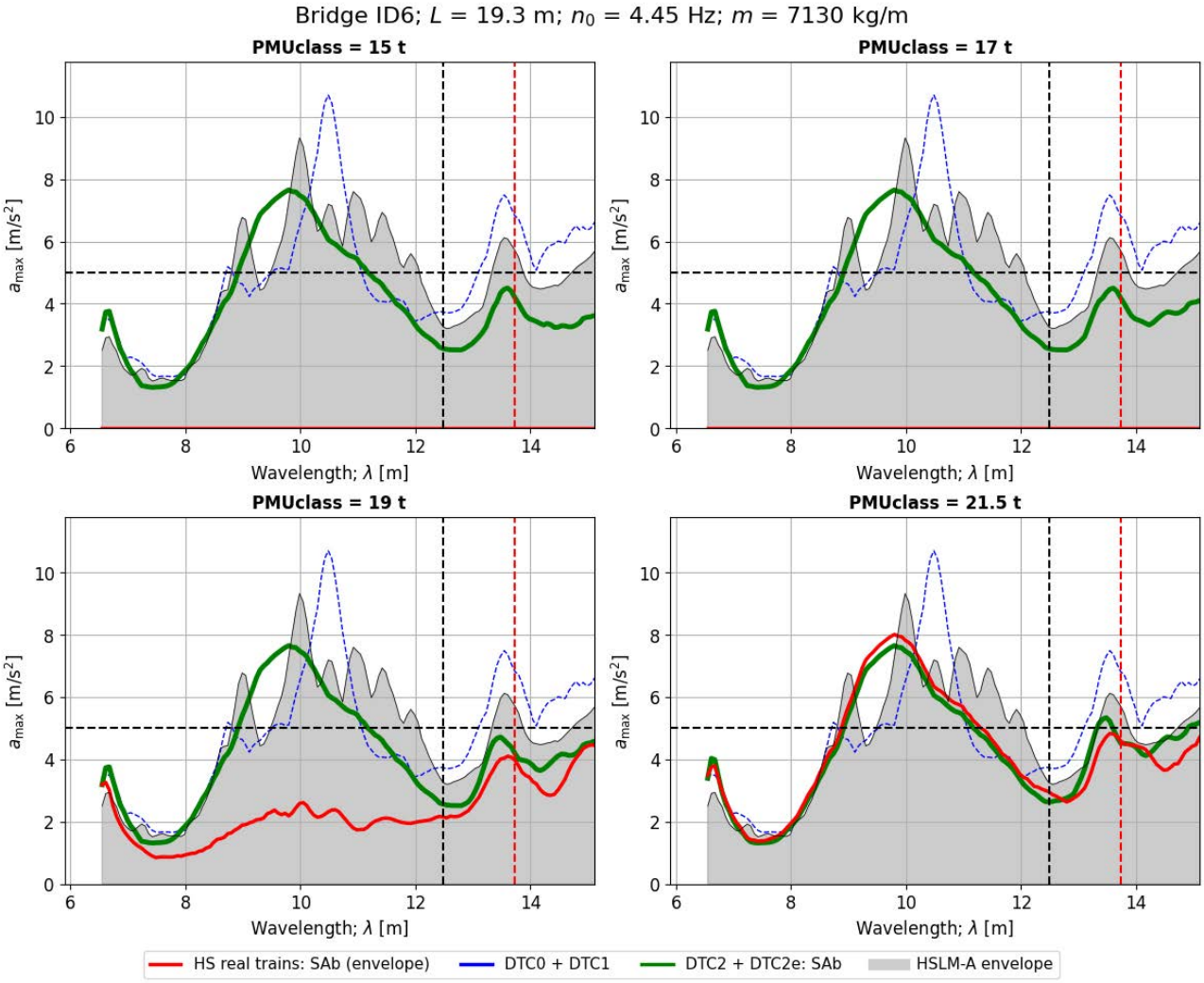

Figure 211. Peak vertical acceleration in the bridge ID6 when subject to real SAb trains of different weight categories, and comparison with the reference SAb train in DTCs. Time-stepping analysis.

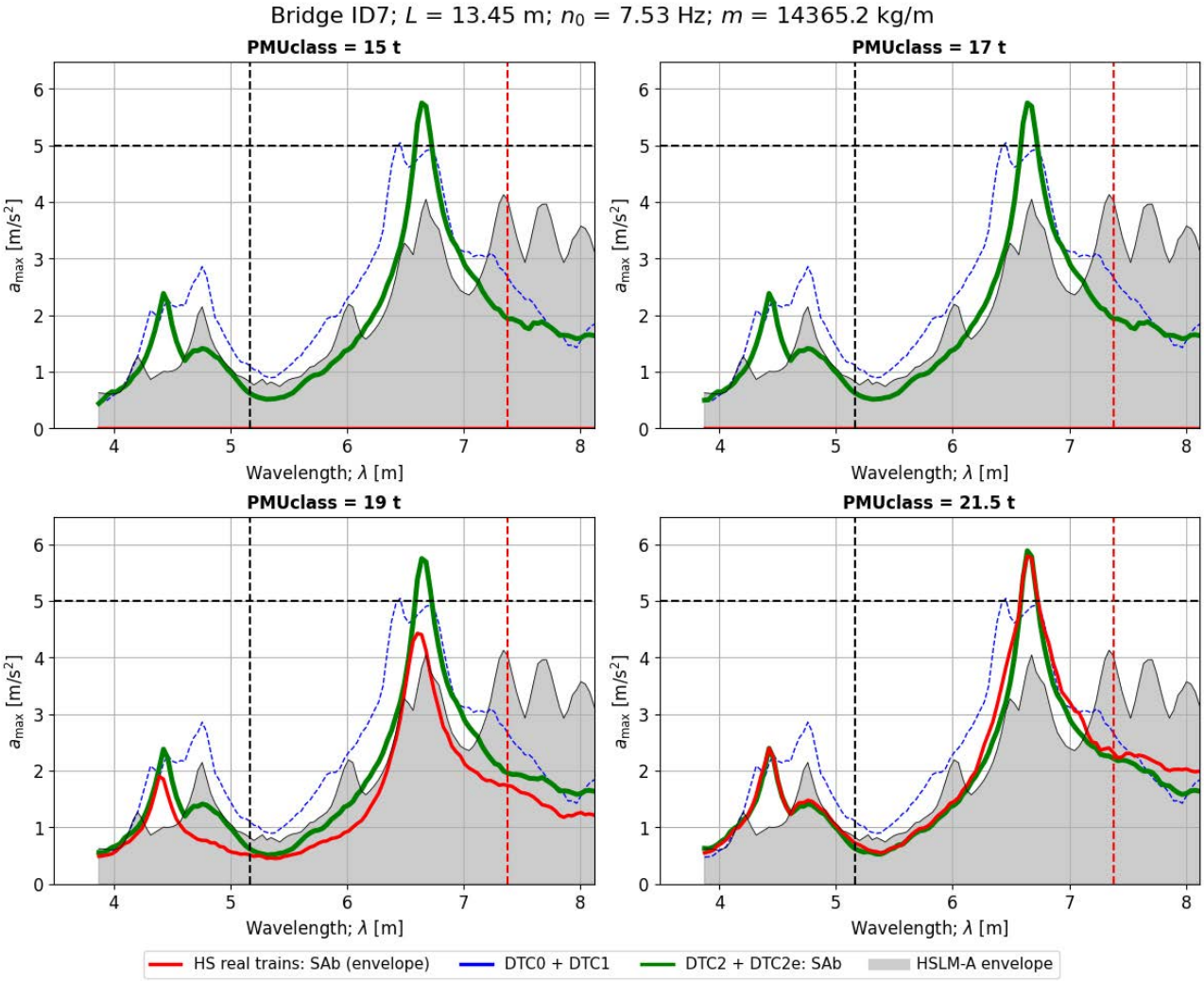

Figure 212. Peak vertical acceleration in the bridge ID7 when subject to real SAb trains of different weight categories, and comparison with the reference SAb train in DTCs. Time-stepping analysis.

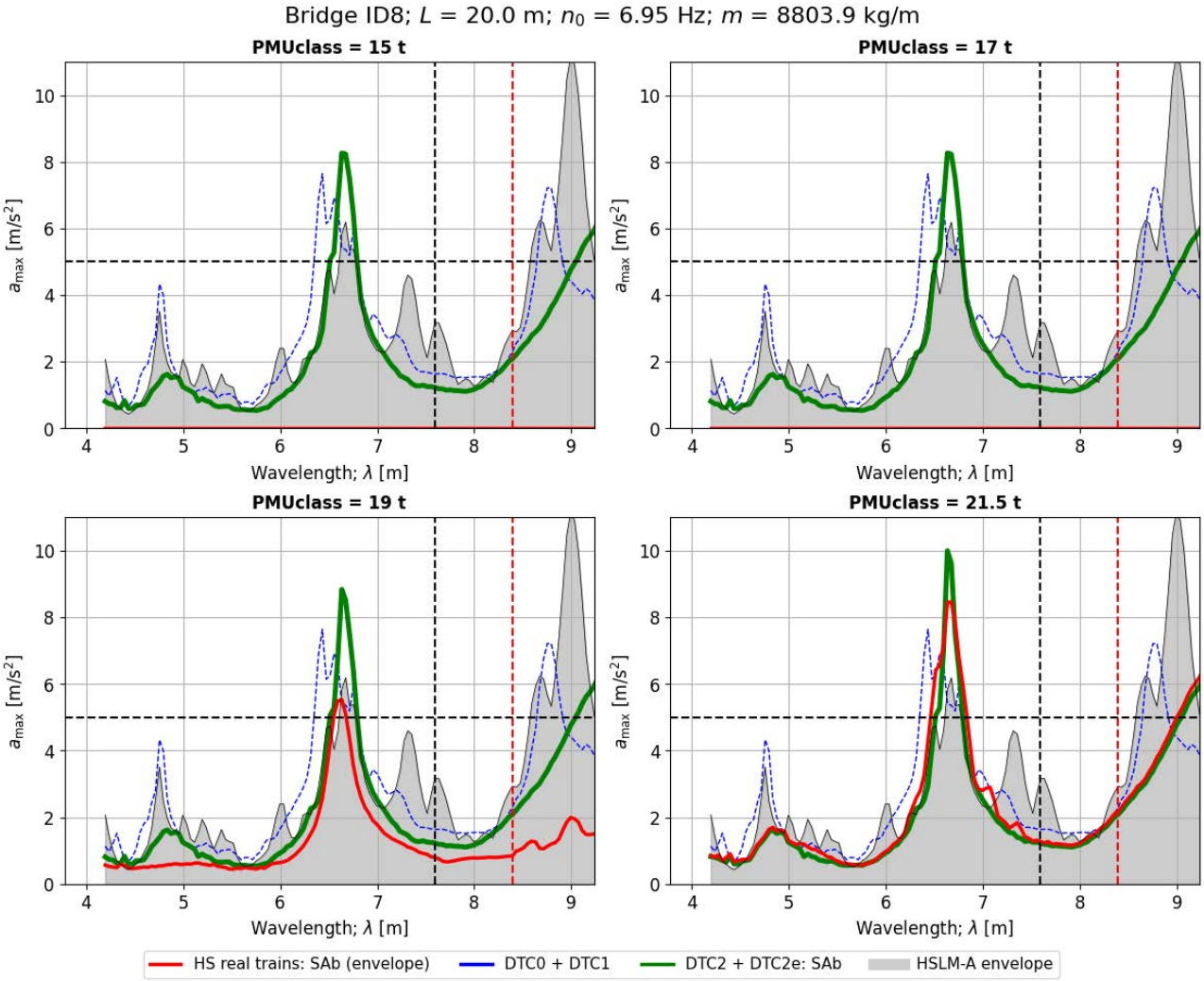

Figure 213. Peak vertical acceleration in the bridge ID8 when subject to real SAb trains of different weight categories, and comparison with the reference SAb train in DTCs. Time-stepping analysis.

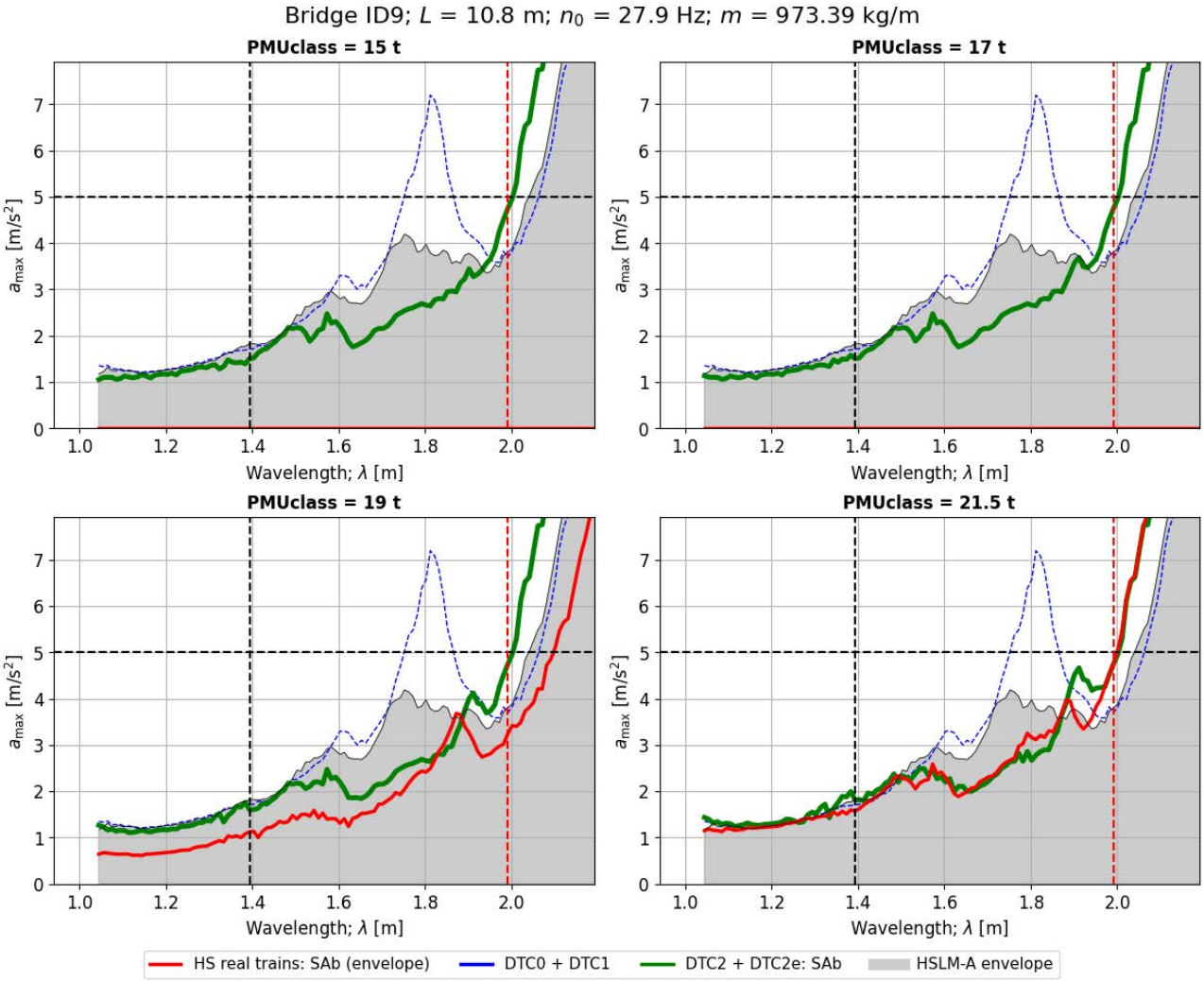

Figure 214. Peak vertical acceleration in the bridge ID9 when subject to real SAb trains of different weight categories, and comparison with the reference SAb train in DTCs. Time-stepping analysis.

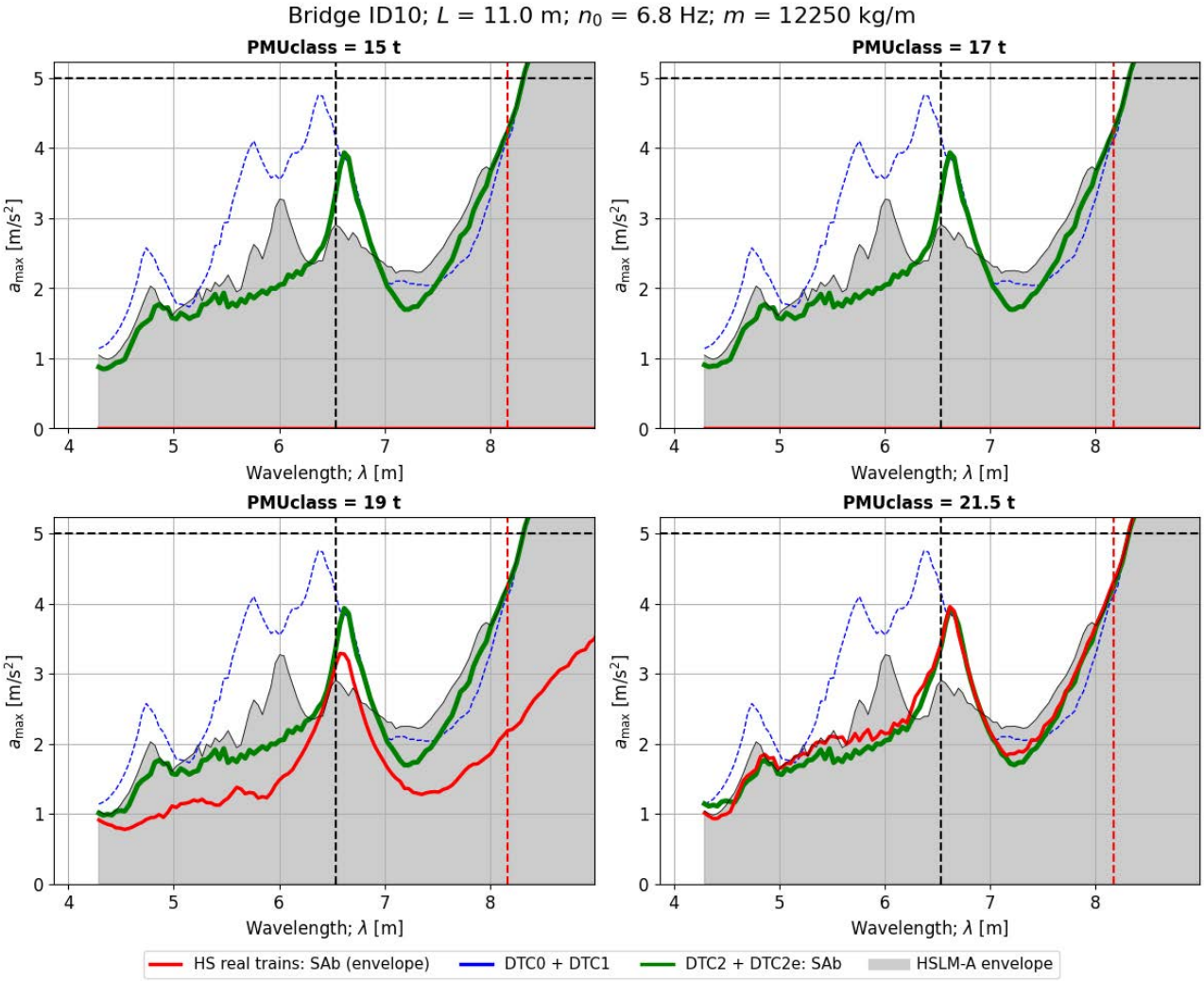

Figure 215. Peak vertical acceleration in the bridge ID10 when subject to real SAb trains of different weight categories, and comparison with the reference SAb train in DTCs. Time-stepping analysis.

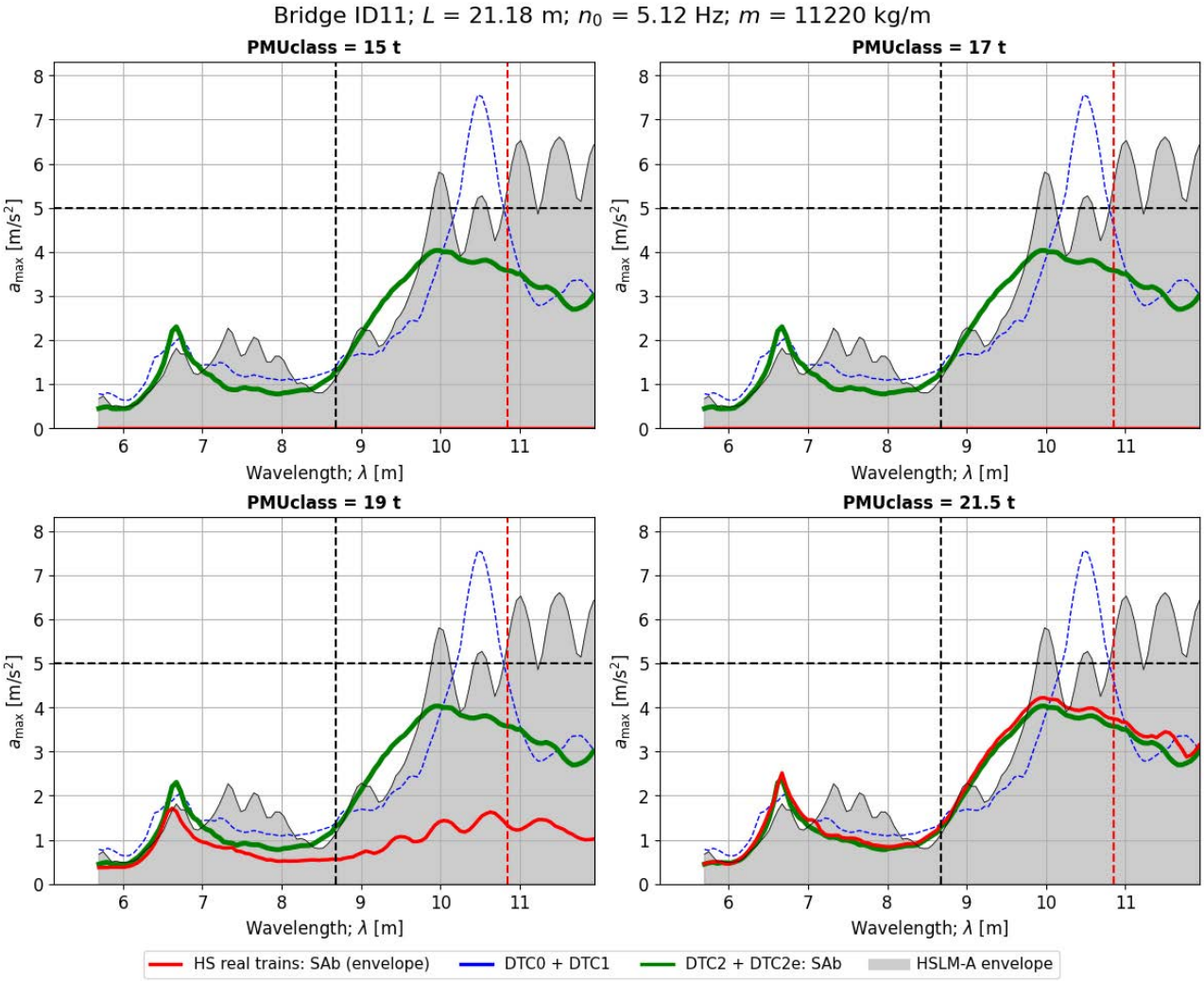

Figure 216. Peak vertical acceleration in the bridge ID11 when subject to real SAb trains of different weight categories, and comparison with the reference SAb train in DTCs. Time-stepping analysis.

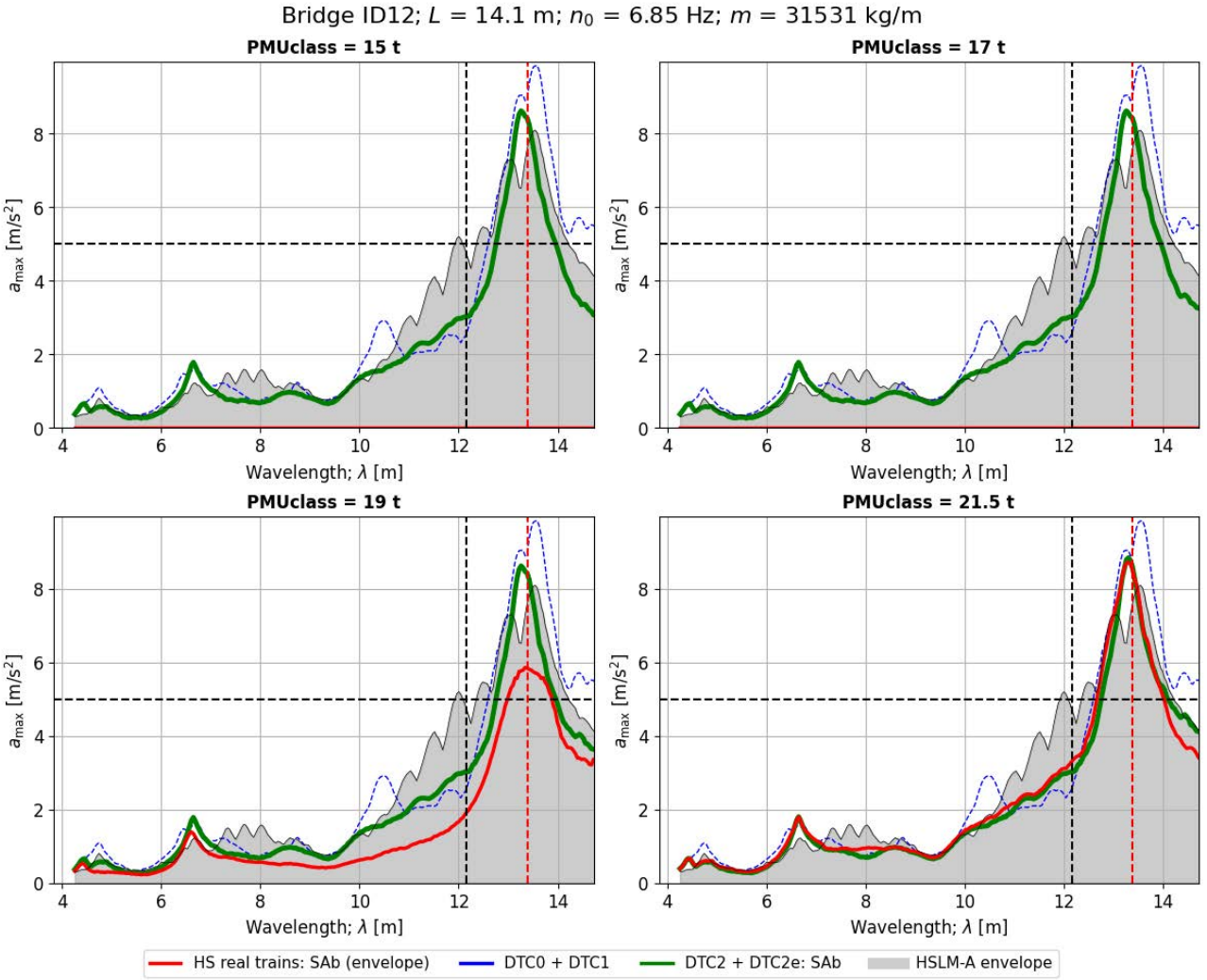

Figure 217. Peak vertical acceleration in the bridge ID12 when subject to real SAb trains of different weight categories, and comparison with the reference SAb train in DTCs. Time-stepping analysis.

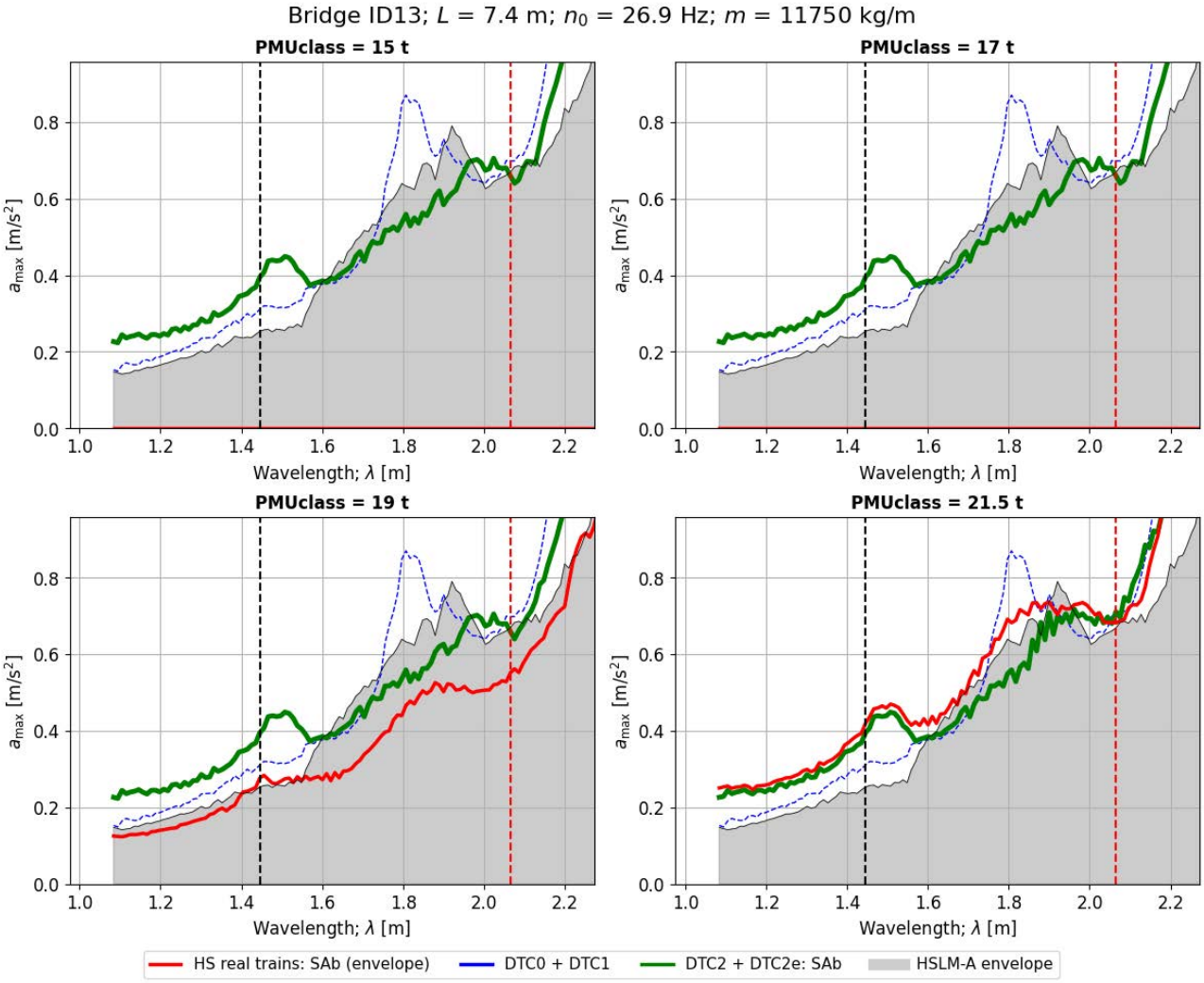

Figure 218. Peak vertical acceleration in the bridge ID13 when subject to real SAb trains of different weight categories, and comparison with the reference SAb train in DTCs. Time-stepping analysis.

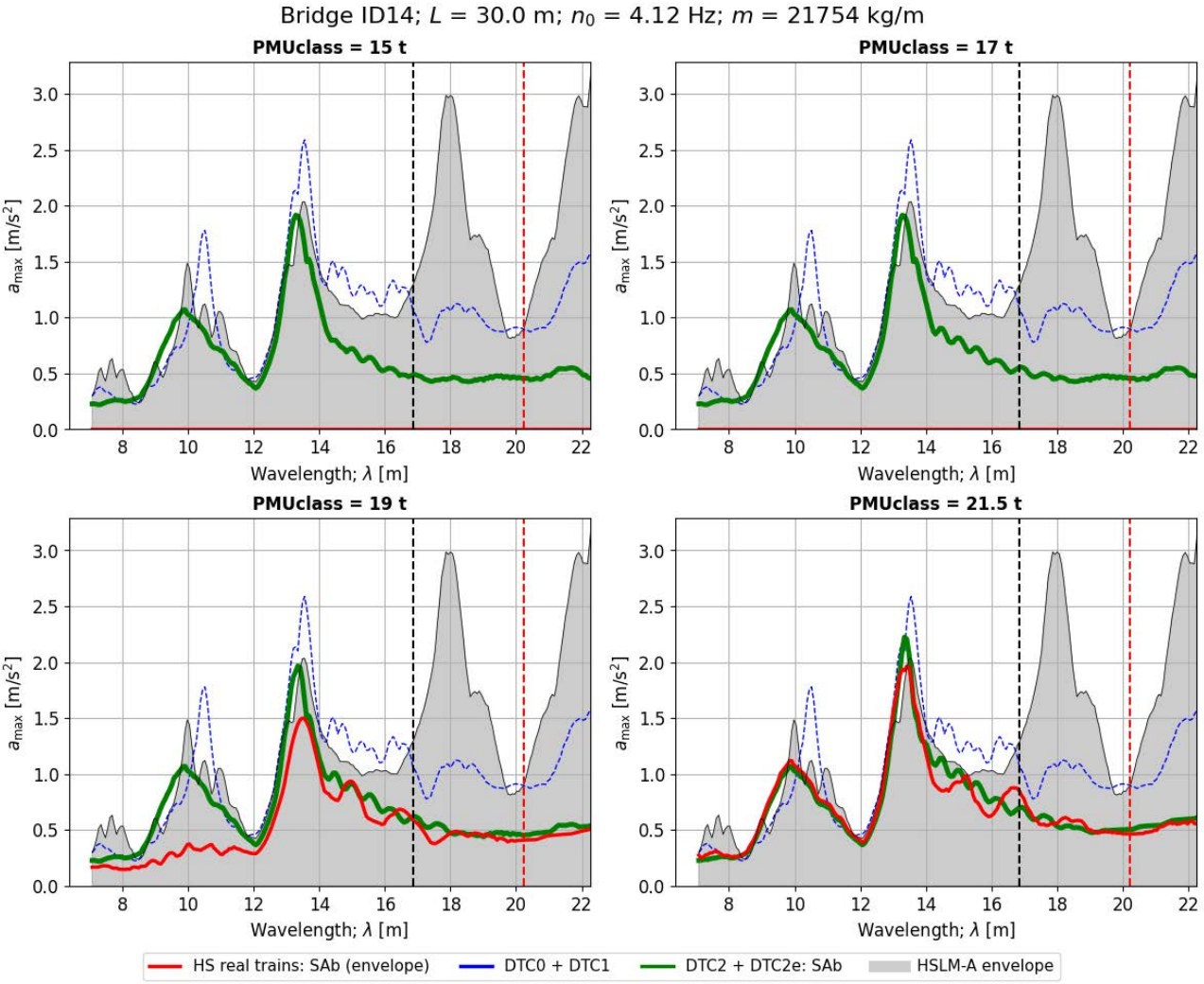

Figure 219. Peak vertical acceleration in the bridge ID14 when subject to real SAb trains of different weight categories, and comparison with the reference SAb train in DTCs. Time-stepping analysis.

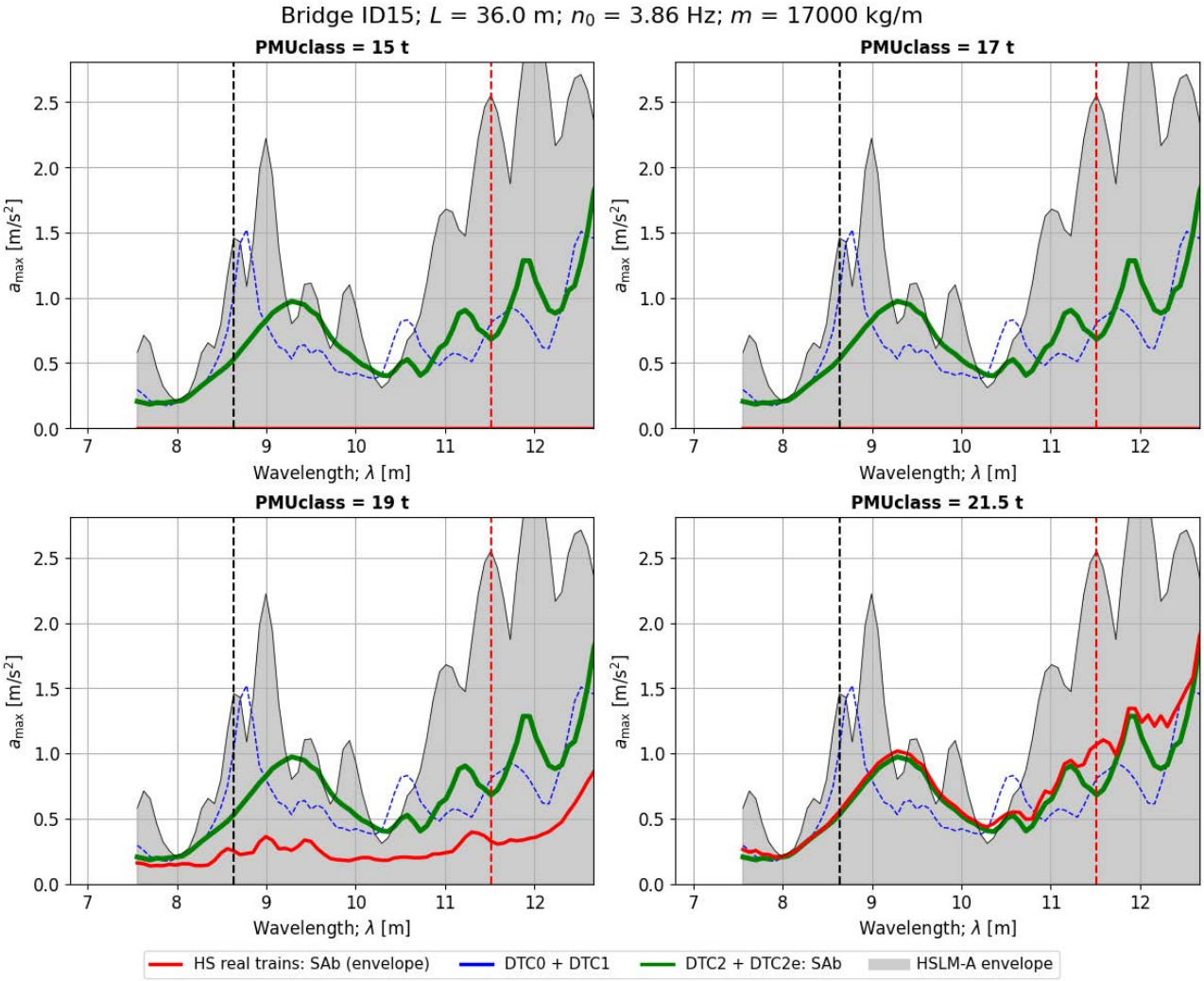

Figure 220. Peak vertical acceleration in the bridge ID15 when subject to real SAb trains of different weight categories, and comparison with the reference SAb train in DTCs. Time-stepping analysis.